

12

AD-A148 462

AFWAL-TR-84-1122

ION IMPLANTATION IN III-V COMPOUND SEMICONDUCTORS



UNIVERSAL ENERGY SYSTEMS, INC.

4401 DAYTON-XENIA ROAD

DAYTON, OH 45432

SEPTEMBER 1984

FINAL REPORT FOR PERIOD 1 AUG 80 - 31 DEC 83

APPROVED FOR PUBLIC RELEASE; DISTRIBUTED UNLIMITED.

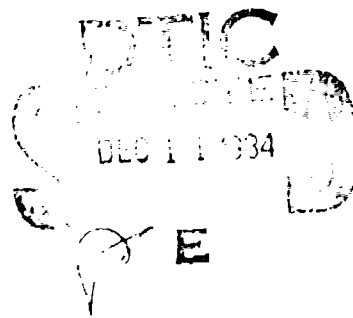
DTIC FILE COPY

AVIONICS LABORATORY

AIR FORCE WRIGHT AERONAUTICAL LABORATORIES

AIR FORCE SYSTEMS COMMAND

WRIGHT-PATTERSON AIR FORCE BASE, OH 45433



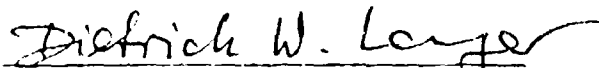
84 12 03 153

NOTICE

When Government drawings, specifications, or other data are used for any purpose other than in connection with a definitely related Government procurement operation, the United States Government thereby incurs no responsibility nor any obligation whatsoever; and the fact that the government may have formulated, furnished, or in any way supplied the said drawings, specifications, or other data, is not to be regarded by implication or otherwise as in any manner licensing the holder or any other person or corporation, or conveying any rights or permission to manufacture use, or sell any patented invention that may in any way be related thereto.

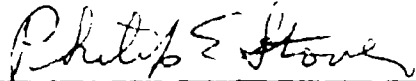
This report has been reviewed by the Office of Public Affairs (ASD/PA) and is releasable to the National Technical Information Service (NTIS). At NTIS, it will be available to the general public, including foreign nations.

This technical report has been reviewed and is approved for publication.



DIETRICH W. LANGER, Research Physicist
Electronic Research Branch
Avionics Laboratory

FOR THE COMMANDER



PHILIP E. STOVER, Chief
Electronic Research Branch
Avionics Laboratory

"If your address has changed, if you wish to be removed from our mailing list, or if the addressee is no longer employed by your organization please notify AFWAL/AADL, W-PAFB, OH 45433 to help us maintain a current mailing list".

Copies of this report should not be returned unless return is required by security considerations, contractual obligations, or notice on a specific document.

REPORT DOCUMENTATION PAGE		READ INSTRUCTIONS BEFORE COMPLETING FORM
1. REPORT NUMBER AFWAL-TR-84-1122	2. GOVT ACCESSION NO. 4D-A148462	3. RECIPIENT'S CATALOG NUMBER
4. TITLE (and Subtitle) ION IMPLANTATION IN III-V COMPOUND SEMICONDUCTORS		5. TYPE OF REPORT & PERIOD COVERED Final Technical Report 1 Aug 80 thru 31 Dec 83
		6. PERFORMING ORG. REPORT NUMBER
7. AUTHOR(s) Dr. Peter P. Pronko Dr. Y. K. Yeo Dr. R. S. Bhattacharya Dr. A. K. Rai		8. CONTRACT OR GRANT NUMBER(s) F33615-80-C-1108
9. PERFORMING ORGANIZATION NAME AND ADDRESS Universal Energy Systems, Inc. 4401 Dayton-Xenia Road Dayton, OH 45432		10. PROGRAM ELEMENT, PROJECT, TASK AREA & WORK UNIT NUMBERS 61102F JON: 2306R201 CCC: 656320
11. CONTROLLING OFFICE NAME AND ADDRESS Avionics Laboratories (AFWAL/AADR) Air Force Wright Aeronautics Laboratories (AFSC) WPAFB, OH 45433		12. REPORT DATE September 1984
		13. NUMBER OF PAGES 372
14. MONITORING AGENCY NAME & ADDRESS (if different from Controlling Office)		15. SECURITY CLASS. (of this report) Unclassified
		15a. DECLASSIFICATION/DOWNGRADING SCHEDULE N/A
16. DISTRIBUTION STATEMENT (of this Report) Approved for public release; distribution unlimited.		
17. DISTRIBUTION STATEMENT (of the abstract entered in Block 20, if different from Report)		
18. SUPPLEMENTARY NOTES		
19. KEY WORDS (Continue on reverse side if necessary and identify by block number) Ion Implantation, GaAs, Hall effect, electrical resistivity, Rutherford Backscattering (RBS), channeling, Proton induced x-ray excitation (PIXE), Transmission electron microscopy (TEM), Mg-implanted GaAs, Ge-implanted GaAs, Se-implanted GaAs, Si-implanted GaAs, S-implanted GaAs, Device isolation, Ohmic contacts		
20. ABSTRACT (Continue on reverse side if necessary and identify by block number) The goal of this program was to address the basic and applied problems associated with (a) ion implantation doping of GaAs, (b) device isolation by ion implantation in GaAs, and (c) Ohmic contact in GaAs. This report presents results of detailed investigation conducted by using various techniques. These results provide an understanding of the interactions of implanted ions with pre-implant impurities and nature of defects; the effect of various annealing procedures an activation		

efficiency, profile distribution, lattice incorporation, and residual damage. A clear indication of the importance of defect complexes in ion implanted GaAs has resulted from this work. Formation of high resistivity layers in n-type GaAs by oxygen implantation has been demonstrated. Systematic studies have been performed to compare surface morphologies, compound formation and diffusion behavior of Au, Au-Ge, and Au-Ge-Ni on GaAs.

Unclassified

PREFACE

This report was prepared by the Universal Energy Systems, Inc. (UES), Dayton, Ohio, under Air Force contract No. F33615-80-C-1108, Project 723 and covers research performed during the period 1 August 1980 through 31 December 1983. The work was performed utilizing the facilities in the Electronic Research Branch of the Air Force Wright Aeronautical Laboratories/Avionics Laboratory at Wright-Patterson Air Force Base, Ohio 45433. The UES program manager for this effort was Dr. Peter P. Pronko, during the period 1 August 1980 through 30 June 1983 and Dr. Y. K. Yeo during the period 1 July 1983 through 31 December 1983. The other UES staff members performing research under this effort were Dr. R. S. Bhattacharya, and Dr. A. K. Rai. Dr. Y. S. Park (AFWAL/AADR) was the Government contract monitor during the period 1 August 1983 through 31 August 1983, and Dr. D. Langer (AFWAL/AADR) was the Government contract monitor during the period 1 September 1983 through 31 December 1983. This report was submitted by the authors in January 1984.

Accession For	
DTIC GAA&I	<input checked="" type="checkbox"/>
DTIC TAB	<input type="checkbox"/>
Unannounced	<input type="checkbox"/>
Justification	
By	
Distribution/	
Availability Codes	
1/50	
1/50	
A-1	

TABLE OF CONTENTS

<u>SECTION</u>	<u>PAGE</u>
I INTRODUCTION	1
II MACHINE AND ASSOCIATED APPARATUS	3
2.1 Ion Machine	3
2.2 Encapsulation	4
2.3 Automated Hall-Effect/Sheet-Resistivity Measurement System	16
2.4 Rutherford Backscattering Analysis System	20
2.5 Electron Microscope	22
III ELECTRICAL PROPERTIES AND DISTRIBUTION OF ION IMPLANTS IN GaAs	25
3.1 Sample Preparation	25
3.2 Electrical Measurements	26
3.3 Mg-Implanted GaAs	29
3.4 Ge-Implanted GaAs	64
3.5 S-Implanted GaAs	83
3.6 Si-Implanted GaAs	112
IV DEFECT STUDIES OF ION-IMPLANTED GaAs	136
4.1 Sample Preparation	136
4.2 Procedures for Defect Analysis	136
4.3 Se-Implanted GaAs - Low Temperature Studies	143
4.4 Si-Implanted GaAs - Damage and Lattice Location	199
4.5 S Implantation in GaAs	253
4.6 Cr Implantation in GaAs	270
4.7 Ar Implantation in GaAs	287
V DEVICE ISOLATION STUDY	301
5.1 Device Isolation By Ion Implantation In GaAs; O ⁺ and H ⁺ Implantation in GaAs	302
5.2 Electrical Measurements of Si- and O- Implanted GaAs	318

TABLE OF CONTENTS (CONCONLUDED)

VI	OHMIC CONTACT STUDY	324
6.1	Au/GaAs	325
6.2	Au-Ge/GaAs	330
6.3	Au-G-Ni/GaAs	334
	REFERENCES	344

LIST OF ILLUSTRATIONS

<u>FIGURE</u>		<u>PAGE</u>
1	Si ₃ N ₄ Pyrolytic Deposition System	6
2	Cold-Wall Reactor for Pyrolytic Deposition of Si ₃ N ₄	9
3	Si ₃ N ₄ Plasma-Enhanced Deposition System	11
4	Plasma-Enhanced Deposition System Reactor Chamber with Small Shower Ring and Shutter Assembly	12
5	Plasma-Enhanced Deposition System Reactor Chamber with Large Shower Ring	14
6	Block Diagram of Automated Hall-Effect/Sheet-Resistivity Measurement System	17
7	Schematic Diagram of the Apparatus Used for PIXE and RBS-C Analysis Using 400 keV van de Graaff	21
8	Schematic Diagram of the Experimental Set Up at Oak Ridge National Laboratory	23
9	Schematic Ray Diagram for Producing an (a) Electron-Optical Image, (b) Diffraction Pattern	23
10	Schematic Diagram of the Hall-Measurement System for the van der Pauw Configuration	27
11	Dependence of Surface-Carrier Concentration (N_s) and Hall Mobility (μ_H) upon Annealing Temperature (T_A) for GaAs:Mg Samples with PED Si ₃ N ₄ Cap	31
12	Dependence of Surface-Carrier Concentration (N_s) and Hall Mobility (μ_H) upon Ion Dose (ϕ) for GaAs:Mg Samples with PED Si ₃ N ₄ Cap	32
13	Dependence of Surface-Carrier Concentration (N_s) and Hall Mobility (μ_H) upon Annealing Temperature (T_A) for $1 \times 10^{13}/\text{cm}^2$ Dose Samples of GaAs:Mg with Three Different Capping Methods	33
14	Dependence of Surface-Carrier Concentration (N_s) and Hall Mobility (μ_H) upon Annealing Temperature (T_A) for $3 \times 10^{14}/\text{cm}^2$ Dose Samples of GaAs:Mg with Three Different Capping Methods	34

LIST OF ILLUSTRATIONS (CONTINUED)

<u>FIGURE</u>		<u>PAGE</u>
15	Dependence of Surface-Carrier Concentration (N_S) and Hall Mobility (μ_H) upon Annealing Temperature (TA) for $1 \times 10^{15}/\text{cm}^2$ Dose Samples of GaAs:Mg with Three Different Capping Methods	35
16	Dependence of Surface-Carrier Concentration (N_S) and Hall Mobility (μ_H) upon Annealing Time for GaAs:Mg Samples with Capless Annealing at 750°C	38
17	Dependence of Electrical Depth Profile upon Capping Method for GaAs:Mg Samples having a Dose of $3 \times 10^{14}/\text{cm}^2$	39
18	Dependence of Electrical Depth Profile upon Capping Method for GaAs:Mg samples having a Dose of $1 \times 10^{15}/\text{cm}^2$	40
19	Dependence of Electrical Depth Profile upon Capping Method for GaAs:Mg Samples having a Dose of $3 \times 10^{15}/\text{cm}^2$	41
20	Dependence of Electrical Depth Profile upon Capping Method for Lower-Dose GaAs:Mg Samples	45
21	Dependence of Electrical Depth Profile upon Annealing Time for GaAs:Mg Samples with PED Si_3N_4 Cap	46
22	SIMS Atomic Profiles of As-Implanted GaAs:Mg Samples	49
23	SIMS Atomic and Electrical Carrier Profiles of $1 \times 10^{13}/\text{cm}^2$ Dose GaAs:Mg Samples with PED Si_3N_4 Cap	52
24	SIMS Atomic and Electrical Carrier Profiles of $1 \times 10^{13}/\text{cm}^2$ Dose GaAs:Mg Samples Annealed Using a Close-Contact-Capless Method	53
25	SIMS Atomic and Electrical Carrier Profiles of $1 \times 10^{14}/\text{cm}^2$ Dose GaAs:Mg Samples with PED Si_3N_4 Cap	55
26	SIMS Atomic and Electrical Carrier Profiles of $1 \times 10^{14}/\text{cm}^2$ Dose GaAs:Mg Samples Annealed Using a Close-Contact-Capless Method	56
27	SIMS Atomic and Electrical Carrier Profiles of $1 \times 10^{15}/\text{cm}^2$ Dose GaAs:Mg Samples with PED Si_3N_4 Cap	57

LIST OF ILLUSTRATIONS (CONTINUED)

<u>FIGURE</u>		<u>PAGE</u>
28	SIMS Atomic and Electrical Carrier Profiles of $3 \times 10^{15}/\text{cm}^2$ Dose GaAs:Mg Samples Annealed Using a Close-Contact-Capless Method	59
29	SIMS Atomic and Electrical Carrier Profiles of GaAs:S Samples Annealed at 900°C with CVD Cap	61
30	Dependence of Surface-Carrier Concentration (N_S) And Hall Mobility (μ_H) upon Annealing Temperature (T_A) for GaAs:Ge	67
31	Dependence of Surface-Carrier Concentration (N_S) and Hall Mobility (μ_H) upon Annealing Temperature (T_A) for an $1 \times 10^{13}/\text{cm}^2$ Dose of Single Ge, Dual (Ge + Ga) and (Ge + As) Implants in GaAs	70
32	Dependence of Surface-Carrier Concentration (N_S) and Hall Mobility (μ_H) upon Annealing Temperature (T_A) for a $3 \times 10^{13}/\text{cm}^2$ Dose of Single Ge, Dual (Ge + Ga) and (Ge + As) Implants in GaAs	71
33	Dependence of Surface-Carrier Concentration (N_S) and Hall Mobility (μ_H) upon Annealing Temperature (T_A) for a $1 \times 10^{14}/\text{cm}^2$ Dose of Single G, Dual (Ge + Ga) and (Ge + As) Implants in GaAs	73
34	Dependence of Surface-Carrier Concentration (N_S) and Hall Mobility (μ_H) upon Annealing Temperature (T_A) for a $3 \times 10^{14}/\text{cm}^2$ Dose of Single Ge, Dual (Ge + Ga) and (Ge + As) Implants in GaAs	75
35	Dependence of Surface-Carrier Concentration (N_S) and Hall Mobility (μ_H) upon Annealing Temperature (T_A) for an $1 \times 10^{15}/\text{cm}^2$ Dose of Single Ge, Dual (Ge + Ga) and (Ge + As) Implants in GaAs	76
36	Dependence of Surface-Carrier Concentration (N_S) and Hall Mobility (μ_H) upon Annealing Temperature (T_A) for a $3 \times 10^{15}/\text{cm}^2$ Dose of Single Ge, Dual (Ge + Ga) and (Ge + As) Implants in GaAs	77
37	Electrical Carrier Profiles of GaAs:Ge Samples	79
38	Dependence of Surface-Carrier Concentration (N_S) and Hall Mobility (μ_H) upon Annealing Temperature (T_A) for GaAs:S	86
39	Dependence of Surface-Carrier Concentration (N_S) and Hall Mobility (μ_H) upon Ion Dose (ϕ) for 120 keV GaAs:S	87

LIST OF ILLUSTRATIONS (CONTINUED)

<u>FIGURE</u>		<u>PAGE</u>
40	Dependence of Surface-Carrier Concentration (N_S) Hall Mobility (μ_H) upon Ion Energy for GaAs:S	88
41	Dependence of Surface-Carrier Concentration (N_S) Hall Mobility (μ_H) upon Ion Dose for 120 and 300 keV GaAs:S	90
42	Electrical Carrier Profiles of 120 keV GaAs:S Samples Annealed at 900°C	94
43	Electrical Carrier Profiles of $1 \times 10^{14}/\text{cm}^2$ Dose GaAs:S Samples Implanted at 120 keV and Annealed at Three Different Temperatures	97
44	Electrical Carrier Profiles of 120 keV GaAs:S Samples with CVD and PED Caps	98
45	Electrical Carrier Profiles of $4 \times 10^{13}/\text{cm}^2$ Dose GaAs:S Samples Implanted at Three Lower Ion Energies	100
46	Electrical Carrier Profiles of $4 \times 10^{13}/\text{cm}^2$ Dose GaAs:S Samples Implanted at Three Higher Ion Energies	101
47	Electrical Carrier Profiles of 300 keV GaAs:S Samples Annealed at 900°C	104
48	SIMS Atomic and Electrical Carrier Profiles of $1 \times 10^{13}/\text{cm}^2$ Dose GaAs:S	106
49	SIMS Atomic and Electrical Carrier Profiles of $1 \times 10^{14}/\text{cm}^2$ Dose GaAs:S	107
50	SIMS Atomic and Electrical Carrier Profiles of $1 \times 10^{15}/\text{cm}^2$ Dose GaAs:S	108
51	Dependence of Surface-Carrier Concentration (N_S) and Hall Mobility (μ_H) upon Annealing Temperature (T_A) for Si-Implanted Cr-doped GaAs	114
52	Dependence of Surface-Carrier Concentration (N_S) and Hall Mobility (μ_H) upon Annealing Temperature (T_A) for Si-Implanted Undoped GaAs	115
53	Dependence of Surface-Carrier Concentration (N_S) and Hall Mobility (μ_H) upon Annealing Temperature (T_A) for Low-Dose Si-Implanted Cr-doped GaAs	117

LIST OF ILLUSTRATIONS (CONTINUED)

<u>FIGURE</u>		<u>PAGE</u>
54	Dependence of Surface-Carrier Concentration (N_S) and Hall Mobility (μ_H) upon Ion Dose for 100 keV Si-Implanted Cr-doped GaAs	118
55	Dependence of Surface-Carrier Concentration (N_S) and Hall Mobility (μ_H) upon Annealing Temperature (T_A) for Low-Dose Si-Implanted Undoped GaA	120
56	Surface-Carrier Concentration (N_S) versus Ion Dose for Two Different GaAs Substrates Implanted with Si	122
57	Surface-Carrier Concentration (N_S) and Hall Mobility (μ_H) versus Ion Energy for Si-Implanted Undoped GaAs	123
58	Electrical Carrier Profiles of Three Lower Si-Dose Cr-Doped GaAs	124
59	Electrical Carrier Profiles of Three Higher Si-Dose Cr-Doped GaAs	126
60	Electrical Carrier Profiles of Three Lower Si-Dose Undoped GaAs	127
61	Electrical Carrier Profiles of Three Higher Si-Dose Undoped GaAs	129
62	Electrical Carrier Profiles of Two Different GaAs Substrates Implanted with Si	130
63	Dependence of Electrical Depth Profile upon Annealing Temperature for Si-Implanted Cr-Doped GaAs	132
64	Dependence of Electrical Depth Profile upon Annealing Temperature for Si-Implanted Undoped GaAs	133
65	Cross Sectional TEM Specimen Preparation	137
66	Schematic Ray Diagram Illustrating the Mechanism of Diffraction Contrast	137
67	Backscattering of Ion from Solid Target	137
68	Ion Scattering from Defects: (a) Channeling in a Perfect Crystal, (b) Dechanneling by Defects, (c) Direct Scattering from Amorphous Layer	141
69	Angular Scan Profiles for Different Projections of a Solute Atom in an Axial Channel	144

LIST OF ILLUSTRATIONS (CONTINUED)

<u>FIGURE</u>		<u>PAGE</u>
70	Channeling Spectra Before and After Annealing at 200°, GaAs:Se ⁺ , 10 ¹³ cm ⁻²	147
71	Channeling Spectra Before and After Annealing at 200, 250, and 300°C, GaAs:Se ⁺ , 1 X 10 ¹³ cm ⁻²	148
72	Channeling Spectra Before and After Annealing at 200°C, GaAs:Se ⁺ 3 X 10 ¹³ cm ⁻²	149
73	Channeling Spectra for GaAs:Se ⁺ , 3 X 10 ¹³ cm ⁻² Before and After Annealing at 200-500°C	151
74	Channeling Spectra for GaAs:Se ⁺ , 7 X 10 ¹³ cm ⁻² , Before and After Annealing at 200°C	152
75	Channeling Spectra for GaAs:Se ⁺ , 7 X 10 ¹³ cm ⁻² , Before and After Annealing at 200-600°C	153
76	Channeling Spectra for GaAs:Se ⁺ , 1 X 10 ¹⁴ cm ⁻² , Before and After Annealing at 200°C	154
77	Channeling Spectra for GaAs:Se ⁺ , 1 X 10 ¹⁴ cm ⁻² , Before and After Annealing at 200-600°C	155
78	Bright-Field Micrograph of GaAs:Se ⁺ , 1 X 10 ¹³ cm ⁻² , After Annealing at 200°C for 90 min (g=220, S ₀₁)	158
79	Bright-Field Micrographs of GaAs:Se ⁺ Annealed at 200°C for 90 min: (a) 3 X 10 ¹³ cm ⁻² , (b) 7 X 10 ¹³ cm ⁻² , g=220	158
80	(a) TED Pattern and (b) X-Section Micrograph of GaAs:Se, 1 X 10 ¹⁴ cm ⁻² , Annealed at 200°C, 90 min	159
81	Bright-Field Micrographs of GaAs:Se ⁺ , (a) 3 X 10 ¹³ cm ⁻² Annealed at 500°C, 30 min, (b) 7 X 10 ¹³ cm ⁻² Annealed at 600°C, 30 min (g=220, S ₀₀)	160
82	(a) TED Pattern, (b) Bright-Field Plan View Micrograph (g=220, S ₀₀) and (c) Weak Beam Dark Field Micrograph of GaAs:Se ⁺ , 1 X 10 ¹⁴ cm ⁻² Annealed at 600°C, 30 min	162
83	TED Pattern of GaAs:Se ⁺ , 5 X 10 ¹³ cm ⁻² Annealed at 200°C, 30 min, (a) Exact <001> Orientation, (b) Slightly Tilted from <001> and (c) <114> Orientation	163

LIST OF ILLUSTRATIONS (CONTINUED)

<u>FIGURE</u>		<u>PAGE</u>
84	Bright-Field Micrograph of GaAs:Se ⁺ , $5 \times 10^{13} \text{cm}^{-2}$ Annealed at 400°C, 15 min (g=220, S_{\perp})	164
85	Dark-Field Micrographs of GaAs:Se ⁺ , $1 \times 10^{14} \text{cm}^{-2}$ Annealed at 200°C, 30 min	164
86	Channeling spectra for GaAs:Se ⁺ , $1 \times 10^{14} \text{cm}^{-2}$ Before and After Annealing at 200°C	167
87	Channeling Spectra for GaAs:Se ⁺ , $5 \times 10^{13} \text{cm}^{-2}$ Before and After Annealing at 200°C	168
88	Channeling Spectra for GaAs:Se ⁺ , $1 \times 10^{14} \text{cm}^{-2}$ Before and After Annealing at 250°C	170
89	Channeling Spectra For GaAs:Se ⁺ , $1 \times 10^{14} \text{cm}^{-2}$ Before and After Annealing at 300 and 400°C	171
90	Channeling Spectra for GaAs:Se After Various Annealing Steps	172
91	Channeling Spectra for GaAs:Se ⁺ , As ⁺ Before and After Annealing at 400°C	174
92	Dose Dependence of Residual Disorder After Annealing at 400°C	175
93	Area under the Disorder Peak of Se-Implanted GaAs Annealed at 400°C for 30 min Plotted Against the Thickness of the Amorphous Layer Produced by Ion Implantation. The Smaller Size Symbols With Numbers Are from Reference. They Are: (1) Average of As ⁺ As ₂ ⁺ 60-keV $1 \times 10^{14} \text{cm}^{-2}$ RT and Ln ₂ T, (2) 120-keV As ₂ ⁺ , $1 \times 10^{15} \text{cm}^{-2}$, (3) 120-keV As ₂ ⁺ , $5 \times 10^{14} \text{cm}^{-2}$, (4) 120-keV As ₂ ⁺ , $1 \times 10^{14} \text{cm}^{-2}$, (5) 100-keV Ar ⁺ , $1 \times 10^{14} \text{cm}^{-2}$, (6) 80-keV Si ⁺ , $1 \times 10^{15} \text{cm}^{-2}$, (7) 180-keV As ⁺ , $1 \times 10^{14} \text{cm}^{-2}$, (8) 80-keV S ⁺ , $1 \times 10^{15} \text{cm}^{-2}$, (9) 80-keV Si ⁺ , $1 \times 10^{16} \text{cm}^{-2}$. Open and Full Symbols Refer to Rt and Ln ₂ T Implantations Respectively	178
94	Normalized Area of Damage Peak Plotted as a Function of Anneal Temperature: Annealing Time was 30 min	157
95	Backscattering Spectra from Aligned and Randomly Oriented GaAs:Se ⁺ for Various Doses of Se ⁺	185

LIST OF ILLUSTRATIONS (CONTINUED)

<u>FIGURE</u>		<u>PAGE</u>
96	Dependence of the Number of Displaced Ga and As Atoms/cm ² as a Function of Se ⁺ Dose	187
97	Comparasion of Experimental and Calculated Damage Profile for GaAs:Se ⁺ (120 keV)	190
98	Backscattering Spectra from Aligned and Randomly Oriented Virgin and Annealed Samples	191
99	Dependence of Dechanneled Fraction on Depth for Annealed Samples Implanted with Various Doses of Se	193
100	TEM Bright Field Micrographs of Samples Implanted with 120 keV Se ⁺ Ions at RT to a Dose of (a) 10 ¹³ cm ⁻² , and (b) 10 ¹⁴ cm ⁻² , Annealed at 900° for 15 min	194
101	TEM Bright Field Micrographs of Sample Implanted with 120-keV Se ⁺ Ions at RT to a Dose of 3 X 10 ¹⁴ cm ⁻² (a) g=220 and (b) g=220, Annealed at 900°C for 15 min	195
102	Surface Carrier Concentrations (N ₃) and Mobility (M _H) as a Function of Anneal Temperature for GaAs:Se	196
103	Carrier Concentration (N) and Mobility (M _H) Profile as a Function of Anneal Temperature for GaAs:Se	198
104	Backscattering Spectra of GaAs:Si (50 and 120 keV, 1 X 10 ¹⁵ cm ⁻²)	200
105	Transmission Electron Diffraction and Micrographs of Specimen #1 (a) TED Pattern After Annealing at 250°C for 15 minutes, (b) Dark Field Micrograph Imaged with twin spot After Annealing at 250°C for 15 minutes, (c) Dark Field Micrograph Imaged With Twin Spot After Annealing at 400°C for 15 minutes (d) and (e) Strong Beam Bright Field, and Dark Field Micrograph, Respectively Imaged With Twin Spot After Annealing at 500°C for 15 min	201
106	Transmission Electron Diffraction and Micrographs of Specimen #2 (a) TED Pattern, After Annealing at 250°C for 15 minutes, (b) Dark Field Micrograph Imaged with Twin Spot After Annealing at 400°C for 15 Minutes, (c) Dark Field Micrograph Imaged with Twin Spot After Annealing at 500°C for 15 minutes (d) Dark Field Micrograph Imaged With Twin Spot After Annealing at 600°C for 90 Minutes and (e) Strong Beam Bright Field Micrograph After Annealing at 700°C for 15 Minutes	203
107	Backscattering Spectra of GaAs:Si (1 X 10 ¹⁵ cm ⁻²) After Annealing at 250°C for 15 min	204

LIST OF ILLUSTRATIONS (CONTINUED)

FIGURE	PAGE
108 Backscattering Spectra of GaAs:Si ($1 \times 10^{15} \text{cm}^{-2}$) After Annealing at 400°C for 15 min	205
109 Backscattering Energy Spectra of 340 keV H^+ Recorded With (a) $\langle 100 \rangle$ Incidence for (100) GaAs Implanted With 60-keV Si^+ to a Dose of $1 \times 10^{15} \text{cm}^{-2}$; _____ as implanted; \square 200+250; \triangle 200+250+300; \blacksquare 350+400+450+500; \bullet 350+...+550+900 $^\circ\text{C}$, This is Same as Virgin (100) GaAs. (b) $\langle 211 \rangle$ Incidence for (211) GaAs; Implantation Parameters same as in (a); _____ as Implanted; \square 200+250+300; \triangle 350+400+450+550; \blacksquare 350+...+550+900 $^\circ\text{C}$; \bullet virgin (211) GaAs	(a) 209 (b) 210
110 Minimum Yield (X_{\min}) Versus the Anneal Temperatures for GaAs:Si $^+$	211
111 Bright-Field Micrographs with $g=220$ After Annealing at 350°C for 30 min (a) (100); (b) (211)	213
112 TED Pattern of (211) Specimen After Annealing at 350°C for 30 min in $\langle 114 \rangle$ Orientation. Dark-Field Micrographs Imaged With Twin Spots (b) (100); (c) (211)	214
113 Bright-Field Micrographs With $g=220$ After Further Annealing at 500°C for 30 min (a) (100); (b) (211)	215
114 Dark-Field Micrographs After Annealing at 500°C for 30 min, Imaged With the Twin Spots (a) (100); (b) (211)	215
115 Backscattering Spectra for GaAs:Si $^+$	220
116 Bright Field Transmission Electron Micrographs of 120 keV Si^+ , $3 \times 10^{15} \text{cm}^{-2}$, Annealed at 850°C for 15 min; (a) $g=(220)$; (b) $g=(220)$. P-Precipate, LD-Line dislocation, DL-D'slocaton loop	221
117 High resolution weak beam image of GaAs:Si (120 keV , $3 \times 10^{15} \text{cm}^{-2}$) annealed at 850°C , 15 min	221
118 Characteristic X-ray spectra for 330 keV H^+ on GaAs:Si $^+$	223
119 (a) $\langle 110 \rangle$ and (b) $\langle 100 \rangle$ Channeling Dips for GaAs:Si Annealed at 850°C	224
120 (a) $\langle 110 \rangle$ and (b) $\langle 100 \rangle$ Channeling Dips for GaAs:Si Annealed at 950°C	(a) 225 (b) 226
121 Backscattering spectra for GaAs:Si $^+(5 \times 10^{15} \text{cm}^{-2})$	227

LIST OF ILLUSTRATIONS (CONTINUED)

<u>FIGURE</u>		<u>PAGE</u>
122	(a) TED Pattern in $\langle 114 \rangle$ orientation, GaAs:Si ⁺ , 5 X 10 ¹⁵ cm ⁻² 850°C, 15 min, (b) and (c) are the Bright and Dark Field Micrographs Respectively	229
123	(a) $\langle 110 \rangle$ and (b) $\langle 100 \rangle$ Channeling Dips for GaAs:Si Annealed at 850°C	(a) 230 (b) 231
124	Bright Field Micrograph of 120 keV Si ⁺ , 5 X 10 ¹⁵ cm ⁻² , 950°C for 15 min	232
125	(a) $\langle 110 \rangle$ and (b) $\langle 100 \rangle$ Channeling Dips for GaAs:Si ⁺ , 5 X 10 ¹⁵ cm ⁻² , 950°C	(a) 233 234
126	Backscattering Spectra for GaAs:Si, 5 X 10 ¹⁵ cm ⁻²	235
127	Bright Field Micrographs of Sample 3 After Annealing at 850°C for 15 min	237
128	$\langle 110 \rangle$ Axial and $\langle 110 \rangle$ Planar Channeling Spectra for GaAs:Si ⁺ , 5 X 10 ¹⁵ cm ⁻²	238
129	Depth Distribution of Disorder of Sample 3 after 850°C Annealing for 15 min	240
130	Weak Beam Dark Field Micrograph of Sample 3, After Annealing at 950°C for 15 min	241
131	(a) $\langle 110 \rangle$ and (b) $\langle 100 \rangle$ Channeling Dips For GaAs:Si ⁺ , 5 X 10 ¹⁵ cm ⁻² , 850°C	242
132	(a) $\langle 110 \rangle$ and (b) $\langle 100 \rangle$ Channeling Dips of Sample 3, Annealed at 950°C	242
133	Positions of Ga and As Atoms in the $[110]$ Plane of the GaAs	243
134	Channeling Spectrum of GaP	245
135	$\langle 110 \rangle$ Channeling Dip of GaP (RBS)	246
136	Characteristic X-ray Spectrum of GaP	247
137	$\langle 110 \rangle$ Channeling Dip of GaP (RBS and PIXE)	248
138	$\langle 110 \rangle$ Channeling Dip of GaAs:Si (5 X 10 ¹⁵ cm ⁻²) Annealed at 950°C	250
139	Depth Profiles of Carrier Concentration (N) and Mobility (M _H) for GaAs:Si ⁺	252

LIST OF ILLUSTRATIONS (CONTINUED)

FIGURE	PAGE
140 Backscattering Spectrum for GaAs:S ⁺ , $1 \times 10^{15} \text{cm}^{-2}$	254
141 TEM Micrographs of Samples Implanted with 120 keV S ⁺ Ions to Doses of (a) $1 \times 10^{15} \text{cm}^{-2}$, Bright Field and (b) $3 \times 10^{15} \text{cm}^{-2}$, Weak Beam Dark Field. The Samples Were Annealed at 800°C for 15 min	256
142 Characteristic X-ray Spectra for GaAs:S ⁺ ($3 \times 10^{15} \text{cm}^{-2}$) Random and Channeled	257
143 (A) <110>, (b) <100> Channeling Dips of GaAs:S ⁺ ($3 \times 10^{15} \text{cm}^{-2}$, 800°C	(a) 258 (b) 259
144 (a) <110>, and (b) <100> Channeling Dips of GaAs:S ⁺ ($3 \times 10^{15} \text{cm}^{-2}$), 800°C	(a) 261 (b) 262
145 (a)<110> (b) <100> Channeling Dips of GaAs:S ⁺ ($3 \times 10^{15} \text{cm}^{-2}$), 900°C	(a) 264 (b) 265
146 <110>Channeling Dip Scanned Parallel to (110) Plane	266
147 Characteristic X-ray Spectra of GaAs With and Without Collimator	272
148 Characteristic X-ray Spectra of GaAs:Cr ⁺ ($5 \times 10^{16} \text{cm}^{-2}$)	274
149 PIXE Calibration Curve for GaAs:Cr ⁺	276
150 Channeling Spectra for GaAs:Cr ⁺ Annealed at 900°C, 15 min	277
151 Electron Micrographs from Specimen Implanted with Chromium to a Dose of $5 \times 10^{16} \text{cm}^{-2}$ and Annealed at 900°C for 15 min (a) Bright Field; (b) Dark Field; and (c) Diffraction Pattern	279
152 Combined RBS-PIXE Channeling Angular Scans for Specimen Implanted with $5 \times 10^{16} \text{Cr/cm}^2$ and Annealed at 900°C for 15 min	280
153 Electron Micrographs for Specimen Implanted With Chromium to a Dose of $5 \times 10^{15} \text{cm}^{-2}$ and Annealed at 900°C for 15 min (a) Bright Field; (b) Weak Beam Dark Field; and (c) Standard Dark Field	282
154 Combined RBS-PIXE Channeling Angular Scans for Specimen of Figure 153 Implanted with $5 \times 10^{15} \text{Cr/cm}^2$ and Annealed at 900°C for 15 min	284

LIST OF ILLUSTRATIONS (CONTINUED)

FIGURE	PAGE
155 Electron Micrographs from Specimen Implanted with Chromium to a Dose of $1 \times 10^{15} \text{cm}^{-2}$, (a) Weak Beam Dark Field; (b) Bright Field Dynamical $S=0$ Condition; and (c) Bright-Field Kinematical $S=1$ Condition	285
156 Bright-Field Micrographs from Specimen Implanted With Chromium to a Dose of $5 \times 10^{14} \text{cm}^{-2}$	285
157 (a) TED Pattern of $\langle 001 \rangle$ Orientation of Ar^+ Implanted GaAs (700 keV, $5 \times 10^{15} \text{cm}^{-2}$). Strong Beam Bright Field Micrographs ($g=220$); (b) As implanted; (c) Annealed at 200°C for 30 min	289
158 (a) TED Pattern in $\langle 114 \rangle$ Orientation of Ar^+ Implanted GaAs (700 keV, $5 \times 10^{15} \text{cm}^{-2}$) After Annealing at 400°C for 30 min. Strong Beam Bright Field Micrographs ($g=220$); (b) Annealed at 400°C for 30 min; (c) Annealed at 600°C for 30 min	290
159 Dark Field Micrographs of Ar^+ Implanted GaAs (700 keV, $5 \times 10^{15} \text{cm}^{-2}$) Imaged with the Twin Spots. (a) Annealed at 400°C for 30 min; (b) Annealed at 600°C for 30 min	291
160 Channeling Spectrum of GaAs: Ar^+	293
161 Strong Beam Bright Field Micrographs of the Ar^+ Implanted GaAs Specimen After Annealing at 850°C for 15 min. (a) Close to the Surface, in Focus; (b) Same as (a), But Slightly Underfocus; (c) Slightly Inside Implanted Layer; (d) Further Inside the Implanted Layer	294
162 Weak Beam Dark-Field Micrograph of GaAs: Ar^+ After Annealing at 850°C , 15 min	296
163 Characteristic X-ray spectra for GaAs: Ar^+	297
164 $\langle 110 \rangle$ Angular Half Scan of GaAs: Ar^+ (700 keV, $5 \times 10^{15} \text{cm}^{-2}$, 850°C , 15 min)	298
165 $\langle 100 \rangle$ Channeling Spectra of GaAs: O^+ (80 keV)	303
166 $\langle 110 \rangle$ Channeling Spectra of GaAs: O^+ (80 keV)	304
167 $\langle 100 \rangle$ Channeling Spectra of GaAs: O^+ (350 keV)	306
168 $\langle 100 \rangle$ Channeling Spectra of GaAs: O^+ (350 keV) annealed at $700^\circ\text{C}/15 \text{ min}$	307

LIST OF ILLUSTRATIONS (CONTINUED)

<u>FIGURE</u>		<u>PAGE</u>
169	Strong Beam Bright Field Micrograph with $g=220$ for 80 keV O^+ Implanted to $5 \times 10^{15} \text{cm}^{-2}$ and Annealed at 700°C for 15 min	308
170	(a) $\langle 100 \rangle$ and (b) $\langle 110 \rangle$ Channeling Spectra of GaAs Before and After Proton Bombardment	(a) 310 (b) 311
171	Minimum Yield X Behind the Surface Peak ($\sim 1000 \text{ \AA}$) Versus Dose of 330 keV H^+	313
172	PIXE Spectra of GaAs in $\langle 110 \rangle$ Direction	315
173	X-ray Minimum Yield as a Function of 330 keV H^+ Dose. The Percentage of Non-Substitutional Atoms (f_{ns}) are Given on the Right Hand Scale	317
174	Sheet Resistivity Versus Annealing Temperature for the 100 keV Si-Implanted GaAs Samples Bombarded With 57 keV Oxygen Ions	320
175	Sheet Resistivity Versus Annealing Temperature for the 200 keV Si-Implanted GaAs Samples Bombarded with 113 keV Oxygen Ions	321
176	SEM Micrographs of Au/GaAs (a) and (b) annealed at 350°C for 15 minutes; (c) and (d) annealed at 425°C for 0.5 minutes	326
177	SEM micrographs of Au/GaAs after annealing at 450°C for 15 minutes (a) Mag. X2k; (b) Mag. X5k	327
178	TED pattern of Au/GaAs (a) annealed at 350°C for 15 minutes; (b) annealed at 425°C for 0.5 minutes; (c) annealed at 450°C for 15 minutes; (d) Bright-field micrograph after annealing at 450°C for 15 minutes	328
179	Rutherford backscattering spectra of He ions from AuGaAs system before and after annealing at 350°C for 15 minutes and 450°C for 15 minutes	329
180	Rutherford backscattering spectra of He ions from Au/GaAs, Au-Ge/GaAs and Au-Ge-Ni/GaAs systems after annealing at 425°C for 15 minutes	331
181	SEM micrographs of Au-Ge/GaAs system (a) annealed at 350°C for 15 minutes; (b) annealed at 425°C for 0.5 minutes; (c) annealed at 450°C for 15 minutes	332

LIST OF ILLUSTRATIONS (CONCLUDED)

<u>FIGURE</u>		<u>PAGE</u>
182	TED pattern of the Au-Ge/GaAs system (a) as deposited; (b) annealed at 350°C for 15 minutes; (c) annealed at 425°C for 0.5 minutes; (d) annealed at 450°C for 15 minutes; (e) Bright and (f) dark-field micrographs after annealing at 450°C for 15 minutes	333
183	Rutherford backscattering spectra of He ions from Au-Ge/GaAs system before and after annealing at 350°C for 15 minutes and 450°C for 15 minutes	335
184	SEM micrographs of Au-Ge-Ni/GaAs system (a) and (b) after annealing at 350°C for 15 minutes; (c) and (d) after annealing at 425°C for 0.5 minutes	336
185	SEM micrographs of Au-Ge-Ni/GaAs system after annealing at 450°C for 15 minutes (a) Mag. X1k (b) Mag. X2k	337
186	(a) Bright field micrograph and (b) TED pattern of the Au-Ge-NiGaAs system after annealing at 350°C for 15 minutes; (c) TED pattern of Au-Ge-Ni/GaAs system after annealing at 450°C for 15 minutes	339
187	(a) Rutherford backscattering spectra of He ions from Au-Ge-Ni/GaAs system after annealing at 350°C for 15 minutes and 450°C for 15 minutes	340
188	(a,b) Rutherford backscattering spectra of He ions from Au-Ge-Ni/GaAs system before and after annealing at 425°C for 0.5 minutes	(a) 341 (b) 342

LIST OF TABLES

TABLE		PAGE
1	Equipment Identification of Automated Hall-Effect/ Sheet-Resistivity Measurement System	18
2	Four Moments Used in the Type-IV Pearson Distributions to Fit SIMS As-Implanted Profiles of Mg Implants in GaAs Implanted at 120 keV for Different Ion Doses	50
3	Summary of the Results of Single Ge and Dual Implantation of (Ge + Ga) and (Ge + As) into Semi-insulating Cr-doped GaAs	81
4	Dependence of Electrical Activation Efficiency upon Ion Energy for a Dose of $4 \times 10^{13}/\text{cm}^2$ and the Equivalent Dose Producing the same LSS peak concentration at the Energy of 130 keV for GaAs=S.	92
5	Implantation Parameters Used to Prepare the Samples for High Temperature Annealing of Si	218
6	Surface Carrier Concentration and Hall Mobility of 120 keV S^+ Implanted Samples	268

SECTION I

INTRODUCTION

The goal of this research program was to address the basic and applied problems associated with ion implantation doping of III - V compound semiconductors. The objectives identified to achieve this goal were to (1) characterize ion implanted III - V compound semiconductors, (2) optimize and achieve reproducibility in the process, and (3) explore the limits of ion implantation as a process for device fabrication. The implanted layers were to be characterized by as many methods as possible in order to establish doping profiles, damage parameters, and electrical properties. This work was pursued, since progress in the application of ion implantation to GaAs device technology has been impeded by difficulties in annealing the implantation damage and in activating the implanted species. Therefore, a need was recognized to investigate annealing processes and the interaction of implanted ions with defects and substrate impurities. This is a particularly acute problem for device applications involving n-active layers and high-conductivity n^+ layers for electronic and optical devices. A need was also recognized to investigate ion implantation as a way to produce electrically isolated regions in device structures.

In order to pursue these goals and objectives, efforts were made to (a) understand the interactions of implanted ions with pre-implant impurities and native defects. This was done through comparison of effects in Cr doped and undoped substrates, (b) systematically investigate various annealing procedures and their effect on activation efficiency and profile distributions, (c) conduct an in-depth examination of implantation induced

damage, the distribution of that damage, and its influence on electrical activation and (d) investigate the structural characteristics of implantation induced damage before and after annealing and relate this to dopant activation, diffusion, and redistribution.

The experimental approach described in this report was designed to meet the goals and objectives stated above and represents a direct technical response of the programmatic scope and work statement. It is the opinion of the authors that this research has resulted in new and innovative techniques for investigating problems in III - V semiconductors. This research has also contributed to the better understanding of the nature of problems associated with the use of GaAs in device structure. In particular, a clear indication of the importance of defect complexes in ion implanted GaAs has resulted from this work. Demonstration of dopant incorporation into the GaAs lattice has been achieved through a variety of measurements, yet continued poor activation efficiency for n type dopants persists. Defect complexing is a highly probable exploration of this effect and should be considered an important problem for future study. The use of ion implantation for device isolation and backgating problems in GaAs is also identified as an important area for continued research and follows from the studies conducted here on oxygen implantation. Deep high energy implants will also be of significance in the emerging field of micron and sub-micron line width devices in CMOS technology where noise triggered latch-up is encountered. These and other areas of ion implantation will serve future needs in III - V compound semiconductor development for both discrete systems and monolithic integrated circuits using bulk, epitaxial and superlattice systems.

SECTION II

MACHINE AND ASSOCIATED APPARATUS

The importance of ion implantation as a semiconductor doping technique is derived from the degree of control available over the implantation process and from the fact that any ion can be implanted into any solid. The three main parameters over which control is exercised are implantation depth, fluence, and impurity species. The depth of penetration of an impurity ion into a host material is dependent upon the host material, the mass and charge of the impurity ion, and the accelerating potential. For a specific host and ion, the penetration depth is directly controlled by the accelerating potential. The fluence or number of impurities implanted per cm^2 is dependent upon the implant area, the impurity beam current at the target, and the amount of time during which the target is exposed to the beam. For a given implanted area and beam current, the fluence is directly controlled by exposure time. Selection of the implant species is accomplished by mass analysis of the ion beam.

2.1 ION MACHINE

The implants reported herein were accomplished by government personnel using a Varian/Extrion Model 400-10AR Ion Implanter located at WPAFB. This implanter has an accelerating energy range of 50-400 keV for singly charged ions of mass less than 140AMU. Mass analysis of the ion beam is performed by a 90° magnet located just before the accelerating column. Analysis is done on a beam at extraction potential (50 keV) and not at full accelerating potential. This pre-acceleration analysis simplifies multiple energy implants, since once parameters are adjusted to produce an ion beam, they

remain fixed and only the acceleration potential needs to be varied. The ion source used on this machine is a hollow cathode Penning discharge type. Provisions to supply the source with one of three possible carrier gasses are provided and selectable from the control consol. After acceleration, the beam passes through a quadrupole for focusing and an X-Y asynchronous scanner to insure large area uniform doping. A neutral particle trap is incorporated into the X scanner. It is achieved by applying a d.c. voltage to the scanner plates. Beam current is measured on 4 corner Faraday cups positioned outside the implant area. These signals are sent to a Model MP-100 Dose Processor. The dose processor is a precision current measuring and integrating instrument which uses an 8080A microcomputer for control. The end station is a model RS-LN 600. Samples up to 2 1/4" diameter are mounted on each face of a cube. The cube is manually indexed and can be set from 0° to 15° off the beam normal. Regardless of sample size the implant area is the entire 2 1/4" diameter. The mounting cubes can be cooled or heated. The implanter is cryo-pumped except for the source region which uses a small diffusion pump.

2.2 ENCAPSULATION

Radiation damage is an inevitable consequence of ion implantation. Bombardment of high-energy ions creates point defects such as vacancies and interstitials, clusters of point defects, and dislocation loops. The amount of damage generated depends upon the ion species, ion dose, dose rate, and the energy and temperature of the substrate. Unfortunately, some damage sites may act as unwanted traps for holes and electrons, or may form vacancy complexes. In addition, all of the as-implanted ions do not become electrically active. Therefore, thermal annealing is required to bring the dopant onto electrically active sites and to remove the unwanted radiation damage. Generally,

annealing temperatures in the range 600-900°C are required to achieve maximum electrical activation of the implanted ions in GaAs. Annealing at this high temperature usually removes the majority of the implanted damage. However, it is known that As can be lost from the surface of GaAs at a temperature as low as 400°C. Therefore, some means of surface protection is required during high-temperature annealing of GaAs.

Usually the surface of the implanted layer is encapsulated, using a thin dielectric film as a protective cap. An effective encapsulant should reliably protect the implanted GaAs surface from decomposition at temperatures up to at least 900°C. It should also prevent outdiffusion of the implanted species. The encapsulant must be easily depositable as a homogeneous layer which adheres well and does not diffuse into or react chemically with GaAs. It must also be mechanically stable and able to withstand high temperatures without blistering, crazing, or creating strain at the interface.

Among the presently known dielectric caps, Si_3N_4 has been demonstrated to be comparable and in many cases superior to the other encapsulants for annealing GaAs. Even with this cap, however, the implantation results have shown a strong dependence upon the deposition method and the particular parameters used. Two Si_3N_4 deposition systems were used over the period of this contract - a chemical-vapor-deposition (CVD) system and a plasma-enhanced deposition (PED) system. Figure 1 is a block diagram of the chemical vapor-deposition system used to encapsulate GaAs with Si_3N_4 . This type of system is also known as a "pyrolytic reactor" since it uses high temperature to initiate the reaction needed to produce the Si_3N_4 . Although high temperature is employed, this is a "cold-wall" type of reactor. The CVD system uses two reactive gases - silane (SiH_4) and

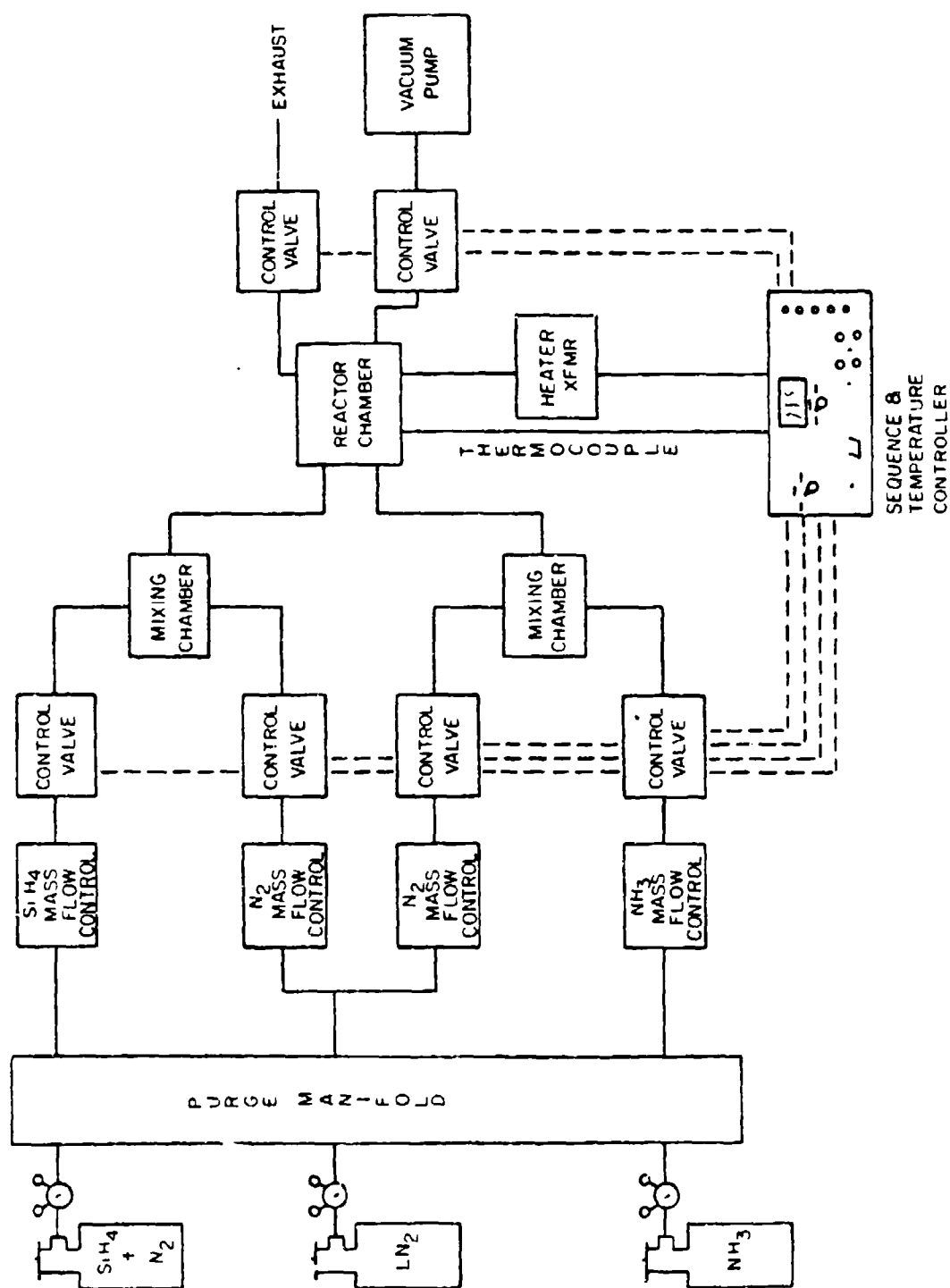


Figure 1 Si_3N_4 Pyrolytic Deposition System

ammonia (NH_3) - and a third diluting gas which is nitrogen. The silane used is a 5% mixture in nitrogen. The other reactant gas is anhydrous ammonia. The nitrogen gas used for diluting and backfilling is obtained from liquid nitrogen in a pressurized storage Dewar. This nitrogen gas is most reliable, pure, and readily available.

As shown in the Figure 1, the three gases enter the purge manifold from where it is possible to purge or flush any part of the entire system with nitrogen gas. This is a requirement because NH_3 is a strong irritant and SiH_4 reacts spontaneously on contact with air. Therefore, air must be flushed out with nitrogen gas before the reacting gases are admitted. The next elements in the system are the gas-flow controllers. These are tapered graduated tube-type flow meters with manual flow control valves for adjusting flow rates. Upon leaving the flowmeters, each gas passes through a pneumatically operated control valve. Pneumatic pressure valves are used here to assure positive shut-off of the gases. These valves, and similar ones located in the exhaust and vacuum pump lines are opened and closed by the sequence and temperature controller through a solenoid and are actuated at different times during the capping cycle. When the system is in "stand-by", the valves in both N_2 lines are open to allow continual flushing through the reaction chamber. Once a sample is loaded, the system is evacuated. All valves are closed with the exception of one in the vacuum pump line which is opened, allowing evacuation of the reaction chamber and all lines to the other control valves. The system is evacuated to less than 1 torr for approximately 5 minutes. At this time, the "vacuum" control valve is closed and the two N_2 valves are opened to allow back filling with N_2 gas. When the system has backfilled to atmospheric pressure, the exhaust valve is opened and the

"purge" mode is initiated, which opens the SiH_4 and NH_3 valves and closes the two N_2 valves. At this time, the heater temperature is raised to 200°C . This rise time takes only about two seconds and is necessary because silane can react at room temperature with trace amounts of oxygen to produce SiO_2 deposit on the substrate. The "purge" mode lasts about 1 minute, after which the two N_2 valves open to dilute the SiH_4 and NH_3 in their respective mixing chambers. This is referred to as the "mixing" mode. At this time, previously established flow rates are checked and readjusted, if necessary. Typical flow rates are as follows:

5% silane in nitrogen	-	68 SCCM
nitrogen-silane carrier	-	500 SCCM
ammonia	-	40 SCCM
nitrogen-ammonia carrier	-	500 SCCM

After about 3 minutes of mixing, the substrate heater temperature is raised to 725°C . The rise time from 200°C to 725°C is less than 8 seconds. The heater remains at this temperature until the required thickness is obtained. At this time, the SiH_4 and NH_3 control valves are closed and the heater temperature is dropped to 200°C and maintained for about 3 minutes while the system flushes out the reactant gases. At this point all control valves are closed except the vacuum pump valve, the system is pumped down again and backfilled with N_2 , and opened. When the vacuum control valve opens, the substrate heater will drop to room temperature. Using the above gas flow parameters and 725°C heater temperature, the Si_3N_4 deposition rate will be 25 to 30 $\text{\AA}/\text{sec}$.

Figure 2 shows the CVD reaction chamber detailing the dispersion arms, hood, graphite heater strip, thermocouple, and exhaust line. The two dispersion arms carry all gases into the reaction chamber and end about an inch apart, facing each other approximately 2 inches above the graphite

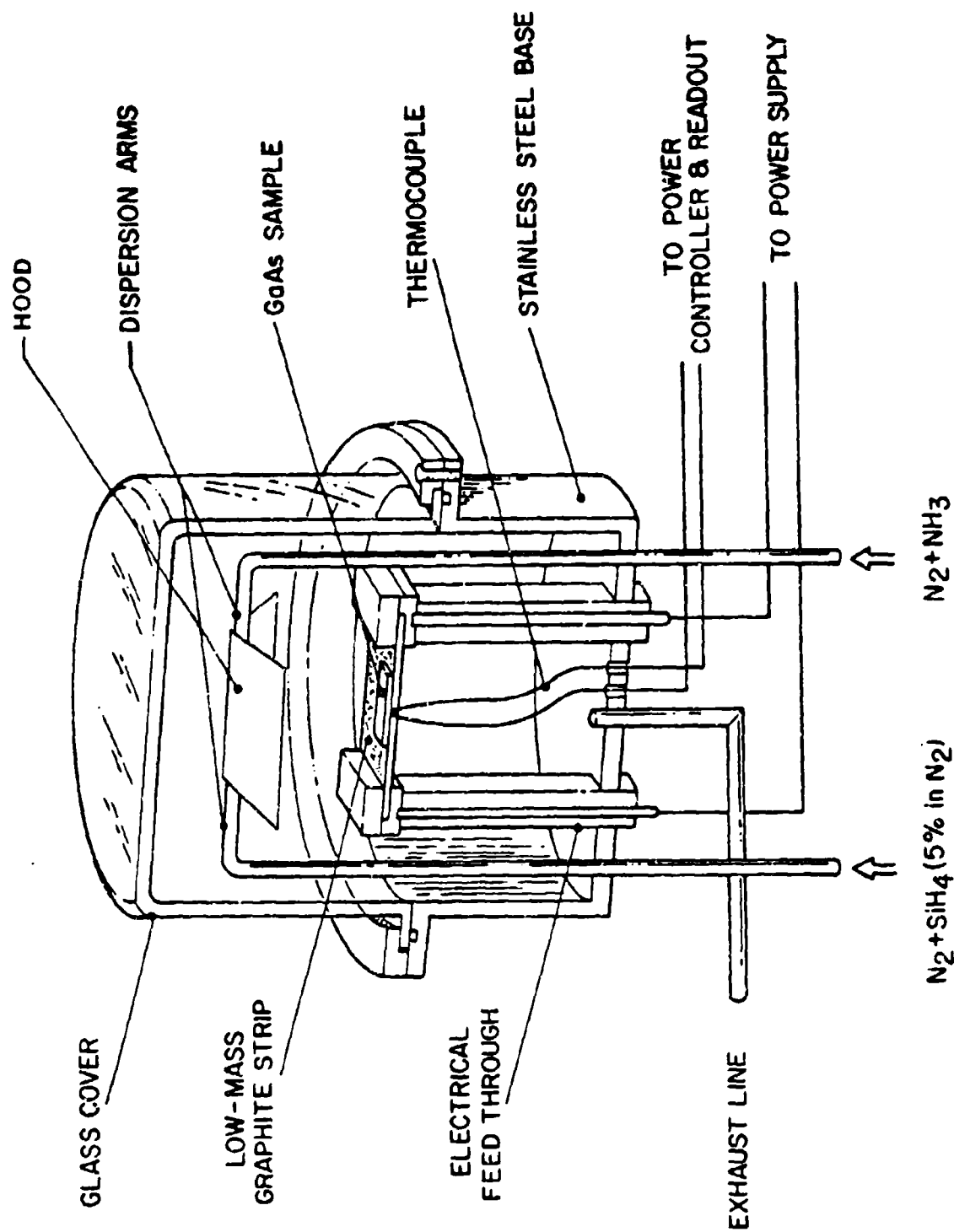


Figure 2 Cold-Wall Reactor for Pyrolytic Deposition of Si_3N_4

heater. The two gas mixtures combine in the chamber under a hood placed over the dispersion arms in such a position as to direct the gases downward to the substrate on the graphite heater strip. The temperature controlling and monitoring thermocouple is inserted into a 1/4" deep hole drilled into the edge of the graphite heater about midway along the length. The thermocouple leads continue through the stainless steel chamber wall unbroken through a rubber vacuum feedthrough to terminals which remain at room temperature. The graphite also has about 1.0 mm diameter holes drilled on each side of the hot zone to improve heat distribution by preventing heat loss to the mounting clamps and electrical feedthroughs. The heater is a low mass graphite strip 51 mm long X 22 mm wide X 1 mm thick. Only an area 15 mm X 20 mm is usable for capping.

The second silicon nitride deposition system is a plasma enhanced deposition (PED) reactor. The PED system is necessary because the high temperature associated with the CVD reactor limits its versatility. It is also impossible to encapsulate large samples in the CVD system. A block diagram of the PED system is shown in Figure 3.

Gas is supplied from two sources. One is 2% silane in argon; the other is N_2 from a liquid nitrogen storage dewar. Following the gas flow in the block diagram, each of these gases flow through their metering valves, flow meters, pneumatically operated control valves, and into the reaction chamber where the silane and nitrogen mix directly over the hot substrate.

Figure 4 shows a vertical cross section of the PED reaction chamber. The silane/argon gas mix enters the chamber through a "shower" ring placed 1 1/2 inches above the heater plate. Nitrogen enters the chamber at the top to drift down through the chamber and mix with the silane over the heated

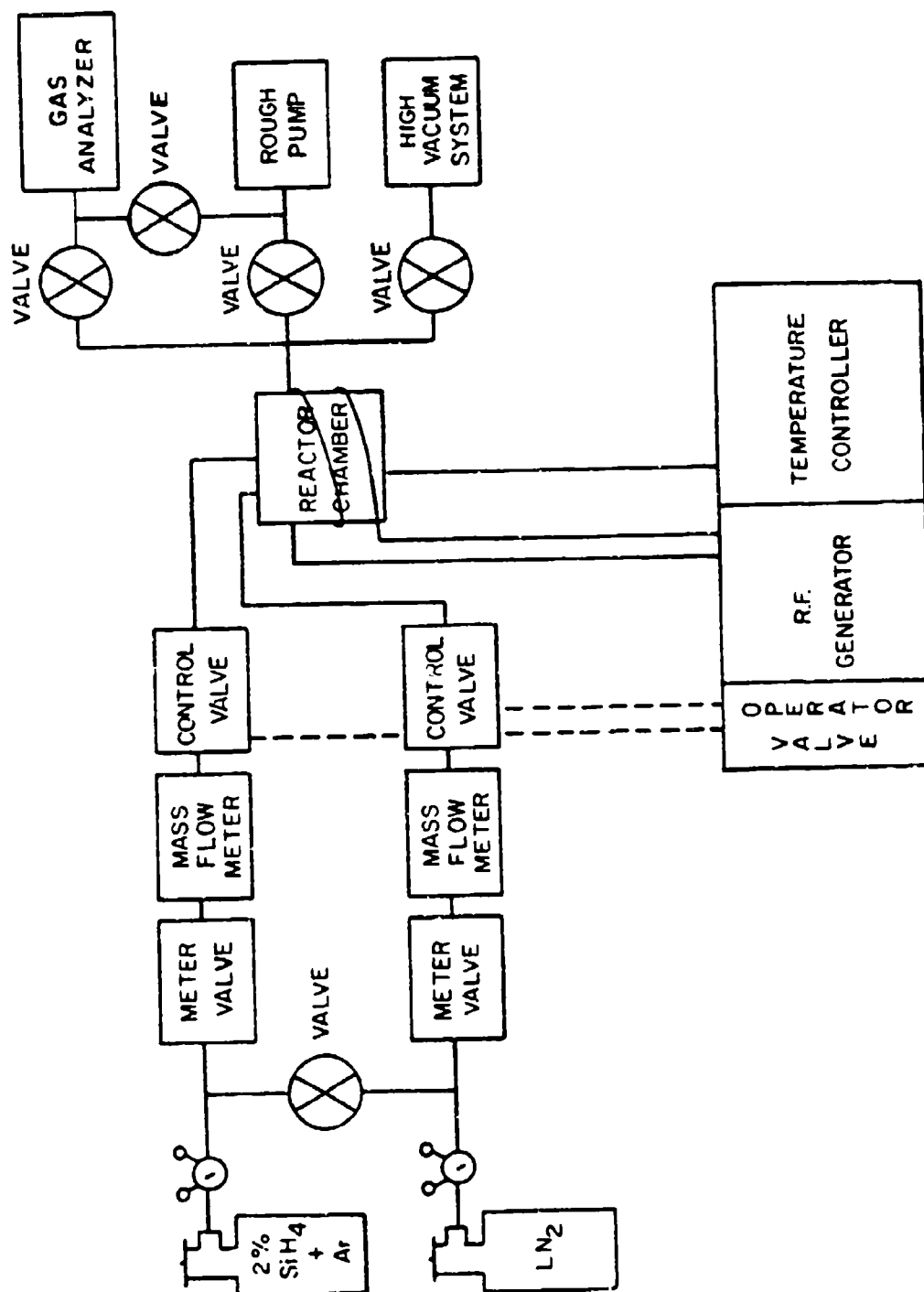


Figure 3 Si_3N_4 Plasma-Enhanced Deposition (PED) System

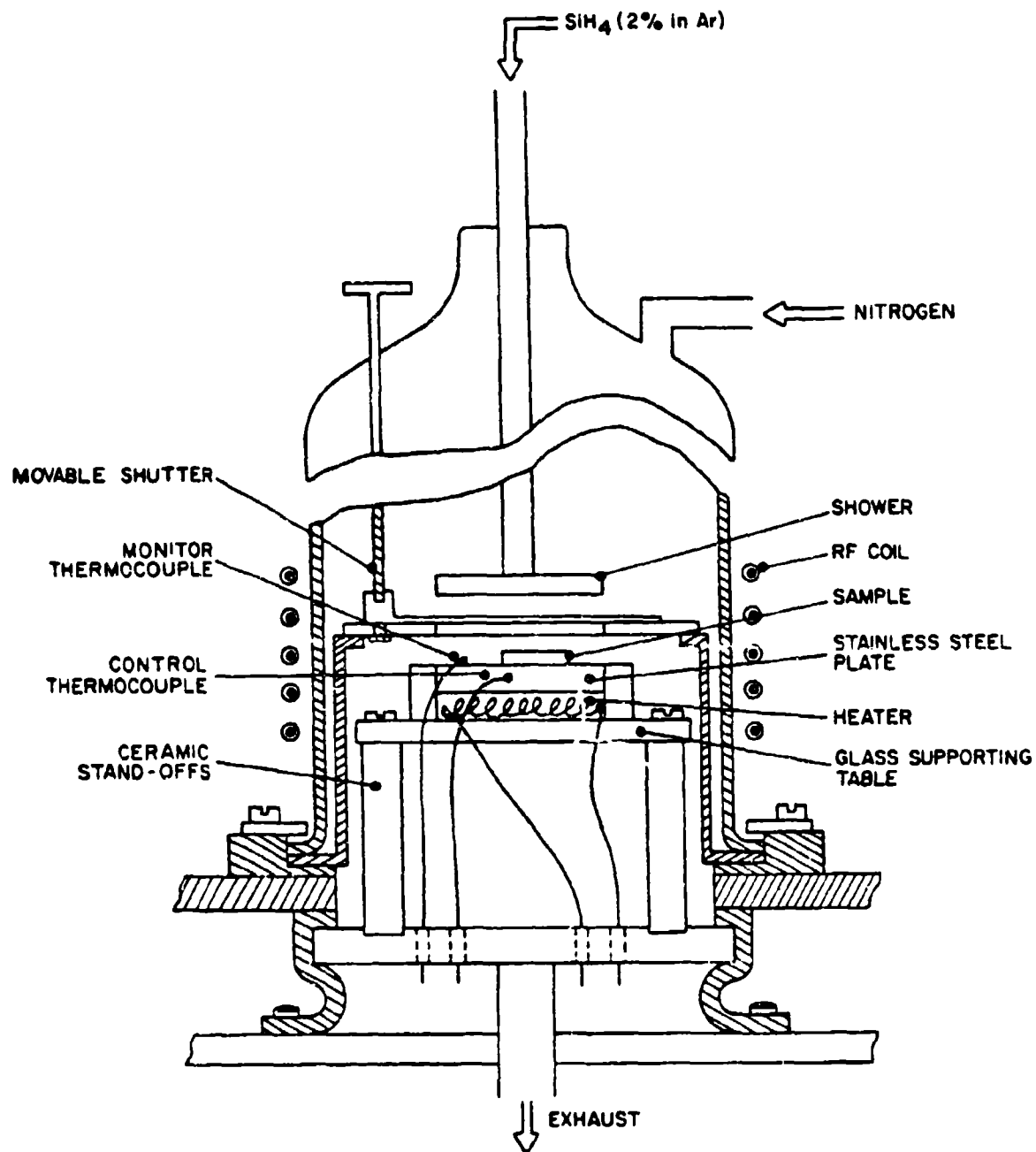


Figure 4 Plasma-Enhanced-Deposition-System Reactor Chamber with Small Shower Ring and Shutter Assembly

area. The shower is 3 inches in diameter and made of 1/4 inch stainless steel tubing which is curved and welded to make a complete ring. On the inside of the ring is a series of holes 1/16 inch in diameter used to direct the gas toward the center of the circle. R.F. plasma is created by a 5 turn coil around the outside of a pyrex chamber, and coupled to a generator operating at 13.56 MHZ.

The substrate heater element was fabricated by making a coil of nichrome wire and placing it in a spiral formation on a quartz plate of 1/4" in thickness. The spiral turns are spaced with quartz strips to prevent short circuiting. The substrate mount is a 3" diameter X 1/8" thick stainless steel disc which is placed over the heater and rests on top of the spacer. A hole of 1/16" in diameter is drilled from the edge of the disc to a point near the center for the thermocouple. This type of heater arrangement is easily capable of 500°C and normally operates at 400°C during deposition. A shutter assembly is placed between the silane shower and substrate mounting plate which can be opened and closed from outside the chamber by a rotatable vacuum feed through. The purpose of the shutter is to protect the sample during a cleaning step in which an N₂ plasma is created which cleans the inside walls of the chamber and removes absorbed gases and vapors.

To improve the cap uniformity over the area of 2-3 inch diameter wafers, it was necessary to increase the diameter of the silane shower ring as shown in Figure 5. Unfortunately the shutter assembly had to be removed when the shower ring was enlarged; therefore, the R.F. cleaning step had to be discontinued. Instead, a longer pumping time in the 10⁻⁶ torr range see equally effective. The R.F. plasma substrate cleaning step also had to be removed because R.F. plasma can produce substrate surface damage when exposed

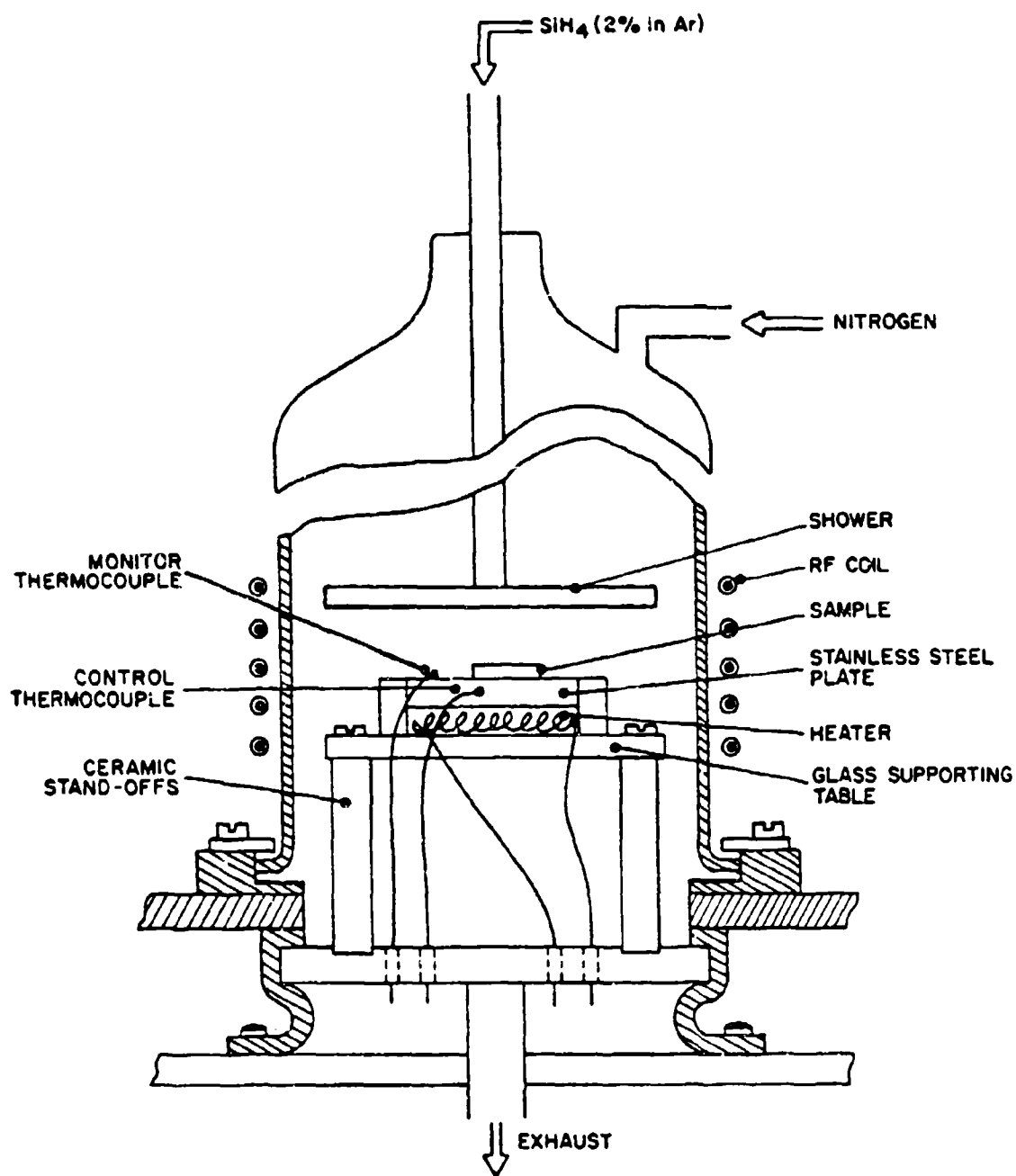


Figure 5 Plasma-Enhanced Deposition System Reactor Chamber with Large Shower Ring

for a long period of time. The following parameters affect Si_3N_4 deposition: R.F. power, silane flow rate, deposition time, N_2 flow rate, substrate temperature, and distance from shower ring to substrate. The last parameter has the greatest effect on cap uniformity and area of deposition. R.F. power is the final adjustment made to obtain the desired index of refraction and the deposition time is selected to obtain required film thickness. The other parameters usually do not have to be changed from run to run.

The substrate temperature of 400°C seems to be the lowest temperature at which consistently good results can be obtained. The sample to be capped is loaded onto the heater, the chamber is closed, and, as shown in Figure 3, the rough pump valve is opened to evacuate the reactor chamber. The substrate heater can be turned on and is usually left "on" from run to run. When the chamber pressure reaches <10 millitorr the roughing valve is closed and the high vacuum valve is opened to further evacuate to $\sim 5 \times 10^{-6}$ torr with the LN_2 trapped high vacuum pump system. After 15 minutes the high vacuum valve is closed and the LN_2 control valve is opened to back fill the chamber with N_2 gas. When the chamber pressure is about 0.5 torr the rough pump valve is opened. When the N_2 flow and chamber pressure have stabilized, the pre-set R.F. power is switched on and then the silane control valve is opened immediately and Si_3N_4 deposition begins. Typical PED system parameters are as follows:

N_2 flowrate - 20 SCCM
 SiH_4 (2% in Ar) - 23 SCCM
Substrate heater - 400°C
System pressure during deposition - 0.5 to 0.6 torr
Time to obtain 100 Å cap - 35 minutes
Index of refraction obtained - 2.0 to 2.05.

Plumbed into the PED system is a quadrupole mass gas analyzer to facilitate monitoring the various gases flowing through the system. The gas sampling point is between the reaction chamber and the rough pump valve. The sample gas flows past the analyzer leak valve where the sample is taken, then it flows directly to the rough pump. System vacuum leaks and some other gas flow problems can often be detected and corrected before they have advanced enough to produce a defective film. As can be seen in Figure 3, it is possible to evacuate the entire system with the high vacuum pump, then back fill with N_2 gas and flush the system by opening the valve between the two gas sources. This is desirable after replenishing the gas supply.

2.3 AUTOMATED HALL-EFFECT/SHEET-RESISTIVITY MEASUREMENT SYSTEM

Hall-effect and sheet-resistivity measurements form an important part of the characterization study of both ion-implanted and undoped semiconductors. Important information obtained by the electrical measurements include conductivity type, sheet resistivity, sheet-Hall coefficient, sheet-carrier concentration, Hall mobility, dopant profile, diffusion coefficient, compensating level, ionization energy, and effective density-of-state mass.

Single Hall-effect measurements generally are easy to carry out manually. However, a computer-controlled system becomes very useful when the process must be repeated many times and sophisticated data must be analyzed in the measurement process, for example, when measuring electrical carrier profiles and investigating temperature dependences. A block diagram of the automated Hall-measurement system is shown in Figure 6. All equipment identification in this figure are given in Table 1. Current control is affected by setting a range and percentage of range, in a constant current source, through the current control board and a D-A converter, respectively.

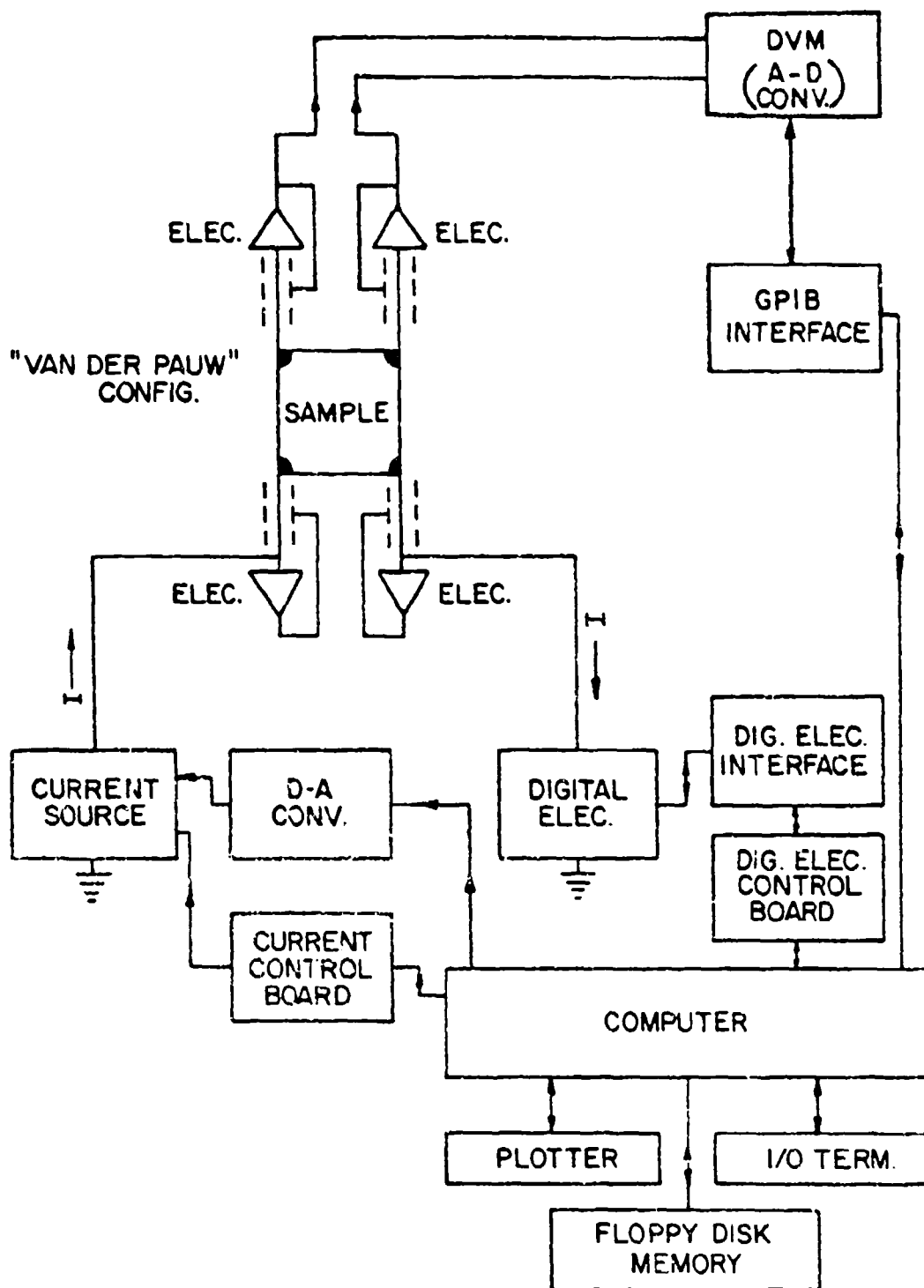


Figure 6 Block Diagram of Automated Hall-Effect/
Sheet-Resistivity Measurement System

TABLE 1

EQUIPMENT IDENTIFICATION OF AUTOMATED HALL-EFFECT/SHEET-RESISTIVITY MEASUREMENT SYSTEM. (ABBREVIATIONS: K = KEITHLEY; DEC = DIGITAL EQUIPMENT CORP.; H-P = HEWLETT-PACKARD)

Equipment Designation	Mfg. and Model No.
ELEC. (Electrometer)	K610CR
DIGITAL ELEC.	K616
DIG. ELEC. INTERFACE	K6162
DIG. ELEC. CONTROL BOARD	K7901-6162 (in K790 mainframe)
CURRENT SOURCE	K725
CURRENT CONTROL BOARD	K7901-725 (in K790 mainframe)
D-A CONV. (D-A converter)	Keeco SNR 488-4
DVM (A-D CONV.)	K6900 Digital Multimeter
GPIB INTERFACE	K55
COMPUTER	DEC PDP11-03 (with IEEE-488 I/O bus)
FLOPPY DISK MEMORY	DEC RXV11
I/O TERM. (I/O Terminal)	DEC LA-36
PLOTTER	H-P 9872A

The seven possible ranges in the K725 current source are 10^{-7} , 10^{-6} , ..., 10^{-1} A, and the D-A converter allows choices within a given range from 0.1 to 99.9%, in 0.1% increments. Thus, currents are available from 10^{-7} to 99.9 mA. Current is read by means of the digital-electrometer interface, in conjunction with the digital-electrometer control board. These latter instruments also allow control of the various digital-electrometer functions.

Each voltage contact is interfaced with an electrometer and operated as a unity-gain amplifier. To minimize the effective cable capacitances--and thus avoid long response times--the inner shield of the triaxial cable is connected to the unity-gain of the electrometer.¹ The particular contact arrangement shown in Figure 6 is the standard van der Pauw configuration.² The voltage is read by a K6900 digital multimeter, with BCD output. The Model 55 General-Purpose Interface Bus (GPIB) provides an interface function between the DVM and the bus conforming to the IEEE Standard 488.

For the van der Pauw configuration, four contacts are placed on the periphery of the sample. Current is passed between two of the contacts (the two electrometers are by-passed for this current mode), and the voltage difference between the other two is read. The current and voltage terminals are then switched between other pairs of contacts, and the process is repeated. Discussions of the van der Pauw method and relevant calculational equations are given in Section 3 of this report.

The central processing unit (computer) for the system is a PDP11-03 with software to control the IEEE-488 I/O bus. In general, programs have been written in the FORTRAN IV language because of its wide-spread use. The peripherals include a DEC LA36 terminal, a RXV11 dual floppy-disk system, and an HP9872A four-pen plotter. The results of measurements are calculated

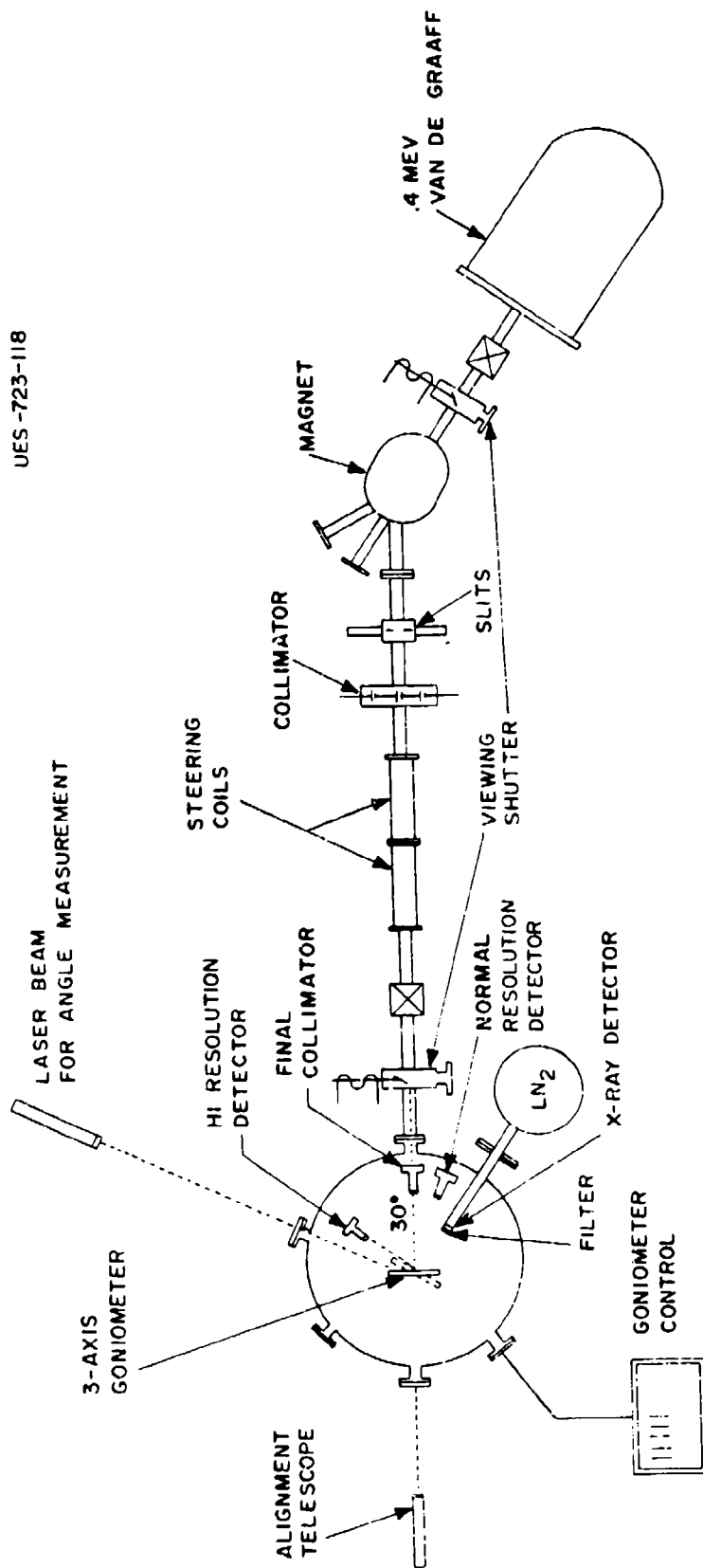
immediately after data are taken. An advantage of the computer is its calculational accuracy, which reduces the frequency of mistakes.

2.4 RUTHERFORD BACKSCATTERING ANALYSIS SYSTEM

A beam of 330 -350 keV H^+ was obtained from a 400 keV Van de Graaff accelerator (Model PN-400) manufactured by High Voltage Engineering Corporation, Massachusetts. A schematic diagram of the experimental set-up for high depth resolution RBS-channeling and PIXE studies are shown in Figure 7.

Both the particle detector and the Si(Li) X-ray detector viewed the target at 30° to the beam direction. The X-ray detector amplifier system has an energy resolution (as measured by the full width at half maximum of a characteristic K X-ray line) of 220 eV in the X-ray range of interest (1-10 keV). The X-ray detector has Be Window $3.46 \mu m$ thick. In addition, $15 \mu m$ thick Mylar foil has been added in front of the detector in order to reduce the intensity of the Ga-L and As-L signals (1.1-1.3 keV) and thus minimize pulse pile up effects that could seriously interfere with the Si-K (1.7 keV) signal. This extra filtering is very selective with the Ga/As-L signal being attenuated by a factor of 50, allowing the Si-K X-ray signal to appear with a signal to background ratio of about 1.8 on the low energy side. This can be improved to about 2.35 by using $22.5 \mu m$ thick Mylar foil which reduces the Ga/As-L signal by a factor of 100. As the window thickness increases, the count rate decreases.

Experiments in the early phase of the contract were performed by using the accelerator facility at the Oak Ridge National Laboratory. In particular, experiments with Cr implanted GaAs were done using their equipment. Besides high energy van de Graaff (H^+ at 1 MeV were used), there were some



UES-723-118

FIGURE 7 Schematic Diagram of the Apparatus Used for PIXE and RBS-C Analysis Using 400 keV van de Graaff

differences in the rest of the set-up. A schematic diagram is shown in Figure 8. Backscattered particles were observed with an annular surface barrier detector cooled to -22°C by a freon refrigerator to improve the detector resolution to 12 keV FWHM. The X-ray detector used a pulsed optical feedback preamplifier system and had an operational energy resolution of 180 eV when mounted in the target chamber. Emitted X-ray were observed at 90° to the incoming beam. This experimental arrangement was such that both the ion scattering and ion-induced X-ray yields were of comparable count rate, and simultaneous spectra could be acquired at reasonable rates for incident beams of 30 nA.

2.5 ELECTRON MICROSCOPE

A tungsten filament produces a coherent parallel beam of electrons, which can be varied in diameter from $0.1\text{ }\mu\text{m}$ to $10\text{ }\mu\text{m}$ at the specimen surface by means of a double condenser lens system in our Hitachi-600 Electron Microscope. The specimen is mounted in a special holder which fits into the bore of the objective lens and enables the specimen to be tilted to $\pm 60^{\circ}$ about two orthogonal axes so that appropriate crystallographic analyses can be done. Electrons passing through the thin specimen are brought into focus in the back focal plane of the objective lens; which acts as a converging lens and thus forms a diffraction pattern at the back focal plane of the objective lens. An inverted image is formed in the first image plane and three subsequent lenses in the column, namely, the diffraction lens, the intermediate lens, and the projector lens are used to magnify this image or to magnify the diffraction pattern. Thus, if the diffraction lens is focused on the back focal plane of the objective lens, a diffraction pattern is magnified and displayed, whereas if the first image plane is imaged by the diffraction

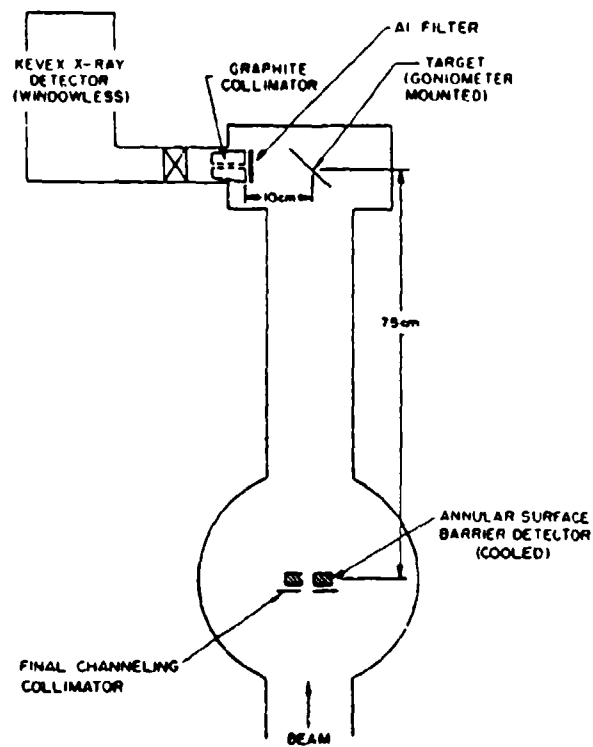


Figure 8 Schematic Diagram of the Experimental Set Up at Oak Ridge National Laboratory

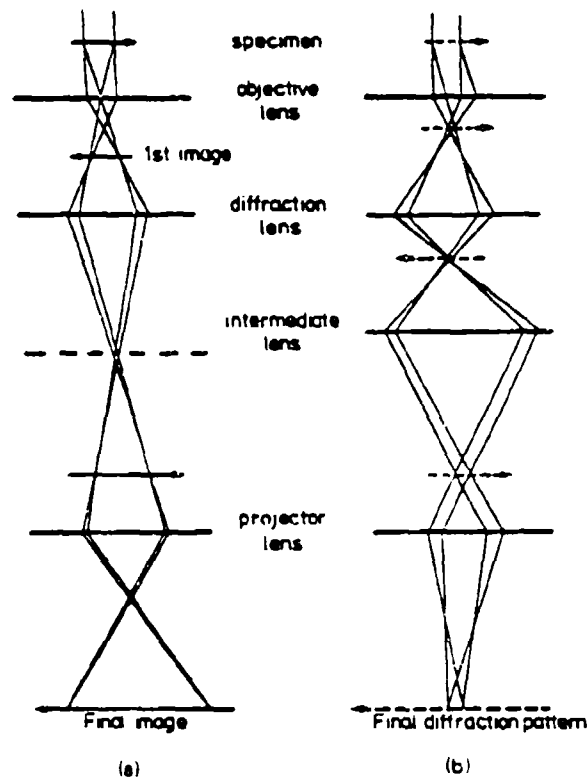


Figure 9 Schematic Ray Diagram for Producing an (a) Electron-Optical Image, (b) Diffraction Pattern

lens, a magnified image of the specimen is produced. In the Hitachi-600 Electron Microscope, magnification can be varied from 10^2 to 3×10^5 times. Schematic ray diagram to produce either an electron micrograph or a diffraction pattern are shown in Figures 9(a) and 9(b).

The analyses of crystal defects are carried out by inserting an aperture in or near the back focal plane of the objective lens to ensure that only one beam contributes to the formation of the image. Also, when the focal length of the diffraction lens is reduced to image the diffraction pattern, an aperture is inserted at the first image plane so that the area of the specimen which is giving rise to the diffraction pattern is defined. This is called selected area diffraction (S.A.D.), and the aperture is called S.A.D. aperture.

Relation Between the Image and the Diffraction Pattern

As seen above, to image the diffraction pattern, the diffraction lens has to be focused on the back focal plant of the objective lens. This can be done by changing the strength of the magnetic field of diffractin lens. Since magnetic lenses produce an image rotation which is related to the strength of the lens, then it is clear that there will be a relative rotation between the diffraction pattern and the corresponding electron micrograph. The magnitude and sense of this rotation need to be established for all operating conditions of the microscope so that the information contained in a diffraction pattern can be correlated with the electron micrograph. We have done this calibration by employing a double exposure technique in which the diffraction pattern and electron image of a crystal of MoO_3 are successively exposed. Crystals of MoO_3 have been grown on the microscope grid with long, straight edges perpendicular to the [100] direction and hence, the angle between the normal to the easily recognizable long edge of the crystal and the [100] direction in the diffraction pattern gives this rotation immediately.

SECTION III

ELECTRICAL PROPERTIES AND DISTRIBUTION OF ION IMPLANTS IN GaAs

3.1 SAMPLE PREPARATION

The substrate materials used, unless specified otherwise, were $\langle 100 \rangle$ -oriented semi-insulating Cr-doped GaAs single crystals obtained from Crystal Specialties, Inc. Prior to implantation, the samples were carefully cleaned with 10% aquasol, de-ionized water, trichloroethylene, acetone, and methanol and then dried with nitrogen gas. They were subsequently free-etched with an $\text{H}_2\text{SO}_4:30\%\text{H}_2\text{O}_2:\text{H}_2\text{O}$ solution in a 3:1:1 ratio by volume for 60 sec. Implantation was carried out at different ion energies to various ion doses at room temperature. The incident ion beam was directed 7° off the $\langle 100 \rangle$ crystal axis to minimize ion-channeling effects. After implantation, the samples were carefully cleaned again and then encapsulated with Si_3N_4 caps either by a chemical-vapor-deposition (CVD) or an rf plasma-enhanced-deposition (PED) system. In rf-plasma deposition of the caps, both sides of the samples were encapsulated with an $\sim 1000 \text{ \AA}$ layer of Si_3N_4 at $\sim 220^\circ\text{C}$ for ~ 10 min. In pyrolytic deposition of the caps, the implanted surfaces of the samples were encapsulated with an $\sim 1000 \text{ \AA}$ layer of Si_3N_4 at $\sim 700^\circ\text{C}$ for ~ 30 s. The samples were then annealed in flowing hydrogen gas for 15 min at various temperatures. The encapsulants were removed by 48% hydrofluoric acid after annealing. In the case of the close-contact capless method, the annealing was accomplished by resting the implanted surface side on top of another polished GaAs substrate during annealing in flow hydrogen gas. Electrical indium contacts were made on the four corners of the square-shaped (typically 0.5×0.5 cm) implanted surface using an ultrasonic iron. The contacts were then

heated at 375°C for 3 min., unless specified otherwise, in flowing argon gas to produce ohmic behavior. Sheet resistivity of the unimplanted Cr-doped substrate capped with Si₃N₄ and annealed at 900°C varied from 10⁷ to 10⁵ Ω/□.

3.2 ELECTRICAL MEASUREMENTS

Hall-effect/sheet-resistivity measurement are made using the standard van der Pauw technique² and an apparatus which utilizes a guarded approach¹ with unity-gain electrometers. A schematic diagram of the Hall-measurement system for the van der Pauw configuration is shown in Figure 10. From measurements of a sample voltage V_c and a sample current I, the sheet resistivity ρ_s for a homogeneous sample is calculated using the equation

$$\rho_s = \frac{\pi}{\ln 2} \frac{V_c}{I}$$

From measurement of a sample current I, a Hall voltage V_H, and a magnetic field B, the sheet-Hall coefficient R_{Hs} is found from the equation

$$R_{Hs} = 10^8 \frac{V_H}{IB} \quad (\Omega\text{-cm}^3/\text{V}\cdot\text{sec})$$

Then the sheet-carrier concentration N_s and Hall mobility μ_H are calculated from the relations

$$N_s = \frac{r}{eR_{Hs}} \quad \text{and} \quad \mu_H = \frac{R_{Hs}}{s}$$

where r is the Hall-to-drift mobility ratio, which is customarily taken to be unity.

Depth profiles of a carrier concentration N and a Hall mobility μ_H are accomplished by combining a layer-removal technique with the Hall and

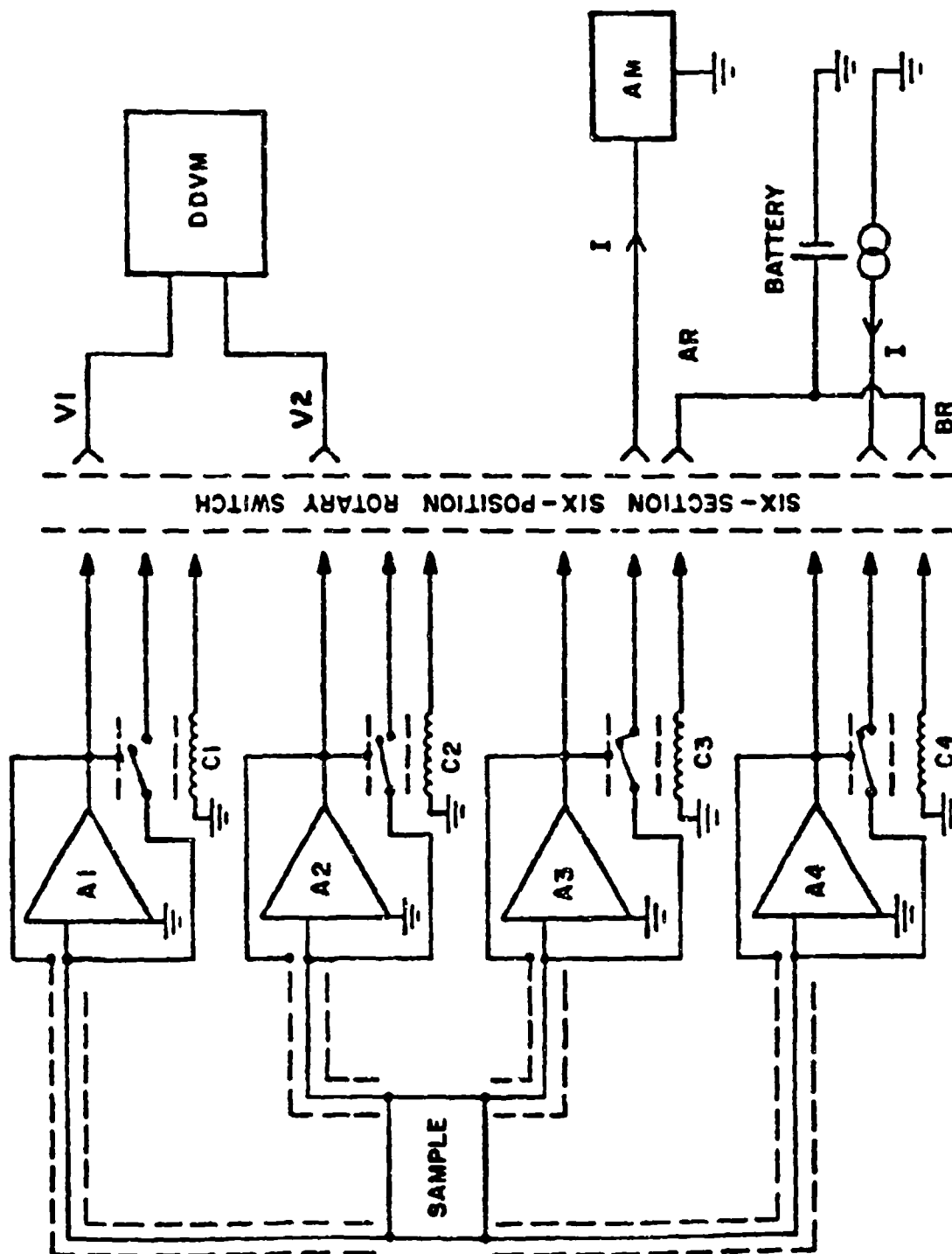


Figure 10. Schematic Diagram of the Hall-Measurement System for the van der Pauw Configuration.

sheet-resistivity measurements. The number of carriers N_i in the i^{th} layer and their Hall mobility μ_{Hi} can be obtained from the relations^{3,4}

$$N_i = \frac{\Delta \frac{1}{\rho_s}_i}{e \mu_{Hi} d_i}$$

where

$$\Delta \frac{1}{\rho_s}_i = \frac{1}{(\rho_s)_i} - \frac{1}{(\rho_s)_{i+1}}$$

and

$$\mu_{Hi} = \frac{\Delta \frac{R_{Hs}}{2}}{\frac{\rho_s}{\rho_s}_i}$$

where

$$\Delta \frac{R_{Hs}}{2} = \frac{(R_{Hs})_i}{\rho_s}_i - \frac{(R_{Hs})_{i+1}}{\rho_s}_{i+1}$$

In the above equations, $(R_{Hs})_i$ and $(\rho_s)_i$ are the sheet-Hall coefficient and the sheet resistivity, respectively, which are measured after removal of the i^{th} layer with thickness d_i .

Successive thin layers of the implanted section were removed using a diluted solution of H_2SO_4 :30% H_2O_2 : H_2O in a 1:1:50 ratio by volume at 0°C . Such an etch produces uniform and damage-free surfaces. A typical etching rate is $\sim 200 \text{ \AA}/\text{min}$. as determined by a Sloan Dektak Surface Profile Measuring System.

3.3 Mg-IMPLANTED GaAs

It is well known that Be, Mg, Zn, and Cd are all p-type dopants in GaAs. Although many studies⁵ on the implantation of Be, Cd, and Zn into GaAs have been done, few electrical studies have been reported for Mg-implanted GaAs. Hence, details of the electrical properties are not well known. The dependence of surface-carrier concentration upon annealing temperature has been reported^{6,7} previously for several ion doses. In the work of Hunsperger et al.⁶ a sputtered SiO₂ cap and n-type substrates were used; in the work of Zölch et al.⁷ a pyrolytic SiO₂ cap and sputtered Si₃N₄ cap, and n-type and semi-insulating substrates were used. Electrical studies on Mg-implanted GaAs have also been carried out previously with pyrolytic Si₃N₄ caps⁸ and plasma deposited Si₃N₄ caps⁹.

In the present work¹⁰, a comparative study of the electrical properties of Mg implants in GaAs has been carried out using rf-plasma-deposited Si₃N₄ caps, pyrolytic Si₃N₄ caps, and close-contact capless annealing methods. For convenience the close-contact capless annealing techniques will be referred to as a type of capping method in this discussion. In particular, the present work contains the first published detailed results of Mg-implanted GaAs using capless annealing methods. The dependence of surface-carrier concentration upon annealing temperature as well as detailed dopant profiles of GaAs implanted to several Mg-ion doses have been measured, and these results are discussed.

3.3.1 Electrical Activation

The results of Hall-effect/sheet-resistivity measurements made on GaAs samples implanted at an ion energy of 120 keV with Mg ions to doses ranging from 1×10^{13} to $3 \times 10^{15}/\text{cm}^2$ and annealed with plasma caps at

temperatures ranging from 600 to 850°C are shown in Figure 11. The electrical activation increases monotonically with annealing temperatures up to 750°C, and then it decreases monotonically with increasing annealing temperature, possibly due to outdiffusion of Mg. The maximum electrical activation occurs at 750°C for all except the lowest dose of $1 \times 10^{13}/\text{cm}^2$, for which the maximum occurs at 800°C. The maximum activation efficiency (surface-carrier concentration divided by ion dose) obtained was 85% for the sample implanted to a dose of $3 \times 10^{13}/\text{cm}^2$ and annealed at 750°C. The annealing behavior of Hall mobilities indicates that lattice damage due to ion bombardment is reduced appreciably even at an annealing temperature of 600°C and that mobilities increase further with annealing temperature.

Figure 12 is a replot of the data at 120 keV, showing surface carrier concentration N_s and Hall mobility μ_H versus implanted ion dose ϕ for the Mg-implanted GaAs samples annealed at various temperatures with PED caps. The dashed straight line represents 100% electrical activation efficiency (surface-carrier concentration divided by implanted-ion dose). Activation efficiencies are generally high for low dose ($< 1 \times 10^{14} \text{ cm}^{-2}$) samples annealed at 750°C, but decrease with increasing ion dose ($3 \times 10^{14} \text{ cm}^{-2}$). Mobilities generally decrease with increasing ion dose at a given annealing temperature.

Surface-carrier concentrations and mobilities are plotted as a function of annealing temperature in Figures 13, 14, and 15 for three different doses of Mg ions, 1×10^{13} , 3×10^{14} , and $1 \times 10^{15}/\text{cm}^2$, respectively, using the three different capping methods. Dashed lines in these figures indicate the results of electrical measurements after annealing with pyrolytic Si_3N_4 caps at temperatures below the deposition temperature

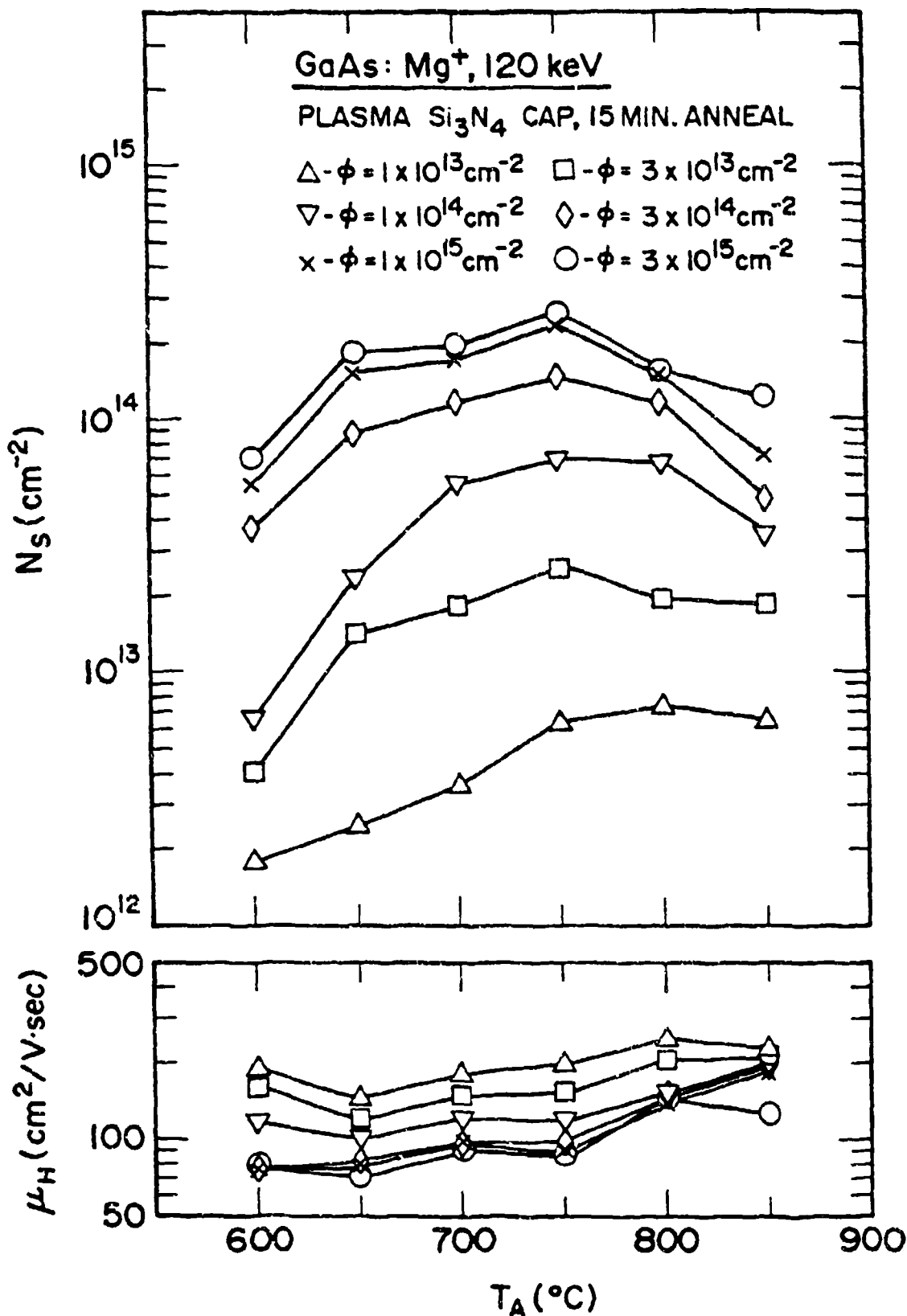


Figure 11 Dependence of Surface-Carrier Concentration (N_s) and Hall Mobility (μ_H) upon Annealing Temperature (T_A) for GaAs:Mg Samples with PED Si₃N₄ Cap

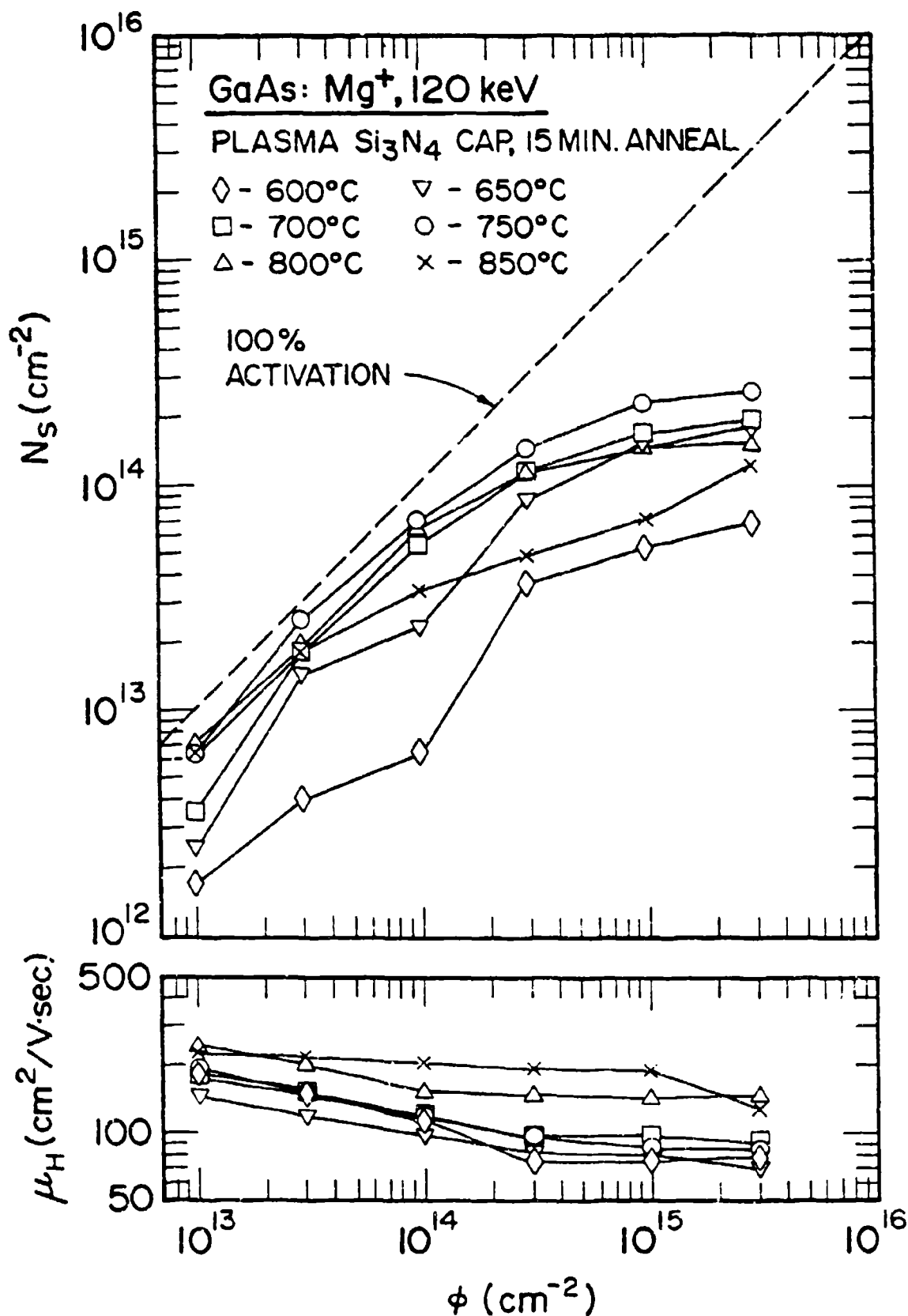


Figure 12 Dependence of Surface-Carrier Concentration (N_s) and Hall Mobility (μ_H) Upon Ion Dose (ϕ) for GaAs:Mg Samples with PED Si₃N₄ Cap

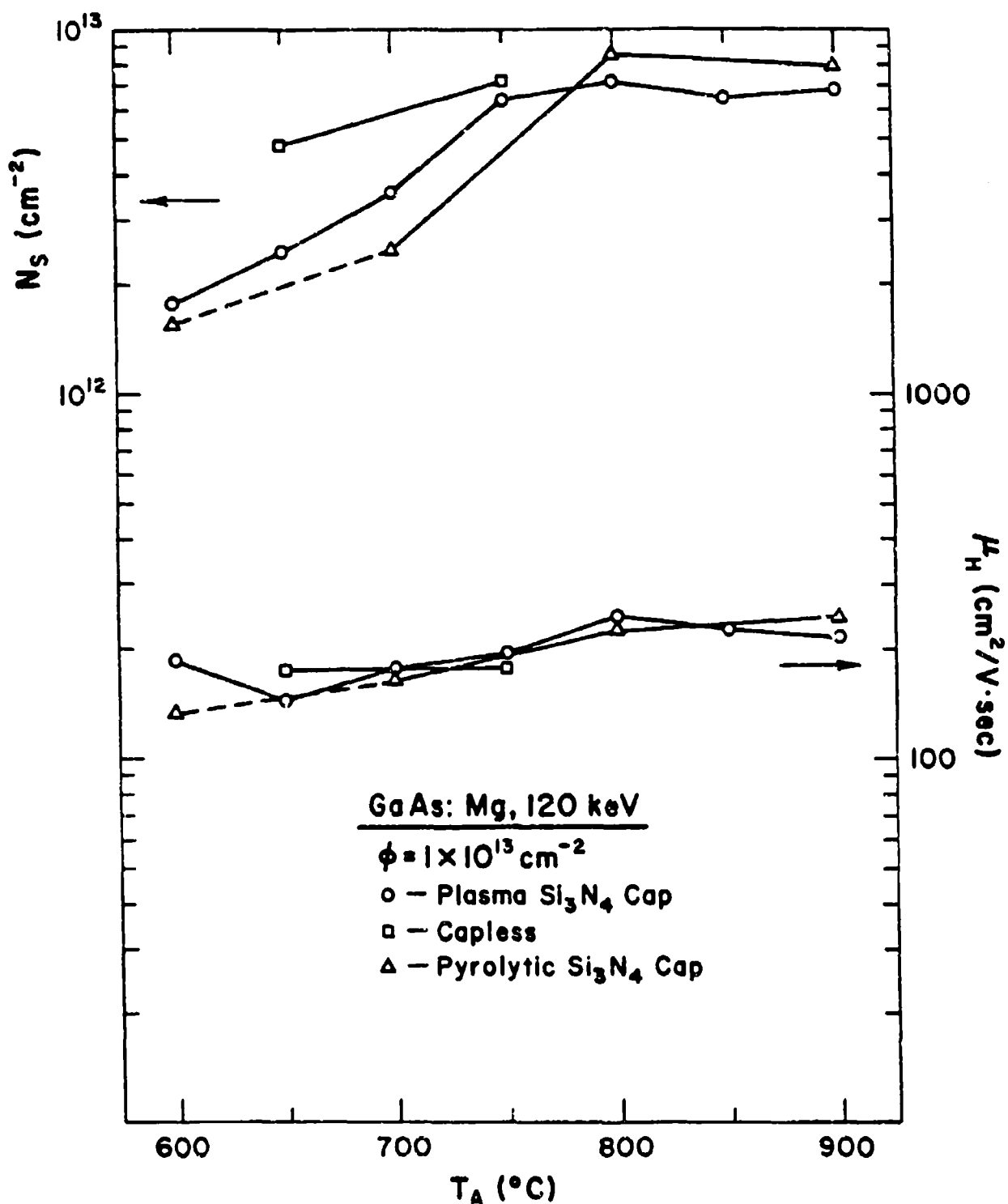


Figure 13 Dependence of Surface-Carrier Concentration (N_s) and Hall Mobility (μ_H) upon Annealing Temperature (T_A) for $1 \times 10^{13}/\text{cm}^2$ Dose Samples of GaAs:Mg with Three Different Capping Methods.

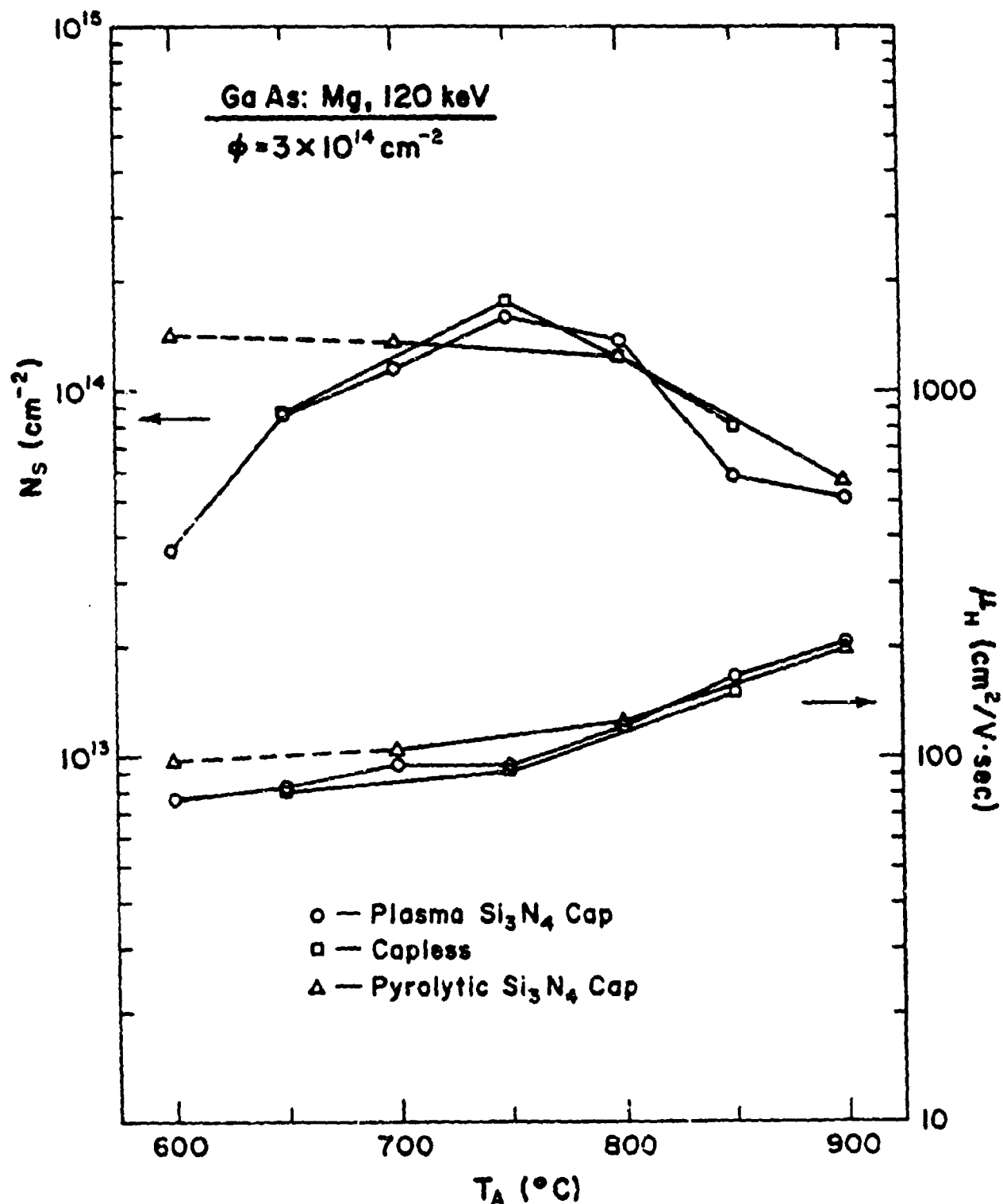


Figure 14 Dependence of Surface-Carrier Concentration (N_S) and Hall Mobility (μ_H) Upon Annealing Temperature (T_A) for $3 \times 10^{14}/\text{cm}^2$ Dose Samples of GaAs:Mg with Three Different Capping Methods

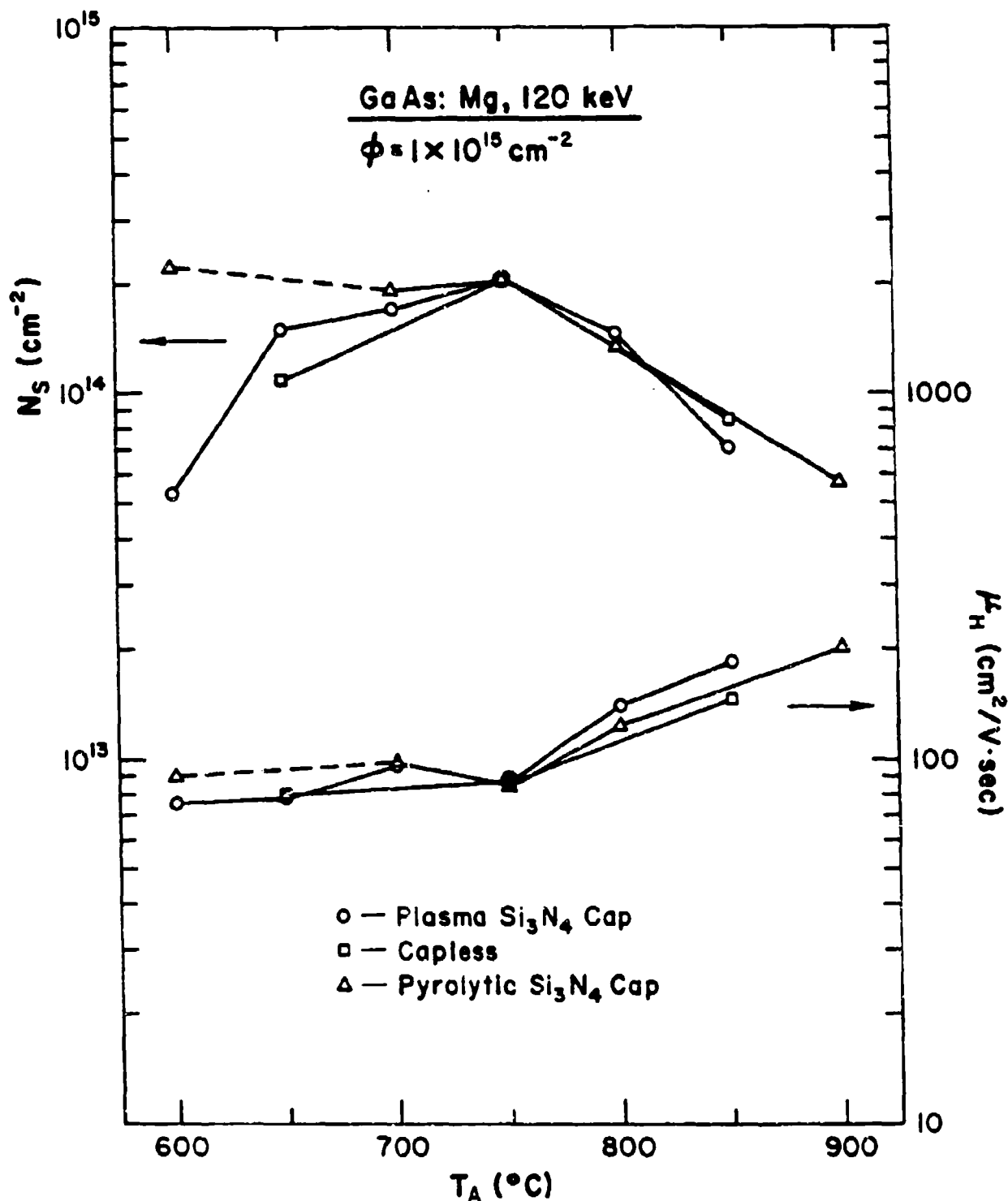


Figure 15 Dependence of Surface-Carrier Concentration (N_S) and Hall Mobility (μ_H) Upon Annealing Temperature (T_A) for $1 \times 10^{15}/\text{cm}^2$ Dose Samples of GaAs:Mg with Three Different Capping Methods

($\sim 700^\circ\text{C}$). At the lowest dose of $1 \times 10^{13}/\text{cm}^2$, it seems that the electrical activation and mobility are relatively unaffected by the high capping temperature of pyrolytic Si_3N_4 caps. However, considerable electrical activation occurs during pyrolytic deposition of the cap for higher doses, and neither the surface carrier concentrations nor the mobilities are altered appreciably during subsequent annealing up to 700°C . Therefore, the results of Mg-implants in GaAs with pyrolytic capping at lower temperatures (below $\sim 700^\circ\text{C}$) for high doses should not be compared directly with the results of other capping methods. A detailed study of GaAs:Mg with pyrolytic capping has been reported previously.⁸

For an ion dose of $1 \times 10^{13}/\text{cm}^2$, as shown in Figure 13, the annealing characteristics of surface-carrier concentration are markedly dependent upon capping. Capless annealing produces better electrical activation than plasma cap annealing, and plasma cap annealing produces better activation than pyrolytic cap annealing at lower annealing temperatures. On the other hand, pyrolytic cap annealing yields better activation than plasma cap annealing at higher annealing temperatures. The maximum electrical activation occurs at around 800°C . Mobilities are comparable for all capping techniques. For an ion dose of $3 \times 10^{14}/\text{cm}^2$, as shown in Figure 14, the annealing behavior of surface-carrier concentrations and mobilities obtained by different capping methods generally agree with one another. The maximum electrical activation occurs at 750°C anneal. Mobilities increase monotonically with annealing temperature for all three capping methods. For an ion dose of $1 \times 10^{15}/\text{cm}^2$, as shown in Figure 15, the electrical activations obtained by different capping methods generally agree well with one another at annealing temperatures $> 750^\circ\text{C}$. Plasma cap annealing gives

better electrical activations than capless annealing at lower annealing temperatures. In particular, the activations and mobilities obtained after annealing at 750°C produce nearly identical results. At higher annealing temperatures, the annealing behaviors of mobilities are somewhat different from one another, with plasma capping yielding the best values.

Although there are some differences in the detailed annealing behavior of surface-carrier concentrations and mobilities depending upon ion dose and annealing temperature, electrical activations show general agreement for the three capping methods investigated at high doses.

Since it has been found⁸ that considerable electrical activation occurs during the short deposition time of pyrolytic capping, a systematic study has been made of activation as a function of annealing time at 750°C, using the capless annealing method for two different doses. The results of this study are shown in Figure 16. The electrical activations obtained after annealing for only 2 min at 750°C were 55% and 67% for ion doses of 3×10^{13} and $1 \times 10^{14}/\text{cm}^2$, respectively. The activation increases further with annealing time and reaches a maximum at around 30 min annealing, with activation efficiencies of 100% and 80% for ion doses of 3×10^{13} and $1 \times 10^{14}/\text{cm}^2$, respectively. The mobility values are surprisingly good even after annealing for only 2 min at 750°C and they increase slightly thereafter for longer annealing times.

3.3.2 Electrical Carrier Profiles

Electrical depth profiles of hole concentrations and Hall mobilities for samples annealed after the three different capping methods and implanted to three different doses of Mg ions, 3×10^{14} , 1×10^{15} , and $3 \times 10^{15}/\text{cm}^2$, are shown in Figures 17, 18, and 19, respectively. The

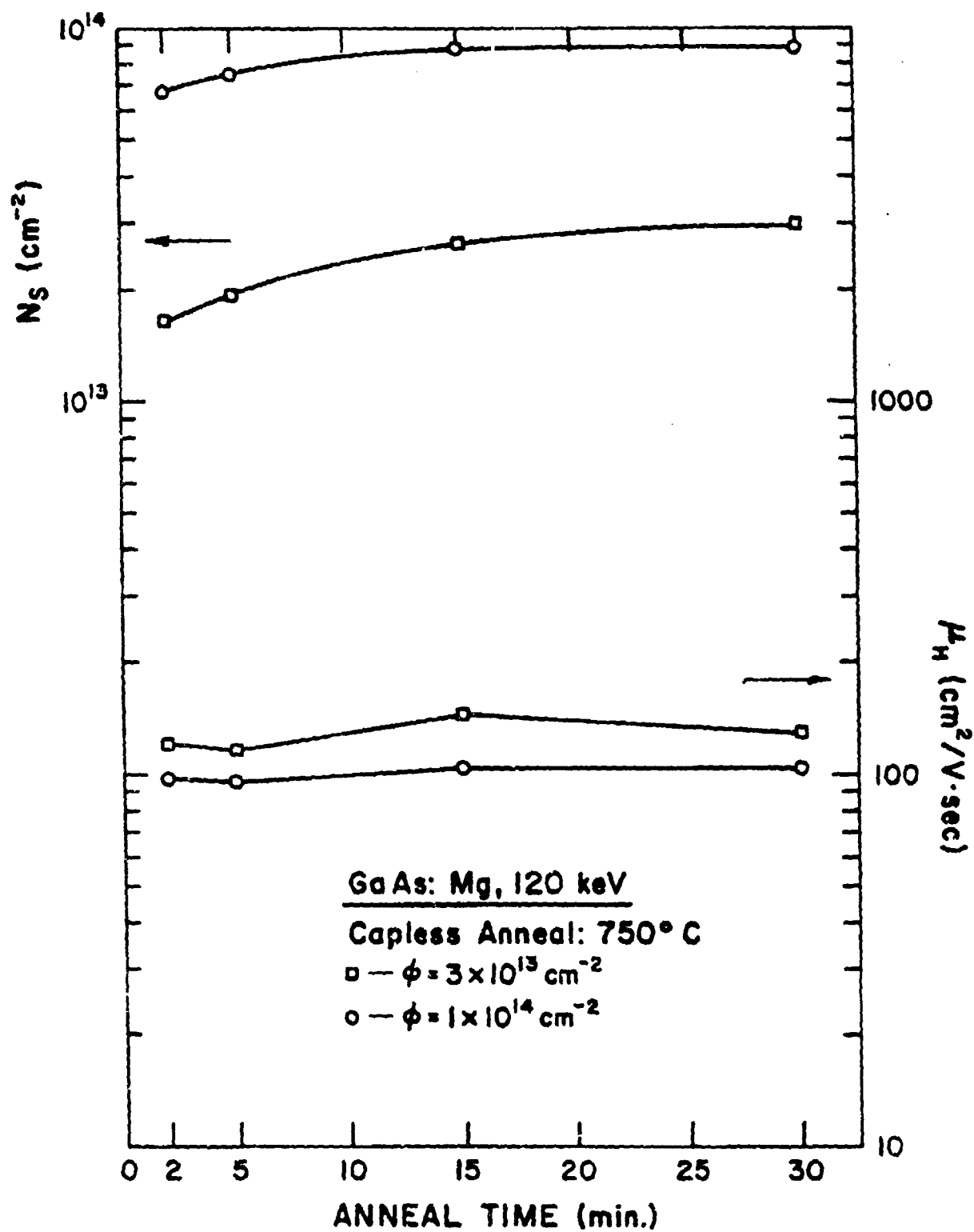


Figure 16 Dependence of Surface-Carrier Concentration (N_S) and Hall Mobility (μ_H) Upon Annealing Time for GaAs:Mg Samples with Capless Annealing at 750°C.

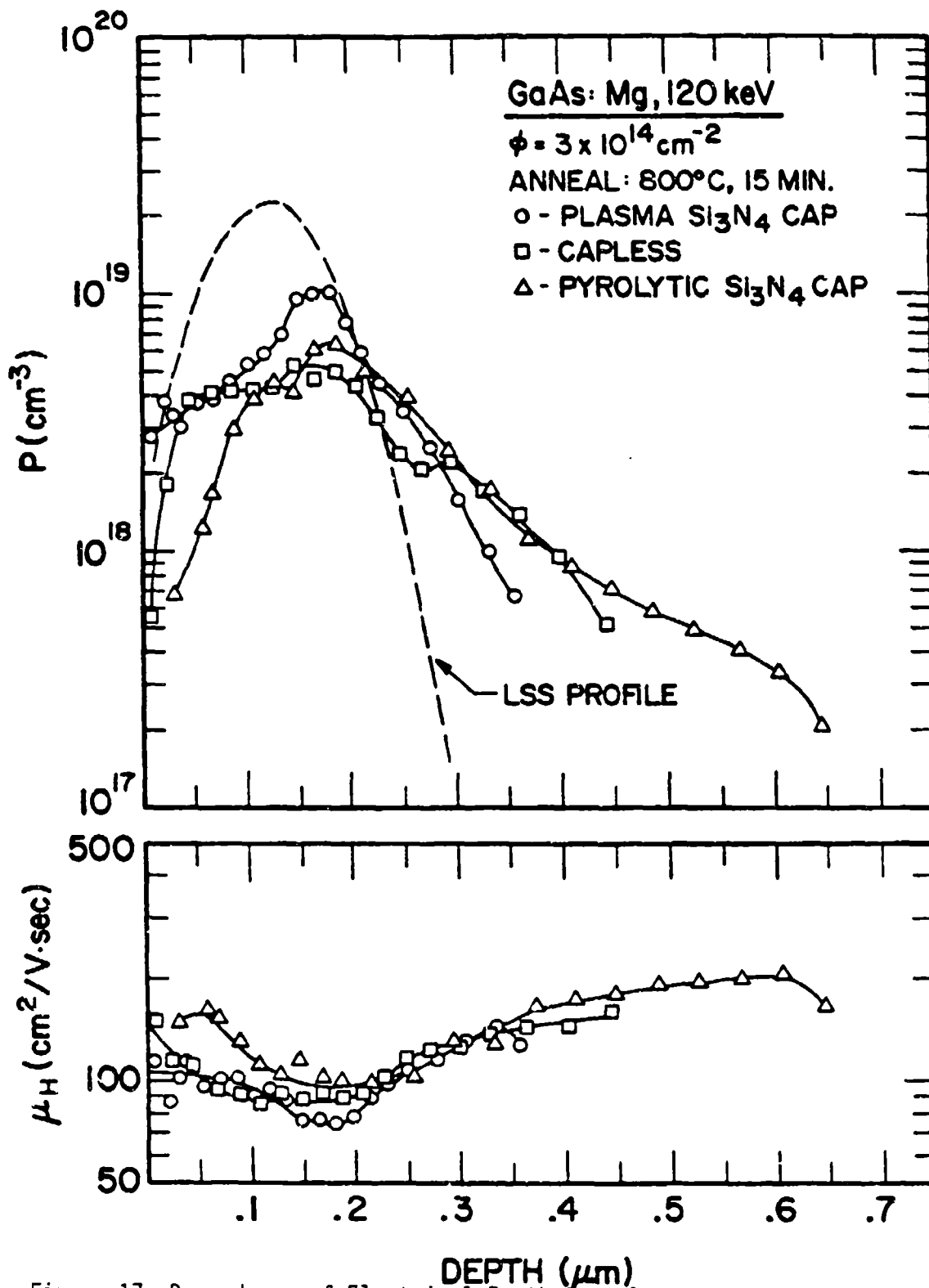


Figure 17 Dependence of Electrical Depth Profile upon Capping Method for GaAs:Mg Samples having a Dose of $3 \times 10^{14}/\text{cm}^2$

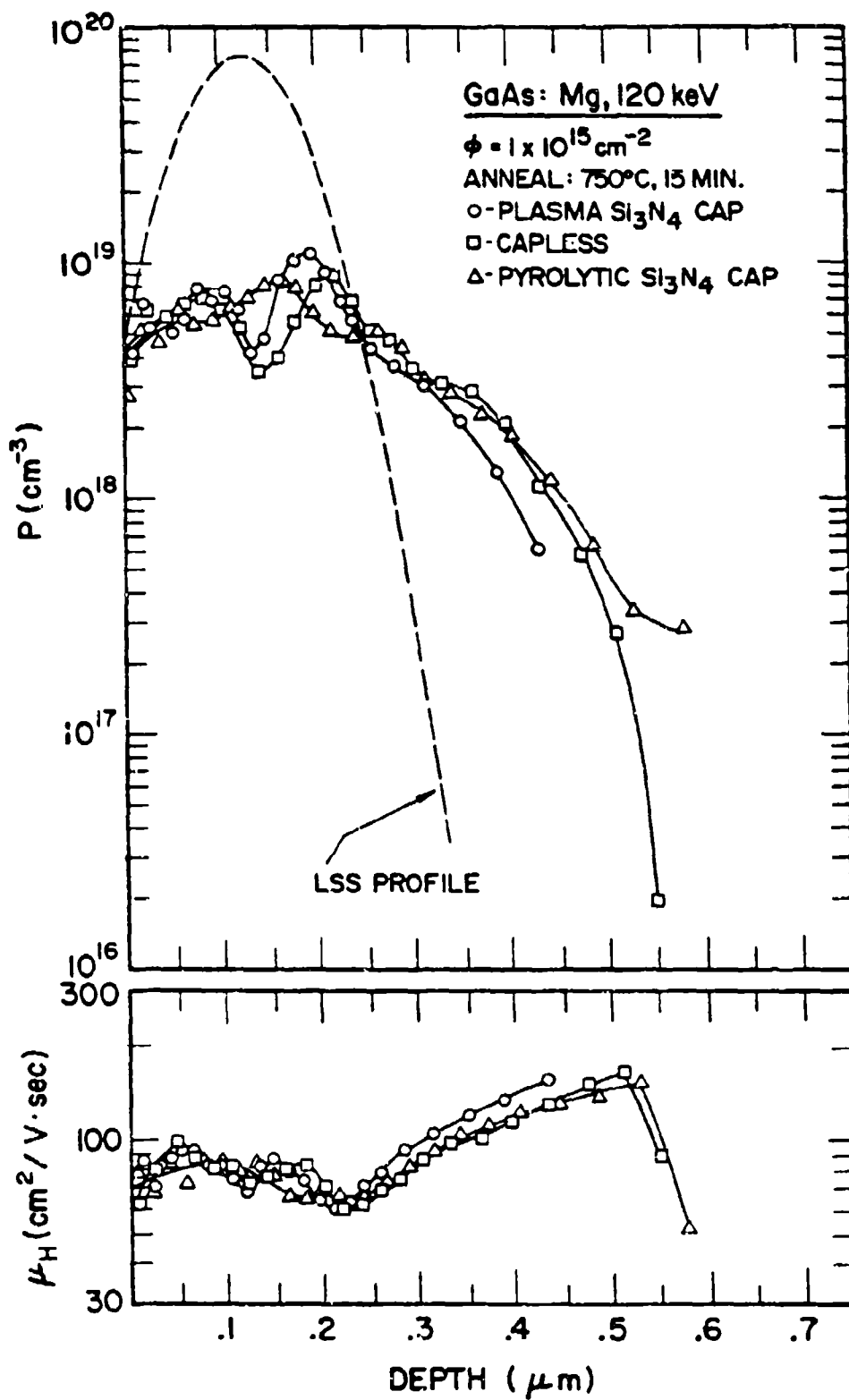


Figure 18 Dependence of Electrical Depth Profile Upon Capping Method for GaAs:Mg Samples having a Dose of $1 \times 10^{15} \text{ e}^-/\text{cm}^2$

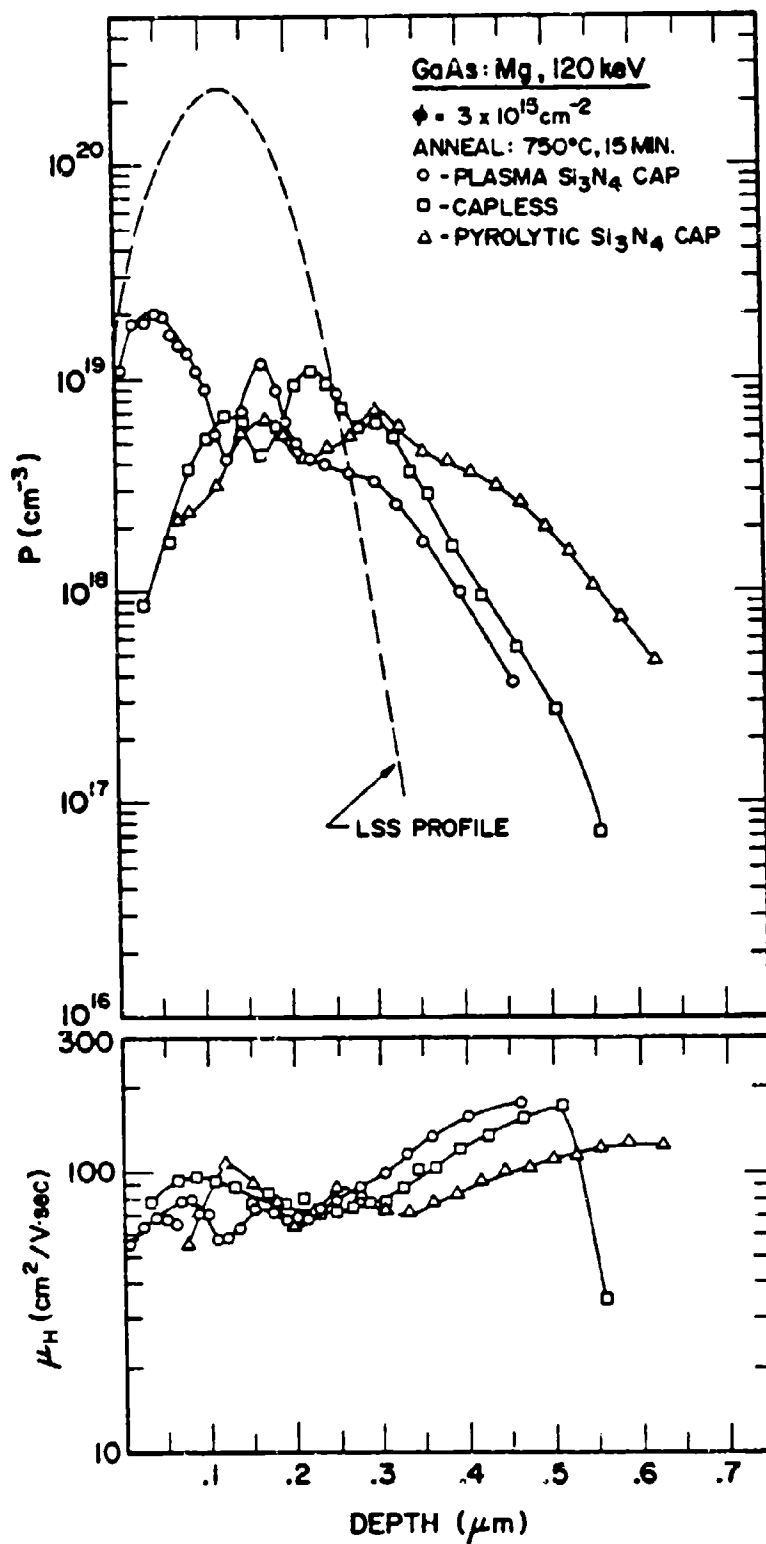


Figure 19 Dependence of Electrical Depth Profile Upon Capping Method for GaAs:Mg Samples having a Dose of $3 \times 10^{15}/\text{cm}^2$

theoretical Lindhard- Scharff- Schiott (LSS)¹¹ profiles are also shown in these figures for comparison purposes. The theory predicts that the peak concentration will occur at $\sim 0.124 \mu\text{m}$ for an ion energy of 120 keV. However, the peak concentrations do not generally occur at the position predicted by the LSS theory, and furthermore, the dopant profile data show a significant redistribution of Mg ions.

For an ion dose of $3 \times 10^{14}/\text{cm}^2$, as shown in Figure 17, the dopant profiles are highly dependent upon capping at the annealing temperature of 800°C , and show a broad indiffusion compared with that predicted by the LSS theory. The peak positions of maximum carrier concentrations are deeper than that of the theoretical curve, but they occur at about the same location ($\sim 0.17 \mu\text{m}$) for all three cappings. The dopant profile of the capless annealed sample exhibits a much broader peak region than the others. Depth profiles of capless and pyrolytic cap annealed samples show deeper tails than that of plasma cap annealed samples. It is evident from Figure 17 that considerably fewer electrically active Mg ions are found near the surface with pyrolytic cap annealing, perhaps due to significant outdiffusion of Mg ions. Mobility profiles show about the same trend for different cappings except in the case of pyrolytic capping near the surface, where values are somewhat higher. The hole mobility is generally higher near the surface, gradually decreases to the region of the maximum hole concentration, and then increases again with a decrease in carrier concentration.

For an ion dose of $1 \times 10^{15}/\text{cm}^2$, as shown in Figure 18, dopant profiles are also dependent upon capping, but to a lesser extent than for other doses shown. These profiles show a redistribution of implanted Mg ions extending to considerable depth into the sample compared with the LSS curve. All three curves generally agree near the surface, but become

significantly different in the peak and tail regions. Clear double peaks of depth profiles have been observed for the capless and plasma cap annealed samples, with minima rather than peaks near the LSS peak region. The reasons for this behavior are not well understood at present. The maximum carrier concentration obtained for this dose was $1 \times 10^{19}/\text{cm}^3$. Deeper profile tails have been observed for capless and pyrolytic cap than for plasma cap annealing. Mobility profiles show generally the same trend for different cappings.

For an ion dose of $3 \times 10^{15}/\text{cm}^2$, as shown in Figure 19, depth profiles of carrier concentrations and mobilities are strongly dependent upon capping and much more complicated than for other doses shown. Clear double peaks of dopant profiles have been observed for all three capping methods. A much deeper profile tail was observed with pyrolytic capping. It can be clearly seen from Figure 19 that significantly reduced numbers of electrically active Mg ions are found near the surface after both capless and pyrolytic cap annealing, possibly due to outdiffusion of Mg ions for these annealing methods. A maximum hole concentration of $2 \times 10^{19}/\text{cm}^3$ was obtained by plasma cap annealing.

Although surface-carrier concentrations shown in Figure 14 and 15 generally agree, dopant profiles in Figure 17-19 for the same dose and annealing temperature are generally highly dependent upon the capping technique. Pyrolytic capped samples usually show deeper profile tails and more outdiffusion of the implanted-Mg ions for the three doses investigated. Capless annealing yields deeper profile tails than plasma cap annealing, but not as deep as pyrolytic cap annealing. Except at depths well inside the sample, mobilities are generally lower ($<100 \text{ cm}^2/\text{V.s}$) for a dose of $1 \times 10^{15}/\text{cm}^2$ or higher in all three capping cases.

Electrical depth profiles of hole concentrations and Hall mobilities for samples annealed both with capless and plasma capping methods and implanted to three low doses of Mg ions, 1×10^{13} , 3×10^{13} , and $1 \times 10^{14}/\text{cm}^2$, are shown in Figure 20. It can be clearly seen from the figure that the depth profiles of carrier concentrations and mobilities are highly dependent upon dose. For samples having doses of 1×10^{13} and $1 \times 10^{14}/\text{cm}^2$, and annealed with a plasma Si_3N_4 cap, the peak concentrations occur at the position predicted by the LSS theory. At an ion dose of $1 \times 10^{14}/\text{cm}^2$, the dopant profile shows much more complicated structure than at lower doses. The depth profiles of carrier concentrations and mobilities differ significantly between the two capping methods for doses of 1×10^{13} and $1 \times 10^{14}/\text{cm}^2$. It is also evident that capless annealing produces deeper dopant profiles than plasma cap annealing for these two doses. However, little difference in profiles of hole concentrations and mobilities has been observed for a dose of $3 \times 10^{13}/\text{cm}^2$. Mobilities for a dose of $3 \times 10^{13}/\text{cm}^2$ or below are much higher in most of the implanted region than for a dose of $1 \times 10^{14}/\text{cm}^2$ until they finally fall off near the substrate.

Depth profiles of hole concentrations and mobilities for samples implanted to an ion dose of $1 \times 10^{14}/\text{cm}^2$ and annealed at 750°C with a plasma Si_3N_4 cap for different annealing times are shown in Figure 21. It has been found that the profiles are very sensitive to annealing time even at the same annealing temperature. Carrier concentrations and mobilities generally increase with annealing time up to 15 minutes throughout the implanted region. Complicated structures in dopant profiles can be seen for an annealing time of 15 minutes or longer. Some surface accumulation of Mg ions has been observed for the 30 minute anneal. This surface accumulation,

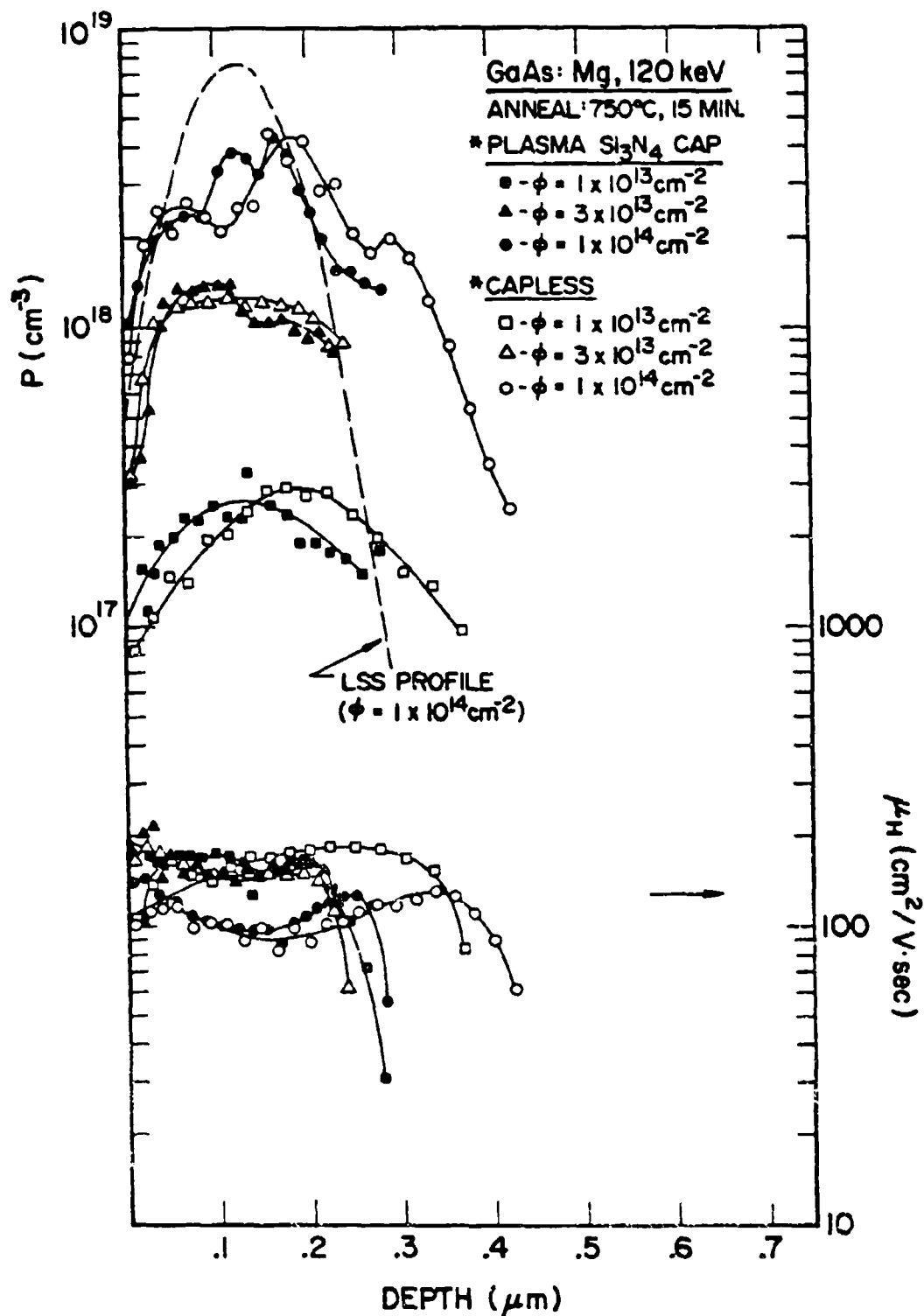


Figure 20 Dependence of Electrical Depth Profile Upon Capping Method for Lower-Dose GaAs:Mg Samples

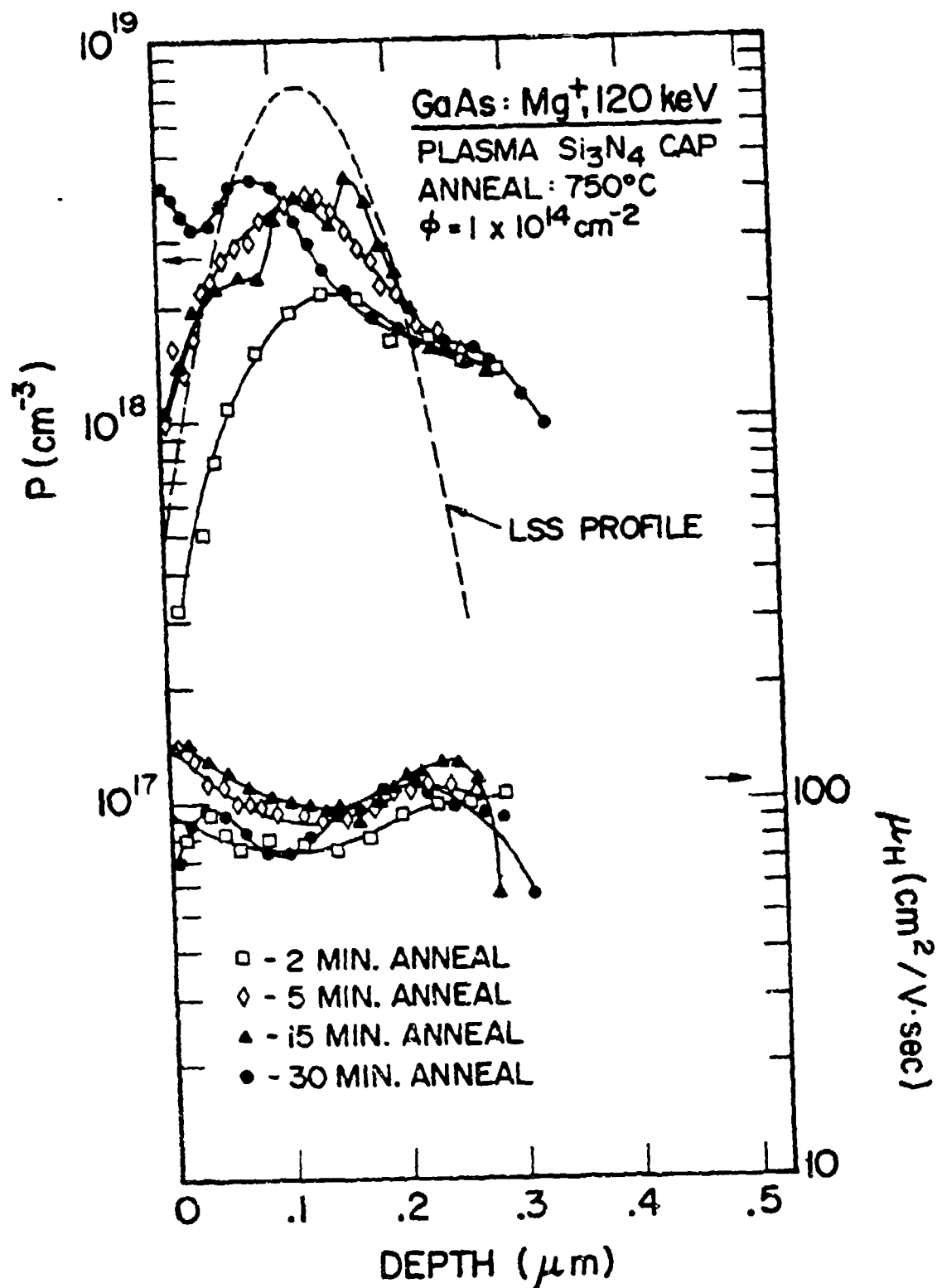


Figure 21 Dependence of Electrical Depth Profile Upon Annealing Time for GaAs:Mg Samples with PED Si_3N_4 Cap

together with low concentrations of Mg ions observed deeper within the sample, may indicate that implanted Mg ions did not out-diffuse more at an annealing time of 30 minutes. It is interesting to note that the tail sections of dopant profiles are nearly independent of annealing time. For the 2 and 30 minute annealings, mobilities are found to be quite low in the surface region.

3.3.3 Atomic Profiles

A few publications⁶⁻¹⁰ dealing with the electrical properties of magnesium-implanted GaAs have appeared in the literature. However, atomic distributions of Mg as-implanted or after annealing is not well known. Although the electrical activation of Mg implants in GaAs has been reported as generally good, carrier profiles have been found to be very sensitive to both implanted ion dose and annealing temperature. Also, carrier profiles generally show much broader distributions than those predicted by the theoretical 'Gaussian' Profiles.

In order to study Mg atomic distributions and to better understand the electrical behavior of Mg implants in GaAs, we have carried out a comparative study of secondary ion mass spectrometry (SIMS) atomic profiles and electrical carrier profiles, and the results are reported here. This work¹² contains, to the best of our knowledge, the first direct comparative study of this kind. In this study, both rf-plasma-deposited Si_3N_4 encapsulation and close-contact capless annealing methods were used as protective mechanisms during sample annealing. For the profile measurements, an annealing temperature of 750°C was chosen specifically because of the maximum electrical activation occurs at this temperature for nearly all doses. Also, the results for Mg-implanted GaAs will be compared with a similar study of sulfur-implanted GaAs. SIMS atomic profiles of Mg and Cr

were measured using oxygen-ion bombardment. Both the chemical etching rate and the sputtering rate were determined using a Sloan Dektak Surface Profile Measuring System.

The results of SIMS atomic profiles made on Mg-implanted GaAs samples implanted at an ion energy of 120 keV for doses ranging from 1×10^{13} to $3 \times 10^{15} \text{ cm}^{-2}$ are shown in Figure 22. The symbols indicate SIMS data taken for as-implanted samples, the solid curves indicate the best-fit curves of type-IV Pearson distributions,¹³ and the dashed curves indicate the Gaussian LSS profiles. In the SIMS analysis, background levels of Mg ($2 \times 10^{15} \text{ cm}^{-3}$) have been subtracted out, and the curves of as-implanted samples have been normalized in such a way that the integrated area under the SIMS output corresponds to the implanted-ion dose. Surface corrections have also been made for the first several data points, which often show abnormally high values, probably attributable to artifacts.

Implantation profiles are usually compared with Gaussian LSS profiles, which are determined by the projected range and the standard deviation of the projected range. For Mg-implanted GaAs, however, it turns out that this simple Gaussian approximation of implantation profiles using only two moments is not suitable, whereas a Pearson distribution of type IV, using four moments (projected range, projected range standard deviation, skewness, and kurtosis) describes the as-implanted profiles accurately over more than two orders of magnitude of the concentration range. In the curve fitting procedures, a theoretical distribution using the four moments as parameters is fitted by trial and error to an experimental distribution. The optimum fits of the type-IV Pearson distributions to experimental profiles for each dose are shown in Figure 22, and the four moments obtained from this fitting procedure are given in Table 2. The LSS range statistics predict that

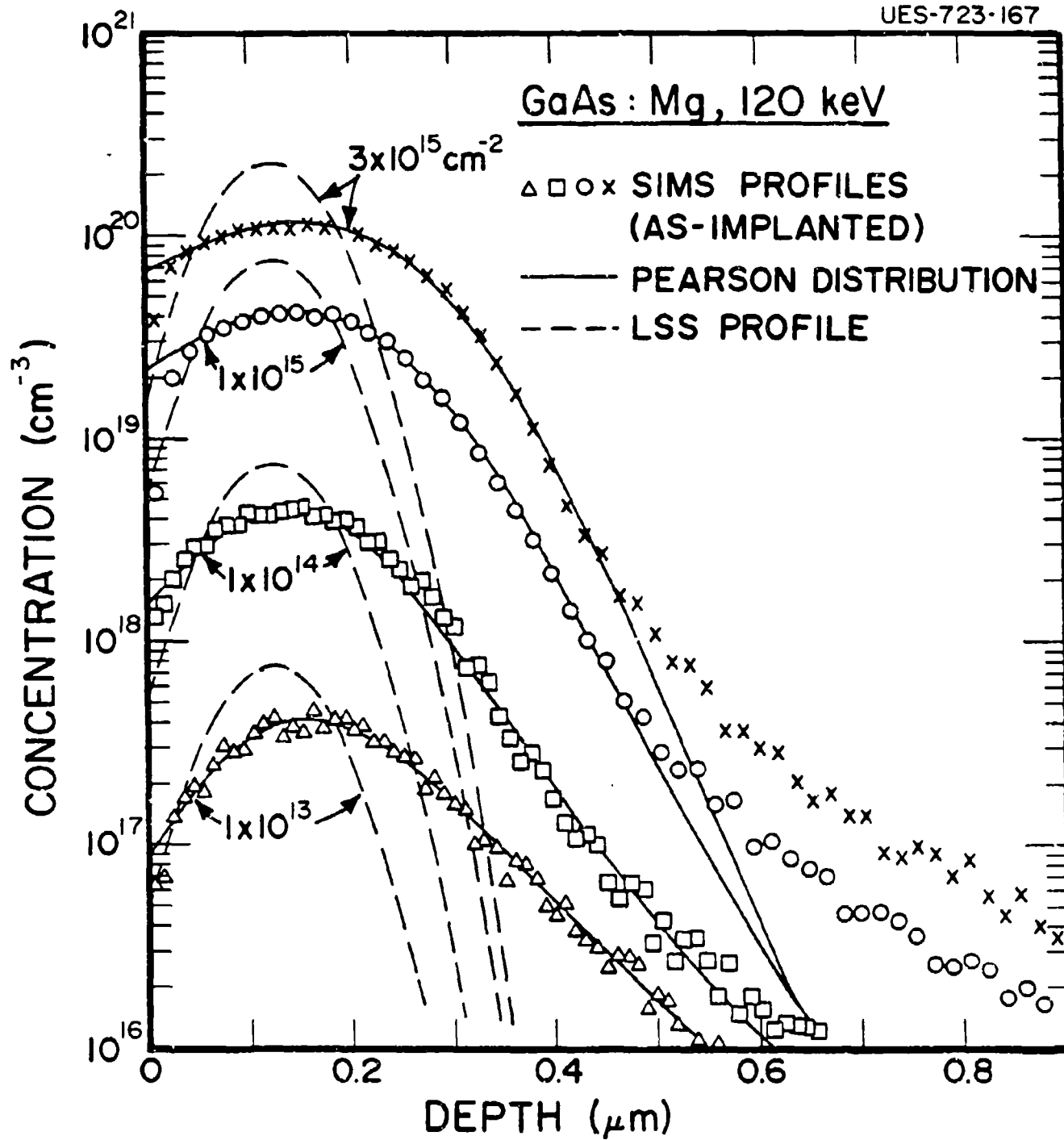


Figure 22 SIMS Atomic Profiles of As-Implanted GaAs:Mg Samples

TABLE 2

FOUR MOMENTS USED IN THE TYPE-IV PEARSON DISTRIBUTIONS TO FIT SIMS AS-IMPLANTED PROFILES OF Mg IMPLANTS IN GaAs IMPLANTED AT 120 keV FOR DIFFERENT ION DOSES.

Ion dose (cm ⁻²)	Projected range (μ m)	Projected range standard deviation (μ m)	Skewness	Kurtosis
1 X 10 ¹³	0.160	0.125	1.0	10
1 X 10 ¹⁴	0.150	0.120	-0.6	10
1 X 10 ¹⁵	0.165	0.150	-1.2	8
3 X 10 ¹⁵	0.155	0.165	-1.2	7

the projected range and the standard deviation of the projected range for the Mg implants in GaAs at 120 keV are 0.124 and 0.053 μm , respectively. However, the projected range and the projected range standard deviation obtained from the curve fitting procedure are nearly 30% and 200 to 300%, respectively, greater than those of the LSS theory. Although the projected ranges for different ion doses are all within 5% of the average value of 0.158 μm , the projected range standard deviation is slightly dose dependent even for the given ion energy of 120 keV, and it increases with ion dose. Both the skewness and kurtosis of the curves are also slightly dose dependent. It might be argued that the inadequate description of the SIMS profiles by the simple LSS theory is due to channeling, but the discrepancies are too great to attribute to channeling alone. Nonetheless, a small residual amount of channeling, which is difficult to suppress completely, might take place, and would be more apparent for the higher doses.

Comparisons of electrical profiles and SIMS profiles made on GaAs samples implanted at an ion energy of 120 keV with a dose of $1 \times 10^{13} \text{ cm}^{-2}$ and annealed at 750°C either with a PED Si_3N_4 cap or by using close-contact capless method are shown in Figures 23 and 24, respectively. For either annealing treatments, no significant amount of Mg outdiffusion was detected by SIMS measurements, and therefore the SIMS data for annealed samples were normalized in the same way as for the as-implanted samples. It can also be seen that no appreciable redistribution of the implanted Mg for this dose has taken place during annealing at 750°C for either annealing method. The SIMS profile shows only a slight amount of Mg accumulation near the peak region. No indiffusion of Mg took place; rather the SIMS profile shows a slightly smaller amount of Mg in the deep side of the implanted layer. By comparing the carrier distributions with the corresponding SIMS

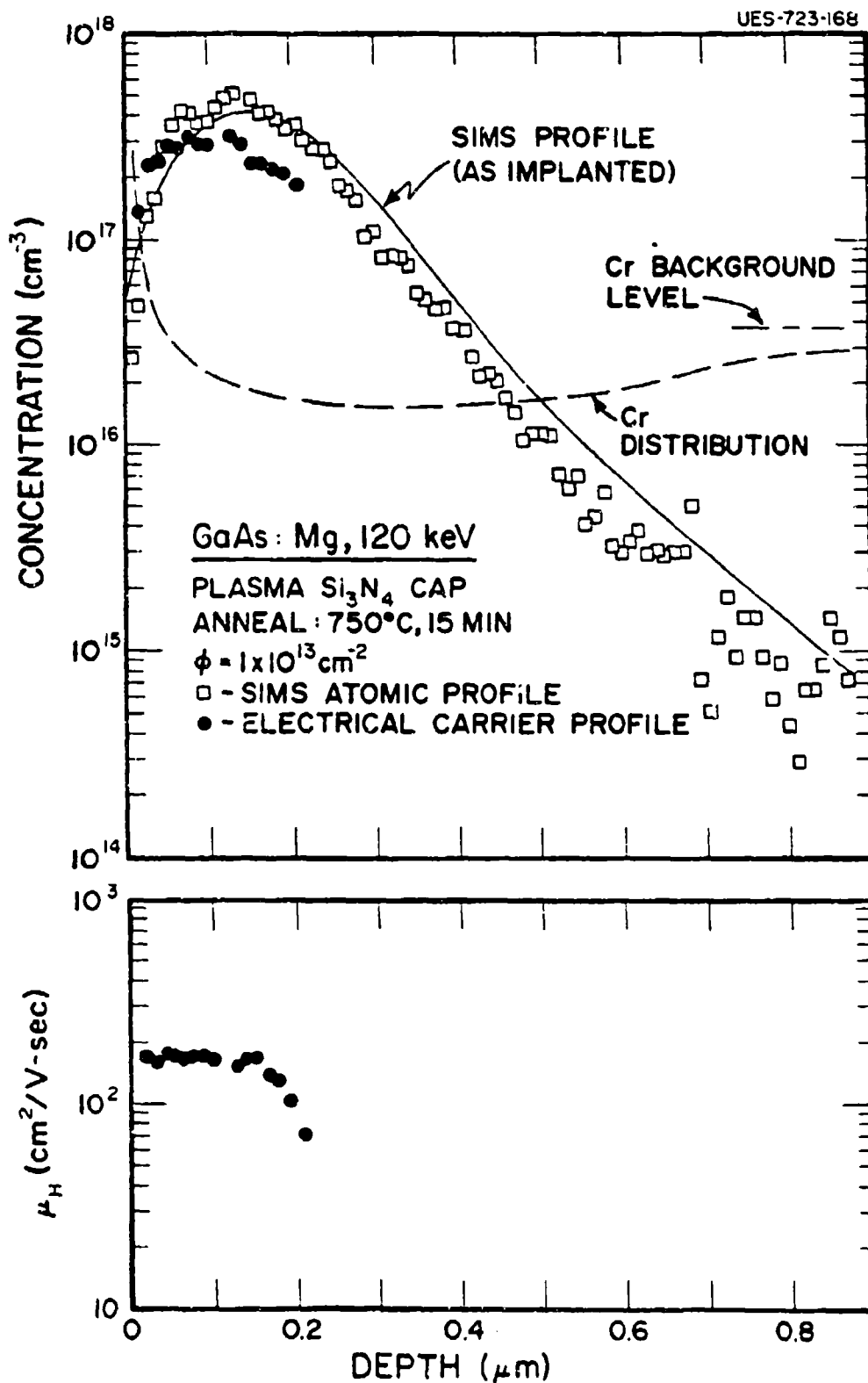


Figure 23 SIMS Atomic and Electrical Carrier Profiles of $1 \times 10^{13}/\text{cm}^2$ Dose GaAs:Mg Samples with PED Si_3N_4 Cap

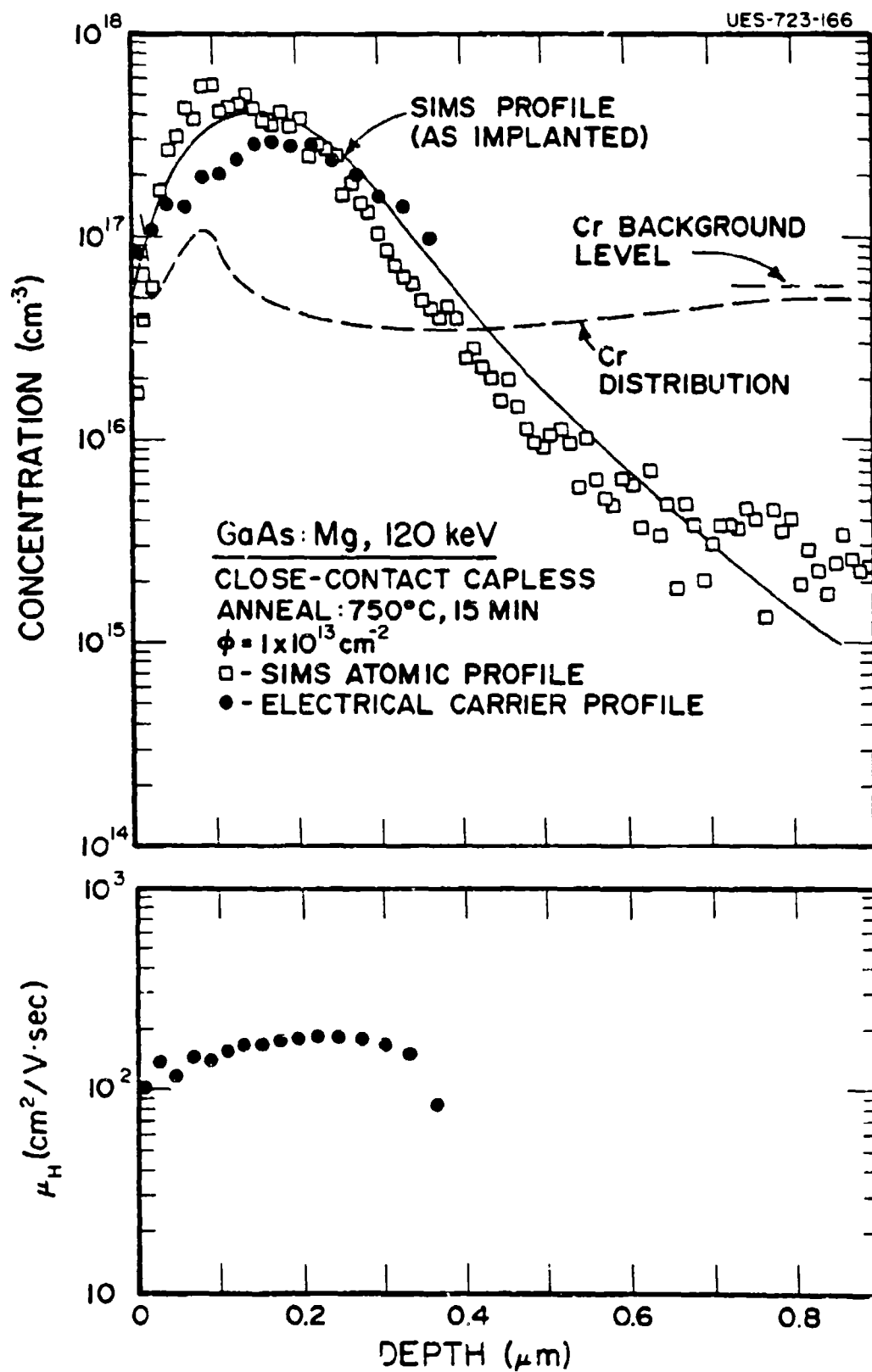


Figure 24 SIMS Atomic and Electrical Carrier profiles of $1 \times 10^{13}/\text{cm}^2$ Dose GaAs:Mg Samples Annealed Using a Close-Contact-Capless Method

profiles, it can be seen that there are some differences between the two profiles in the case of both annealing treatments. In particular, nearly 25% of the implanted ion dose is not electrically active in the peak-concentration region. although values of mobilities are reasonably good in this region, damage induced by ion implantation apparently is not completely annealed out. For this dose and 750°C anneal, the electrical activation efficiencies obtained were about 60% for the PED cap and about 75% for the capless annealed samples. As mentioned earlier, both electrical activation and mobility are improved by increasing the annealing temperature to 800°C.

The results of electrical profiles and SIMS profiles for a dose of $1 \times 10^{14} \text{ cm}^{-2}$ and 750°C anneal, either with a PED cap or by capless method are shown in Figure 25 and 26, respectively. By comparing the number of Mg ions for the annealed samples with that for as-implanted samples, it was found that a small amount ($\sim 13\%$) of the implanted Mg was lost by outdiffusion. In spite of this, the SIMS profiles for the annealed samples follow extremely well those for the as-implanted SIMS profiles in most of the implanted region for both annealing treatments. Furthermore, it appears that no indiffusion of Mg takes place for this dose and annealing temperature. The electrical carrier profiles also follow the SIMS profiles very closely for the annealed samples. Of the remaining Mg implants, nearly 90% or more were electrically activated in the peak-concentration region. Therefore, the resultant electrical activation efficiencies are very good, that is, 70% of the implanted ion dose for the PED cap and 88% for the capless annealed samples.

A similar comparison of electrical and SIMS profiles made on GaAs:Mg samples annealed at 750°C with a PED Si_3N_4 cap for a dose of $1 \times 10^{15} \text{ cm}^{-2}$ is shown in Figure 27. For this high dose, nearly 62% of the

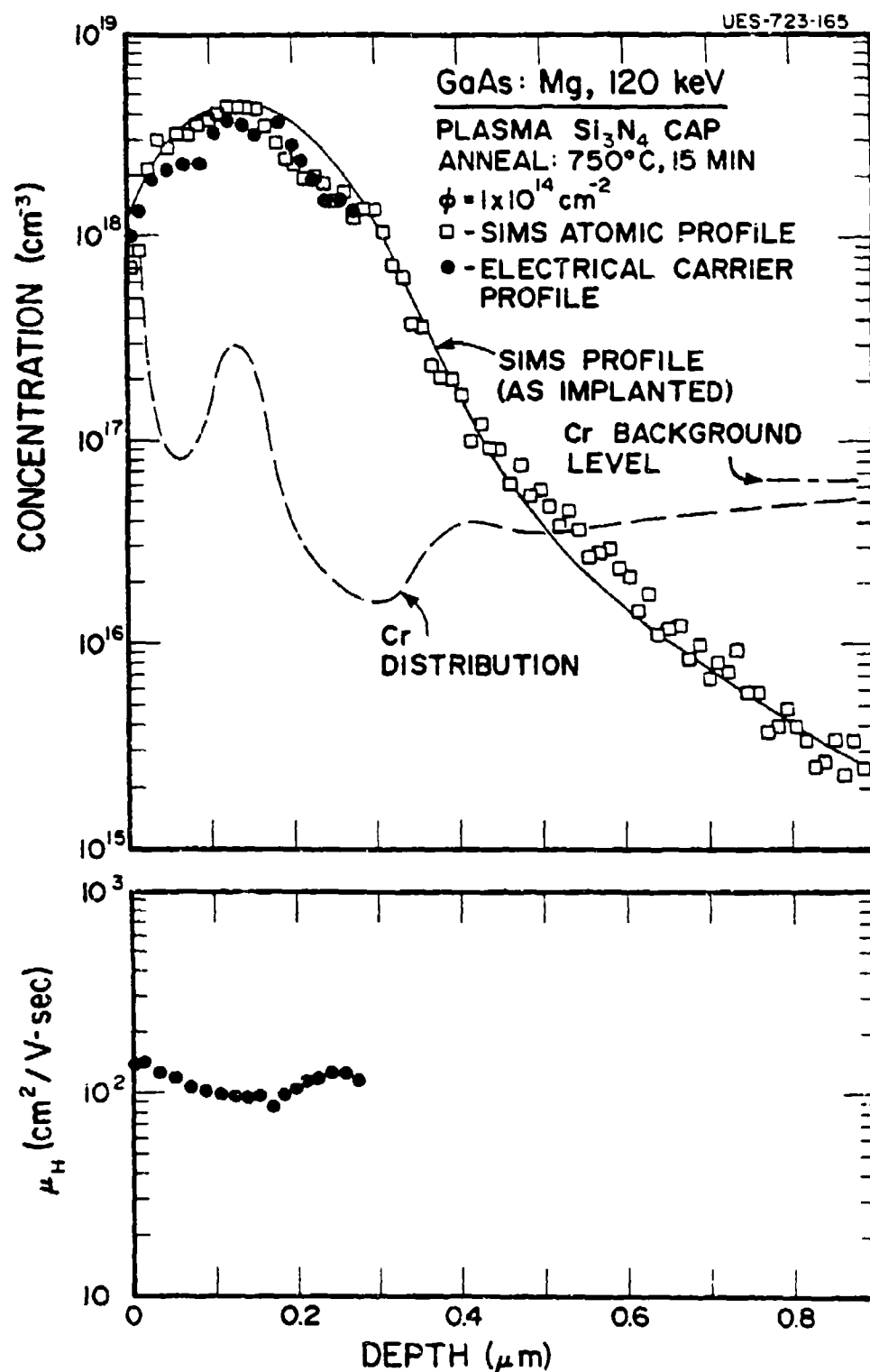


Figure 25 SIMS Atomic and Electrical Carrier Profiles of $1 \times 10^{14}/\text{cm}^2$ Dose GaAs:Mg Samples with PED Si_3N_4 Cap

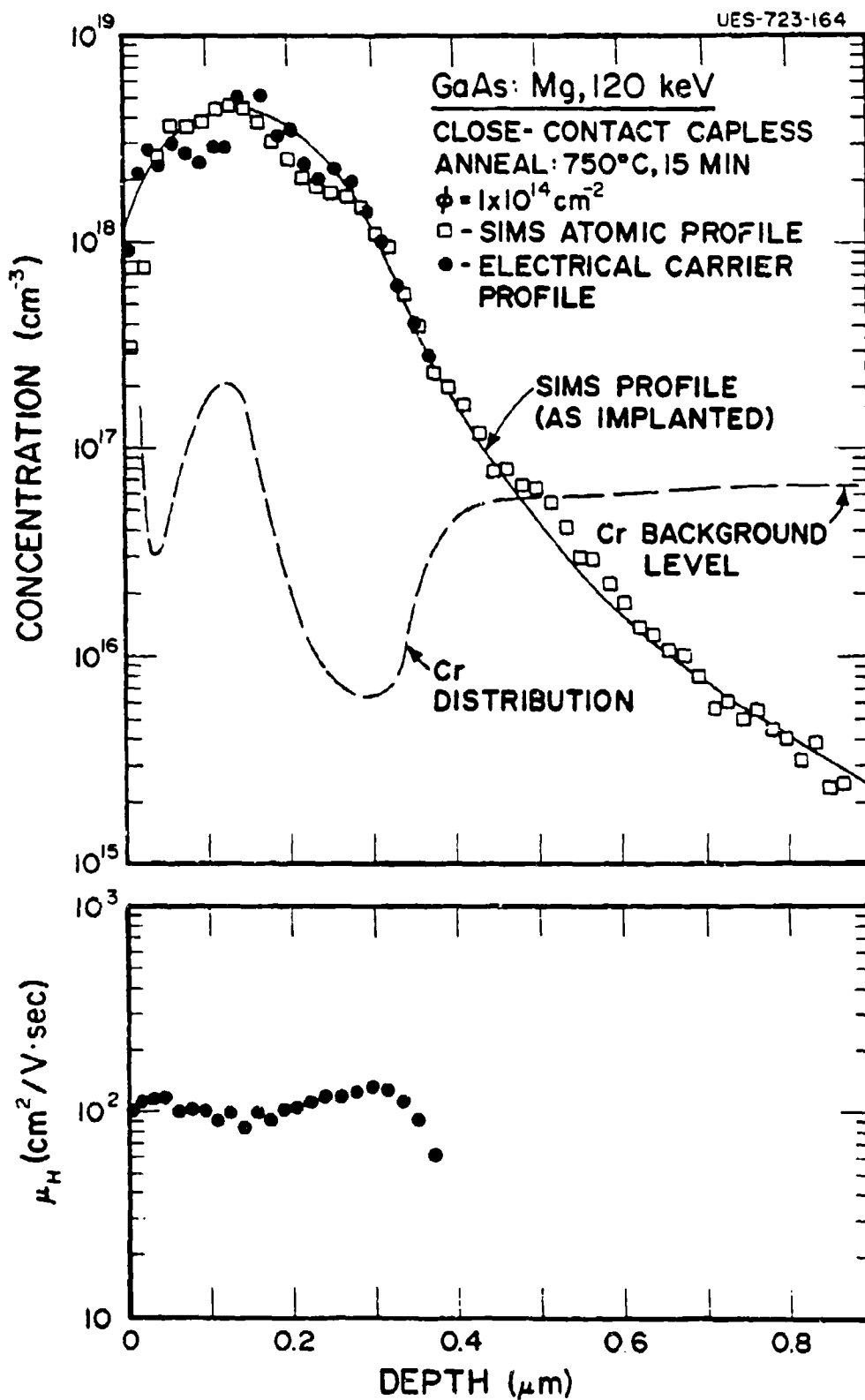


Figure 26 SIMS Atomic and Electrical Carrier Profiles of $1 \times 10^{14}/\text{cm}^2$ Dose GaAs:Mg Samples Annealed Using a Close-Contact-Capless Method

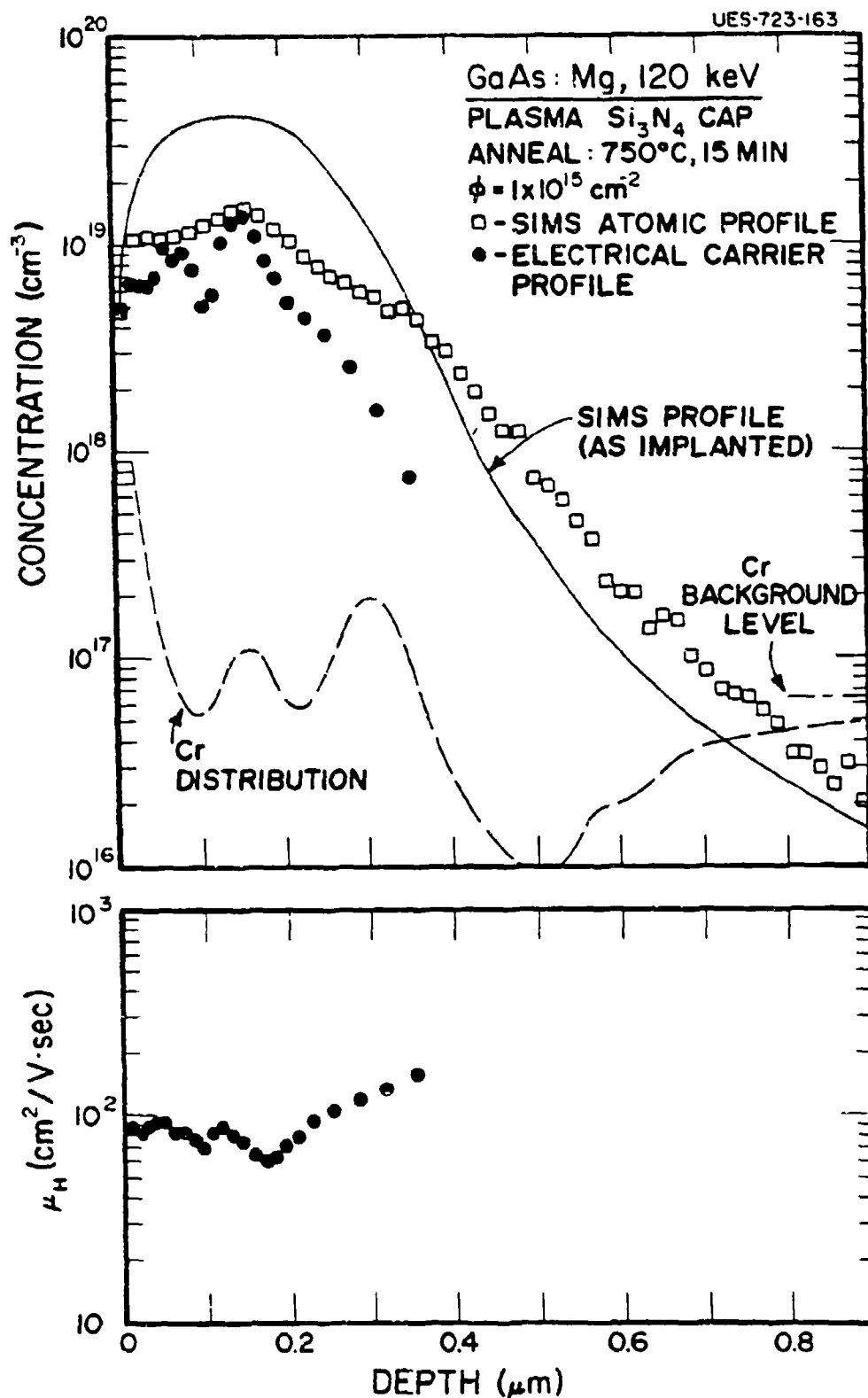


Figure 27 SIMS Atomic and Electrical Carrier Profiles of $1 \times 10^{15}/\text{cm}^2$
 Dose GaAs:Mg Samples with PED Si_3N_4 Cap

implanted Mg appears to be outdiffused during thermal annealing. Some of this loss, which occurs mostly from the Mg located in the peak-concentration region, could be attributed to the solubility limit of Mg in GaAs. Also, there can be seen a slight indiffusion of the implanted Mg in the tail section of the profile. Even among the remaining Mg, only about 54% is electrically active, and the carrier profile deviates substantially from the SIMS distribution of the annealed sample. The large amount of Mg outdiffusion and the partial electrical activation of the remaining Mg can account for the low electrical activation efficiency of 20% obtained for this dose.

The results of electrical and SIMS atomic profiles made on samples annealed at 750°C using the close-contact capless method for a dose of $3 \times 10^{15} \text{ cm}^{-2}$ are shown in Figure 28. For this dose, the amount of Mg outdiffusion upon annealing is even greater, almost 81% of the implanted ion dose. A slight amount of Mg indiffusion can also be seen in the tail region of the profile. In addition to the severe Mg outdiffusion, only about 35% of the remaining Mg is electrically active. Consequently, the electrical activation efficiency is very low, only about 7% of the implanted ion dose. Although the carrier profile deviates substantially from the SIMS profile of the annealed sample, the shapes of both curves are very similar. For the two higher doses, the mobilities are generally low ($< 100 \text{ cm}^2/\text{V}\cdot\text{sec}$) in most of the implanted region.

Cr profiles together with Cr-background levels of the GaAs:Mg samples are also shown in Figure 23-28. The Cr profiles are flat before annealing for all doses, but the Cr redistributes during annealing. A surface accumulation of Cr is generally observed for all doses upon annealing, followed by a Cr-depleted region and one or two peaks in the Cr distribution. Most peaks are located near the implanted peak region. Apparently the Cr is

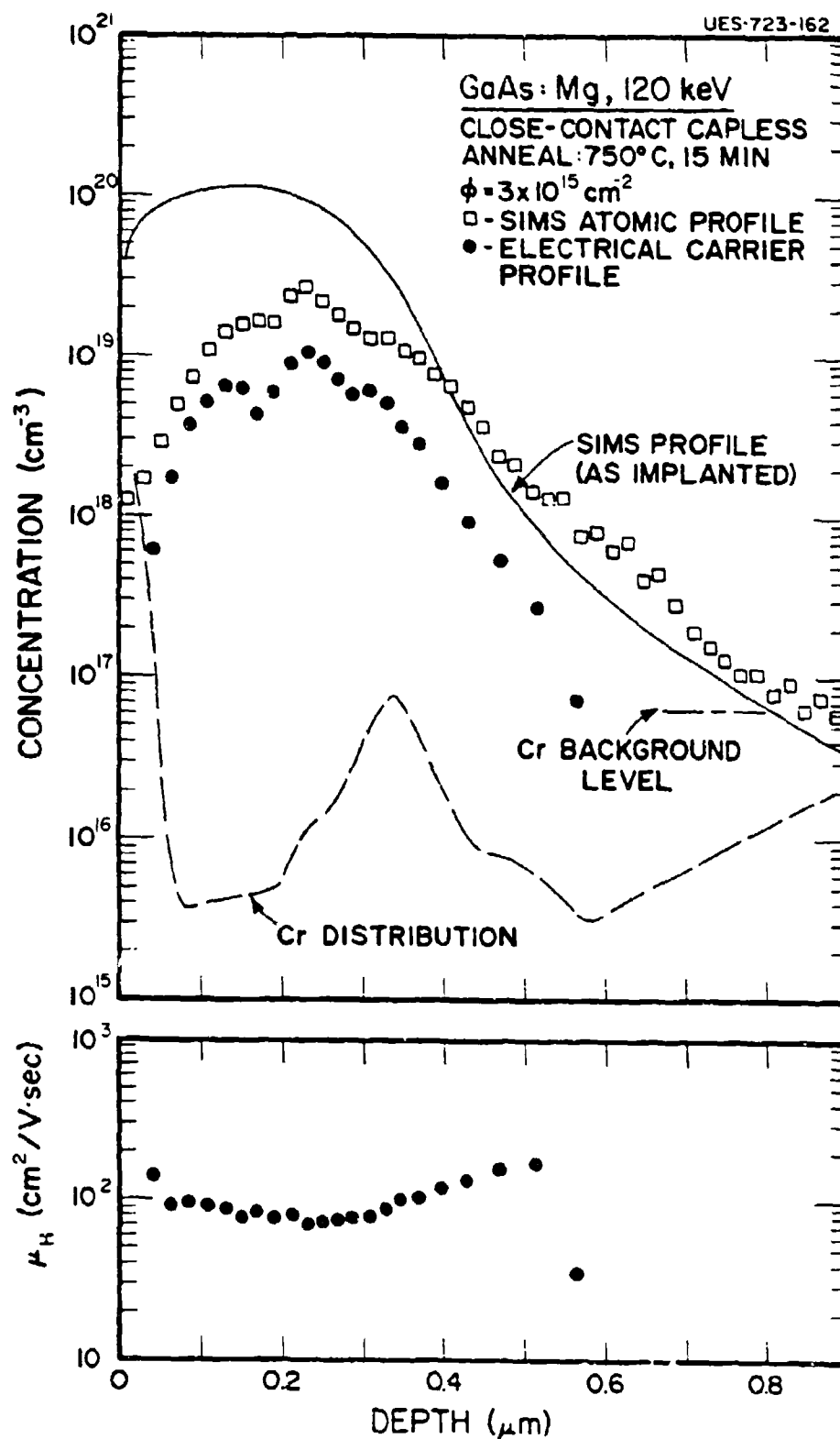


Figure 28 SIMS Atomic and Electrical Carrier Profiles of $3 \times 10^{15}/\text{cm}^2$ Dose GaAs:Mg Samples Annealed Using a Close-Contact-Capless Method

gettered in regions where defects and/or implanted damage are great as reported by Vasudev et al.¹⁴ However, at present we can not determine any direct correlation between Cr redistribution and the electrical carrier profile. Carrier concentrations are probably too high to exhibit the effect of the Cr redistribution.

It is interesting to compare the results of Mg-implanted GaAs, which produces a p-type layer, with those of sulfur-implanted GaAs, which produces an n-type layer. Detailed results of a comparative study of SIMS atomic profiles and electrical carrier profiles for S implants in GaAs will be reported later. Figure 29 shows an overall picture of the carrier profiles and SIMS profiles (both annealed and unannealed) made on samples implanted with S at an ion energy of 120 keV for three ion doses and annealed at 900°C. In comparing both ion species, it must be remembered that the annealing temperatures are different - 750°C for Mg implants and 900°C for S implants. However, in each case the basic behavior of the implant is presented at its own optimum annealing temperature.

In contrast to the results for Mg implants, it has been observed that for low dose ($\approx 1 \times 10^{13} \text{ cm}^{-2}$), the implanted S undergoes substantial redistribution during annealing at 900°C throughout the entire implanted region, while for high dose ($\approx 1 \times 10^{14} \text{ cm}^{-2}$), S redistributes to a much lesser extent in the implanted peak region. Sulfur implants in GaAs before annealing generally follow the theoretical LSS profiles except in the deep side of the implanted layer. Significant indiffusion of S takes place during annealing for all doses, whereas no significant indiffusion of Mg takes place for any dose. Also it has been observed that there is no appreciable sulfur outdiffusion during annealing at 900°C at any dose, while a substantial amount of Mg outdiffusion takes place during annealing at 750°C for high doses ($\approx 1 \times$

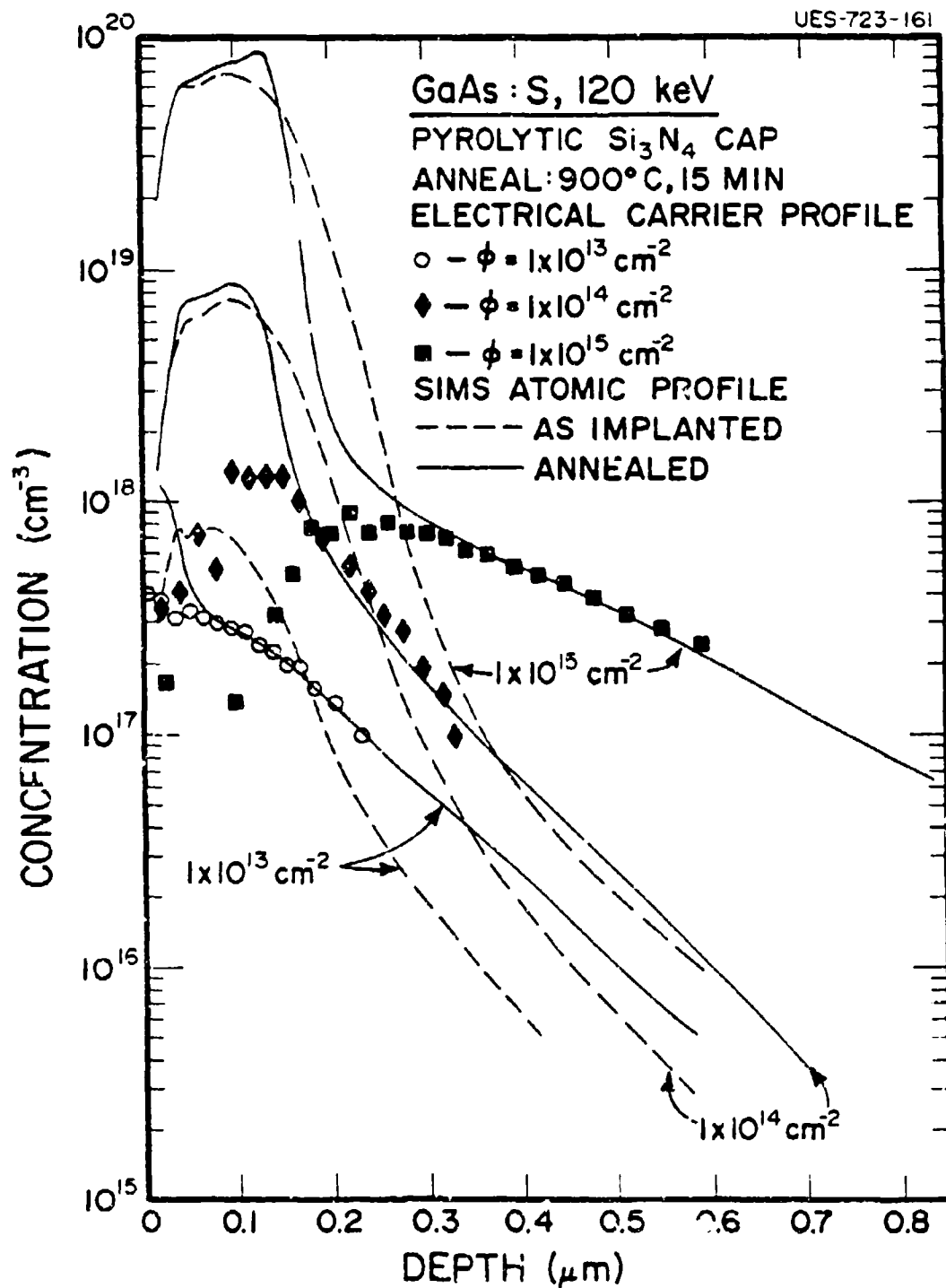


Figure 29 SIMS Atomic and Electrical Carrier Profiles of GaAs:S Samples
 Annealed at 900°C with CVD Cap

10^{14} cm^{-2}). It is believed that the observed low electrical activation for GaAs:S is not caused chiefly, if at all, by outdiffusion of S, but by a substantial amount of inactivated S due to precipitates and/or residual defects, whereas for GaAs:Mg, the outdiffusion of Mg is the main cause for the low electrical activation for high dose ($\geq 1 \times 10^{14} \text{ cm}^{-2}$). As shown in the figures, the maximum carrier concentration of Mg implants is about one order of magnitude higher than that of S implants.

3.3.4 Summary

Mg-implanted GaAs produces p-type conductivity, with maximum electrical activation occurring at 750°C for ion doses $> 3 \times 10^{13} / \text{cm}^2$. Lattice damage due to ion bombardments is reduced appreciably even at an annealing temperature of 600°C . Although electrical activations for an ion dose of $1 \times 10^{13} / \text{cm}^2$ are markedly dependent upon capping, activations for higher doses show general agreement for the three capping methods investigated. Most of the electrical activation occurs after very short anneal time for the Mg-implanted samples. The mobilities are surprisingly good even after annealing at 750°C for only 2 minutes.

The results of the comparative study of the three capping/anneal methods used in these investigations do not permit an unqualified conclusions that any one is superior to the others. The advantages of one method over the others may be dependent upon application. In general, pyrolytic caps appear to be slightly better in terms of activation at higher annealing temperatures for all doses examined, although their higher deposition temperature makes them less suitable at lower annealing temperatures. Plasma caps are preferable at lower annealing temperatures, where capless annealing is also effective.

Peak positions of carrier profiles generally do not agree with those of LSS theory, and significant redistribution of Mg ions takes place. The carrier profiles are found to be highly dependent upon implanted ion dose, anneal temperature, anneal time, and capping/anneal method. Carrier profile structures become more complicated as the ion dose increases, exhibiting double peaks at high doses. The maximum carrier concentration obtained was $2 \times 10^{19}/\text{cm}^3$. In general, pyrolytic capping results in more outdiffusion than other cappings. Although capless annealing generally yields slightly deeper profiles than plasma cap annealing, the capless method used in this study has proved very effective. It may be worthwhile to point out that the close-contact capless method used in this study is simple, rapid, and reproducible.

We also found that Mg implants in GaAs before annealing do not follow Gaussian LSS profiles but can be represented by the type-IV Pearson distributions. Mg implants do not show significant indiffusion during annealing at 750°C for the doses investigated here. For low dose ($\leq 1 \times 10^{14}/\text{cm}^2$), the SIMS profiles of annealed samples follow very closely those of as-implanted samples. However, the amount of Mg outdiffusion increases substantially with implanted ion dose during annealing for high dose ($> 1 \times 10^{14}/\text{cm}^2$). The percentage of outdiffusion is found to be 13, 62, and 81% of the implanted dose for doses of 1×10^{14} , 1×10^{15} , and $3 \times 10^{15}/\text{cm}^2$, respectively. Consequently, electrical activation efficiencies show a strong dependence on the implanted ion dose. It is believed that the outdiffusion of Mg is the main source of poor electrical activation efficiencies at high doses. These results suggest that the decrease in activation efficiency for the samples annealed at higher temperatures may also be due to Mg outdiffusion. Although most of the Mg ions become

electrically active upon annealing at low doses, a considerable number of the remaining Mg ions for high doses do not become electrically active, probably due to residual defects. In general, electrical carrier profiles follow roughly the SIMS atomic profiles of annealed samples, showing almost perfect agreement for a dose of $1 \times 10^{14}/\text{cm}^{-2}$. Results obtained in this study suggest that Mg implantation into GaAs is a good candidate for device fabrication of p-type layers, because of its predictable carrier profiles and reasonably good electrical activation and mobility for low doses.

3.4 Ge-IMPLANTED GaAs

The concept of dual implantation in compound semiconductors, as proposed by Heckingbottom and Ambridge¹⁵, has been tested by several workers to improve the electrical activity and inhibit the diffusion of certain implant species. This approach is based on the maintenance of stoichiometry in the host lattice in order to avoid compensation due to vacancy complexes with the dopant. In the case of amphoteric dopants, dual implantation permits shifting the probability of lattice site occupancy by the dopant to favor either n- or p-type activity. By control and shift of defect stoichiometry in GaAs, precise control of the behavior of the dopants can be attained.

Some degree of success has been achieved in the production of high carrier concentrations by dual implantation. For example, in comparison with Se single implants into GaAs, donor activity enhanced by the implantation of an equal dose of Ga has been reported.¹⁶⁻¹⁸ The improvement of p-type activity has been observed as a result of the dual implantation of C and Ga into GaAs.¹⁹ Dual implants of Zn or Cd and As into GaAs have been found to considerably decrease the diffusion of the implanted Zn or Cd.^{20,21}

We have employed the technique of dual implantation in order to study the amphoteric behavior of Ge implants in GaAs²² and to elucidate the

interaction mechanisms of implanted ions with native and induced type defects in the host crystal. An understanding of the physics involved in the behavior of Ge implants is particularly important in applications where the amphoteric nature of the dopant is used to advantage. Ge has been widely used as a dopant in epitaxial layers of GaAs because of its low diffusivity. Ge has also been utilized to produce stable, reliable, and reproducible ohmic contacts to n-type GaAs by methods which achieve high densities of Ge almost exclusively on Ga lattice sites.²³ More recently, the feasibility of fabricating p/n junctions and p/n multilayers using Ge dopants in GaAs by molecular beam epitaxy has been demonstrated.²⁴

The single implants of Ge in GaAs have shown amphoteric behavior, where the conductivity type, electrical activity, and carrier mobility depend critically upon ion dose and annealing temperature.²⁵ Low doses of the Ge implant appear to favor substitution into As sites, resulting in p-type activity, while high doses show n-type activity due to preferential occupation of Ga sites by the Ge ions.

The addition of Ga by dual implantation of Ga and Ge into GaAs²⁶ is expected to favor As site occupancy by the Ge ions and an enhancement of p-type activity, while the addition of As²⁷ would encourage Ga site occupancy and result in enhancement of n-type activity. Although a dual implantation with amphoteric dopants such as Ge is expected to be more complicated than with Group II or Group VI dopants of the periodic table, in which case the dopants locate almost exclusively on one of the sub-lattice sites, the above expectations are generally consistent with the experimental results reported here.

The single and dual implantations were carried out at an energy of 120 keV with doses ranging from 5×10^{12} to $3 \times 10^{15}/\text{cm}^2$ at room

temperature into semi-insulating Cr-doped GaAs. In the case of the dual implantations, Ga or As ions were implanted after the Ge implants. In each case, equal doses of the dual implants were used. During annealing the samples rested cap-side down on bare GaAs substrates in order to improve the performance of the caps. In this way, the caps held very successfully at temperatures as high as 1000°C. No sign of surface degradation could be observed by visual inspection. It should be pointed out that contacts made on the (Ge + Ga) dual implants usually showed good ohmic behavior even without ohmic anneal.

Similar GaAs control samples, implanted with the same dose of Ga or As alone were also prepared by the same procedures, and annealed at various temperatures. The test samples did not show appreciable electrical activity, and in most cases no Hall effect could be observed.

3.4.1 Ge Single Implants

Figure 30 shows the results of electrical measurements made on semi-insulating Cr-doped GaAs samples implanted with Ge to ion doses ranging from $5 \times 10^{12}/\text{cm}^2$ to $3 \times 10^{15}/\text{cm}^2$ and annealed at various temperatures. The anneal behavior of the sheet-carrier concentration indicates that for samples having an ion dose of $< 3 \times 10^{13}/\text{cm}^2$, the electrical activity increases monotonically with anneal temperature. The highest electrical activation efficiency obtained was 38% for an ion dose of $10^{13}/\text{cm}^2$ and annealed at 950°C for 15 minutes. Below 850°C the electrical activity is very low for samples having an ion dose of $< 10^{13}/\text{cm}^2$, although definite p-type conductivity (solid lines) becomes apparent at around 750°C. For samples implanted to an ion dose of $10^{14}/\text{cm}^2$, the electrical activity increases gradually with anneal temperature, yielding the highest activation (11%) at about 850°C, and then decreases at higher anneal temperatures. The

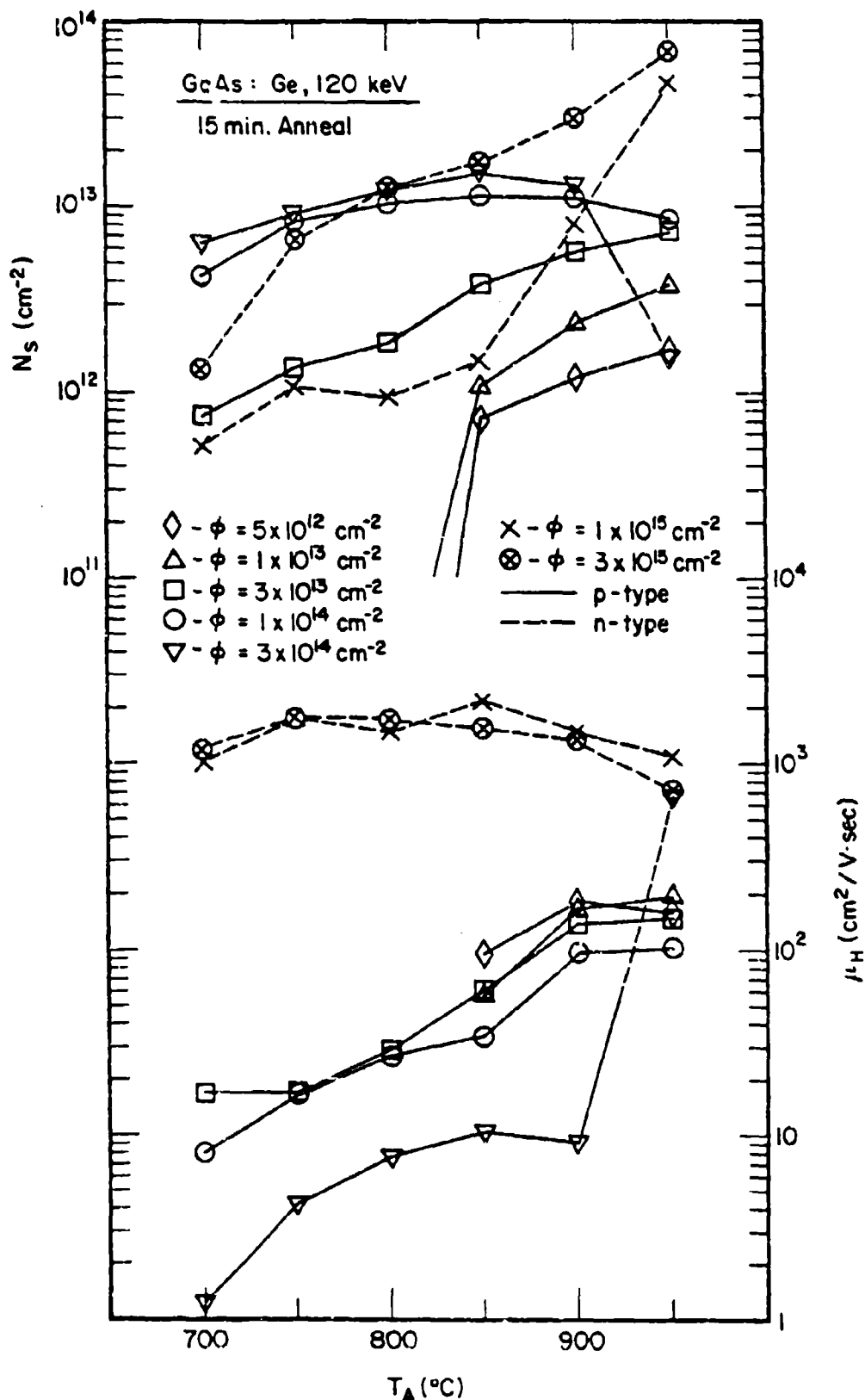


Figure 30 Dependence of Surface-Carrier Concentration (N_s) And Hall Mobility (μ_H) upon Annealing Temperature (T_A) for GaAs:Ge

anneal behavior for an ion dose of $3 \times 10^{14}/\text{cm}^2$ is similar to that for $10^{14}/\text{cm}^2$ up to 900°C . However, the electrical activation drops sharply (to 0.5%) at 950°C accompanied by conductivity type conversion (indicated by dashed lines in the figure). For the two highest doses, the implanted layer is n-type at all anneal temperatures and the electrical activity increases with anneal temperature, but the activation efficiencies are low (only 5% and 2% for ion doses of 10^{15} and $3 \times 10^{15}/\text{cm}^2$, respectively, even after annealing at 950°C for 15 minutes.

The anneal behavior of the carrier mobility indicates that the mobility increases with anneal temperature for samples having doses of $<10^{14}/\text{cm}^2$, which implies that the lattice damage due to ion bombardment is appreciably reduced with increasing anneal temperatures. However, the mobilities of samples with an ion dose of $3 \times 10^{14}/\text{cm}^2$ remain low - below about $10 \text{ cm}^2/\text{V}\cdot\text{sec}$ with the sample remaining p-type up to 900°C anneal. The mobility increases with anneal temperature up to 850°C , levels off, and then increases sharply at an anneal temperature of 950°C , becoming n-type as indicated by the dashed line. The low value of mobility at this dose may be due to high electrical compensation. The mobility anneal behavior of n-type layers is different from that of p-type layers. The mobilities for the two highest doses remain essentially constant for all anneal temperatures. The slight decrease in mobility above 900°C , although accompanied by increasing activation, may be somewhat related to lattice defects created during high-temperature anneal.

As shown, the electrical behavior of Ge implants in semi-insulating Cr-doped GaAs is very complicated, producing both p- and n-type activity depending upon both ion dose and anneal temperature. This behavior is in contrast to the n-type activity for all doses reported by

Surridge and Sealy²⁸ and is unlike that of implanted silicon which produces only n-type activity.²⁹ Even though no theory is available to explain present experimental results, the general electrical behavior suggests that in samples of lower dose and anneal temperature, the implanted Ge ions go into As sites preferentially, producing p-type activity. As the Ge-ion dose and anneal temperature increase, increasing numbers of Ge ions go into Ga sites than into As sites, producing, n-type activity; the compensation level still remains high. There is a possibility that defects such as As or Ga vacancies (both intrinsic and extrinsic), or residual damage may influence the electrical activity. However, it is evident that the amphoteric electrical behavior is due mainly to the implanted Ge ions because: (1) no significant number of acceptors or donors has been found in the unimplanted substrates, even after annealing at 900 or 950°C; (2) not only p-type but also n-type activation continues to increase monotonically with anneal temperature as high as 950°C, except for the two intermediate doses which are nearing the type conversion; and (3) no distinct Hall effect due to damage produced by krypton implantation has been observed from samples having doses of 10^{14} and 10^{15} Kr^+ -ions/ cm^2 .

3.4.2 (Ge + Ga) and (Ge + As) Dual Implants

The results of electrical measurements made on semi-insulating Cr-doped GaAs implanted with (Ge + Ga) and (Ge + As) to ion doses ranging from 10^{13} to $3 \times 10^{15}/\text{cm}^2$ and annealed at various temperatures, together with the comparable variation for the single implanted Ge, are shown in Figures 2-7.

For doses of $10^{13}/\text{cm}^2$ (Figure 31) and $3 \times 10^{13}/\text{cm}^2$ (Figure 32), p-type conductivity has been observed for both single and dual implants at all anneal temperatures. The annealing behavior of the sheet-carrier concentration indicates that electrical activity increases

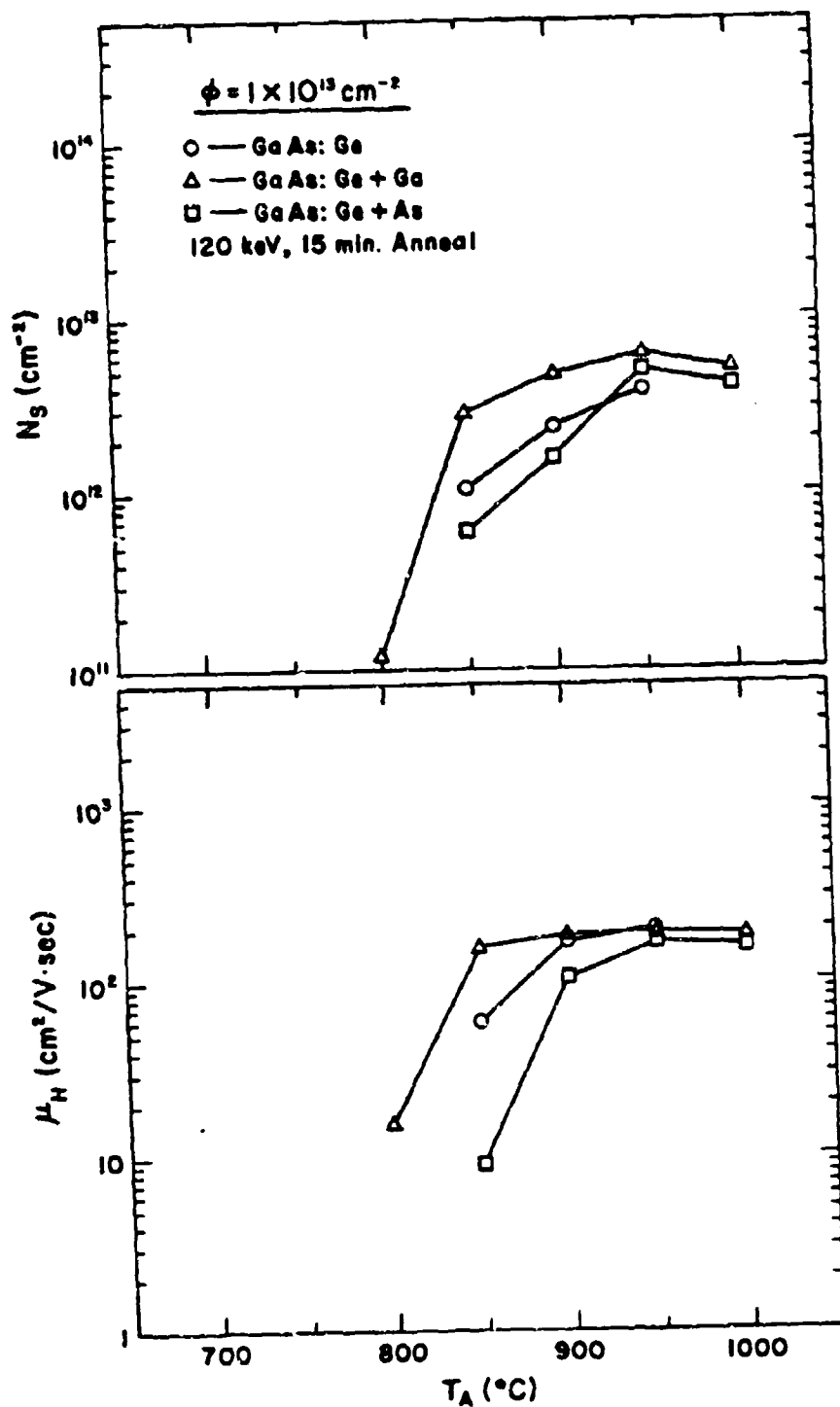


Figure 31 Dependence of Surface-Carrier Concentration (N_s) and Hall Mobility (μ_H) upon Annealing Temperature (T_A) for an $1 \times 10^{13}/\text{cm}^2$ Dose of single Ge, Dual (Ge + Ga) and (Ge + As) Implants in GaAs

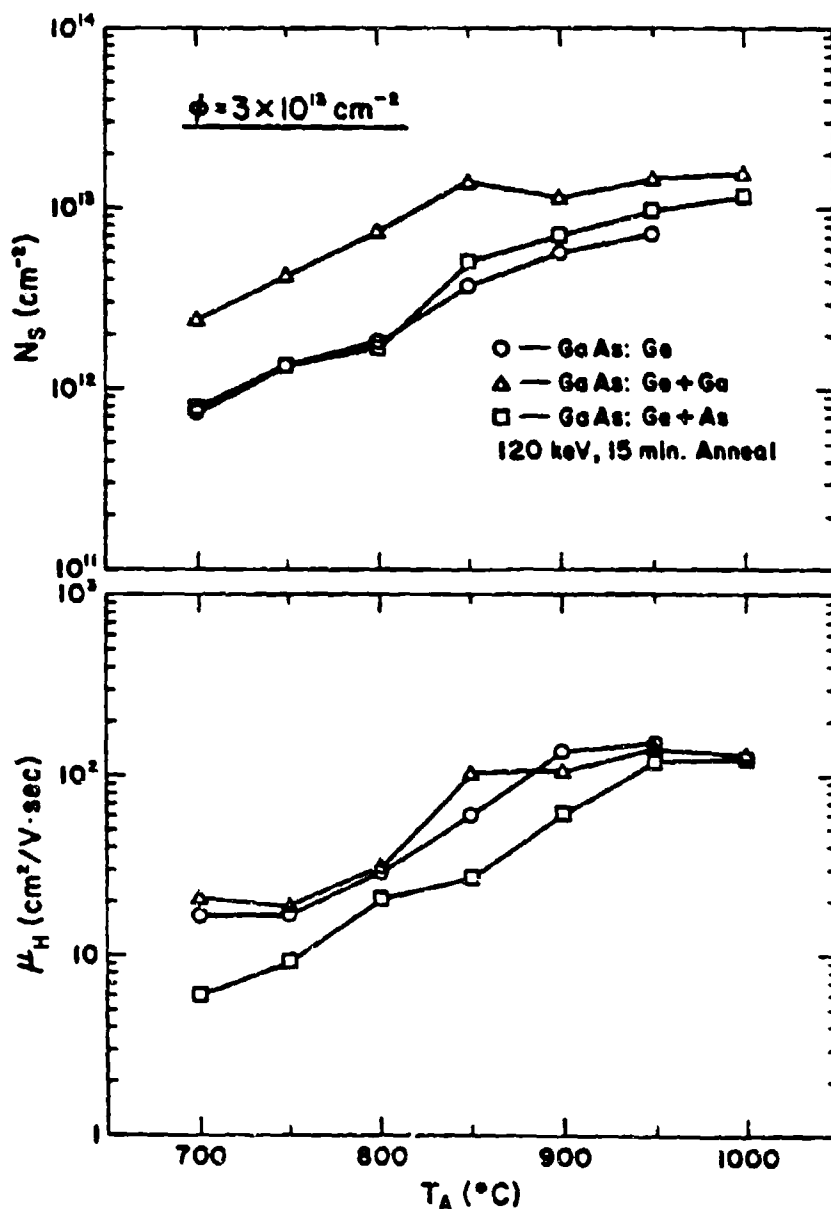


Figure 32 Dependence of Surface-Carrier Concentration (N_s) and Hall Mobility (μ_H) upon Annealing Temperature (T_A) for a $3 \times 10^{13}/\text{cm}^2$ Dose of single Ge, Dual (Ge + Ga) and (Ge + As) Implants in GaAs

monotonically with annealing temperature, though for a dose of $10^{13}/\text{cm}^2$ a slight decrease in the electrical activation has been observed between 950 and 1000°C anneal. For the (Ge + Ga) implants, an enhancement of p-type activity is seen at all anneal temperatures. At the 950°C anneal and $10^{13}/\text{cm}^2$ dose, where the single Ge implants has its highest measured activation of 38%, the (Ge + Ga) implants yield a maximum efficiency of 61%.

The (Ge + As) implants show, on the other hand, a decrease in p-type activation for the $10^{13}/\text{cm}^2$ dose annealed at 850 and 900°C as expected. In all other cases, however, the activation after dual implantation is comparable to, or even higher than, that due to the Ge single implantation. This result is somewhat surprising since dual implants of (Ge + As) are expected to result in a reduction of p-type activity. The reason for this result cannot be adequately explained at present.

The annealing behavior of the Hall mobility indicates that the mobility increases with annealing temperature due to damage annealing to values in the range of 100-200 $\text{cm}^2/\text{V}\cdot\text{sec}$ as expected. At the lower anneal temperatures, mobilities of the (Ge + Ga) dual implants are somewhat higher, but at the highest annealing temperatures they are comparable with the mobilities of the Ge single-implanted samples.

For an ion dose of $10^{14}/\text{cm}^2$ (Figure 33), the effect of dual implantation is very dramatic. The p-type activity of the Ge single implant is enhanced in the (Ge + Ga) dual implants by a factor of 5 at 700°C with somewhat improved mobility. At 900°C the (Ge + Ga) dual implants give an activation efficiency of 27% and mobility of about 83 $\text{cm}^2/\text{V}\cdot\text{sec}$, while the activation efficiency and mobility of the Ge single implant are 11% and about 96 $\text{cm}^2/\text{V}\cdot\text{sec}$, respectively. At this dose, the conductivity of the (Ge + As) implants converts to n-type, and a sharp drop in activation efficiency

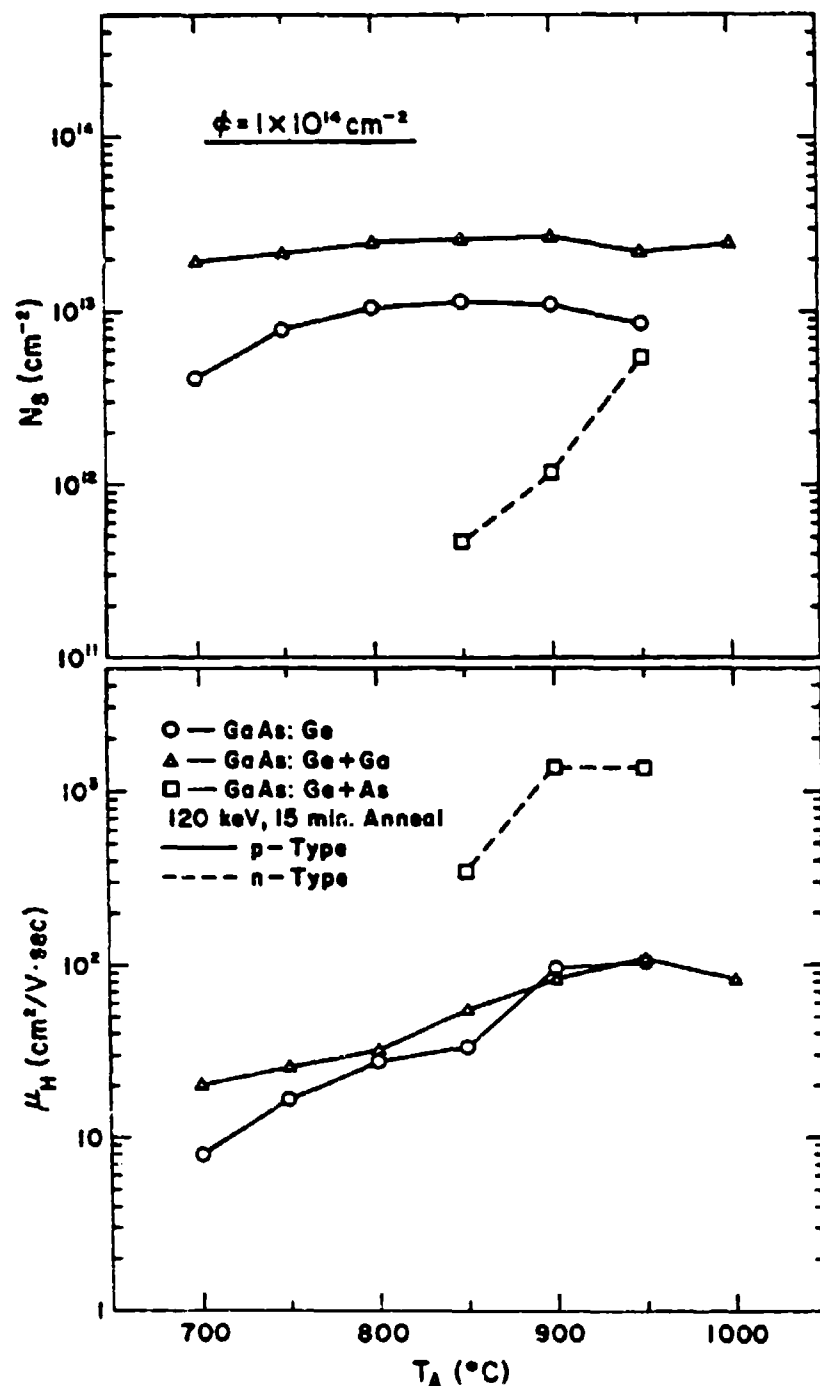


Figure 33 Dependence of Surface-Carrier Concentration (N_s) and Hall Mobility (μ_H) upon Annealing Temperature (T_A) for an $1 \times 10^{14}/\text{cm}^2$ Dose of single G, Dual (Ge + Ga) and (Ge + As) Implants in GaAs

occurs probably due to high electrical self-compensation. The mobility increases with annealing temperatures toward values representative of n-type mobilities.

Figure 34 shows the variation of surface carrier concentration and mobility as a function of the annealing temperature for the $3 \times 10^{14}/\text{cm}^2$ dose. At this dose, the p-type activity (solid lines) of the Ge single implant, which persists up to 900°C , is enhanced significantly by the (Ge + Ga) dual implants. At $700\text{--}750^\circ\text{C}$, the greatest enhancement of p-type activity by a factor of 8 was obtained over that of the Ge single implant. It is interesting to note that the conversion of p- to n-type activity of the Ge single implant above 900°C is inhibited by the (Ge + Ga). Up to 900°C , the dual implantation shows some improvement of p-type mobility over the single implantation, although mobilities are very low in this region due to self-compensation.

For the (Ge + As) dual implants, n-type conductivity (dashed lines) has been observed at all annealing temperatures. The activation efficiency also increases rapidly with annealing temperature up to 24% at 1000°C . The mobility of n-type samples remains low at annealing temperatures of 850°C or below, increases with T_A to 900°C , and then decreases slightly with annealing temperature. The low value of mobility below 850°C for this dose may be due to high electrical self-compensation under conditions which promote type conversion.

For the two highest doses of 10^{15} and $3 \times 10^{15}/\text{cm}^2$ (Figures 35 and 36), the (Ge + Ga) dual implants yield p-type activity for T_A up to 900°C . The n-type activity of the Ge single implant is inhibited by the addition of Ga. After high temperature annealing at 950°C or above,

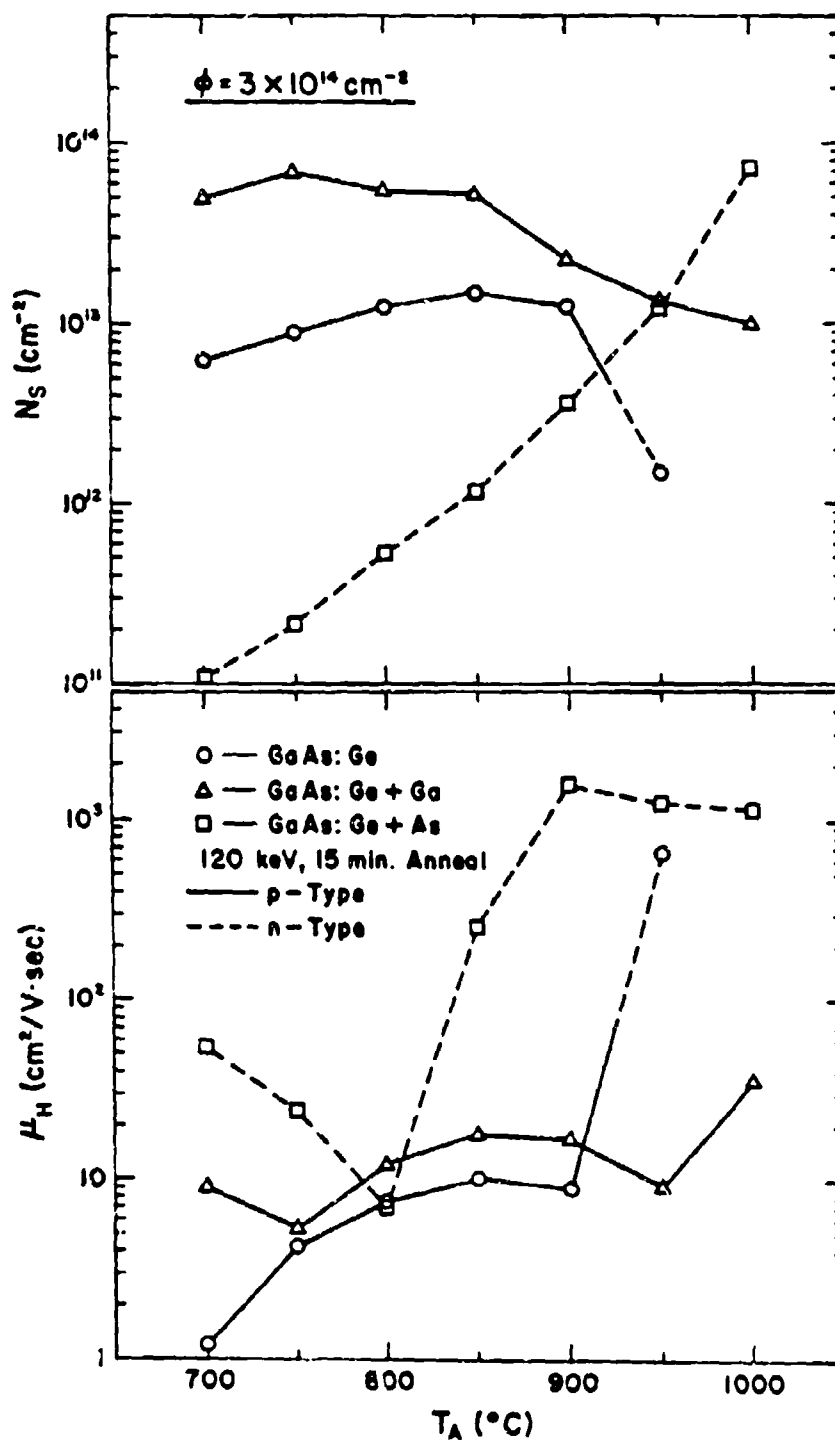


Figure Dependence of Surface-Carrier Concentration (N_s) and Hall Mobility (μ_H) upon Annealing Temperature (T_A) for a $3 \times 10^{14}/\text{cm}^2$ Dose of single Ge, Dual (Ge + Ga) and (Ge + As) Implants in GaAs

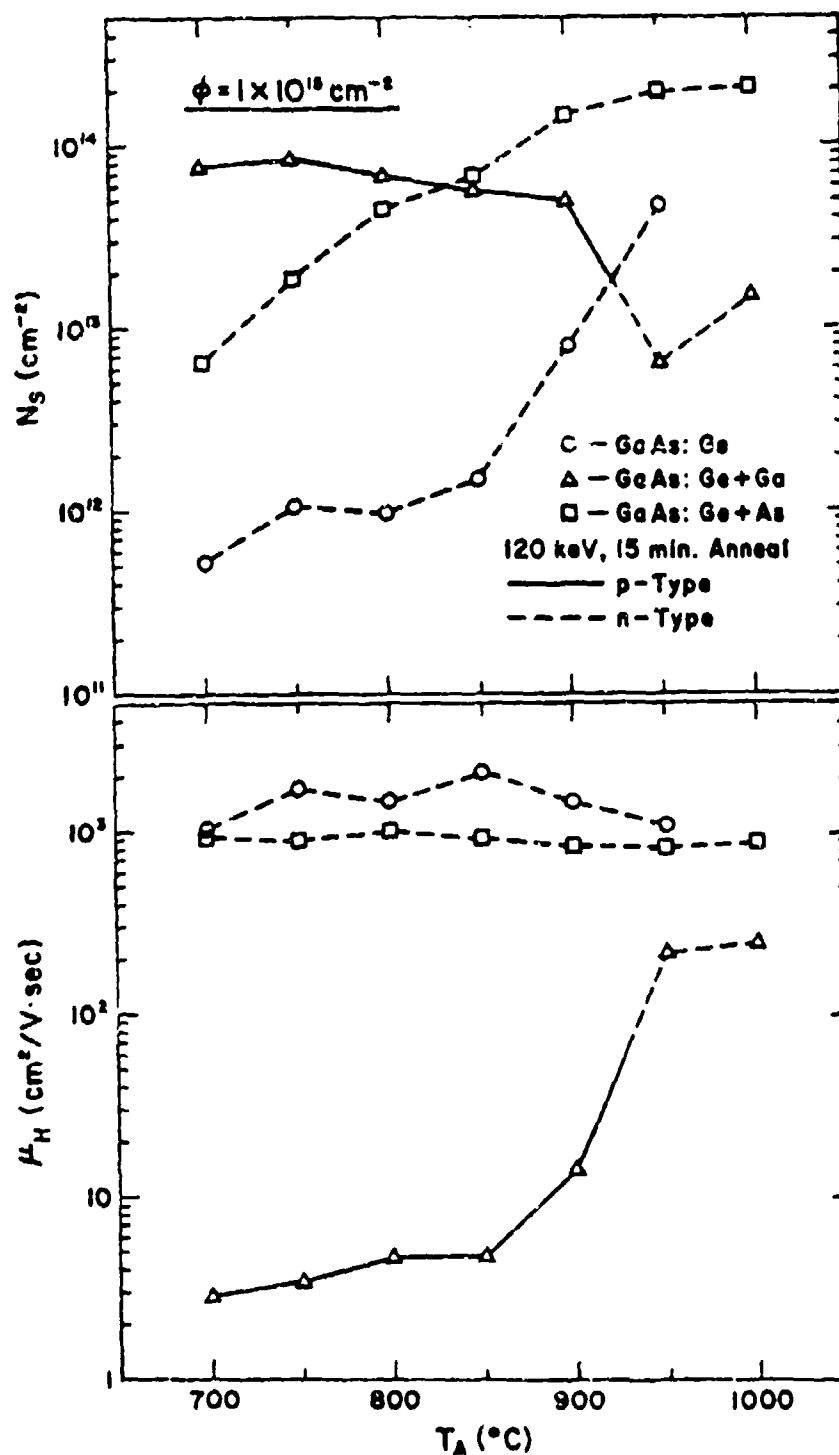


Figure 35

Dependence of Surface-Carrier Concentration (N_s) and Hall Mobility (μ_H) upon Annealing Temperature (T_A) for an $1 \times 10^{15}/\text{cm}^2$ Dose of Single Ge, Dual (Ge + Ga) and (Ge + As) Implants in GaAs

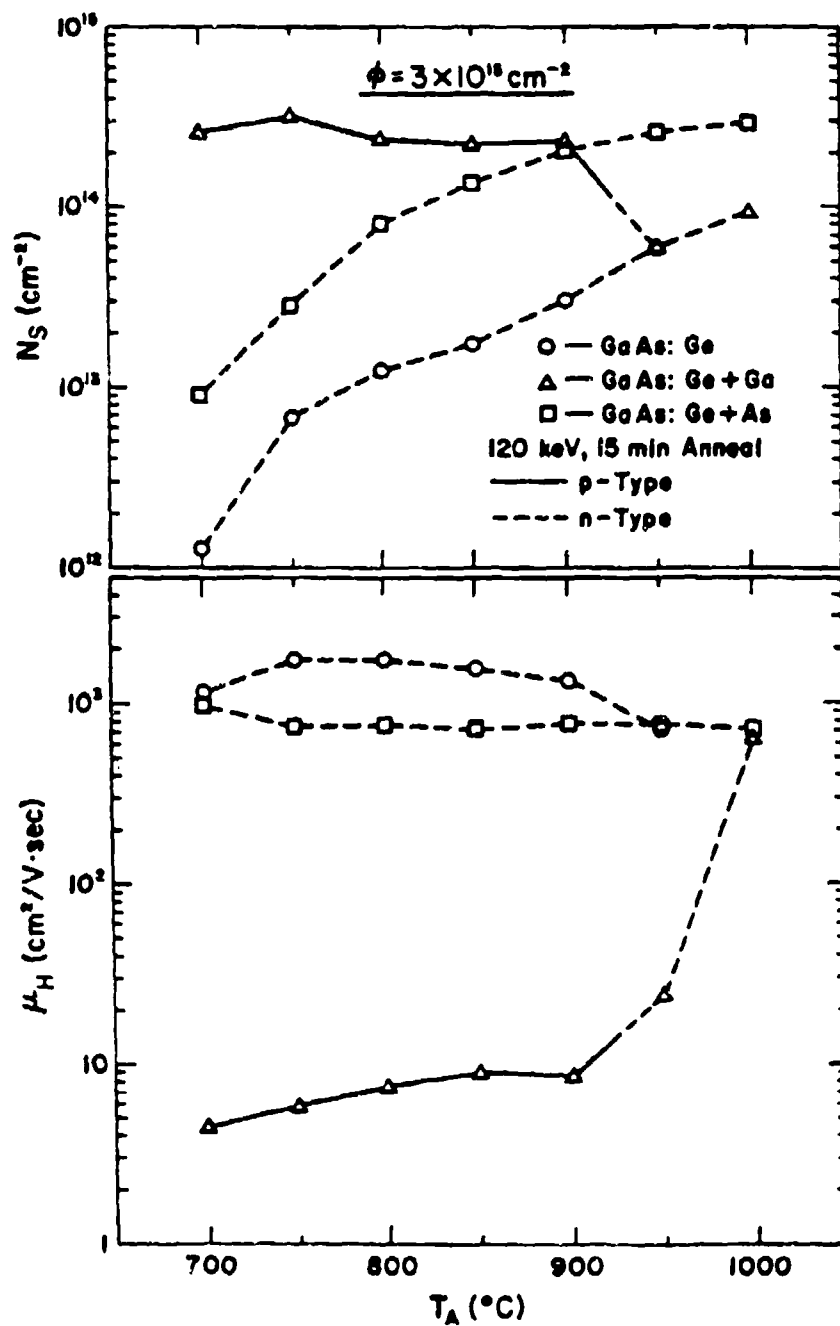


Figure 36

Dependence of Surface-Carrier Concentration (N_s) and Hall Mobility (μ_H) upon Annealing Temperature (T_A) for a $3 \times 10^{15}/\text{cm}^2$ Dose of Single Ge, Dual (Ge + Ga) and (Ge + As) implants in GaAs

the p-type conductivity of the dual implants becomes n-type. The (Ge + As) dual implants in this dose range show n-type activation which is greatly enhanced over that of the Ge single implant at all annealing temperatures. In most cases, the activation is increased by about one order of magnitude and by as much as 45 times for a $10^{15}/\text{cm}^2$ dose and 850°C anneal. However, mobilities are generally reduced by a factor of about 2 at those dose levels. At 950°C for the $10^{15}/\text{cm}^2$ dose, an activation efficiency of 19.5% and mobility of 843 $\text{cm}^2/\text{V}\cdot\text{sec}$ were obtained for the (Ge + As) dual implants compared with an activation efficiency of 4.7% and mobility of 1109 $\text{cm}^2/\text{V}\cdot\text{sec}$ for the Ge single implant.

3.4.3 Electrical Carrier Profiles

In order to examine the implanted layers in more detail, efforts were made to obtain the electrical profiles of Ge implants in GaAs by differential Hall measurements in conjunction with the chemical etch layer-removal technique. Preliminary profiles of the Ge implants in samples having doses of $10^{14}/\text{cm}^2$ annealed at 800 and 850°C and $10^{15}/\text{cm}^2$ annealed at 900°C are shown in Figure 37. The Ge implants in samples with $10^{14}/\text{cm}^2$ annealed at 800 and 850°C which displayed p-type activity, are electrically distributed within a region of the atomic distribution predicted by the LSS theory (dashed line). Both samples show a structure in the vicinity of the peak concentration and some indication of a surface pile-up of the Ge implant as a result of redistribution is seen in the 850°C anneal sample. A similar redistribution and structure has also been observed in the electrical profiles of Mg implants in semi-insulating Cr-doped GaAs.⁹ It was speculated there that the structure observed near the LSS peak position could be due to Cr redistribution and/or implantation damage-induced

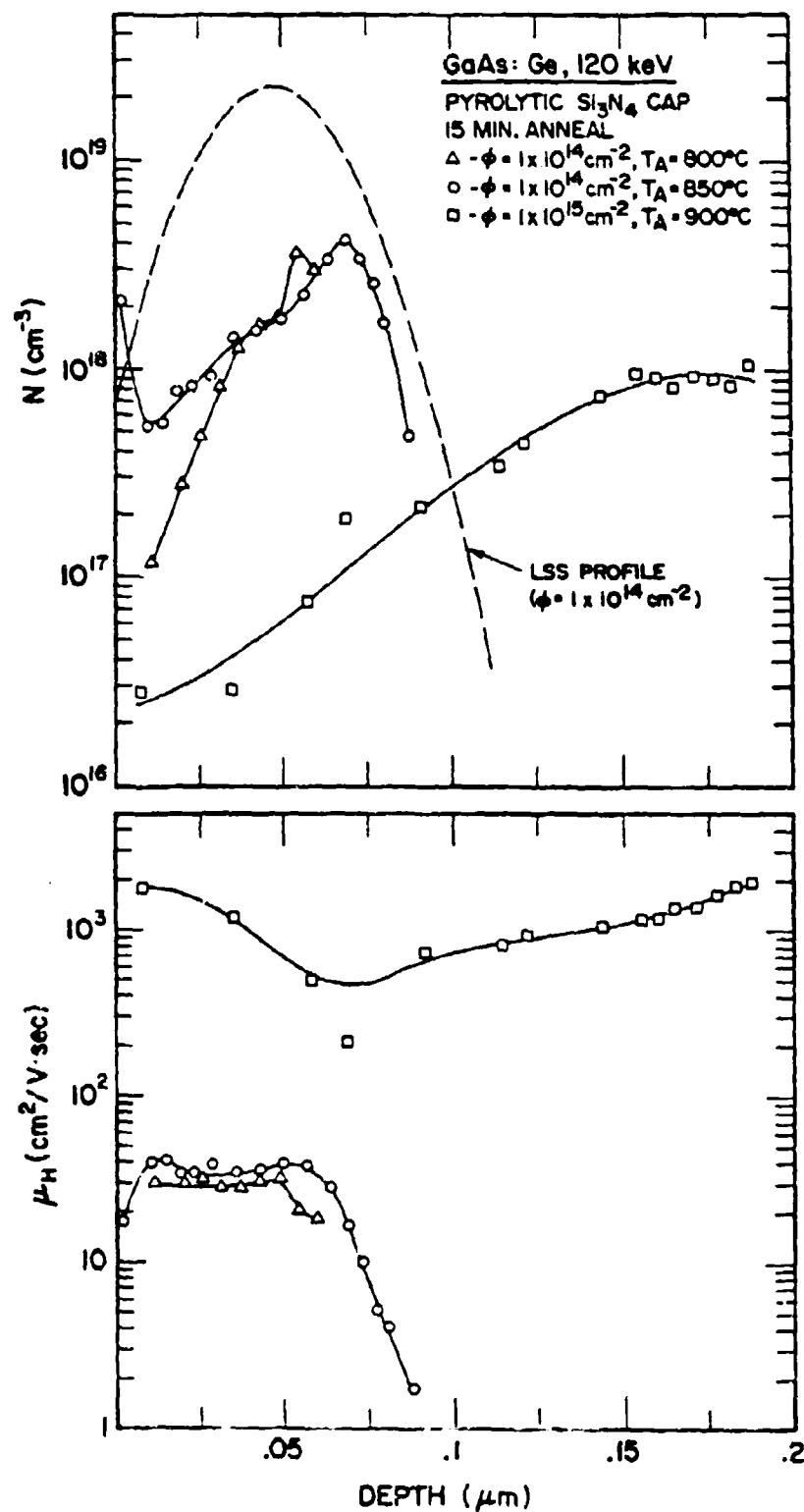


Figure 37 Electrical Carrier Profiles of GaAs:Ge Samples

redistributions of the Mg implants. SIMS analysis is underway to check this hypothesis for Ge implants.

For the $10^{15}/\text{cm}^2$, 900°C anneal sample, which showed n-type conductivity, the profile shows a rather broad distribution extending into the bulk of the sample. Because of the high ion dose and annealing temperature involved for this specimen, damage-enhanced diffusion may be a dominant mechanism affecting the electrical behavior of the Ge implants occupying Ga sites.

It should be pointed out that measured profiles, in the case of amphoteric dopants like Ge, may be significantly affected by regions of high self-compensation. Thus, such measured carrier profiles may differ at times from Ge-ion profiles, depending on the compensation level.

3.4.4 Summary

Table 3 summarizes the result of single Ge and dual implantation of (Ge + Ga) and (Ge + As) into semi-insulating, Cr-doped GaAs.

Single implants of Ge into GaAs have been shown to produce p-type or n-type conducting layers depending upon ion dose and annealing temperature. In samples having low doses ($<10^{14}/\text{cm}^2$), the implanted Ge ions occupy As sites preferentially, producing p-type conductivity at all annealing temperatures from 700 to 950°C . A maximum efficiency of 38% was obtained at a dose of $10^{13}/\text{cm}^2$ and an annealing temperature of 950°C . For high doses ($>10^{15}/\text{cm}^2$), more Ge ions occupy Ga sites than As sites, producing n-type activity at all annealing temperatures with maximum activation efficiency of only 5%. The transition from p- to n-type conductivity occurs at the intermediate dose of $3 \times 10^{14}/\text{cm}^2$ and an annealing temperature between 900 and 950°C .

TABLE 3

Summary of the result of single Ge and dual implantation of (Ge + Ga) and (Ge + As) into semi-insulating, Cr-doped GaAs. Implantation was performed at 120 keV with an equal dose of Ge, Ga, or As. Ion dose and anneal temperature required for p- or n-type conductivity is summarized.

Conductivity/Implantation	GaAs:Ge	GaAs:(Ge + Ga) (p-type activity enhanced)	GaAs:(Ge + As) (n-type activity enhanced)
P-Type	$\phi \sim 1 \times 10^{14} \text{ cm}^{-2}$ or below	ϕ - ALL	$\phi \sim 3 \times 10^{13} \text{ cm}^{-2}$ or below
	T_A - up to 950°C	T_A - up to 900°C	T_A - all
Type Conversion	$\phi \sim 3 \times 10^{14} \text{ cm}^{-2}$	$\phi > 1 \times 10^{15} \text{ cm}^{-2}$	$\phi \sim 1 \times 10^{14} \text{ cm}^{-2}$
	T_A - 900-950°C	T_A 900-950°C	T_A - all
N-Type	$\phi \sim 1 \times 10^{15} \text{ cm}^{-2}$ or above	$\phi \sim 1 \times 10^{15} \text{ cm}^{-2}$ or above	$\phi \sim 1 \times 10^{14} \text{ cm}^{-2}$ or above
	T_A - all	T_A 950°C or above	T_A - all

Dual implantation of Ge and Ga into GaAs indicates that the amphoteric electrical behavior of Ge is significantly changed from that of Ge single implantation. The dual implants have produced p-type conductivity for all doses ($< 3 \times 10^{15}/\text{cm}^2$) for an annealing temperature of up to 900°C. The p-type electrical activity of Ge in the dual implantation has been found to be improved significantly over that of the single implantation for all doses of $< 3 \times 10^{14}/\text{cm}^2$, while the original n-type of the Ge single implant has been found to change to p-type for doses of $> 10^{15}/\text{cm}^2$, except at anneal temperatures higher than 900°C.

Dual implantation of Ge and As into GaAs has produced a significant enhancement of n-type activity for ion doses of $> 10^{15}/\text{cm}^2$, a conductivity-type conversion for intermediate doses, and little effect upon p-type activity for ion doses of $< 3 \times 10^{13}/\text{cm}^2$. In most cases, the electrical activation continues to increase with annealing temperature up to 1000°C. The maximum electrical activation efficiency obtained for these dual implants was 50% at an ion dose of $10^{13}/\text{cm}^2$ for the p-type samples and 24% at an ion dose of $3 \times 10^{14}/\text{cm}^2$ for the n-type samples.

In conclusion, we have found that the electrical activity of the amphoteric dopant Ge in GaAs can be modified in a predictable manner by controlling dose level and annealing temperature, or by dual implantation of (Ge + Ga) and (Ge + As). Although the possibility exists that defects such as As and Ga vacancies, or their complexes, may influence electrical activity, it is evident that the results obtained are due mainly to the amphoteric nature of the implanted Ge ions.

3.5 SULFUR-IMPLANTED GaAs

Sulfur-implanted GaAs has been used in fabricating various microwave devices. Although a number of publications³⁰⁻⁴⁰ dealing with the electrical properties of GaAs:S have appeared in the literature, the fundamental difficulties encountered for this dopant are still not well understood. Moreover, each paper contains range-limited results of dependence upon ion dose, ion energy, and annealing temperature. In general, electrical activation efficiencies of GaAs:S are reported to be very low, mostly below ~50%, although some improvements with elevated temperature implantations³³ have been realized. In most cases, the maximum electron concentrations reported for S implants are also very low (below $\sim 5 \times 10^{17} \text{ cm}^{-3}$) regardless of the ion doses used. Also, diffusion of S during annealing has usually been reported to be significant.

In order to better understand the factors affecting electrical activation and carrier depth distributions, and thereby obtain useful information for device applications, we have undertaken a comprehensive study of electrical properties of S-implanted GaAs. The electrical activation and carrier profiles have been measured as a function of ion dose, ion energy, and annealing temperature. Also, the electrical depth profiles have been compared with the SIMS atomic profiles. All of the results⁴¹⁻⁴³ will be discussed in this report. Especially, this work contains, to the best of our knowledge, the first direct comparative study of the SIMS and electrical profiles for S-implanted GaAs. Also, no systematic study of electrical property dependence of S implants in GaAs upon implanted-ion energy has been reported, and such dependence is not well understood at present.

Room-temperature implantations were carried out in a nonchanneling direction at ion energies ranging from 40 to 600 keV to doses ranging from 4×10^{12} to 4×10^{15} ions/cm². SIMS atomic profiles of sulfur were measured using cesium-ion bombardment while the Cr distributions were measured using oxygen-ion bombardment. The sputtering rate was determined using a Sloan Dektak Surface Profile Measuring System.

3.5.1 Electrical Activation

The results of Hall effect/sheet resistivity measurements made on GaAs samples, implanted with S ions at an energy of 120 keV to doses ranging from 5×10^{12} to 1×10^{15} cm⁻² and annealed with pyrolytic Si₃N₄ caps at temperatures ranging from 700 to 900°C, are shown in Figure 38. The electrical activation increases monotonically with annealing temperature up to 900°C for all except the lowest dose of 5×10^{12} cm⁻², for which the activation begins to level out at around 800°C. A maximum activation efficiency of 57% was obtained for the sample implanted to a dose of 1×10^{13} cm⁻² and annealed at 900°C. Electrical activations for samples capped by plasma-enhanced deposition were also investigated, and activations were, in general, slightly higher than for samples with pyrolytic caps. However, the anneal behavior of surface carrier concentration and mobility shows about the same trend for both caps.

The anneal behavior of electron Hall mobilities indicates that mobilities for low doses ($< 1 \times 10^{13}$ cm⁻²) increase with annealing temperature up to 850°C, and then level out at higher temperatures, while the mobilities for high doses ($< 1 \times 10^{14}$ cm⁻²) show their maxima at around 750°C, and then decrease with annealing temperature. It seems that implantation damage can be annealed reasonably well at around 800°C. The

decrease in mobility with increasing annealing temperature for high doses may be partly due to the increase in carrier concentrations.

Figure 39 is a replot of the data at 120 keV, showing surface carrier concentration versus implanted dose at different annealing temperatures, compared with a straight line which represents 100% activation efficiency. Activation efficiencies are generally high for low dose ($< 3 \times 10^{13} \text{ cm}^{-2}$) samples annealed at higher temperatures, but decrease with increasing ion doses. A sharp drop in activation efficiency for doses above $1 \times 10^{14} \text{ cm}^{-2}$ for 900°C anneal may be attributed to unannealed damage or S precipitates. The figure also clearly shows a significant increase in activation efficiency with annealing temperature for all doses.

The results of electrical measurements made on GaAs samples implanted with S to an ion dose of $4 \times 10^{13} / \text{cm}^2$ at various ion energies and annealed at several temperatures are shown in Figure 40. The electrical activation for this dose level increases with ion energy up to 300 keV and then decreases with further increase in energy at all anneal temperatures. The figure also shows that the activation increases with anneal temperature at a given ion energy. The highest electrical activation efficiency obtained was 80% for an energy of 300 keV and 950°C anneal. In spite of the sharp variation in electrical activation, mobilities are nearly independent of ion energies. Also the mobility data indicate that considerable implantation damage still remains even after annealing at 850°C, and recovers gradually as the anneal temperature increases further.

It was found that, for the ion dose of $4 \times 10^{13} / \text{cm}^2$ and 900°C anneal, the surface carrier concentration N_s , increases approximately according to $N_s \sim 1.5 \times 10^{12} E^{0.5}$ for ion energies E up to 300 keV, and

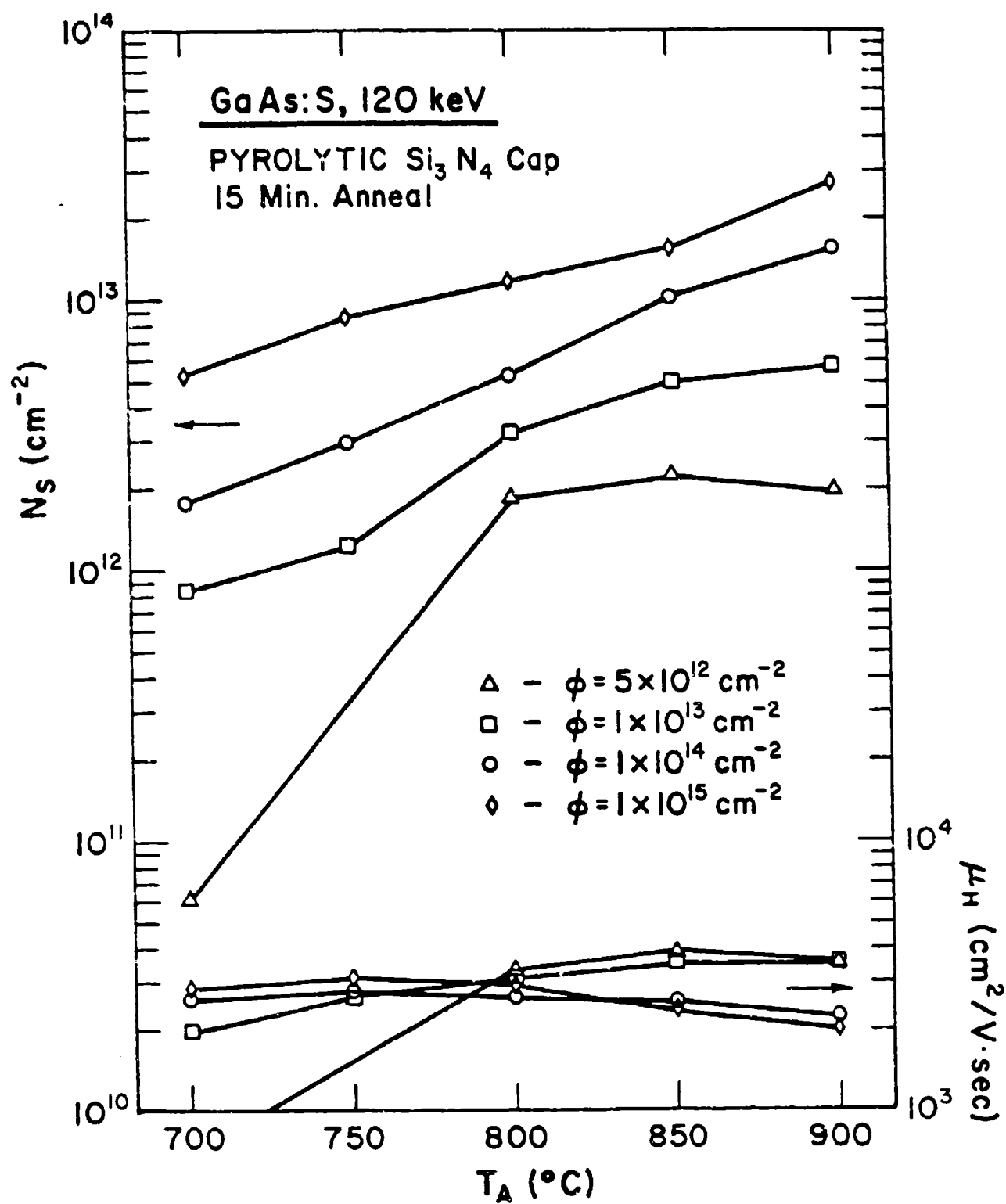


Figure 38

Dependence of Surface-Carrier Concentration (N_S) and Hall Mobility (μ_H) upon Annealing Temperature (T_A) for GaAs:S

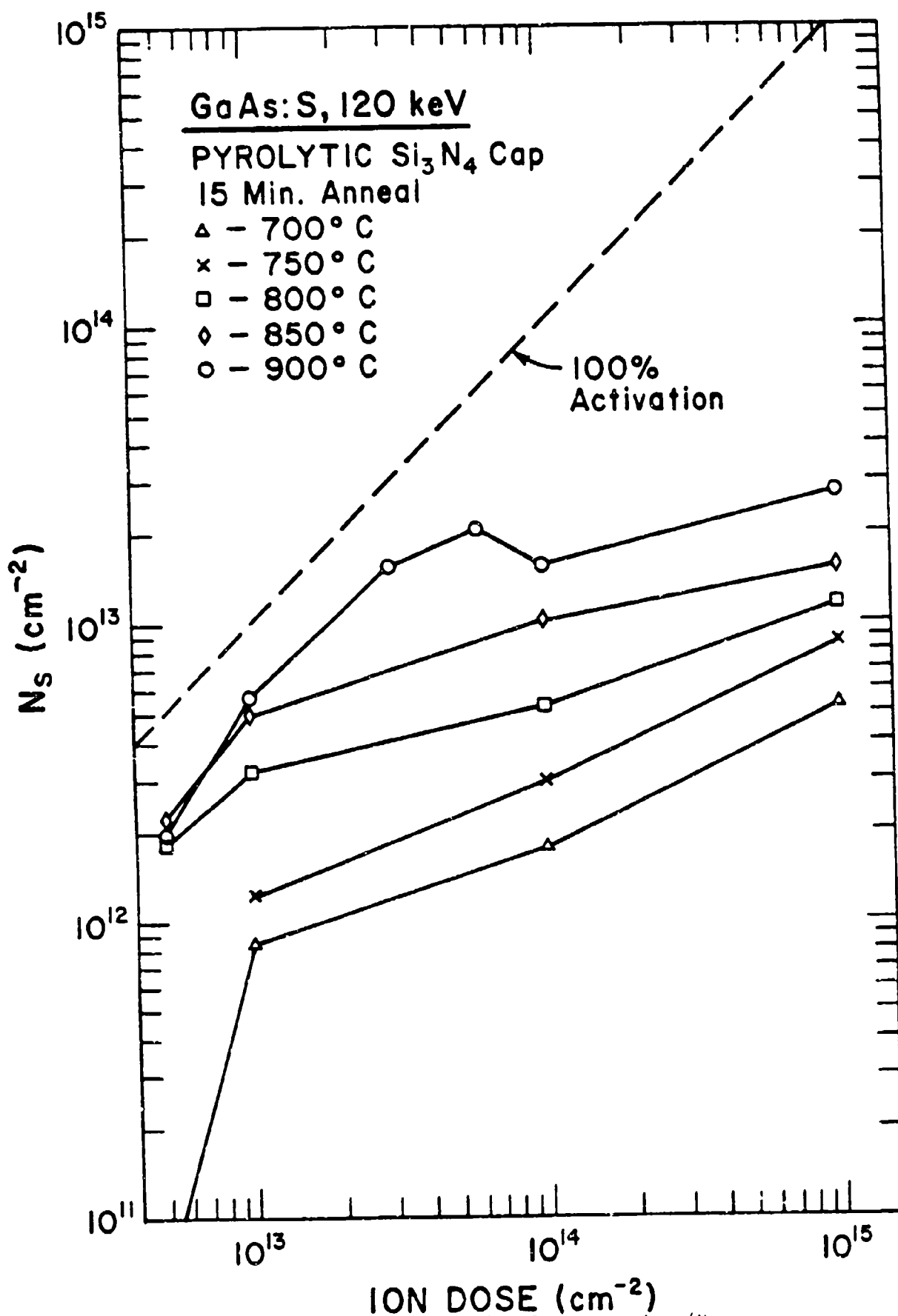


Figure 39

Dependence of Surface-Carrier Concentration (N_S) and Hall Mobility (μ_H) upon Ion Dose (Φ) for 120 keV GaAs:S

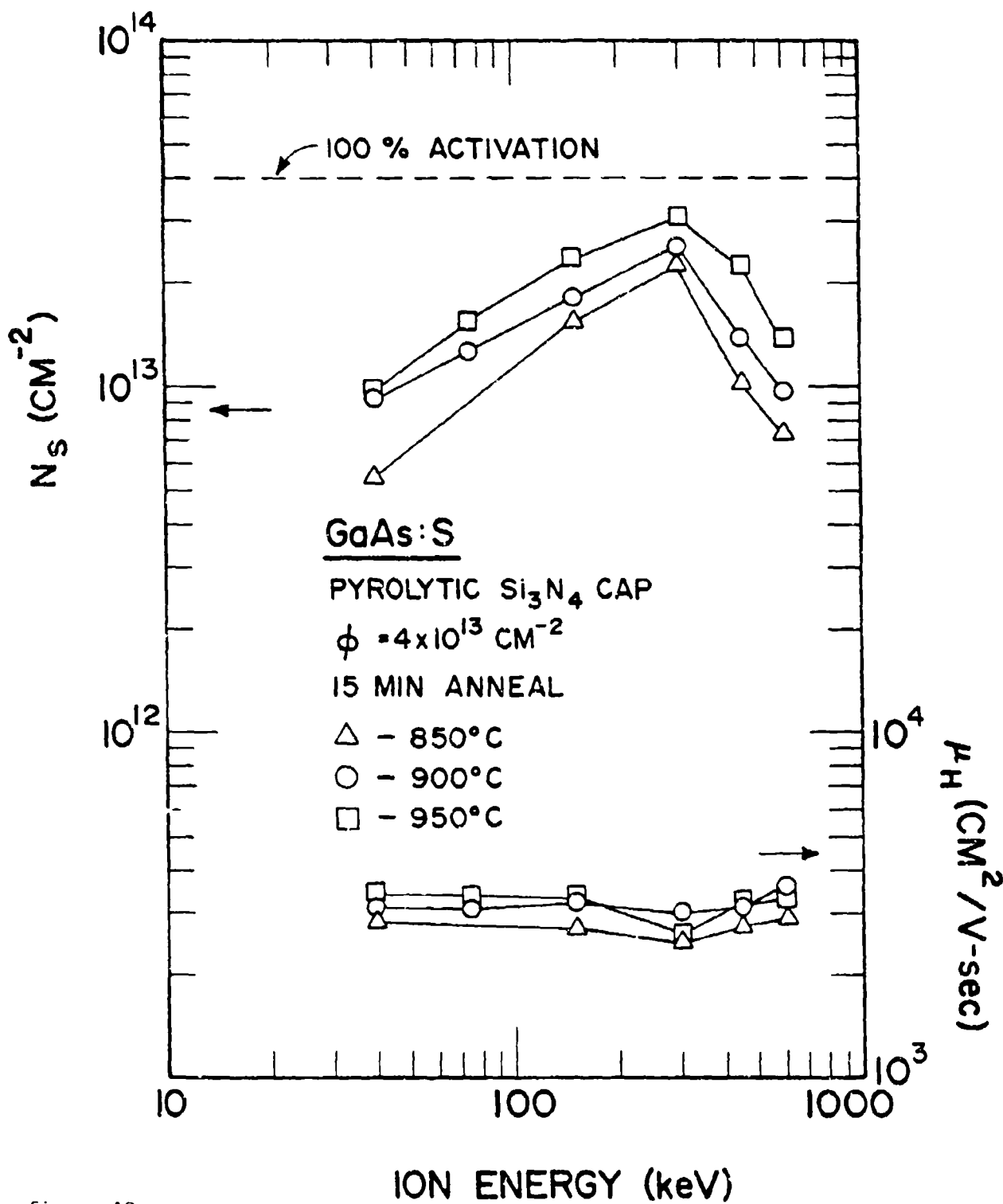


Figure 40

Dependence of Surface-Carrier Concentration (N_S) Hall Mobility (μ_H) upon Ion Energy for GaAs:S

then decreases with $N_S \sim 1.4 \times 10^{17} E^{-1.5}$ for energies above 300 keV. The increase in activation with ion energy for the GaAs:S samples has been reported^{34,35} previously for energies up to 400 keV. However, there has been no report, to the best of our knowledge, that further increase in energy results in decreasing electrical activation. Eisen *et al.*³⁴ attributed the increase in activation with ion energy to the fact that less S outdiffusion is expected during anneal for higher-energy implanted samples due to greater depths than for lower energy. However, this explanation does not account adequately for the overall behavior observed. The results reported here indicate that the activation dependence upon ion energy is much more complicated. However, this explanation does not account adequately for the overall behavior observed, and in particular, for the decreasing activation with further increase in ion energy. Moreover, our SIMS data show no significant outdiffusion of S for samples capped with our Si_3N_4 caps. A detailed analysis of ion energy-dependent electrical properties of GaAs:S has been reported⁴¹ by the authors. By comparison with the data of 120 keV, it has been found that the effects of implantation energy and ion dose on the expected activation can be correlated approximately (up to 300 keV) in terms of an as-implanted peak concentration.

Surface-carrier concentrations and Hall mobilities for samples annealed at 900°C are plotted as a function of ion dose for ion energies at 120 and 300 keV in Figure 41. The activation efficiencies remain relatively constant up to a dose of about $4 \times 10^{13}/cm^2$. However, they decrease appreciably as the dose increases above $4 \times 10^{13}/cm^2$. The figure also shows that the activation at 300 keV is higher than at 120 keV for doses below about $1 \times 10^{14}/cm^2$, whereas there is little difference in electrical

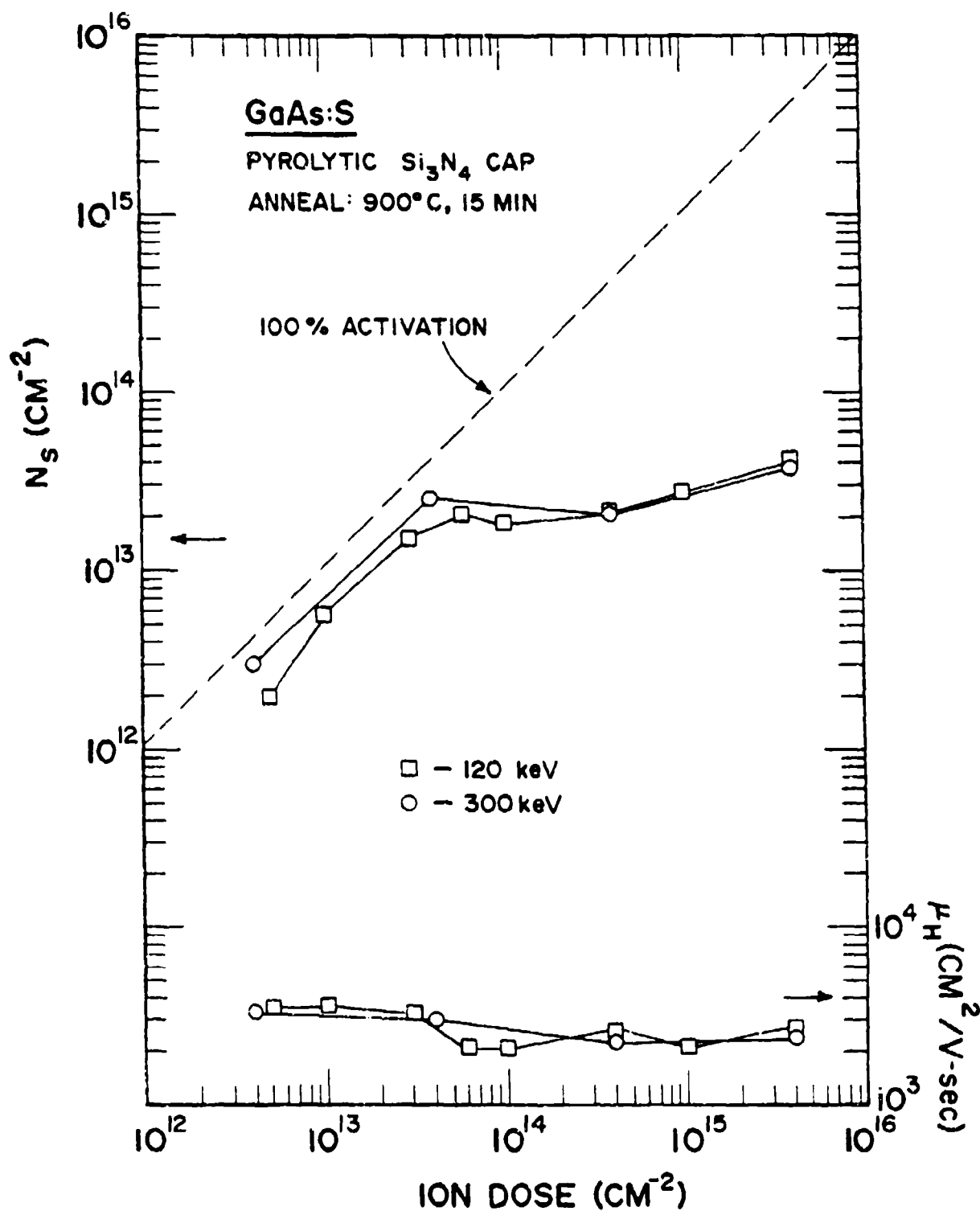


Figure 41 Dependence of Surface-Carrier Concentration (N_S) Hall Mobility (μ_H) upon Ion Dose for 120 and 300 keV GaAs:S

activation for ion energies of 120 and 300 keV for doses above $4 \times 10^{14}/\text{cm}^2$. Mobilities are seen to be about the same between the two ion energies for all doses.

A correlation has been found between the dependence of electrical activation efficiency on ion energy and on ion dose, as shown in Table 4. In the first three columns are listed the measured electrical activation efficiency and LSS peak concentrations for various ion energies, all at the dose of $4 \times 10^{13}/\text{cm}^2$. The activation efficiencies listed in column 5 for 120 keV were obtained from Figure 41 for equivalent doses producing the same LSS peak concentrations as those in column 3 for the dose of $4 \times 10^{13}/\text{cm}^2$. It can be seen from this table that there is agreement in these activation efficiencies for energies up to 300 keV, although there is a significant difference between the two activation efficiencies for energies about 300 keV. The table suggests that the effects of implantation energy and ion dose on the expected activation can be correlated approximately (up to 300 keV) in terms of a single parameter -- the as-implanted peak concentration. For example, the activation efficiency for a dose of $4 \times 10^{13}/\text{cm}^2$ and energy of 75 keV is 32%. In good agreement with that, the estimated activation efficiency for the equivalent dose ($5.8 \times 10^{13}/\text{cm}^2$) producing the same LSS peak concentration ($5.2 \times 10^{18}/\text{cm}^3$) at 120 keV is 35%. In general one may observe that, for energies up to about 300 keV, increasing ion energy at a given dose level ($4 \times 10^{13}/\text{cm}^2$) has an effect on the activation efficiency similar to that of lowering the implanted ion dose at a given ion energy (120 keV). However, this is not the case for higher energy implantations.

TABLE 4. Dependence of electrical activation efficiency upon ion energy for a cost of $4 \times 10^{13} \text{ cm}^{-2}$ and the equivalent dose producing the same LSS peak concentration at the energy of 120 keV for GaAs:S.

Ion dose = $4 \times 10^{13} / \text{cm}^2$		Ion energy = 120 keV		
Ion energy (keV)	Measured electrical activation efficiency (%)	Calculated LSS peak concentration (cm^{-3})	Equivalent dose producing the same LSS peak concentration (cm^{-2})	Activation efficiency estimated from Fig 41 (%)
40	23	8.5×10^{18}	9.6×10^{13}	19
75	32	5.2×10^{18}	5.8×10^{13}	35
150	45	3.0×10^{18}	3.4×10^{13}	48
300	64	1.8×10^{18}	2.0×10^{13}	54
450	35	1.4×10^{18}	1.5×10^{13}	55
600	24	1.1×10^{18}	1.3×10^{13}	56

3.5.2 Electrical Carrier Profiles

Electrical depth profiles of carrier concentrations and Hall mobilities for samples implanted at an ion energy of 120 keV to doses ranging from 5×10^{12} to $1 \times 10^{15} \text{ cm}^{-2}$ and annealed at 900°C with a pyrolytic Si_3N_4 cap are shown in Figure 42. The theoretical Lindhard-Scharff-Schiott (LSS) profile for an ion dose of $3 \times 10^{13} \text{ cm}^{-2}$ is also shown in this figure for comparison. The theory predicts that the peak concentration will occur at $\sim 0.09 \mu\text{m}$ for an ion energy of 120 keV. However, the peak concentrations generally do not occur at the position predicted by the LSS theory. Furthermore, the carrier profile data show a high dependence on ion dose and a significant redistribution of the implanted-S ions. In contrast to our results, Woodcock et al.³⁶ have reported that S ions implanted at room temperature have peaks of carrier concentration close to the predicted ranges even at high doses.

For an ion dose of $1 \times 10^{13} \text{ cm}^{-2}$ or below, the profiles show no clear peaks and show more carrier concentrations near the surface, indicating a tendency of sulfur accumulation near the surface. For doses greater than $1 \times 10^{13} \text{ cm}^{-2}$, clear peaks in carrier profiles have been observed for all doses, and the positions of peak carrier concentrations move deeper into the substrate as the dose increases. Increasing depths of peak positions with ion dose have also been reported by Sansbury et al.³⁷ Indiffusion of implanted-S ions can be seen for all doses by comparing the electrical profiles with the LSS profiles, but is more significant for higher doses, producing long diffusion tails for the two highest doses. Presumably, the diffusion is greatly enhanced during annealing by the presence of implantation-induced damage. One may also notice that a significantly reduced

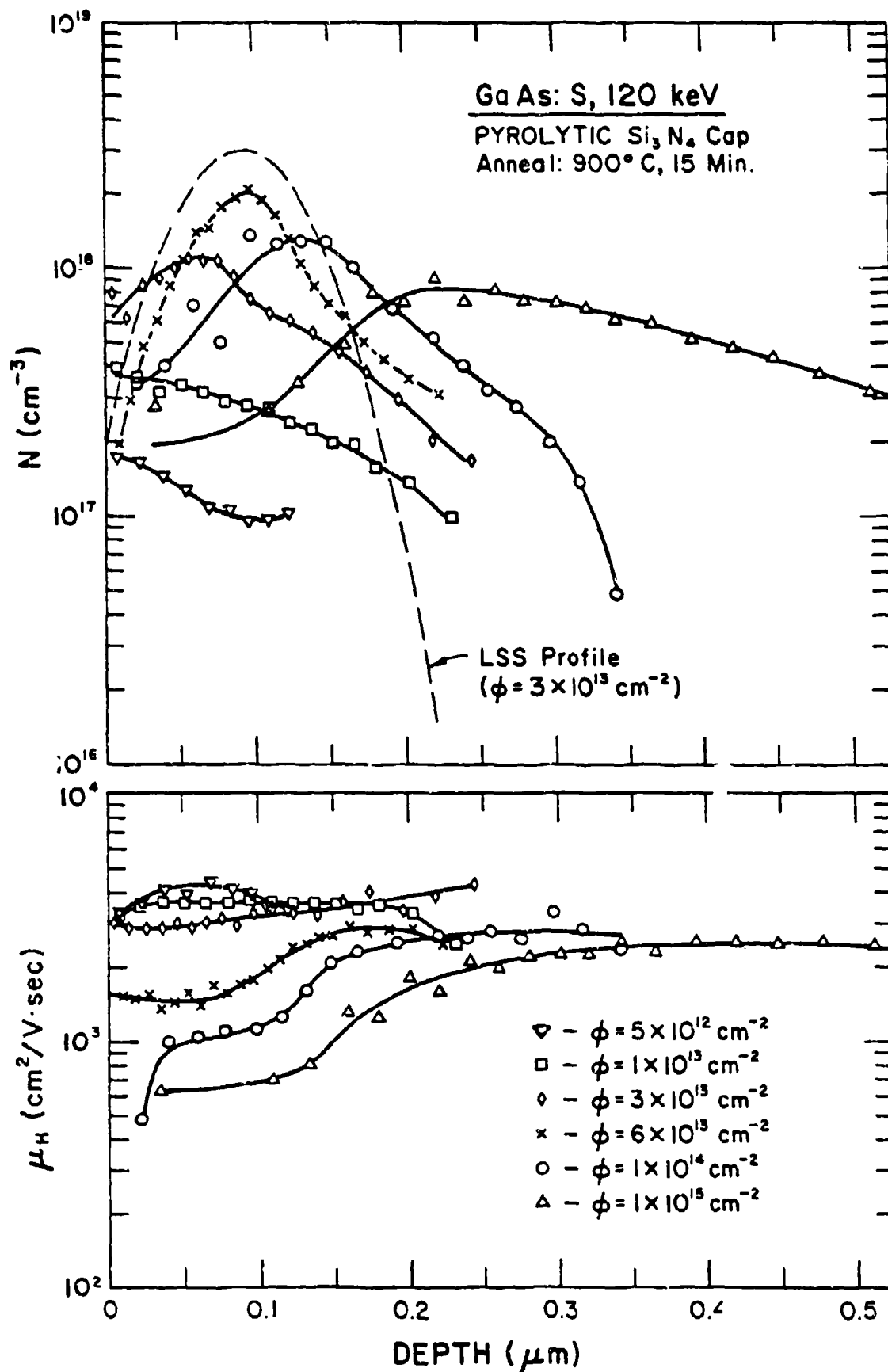


Figure 42 Electrical Carrier Profiles of 120 keV GaAs:S Samples
Annealed at 900°C

number of carriers can be found near the surface for the two highest doses.

For an ion dose of $6 \times 10^{13} \text{ cm}^{-2}$, the carrier profile is quite different from the others. The maximum carrier concentration obtained is $2 \times 10^{18} \text{ cm}^{-3}$, with the concentration peak occurring at the same position as predicted by the theory. Moreover, it has been found that the carrier profile agrees well with the proportionately reduced LSS profile for this dose (by a factor of ~ 3) in most of the implanted region except in the deeper region of the substrate. The reduction factor of ~ 3 is in agreement with an electrical activation efficiency of $\sim 34\%$ obtained for this sample. This may suggest that most of the implanted-S ions remain as implanted but only a fraction of the implanted ions become electrically activated at this dose. The profile also indicates that the implanted ions are activated slightly more in the deeper region of the sample than near the surface, producing a small diffusion tail.

The mobilities for doses $< 3 \times 10^{13} \text{ cm}^{-2}$ are much higher throughout the implanted region than those for the higher dose. The mobility values for the two highest doses are especially low near the surface region and the values increase gradually with depth to about $2500 \text{ cm}^2/\text{V sec}$. The reductions of both carrier concentrations and mobilities in the surface region for higher doses may be due to the implantation-induced defects or to the electrically inactivated-S ions (activation efficiencies are only 16% and 3% for doses 1×10^{14} and $1 \times 10^{15} \text{ cm}^{-2}$, respectively). Some more discussion will be given later.

The reasons for changes in the carrier-peak-concentration positions and magnitudes are complicated. The carrier profiles could be affected, in general, by the redistribution of the implanted sulfur, electrically inactivated sulfur, or unannealed damage, all depending upon the

ion doses. Whatever the dominant factor may be for each dose level, recent results of profile data show much higher peak concentrations ($>1 \times 10^{18} \text{ cm}^{-3}$ for doses $>3 \times 10^{13} \text{ cm}^{-2}$) than the values previously reported.³⁴⁻⁴⁰ It may be noted that Sansbury et al.³⁷ obtained a maximum carrier concentration of about $2 \times 10^{17} \text{ cm}^{-3}$, almost independent of the ion dose. This result could be due to the relatively low annealing temperature (700°C) used.

Depth profiles of the carrier concentrations and Hall mobilities for samples implanted to an ion dose of $1 \times 10^{14} \text{ cm}^{-2}$ at an ion energy of 120 keV and annealed at different temperatures are shown in Figure 43. Carrier and mobility profiles are shown to be highly dependent upon annealing temperature. The carrier concentrations increase with annealing temperatures, showing peaks at a slightly greater depth than the theory predicts. It can also be seen that indiffusion of S takes place at this dose level: the higher the annealing temperature, the more indiffusion. Both the carrier concentrations and mobilities are significantly lower near the surface at all annealing temperatures. The mobilities for the 750°C anneal are generally lower than for the 800°C anneal. This indicates that significant damage remains after a 750°C anneal for 15 min.

Electrical profiles of carrier concentrations and Hall mobilities for samples implanted to two doses of S ions at an ion energy of 120 keV and annealed with either pyrolytic or plasma-deposited Si_3N_4 caps are shown in Figure 44. It can be seen that both caps produce nearly identical profiles of carrier concentrations and mobilities. A maximum carrier concentration of $2.5 \times 10^{18} \text{ cm}^{-3}$ was obtained for the sample having a dose of $1 \times 10^{14} \text{ cm}^{-2}$ and annealed at 900°C with a plasma-deposited cap. This is,

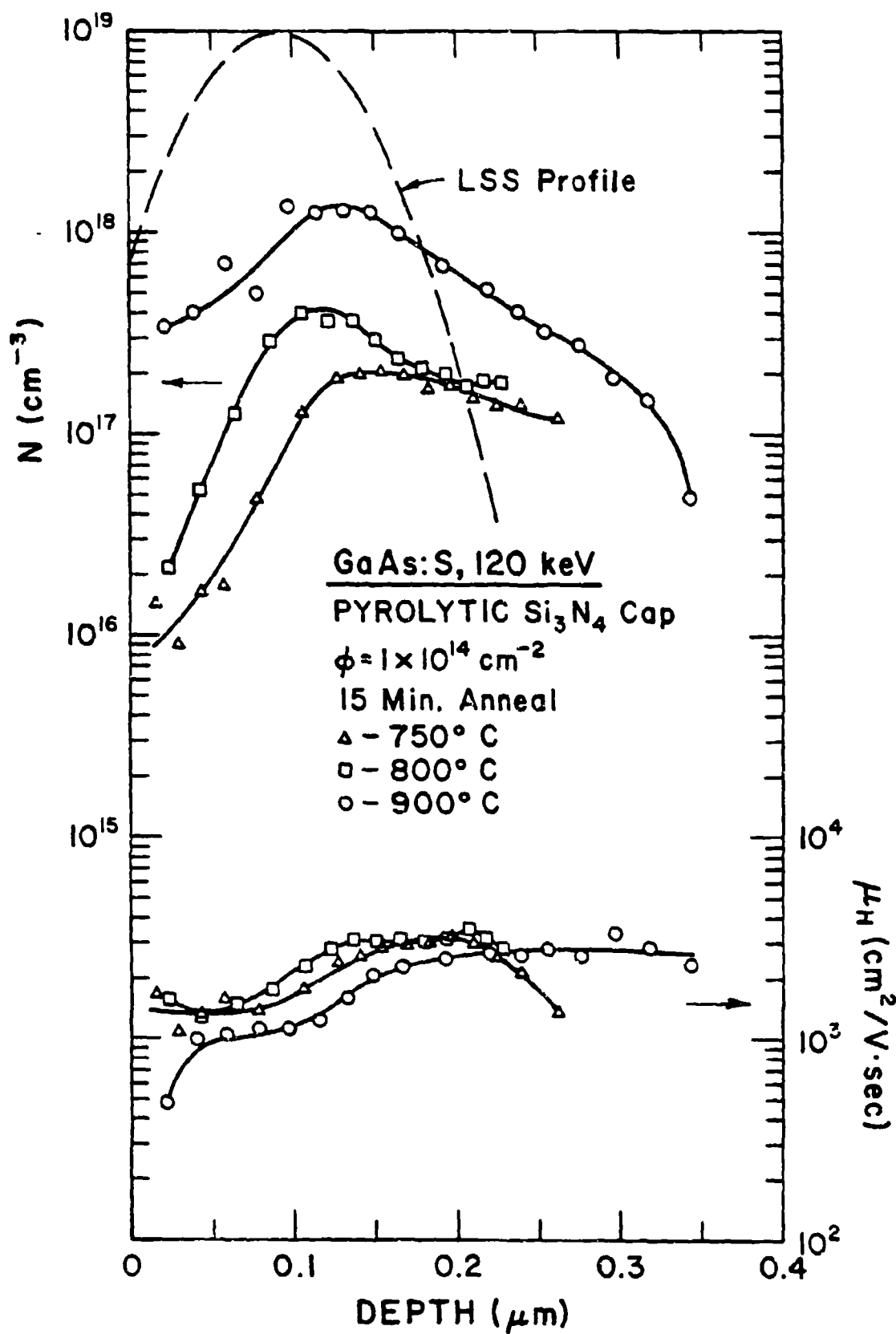


Figure 43 Electrical Carrier Profiles of $1 \times 10^{14}/\text{cm}^2$ Dose GaAs:S Samples Implanted at 120 keV and Annealed at Three Different Temperatures

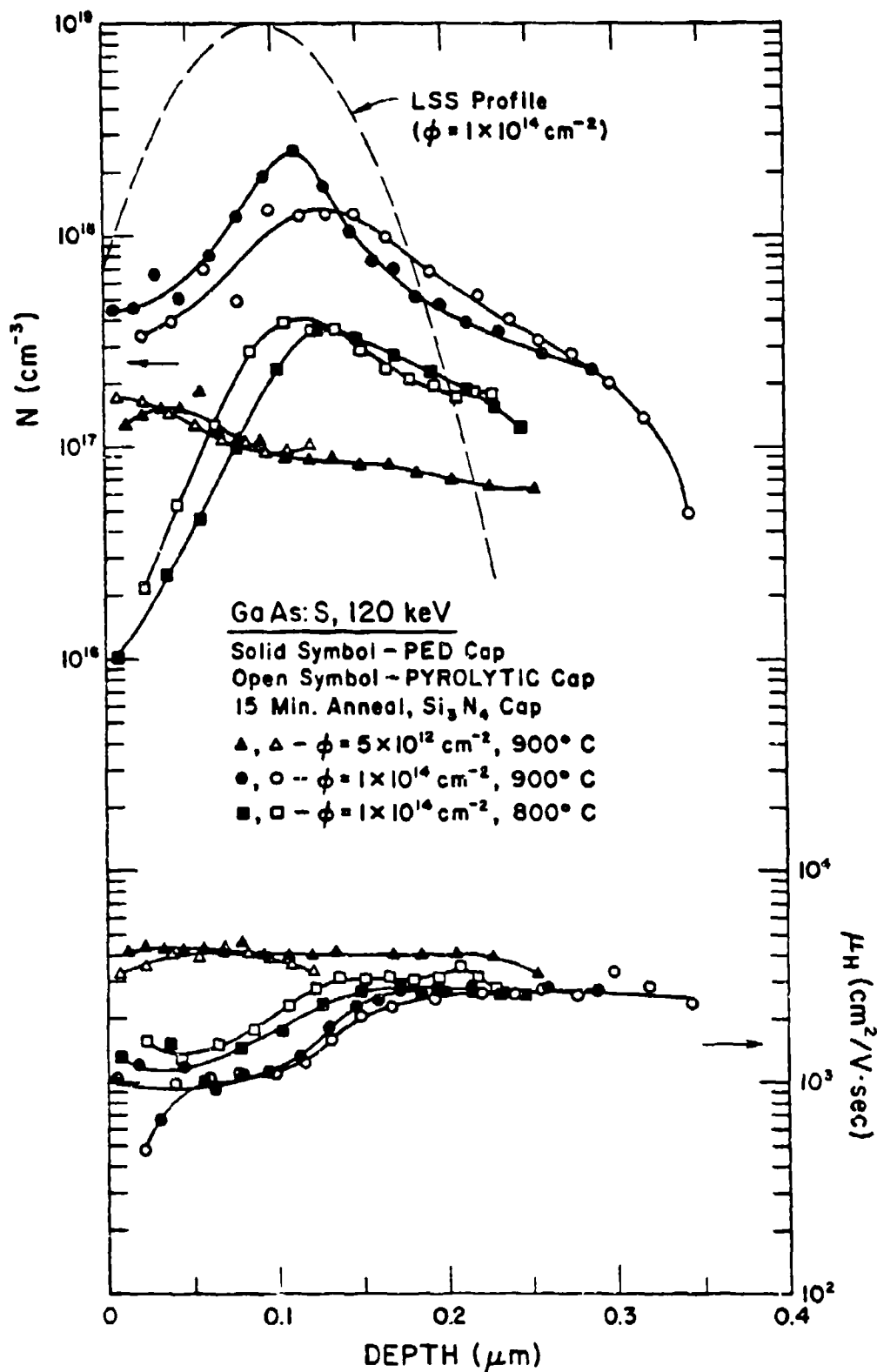


Figure 44 Electrical Carrier Profiles of 120 keV GaAs:S Samples with CVD and PED Caps

to the best of our knowledge, the highest value reported yet for S-implanted GaAs. It seems from our results that the higher annealing temperature ($\sim 900^\circ\text{C}$) and intermediate ion dose ($\sim 1 \times 10^{14} \text{ cm}^{-2}$) are required to achieve maximum carrier concentrations greater than $1 \times 10^{18} \text{ cm}^{-3}$ for S-implanted GaAs.

Electrical depth profiles of carrier concentrations and Hall mobilities for samples implanted to a dose of $4 \times 10^{13} / \text{cm}^2$ at various ion energies and annealed at 900°C are shown in Figures 45 and 46. The theoretical Lindhard-Scharff-Schiott (LSS) profiles for the various ion energies are also shown for comparison. The profile data show a redistribution of implanted-S ions. Peak concentrations do not occur at the positions predicted by the theory, but all occur at positions much closer to the surface, regardless of the implanted energy. The maximum carrier concentration obtained was $1 \times 10^{18} / \text{cm}^3$ for the 75 keV sample. Furthermore, the profiles are seen to be highly dependent upon ion energies. Measured peak carrier concentrations decrease with increasing energy except at 40 keV, for which case the peak concentration is lower than at 75 keV. However, the electrical profiles for different ion energies do not quite vary in the same way as the LSS profiles. The trend shown in the electrical profiles is also found in SIMS (Secondary Ion Mass Spectroscopy) atomic profiles performed on similar samples. Significant redistribution of the implanted S results after thermal annealing when the implanted-S concentration is below about $5 \times 10^{18} / \text{cm}^3$, whereas the S does not redistribute appreciably at the higher-implanted concentrations, presumably due partly to sulfur precipitates. Consequently, this behavior of the S atomic redistribution greatly affects the electrical profiles and the resultant net activation.

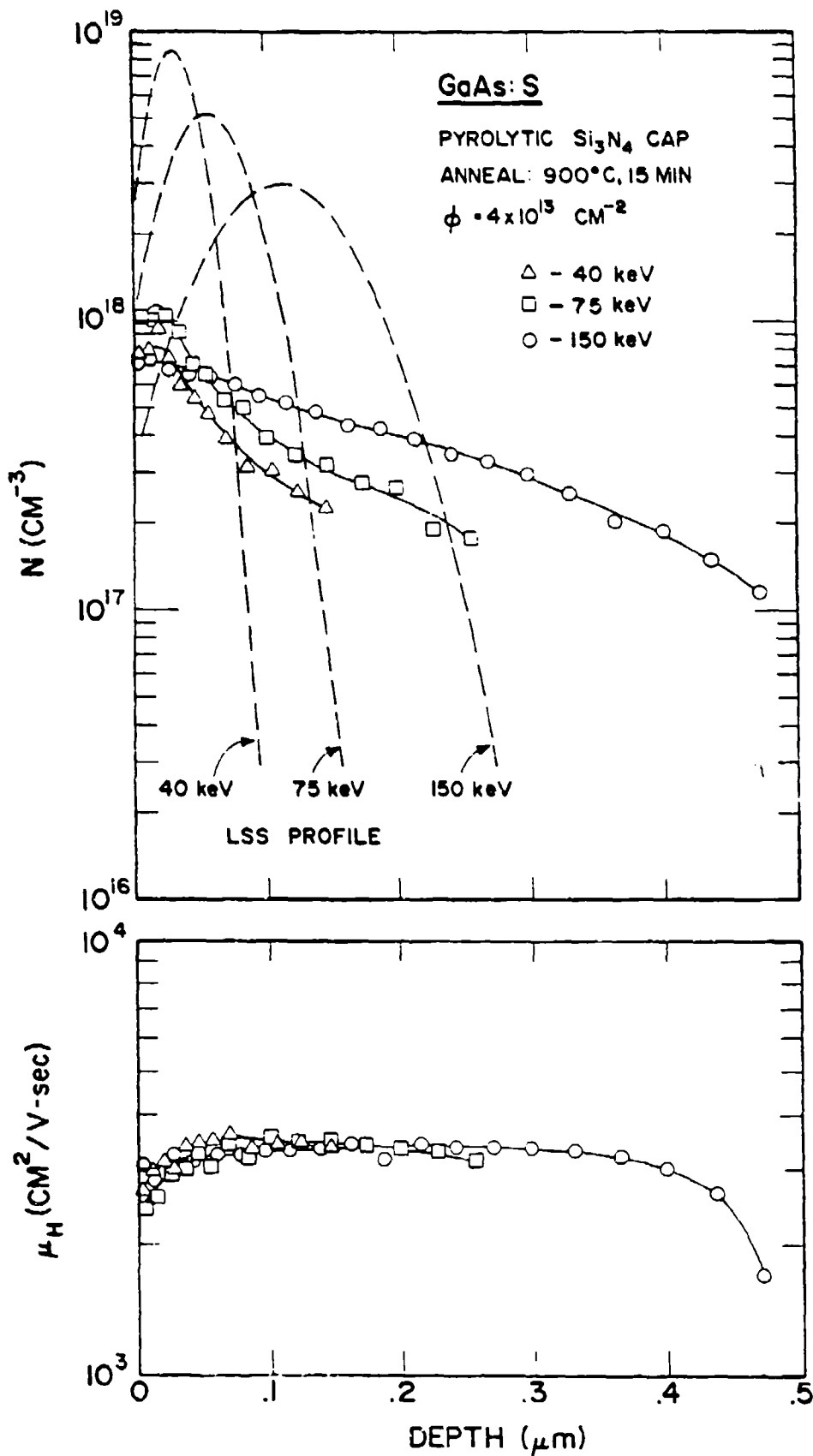


Figure 45 Electrical Carrier Profiles of $4 \times 10^{13}/\text{cm}^2$ Dose GaAs:S Samples Implanted at Three Lower Ion Energies

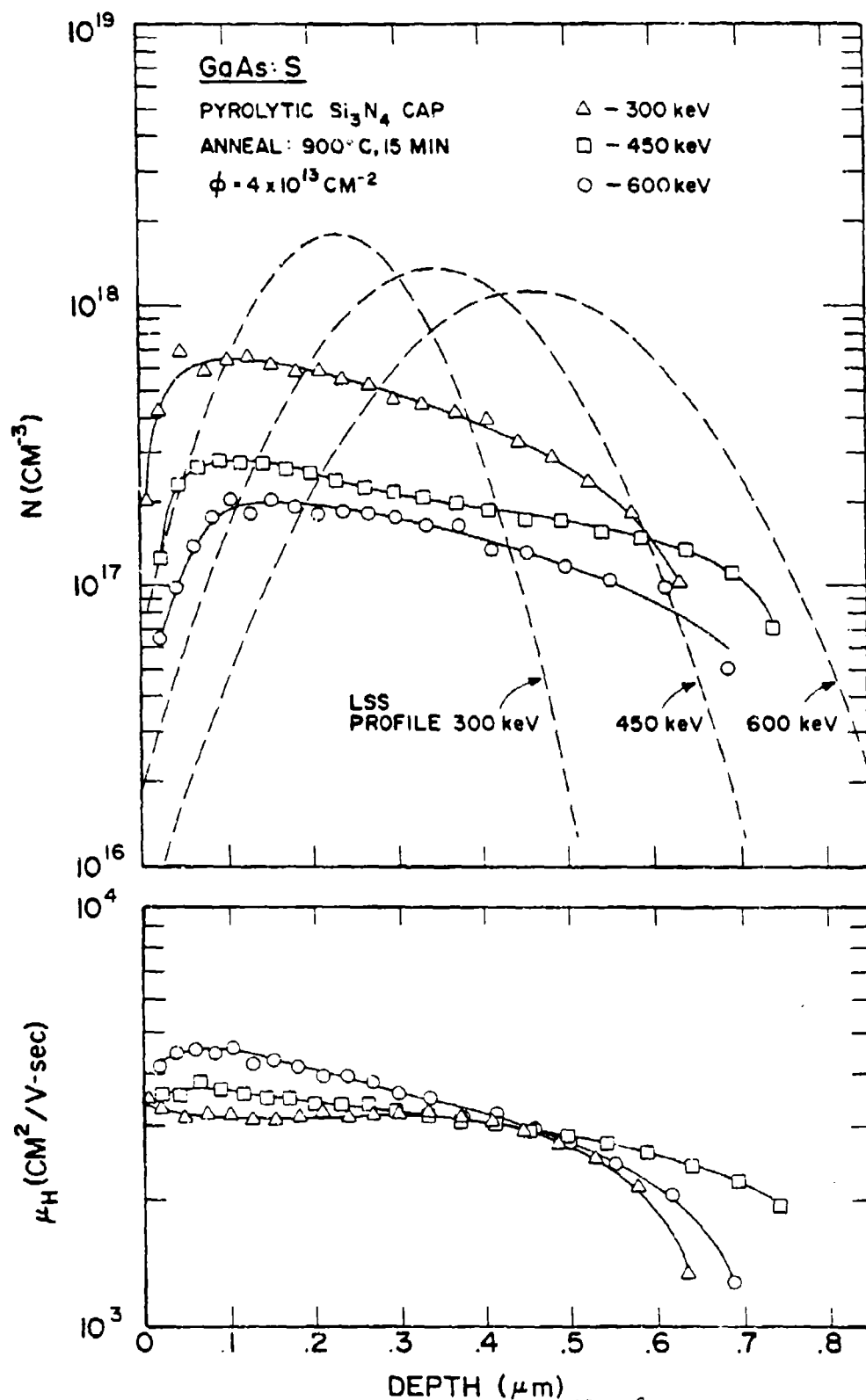


Figure 46 Electrical Carrier Profiles of $4 \times 10^{13}/\text{cm}^2$ Dose GaAs:S Samples Implanted at Three Higher Ion Energies

Other factors may affect the electrical profiles as well. The peak carrier concentrations for the two lower energies can be considered within the high dose regime, and therefore are believed to be partly limited by a solid solubility. Also, carrier concentrations for the two higher energies are significantly lower throughout the implanted regions, probably due to various compensating effects. For example, no carriers are found deep in the implanted region of the 600 keV sample. Even though we also observed Cr redistribution upon thermal annealing from SIMS measurements, we have not been able to make any direct correlation between the redistributed-Cr level and the carrier profiles at present.

Up to the ion energy of 150 keV, the electrically active layers extend to roughly twice the projected ranges of the original implants, indicating a significant indiffusion of the implanted sulfur ions. On the other hand, less sulfur indiffusion takes place for further increase in ion energy. The profiles for the two higher ion energies are rather flat, and the carrier concentrations are notably reduced throughout the active layers.

It appears that the electrical activation as well as the carrier profiles are highly dependent upon the implanted peak concentrations and the depths of the original implants. For an intermediate dose (e.g., $4 \times 10^{13}/\text{cm}^2$), the activation is poor at lower energies (high dose regime) presumably due to unannealed residual damage and S precipitates as well as some outdiffusion, and improves as the ion energy increases, effectively lowering the ion dose. The activation becomes poor again at higher energies, probably due to additional compensation arising from the increased depth of the redistributed S. Compensating effects may be especially significant in the case of Cr-doped semi-insulating GaAs.

Electrical depth profiles of carrier concentrations and Hall mobilities for samples implanted at an ion energy of 300 keV with doses ranging from 4×10^{12} to $4 \times 10^{15} \text{ cm}^{-2}$, and annealed at 900°C , are shown in Figure 47. Electrical activation efficiencies are 74%, 64%, 5%, and 1% for doses of 4×10^{12} , 4×10^{13} , 4×10^{14} , and $4 \times 10^{15} \text{ cm}^{-2}$, respectively. The activation efficiency drops sharply as the dose increases. A redistribution of sulfur takes place for all doses, showing a significant indiffusion of the implanted sulfur for all except the lowest dose. For the two low doses, a considerable number of carriers is found near the surface, whereas for the two high doses, no carriers are found at all well into the implanted region. Mobilities are also very low in most of the implanted region for high doses. The results of SIMS profiles for samples implanted at 300 keV to a dose of $4 \times 10^{13} \text{ cm}^{-2}$ and annealed at 840°C have recently been reported by Wilson et al.⁴⁴ showing a significant redistribution of the sulfur throughout the implanted region during annealing. Also, Evans et al.⁴⁵ reported results of SIMS data for samples implanted at 300 keV to a dose of $4 \times 10^{15} \text{ cm}^{-2}$ and annealed at 840°C . This study indicated no significant redistribution of sulfur at concentrations above $5 \times 10^{18} \text{ cm}^{-3}$ but showed a significant indiffusion of sulfur below this concentration. Our present electrical carrier profiles are consistent with the SIMS data cited above.

3.5.3 Atomic Profiles

A comparative study of SIMS atomic profiles and electrical carrier profiles for S-implanted GaAs has also been made in order to better understand the electrical behavior of the sulfur implants, and detailed results were reported⁴² recently.

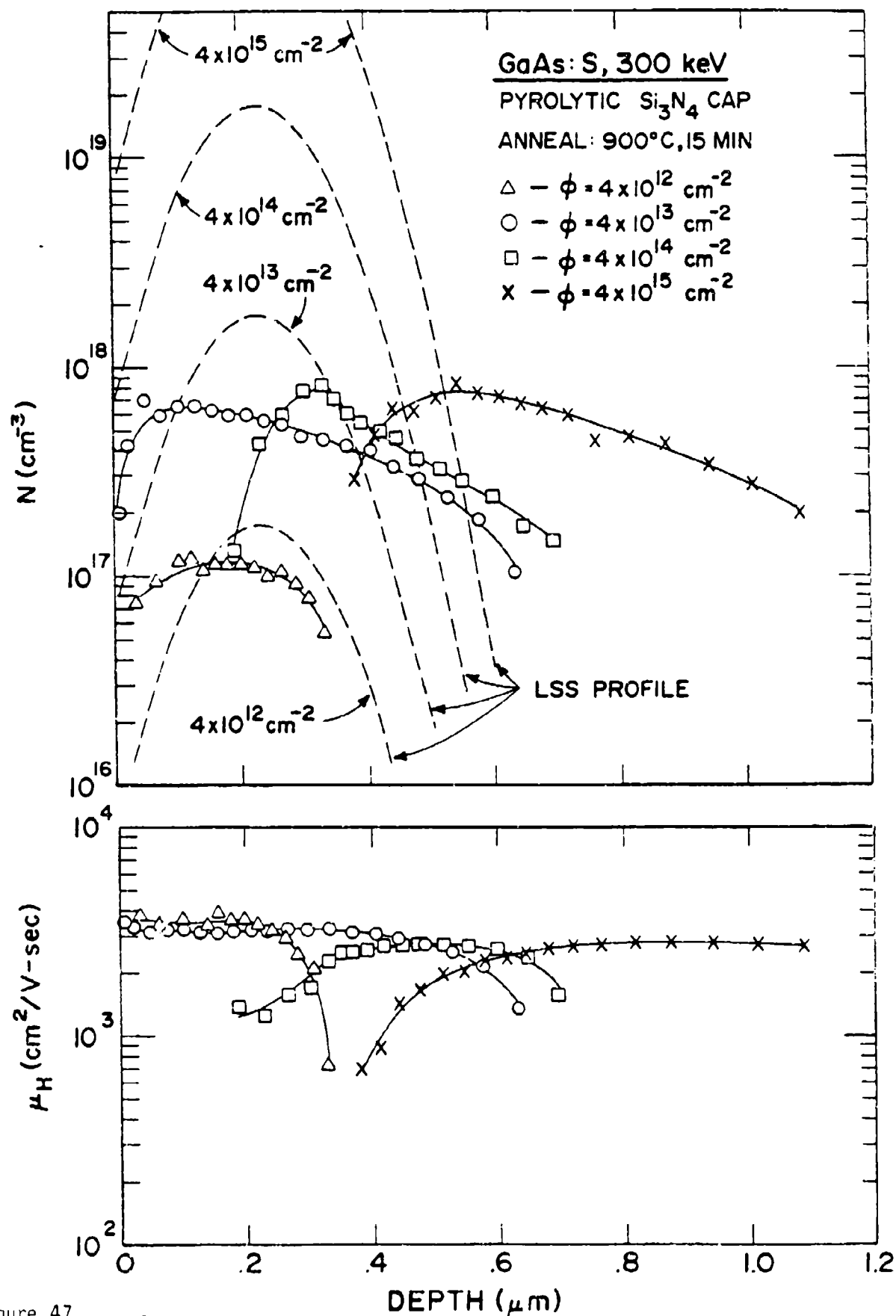


Figure 47

Electrical Carrier Profiles of 300 keV GaAs:S Samples Annealed at 900°C

SIMS atomic profiles of S were measured using cesium-ion bombardment and negative-ion spectroscopy, while the Cr distributions were measured using oxygen-ion bombardment and positive-ion spectroscopy. Both the chemical-etching rate and the sputtering rate were determined using a Sloan Dektak.

The results of electrical profiles and SIMS atomic profiles made on GaAs samples implanted at an ion energy of 120 keV to doses of 1×10^{13} , 1×10^{14} , and $1 \times 10^{15} \text{ cm}^{-2}$, and annealed at 900°C are shown in Figures 48, 49, and 50, respectively. Only representative points of SIMS data toward the deep side of the annealed samples are plotted for clarity. The theoretical Lindhard-Scharff-Schiott (LSS) curves are also plotted in all figures for comparison purposes. In the SIMS analysis, background levels of S have been subtracted, and the curves of as-implanted samples have been normalized in such a way that the integrated area under the SIMS output corresponds to the implanted-ion doses. For the annealed samples, there is no observable amount of S outdiffusion, and therefore, the SIMS data have been normalized in the same way as for the as-implanted samples. Surface corrections have also been made for the first several data points, which show abnormally high values, probably attributable to artifacts. Such artifacts near the surface have also been observed even for samples which were capped but not annealed. For all samples, the S background level was found to be approximately $2.5 \times 10^{16} \text{ cm}^{-3}$. This background may be due to residual S present in the bulk GaAs. The small dip in the SIMS profiles near the surface can be accounted for by the secondary ionization mechanism involving the native oxide. Similar dips have been observed⁴⁶ for the case of Se implants in GaAs.

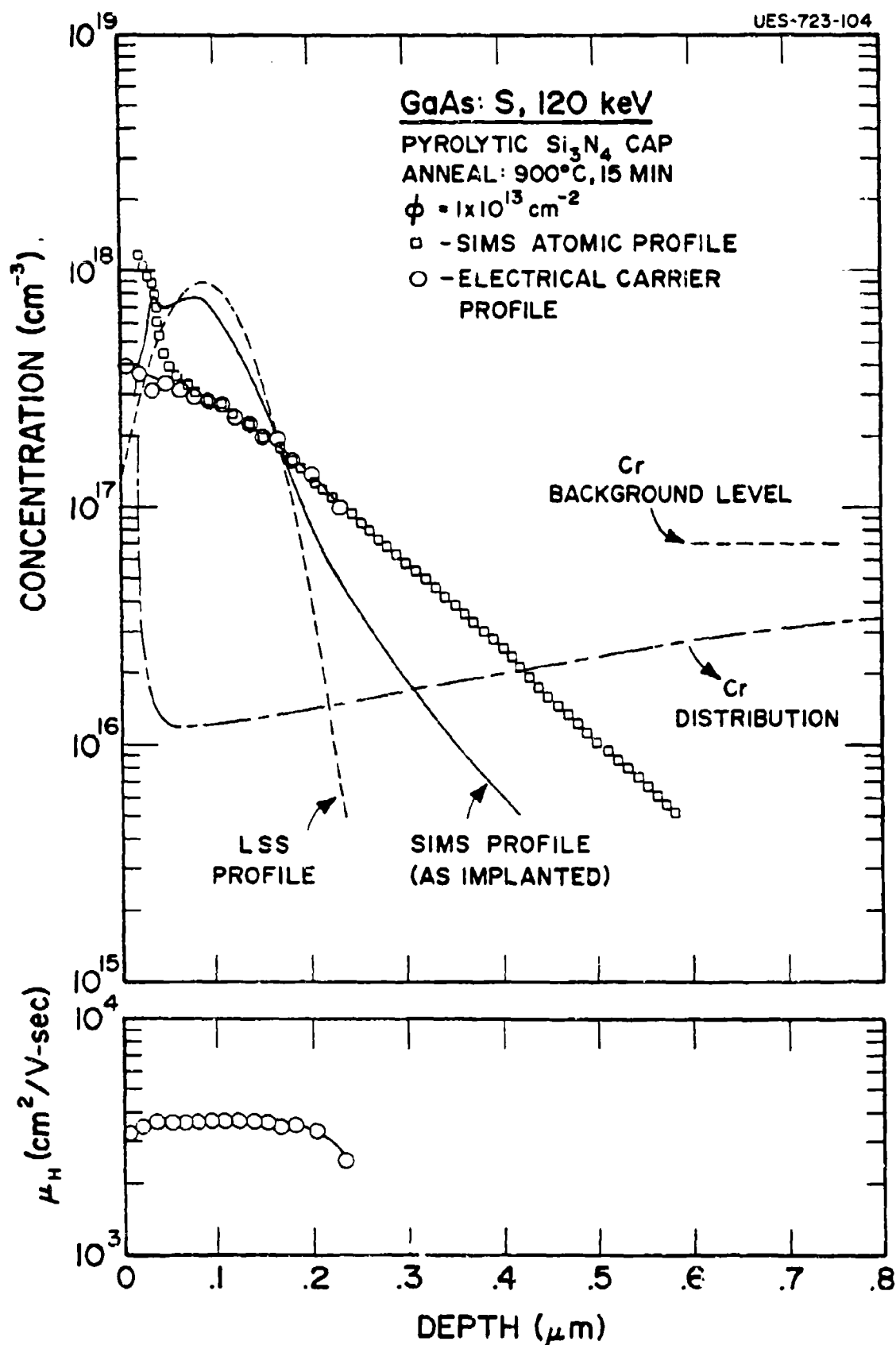


Figure 48 SIMS Atomic and Electrical Carrier Profiles of $1 \times 10^{13}/\text{cm}^2$ Dose GaAs:S

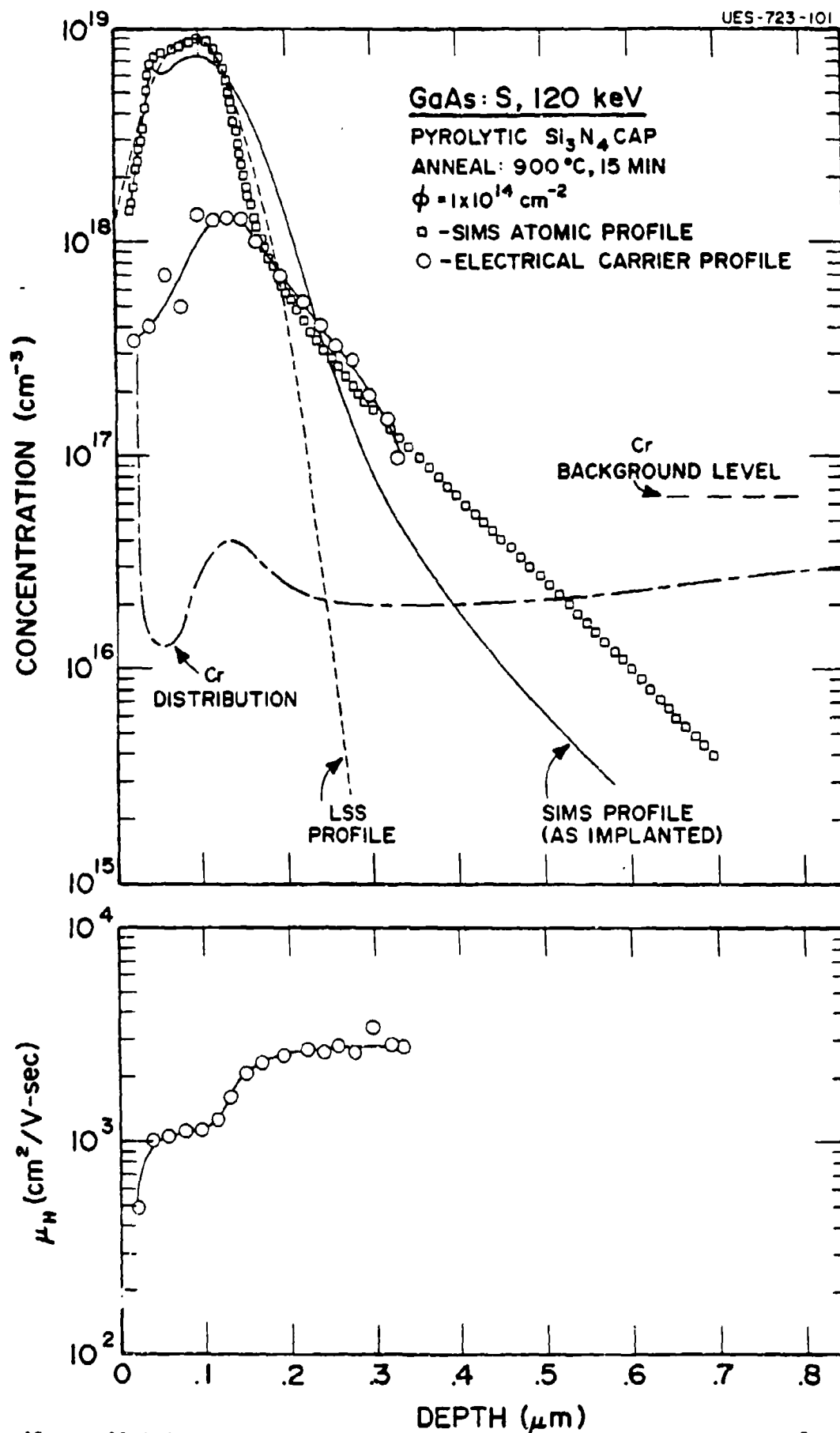


Figure 49

SIMS Atomic and Electrical Carrier Profiles of $1 \times 10^{14}/\text{cm}^2$
 Dose GaAs:S

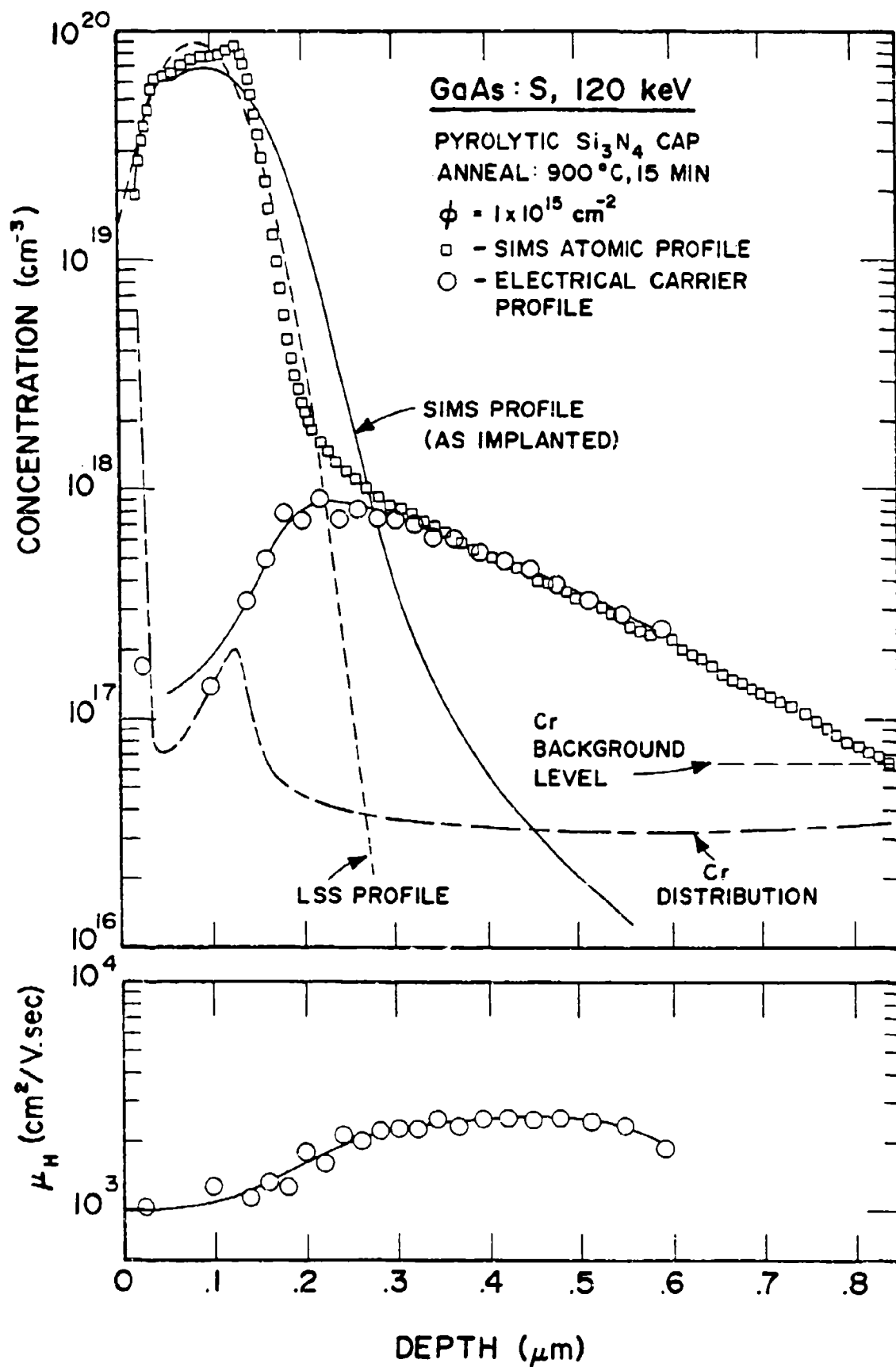


Figure 50 SIMS Atomic and Electrical Carrier Profiles of $1 \times 10^{15}/\text{cm}^2$ Dose GaAs:S

One of the most important findings of our experimental results is that, deep in the doped sample, the electrical carrier profiles follow the SIMS atomic profiles after annealing very closely for all three doses. This behavior is in marked contrast to the results reported by Lidow et al.⁴⁷ in similar work with Se-implanted GaAs. It has also been found that during thermal anneal, the redistribution of the S implant depends strongly on the ion dose, especially in the peak region. However, sulfur indiffusion takes place at all dose level upon thermal annealing, although the indiffusion may not be as severe as generally believed. This is clear from the figures when one compares the as-implanted profile (rather than the customary LSS profile) with that of the annealed sample. The as-implanted profiles of S in GaAs do not closely follow a simple Gaussian profile, and the former is usually deeper than the latter. This may be due partly to the experimental error and/or ion channeling contribution.

As shown in Figure 48, the implanted S redistributes significantly upon annealing over the entire implanted region for a dose of $1 \times 10^{13} \text{ cm}^{-2}$, which produces an as-implanted peak of $7.8 \times 10^{17} \text{ cm}^{-3}$. Some accumulation of S can clearly be seen near the surface, although most of this sulfur is not electrically activated. The inactivated S near the surface and in the tail region are about 30% and 10% of the implanted ion dose, respectively, accounting for the electrical activation efficiency of about 60% of this dose. The reasons for the S inactivation near the surface are not well understood at present, but may be related to residual surface defects. Since little, if any, outdiffusion of S is found to occur, the observed low electrical activation cannot be attributed to an outdiffusion effect, as suggested, for example, by Eisen et al.,³⁴ in the case of sputtered

Si_3N_4 caps. The mobility remains essentially flat throughout the entire region except near the surface and deep side of the sample.

In contrast with the low-dose case, as shown in Figures 49 and 50, the implanted S does not redistribute upon annealing as dramatically for high doses ($>1 \times 10^{14} \text{ cm}^{-2}$), which produce an as-implanted peak of about $7.5 \times 10^{18} \text{ cm}^{-3}$ or above. In this case, the S-atomic profiles of the annealed samples match very well with those of the as-implanted samples near the surface, although a slight change in S distribution occurs in the implanted peak region. The reasons for the lesser degree of S redistribution near the surface and peak region of the high-dose samples are not understood well at present. However, this may be partly due to the presence of immobile precipitates of S and disorder remaining even after annealing. In addition, these defects inhibit most of the S in the implanted peak region from becoming electrically active. In contrast, the S atoms in the less damaged region diffuse appreciably, and become electrically active. The inactivated sulfur near the surface and peak region is about 81% and 97% for doses of 1×10^{14} and $1 \times 10^{15} \text{ cm}^{-2}$, respectively, accounting for the very low electrical-activation efficiencies of 18% and 2.7%, respectively. The amount of inactivated S in the tail region is negligible and is only about 1% or less for these dose levels. Similar behavior of Se-implanted GaAs for high dose has been reported previously by Lidow et al.,⁴⁸ and they attributed this to the selenium precipitates. One may notice that carrier mobilities for high doses are significantly lower near the surface and in most of the implanted peak region, where presumably the S precipitates and unannealed damage are large.

The Cr profile for the S-implanted sample is flat before annealing. However, the Cr redistributes upon annealing, in a manner which depends on the implanted S dose. The absolute concentration of Cr was calculated by reference to a standard GaAs sample implanted with Cr, and the background levels (typically $\sim 6.5 \times 10^{16} \text{ cm}^{-3}$) are indicated in the figures. For a S fluence of $1 \times 10^{13} \text{ cm}^{-2}$, a surface accumulation of Cr is observed, followed by a depleted region about 3-4 μm deep. For high doses ($> 1 \times 10^{14} \text{ cm}^{-2}$) of implanted S, the Cr distribution curves show a peak near the implanted peak region in addition to a surface accumulation. Apparently, the Cr is gettered in the regions where defects and/or implanted damage are great as reported by Vasudev et al.¹⁴ However, at present we cannot determine any direct correlation between Cr redistribution and the electrical depth profile. Carrier concentrations may be too high to exhibit the effect of the Cr redistribution.

3.5.4 Summary

Through a comprehensive study of S implants in GaAs, it has been found that both electrical activation efficiency and carrier profiles are highly dependent upon the annealing temperature, the implanted peak concentration, and the implanted depth. The implanted S undergoes substantial redistribution during thermal annealing throughout the entire implanted region for an implanted peak concentration below about $5 \times 10^{18} \text{ cm}^{-3}$, whereas the S redistributes to a much lesser extent in the implanted peak region and near the surface for higher implanted peak concentration, although significant S indiffusion takes place in the deep side of the implanted layer. The electrical carrier profiles are greatly affected by this S redistribution. The electrical activation efficiencies are generally high for the samples

having low implanted peak concentrations, but they are limited by a considerable amount of inactivated S near the surface for low ion energies and by greater compensation for high ion energies. On the other hand, the electrical activation efficiencies are very poor for samples having high implanted peak concentrations due to a large amount of unannealed disorder and/or sulfur precipitates, producing a significantly lower number of carriers and low mobilities near the surface and the implanted peak region. It is believed that the observed low electrical activation is not caused chiefly, if at all, by outdiffusion of sulfur, but by a substantial amount of inactivated sulfur. High annealing temperatures ($>900^{\circ}\text{C}$) are generally required to achieve better electrical activation. A maximum electrical activation efficiency of 80% and a maximum carrier concentration of $2.5 \times 10^{18} \text{ cm}^{-3}$ were obtained under appropriate conditions for GaAs:S implanted at room temperature.

3.6 Si-IMPLANTED GaAs

Silicon-implanted GaAs has been widely used for the fabrication of various devices such as field-effect transistors and integrated circuits, because Si is a light atom and hence it has sufficient ion range for many device requirements. Moreover, for low-dose Si implants, high electrical activation efficiencies are generally achieved with room temperature implantation. Although a number of publications^{29, 36, 37, 49-52} dealing with the electrical properties of Si implants in GaAs have appeared in the literature, the fundamental difficulties encountered with this dopant are still not well understood. In particular, no comprehensive study has been reported, to the best of our knowledge, for low-dose Si implants in GaAs in spite of the wide use in device fabrication. Moreover, there are inconsistent

reports about depth profiles of electrical carrier concentrations and diffusion of Si during annealing. Also, most previous studies have been made using Cr-doped semi-insulating GaAs, and only a few studies have been done using undoped semi-insulating GaAs.

3.6.1 Electrical Activation

Si, like Ge, is an amphoteric dopant in GaAs; therefore, theoretically, it should be possible to produce n- or p-type conductivity. However, the implanted Si has been found to be an n-type dopant in GaAs, which implies that the implanted Si ions preferentially go into Ga sites.

The results of Hall-effect/sheet-resistivity measurements made on both Cr-doped and undoped semi-insulating GaAs implanted with Si at an ion energy of 120 keV to doses ranging from 3×10^{12} to $3 \times 10^{15} \text{ cm}^{-2}$ and annealed at various temperatures are shown in Figures 51 and 52. Here the undoped GaAs substrates were obtained from Cambridge Instruments, Ltd. For both substrates, the annealing behavior of surface-carrier concentrations is highly dependent upon ion dose and annealing temperature. For a dose of $1 \times 10^{13} \text{ cm}^{-2}$ or below, the maximum electrical activation occurs at the 850°C anneal, while for doses of 3×10^{13} and $1 \times 10^{14} \text{ cm}^{-2}$, the maximum occurs at the 900°C anneal. However, for doses above $3 \times 10^{14} \text{ cm}^{-2}$, the electrical activation increases monotonically with annealing temperature as high as 950°C. The highest electrical activation efficiency obtained was about 90% for the sample implanted to a dose of $1 \times 10^{13} \text{ cm}^{-2}$ and annealed at 850°C. The highest surface-carrier concentration obtained was nearly $1 \times 10^{14} \text{ cm}^{-2}$ for the sample implanted to a dose of $3 \times 10^{15} \text{ cm}^{-2}$ and annealed at 950°C. For a dose of $3 \times 10^{12} \text{ cm}^{-2}$, the electrical activation for the undoped substrates is higher than that for the Cr-doped GaAs, whereas

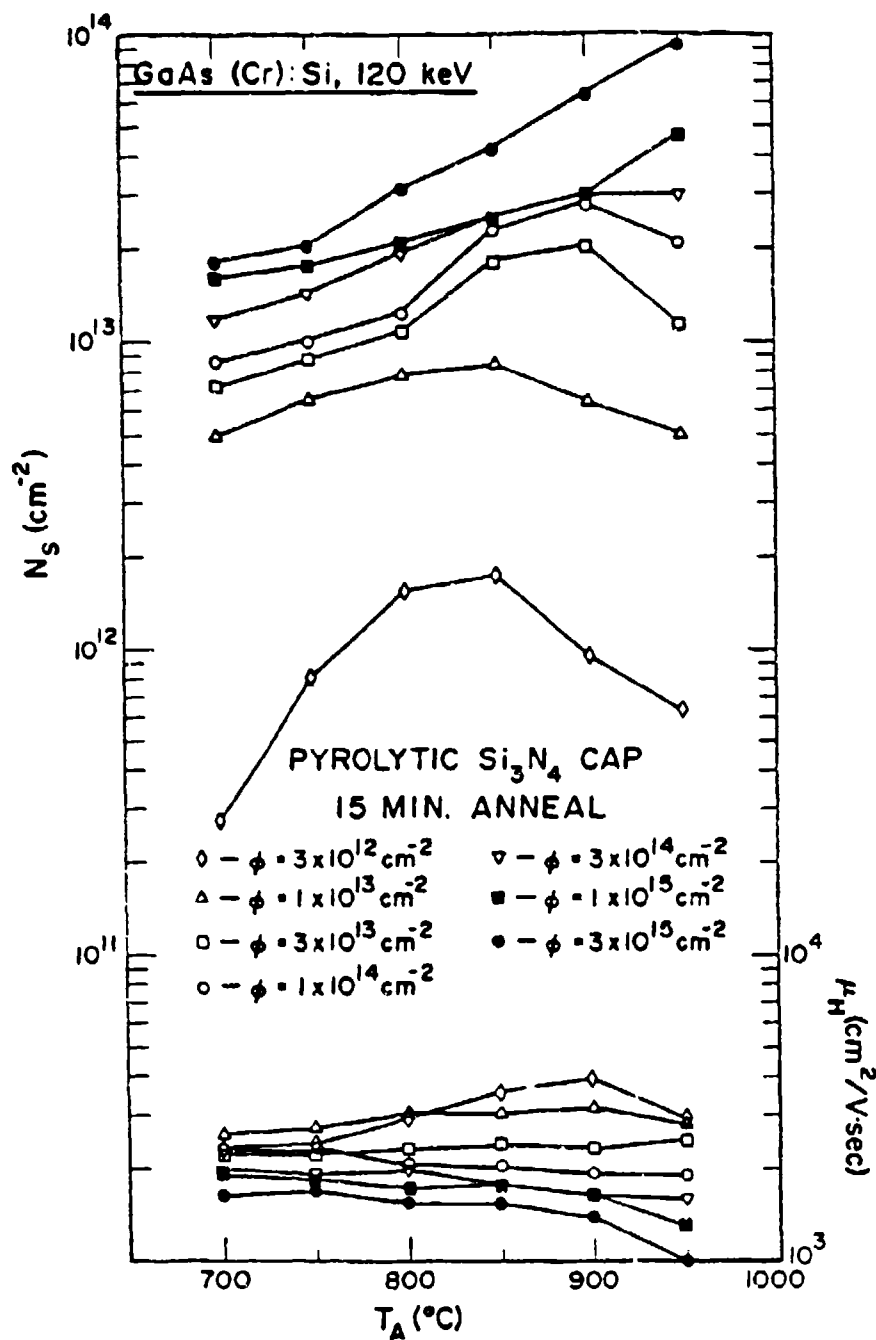


Figure 51 Dependence of Surface-Carrier Concentration (N_S) and Hall Mobility (μ_H) upon Annealing Temperature (T_A) for Si-Implanted Cr-doped GaAs

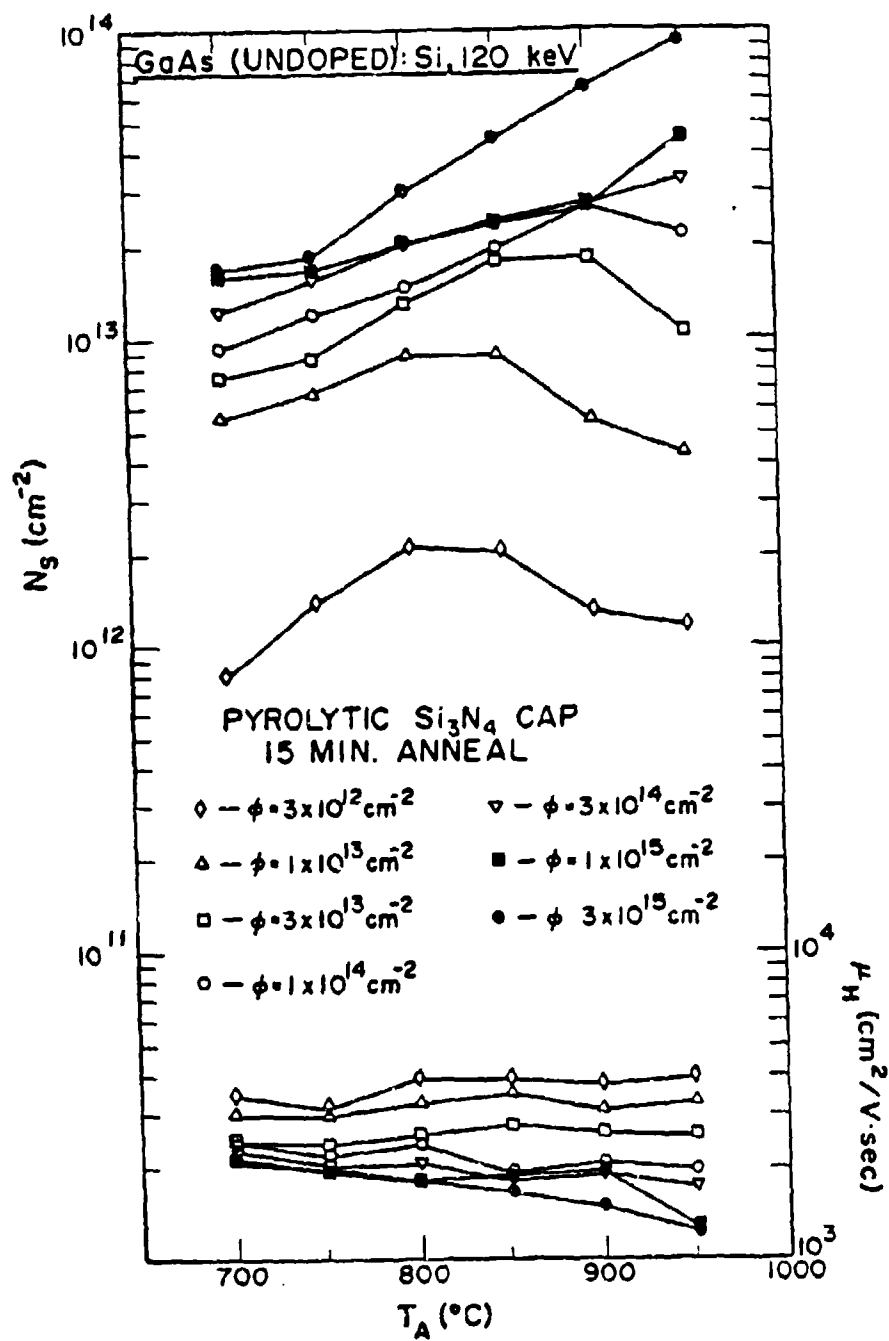


Figure 52 Dependence of Surface-Carrier Concentration (N_s) and Hall Mobility (μ_H) upon Annealing Temperature (T_A) for Si-Implanted Undoped GaAs

for higher doses, the activation is about the same for both substrates. The mobilities for the undoped substrates are generally higher than those for the Cr-doped substrates.

We investigated low-dose Si implants in GaAs in more detail, and the results of Hall measurements made on Cr-doped GaAs substrates implanted with Si at an energy of 100 keV to doses ranging from 1×10^{12} to $1 \times 10^{13} \text{ cm}^{-2}$ are shown in Figure 53. These results clearly show that the maximum electrical activation occurs at the 850°C anneal for all doses. The highest activation efficiency obtained was 89% for the sample implanted to a dose of $8 \times 10^{12} \text{ cm}^{-2}$. The decrease in electrical activation at the 900°C anneal may be due to outdiffusion of implanted Si ions. For the sample implanted with $2 \times 10^{12} \text{ cm}^{-2}$ and annealed at 800°C, no appreciable electrical activation has been observed. Samples having a dose of $1 \times 10^{12} \text{ cm}^{-2}$ have also been investigated, but no measurable electrical activation was obtained even at the 900°C anneal. The annealing behavior of the Hall mobility indicates that mobilities obtained after the 850°C anneal increased significantly from the values of the 800°C anneal for all except the dose of $1 \times 10^{13} \text{ cm}^{-2}$. However, the mobilities did not increase further after annealing the samples at 900°C. The mobilities for a dose of $1 \times 10^{13} \text{ cm}^{-2}$ remained about the same at three different annealing temperatures. Generally, mobilities are higher for low-dose samples than for high-dose samples.

Figure 54 is a replot of the data for Cr-doped substrates, showing surface carrier concentration versus implanted dose at different annealing temperatures. A straight line represents 100% activation efficiency. Activation efficiency clearly increases with ion dose up to

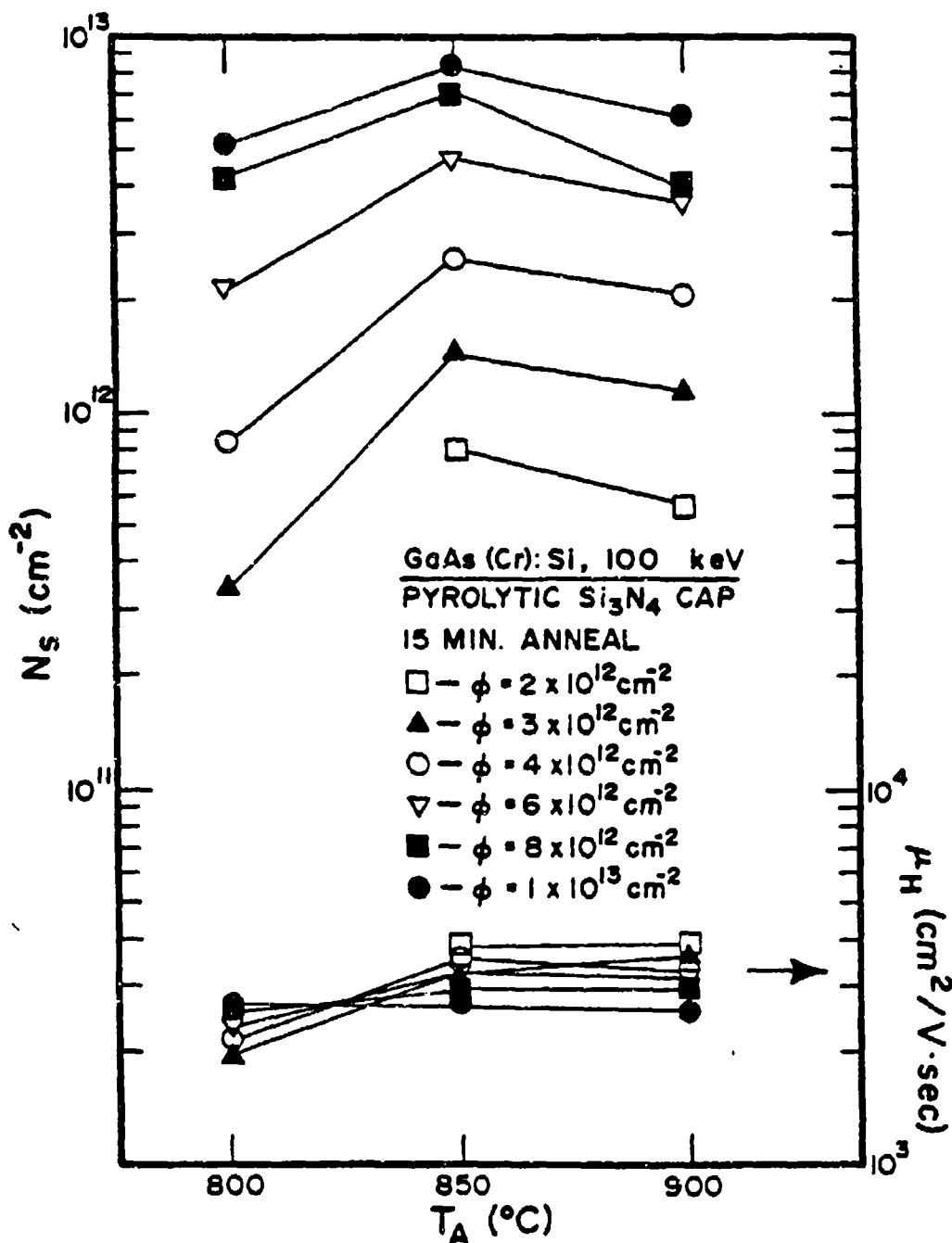


Figure 53 Dependence of Surface-Carrier Concentration (N_s) and Hall Mobility (μ_H) upon Annealing Temperature (T_A) for Low-Dose Si-Implanted Cr-doped GaAs

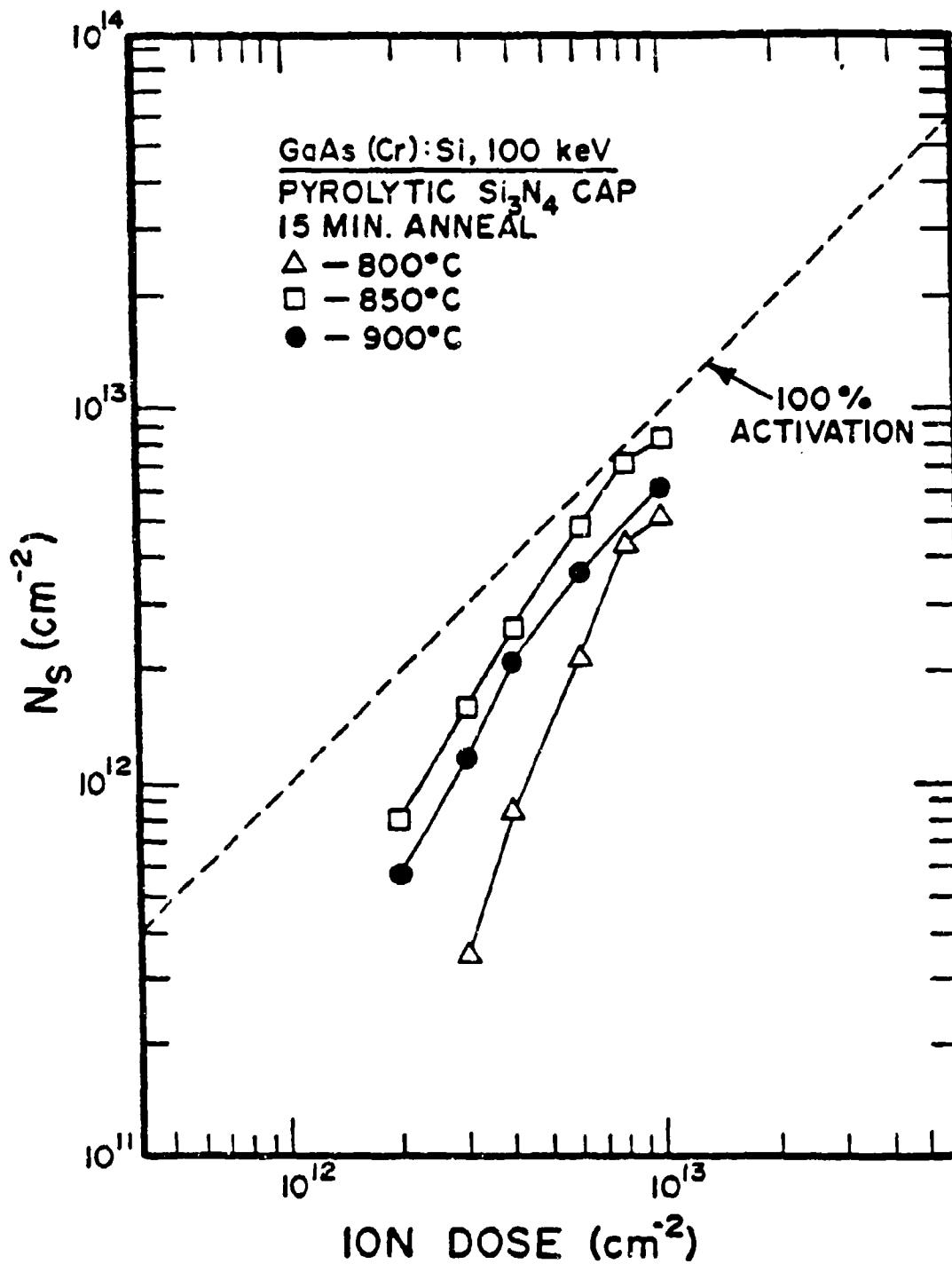


Figure 54 Dependence of Surface-Carrier Concentration (N_s) and Hall Mobility (μ_H) upon Ion Dose for 100-keV Si-Implanted Cr-doped GaAs

$8 \times 10^{12} \text{ cm}^{-2}$ and decreases slightly at an ion dose of $1 \times 10^{13} \text{ cm}^{-2}$. From this figure, we can deduce that the electrical activation for doses lower than $2 \times 10^{12} \text{ cm}^{-2}$ is very poor. The cut-off dose below which no appreciable electrical activation can be obtained is around $1 \times 10^{12} \text{ cm}^{-2}$.

The results of Hall measurements made on undoped GaAs substrates implanted with Si ions are also shown in Figure 55. The maximum electrical activation occurs at the 850°C anneal for most doses as in the case of Cr-doped substrates. However, the surface carrier concentrations for doses of 3×10^{12} and $4 \times 10^{12} \text{ cm}^{-2}$ are nearly the same for three annealing temperatures. The activation efficiency increases with ion dose up to a dose of $6 \times 10^{12} \text{ cm}^{-2}$ except for the 800°C anneal, and then it decreases slightly with increasing dose. Electrical activation for the undoped GaAs substrates is, in general, slightly higher at all annealing temperatures than that for Cr-doped GaAs for doses up to $6 \times 10^{12} \text{ cm}^{-2}$, whereas for higher doses, the activation is about the same for both substrates. The highest electrical activation efficiency obtained for undoped GaAs substrates was 87% for the sample to a dose of $6 \times 10^{12} \text{ cm}^{-2}$ and annealed at 850°C. The annealing behavior of the Hall mobility indicates that mobility is nearly independent of annealing temperature. It seems that lattice damage due to ion bombardment can be annealed well even at around 800°C for these undoped GaAs substrates. Furthermore, the mobilities are considerably higher for undoped substrates than for Cr-doped substrates at all annealing temperatures and doses.

Since the optimum annealing temperature for most of the Si-implanted GaAs is 850°C, surface-carrier concentrations obtained at the 850°C anneal have been compared for two different substrates, and the results

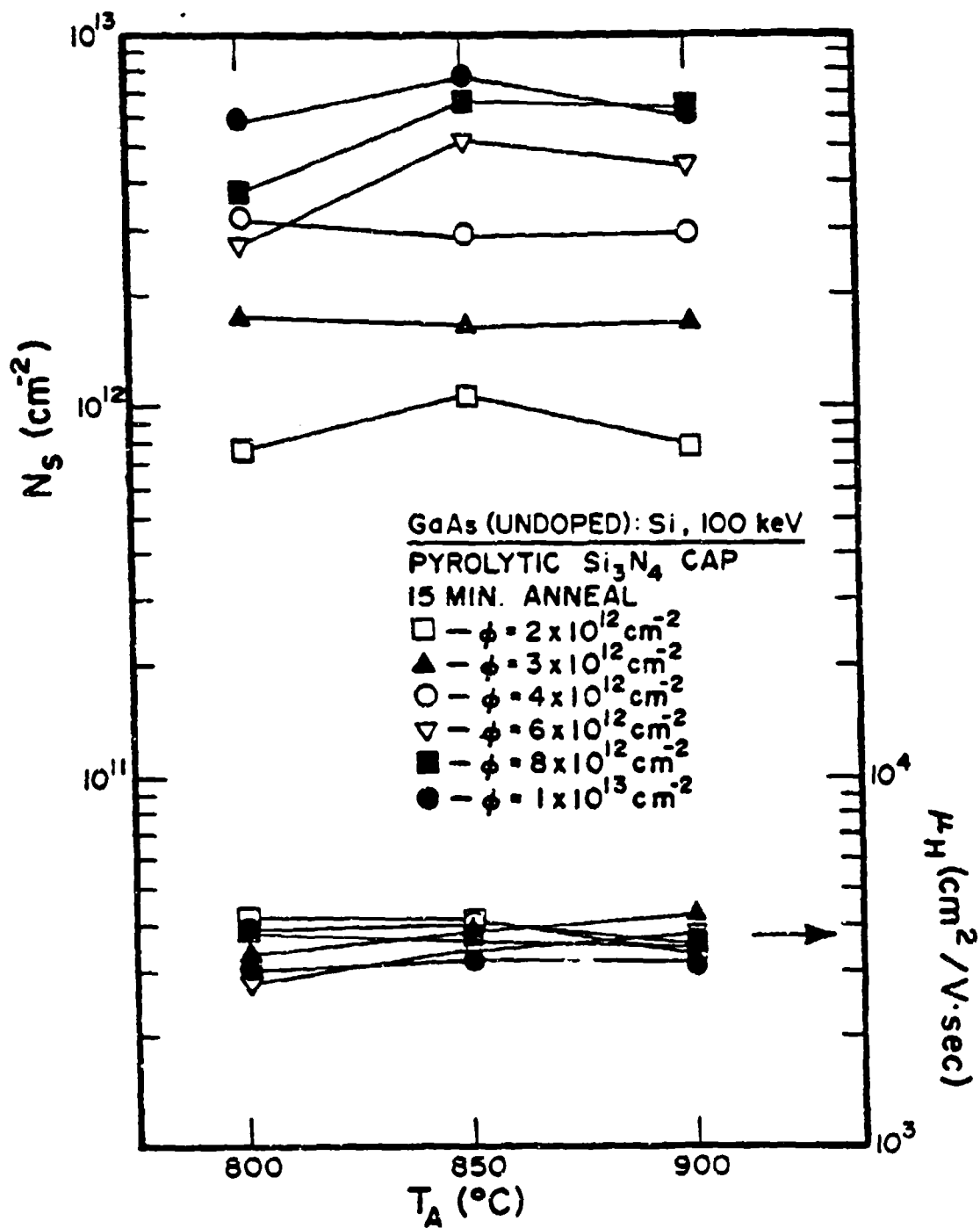


Figure 55 Dependence of Surface-Carrier Concentration (N_s) and Hall Mobility (μ_H) upon Annealing Temperature (T_A) for Low-Dose Si-Implanted Undoped GaAs

are shown in Figure 56. For low-dose implants ($< 6 \times 10^{12} \text{ cm}^{-2}$), the electrical activation for undoped GaAs substrates is slightly better than for Cr-doped substrates, whereas for the two higher doses, the reverse is true. For both substrates, the electrical activation efficiency increases with ion dose up to about $6 \sim 8 \times 10^{12} \text{ cm}^{-2}$, and then it decreases with increasing ion dose.

The results of electrical measurements made on undoped GaAs substrates implanted with Si to an ion dose of $4 \times 10^{12} \text{ cm}^{-2}$ at various ion energies and annealed at 850°C are shown in Figure 57. The electrical activation as well as the mobility for this dose level clearly increases with ion energy. The reasons for this increase in electrical activation efficiency with ion energy are not well understood at present. The highest electrical activation efficiency was 85% for an ion energy of 300 keV.

3.6.2 Electrical Carrier Profiles

Electrical depth profiles of carrier concentration and Hall mobility for Cr-doped substrates implanted with Si at an ion energy of 100 keV and annealed at 850°C are shown in Figure 58 for the three lower dose samples. In the profile measurements, an annealing temperature of 850°C was especially chosen because the maximum electrical activation occurred at this temperature. The theoretical LSS profile for an ion dose of $4 \times 10^{12} \text{ cm}^{-2}$ is also shown in this figure for comparison. The theory predicts that the peak concentration will occur at $\sim 0.085 \mu\text{m}$ for an ion energy of 100 keV. For an ion dose of $3 \times 10^{12} \text{ cm}^{-2}$ or below, the profiles show no clear peaks and the active layers extend only to about $0.075 \mu\text{m}$. Nearly all the Si ions in these active layers are electrically active, whereas the Si ions beyond the depth of about $0.075 \mu\text{m}$ are not electrically active at all or they are

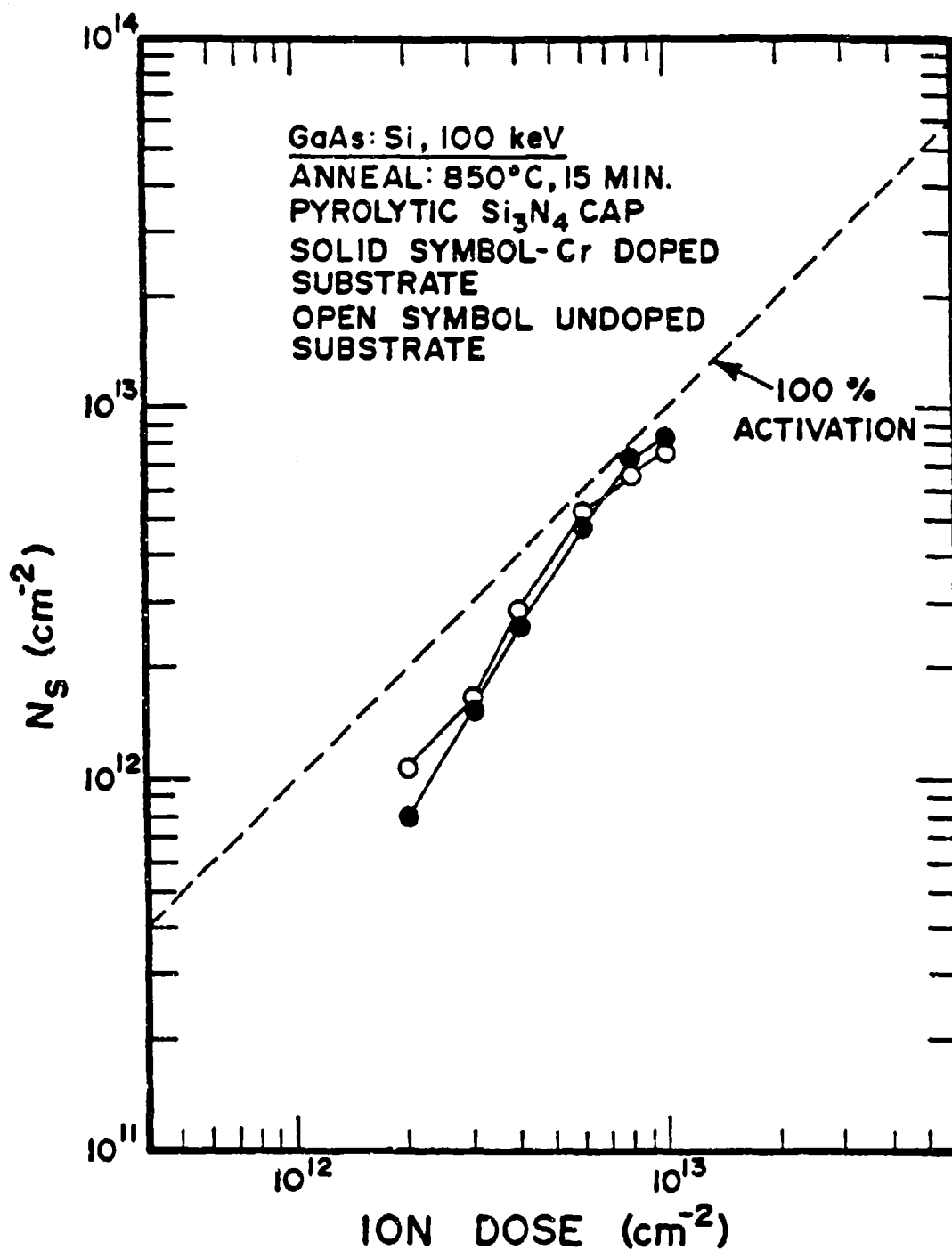


Figure 56 Surface-Carrier Concentration (N_s) versus Ion Dose for Two Different GaAs Substrates Implanted with Si

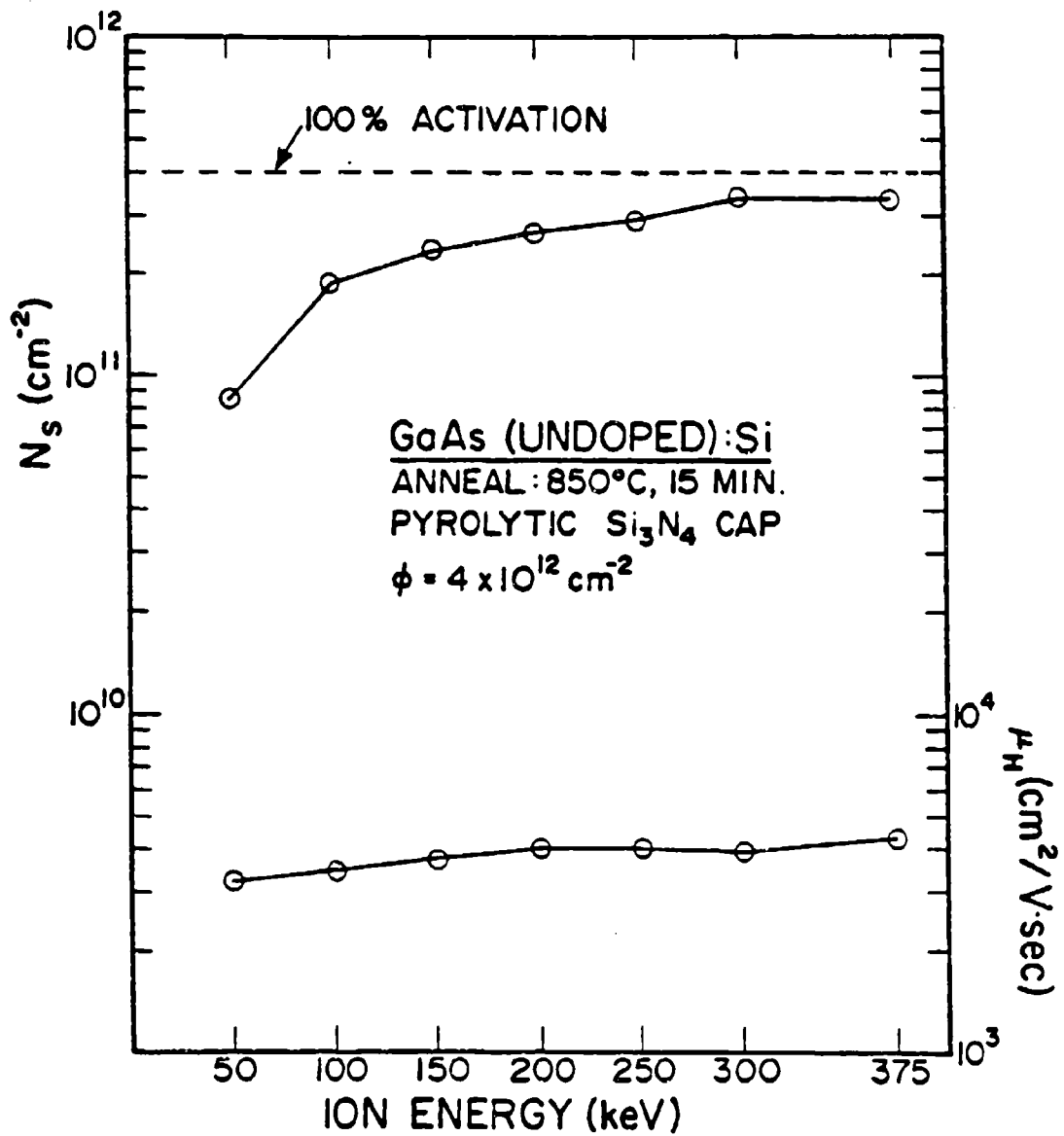


Figure 57 Surface-Carrier Concentration (N_s) and Hall Mobility (μ_H) versus Ion Energy for Si-Implanted Undoped GaAs

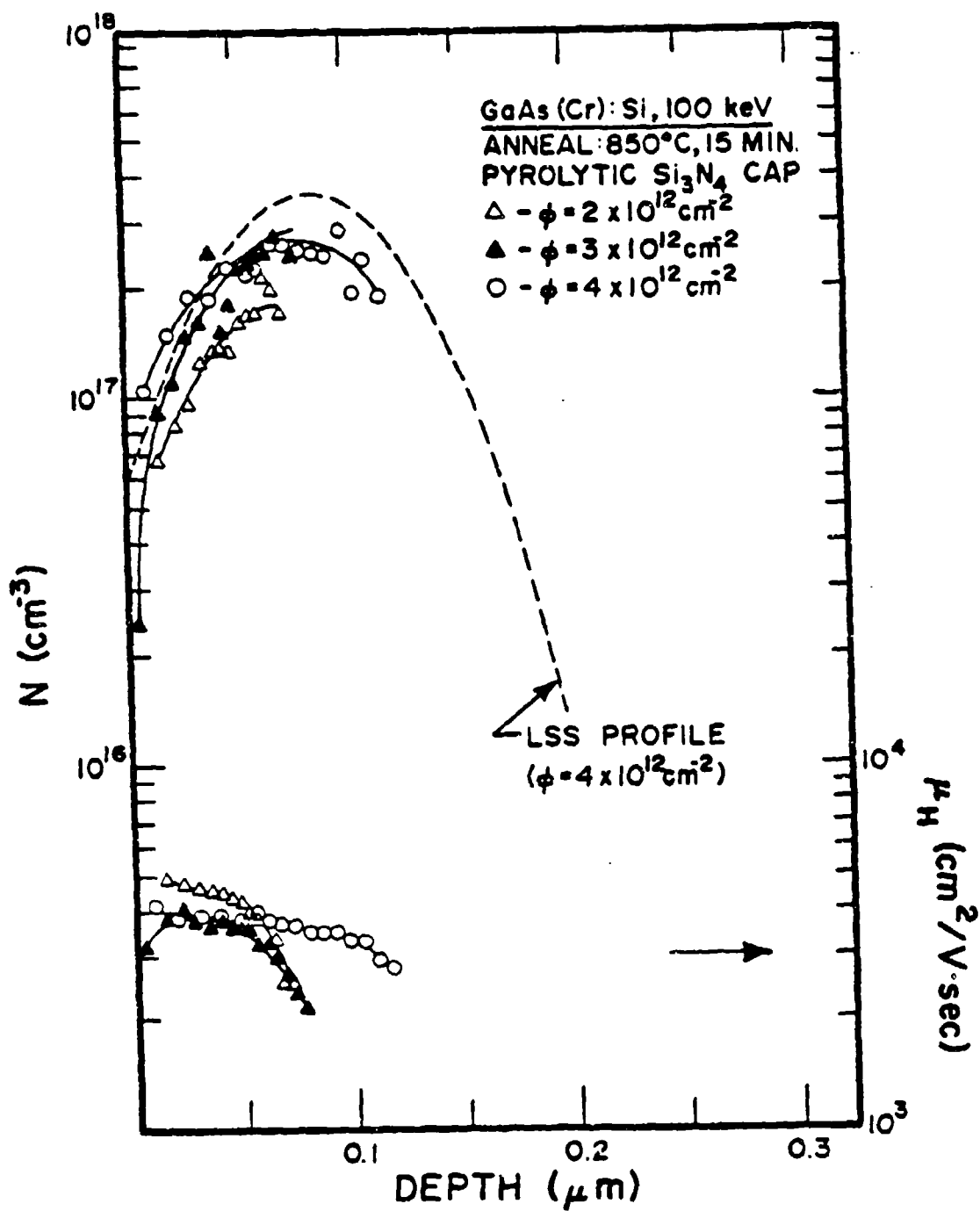


Figure 58 Electrical Carrier Profiles of Three Lower Si-Dose Cr-doped GaAs

completely compensated. Therefore, the electrical activation efficiencies are about 40~50% for these donors. Nevertheless, the maximum carrier concentrations obtained are about the same values predicted by the theory. The mobilities are high near the surface, and they decrease rapidly as the depth increases. For a dose of $4 \times 10^{12} \text{ cm}^{-2}$, the depth of an electrically active region is deeper than those for lower doses, extending roughly to $0.12 \mu\text{m}$. The mobilities decrease gradually with increasing depth.

Electrical depth profiles of Si implants in Cr-doped GaAs substrates for three higher doses are shown in Figure 59. The LSS profile for a dose of $1 \times 10^{13} \text{ cm}^{-2}$ is also shown in this figure. For doses of 6×10^{12} and $1 \times 10^{13} \text{ cm}^{-2}$, the carrier concentrations near the surface are higher than the values predicted by the theory. The carrier profile of a dose of $3 \times 10^{12} \text{ cm}^{-2}$ is much different from the others. The profile is much broader, and the carrier-peak position is deeper than the LSS peak position. For a dose of $1 \times 10^{13} \text{ cm}^{-2}$, the carrier profile follows generally very closely to the theoretical profile, and the peak-carrier concentration as well as the carrier-peak position agree with the theory. The mobilities for these three doses are initially higher near the surface, and then decrease gradually with increasing depth.

Electrical depth profiles of carrier concentration and Hall mobility for undoped substrates implanted with Si to the three lower doses and annealed at 350°C are shown in Figure 60. The LSS profile shown in this figure is for a dose of $4 \times 10^{12} \text{ cm}^{-2}$. The shapes of the carrier profiles are quite different from one another. The carrier profile for a dose of $2 \times 10^{12} \text{ cm}^{-2}$ initially follows the LSS profile closely up to a few hundred angstroms. Thereafter, the carrier concentrations continue to increase with

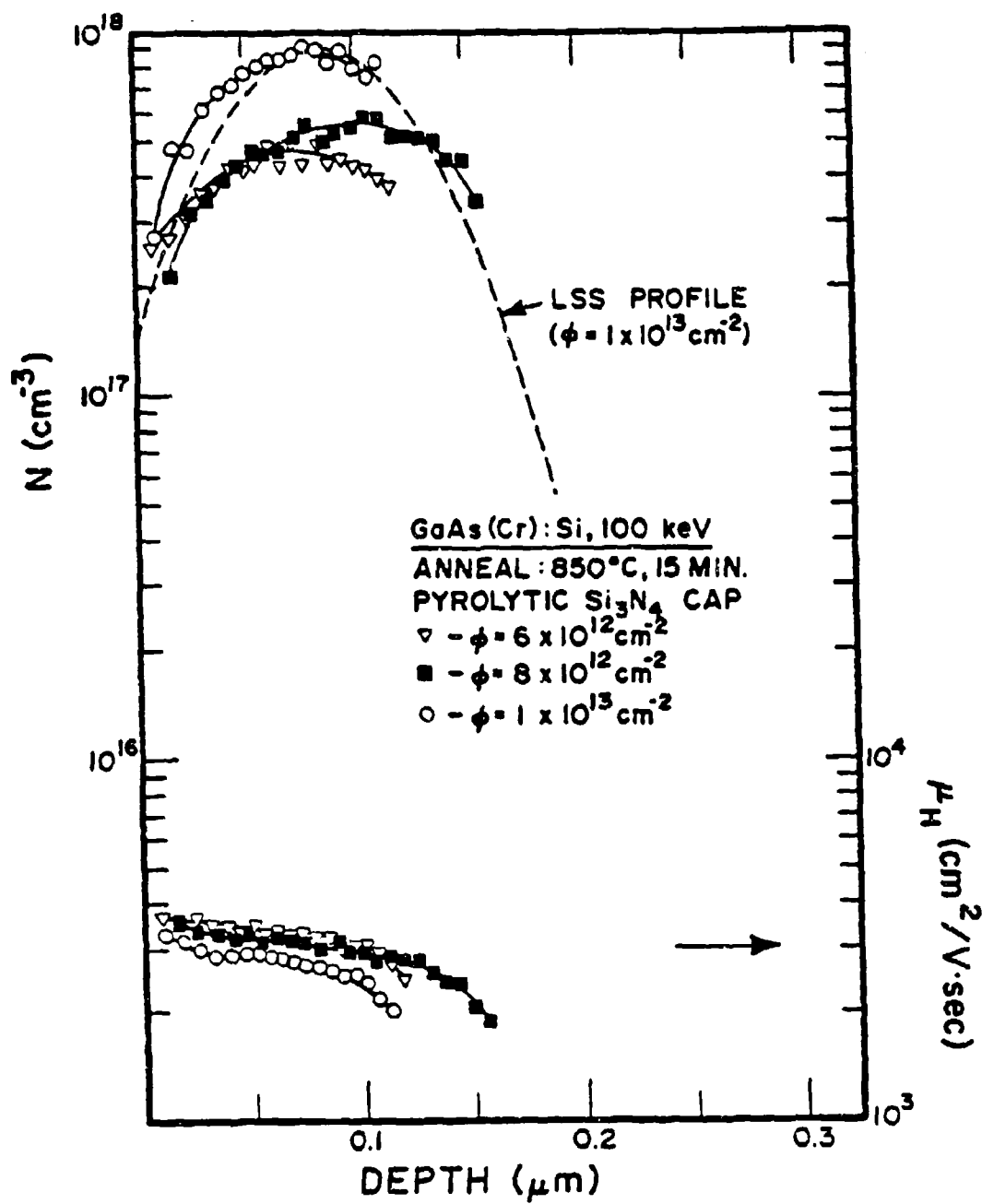


Figure 59 Electrical Carrier Profiles of Three Higher Si-Dose Cr-Doped GaAs

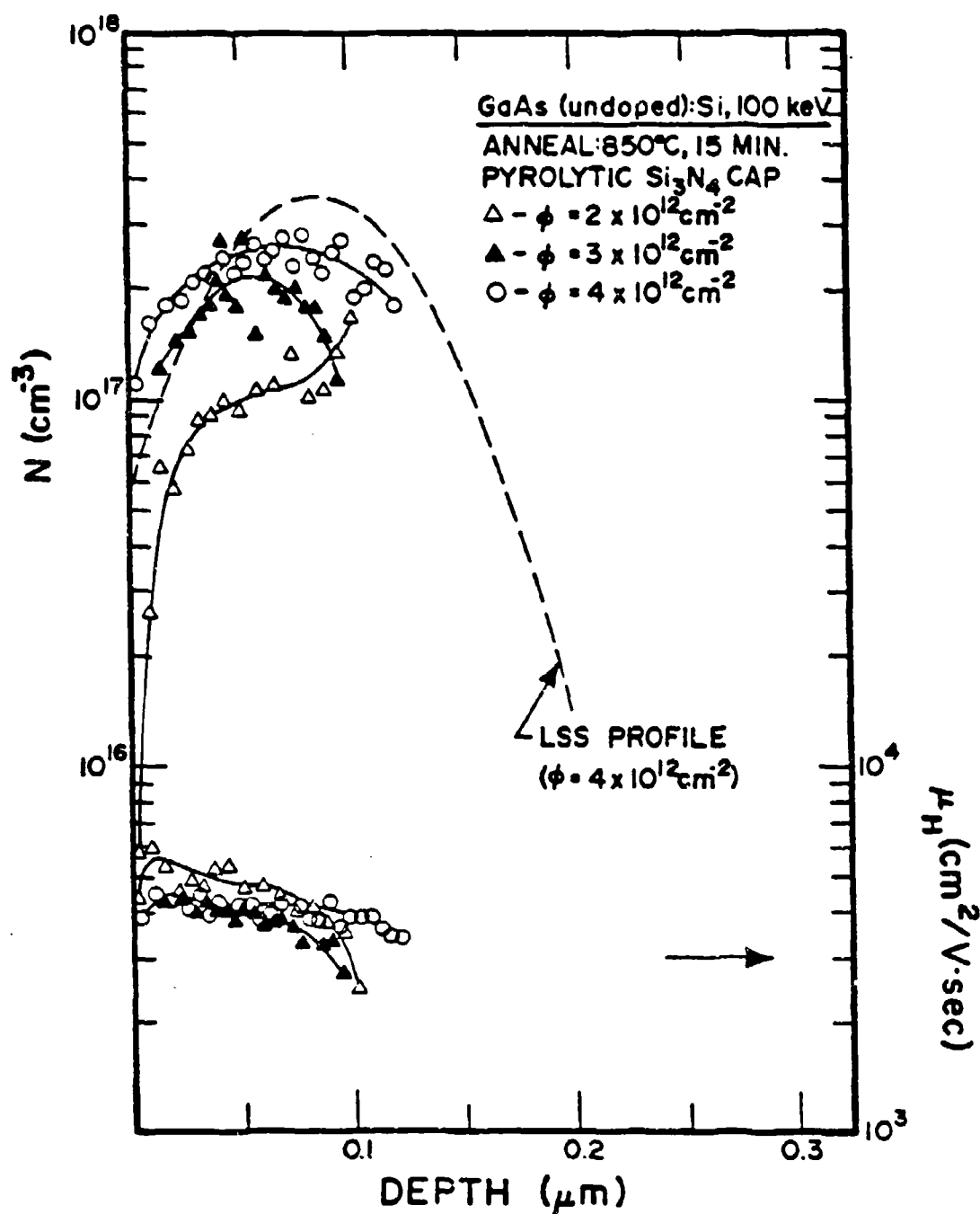


Figure 60 Electrical Carrier Profiles of Three Lower Si-Dose Undoped GaAs

depth up to the end of the active layer. For the two higher doses, the positions of peak carrier concentrations are closer to the surface than those of the theoretical peak carrier concentrations. Also, the carrier concentrations near the surface are higher than the values predicted by the theory.

Electrical depth profiles of Si implants in undoped GaAs substrates for three higher doses are shown in Figure 61. The LSS profile for a dose of $1 \times 10^{13} \text{ cm}^{-2}$ is also shown in this figure for comparison. The carrier profiles for these doses extend deep into the sample. Although the peak concentrations are much lower than the values predicted by the theory, the positions of peak-carrier concentrations agree with the position predicted by the LSS theory for all these doses. The mobilities decrease very slowly with increasing depth, and the trends of the mobility-depth profiles are about the same for all three doses.

Electrical profiles of carrier concentration and Hall mobility for both Cr-doped and undoped GaAs substrates implanted with three doses of Si ions at an energy of 100 keV and annealed at 850°C are shown in Figure 62. It can be clearly seen that the carrier concentrations in the Cr-doped substrates are higher than those in the undoped substrates throughout the entire active region for the given dose, whereas the reverse is true for mobilities. However, the depths of electrically active layers for undoped substrates are greater than those of Cr-doped substrates at a given dose. The shallower active layers of the Cr-doped substrates suggest that electrical compensation in the deep side of the sample is greater for the Cr-doped substrates than for the undoped substrates.

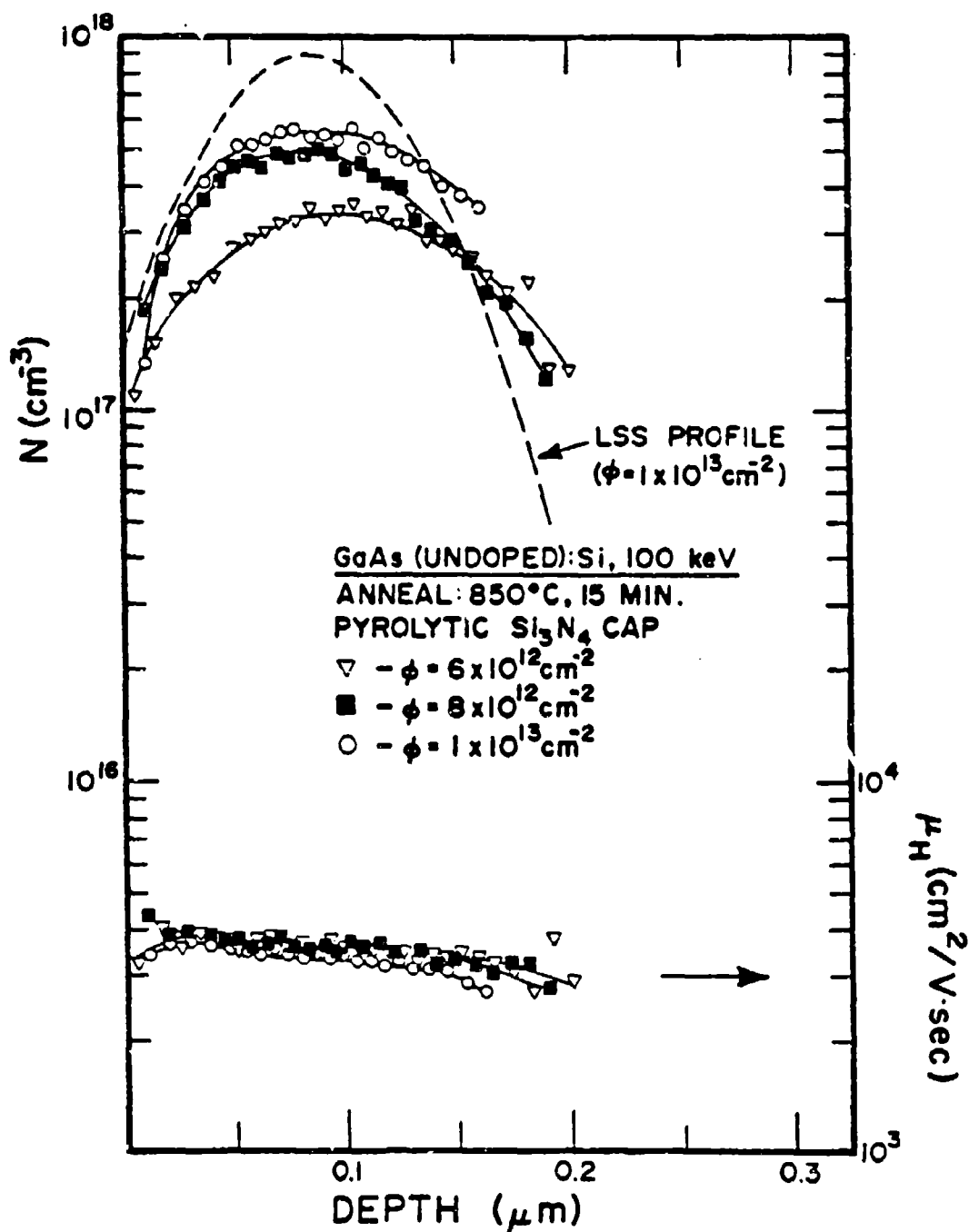


Figure 61 Electrical Carrier Profiles of Three Higher Si-Dose Undoped GaAs

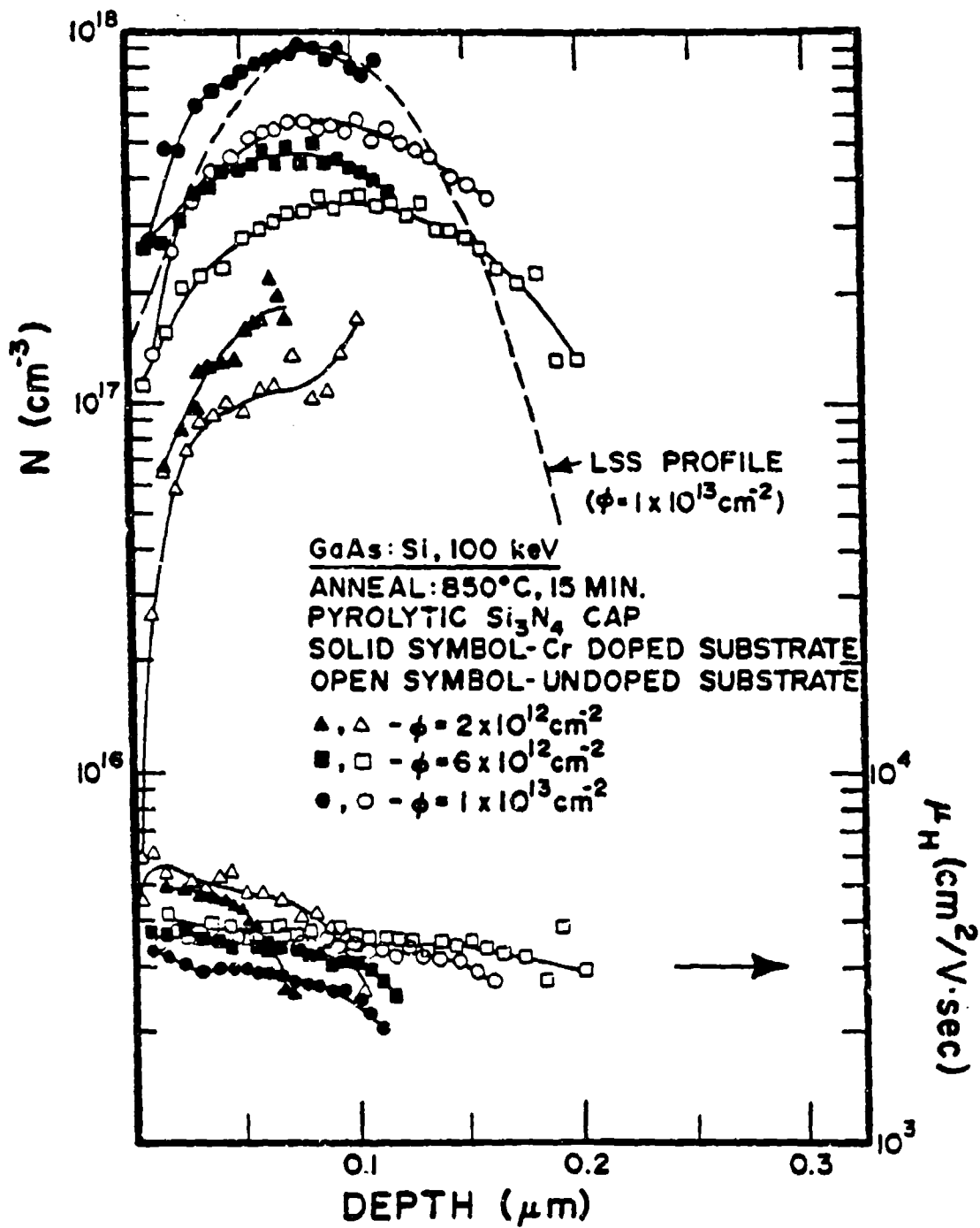


Figure 62 Electrical Carrier Profiles of Two Different GaAs Substrates Implanted with Si

Depth profiles of the carrier concentration and hall mobility for Cr-doped substrates implanted with Si to a dose of $6 \times 10^{12} \text{cm}^{-2}$ and annealed at three different temperatures are shown in Figure 63. Carrier and mobility profiles are shown to be highly dependent upon the annealing temperature. The carrier concentration of the sample annealed at 850°C is significantly higher than those of the samples annealed at either 800 or 900°C. The carrier concentrations for the 800 and 900°C anneals increase with depth, and the profiles show no clear peaks. Both the carrier concentrations and mobilities of the sample annealed at 800°C are significantly lower than those of the sample annealed at 850°C. This indicates that significant implantation damage remains even after annealing at 800°C for this dose. The low activation efficiency observed at this annealing temperature may be due to this unannealed damage. Also, the active region for the 800°C anneal is very shallow and no carriers are found beyond the projected range. The carrier concentrations of the sample annealed at 900°C are also very low compared with those of the 850°C anneal in most of the active region. This is probably due to outdiffusion of the implanted Si ions.

Electrical profiles for undoped substrates implanted with Si to a dose of $6 \times 10^{12} \text{cm}^{-2}$ and annealed at three different temperatures are shown in Figure 64. The carrier concentrations decrease with increasing annealing temperature. However, the active layer for the 800°C anneal is much shallower than those for higher temperature anneals, showing no carriers beyond around the projected range. The redistribution of the implanted Si ions seems to take place well into the damage-free region at an annealing temperature of 850°C or above. The carrier concentrations of the sample annealed at 900°C are much lower than those for an 850°C anneal, and this may

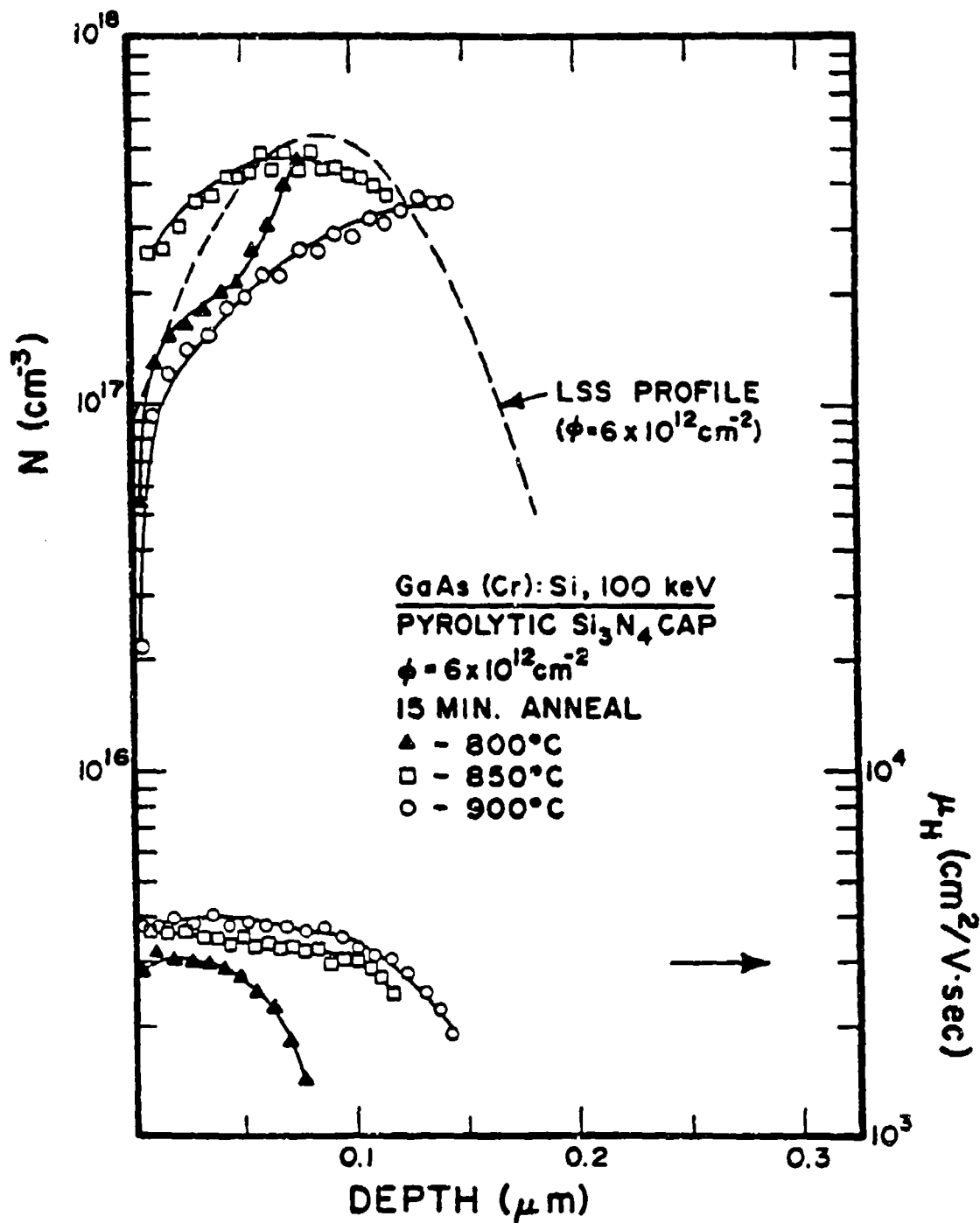


Figure 63 Dependence of Electrical Depth Profile upon Annealing Temperature for Si-Implanted Cr-Doped GaAs

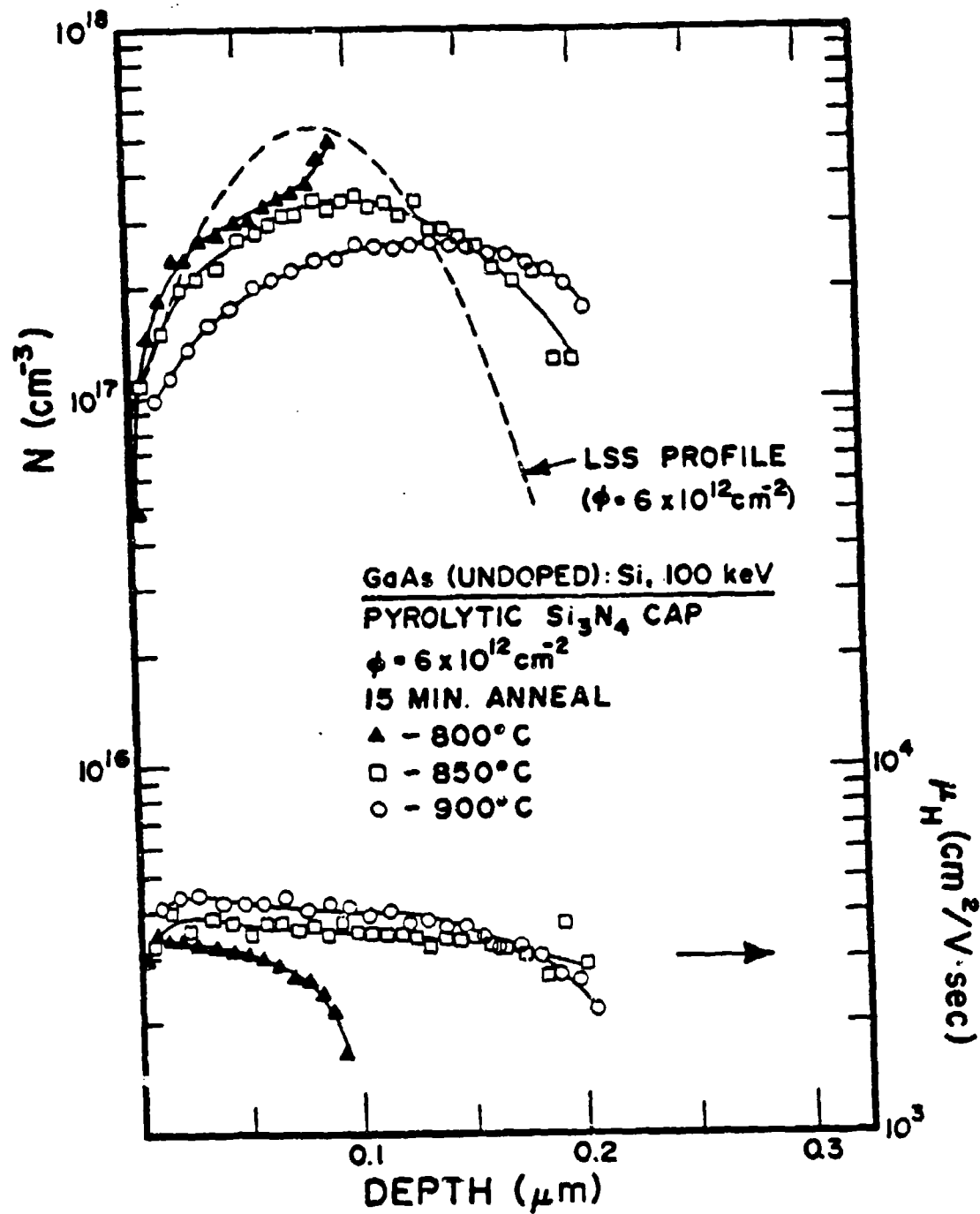


Figure 64 Dependence of Electrical Depth Profile upon Annealing Temperature For Si-Implanted Undoped GaAs

be due to outdiffusion of the implanted Si ions. The mobilities for the 800°C anneal decrease sharply with increasing depth, whereas the mobilities for higher temperature anneal decrease gradually.

3.6.3 Summary

Through a comprehensive study of electrical properties of Si implants in both Cr-doped and undoped GaAs, it has been found that both electrical activation efficiency and carrier profiles are highly dependent upon the annealing temperature, the ion dose, and the type of substrate. For a dose of $1 \times 10^{13} \text{ cm}^{-2}$ or below, the maximum electrical activation occurs at the 850°C anneal, while for doses of 3×10^{13} and $1 \times 10^{14} \text{ cm}^{-2}$, the maximum occurs at the 900°C anneal. However, for doses above $3 \times 10^{14} \text{ cm}^{-2}$, the electrical activation increases monotonically with annealing temperature as high as 950°C. The electrical activation efficiencies increase with ion dose up to about $6 \sim 8 \times 10^{12} \text{ cm}^{-2}$, and then they decrease at higher doses. The highest electrical activation efficiency obtained was about 90% for both substrates. The cut-off dose below which no appreciable electrical activation can be measured is around $1 \times 10^{12} \text{ cm}^{-2}$. The electrical activations and mobilities of undoped GaAs are, in general, higher than those of Cr-doped GaAs at all annealing temperatures for low doses, whereas the activation is about the same for both substrates for higher doses. The electrical activations and mobilities also depend upon the ion energy for a given dose, and they increase with ion energy. In general, the carrier profiles do not follow the theoretical LSS profiles. The depth profiles of carrier concentrations for undoped GaAs implanted with higher doses ($> 6 \times 10^{12} \text{ cm}^{-2}$) are much broader than those for Cr-doped GaAs. However, for a given dose, the carrier concentrations of the Cr-doped

substrates are much higher than those of the undoped substrates, and the reverse is true for the mobility profiles. The profiles for a dose of $6 \times 10^{12} \text{ cm}^{-2}$ show that significant Si implantation damage still remains even after the 800°C anneal. Also the profiles indicate that significant Si outdiffusion occurs for the samples annealed at 900°C for both substrates.

SECTION IV

DEFECT STUDIES OF ION IMPLANTED GaAs

4.1 SAMPLE PREPARATION

Samples for TEM analysis are made in the following manner.

4.1.1 Plan View

2 x 2 mm² TEM specimens can be made by thinning from the backside using Bromine-methanol solution in a conventional jet thinner. For plan view specimens, when placed inside the microscope, the electron beam direction will be perpendicular to the interface.

4.1.2 Cross Sectional (x) View

3 x 2 mm² specimen should be glued together face to face with a blank 5 x 4 mm² piece of GaAs, as shown in Figure 65(a). The sandwich thus made should be mounted on a circular glass disk with two supporting pieces of Si (1 cm x 0.5 cm) as shown in Figure 65(b). Then it should be mechanically polished down (parallel to the interface) to a thickness of ~60 μm. The specimen should then be taken out by dissolving the glue, and be mounted on a piece of Si. Finally, it will be thinned by ion beam. For the x-sectional specimen, the electron beam will be parallel to the interface.

RBS-channeling and PIXE analyses were carried out on 1 x 1 cm² specimens.

4.2 PROCEDURES FOR DEFECT ANALYSIS

4.2.1 Image Formation in Transmission Electron Microscopy

It was pointed out earlier that to form an electron image (electron micrograph) of the specimen, an objective aperture is inserted in the back focal plane of the objective lens. Usually only one beam is allowed

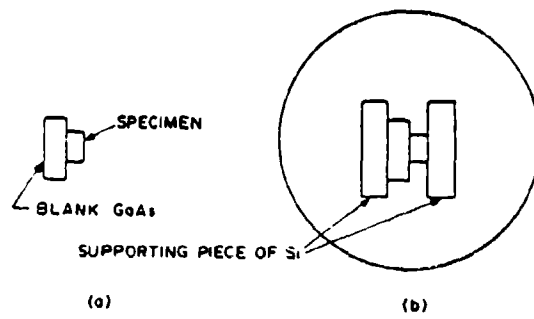
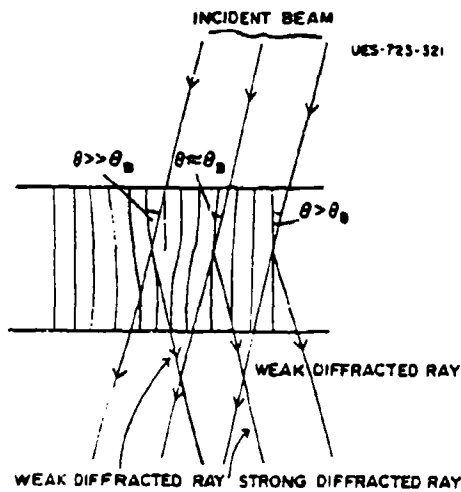
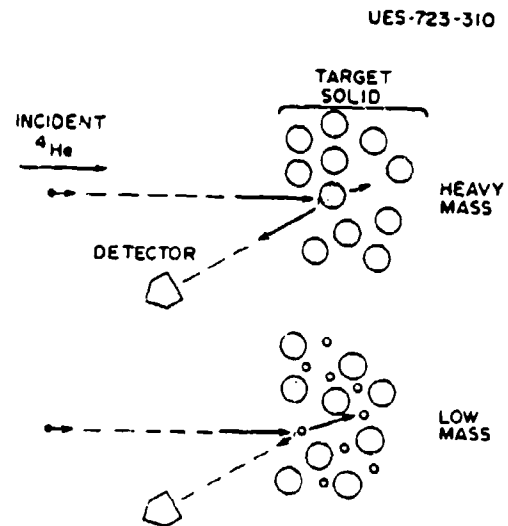


Figure 65 Cross Sectional TEM Specimen Preparation

Figure 66 Schematic Ray Diagram
Illustrating the Mechanism
of Diffraction ContrastFigure 67 Backscattering of Ion
from Solid Target

through this aperture to analyze the crystal defects. If the transmitted beam is selected, then a bright field image is formed, whereas dark field image is formed if a diffracted beam is selected. The Hitachi-600 microscopes incorporate deflection coils above the specimen to enable any diffracted beam to be deflected down the optic axes of the microscope so that high resolution dark field images can be produced. By tilting the beam in this way, the spherical aberration, which reduces the resolution of micrographs taken with off axes rays, is kept to the minimum.

The mechanism through which an image is formed when only one beam is allowed to pass through the objective aperture is called the diffraction contrast mechanism. The mechanism of diffraction contrast can be easily appreciated from the schematic ray diagram shown in Figure 66. The edge dislocation shown in this Figure will bend the crystal planes illustrated. The Bragg condition for diffraction is locally satisfied. Remote from the dislocation, these planes are not bent and do not satisfy this condition. Thus, from this simple ray diagram, it would be expected that the amplitude of the diffracted beam at the exit surface of the crystal would be small everywhere except in the region close to, and one side of, the dislocation where the amplitude would be large. The diffraction lens simply magnifies the information contained in the first image plane. The final image obtained from a specimen will simply be a representation of the variation in intensity of the electrons leaving the crystal in the direction defined by the beam which is selected by the objective aperture. On the basis of Figure 66, it would be expected that the image formed in bright field would show a dark line associated with the image of the dislocation line and conversely, that the dark field image would be a bright line.

4.2.2 Analysis of the Electron Diffraction Patterns

Knowledge of the camera constant λL greatly simplifies indexing of diffraction patterns and is essential for the identification of second phases. The value of λL should be known for all the diffraction magnifications. The usual way of knowing λL is by forming a diffraction pattern of a standard substance (Au) and using the relationship $\lambda L = Rd$ where R is the radius of the diffraction ring and d is the corresponding interplanar spacing. Accurate determination of λL is possible in some cases like a thin alloy film containing precipitates where the matrix diffraction pattern can act as a suitable standard for measurement of the precipitate diffraction pattern.

4.2.3 Rutherford Backscattering (RBS) and Proton Induced X-ray Excitation (PIXE)

When an incident ion beam is chosen so as to allow deep penetration in a solid material, but with an energy kept below where nuclear resonance effects would complicate the scattering, the scattering is simple coulombic repulsion and is accurately described by the Rutherford cross section. The ion beam is usually H or He, typically H^+ at 200-400 keV and He^+ at 1-3 MeV. These energies allow analysis of the upper micron of the surface and are below the nuclear reaction threshold for most elements with atomic number above 8. If the projectile hits a very heavy target nucleus as shown in Figure 67, the target nucleus will absorb little energy and the backscattered ion will retain most of its energy. If, however, it scatters from a very light target nucleus, the target nucleus will absorb most of the energy leaving the projectile at a low energy. Since the backscattered projectile's energy can be measured to better than 1 %, one can deduce from

the final projectile energy, the mass of the target atom. Thus, one can mass analyze the target elements. However, the technique is more sensitive to heavier elements in a lighter substrate because the cross section for scattering is proportional to $(Z_{\text{TGT}})^2$. As the projectile penetrates the solid, it will lose small amounts of energy to collisions with the electron sea of the solid. From the known energy loss of the ion in a given material, one can obtain information of the depth distribution of the impurity in a solid target. However, as mentioned earlier, RBS is not sensitive in detecting low mass impurity in a heavy mass substrate which is the case for most of the ions implanted in GaAs. In that case, PIXE can be used in detecting the impurities. In this mode, one sacrifices depth resolution on the impurity analysis since PIXE is not well suited to depth resolved information.

4.2.4 Channeling

Channeling is the steering of a beam of energetic ions into the open spaces (channels) between close-packed rows or planes of atoms in a crystal as shown schematically in Figure 68. The steering is the result of a correlated series of small-angle screened coulomb collisions between an ion and the atoms bordering the channel. Thus, the channeled ions do not penetrate closer than the screening distance to the atomic nuclei. Therefore, the probability of large angle Rutherford backscattering and X-ray excitation is greatly reduced compared with the probability of such interactions in a random direction. Consequently, a large reduction in yield of such interactions with host crystal is observed when the ion beam is incident at small angles (less than the critical angle for channeling) to a close-packed direction. The normalized yield from such interactions is defined as the

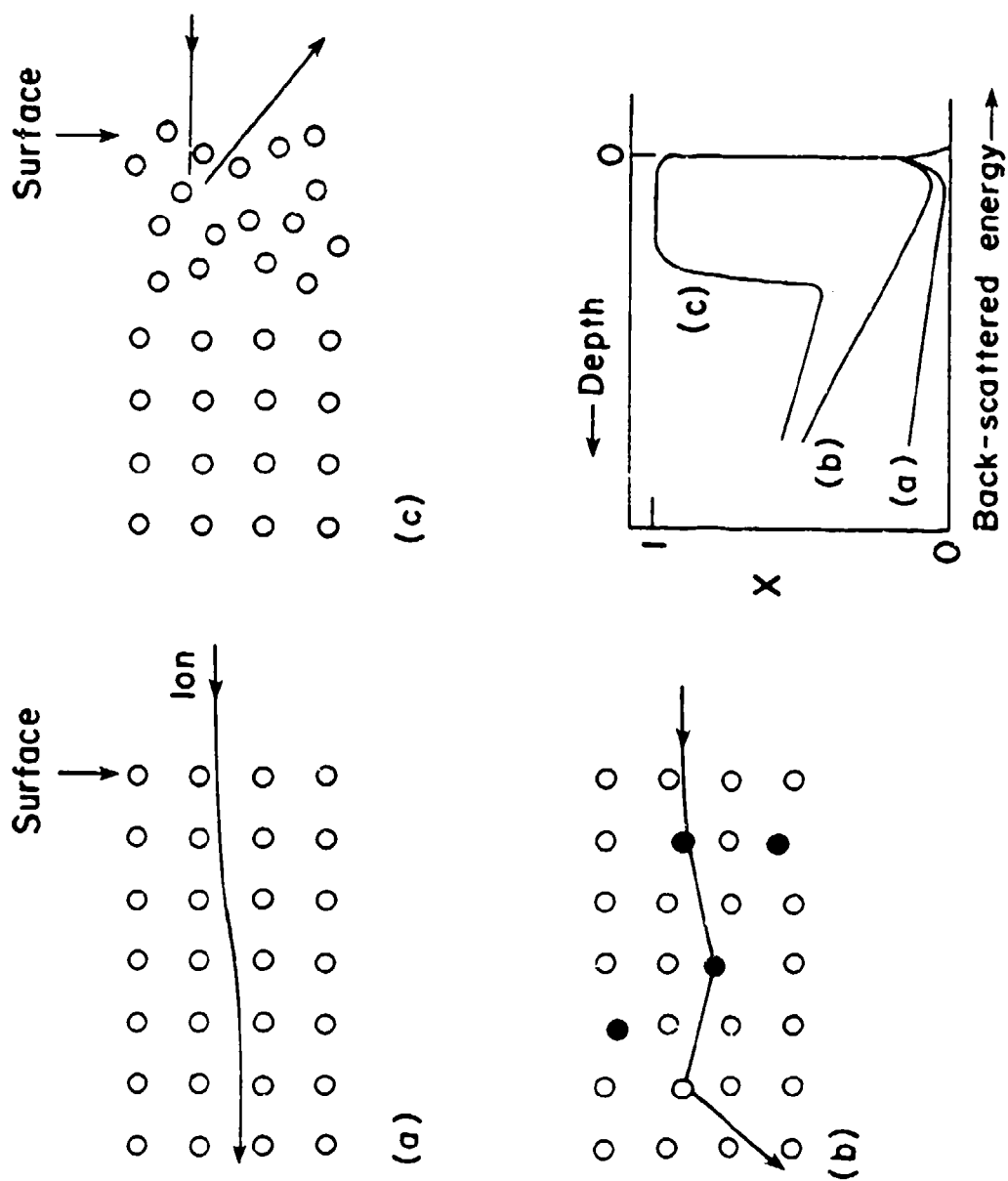


Figure 68 Ion Scattering from Defects: (a) Channeling in a Perfect Crystal, (b) Dechanneling by Defects, (c) Direct Scattering from Amorphous Layer

ratio of the yield for ions incident at an angle ψ to the yield for a randomly directed beam. At $\psi=0$, the normalized yield is called the minimum yield which is a measure of the crystal quality.

4.2.5 Displacement of Host Atoms

Ion implantation induces displacement of host atoms in a crystal lattice which can be measured by channeling. Channeled ions are affected by displaced host atoms in two important ways as illustrated in Figure 68.⁵³ When the concentrations of displaced atoms are small, the gradual deflection of channeled ions (dechanneling) out of channels by multiple scattering is the major effect. The normalized yield χ is a measure of the fraction of dechanneled ions, and the rate of change of χ with depth is proportional to the concentration of displaced host atoms.⁵⁴ For large concentrations ($>10\%$) of displaced host atoms, the probability of single large angle collisions with displaced host atoms becomes important. If a near-surface layer of the crystal is completely disordered (amorphised), as shown in Figure 68(c), χ becomes equal to unity for that layer. Since the ions lose energy as they penetrate into the crystal, the energy increment over which $\chi=1$ corresponds to the thickness of the amorphous region.

4.2.6 Lattice Location of Impurity Atoms in a Crystal Lattice

The lattice site location of an impurity atom in a crystal lattice can be determined quite directly from channeling experiments by measuring the normalized yield χ_h from host atoms and from impurity atoms, χ_i . If the impurity atoms are located on substitutional lattice positions, then $\chi_h = \chi_i$ for any angle ψ . From the values of the minimum yield (i.e., at $\psi=0$) for host and impurity signal, one can determine the fraction of impurity atoms on sites along a particular axis using the relation,

In addition to the measurements of aligned yields, angular scans through low index axial and planar channels are valuable in both qualitative and quantitative determinations of impurity atom locations. Different projections of impurity atoms into a channel will result in different angular profiles characteristic of that position as shown in Figure 69. A comprehensive review of the techniques described above can be found in References 53 and 54.

4.3 Se^+ IMPLANTED GaAs/LOW TEMPERATURE ANNEALING STUDIES

Low temperature epitaxial regrowth of ion implanted amorphous layers in elemental and compound semiconductors has important implications for electronic device applications. It has been established in recent papers⁵⁵⁻⁵⁹ that GaAs surface layers rendered amorphous by high dose ion implantation do not completely reorder during subsequent annealing at low temperatures. Gamo et al.⁵⁵ have studied the reordering of amorphous layers produced by implantation of Zn and Se ions in GaAs held at liquid nitrogen temperature (LN_2T). It was observed that after annealing at temperatures between 200-500°C, a considerable amount of channeling disorder remained. However, for anneals at 600°C, a complete recovery was observed. Similar experiments with Ar implanted GaAs were carried out recently by Williams and Austin.⁵⁶ They found that although GaAs layers can be recrystallized epitaxially at temperatures below 250°C, an appreciable amount of channeling disorder remains which is totally removed at 400°C for an implant dose of $3 \times 10^{13} \text{ cm}^{-2}$. But the recrystallization behavior has been found to be

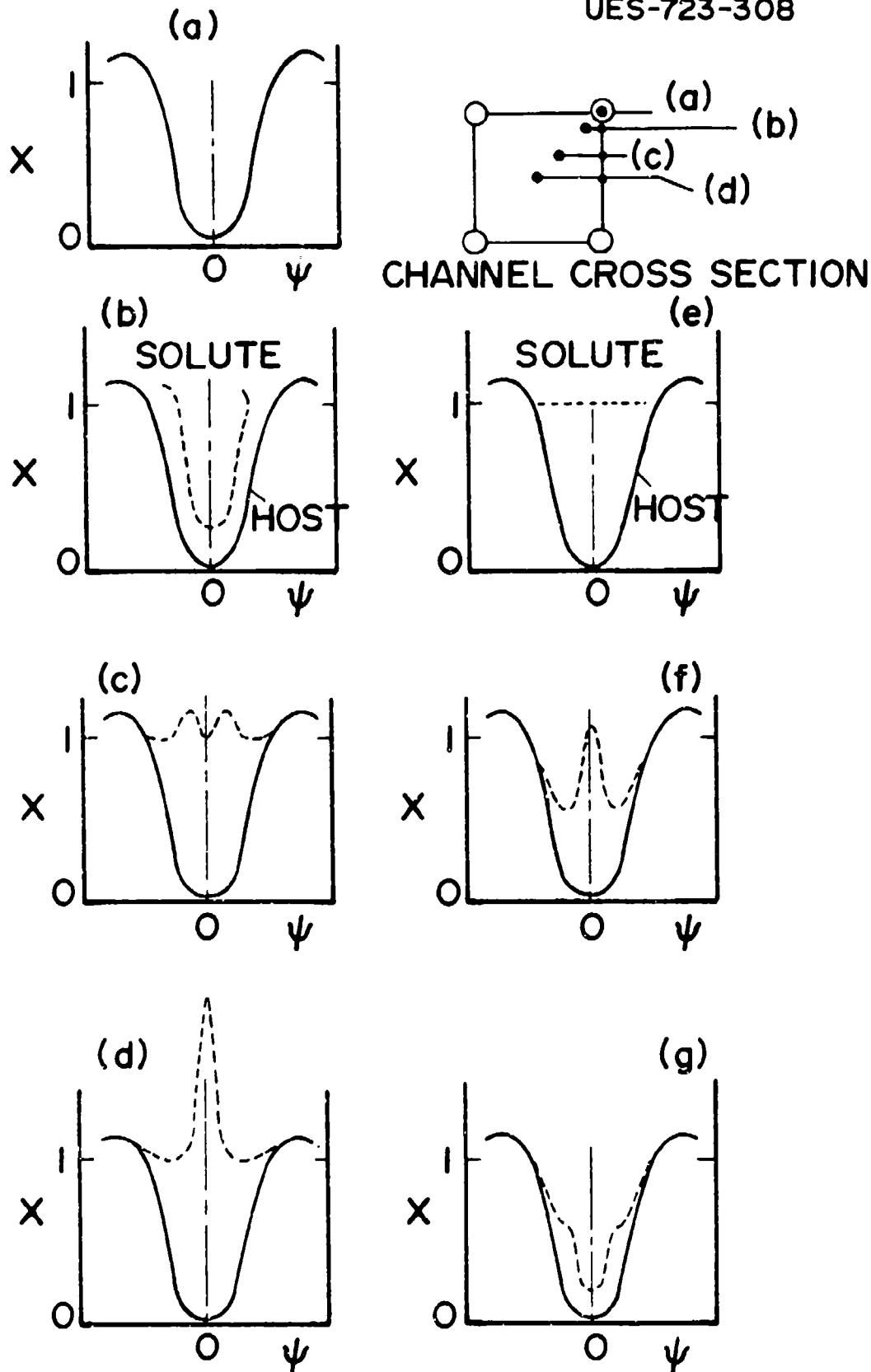


Figure 69 Angular Scan Profiles for Different Projections of a Solute Atom in an Axial Channel

quite complex depending on the implant conditions of dose and substrate temperature. Kular et al.⁵⁷ have studied the recrystallization behavior of Zn implanted GaAs in the temperature range 300-900°C. They found that high level of damage, mostly in the form of twinned single crystals, remained after annealing up to ~500°C. Above this temperature, most twins disappear, leaving dislocation loops as the major residual damage. Grimaldi et al.⁵⁸ have studied the epitaxial regrowth of GaAs implanted with Si, S, As, and Ar ions of various doses and energies. They found that annealing at 400°C for 60 min led to the regrowth of the implanted layer with various amounts of residual channeling disorder. This residual disorder increased with increasing thickness of their original amorphous layer. Transmission electron microscopy (TEM) analysis showed that the residual defects are mostly microtwins. However, a 400 Å thick amorphous layer was found to grow epitaxially without the formation of microtwins. In order to understand these results, they suggested a model in which the growing crystal front accumulates local defects and eventually begins to condense these into clusters. They have proposed that this cluster formation and/or the precipitation of bulk Cr act as nucleation centers for the growth of microtwins.

In view of these results, we feel that a detailed study of both isochronal and isothermal annealing behavior is important and that such an investigation would enable us to better understand the mechanism of epitaxial growth in GaAs and the development of residual defect structures at various stages of the annealing process. We have concentrated our attention on GaAs implanted with various doses of Se both at LN₂T and room temperature (R.T.). Rutherford backscattering-channeling (RBS-C) and TEM were used to study the contents and the nature of defect micro-structures respectively in these annealed samples.

Cr-doped semi-insulating GaAs wafers with (100) orientation were implanted with 120 keV Se^+ ions in a non-channeling direction at LN_2 temperature and at room temperature with fluences ranging from 1×10^{13} to $1 \times 10^{14} \text{ cm}^{-2}$. First, the results will be described for implantation at LN_2 .

Figure 70 shows the channeling spectra obtained from the sample implanted with 120 keV Se^+ (at LN_2) to a dose of $1 \times 10^{13} \text{ cm}^{-2}$. The as-implanted damage is rather small, being characterized by a minimum yield (χ_{MIN}) of 0.16 behind the damage peak as compared to about 0.036 for a virgin sample. Annealing the sample at 200°C for 30 min annealing leads to almost complete recovery of the damage as indicated by the channeling spectrum. An additional 30 min annealing leads to total recovery of the damage. Figure 71 shows the isochronal annealing behavior of the same sample ($1 \times 10^{13} \text{ cm}^{-2}$) at 200°C , 250°C , and 300°C , all for 30 min. The damage recovery is complete at 250°C . Channeling spectra of the sample implanted to a dose of $3 \times 10^{13} \text{ cm}^{-2}$ is shown in Figure 72. The damage in this sample has reached to the level of a random spectrum indicating that the surface layer has become amorphous. The thickness of the amorphous layer is 660 \AA . Annealing at 200°C for 30 min has led to the reduction of the thickness to about 400 \AA . Thus the layer has regrown epitaxially from the interface at the rate of $\sim 7.3 \text{ \AA/min}$. Further annealing for 30 min has led to the reduction of the damage peak with the maximum damage lying very close to the surface. Increasing the annealing time to 90 min and then to 120 min leads to further reduction of the area of the damage peak which, however, stops at 120 min. The residual damage at this stage is quite highly characterized by a minimum yield of 0.33 as compared to 0.036 for a virgin sample. The

120 keV Se^+ \longrightarrow GaAs (100) LN_2T

DOSE $1 \times 10^{13} \text{ cm}^{-2}$

UES-723-135

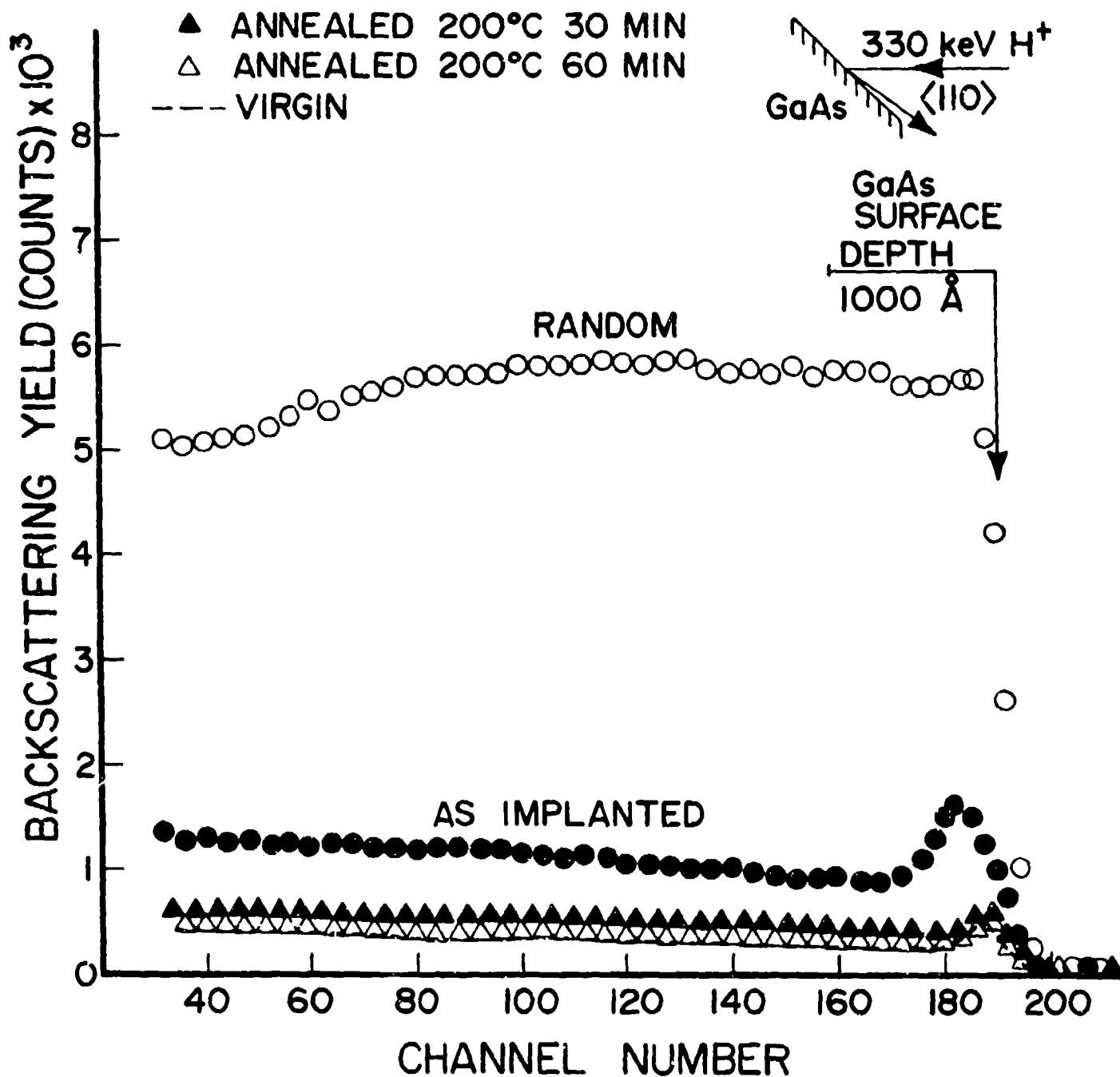


Figure 70 Channeling Spectra Before and After Annealing
 at 200°, GaAs:Se⁺, 10^{13} cm^{-2}

120 keV $\text{Se}^+ \rightarrow \text{GaAs (100) LN}_2\text{T}$

DOSE $1 \times 10^{13} \text{ cm}^{-2}$

UES-723-137

- ANNEALED 200°C 30 MIN
- △ ANNEALED 250°C 30 MIN
- ANNEALED 300°C 30 MIN
- VIRGIN

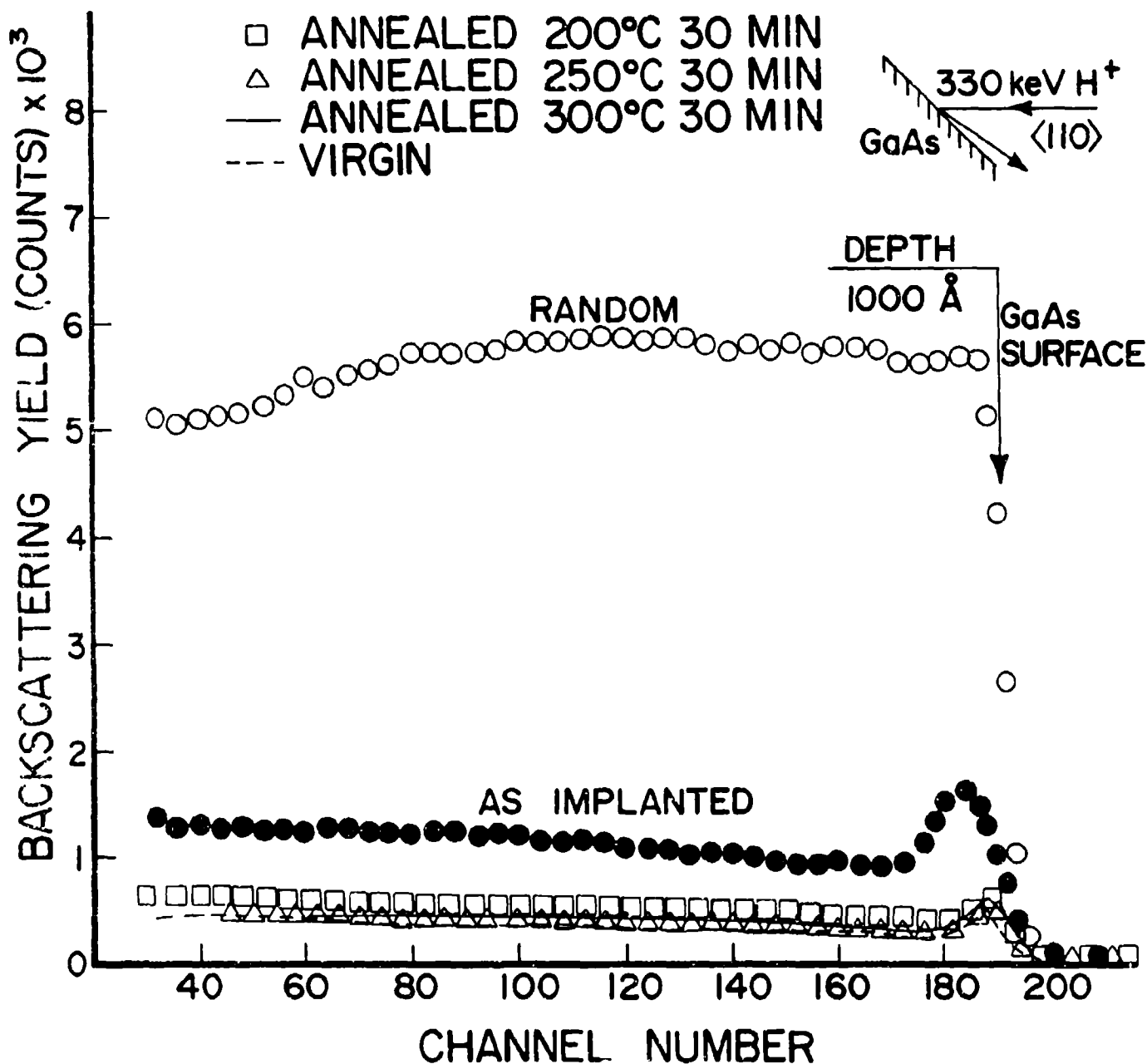


Figure 71 Channeling Spectra Before and After Annealing at 200, 250, and 300°C, GaAs:Se⁺, $1 \times 10^{13} \text{ cm}^{-2}$

120 keV Se^+ \longrightarrow GaAs (100) LN_2T

DOSE $3 \times 10^{13} \text{ cm}^{-2}$

UES-723-131

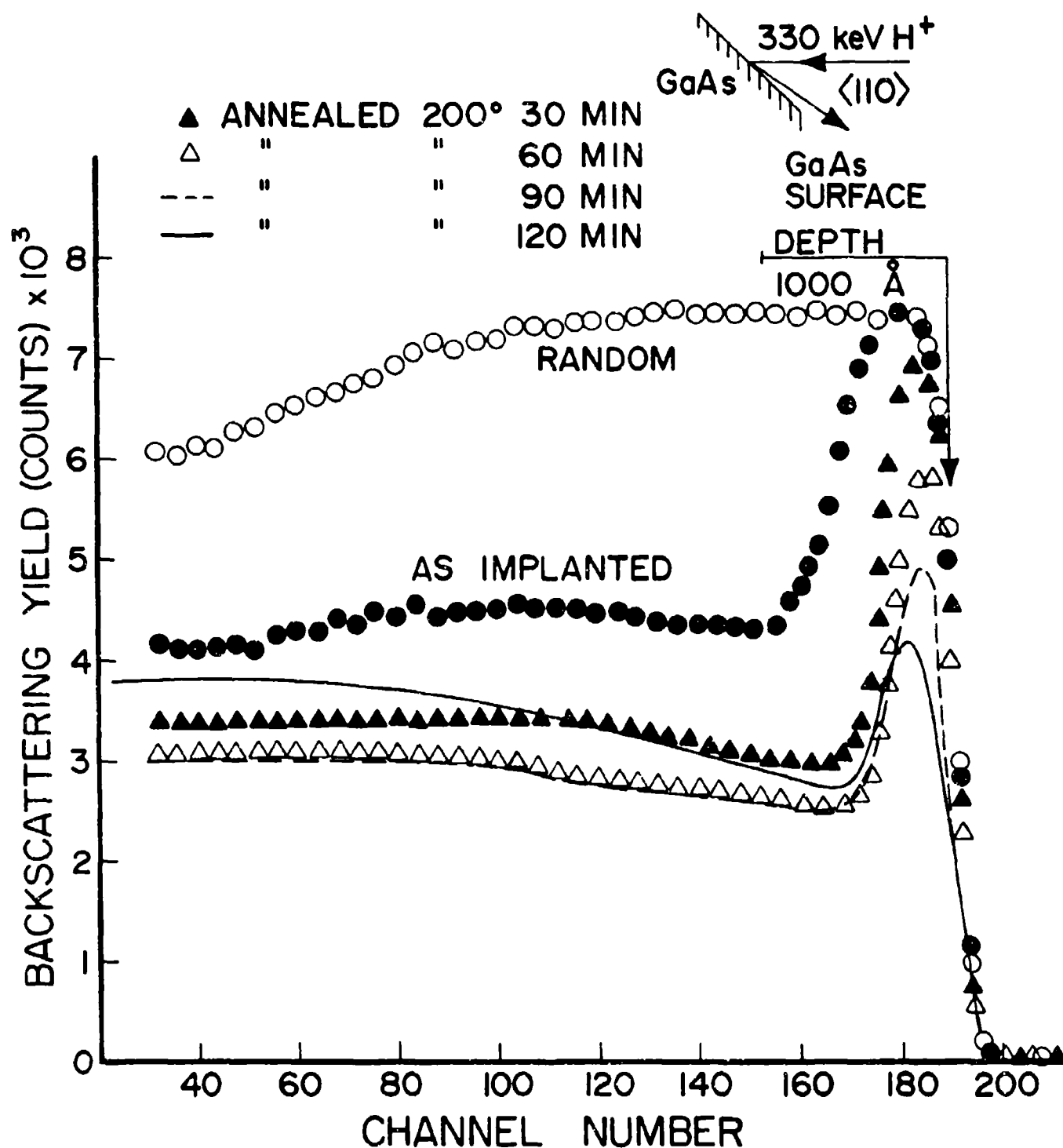


Figure 72 Channeling Spectra Before and After Annealing at 200°C, $\text{GaAs:Se}^+ 3 \times 10^{13} \text{ cm}^{-2}$

isochronal annealing behavior of this sample at temperatures ranging from 200-500°C with a temperature increment of 50°C and annealed for 30 min is shown in Figure 73. It can be seen that almost total recovery is obtained at 500°C. The annealing behavior of the sample implanted to a dose of $7 \times 10^{13} \text{ cm}^{-2}$ and annealed at 200°C for various times is shown in Figure 74. The thickness of the as-implanted amorphous layer was about 750 Å which has reduced to about 600 Å after annealing for 20 min at 200°C. The epitaxial growth rate at this stage is about 5 Å/min. The spectrum after annealing for another 30 min shows that the layer is no longer amorphous but has large amounts of damage centered around a depth of ~ 250 Å below the surface. A little further recovery of damage takes place when the sample is annealed for another 30 min. Further increase of time does not lead to any more damage recovery. Isochronal annealing behavior of the same sample at temperatures ranging from 200-600°C is shown in Figure 75. Here it can be seen that the complete annealing of damage requires a temperature of 600°C. Figure 76 shows the annealing behavior of $1 \times 10^{14} \text{ cm}^{-2}$ implant at 200°C for 30, 60, and 90 minutes. The original thickness of the amorphous layer was 850 Å which decreased to about 710 Å thus yielding a growth rate of ~ 4.7 Å/min. It grows further as the time increases to 60 and 90 min with decreasing rate of growth. Further increases in time does not lead to any more regrowth. The residual layer in this case remains amorphous as opposed to the previous implant of $7 \times 10^{13} \text{ cm}^{-2}$ where the layer became crystalline with heavy residual damage after 60 min anneal. The isochronal annealing behavior of the $1 \times 10^{14} \text{ cm}^{-2}$ sample is shown in Figure 77. The behavior is similar to the earlier case of $7 \times 10^{13} \text{ cm}^{-2}$ except for the fact that now there is some residual disorder after annealing at 600°C for 30 min as revealed by comparison to the channeled spectra of a virgin sample.

120 keV Se^+ \longrightarrow GaAs (100) LN_2T

DOSE $3 \times 10^{13} \text{ cm}^{-2}$

UES-723-132

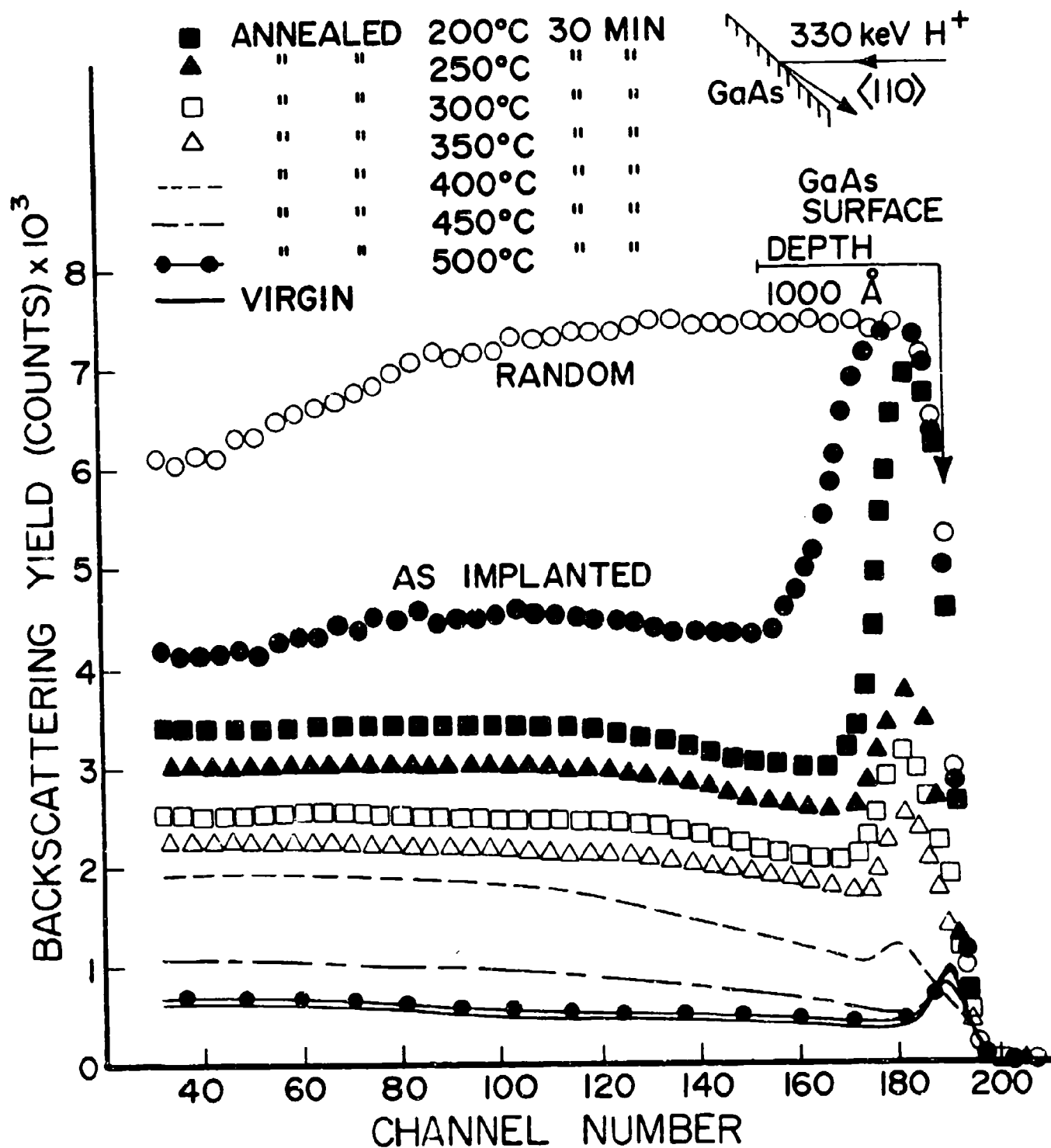


Figure 73 Channeling Spectra for GaAs:Se⁺, $3 \times 10^{13} \text{ cm}^{-2}$
Before and After Annealing at 200-500°C

120 keV Se^+ \longrightarrow GaAs (100) LN_2T

DOSE $7 \times 10^{13} \text{ cm}^{-2}$

UES-723-130

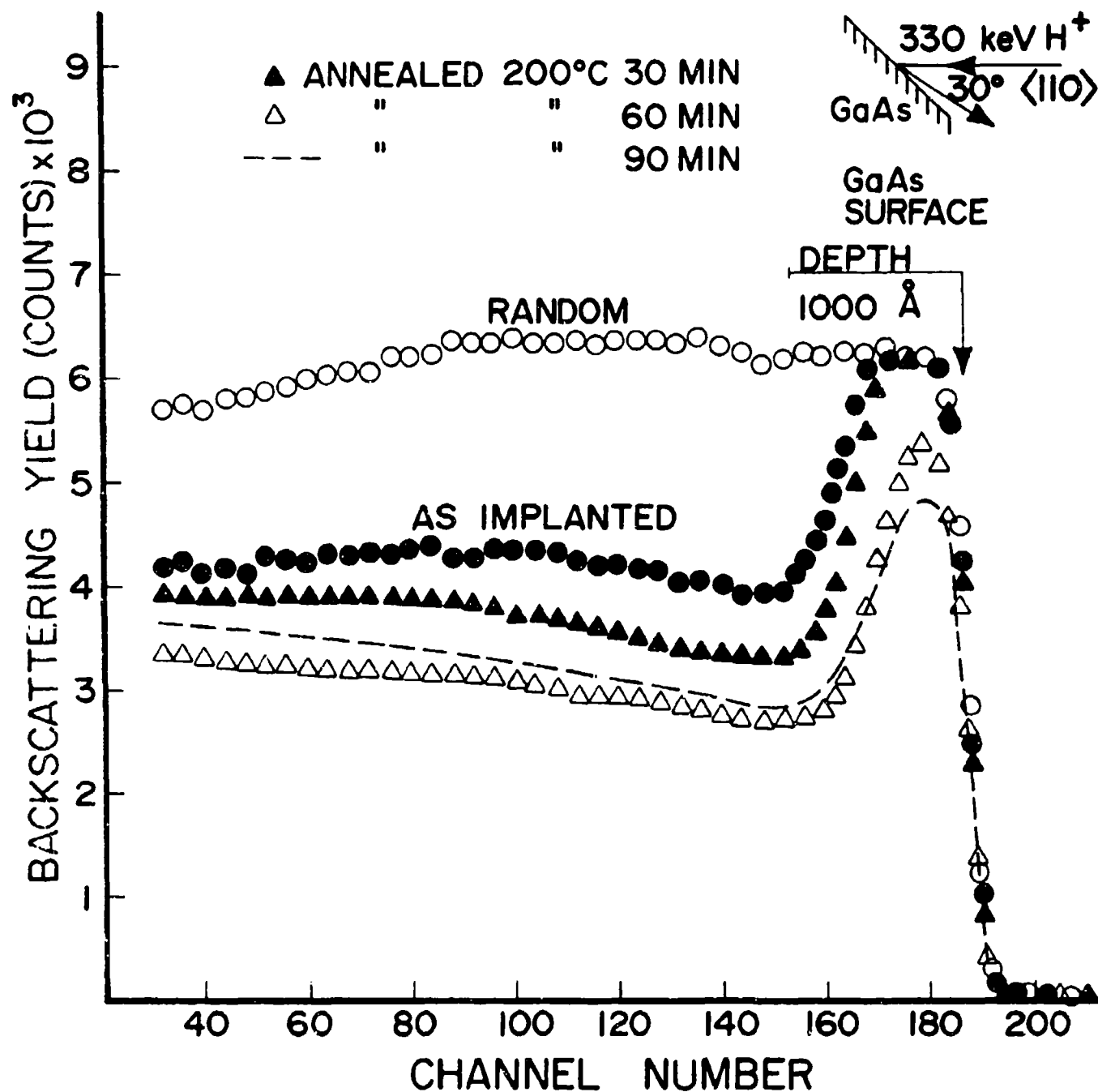


Figure 74 Channeling Spectra for GaAs: Se^+ , $7 \times 10^{13} \text{ cm}^{-2}$, Before and After Annealing at 200°C

120 keV Se^+ \longrightarrow GaAs (100) LN_2T

DOSE $7 \times 10^{13} \text{ cm}^{-2}$

UES-723-133

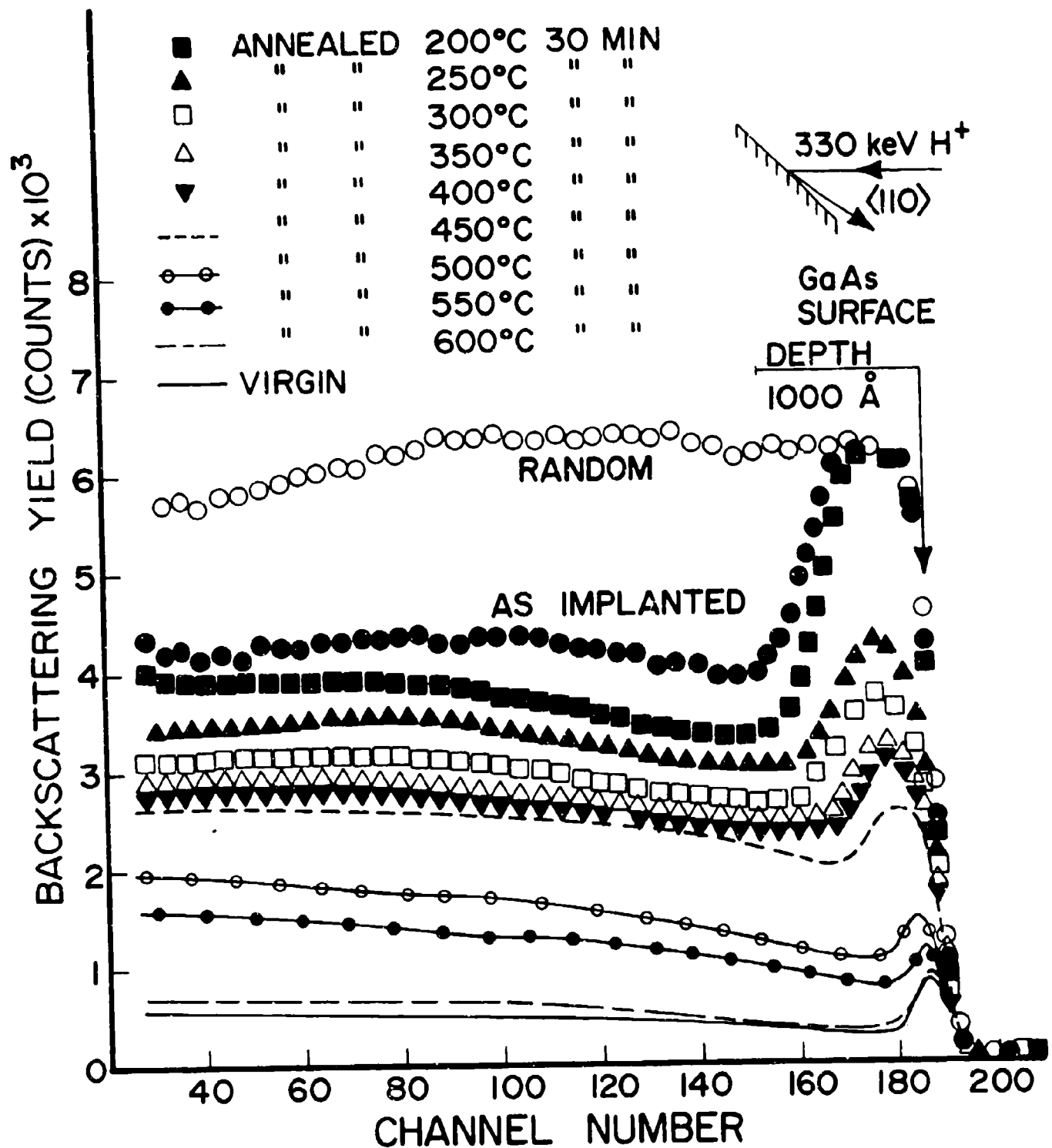


Figure 75 Channeling Spectra for GaAs:Se⁺, $7 \times 10^{13} \text{ cm}^{-2}$, Before and After Annealing at 200-600°C

120 keV Se^+ \rightarrow GaAs (100) LN_2 T

DOSE $1 \times 10^{14} \text{ cm}^{-2}$

UES-723-136

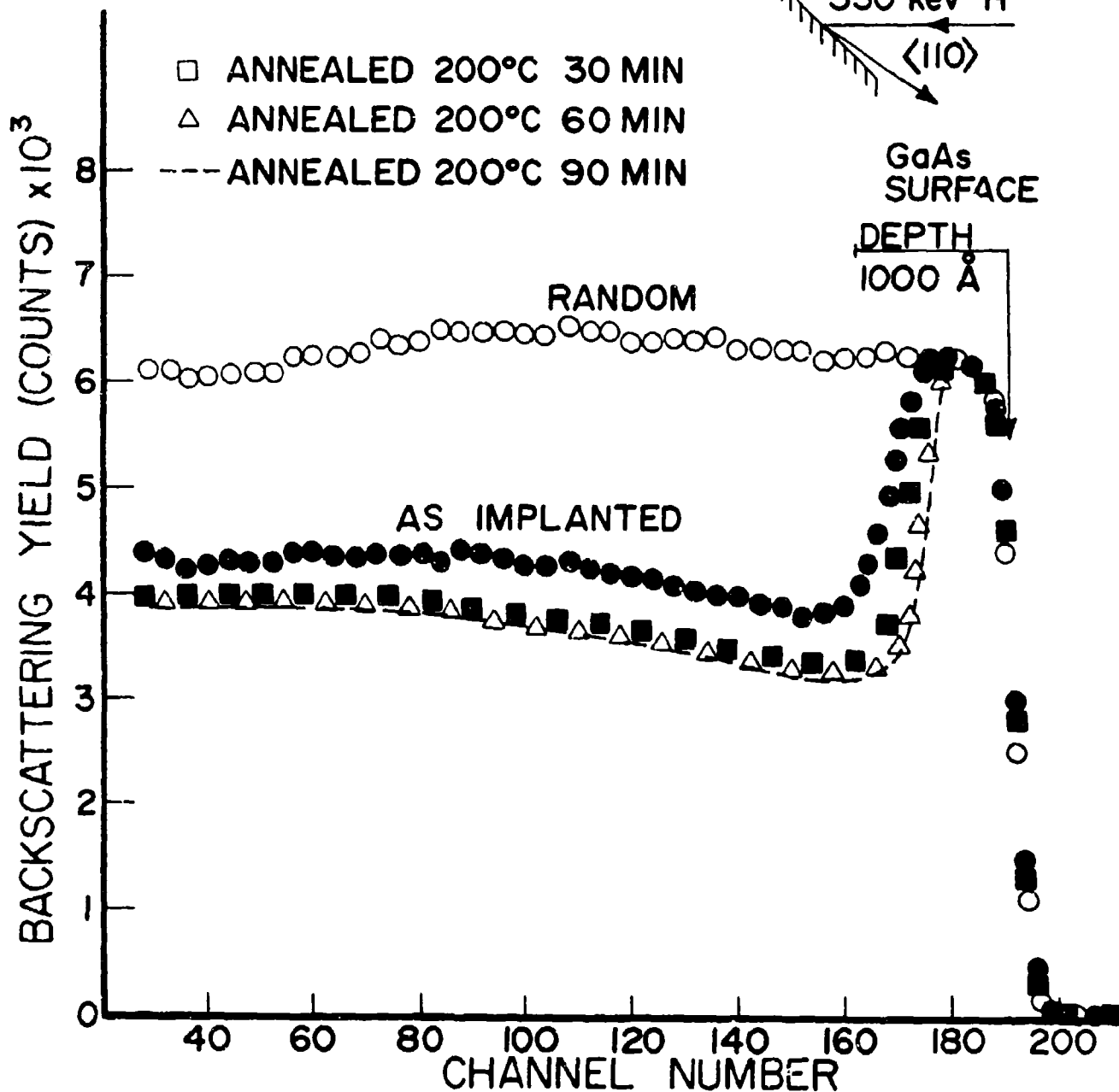


Figure 76 Channeling Spectra for GaAs: Se^+ , $1 \times 10^{14} \text{ cm}^{-2}$, Before and After Annealing at 200°C

120 keV Se⁺ → GaAs (100) LN₂T

DOSE $1 \times 10^{14} \text{ cm}^{-2}$

UES-723-134

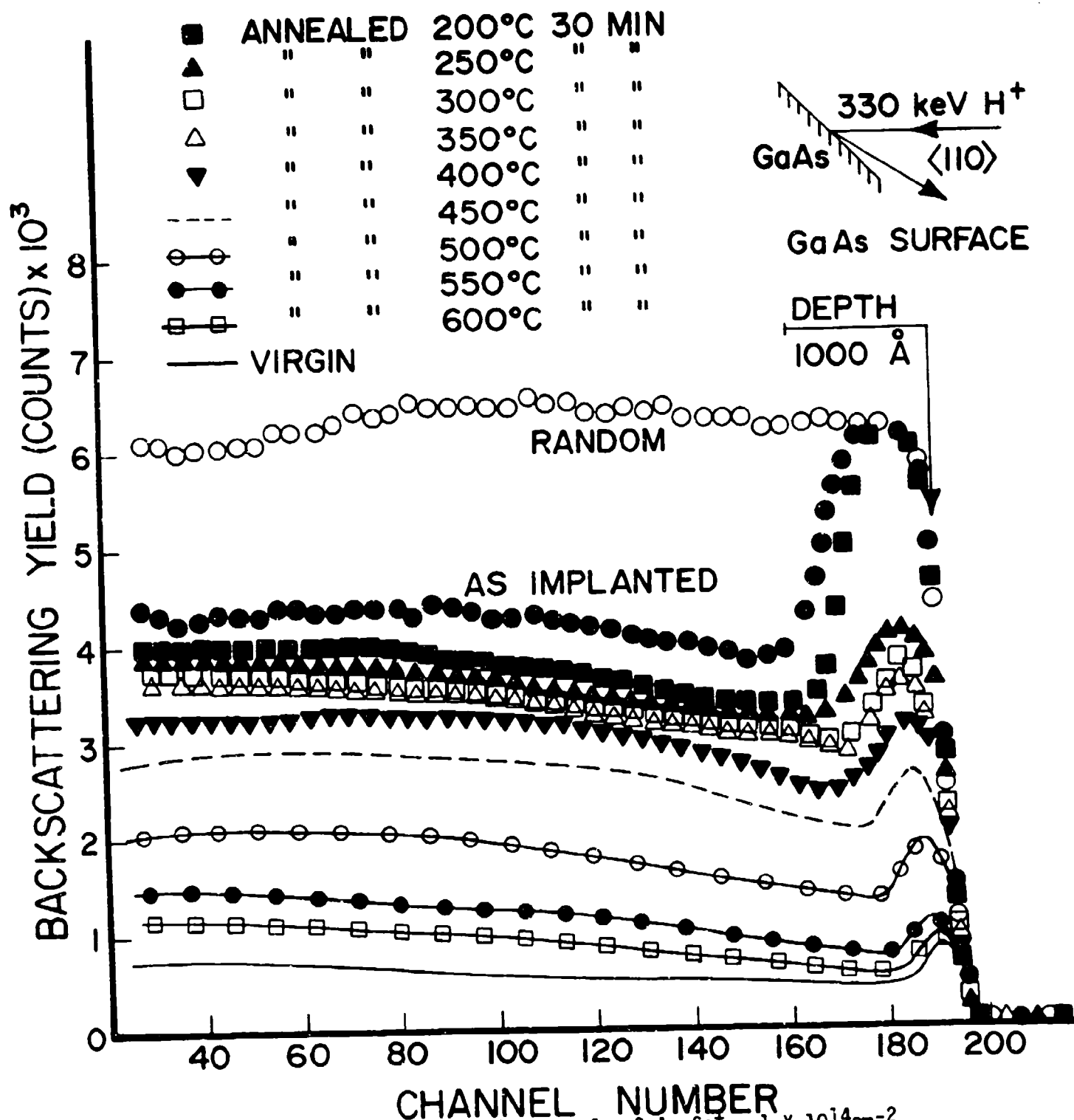


Figure 77

Channeling Spectra for GaAs:Se⁺, $1 \times 10^{14} \text{ cm}^{-2}$,
Before and After Annealing at 200-600°C

Experiments with samples implanted at R.T. exhibited a similar nature of the regrowth behavior with the only difference being lower regrowth rate and higher residual disorder after annealing at a given temperature for a given time. For instance, the rate of growth at 200°C of $1 \times 10^{14} \text{ cm}^{-2}$ implant at R.T. was measured to be about 2.8 Å/min as compared to 4.7 Å/min for LN₂T implant. Similarly, higher residual disorder after annealing at 400°C was obtained for a R.T. implant as compared to the LN₂T implant of the same dose (see Figure 94).

TEM analysis was carried out on the samples of Figures 70-77 after their final annealing treatment. Dislocation loops and precipitates are found in the bright field plan view micrographs of Figure 78 which correspond to samples of Figures 70 and 71. Dislocation loops are distinguished from the precipitates by imaging under $\pm g$ conditions under which dislocation loops exhibit inside/outside contrast whereas precipitates do not. Transmission electron diffraction (TED) patterns from both specimens show no indication of the presence of microtwins or any residual amorphous layer. However, TED patterns corresponding to samples of Figures 72 and 73 show the presence of microtwins. Bright field micrographs from these same specimens, Figures 79(a,b) respectively, also show that microtwins are present. The projected length of these twins are estimated from dark field micrographs (not shown here) and are found to lie between 400-2,000 Å for the $3 \times 10^{13} \text{ cm}^{-2}$ implant and 500-2,500 Å for the $7 \times 10^{13} \text{ cm}^{-2}$ implant. The TED pattern of the sample implanted at LN₂T with a dose of $1 \times 10^{14} \text{ cm}^{-2}$ and annealed at 200°C for 90 min shows the presence of both microtwins and a residual amorphous layer (Figure 80a). A TEM cross sectional view of this sample is presented in Figure 80b. It shows that the amorphous layer is ~ 480 Å thick

120 keV Se⁺ → GaAs (100)

LN₂T

UES-723-129

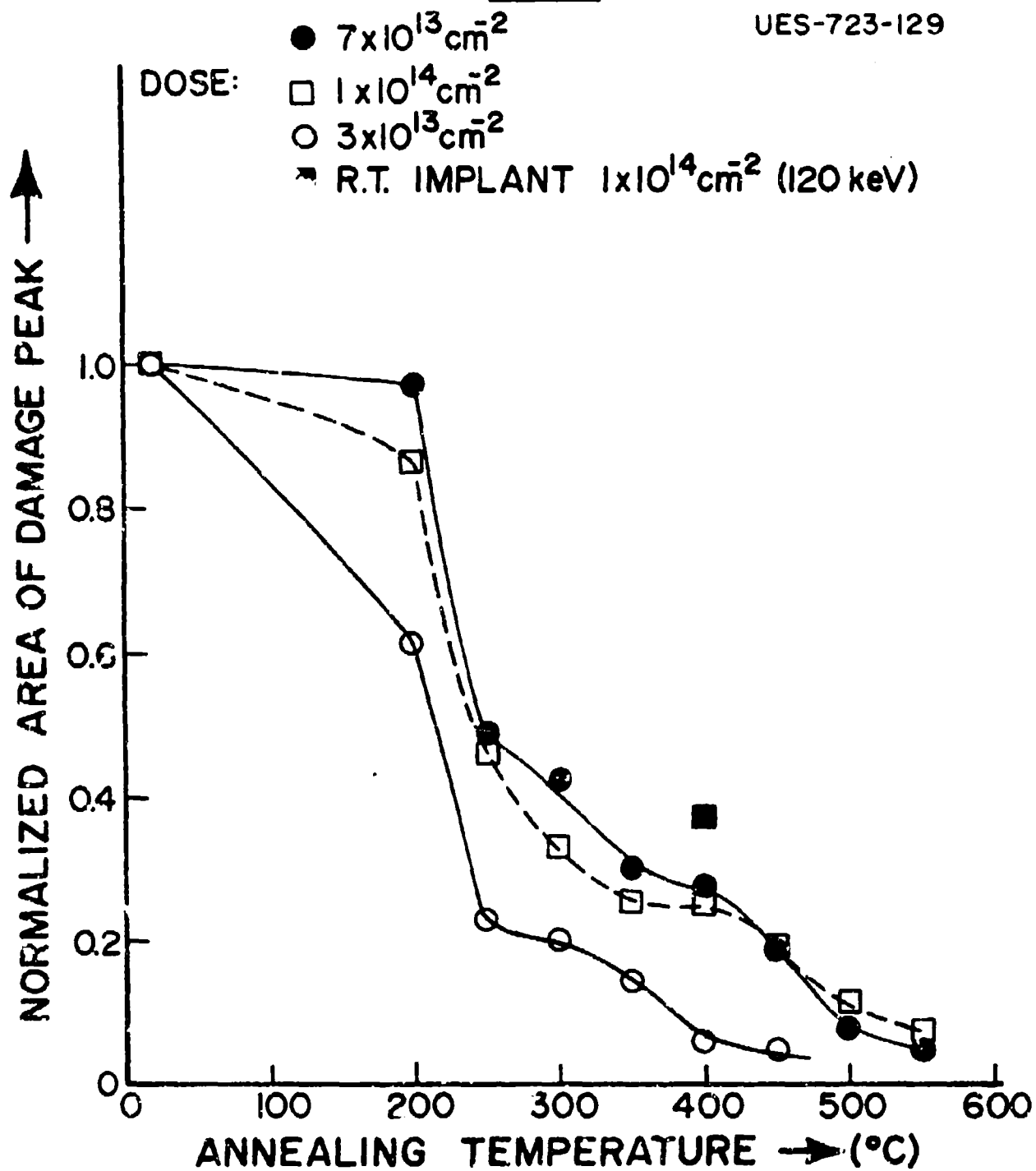


Figure 94 Normalized Area of Damage Peak Plotted as a Function of Anneal Temperature: Annealing Time was 30 min

UES-723-183



Figure 78 Bright-Field Micrograph of GaAs:Se⁺, $1 \times 10^{13} \text{ cm}^{-2}$,
After Annealing at 200°C for 90 min (g=220, S=1)

UES-723-182

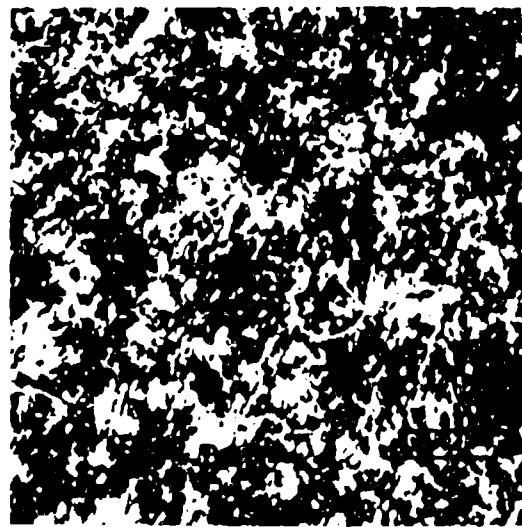
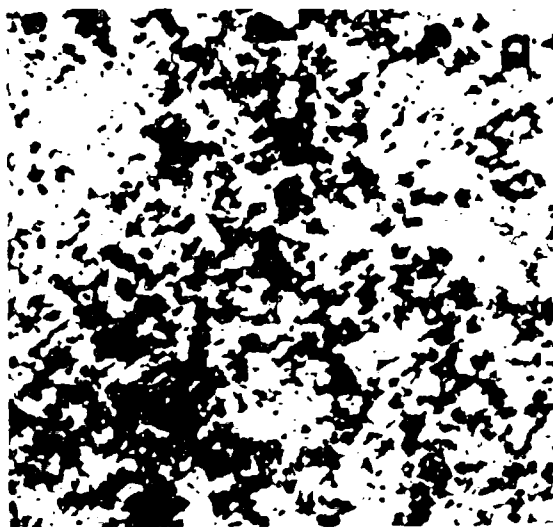
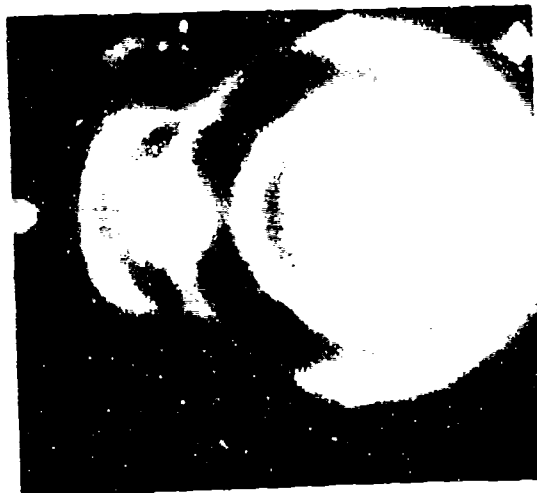


Figure 79 Bright-Field Micrographs of GaAs:Se⁺ Annealed At
200°C for 90 min: (a) $3 \times 10^{13} \text{ cm}^{-2}$,
(b) $7 \times 10^{13} \text{ cm}^{-2}$, g=220

UES-723-179



UES-723-178

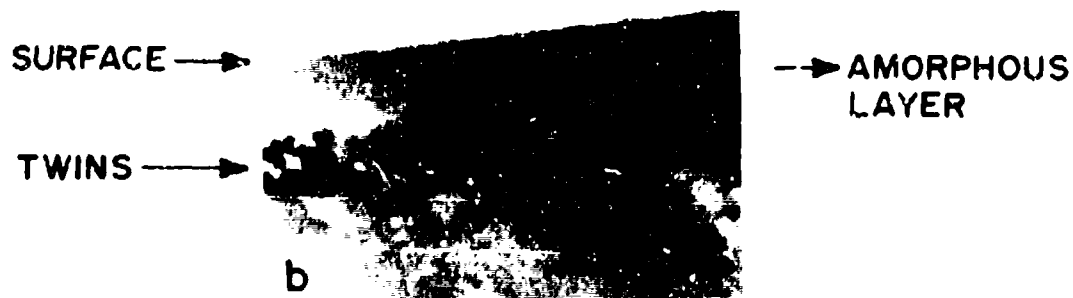


Figure 80 (a) TED Pattern and (b) X-Section Micrograph of GaAs:Se, $1 \times 10^{14} \text{ cm}^{-2}$, Annealed at 200°C , 90 Min

UES-723-180

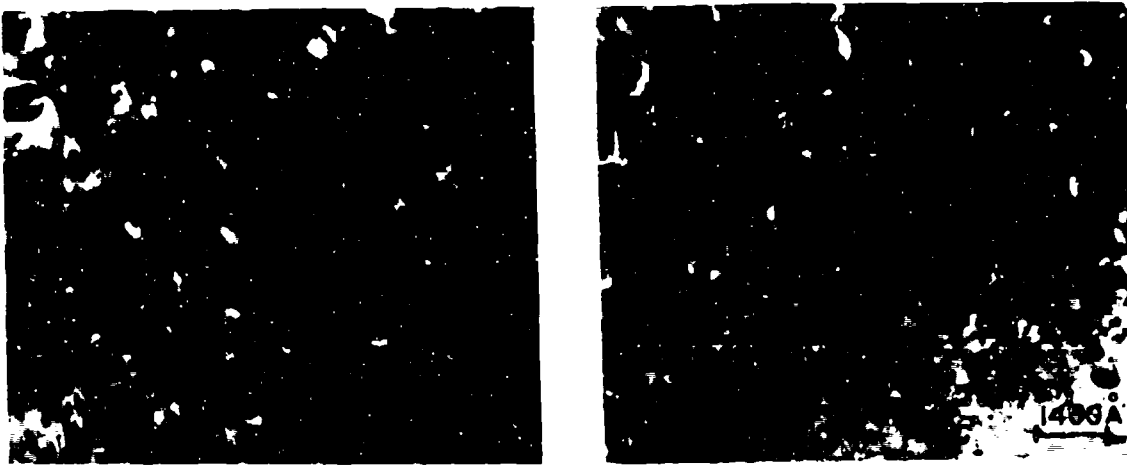


Figure 81 Bright-Field Micrographs of GaAs:Se⁺,
(a) $3 \times 10^{13} \text{ cm}^{-2}$ Annealed at 500°C, 30 Min,
(b) $7 \times 10^{13} \text{ cm}^{-2}$ Annealed at 600°C, 30 Min
(g=220, S=0)

which is very close to the thickness ($\sim 500 \text{ \AA}$) measured by channeling (see Figure 76). It also shows a rough, non-uniform growth front associated with the microtwins.

Returning to the samples isochronally annealed to 600°C after implantation at $3 \times 10^{13} \text{ cm}^{-2}$ and $7 \times 10^{13} \text{ cm}^{-2}$ (Figures 73 and 75 respectively), the TEM bright field micrographs of Figure 81(a,b) show no microtwins but rather the presence of dislocation loops and small precipitates of about 40 \AA average diameter. These precipitates manifest themselves in the form of black-white contrast under dynamical diffraction conditions. From contrast behavior under different diffraction conditions, it was determined that they have spherical symmetry. The $1 \times 10^{14} \text{ cm}^{-2}$ LN_2T implant annealed at 600°C for 30 min shows through the TED pattern, bright field, and dark field picture (Figures 82a-c) the presence of some microtwins along with dislocation loops and precipitates.

TEM investigations of the samples implanted at R.T. were also carried out. Figures 83(a)-(c) shows the TED patterns of the specimen implanted at R.T. with a dose of $5 \times 10^{13} \text{ cm}^{-2}$ and annealed at 200°C for 30 min. Twin spots along with matrix spots can be observed after tilting slightly from (001) orientation (Figure 83b). Figure 84c is the TED pattern in a $\bar{1}14$ orientation. From these TED patterns, microtwins are identified to be on (111) planes with a burger vector $a/6\langle 112 \rangle$ type. The projected length of the twins ($200\text{-}600 \text{ \AA}$) for R.T. implantation are smaller than those associated with the LN_2T implant. A TEM bright field picture (Figure 84) of the same implant annealed at 400°C for 15 min shows the presence of dislocation loops near the surface with underlying twins. RBS-channeling of the same sample showed⁵⁶ the presence of a buried amorphous layer before annealing and

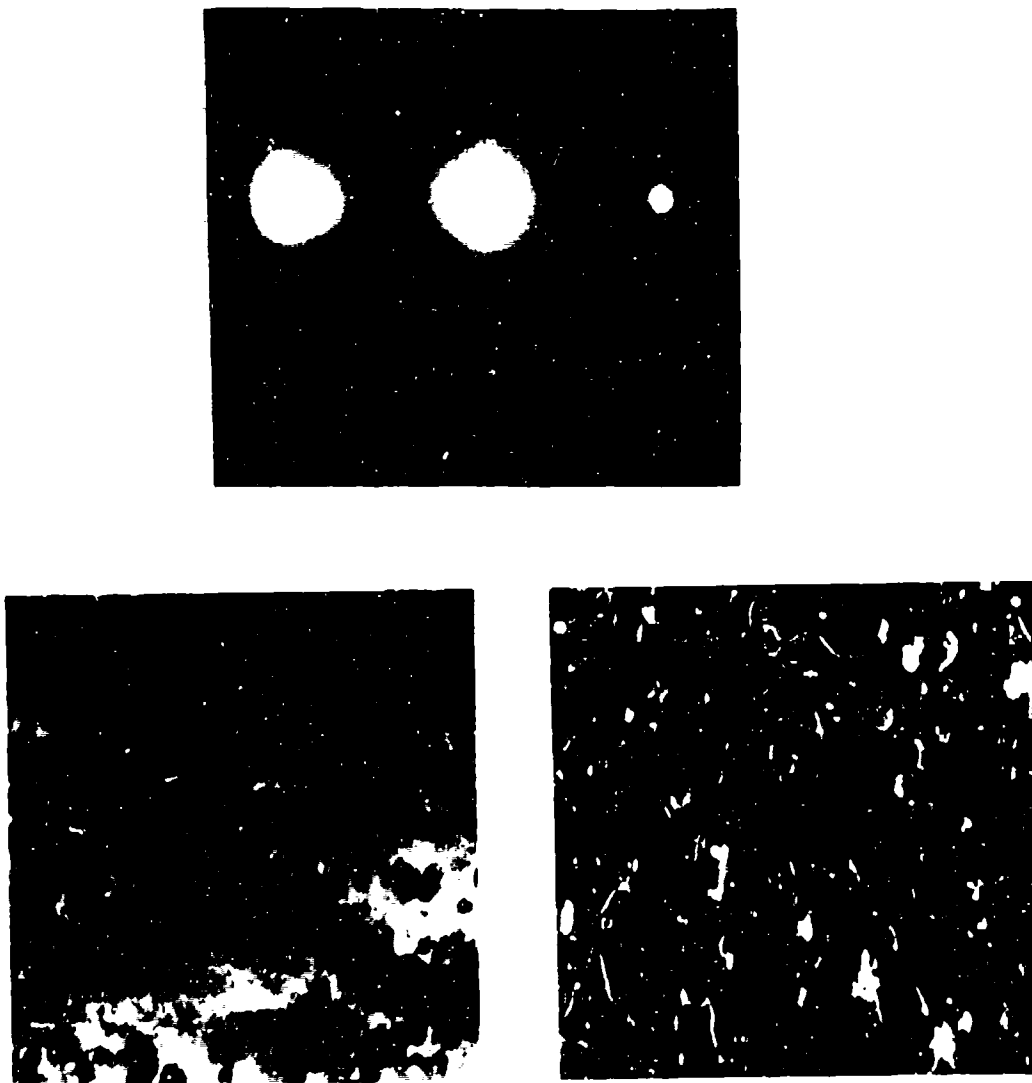


Figure 82 (a) TED Pattern, (b) Bright-Field Plan View Micrograph ($g=220$, $S=0$) and (c) Weak Beam Dark Field Micrograph of GaAs:Se^+ , $1 \times 10^{14} \text{ cm}^{-2}$ Annealed at 600°C , 30 Min

UES-723-176

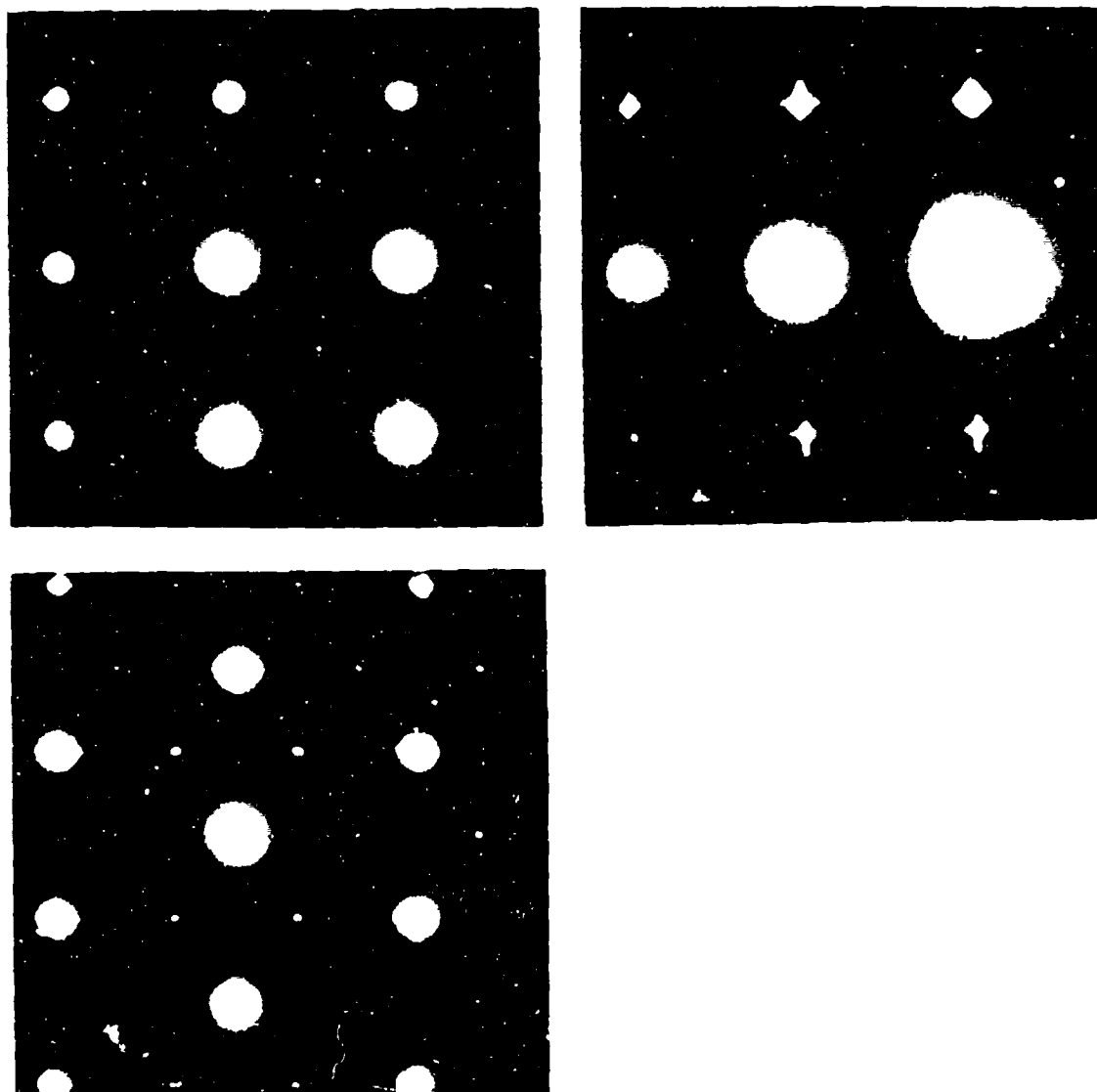


Figure 83 TED Pattern of GaAs:Se⁺, $5 \times 10^{13} \text{ cm}^{-2}$, Annealed at 200 C, 30 Min, (a) Exact <001> Orientation, (b) Slightly Tilted from <001> and (c) <114> Orientation

UES-723-184



Figure 84 Bright-Field Micrograph of GaAs:Se⁺, $5 \times 10^{13} \text{ cm}^{-2}$,
Annealed at 400°C, 15 in (g=220, S₀₁)

UES-723-177

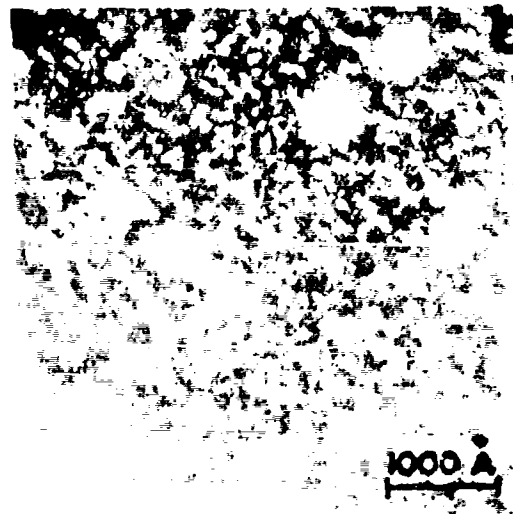
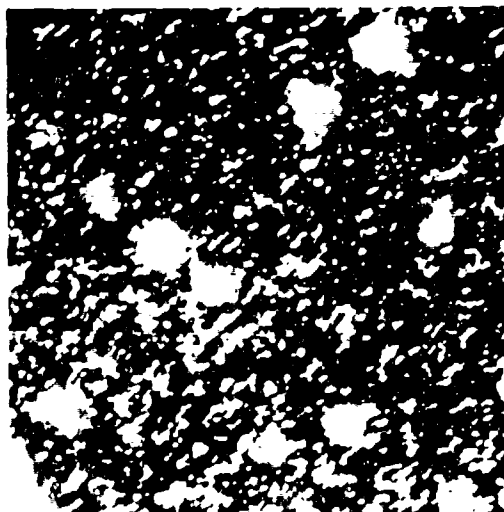


Figure 85 Dark-Field Micrographs of GaAs:Se⁺, $1 \times 10^{14} \text{ cm}^{-2}$,
Annealed at 200°C, 30 Min

regrowth from both sides of the amorphous-crystalline interface. TEM bright field micrographs of the $1 \times 10^{14} \text{ cm}^{-2}$ R.T. implant, annealed at 200°C for 30 min, show the presence of twins below the amorphous layer similar to the case of LN_2T implant. However, the sizes of the twins ($200\text{--}600 \text{ \AA}$) are smaller than that in the LN_2T implant. The dark field pictures (Figures 85a,b) show that twins are lying in at least two $\{111\}$ planes. Micrographs of the same implants after annealing at 300°C and 400°C for 30 min show the presence of twins alone with the higher density occurring at 300°C as compared to 400°C .

In order to determine the volume concentration of twinned regions, dechanneling analysis following Foti et al.⁶⁰ was performed. As the twins lie in $\{111\}$ planes, particles channeled along $\langle 110 \rangle$ direction in the host crystal will enter and move through the twinned lattice along the $\langle 114 \rangle$ direction. The dechanneling as observed in the channeled spectra (Figures 72 and 74) is, therefore, a linear combination of dechanneling in $\langle 110 \rangle$ and $\langle 114 \rangle$ lattices. Knowing the dechanneling rate along $\langle 114 \rangle$ direction, which is about 13 times higher than the $\langle 110 \rangle$ direction and applying single scattering formalism^{64,65} for dechanneling in the host and twinned lattices, one can determine the volume concentration of twinned regions. We have found about 50% and 40% twinned material in $7 \times 10^{13} \text{ cm}^{-2}$ and $3 \times 10^{13} \text{ cm}^{-2}$ implants respectively after they were annealed at 200°C for 120 min.

Measurements of the damage distribution after implantation at room temperature for doses in the range 5×10^{12} – $3 \times 10^{15} \text{ cm}^{-2}$ indicate that the damage level increases with ion dose and reaches an amorphous level at a fluence of $1 \times 10^{14} \text{ cm}^{-2}$ which can be regarded as the threshold dose sufficient to create an amorphous layer extending from the surface to some

depth. The thickness of this amorphous layer is $\sim 760 \text{ \AA}$ which increases with the dose up to $\sim 1,000 \text{ \AA}$ at $2 \times 10^{15} \text{ cm}^{-2}$.

Two sets of samples implanted at a dose of 1×10^{14} and $5 \times 10^{13} \text{ cm}^{-2}$ were chosen for low temperature annealing studies. Figure 86 shows the results of annealing at 200°C for samples implanted to a dose of $1 \times 10^{14} \text{ cm}^{-2}$. Annealing for 30 minutes at 200°C caused some recovery of crystallinity at the interface between the amorphous layer and the underlying crystal. This is indicated by a shift of the rear edge of the aligned spectrum toward the surface. The thickness has reduced from 760 to 675 \AA resulting in an average growth rate of 2.8 \AA/min . Further annealing of the same sample for 60 min at 200°C result in a reduction of thickness to 540 \AA . The average growth rate at this stage is about 2.3 \AA/min . This sample was annealed again at 200°C for 90 min with no further noticeable growth. It may be mentioned that Williams and Austin⁵⁶ have measured a growth rate of $\sim 50 \text{ \AA/min}$ at 150°C for Ar-implanted ($5 \times 10^{13} \text{ cm}^{-2}$) GaAs which was held at liquid nitrogen temperature during the implantation. This large difference in the growth rate is probably because of the fact that dynamic annealing during room temperature implantation produces defect complexes which inhibit proper epitaxial growth in the $150\text{-}250^\circ\text{C}$ range. Figure 87 shows the annealing behavior of a sample implanted to dose of $5 \times 10^{13} \text{ cm}^{-2}$. Annealing at 200°C for 30 min has resulted in a growth of the crystal from both directions indicating the presence of a crystalline layer at the surface of the as-implanted sample which was not quite evident from the initial appearance of the spectrum. A high concentration of defective material centered around 350 \AA below the surface remains after the first anneal period. Further annealing of this sample resulted in a shrinkage of the damaged region from

120 keV $\text{Se}^+ \rightarrow \text{GaAs (100)}$
DOSE $1 \times 10^{14} \text{ cm}^{-2}$

UES-723-110

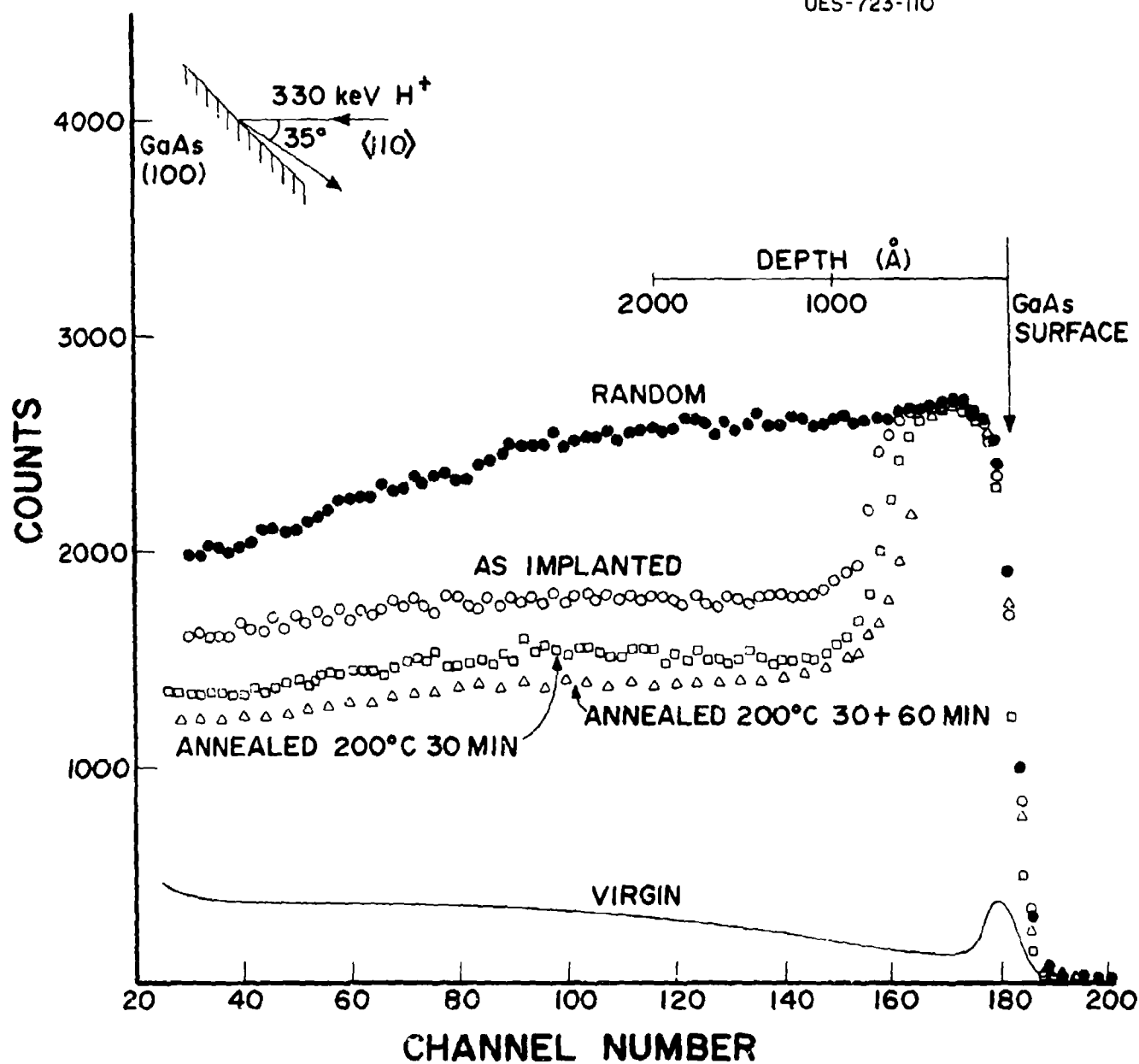


Figure 36 Channeling spectra for GaAs:Se⁺, $1 \times 10^{14} \text{ cm}^{-2}$
Before and After Annealing at 200°C

120 keV Se^+ \rightarrow GaAs (100)
DOSE $5 \times 10^{13} \text{ cm}^{-2}$

UES-723-108

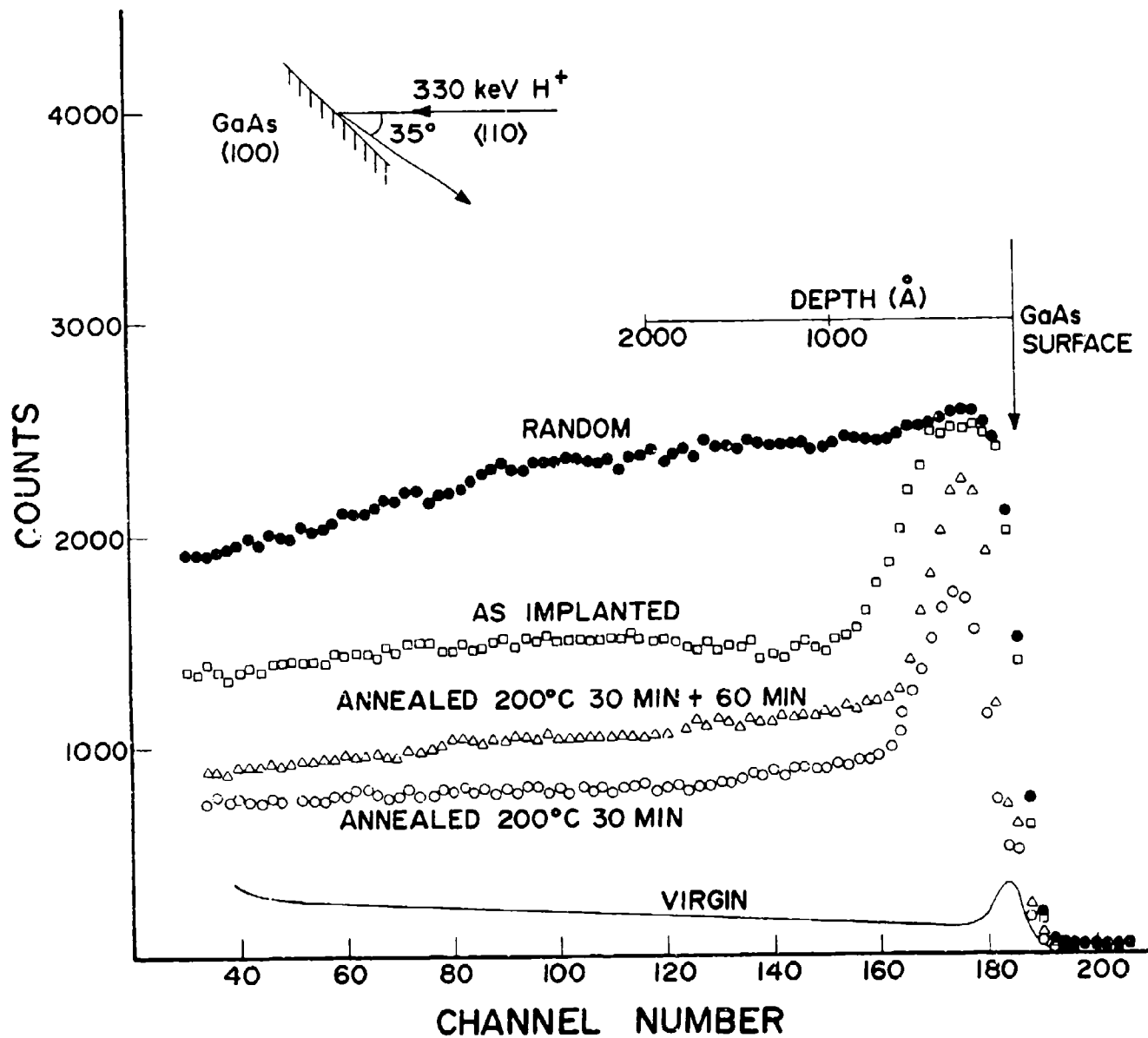


Figure 87 Channeling Spectra for GaAs:Se⁺, $5 \times 10^{13} \text{ cm}^{-2}$
Before and After Annealing at 200°C

both sides with, however, an associated increase in the concentration of defects in the remaining damage zone as compared to that present after the first anneal. These defect structures have apparently evolved ahead of the advancing annealing fronts. No further recovery was observed when this sample was annealed again at 200°C for 90 min. Figure 88 shows the results of the $1 \times 10^{14} \text{ cm}^{-2}$ implanted sample annealed at 250°C for 30 min. The interface is observed, in this case, to move toward the surface at a rate of $\sim 9 \text{ Å/min}$. After 60 min anneal, the layer is no longer amorphous but high dechanneling indicates the presence of large amounts of disorder which remains unchanged even for longer anneal times. Results of annealing of the $1 \times 10^{14} \text{ cm}^{-2}$ implant at 300°C and 400°C are shown in Figure 89. Although regrowth has taken place throughout the layers for both 300°C and 400°C, there remains a high level of disorder. Longer time annealing of these samples does not lead to reduction in damage level. Damage recovery is similar for $5 \times 10^{13} \text{ cm}^{-2}$ implant, except that in addition to growth from the interface there is a growth from the surface as well, indicating that the amorphous layer again did not reach entirely to the surface.

Some of the above described samples were subjected to higher temperature annealing which was performed at 600°C for 30 min. Channeling measurements (Figure 90) indicate that good recovery of the residual damage has taken place in all of them. However, the minimum yields are higher compared to that from a virgin crystal. The best recovery has taken place in the sample that was annealed at 600°C for 30 min in one step.

We have also investigated the implanted dose and initial amorphous layer thickness dependence of the epitaxial regrowth behavior. For this purpose Cr-doped semi-insulating GaAs(100) wafers held at liquid-nitrogen (LN_2)

120 keV $\text{Se}^+ \rightarrow \text{GaAs (100)}$

DOSE $1 \times 10^{14} \text{ cm}^{-2}$

UES-723-III

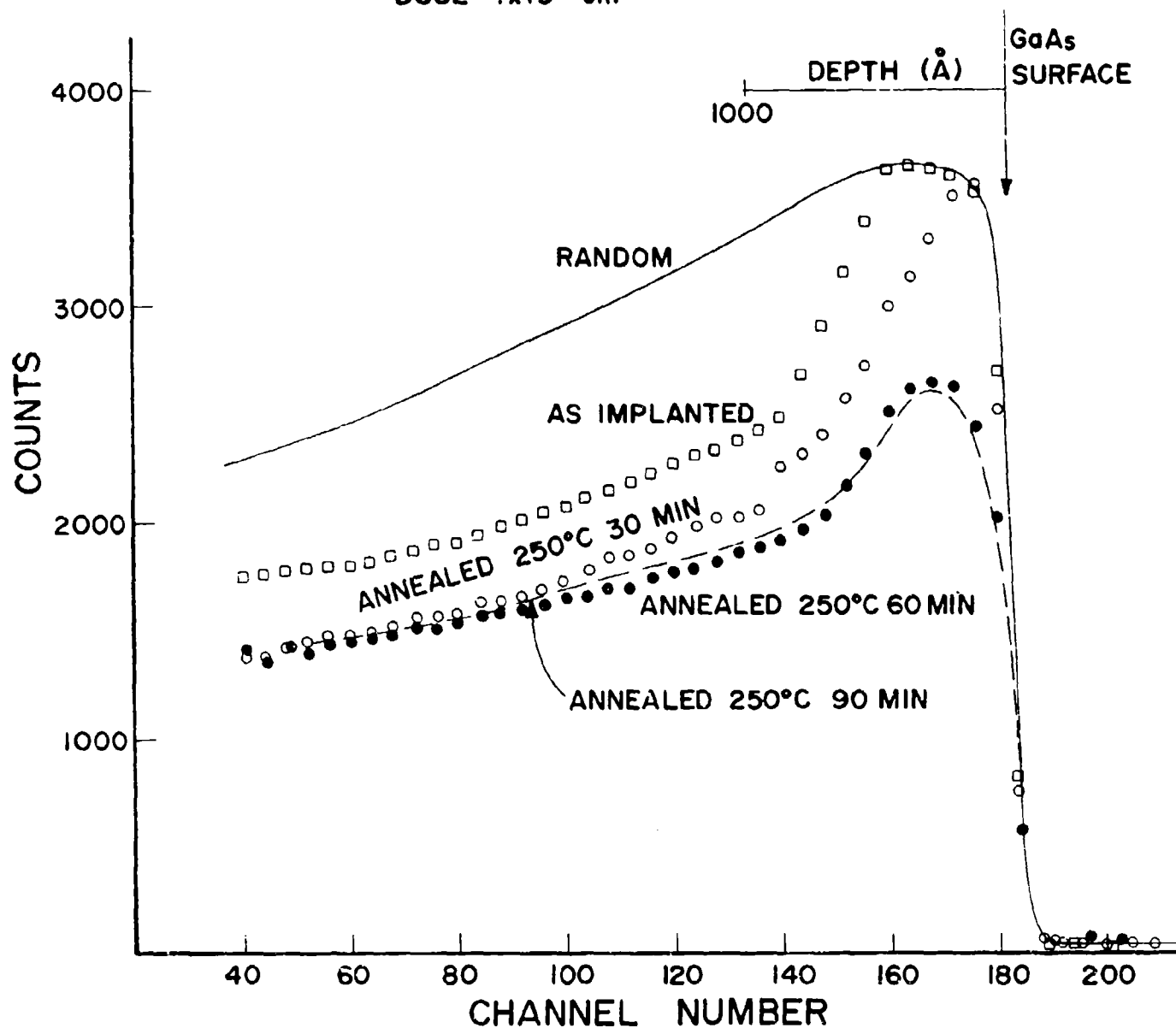


Figure 88 Channeling Spectra for GaAs:Se⁺, $1 \times 10^{14} \text{ cm}^{-2}$
Before and After Annealing at 250°C

120 keV $\text{Se}^+ \rightarrow \text{GaAs (100)}$

DOSE $1 \times 10^{14} \text{ cm}^{-2}$

UES-723-109

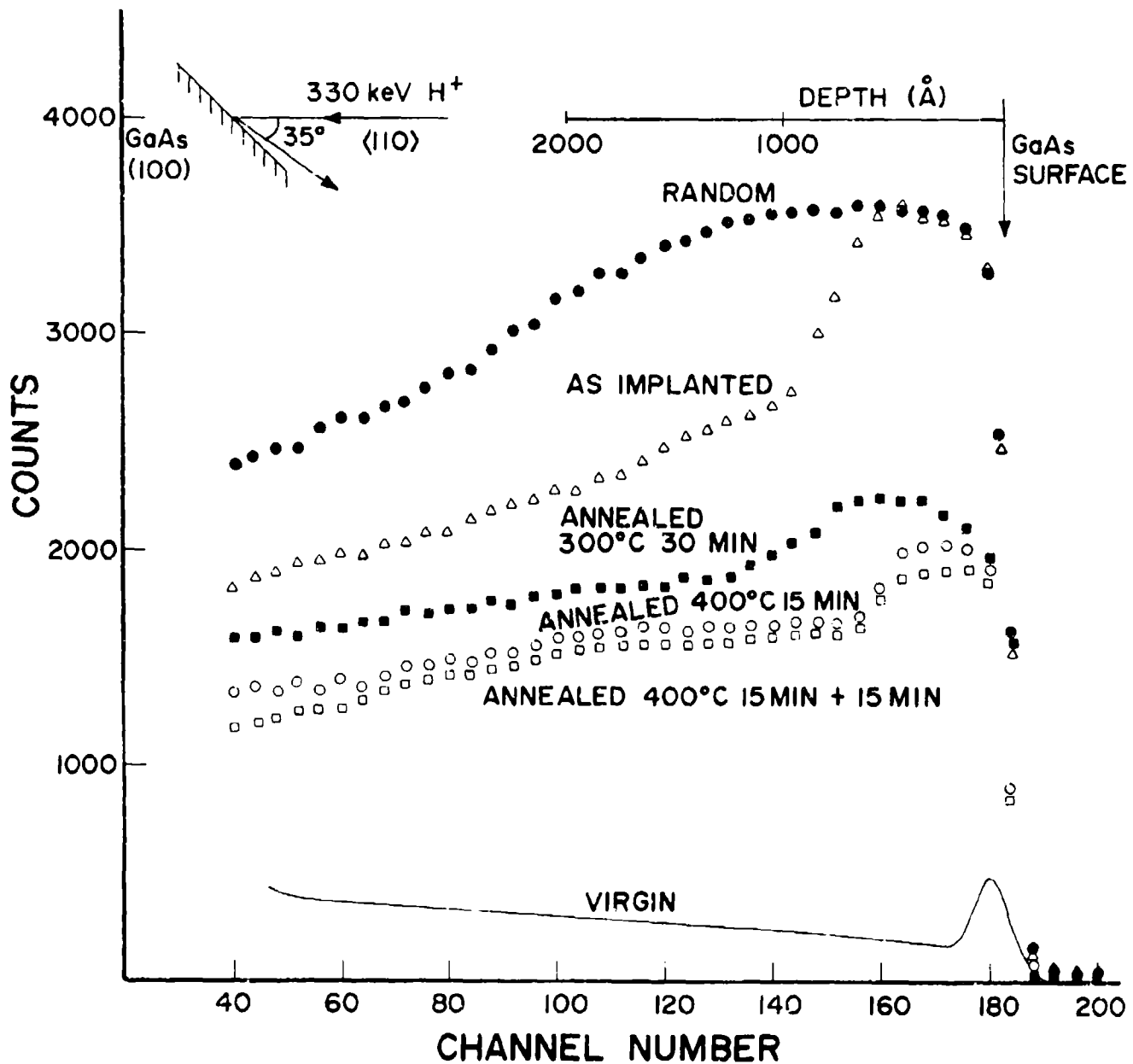


Figure 89 Channeling Spectra for GaAs:Se⁺, $1 \times 10^{14} \text{ cm}^{-2}$.
Before and After Annealing at 300 and 400°C

120 keV $\text{Se}^+ \rightarrow \text{GaAs (100)}$

UES-723-113

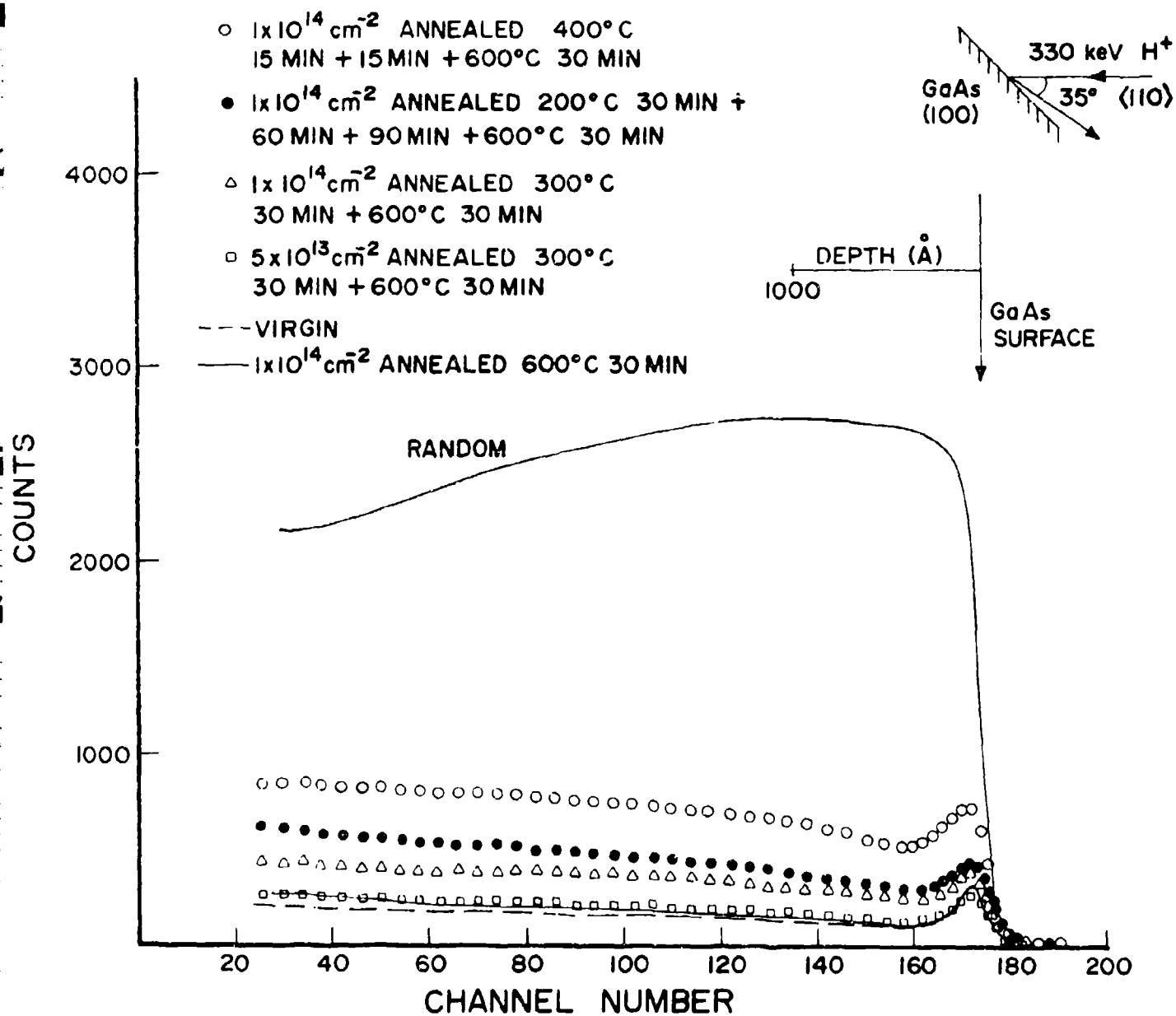


Figure 90 Channeling Spectra for GaAs:Se After Various Annealing Steps

temperature were implanted with 120 keV Se^+ ions to doses of 3×10^{13} , 7×10^{13} , and $1 \times 10^{14} \text{ cm}^{-2}$, and with 240 keV As^+ ions to a dose of $1 \times 10^{14} \text{ cm}^{-2}$. In addition R.T. implantations with 120 keV Se^+ ions to doses of $5 \times 10^{13} \text{ cm}^{-2}$ and $1 \times 10^{15} \text{ cm}^{-2}$ were also chosen for this study.

Figure 91 shows the example of typical RBS spectra of 330 keV H^+ ions impinging along the $\langle 110 \rangle$ axis of GaAs crystals implanted with 120 keV Se^+ to doses of 3×10^{13} and $7 \times 10^{13} \text{ cm}^{-2}$ and 240 keV As^+ to a dose of $1 \times 10^{14} \text{ cm}^{-2}$. The channeling spectra after annealing at 400°C for 30 min indicate that the recrystallization of the amorphous layer is complete for all doses. However, various amounts of disorder remain. The sample implanted at a dose of $3 \times 10^{13} \text{ cm}^{-2}$ at LN_2 temperature showed the best recovery as compared to the higher dose implantes. In order to clarify the correlation between the implant dose and residual damage after annealing, we have plotted in Figure 92 the areas of the disorder peaks against the ion doses. It is clear that there is an abrupt increase in the residual disorder at a dose above $3 \times 10^{13} \text{ cm}^{-2}$. The residual damage increases by almost a factor of 5 when the Se ion dose increases from 3×10^{13} to $7 \times 10^{13} \text{ cm}^{-2}$ while the thickness increases by only about 10% (see Figure 91). Thus Figure 92 represents a dose dependence of residual damage at approximately constant damage thickness. Increases in dose beyond $7 \times 10^{13} \text{ cm}^{-2}$ produce very little or no change in residual defect concentrations after annealing.

To compare our result with that of Grimaldi et al.⁵⁸, we have incorporated our data into their plot of disorder peak area versus thickness. This plot was made by normalizing the residual disorder of our As^+ -implanted sample with their straight line. Clearly the maximum deviation from their straight line is found for $3 \times 10^{13} \text{ cm}^{-2}$ which is the critical dose of

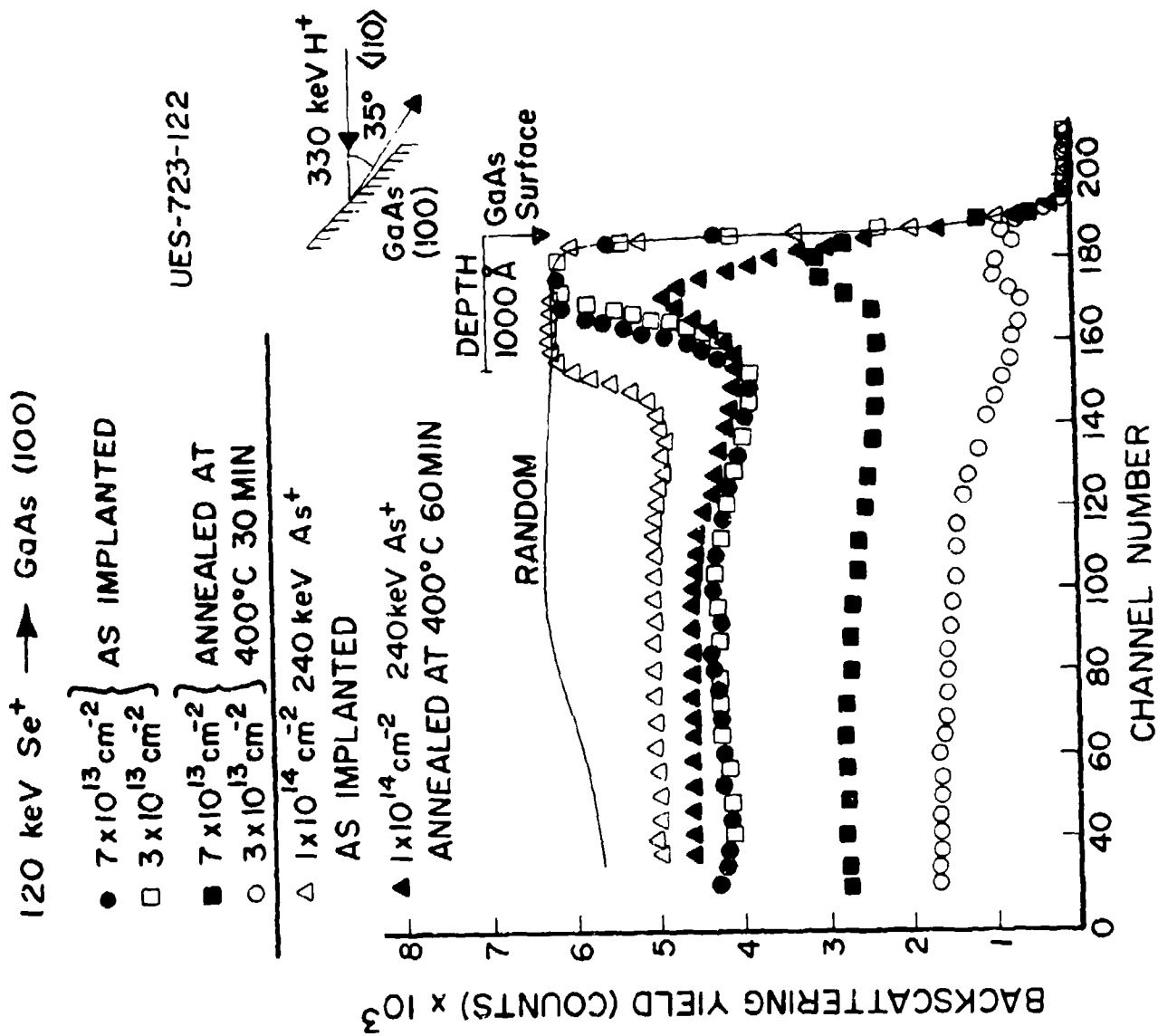


Figure 91 Channeling Spectra for GaAs:Se⁺, As⁺ Before and After Annealing at 400°C

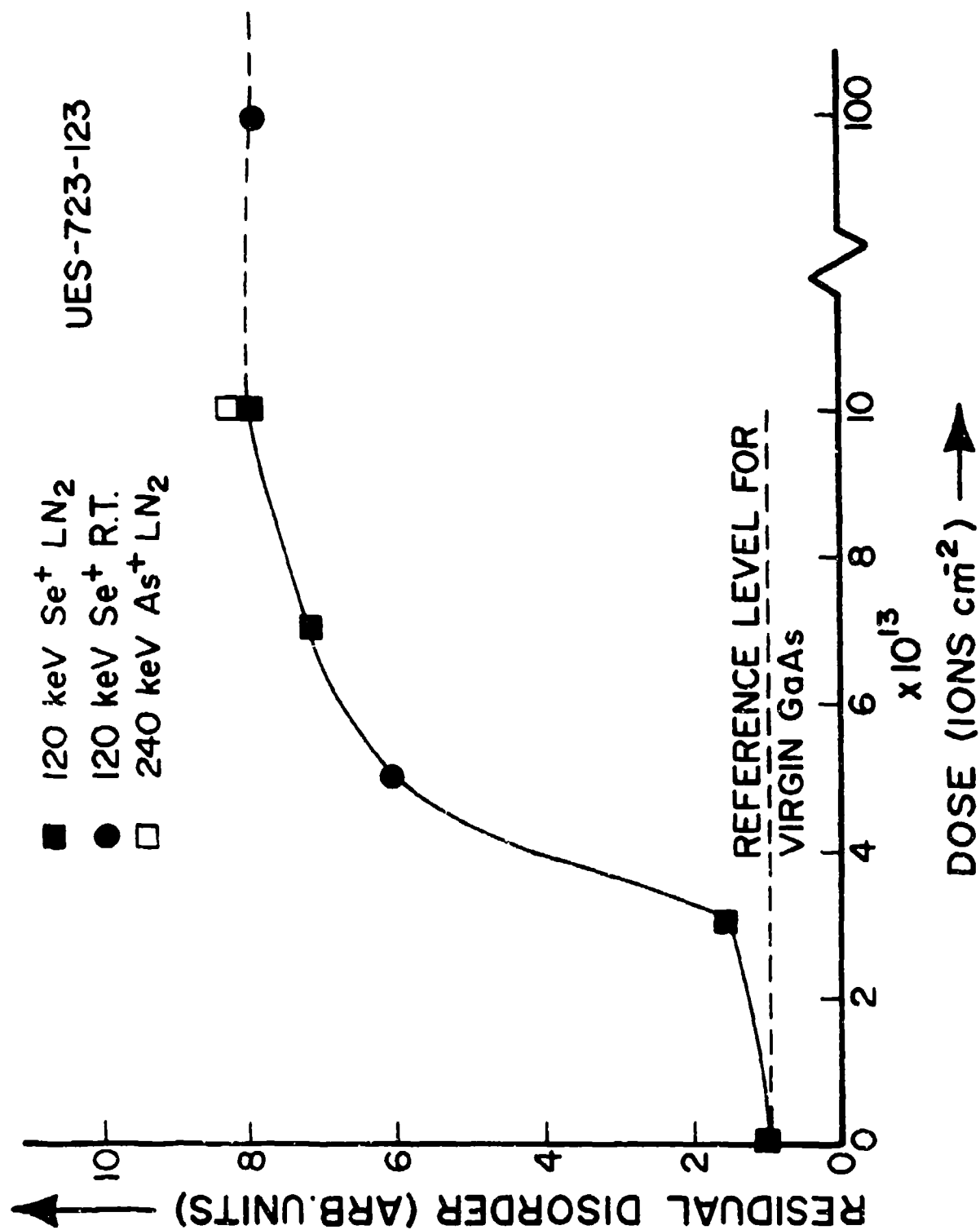


Figure 92 Dose Dependence of Residual Disorder After Annealing at 400°C

amorphization at LN_2 temperature. The residual disorder for higher doses seems to follow the linear dependence on thickness in accordance with the observation of Grimaldi et al. for other implants. We have also investigated the influence of stepwise annealing; starting from 200°C for 30 min up to 400°C for 30 min (in steps of 50°C) on the final residual disorder after 400°C anneal. No difference in residual disorder has been observed from the onstep anneal at 400°C for 30 min shows the same level of residual disorder as observed after annealing at 400°C for 60 min.

For doses above the threshold dose of amorphization, the substrate temperature during implantation does not have any influence on the damage annealing process in agreement with the observation of Grimaldi et al.⁵⁸ However, in the region of the threshold dose for amorphization, substrate temperature seems to have an influence on the annealing behavior. For instance, the dose of $5 \times 10^{13} \text{ cm}^{-2}$ at R.T. was just sufficient or slightly less than the dose required to amorphize the layer. The channeled spectrum showed that the central region of the damage peak reached the random level indicating the presence of crystalline region near the surface. The residual disorder after annealing of this sample was much higher than the $3 \times 10^{13} \text{ cm}^{-2} \text{ LN}_2$ implant and follows the linear dependence on thickness.

Although the present results strengthen the conclusion drawn by Grimaldi et al.,⁵⁸ namely that the thickness of the initial amorphous layer is the most important parameter that determines the regrowth after low-temperature annealing, the situation near the threshold dose for amorphization is different. Williams and Austin⁵⁶ have found that the damage annealing for Ar^+ and S^+ implants at the threshold dose ($3 \times 10^{13} \text{ cm}^{-2} \text{ LN}_2$) for amorphization at a thickness of $1,000 \text{ \AA}$ is almost complete after annealing at

250°C. Our results show that a layer of 650 Å ($3 \times 10^{13} \text{ cm}^{-2} \text{ Se}$) has grown with very little residual disorder (Figure 93) after annealing at 400°C. These results then argue against the suggestion of Grimaldi et al. viz, that the amorphous layer has to be thinner than 400 Å in order for complete defect-free regrowth after annealing at low temperature. In an attempt to explain their own results, Williams and Austin⁵⁶ have suggested that at the threshold dose of amorphization very little disruption of stoichiometry takes place thus allowing a better regrowth. The stoichiometry may get extensively disrupted and reach a steady-state condition at a high dose, which would then inhibit epitaxial growth and result in a high residual disorder after annealing. This suggestion, however, is inconsistent with the good regrowth of a 400-Å-thick amorphous layer produced by high dose As_2^+ implantation. Grimaldi et al.⁵⁸ have suggested that during annealing, the growing crystal front accumulates point defects which collapse into clusters and these clusters of defects promote the formation of microtwins. A thickness of 400 Å, then, is the maximum distance that the interface can move before these defects begin to aggregate or precipitate. These alternate explanations given above are not adequate in reconciling the good regrowth at low (threshold) dose and at the same time, the thickness dependence of residual damage at high doses.

4.3.1 Discussion

It is clear from the results described so far that the low temperature annealing of amorphous GaAs leads to the formation of microtwins as it grows epitaxially from the interface. The annealing starts at 200°C but stops after a certain time, depending on the implantation dose (amount of damage). For doses below that required to amorphize the layer, annealing

DISORDER PEAK AREA AFTER ANNEALING 400°C

UES-723-121

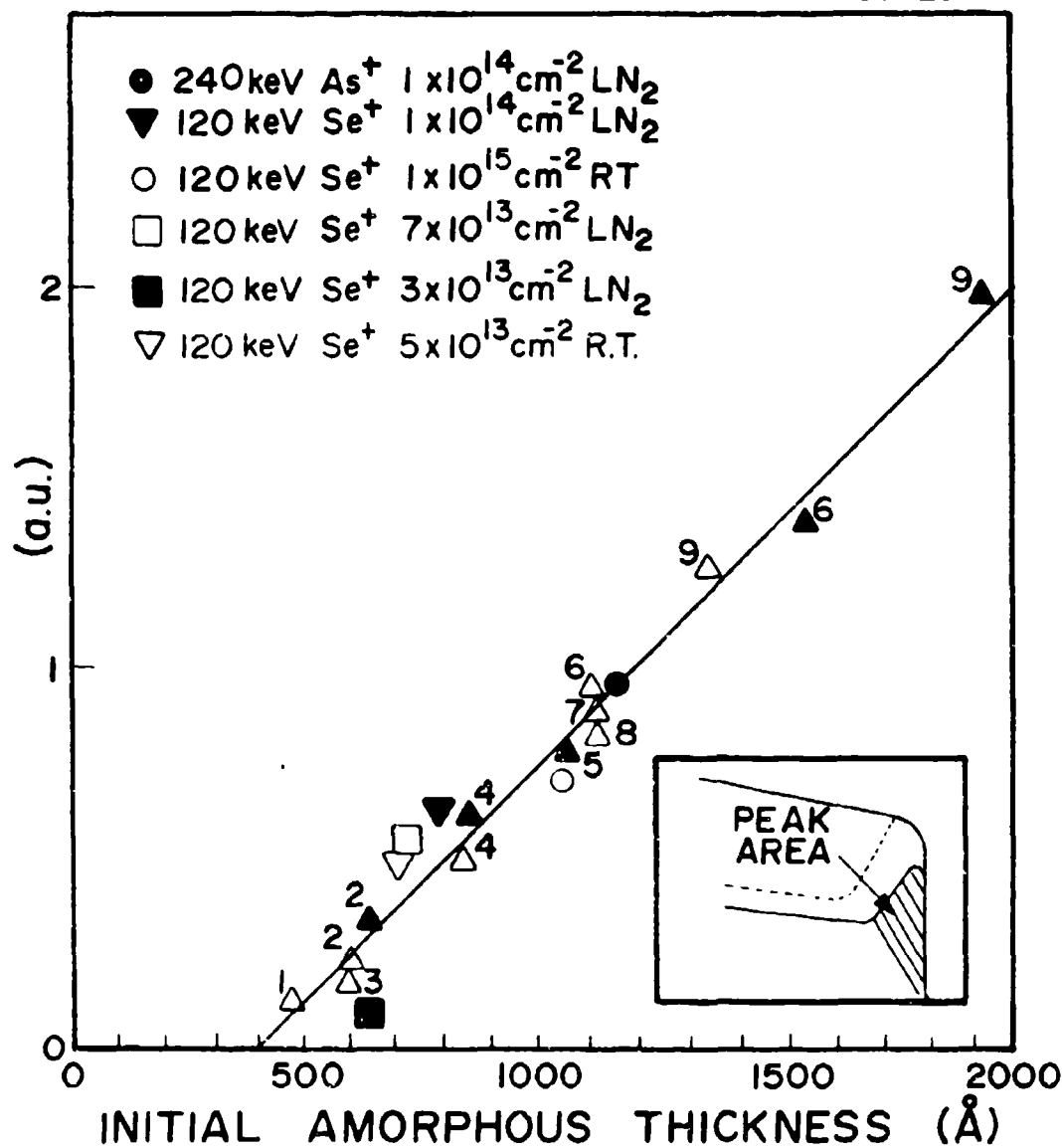


Figure 93 Area under the Disorder Peak of Se-Implanted GaAs Annealed at 400°C for 30 min Plotted Against the Thickness of the Amorphous Layer.

takes place without the formation of microtwins. This may be the reason for higher electrical activation at elevated temperature implantation and subsequent annealing because the damage is not likely to reach the amorphous level at 200°C or 300°C. However, other effects could be involved and will be discussed below. Isochronal annealing studies show that as the implantation dose increases, higher temperature are required to bring the residual defect level close to that of the virgin sample. For instance, complete recovery, as measured by channeling, is obtained after annealing at 500°C for 30 min for $3 \times 10^{13} \text{ cm}^{-2}$ implant (Figure 73). However, for $1 \times 10^{14} \text{ cm}^{-2}$ implant, even after annealing at 600°C for 30 min, there is some residual damage visible by channeling (Figure 77). TEM showed the presence of some microtwins in this case, whereas no microtwins were found to be present in the $3 \times 10^{13} \text{ cm}^{-2}$ implant annealed at 500°C for 30 min.

In order to distinguish between the various annealing stages, we have plotted the damage peak areas after annealing as a function of anneal temperature in Figure 30 for various doses. One clear annealing stage can be seen for all doses at about 250°C. The second annealing stage is at about 400°C for $3 \times 10^{13} \text{ cm}^{-2}$ implant increasing to $\sim 500^\circ\text{C}$ for the $7 \times 10^{13} \text{ cm}^{-2}$ and $1 \times 10^{14} \text{ cm}^{-2}$ implants. The lower stage is associated with the migration of atoms at the crystalline-amorphous interface resulting in the epitaxial regrowth. For those samples not made totally amorphous by the implantation, this stage corresponds to recovery of individual amorphous zones. This requires only short range migration and is possible at low temperature. The second recovery stage is associated with the annealing of microtwins. Dislocation loops and precipitates are found to remain after microtwins disappear at about 500-600°C, depending on the dose of Se. Correlations have

been made between the number of atoms involved in precipitation with the number of implanted atoms by assuming that the precipitates are of spherical shapes. Details of the black-white contrast analysis support this assumption since the g vector is parallel to the black-white vector l implying three-dimensional symmetry. The number of atoms associated with these black-white clusters is based on the average volume of the observed spherical precipitates. Numbers thus obtained correspond very closely with the number of implanted atoms indicating that almost all of the implanted Se atoms form precipitates. Poor or no electrical activation⁶¹ at low temperature ($\sim 600^\circ\text{C}$) for Se in GaAs can therefore, be explained as due to the precipitation of dopants.

Grimaldi et al.⁵⁸ have also observed the formation of twins after low temperature annealing of GaAs implanted with various ions. They suggest that the growing crystal front accumulates local defects which eventually collapse into clusters. These clusters of defects then act as nucleation centers for microtwins. The nature of these clusters or the process of their formation is not very clear. Grimaldi et al.⁵⁸ have suggested that Cr may be involved since Cr is known to be mobile at low temperatures. In order to study the influence of Cr in the recrystallization behavior, we have implanted an undoped crystal with 120 keV Se^+ at a dose of $1 \times 10^{14} \text{ cm}^{-2}$. Channeling analysis after annealing the samples at 300°C for 30 min show exactly the same level of residual damage as that of a Cr doped sample implanted and annealed in an identical manner. TEM investigation of the sample also showed no difference in the twin characteristics or concentration compared to a Cr-doped sample. Thus, we conclude that Cr does not play any significant role in the formation of these microtwins.

Recently Speriosu et al.⁶² have suggested, from their X-ray diffraction studies, that there exists a region near the interface where both point defects and extended defects, such as misfit dislocations, coexist after implantation but before annealing. These extended defects are proposed to act as nucleation centers for microtwins which then act to seriously hinder the perfect crystalline regrowth. In an attempt to verify the model of Speriosu et al.⁶² as regards the presence of line defects at the crystalline-amorphous interface we have examined the as implanted amorphous-crystalline interface by TEM. The samples were prepared by controlled chemical etching of the amorphous layer leaving a thin amorphous region (100-200 Å) on the surface and then jet thinning from the backside. No dislocations or twins were observed at the interface. It is very unlikely that if they were present, they would be below the detection limit of the electron microscope. Therefore, although the evolution of damage up to amorphousness in GaAs may be very different from that in Si or Ge, it does not appear to be accompanied by the formation of extended defects at the amorphous-crystalline interface. It should be mentioned that Speriosu et al.⁶² made an attempt to detect the extended defects by X-ray topography, but failed to see any as well.

Finally, the suggestion that the stoichiometric imbalance produced by preferential sputtering⁶³ and/or by different energy sharing of constituent atoms is the cause of the development of twins after low temperature annealing needs some consideration. It has been shown⁶⁴ that preferential sputtering causes the loss of As from the surface at low ion energies. This behavior is expected to be similar at higher energies required for implantation. The stoichiometry change at the surface is thought to propagate into the bulk by

the movement of enriched Ga surface atoms inward or the movement of As atoms outward thereby replenishing the depletion of As atoms at the surface. Thus, the composition over the whole layer up to a thickness comparable to the range of the projectile ion is changed. Epitaxial regrowth requires the restoration of the stoichiometry which can take place by the migration of the As atoms from the bulk into the growing front. Excess Ga atoms may form anti-site pairs or precipitate and form clusters that will promote the formation of microtwins. One can check the influence of preferential sputtering phenomenon on the regrowth behavior of GaAs by implanting the sample through a layer of some other material deposited on GaAs. We have performed such experiments by depositing 500 Å of Si_3N_4 on GaAs and implanting with 120 keV Se^{++} (equivalent to 240 keV Se^+) at a dose of $1.5 \times 10^{14} \text{ cm}^{-2}$. After implantation, the Si_3N_4 layer is stripped off chemically and the as-implanted damage is examined by ion channeling. An amorphous layer of thickness 560 Å has been found on the surface. Annealing at 300°C for 30 min resulted in the regrowth of the layer with the same level of residual damage as that of the sample implanted without a cap. TEM studies also show a similar nature for the microtwins as was found in uncapped samples. It can, therefore, be stated with reasonable assurance that sputtering does not influence the regrowth behavior in GaAs. This implies that at the level of dose used in the present experiments, the preferential sputtering is probably insignificant.

However, variations in collision cross section, maximum energy transfer and recoil range distribution of each of the constituent atoms in a binary lattice may cause a nonstoichiometric distribution of host atoms after ion implantation. Christel and Gibbons⁶⁵ have shown from theoretical

calculations using the Boltzman transport equation that ion implantation produces separate zones of vacancies and interstitials; vacancies being closer to the surface region and interstitials at depths exceeding R_p . Because of the differences in the threshold energies⁶⁶ for displacement of Ga and As, a slight non-stoichiometric distribution of vacancies and interstitials are expected. As regrowth occurs during annealing, these interstitials may coalesce to form clusters that could promote the occurrence of lattice bonding errors leading to microtwin formation. However, no direct experimental results are available to support the claim of separate vacancy-interstitial distributions after ion implantation, although indirect evidence supports the existence of such an effect.⁶⁷

While discussing the transformation from the amorphous to crystalline state during solid phase regrowth of silicon, Drosd and Washburn⁶⁸ have recently concluded that the $\langle 100 \rangle$ amorphous/crystalline (α/c) interface is expected to advance without the formation of microtwins. Microtwins are expected to form in the case of growth on $\langle 111 \rangle$ surfaces only. As the crystal structure of Si and GaAs are exactly similar except for the fact that alternate sites are occupied by two different kinds of atoms, one can expect that the same analyses should be applicable in the case of GaAs. This implies that, for the α/c interface to advance, both Ga and As atoms should be available in the region close to the interface so that they can take their correct positions. Only when stoichiometric imbalance exists at the interface, can one have cluster formation of excess atoms that may act as nucleation centers for the growth of microtwins at low temperatures.

It may be that the formation of microtwins is more directly related to some intrinsic property of GaAs. For example, if the α/c interface is

non-uniform or rough prior to its being subjected to annealing, i.e., the interface, instead of being planar, consists of hills and valleys, the hills may get bounded by inclined $\langle 111 \rangle$ planes which would then help in the growth of microtwins upon annealing. An extremely rough non-uniform growth front was observed in the cross-sectional TEM micrograph of the $1 \times 10^{14} \text{ cm}^{-2}$ implant (annealed at 200°C for 90 min, Figure 80), suggesting that the initial interface in these low temperature annealed samples may be sufficiently non-planar to result in microtwin growth from $\langle 111 \rangle$ faceting. The differences in size of the residual twins observed for LN_2 and room temperature implants may be a consequence of this effect in as much as two dimensional diffusion at room temperature may result in an interface smoothing compared to similar samples prepared at liquid nitrogen temperature. It was observed in this work that twins from LN_2 implants were larger than from R.T. implants.

4.3.2 High Temperature Annealing

Cr-doped semi-insulating GaAs wafers (grown by horizontal Bridgman technique) with (100) orientation were implanted with 120 keV Se^+ ions in a nonchanneling direction at room temperature to doses ranging from 5×10^{12} to $3 \times 10^{15} \text{ cm}^{-2}$.

After the implanted damage analyses, the samples were capped by plasma-deposited Si_3N_4 , and annealed in flowing hydrogen gas at 900°C for 15 min. The samples were then uncapped and reanalyzed by using RBS channeling and TEI.

4.3.3 Results and Discussion

Rutherford backscattering and channeling

The analysis of the implanted nonannealed sample for various doses is shown in Figure 95. The damage in the surface layer increases as a

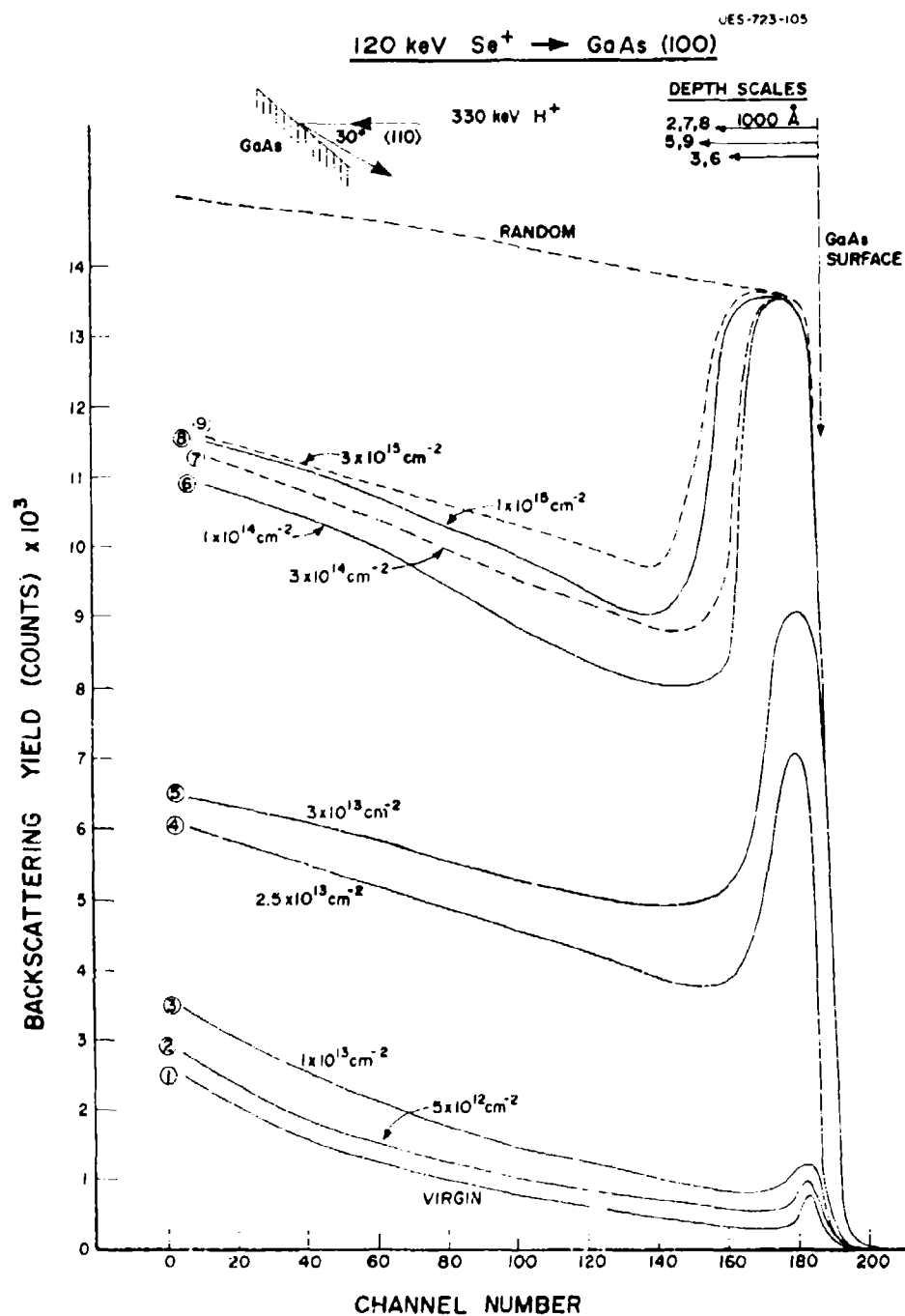


Figure 95 Backscattering Spectra from Aligned and Randomly Oriented GaAs:Se^+ for Various Doses of Se^+

function of Se^+ ion dose, and reaches the effective random reference level at a dose of $1 \times 10^{14} \text{ cm}^{-2}$. Thus the threshold dose of amorphization for 120 keV Se^+ , with the substrate at room temperature, would be very close to $1 \times 10^{14} \text{ cm}^{-2}$. The thickness of this amorphous layer is $\sim 800 \text{ \AA}$, which increases with ion dose up to a thickness of $1,000 \text{ \AA}$, at a dose of $3 \times 10^{15} \text{ cm}^{-2}$. Knowing the area A under the damage peaks of Figure 95, and height H of the random spectrum, one can calculate the number of displaced atoms/ cm^2 from the relation $N_D = (A/H) \partial E / [\epsilon]$, where ∂E is the energy width of a channel and $[\epsilon]$ is the stopping cross section factor.

The build-up of the disorder, in terms of number of displaced atoms cm^2 as a function of Se^+ ion dose, is shown in Figure 96. A linear increase of disorder at low dose is observed which approaches a saturation at higher doses. From the slope of the linear part, the number of displaced Ga and As atoms per incident ion can be determined, and is found to be $\sim 10,000$. A rough estimation, using collision cascade theory⁶⁹ and assuming a threshold displacement energy for Ga and As atoms equal 25 eV, yields a number close to 30,000. This difference is understandable from the fact that a considerable amount of annealing takes place during room temperature implantation. In fact, our recent experiments with Se implantation at liquid nitrogen temperature show a much closer agreement with the calculated number. Earlier studies⁷⁰ on Sb-implanted Si at room temperature and liquid nitrogen temperature, have shown a similar kind of result with the present study in GaAs. It was determined, for example, that one Sb ion at 200 keV produces 6,500 displaced Si atoms at room temperature, and 18,000 atoms at liquid nitrogen temperature.

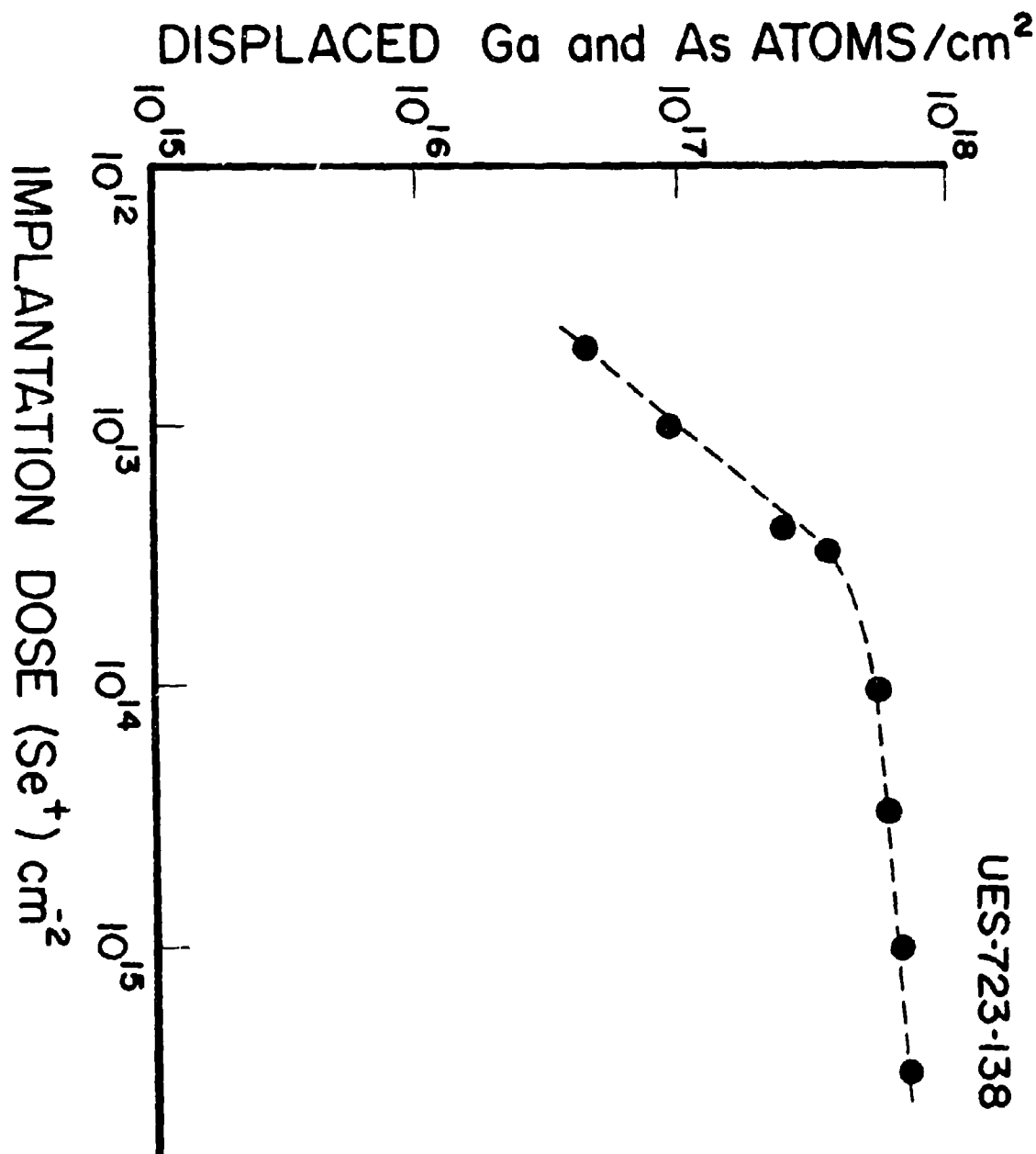


Figure 96 Dependence of the Number of Displaced Ga and As Atoms/cm² as a Function of Se⁺ Dose

One can also extract the disorder distribution from the observed backscattering spectra in Figure 95. For this purpose, one may define a reduced yield

$$\chi(t) = \frac{\chi_2(t) - \chi_1(t)}{1 - \chi_1(t)}$$

where $\chi_2(t)$ and $\chi_1(t)$ are the backscattering yields from an annealed implanted sample and virgin sample from depth t , respectively, normalized to the yield for random incidence. $\chi(t)$ is related to the number of displaced atoms $N_D(t)$ by⁷¹:

$$\chi(t) = (N_D(t)/N) + P(t) \quad 1 - (N_D(t)/N)$$

where N is the density of substrate atoms and $P(t)$ is the probability that a particle has been scattered through an angle larger than the critical angle ψ_c , after penetration over a path length t . $P(t)$ can be calculated by using single, plural, or multiple scattering theory. Hart⁷² has shown that the single scattering theory of dechanneling gives a good description of the dechanneling of low-energy H^+ and He^+ in heavily damaged Si lattice.

Assuming that the same theory applies to heavily damaged GaAs also, we can write

$$P(t) = 1 - \exp(-\sigma_D \int_0^t N_D(t^1) dt^1)$$

where σ_D is given by

$$\sigma_D = \pi \frac{z_1 z_2 e^2}{E_1} \frac{1}{\psi_c^2}$$

which can be taken independent of t for $S_c \ll E_1$, where S_c is the stopping power and E_1 is the incident energy.⁷³ For 330 keV H^+ incident along $\langle 110 \rangle$ direction of GaAs, we determine $\psi_c = 0.84^\circ$ and $\sigma_D = 2.84 \times 10^{-18} \text{ cm}^{-2}$.

Finally, using the iteration procedure of Feldman and Rodgers,⁷¹ a disorder distribution can be evaluated from Figure 95. Figure 97 shows the disorder distribution for two doses, one for $1 \times 10^{14} \text{ cm}^{-2}$, where the layer became amorphous, and another for $3 \times 10^{13} \text{ cm}^{-2}$, which is below amorphous level. We compared our experimental results with computer simulations using the Monte Carlo program TRIM.⁷⁴ There is no provision of considering a compound target, we have used the atomic number and mass of Ge with the density of GaAs for the calculation. Lindhard's electronic stopping cross section is adjusted by a factor $C_k = 1.59$. Figure 97 contains the disorder distribution obtained by following 2,000 particles, which agrees very well with the experimental curve for doses below the amorphous level. The distributions here are normalized to the maximum. The nonzero damage at large depth in the experimental damage distributions is an artifact of using Single Scattering Theory, as discussed by Feldman and Rodgers.⁷¹

An example of a channeling spectrum after annealing of the implanted samples at 900°C for 15 min, is shown in Figure 98. In order to avoid overlapping, only one spectrum (that for highest dose of implantation

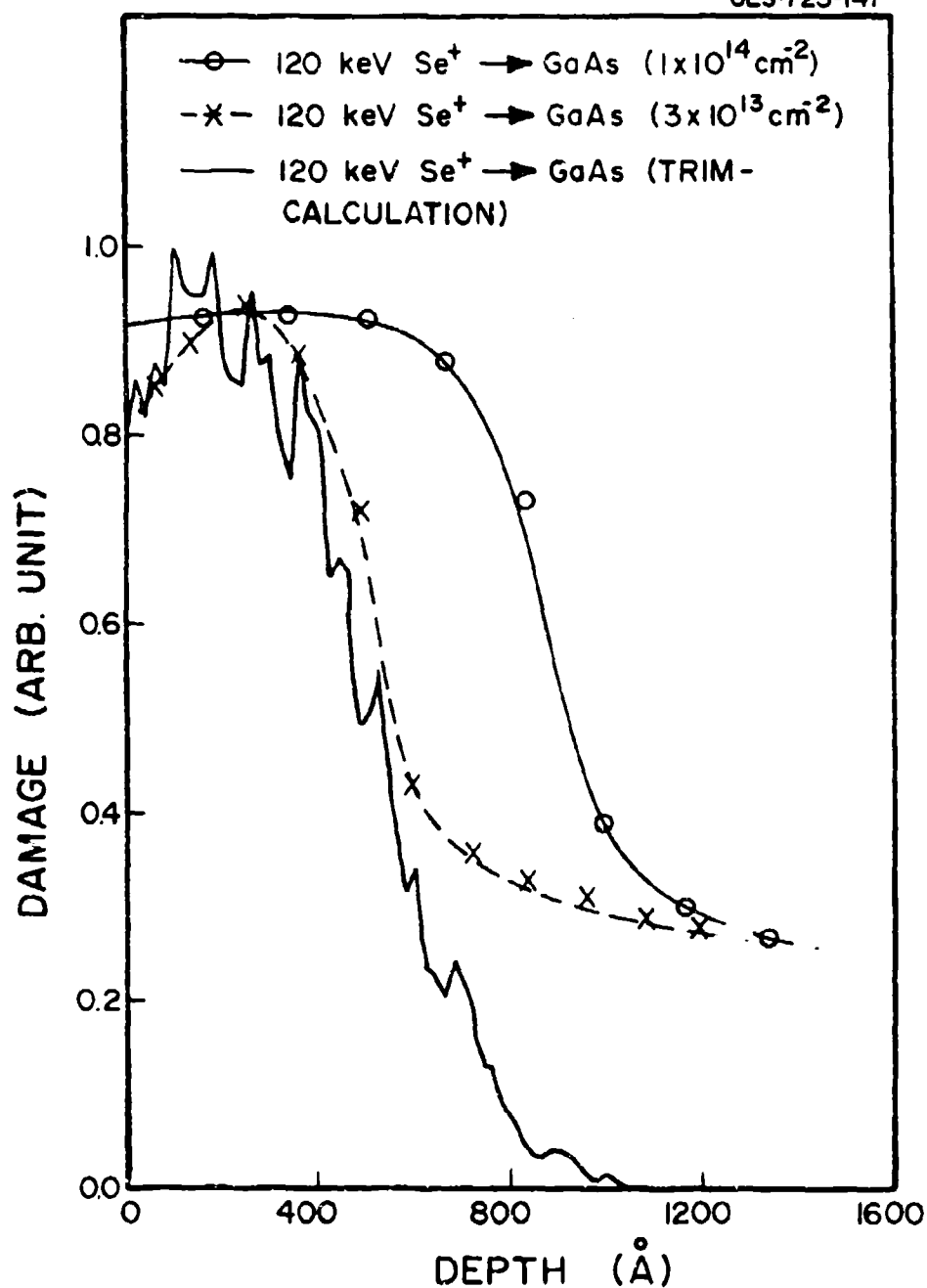


Figure 97 Comparison of Experimental and Calculated Damage Profile for GaAs:Se⁺ (120 keV)

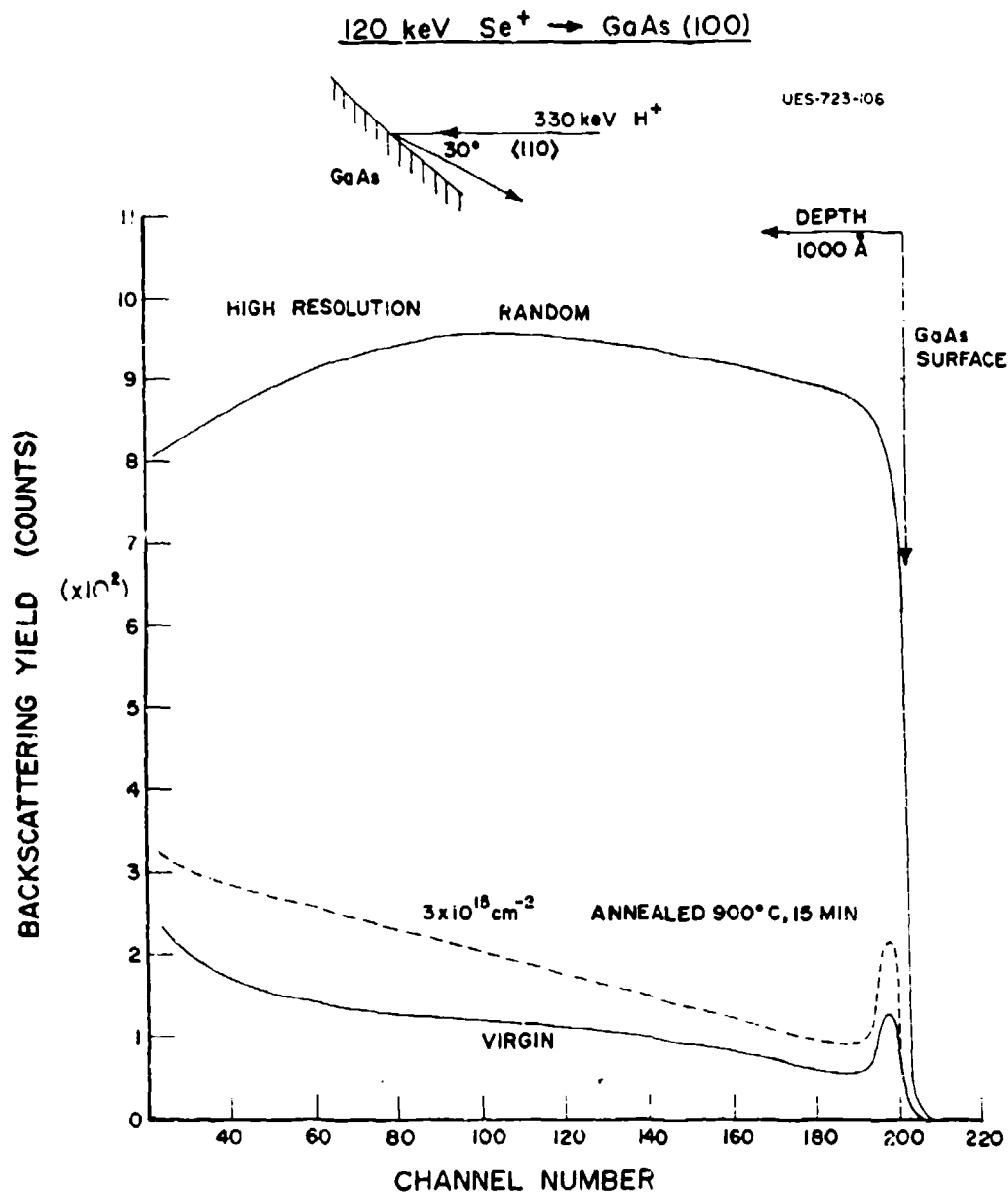


Figure 98 Backscattering Spectra from Aligned and Randomly Oriented Virgin and Annealed Samples

$3 \times 10^{15} \text{ cm}^{-2}$) is shown in comparison to that from a virgin sample. Spectra for all other doses lie between these two.

Figure 99 shows the minimum yield χ_{\min} compared to the virgin sample.

Transmission Electron Microscopy

TEM examination reveals that there are no observable defects in these samples implanted to doses of $5 \times 10^{12} \text{ cm}^{-2}$ and annealed at 900°C for 15 min. The damage was sparse in the sample implanted with $3 \times 10^{13} \text{ cm}^{-2}$ and consisted of small loops of sizes $< 50 \text{ \AA}$ in diameter [Figure 100(a)]. For samples implanted with $1 \times 10^{14} \text{ cm}^{-2}$ and $3 \times 10^{14} \text{ cm}^{-2}$, TEM micrographs show [Figure 100(a) and Figure 100(b)] coarser damage as compared to that in $3 \times 10^{13} \text{ cm}^{-2}$. In these specimens, we found black-white contrast under dynamical diffraction conditions. These contrast features are the characteristics of small dislocation loops, as well as of small precipitates. To distinguish between the two, we took two bright field pictures of the same area with different g vectors, as shown in Figure 101[(a) and (b)] for $3 \times 10^{14} \text{ cm}^{-2}$ implant. Analysis shows that some of the black-white contrast appears due to the presence of small precipitate of sizes $\sim 70 \text{ \AA}$. Most of the defects, however, are dislocation loops of various sizes. Some line dislocations were also found in this sample. Similar analysis for $1 \times 10^{14} \text{ cm}^{-2}$ and $1 \times 10^{15} \text{ cm}^{-2}$ implant reveals that the defects are similar in nature to that of $3 \times 10^{14} \text{ cm}^{-2}$ implant.

Electrical Measurements

Figure 102 shows surface carrier concentrations N_s and Hall mobilities μ_H plotted as a function of anneal temperature for three different doses. The electrical activation increases monotonically with

HIGH RESOLUTION $\langle 110 \rangle$ CHANNELING IN GaAs

120 keV $\text{Se}^+ \rightarrow \text{GaAs}$

UES-723-124

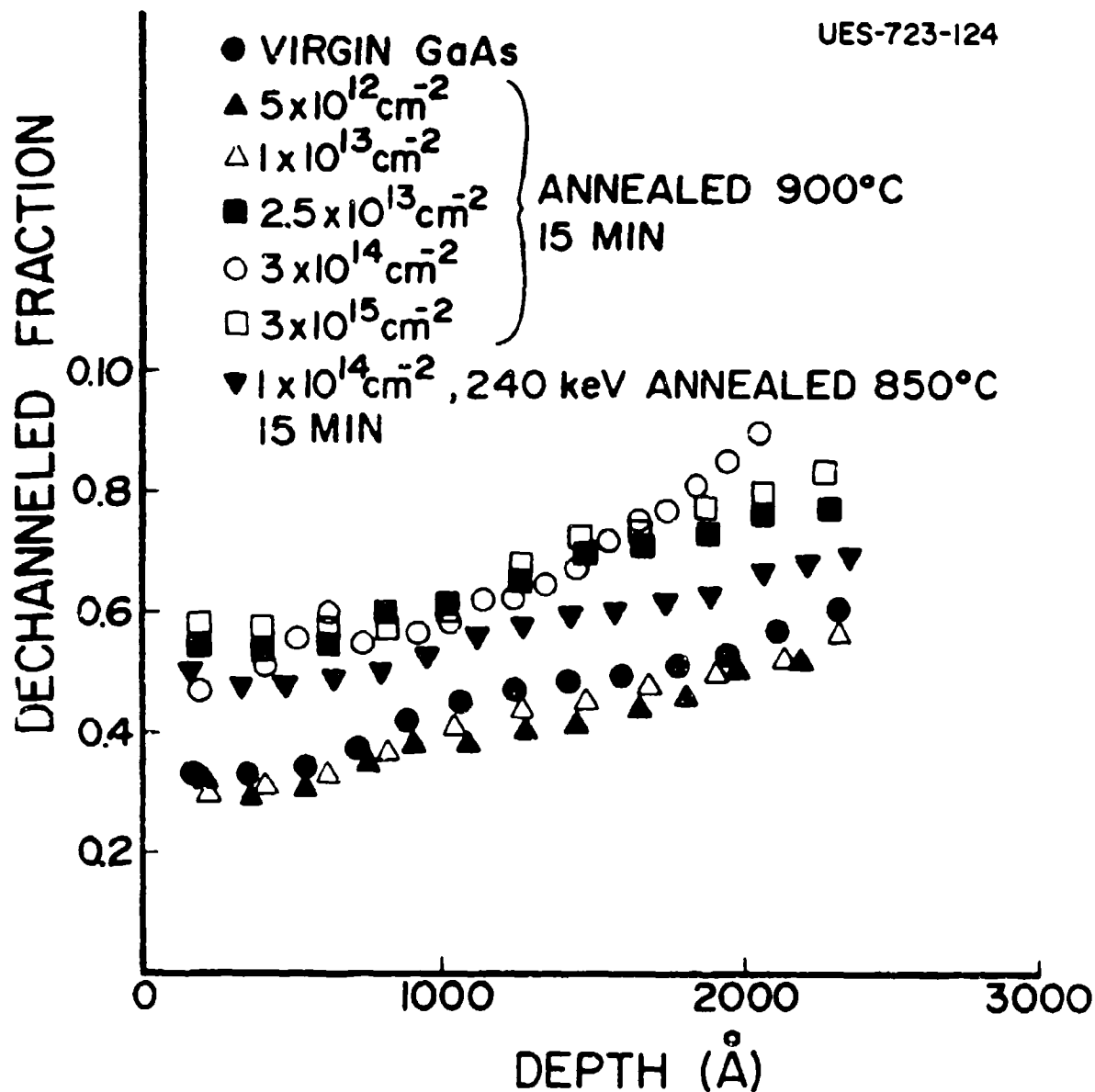


Figure 99 Dependence of Dechanneled Fraction on Depth for Annealed Samples Implanted with Various Doses of Se

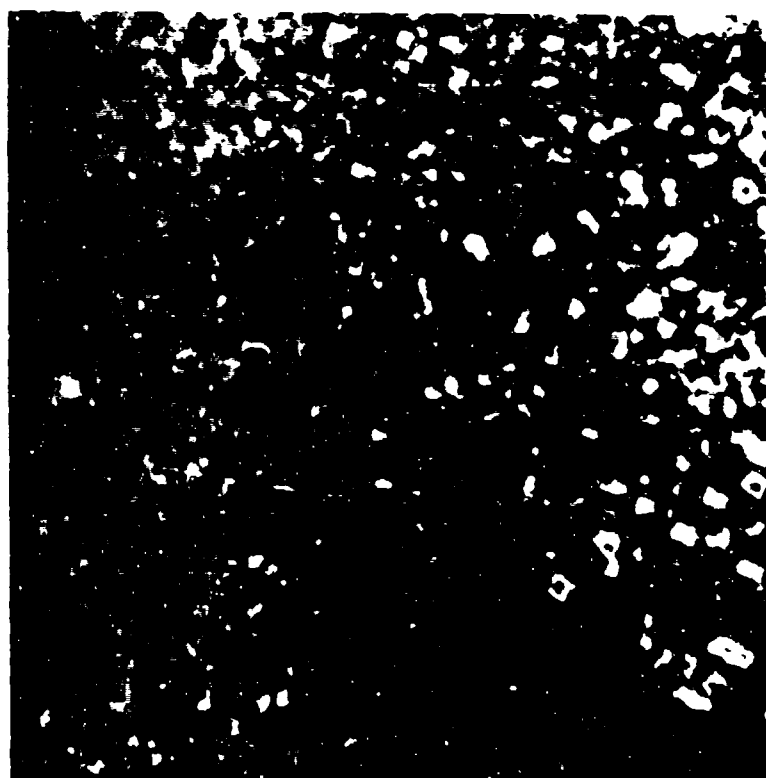
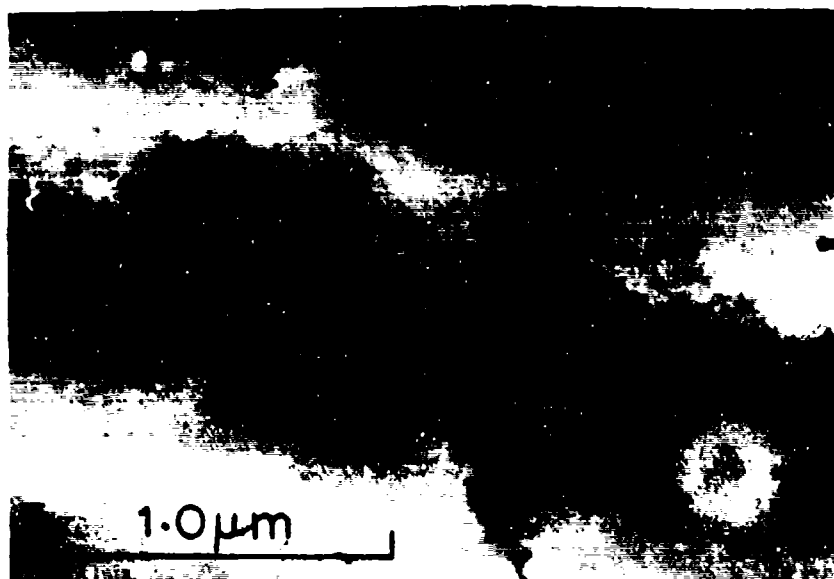


Figure 100 TEM Bright-Field Micrographs of Samples Implanted With 120 keV Se^+ Ions at RT to a Dose of (a) 10^{13}cm^{-2} , and (b) 10^{14}cm^{-2} , Annealed at 900°C for 15 Min

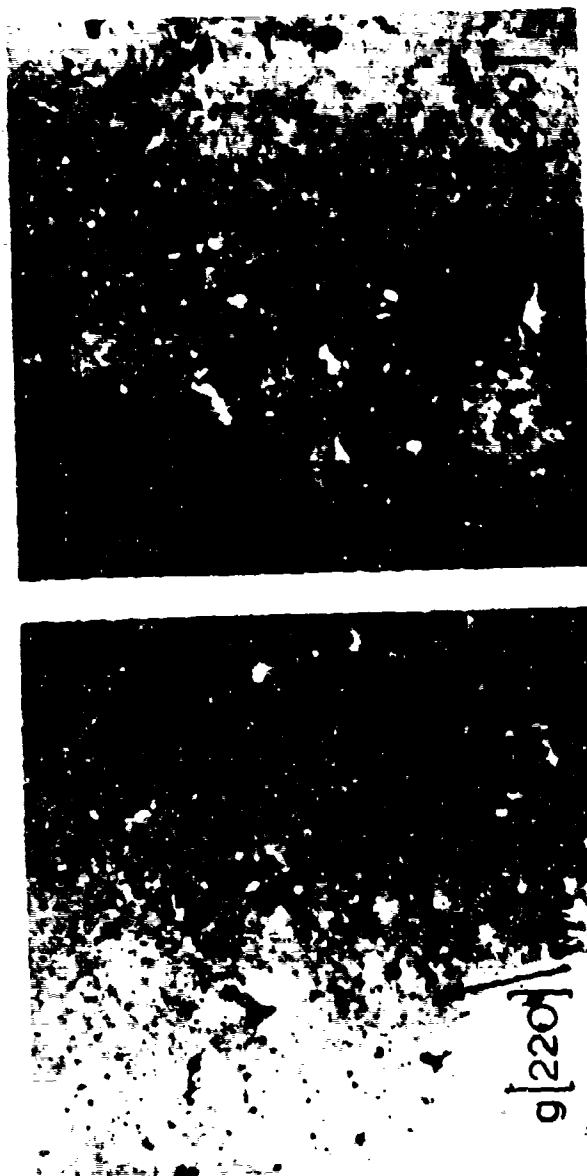


Figure 101 TEM Bright-Field Micrographs of Sample Implanted
With 120 keV Se^+ Ions at RI to a dose of $3 \times 10^{14} \text{cm}^{-2}$,
(a) $g=220$ and (b) $g=220$, 900°C , 15 Min

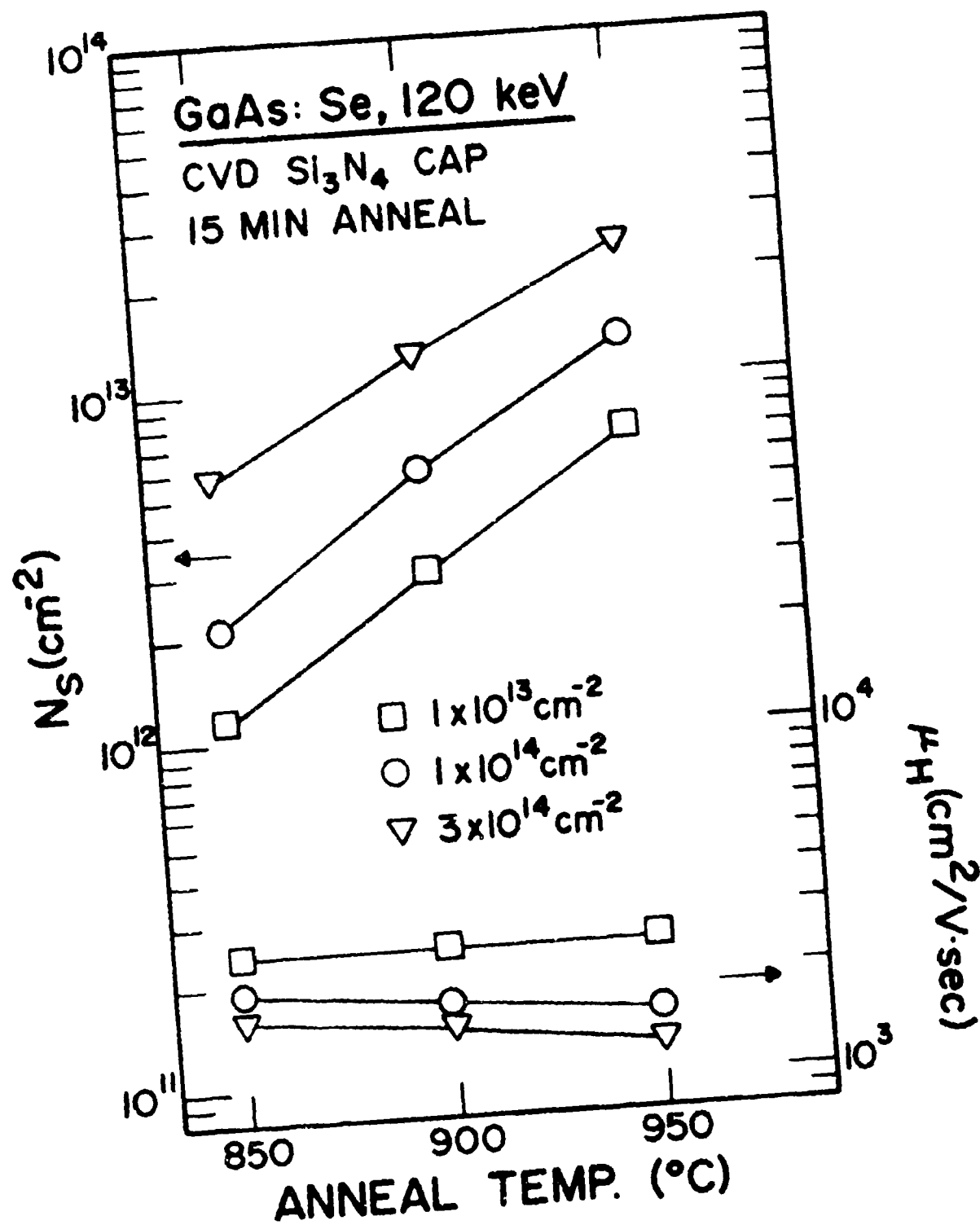


Figure 102 Surface Carrier Concentrations (N_s) and Mobility (μ_H) as a Function of Anneal Temperature for GaAs:Se

anneal temperature for all doses. The activation efficiency is highest for $1 \times 10^{13} \text{ cm}^{-2}$ at all temperatures, which decreases drastically at higher doses. For instance, at 900°C , the activation efficiency is 30% for $1 \times 10^{13} \text{ cm}^{-2}$, which goes down to 6% and 4% for $1 \times 10^{14} \text{ cm}^{-2}$ and $3 \times 10^{14} \text{ cm}^{-2}$, respectively. This reduction in activation efficiency correlates to the presence of residual damage as observed in channeling for the higher doses, which was later identified by TEM as dislocation loops and small precipitates. The mobility data indicate that implantation damage can be annealed reasonably well at around 850°C . Decreases in mobility with increasing anneal temperature for high doses may result from the increase in carrier concentrations.

Figure 103 shows the depth profiles of the carrier concentrations and Hall mobilities for samples implanted at 120 keV to a dose of $3 \times 10^{14} \text{ cm}^{-2}$, and annealed at 900°C or 950°C . Carrier concentrations are highest ($1 \times 10^{19} \text{ cm}^{-3}$) near the surface in both cases, gradually decrease with increasing depth up to about 500 Å and then become nearly flat until they finally fall off rapidly near the substrate. The carrier profile for the sample annealed at 950°C shows a significant effective indiffusion of Se. Similar indiffusion in the carrier concentration has been observed by Gamo et al.⁷⁵ for 400 keV Se implanted at 350°C , which was annealed at 900°C for 10 min. The mobilities are very low ($\sim 1,000 \text{ cm}^2/\text{V sec}$) near the surface, which increase with depth up to about $3,000 \text{ cm}^2/\text{V sec}$. The channeling spectra of the annealed samples (see Figure 98, 900°C for 15 min) showed higher surface peaks (also larger peak areas) as compared to that of virgin sample, indicating the presence of disorder in the surface region, which is probably the reason for lower mobility near the surface.

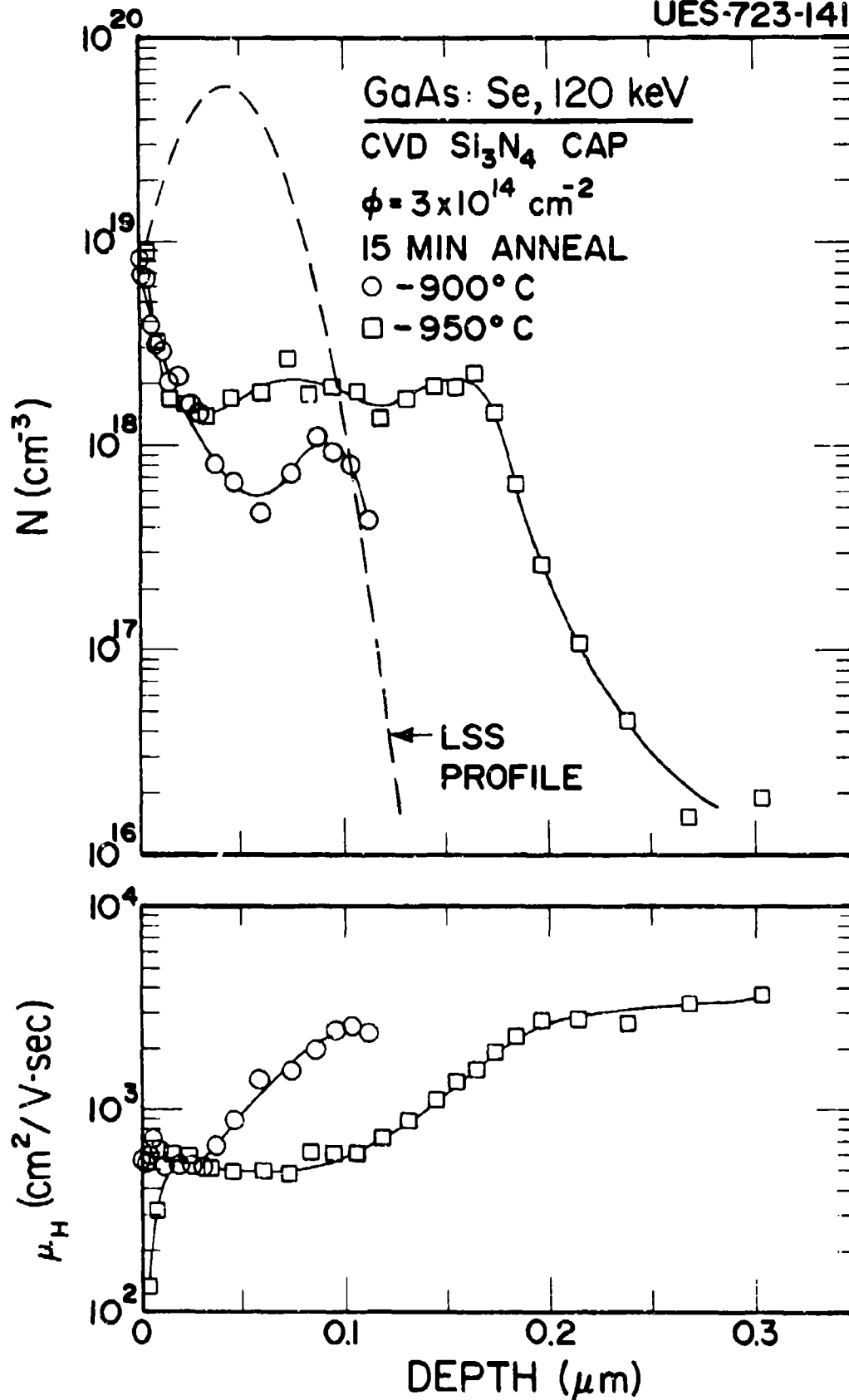


Figure 103 Carrier Concentration (N) and Mobility (μ_H) Profile as a Function of Anneal Temperature for GaAs:Se

4.4 Si IMPLANTED GaAs - DAMAGE AND LATTICE LOCATION

4.4.1 Low Temperature Annealing

Similar studies as in the case of Se implanted GaAs were conducted for samples implanted with Si. It is found, in general, a very similar annealing behavior as described earlier for Se implanted GaAs. Some results will be presented here of the residual damage and microstructure after annealing at low temperatures ($<700^{\circ}\text{C}$) and their dependence on original amorphous layer thickness keeping other parameters fixed. Cr loped semi-insulating GaAs wafers with (100) orientation were implanted with 50 keV and 120 keV Si^+ ions in a non-channeling direction at a dose of 1×10^{15} ions/ cm^2 . From here on we call the specimen implanted with 50 keV Si^+ ions as Sample 1 and the one implanted with 120 keV of Si^+ ions as Sample 2.

4.4.2 Results

The as implanted TEM specimens of Samples 1 and 2 have been examined in the electron microscope under the electron diffraction mode (TED). In both the samples, the layer has been found to be amorphous. RBS-channeling results of the as-implanted samples are shown in Figure 104. The backscattering yield from the damaged layer of the unannealed specimens in a channeling direction reached close to the random level thus supporting the TED observation of the creation of amorphous layer after implantation. The thickness of the amorphous layer can be determined from these spectra and found to be $\sim 350 \text{ \AA}$ and $\sim 1,350 \text{ \AA}$ for Samples 1 and 2, respectively. After annealing at 250°C for 15 minutes, the TED pattern of Sample 1 shows that the implanted layer has been recrystallized. Figure 105(a) shows the TED pattern of Sample 1 after annealing at 250°C for 15 minutes in $\langle 114 \rangle$ orientation. As can be seen, GaAs matrix spots are presented together with some extra spots.

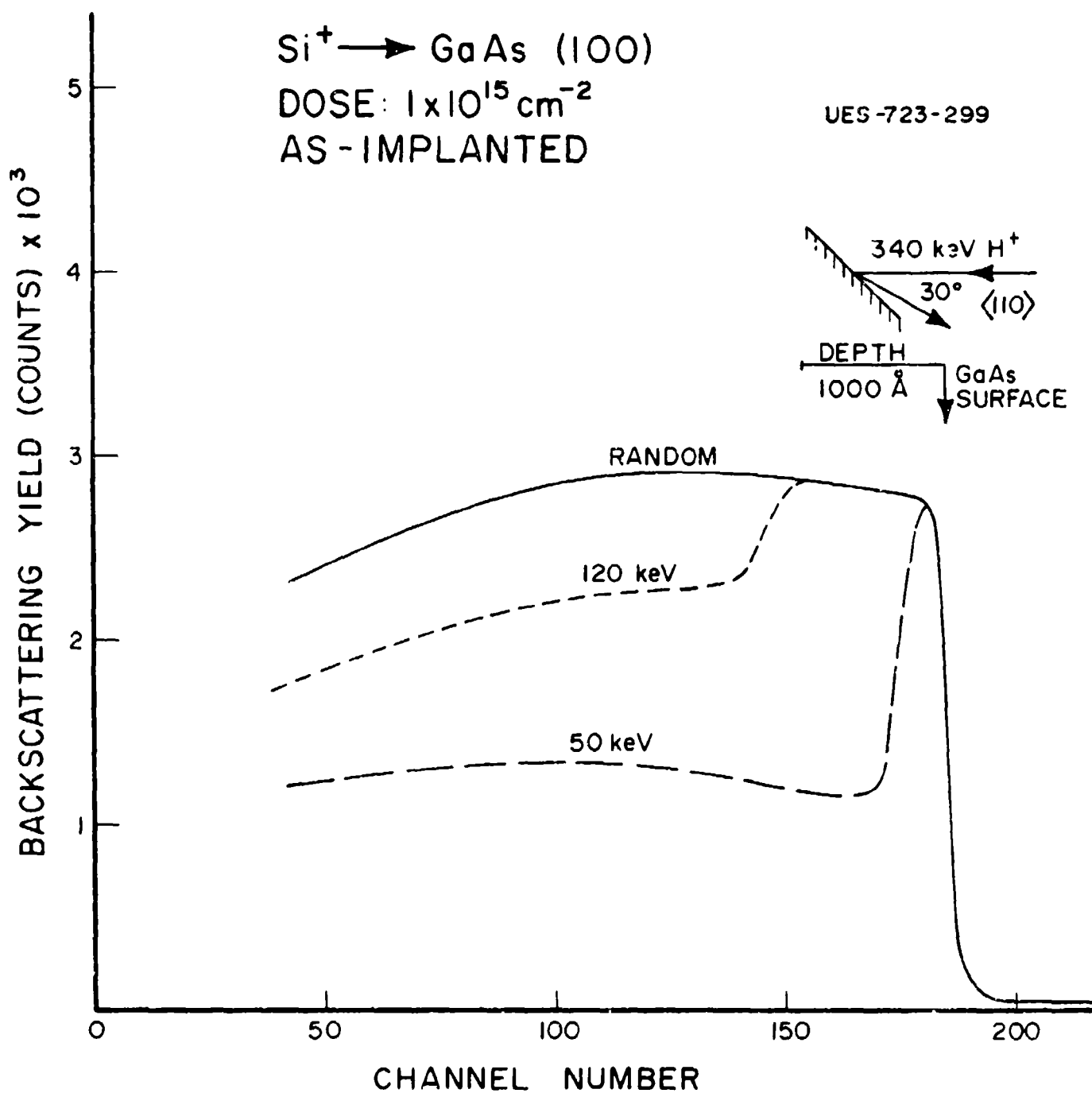
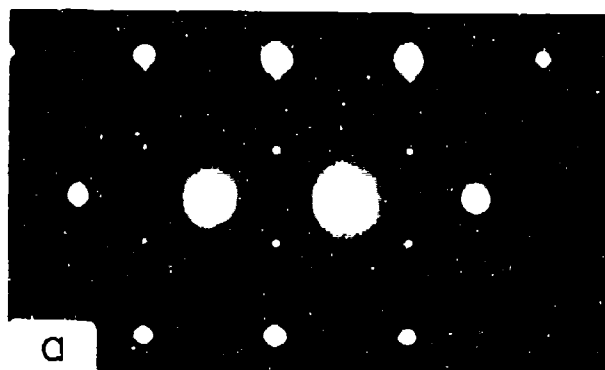


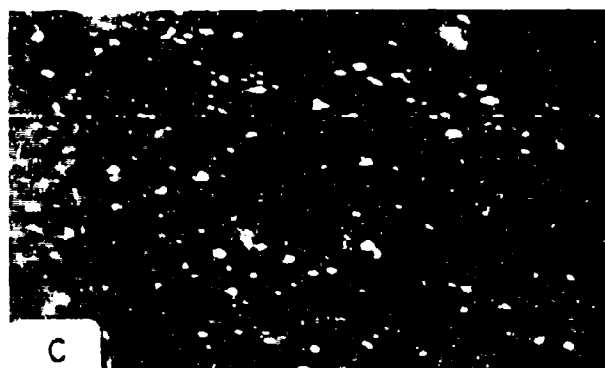
Figure 104 Backscattering Spectra of GaAs:Si
(50 and 120 keV, $1 \times 10^{15} \text{ cm}^{-2}$)
200



TED Pattern After Annealing at 250°C for 15 Minutes



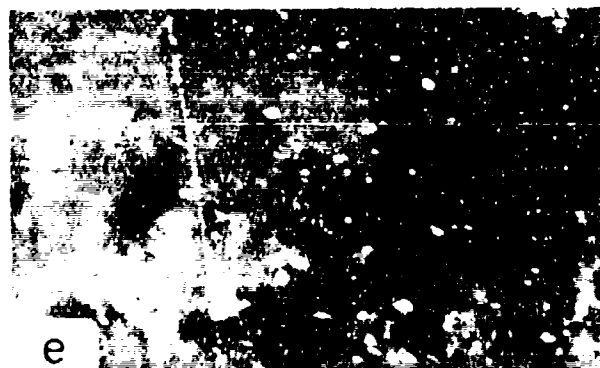
Dark Field Micrograph Imaged with Twin Spot After Annealing at 250°C for 15 Minutes



Dark Field Micrograph Imaged With Twin Spot After Annealing at 400°C for 15 Minutes



Strong Beam Bright Field Micrograph Imaged With Twin Spot After Annealing At 500°C for 15 Minutes

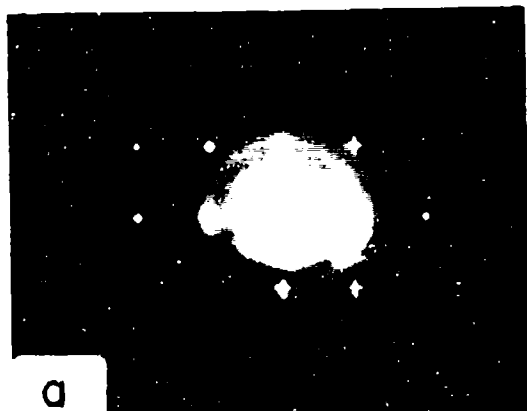


Dark Field Micrograph Imaged With Twin Spot After Annealing at 500°C for 15 Minutes

Figure 105 Transmission Electron Diffraction and Micrographs of Specimen #1

The extra spots are observed to be present at $1/3 \langle 511 \rangle$ and $2/3 \langle 511 \rangle$ positions. Following the analysis of Pashley and Stowell,⁷⁶ it was found that the extra spots are due to twins lying on $\langle 111 \rangle$ planes. Figure 105(b) represents the dark field micrograph of Sample 1 at 250°C for 15 minutes imaged with one of the twin spots. The twin sizes are found to vary from 50 Å to 450 Å. Figure 106(a) shows the TED pattern of Sample 2 annealed at 250°C for 15 minutes. The presence of amorphous ring together with the matrix and twin spots shows that only a part of the amorphous layer is recrystallized. The near surface region remained amorphous. The twins seemed to be lying at the interface of the amorphous layer and the crystalline substrate. Similar results have been found from the cross-sectional TEM studies in Se implanted GaAs by Bhattacharya et al,⁷⁷ RBS-C spectra (Figure 107) show that Sample 1 has become crystalline with high residual damage. However, an amorphous layer is still present in Sample 2, the thickness of which is smaller ($\sim 1,100$ Å) than the original thickness ($\sim 1,350$ Å). Thus, ~ 250 Å has grown epitaxially from the interface.

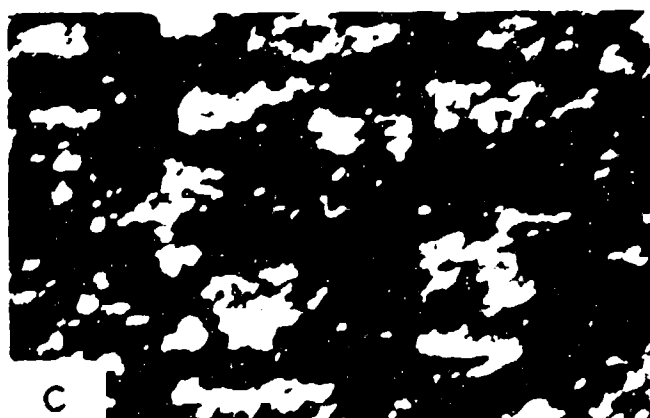
After annealing Sample 1 at 400°C for 15 minutes, twin spots are found to be present in the TED pattern. Figure 105(c) shows the dark field micrograph imaged with one of the twin spots. The twin sizes are found to be about the same as in the case of 250°C anneal. TED pattern of Sample 2 after 400°C anneal shows the presence of GaAs matrix spots and twin spots. No amorphous ring has been found to be present. Figure 106(b) shows the dark field micrograph imaged with one of the twin spots. The twin sizes (150-1,500 Å) were found to be bigger than that of Specimen 1. RBS-C spectra after 400°C annealing is shown in Figure 108. Sample 1 shows a good crystalline quality with dechanneling level still higher than that of virgin



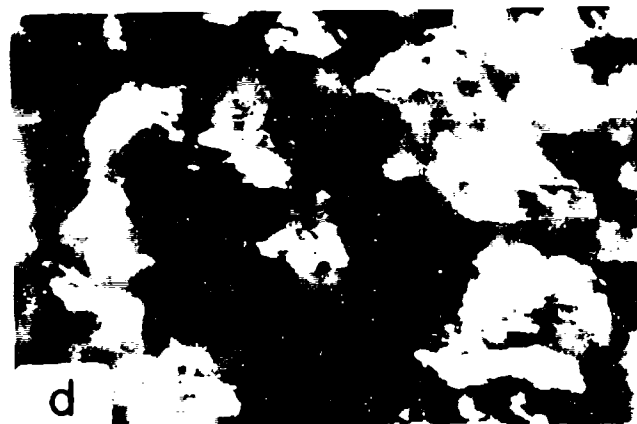
TED Pattern After Annealing at 250°C for 15 Minutes



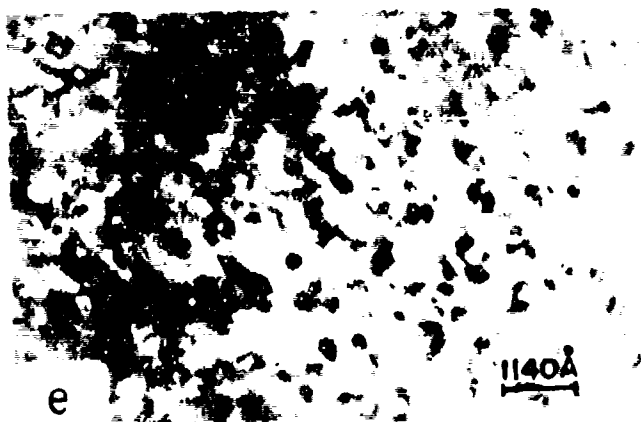
Dark Field Micrograph Imaged with Twin Spot After Annealing at 400°C for 15 Minutes



Dark Field Micrograph Imaged with Twin Spot After Annealing at 500°C for 15 Minutes



Dark Field Micrograph Imaged with Twin Spot After Annealing at 600°C for 90 Minutes



Strong Beam Bright Field Micrograph After Annealing at 700°C for 15 Minutes

Figure 106 Transmission Electron Diffraction and Micrographs of Specimen #2

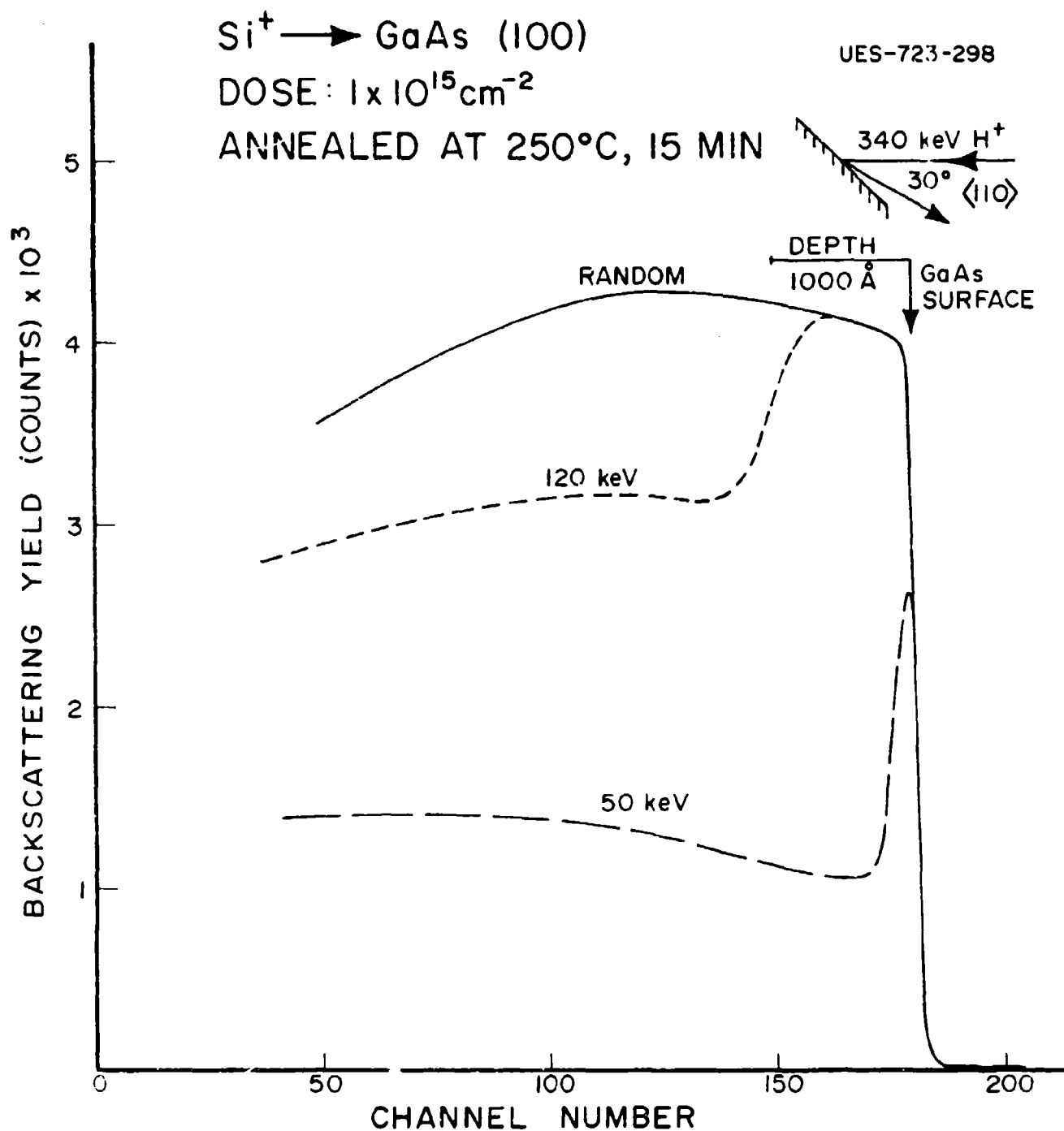


Figure 107 Backscattering Spectra of GaAs:Si ($1 \times 10^{15} \text{ cm}^{-2}$)
 After Annealing at 250°C for 15 min

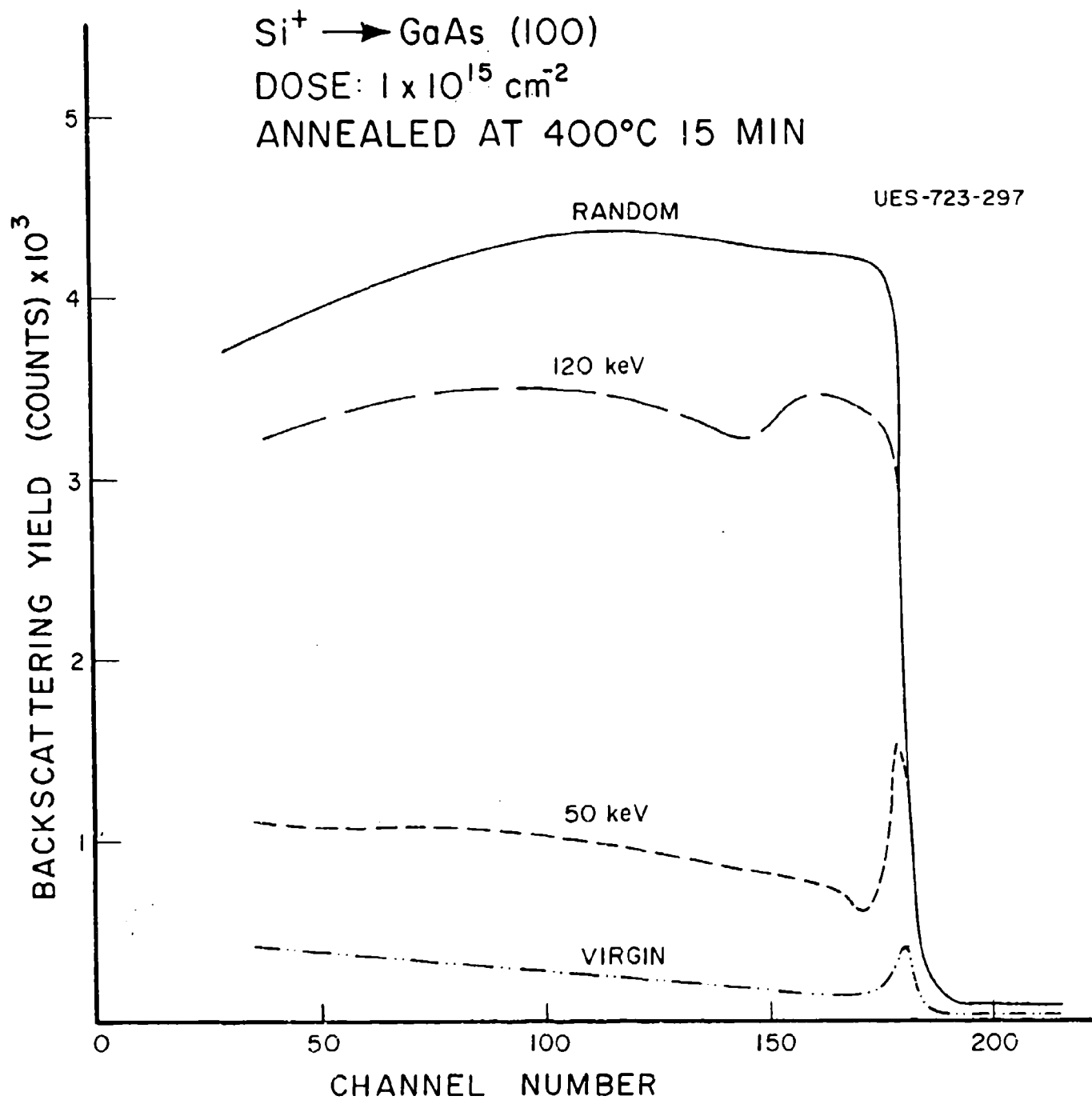


Figure 108 Backscattering Spectra of GaAs:Si ($1 \times 10^{15} \text{ cm}^{-2}$)
After Annealing at 400°C for 15 min

crystal due to the presence of some twins and dislocation loops as observed by TEM. Sample 2 shows very high dechanneling level, although the layer has become crystalline.

Further annealing of Sample 1 at 500°C for 15 minutes leads to the reduction of the number density of microtwins. This is shown in Figures 105(d) and 105(e) where a strong beam bright field and dark field micrographs imaged with one of the twin spots are presented. Dislocation loops are also found to be present. The presence of twins has also been Confirmed by the TED pattern.

Twin spots are found to be still present in the TED pattern after annealing Sample 2 at 500°C for 15 minutes. Figure 106(c) shows the dark field micrograph imaged with one of the twin spots after annealing at 500°C. Figure 106(d) shows the dark field micrograph of Sample 2 annealed at 600°C for 90 minutes imaged with one of the twin spots. It can be seen that the number density of twins has decreased considerably. Figure 106(e) is a bright field micrograph of Sample 2 annealed at 700°C for 15 min. showing the presence of dislocation loops but no twins.

It is clear from the annealing study of Specimen 1 that the amorphous layer has been fully recrystallized after annealing at 250°C. The recrystallized layer is found to contain microtwins. These microtwins lie on $\langle 111 \rangle$ planes of GaAs. Annealing at 400°C does not change the size and the number density of microtwins. After annealing at 500°C, the number density of twins has decreased considerably. Dislocation loops were also found to be present at 500°C. A temperature of about 550°C to 600°C is required for complete annealing of the microtwins. Grimaldi et al.⁵⁸ have suggested that at 400°C, a thin amorphous layer of GaAs can be grown without nucleation of

twins provided the initial amorphous layer is $\leq 400 \text{ \AA}$ or less. This is in contradiction to our observation for Si implanted GaAs. We needed a temperature of about 550°C to anneal microtwins in the case of 350 \AA thick layer and 700°C for a layer of $1,350 \text{ \AA}$. The above observation shows that for thin amorphous layer of GaAs (low energy implant), the microtwins can be annealed out at lower temperature than that for thicker amorphous layer (high energy implant). Thus, lower energy implantations or thinner initial amorphous layer may provide higher electrical activation efficiency in GaAs at lower anneal temperatures.

Most of the studies so far have been carried out with (100) crystals of GaAs. Very few reports are available in the literature on the orientation dependence of annealing behavior of GaAs. Gamo et al.⁵⁵ have studied the recrystallization behavior of (100), (110), and (111) GaAs using Rutherford backscattering (RBS) in combination with channeling techniques. No significant orientation dependence was observed. The residual damage in (111) GaAs was slightly higher as compared to that in (100) and (110) GaAs. In contrast, studies⁷⁸ on the annealing behavior in epitaxial regrowth of silicon showed that there is a large difference between the residual damage in (111) compared to (100) and (110) orientation. For example, the regrowth rate for (111) orientation was found to be about a factor of 20 slower compared to (100) orientation, and the microtwins were found to be present only in the (111) oriented Si except in special cases like inert gas ion implanted Si where microtwins are observed also in (100) crystals after annealing.⁷⁹

We have performed comparative studies on the low temperature annealing behavior of (100) and (211) GaAs. The results show that the recovery rate in (211) GaAs is much slower compared to that in (100) GaAs.

Undoped GaAs wafers with (100) and (211) orientations were implanted with 60 keV Si^+ ions in a nonchanneling direction at room temperature to a dose of $1 \times 10^{15} \text{ cm}^{-2}$. Figures 109(a) and 109(b) show the channeling spectra obtained from (100) and (211) samples implanted with 60 keV Si^+ to a dose of $1 \times 10^{15} \text{ cm}^{-2}$. The backscattered intensity from the damaged layer of the unannealed samples in a channeling direction reached close to the random level thus indicating a high level of damage near the surface. TEM examination revealed that the surface layers of both samples have transformed into the amorphous phase after implantation. The annealing has been carried out from 200°C up to 550°C, all for 30 min, with increments of 50°C. No change in the channeling spectra was noticed for both samples, after annealing at 200°C for 30 min. This is a contrast to our earlier findings⁷⁷ with Se implanted GaAs where we found that the annealing starts at 200°C. In the present case, the annealing starts at 250°C for both (100) and (211) samples. The damage recovery, however, is much better for (100) compared to (211). This trend is reflected also during further annealing at higher temperatures. These results are combined in Figure 110 where we plotted the minimum yield (χ_{min}), determined by dividing the channeled yield just behind the damage peak by the random yield in the same region, versus the anneal temperature. Channeling experiments were also carried out along $\langle 110 \rangle$ direction of the same (100) specimen.

Two clear annealing stages were found for (100); one at 250°C, and the other at 450°C. For (211), the annealing seems to be very slow. After annealing at 550°C, very little damage is observed in (100) samples, whereas in the (211) sample, a substantial amount of damage still remained. The samples were annealed again at 900°C after capping with plasma deposited

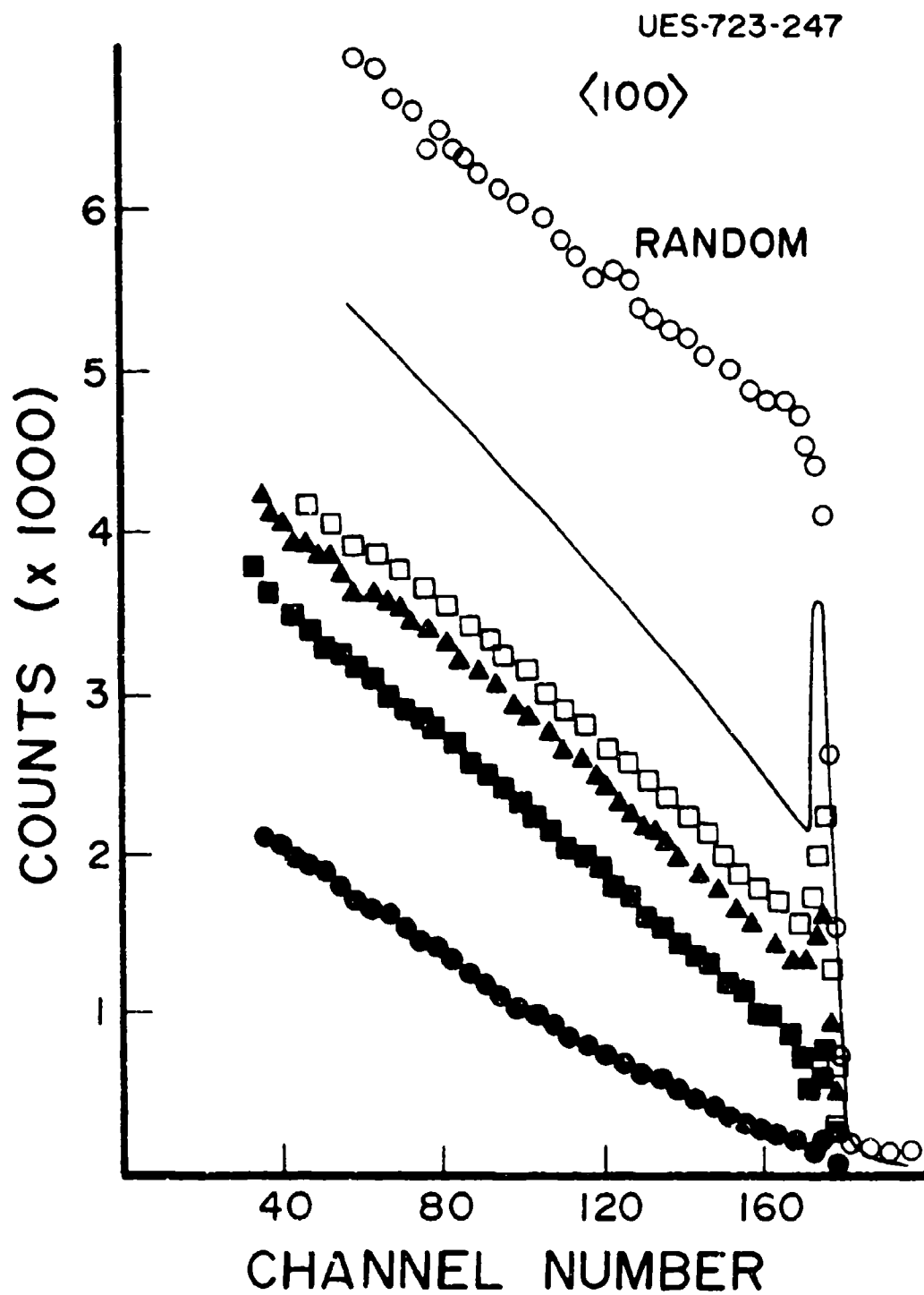


Figure 109 (a) 60-keV Si⁺, $1 \times 10^{15} \text{cm}^{-2}$; _____ as implanted; \square 200+250; \blacktriangle 200+250+300; \blacksquare 350+400+450+500; \bullet 350+... +550+900°C, this is same as virgin (100) GaAs.

UES-723-246

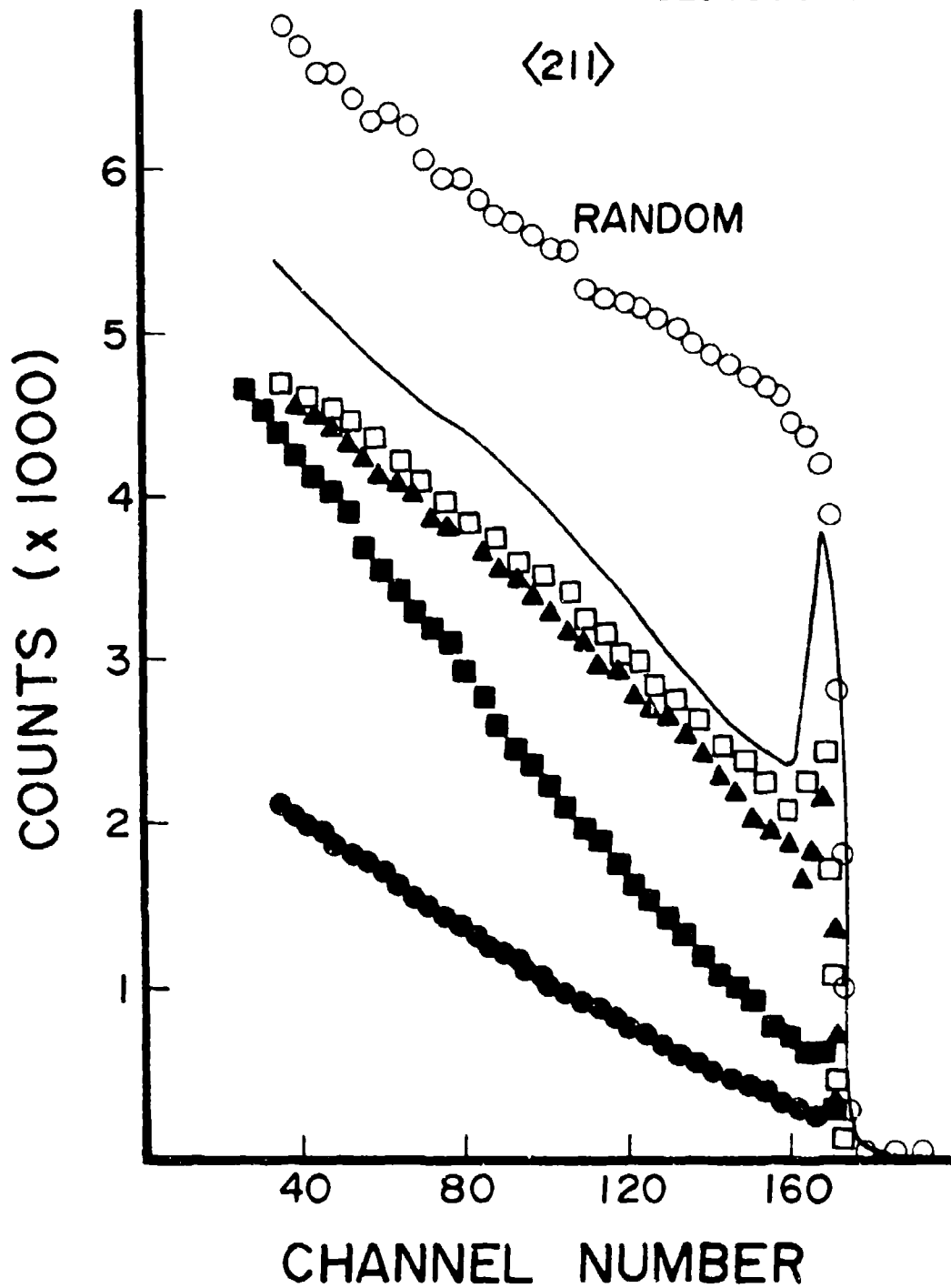


Figure 109 (b) RSB Spectra of (211) GaAs; 60-keV Si⁺,
 $1 \times 10^{15} \text{ cm}^{-2}$; _____ as implanted;
 □ 200+250+300; ▲ 350+400+450+550;
 ■ 350+... +550+900°C, ● virgin (211) GaAs
 210

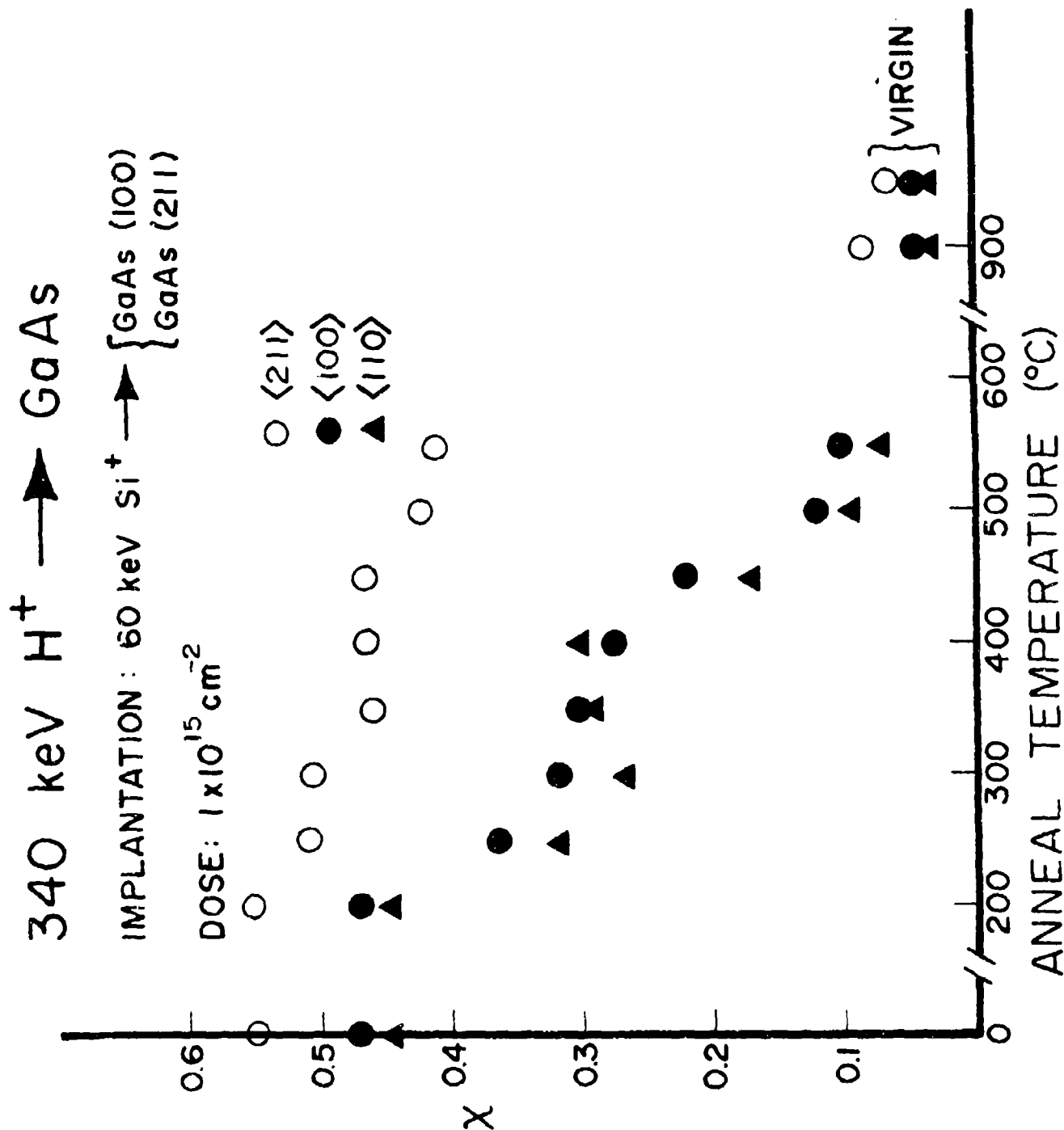
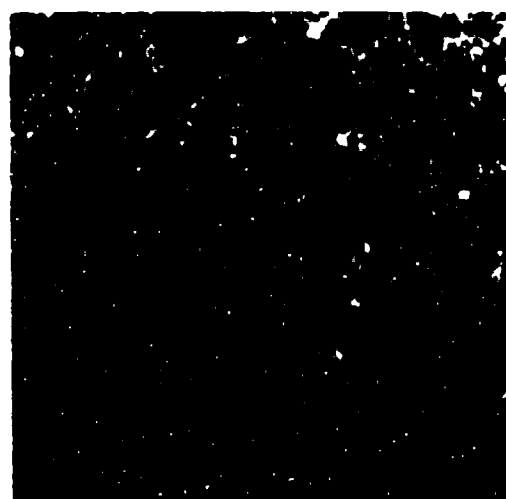


Figure 110 Minimum Yield (X_{min}) Versus the Anneal Temperatures for GaAs: Si^+

Si_3N_4 . The (100) sample showed channeling quality as good as a virgin crystal, although (211) had some damage left (see Figure 110).

Figure 111a, and b are the strong beam bright field micrographs of the surface layers of the (100) and (211) specimens annealed at 350°C for 30 min, respectively. Twins are found to be present, as has been confirmed by Transmission Electron Diffraction (TED) patterns, in both the specimens. Also dislocation loops of $\approx 100 \text{ \AA}$ diameter are found to be present in both samples. The total damage density is clearly higher in (211) as compared to that in (100). Figure 112a shows the (TED) pattern of the (211) sample in $\langle 114 \rangle$ orientation. Extra diffraction spots are found to be present together with the basic GaAs spots. These extra spots are found to lie at $(1/3) \langle 511 \rangle$ positions. Following the analysis of Pashley and Stowell,⁷⁶ it has been determined that these extra spots are twin spots from twins on $\langle 111 \rangle$ planes. Similar diffraction analysis on (100) specimens reveal that the twins here also lie on $\langle 111 \rangle$ planes. Figure 112b, and c are the dark field micrographs imaged with the twin spot for (100) and (211) samples respectively. The twin sizes in the (100) specimen were found to vary from 50 \AA to 400 \AA whereas in (211) some larger twins (50 \AA to 750 \AA) were also found to be present in addition to the smaller ones. However, the volume occupied by the twins seems to be nearly the same in both the specimens. This implies that the denser damage network in (211) as seen in Figure 111b as compared to that in (100) (Figure 47a) is due to dislocations.

Figure 113a, and b are the strong beam bright field micrographs of the same (100) and (211) specimens respectively, annealed at 500°C for 30 min. Most of the damage has annealed out in the (100) specimen, leaving behind some dislocation loops of sizes varying from 80 \AA to 200 \AA . Some microtwins of sizes between (100 \AA to 600 \AA) as observed in the dark field



UES-723-243

Figure 111 Bright-Field Micrographs with $g=220$ After Annealing at 350°C for 30 Min (a) (100); (b) (211)

UES-723-242

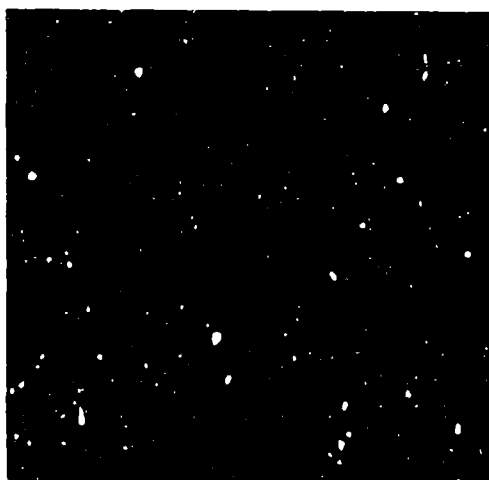
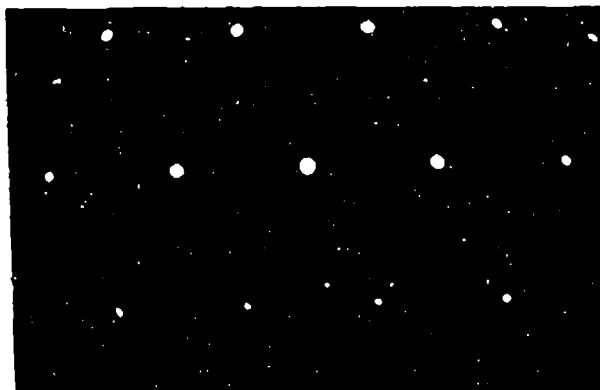


Figure 112 TED Patterson of (211) Specimen After Annealing at 350°C for 30 Min in $\langle 114 \rangle$ Orientation. Dark-Field Micrographs Imaged With Twin Spots (b) (100); (c) (211)

UES-723-244

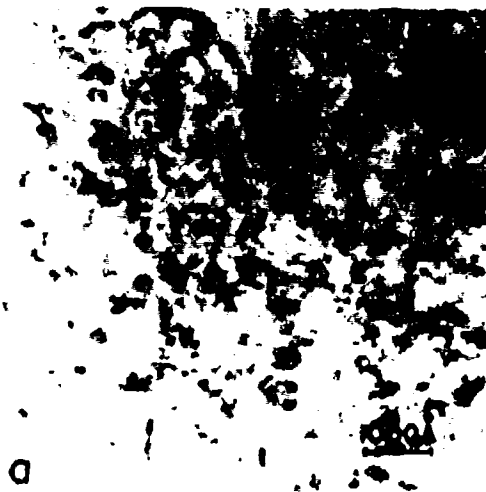


Figure 113 Bright-Field Micrographs With $g=220$ After Further Annealing at 500°C for 30 Min (a) 100; (b) (211)

UES-723-245

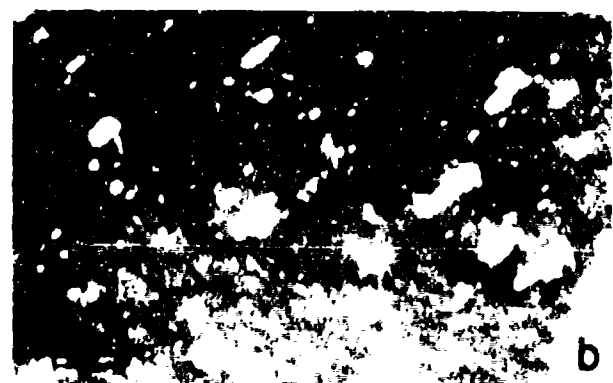
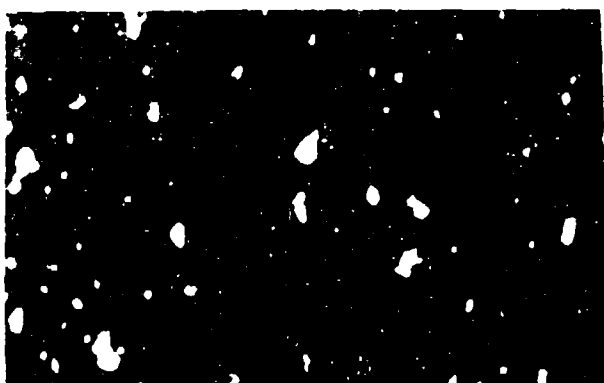


Figure 114 Dark-Field Micrographs After Annealing at 500°C for 30 Min, Imaged With the Twin Spots (a) (100); (b) (211)

micrographs (Figure 114) imaged with the twin spots. However, more damage remained in (211) as compared to that in (100). A high density of dislocation loops and tangles in addition to microtwins are found to be present in (211). The sizes of some of the microtwins are larger in (211) as compared to that in (100) as can be seen in the dark field micrograph (Figure 114). Here again the volume occupied by the microtwins appears to be approximately equal in both the specimens. The high dechanneling, as observed in (211) after annealing at 500°C as compared to that in (100) is caused by a higher density of dislocation networks in (211). Thus, the higher resistance in the annealing of damage in (211) as compared to (100) is due to the higher rate of development of the dislocation tangles and loops in (211). The formation and annealing rate of twins are approximately the same in both specimens.

The present experiments show that there is appreciable difference between the damage recovery rate for (100) and (211) oriented GaAs. At 550°C, the difference in the residual damage is about a factor of four. In the case of Si,³⁰ a difference of a factor of five has been reported for the regrowth rate in (100) and (211) at 550°C. This similarity may apparently indicate a similar epitaxial regrowth process for both Si and GaAs. However, the previous experiments on the orientation dependence of the damage recovery behavior for GaAs showed no significant difference between (100), (110), and (111) orientations. This is in contradiction to the damage recovery behavior in Si in which case the recovery rate for (111) was found to be about 20 times slower than the (100). Also, the twinning was only observed in the case of (111) orientation in Si. This difference in Si was explained later by Drosd and Washburn⁶⁸ using an atomistic model where it was considered that for

transformation from the amorphous phase to the crystalline phase, an atom must make two undistorted bonds with the crystal. From this viewpoint, it was shown that in a diamond cubic crystal, the (100) interface can move easily by satisfying the above mentioned requirements with the migration of a single atom from the amorphous phase to the crystalline phase whereas for the (110) and (111) interface to move epitaxially, incorporation of two and three atoms units, respectively, are required. In the (111) case, the three atom unit can become a part of the crystal in two different orientations; one among them will make distorted bonds, thus leading to the twin formation. This also explains why the regrowth rate in (111) Si is slower than (100). One would expect this model to explain the annealing behavior in GaAs also, because of the similarity in structure. However, the complex annealing behavior of GaAs as compared to that of Si as discussed earlier clearly indicates that additional requirements must be satisfied to explain the observations in GaAs. Part of these requirements will undoubtedly involve the continued integrity of the GaAs binary molecular association during the epitaxial process.

4.4.3 High Temperature Annealing of Si Implanted GaAs

Cr-doped semi-insulating GaAs(100) wafers were implanted with Si^+ ions at an angle about 8° off the $\langle 100 \rangle$ axis to avoid channeling. These wafers were obtained from Crystal Specialties, Inc., and were grown by Czochralski method. Cr concentration in these wafers were measured by secondary ion mass spectroscopy and were found to be of $\sim 6.5 \times 10^{15} \text{ cm}^{-3}$. Three samples were prepared; Sample 1 by implanting 120 keV Si with a dose of $3 \times 10^{15} \text{ cm}^{-2}$, Sample 2 by implanting 120 keV Si with a dose of $5 \times 10^{15} \text{ cm}^{-2}$, and Sample 3 by implanting multiple energies (50-400) keV and

doses totaling $5 \times 10^{15} \text{ cm}^{-2}$. The multiple energies and doses were chosen in such a way as to produce a flat concentration profile. Table 5 shows the sequence of implantation parameters used to prepare the Samples that were studied.

TABLE 5 IMPLANTATION PARAMETERS USED TO PREPARE THE SAMPLES FOR HIGH TEMPERATURE ANNEALING OF Si

Sample Number	Energy (keV)	Current density ($\mu\text{A cm}^{-2}$)	Dose (cm^{-2})
1	120	0.11	3×10^{15}
2	120	0.11	5×10^{15}
3	50	0.36	3.95×10^{14}
	100	0.44	6.6×10^{14}
	200	0.44	1.05×10^{15}
	300	0.44	1.32×10^{15}
	400	0.44	1.58×10^{15}

For the multiple energy implant and calculated depth distribution shows a nearly flat top extending to a depth of 4,000 Å at a concentration level $1 \times 10^{20} \text{ cm}^{-2}$. The temperature of the target during implantation could not be measured. However, the temperature of the block on which the samples were mounted had been found to increase to 200°C-220°C for a power density of 0.7 W cm^{-2} . At the maximum implantation energy used in the present experiments, a power density of 0.18 W cm^{-2} had been deposited which would correspond to a temperature $\sim 60^\circ\text{C}$ if a good thermal contact is assumed. This was not the case for Sample 3, as will be discussed later.

4.4.4 Results

Sample 1

RBS-C analyses of this sample showed that the layer had become amorphous up to a depth of $\sim 1,350 \text{ \AA}$. After annealing at 850°C for 15 min, the layer becomes crystalline as shown in Figure 115. The minimum yield (χ_{\min}) as measured behind the surface peak is 0.11, which is higher than the χ_{\min} of the virgin crystal (~ 0.037) thus indicating the presence of residual damage. Figures 116(a) and 116(b) are the bright field (BF) transmission electron micrographs of this sample. These micrographs are of the same area taken with two different g vectors under dynamical diffraction conditions ($s \neq 0$). The different types of defects are delineated on the micrograph (Figure 116). Besides dislocation loops and line dislocations, defects showing black-white contrast are also present. The black-white directions are parallel to the g vectors in both the micrographs, confirming that the defects giving rise to this type of contrast are precipitates.⁸¹ the average diameter of these precipitates was found to be about 60 \AA . Figure 117 is the high resolution weak beam images of the same area. A quantitative evaluation of the percentage of dopant precipitation has been done by assuming a spherical nature of the precipitates and by measuring the average diameter of the particles in terms of the width of the region separating the black-white lobes. Using this diameter, we calculated the total number of implanted atoms associated with the particles in a given area. This number divided by the area will give the areal density which can then be directly compared with the dose of the implanted ions to get the percentage of dopant precipitation. In this specimen, the dopant precipitation was found to be about 4%. It should be mentioned here that the TEM examinations of a virgin crystal before and

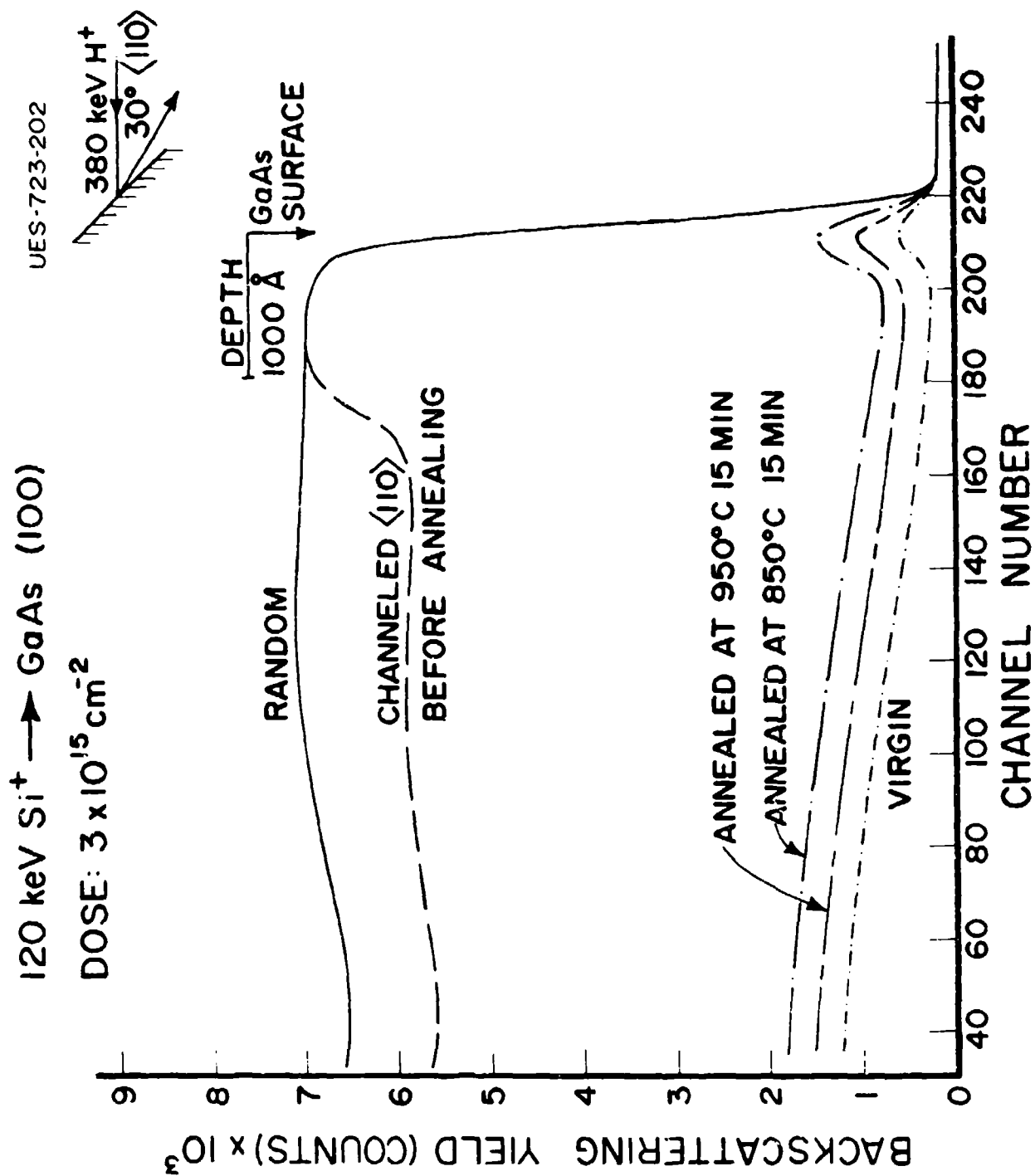


Figure 115 Backscattering Spectra for GaAs:Si⁺

UES-723-217

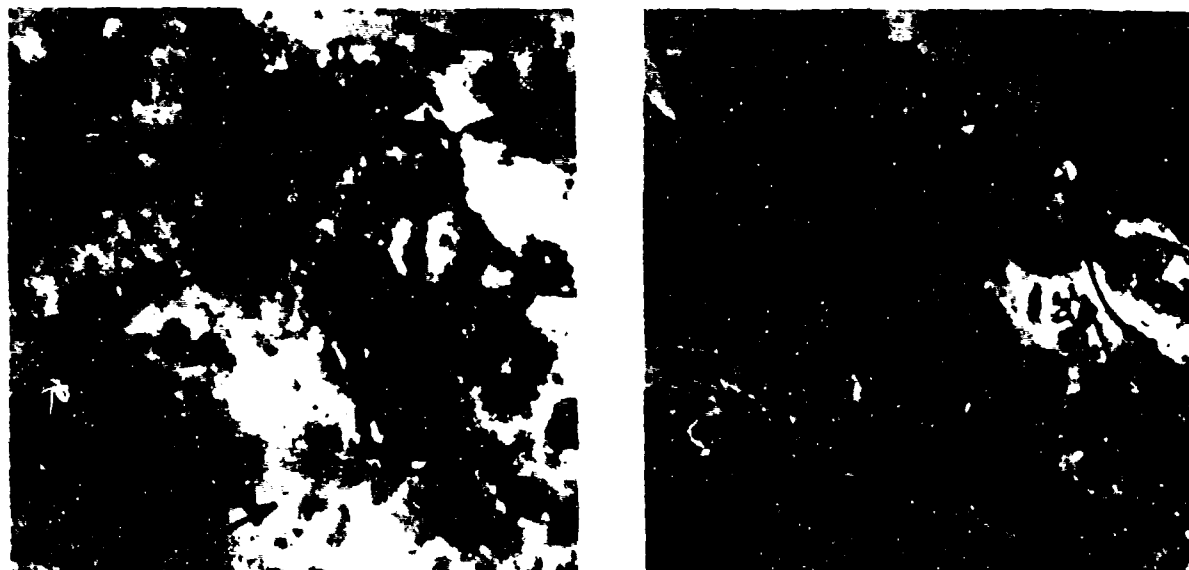


Figure 116 Bright-Field Transmission Electron Micrographs of 120 keV Si^+ , $3 \times 10^{15} \text{ cm}^{-2}$, Annealed at 850°C for 15 Min; (a) $g=(220)$; (b) $g=(220)$. P-Precipitate, LD-Loose Dislocation, DL-Dislocation Loop

UES-723-218



Figure 117 High Resolution Weak Beam Image of GaAs:Si (120 keV, $3 \times 10^{15} \text{ cm}^{-2}$) Annealed at 850°C , 15 Min

after annealing under similar conditions do not reveal any of the defects described above.

The location of the implanted Si atoms were determined from channeling experiments. PIXE spectra were collected as a function of tilt angle across $\langle 100 \rangle$ and $\langle 110 \rangle$ directions. Examples of X-ray emission spectra collected for random and channeling directions are shown in Figure 118. The area under the peaks of the Si and Ga K X-ray can be obtained from these spectra. These yield values are plotted as a function of tilt angle [Figures 119(a) and 119(b)] for the X-ray along with the simultaneous RBS yield for the matrix originating from a depth similar to the range ($\sim 2,000 \text{ \AA}$) of the implanted Si ions. About 60% attenuation of Si signal along both $\langle 100 \rangle$ and $\langle 110 \rangle$ directions was observed after annealing at 850°C for 15 min. Angular scans after 950°C anneal, however, shows [Figures 120(a) and 120(b)] somewhat lower attenuation ($\sim 50\%$), indicating that the annealing at 950°C causes some Si atoms to move out of substitutional sites.

Although RBS-C shows (Figure 115) a smaller reduction to dechanneling ($\mu_{\text{min}} = 0.08$) after 950°C indicating further recovery of damage, TEM examinations shows similar kinds of defects as observed after 850°C anneal. However, the amount of precipitation was found to be lower ($\sim 2\%$) after 950°C anneal. Thus the increased channeling yield for Si atoms after 950°C anneal indicates a larger nonsubstitutional fraction for Si but with these atoms remaining randomly distributed in solution.

Sample 2

RBS-C measurements after implantation show that the layer is amorphous up to a depth of $\sim 1,400 \text{ \AA}$ (Figure 121). After annealing at 850°C for 15 min, the layer has become crystalline. However, comparison of the

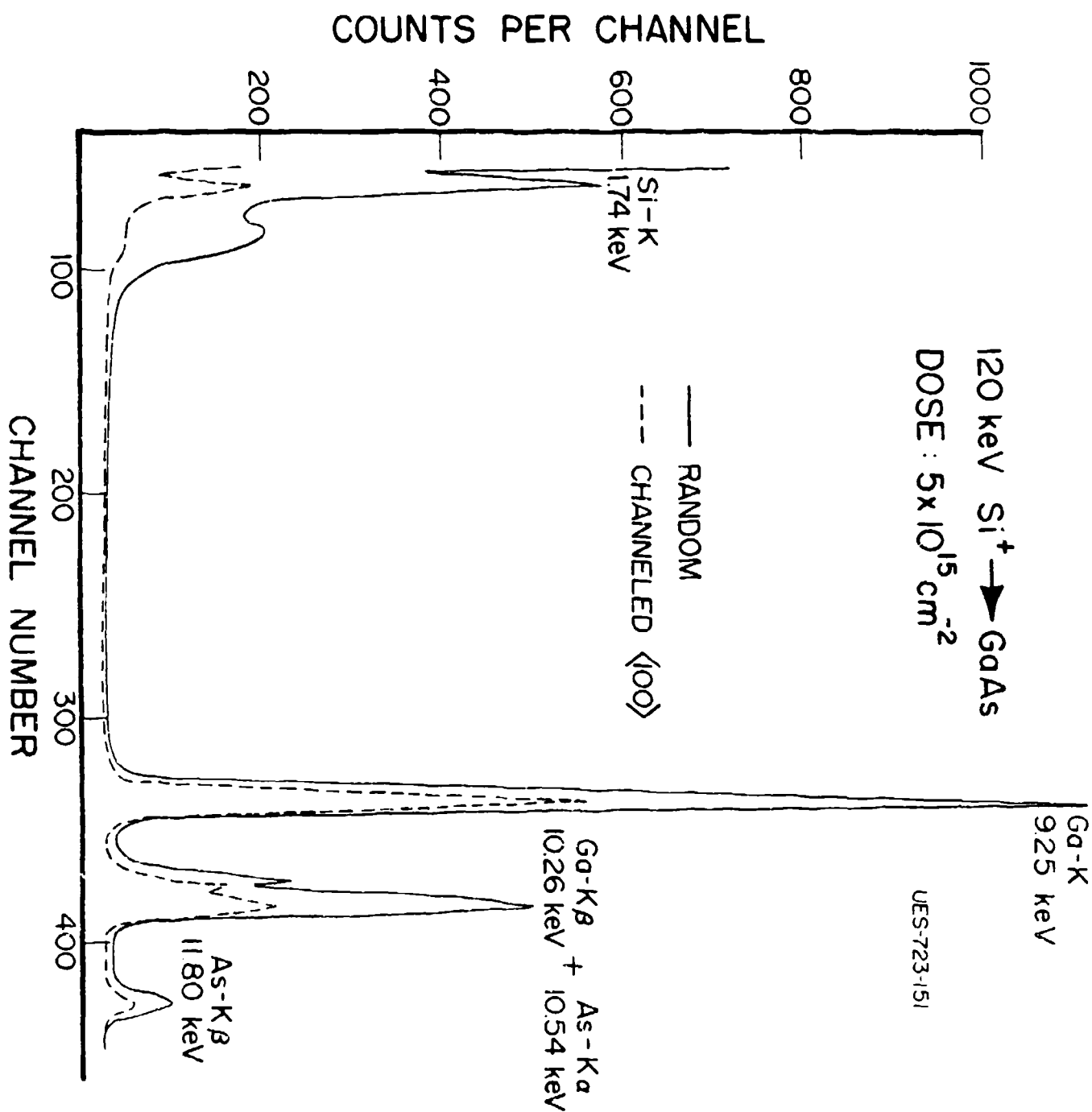
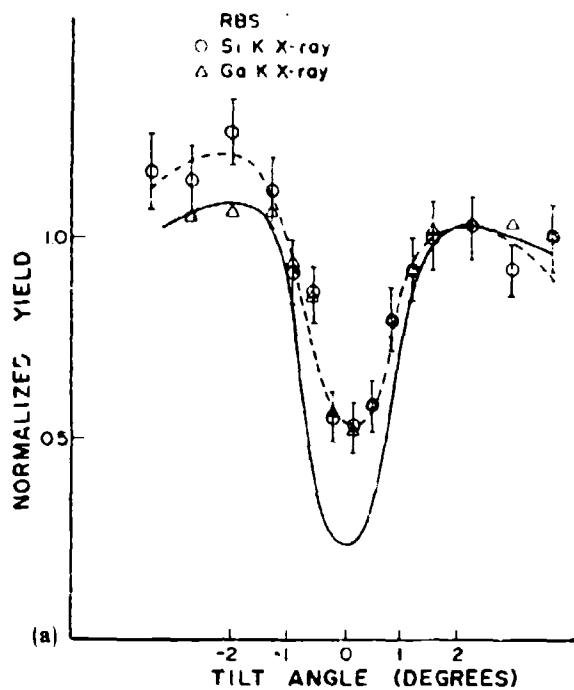


Figure 118 Characteristic X-ray spectra for 330 keV H^+ on GaAs:Si^+

120 keV Si \rightarrow GaAs
DOSE: $3 \times 10^{15} \text{ cm}^{-2}$
ANNEALED AT 850°C 15 MIN $\langle 110 \rangle$



120 keV Si \rightarrow GaAs
DOSE: $3 \times 10^{15} \text{ cm}^{-2}$
ANNEALED AT 850°C 15 MIN $\langle 100 \rangle$

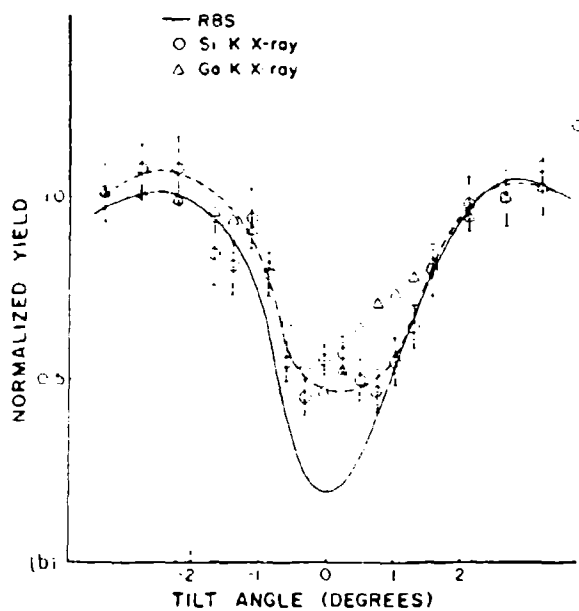


Figure 119 (a) $\langle 110 \rangle$ and (b) $\langle 110 \rangle$ Channeling Dips for GaAs:Si
Annealed at 850°C

120 keV Si \rightarrow GaAs

DOSE: $3 \times 10^{15} \text{ cm}^{-2}$

UES-723-206

ANNEALED AT 950°C 15 MIN $\langle 110 \rangle$

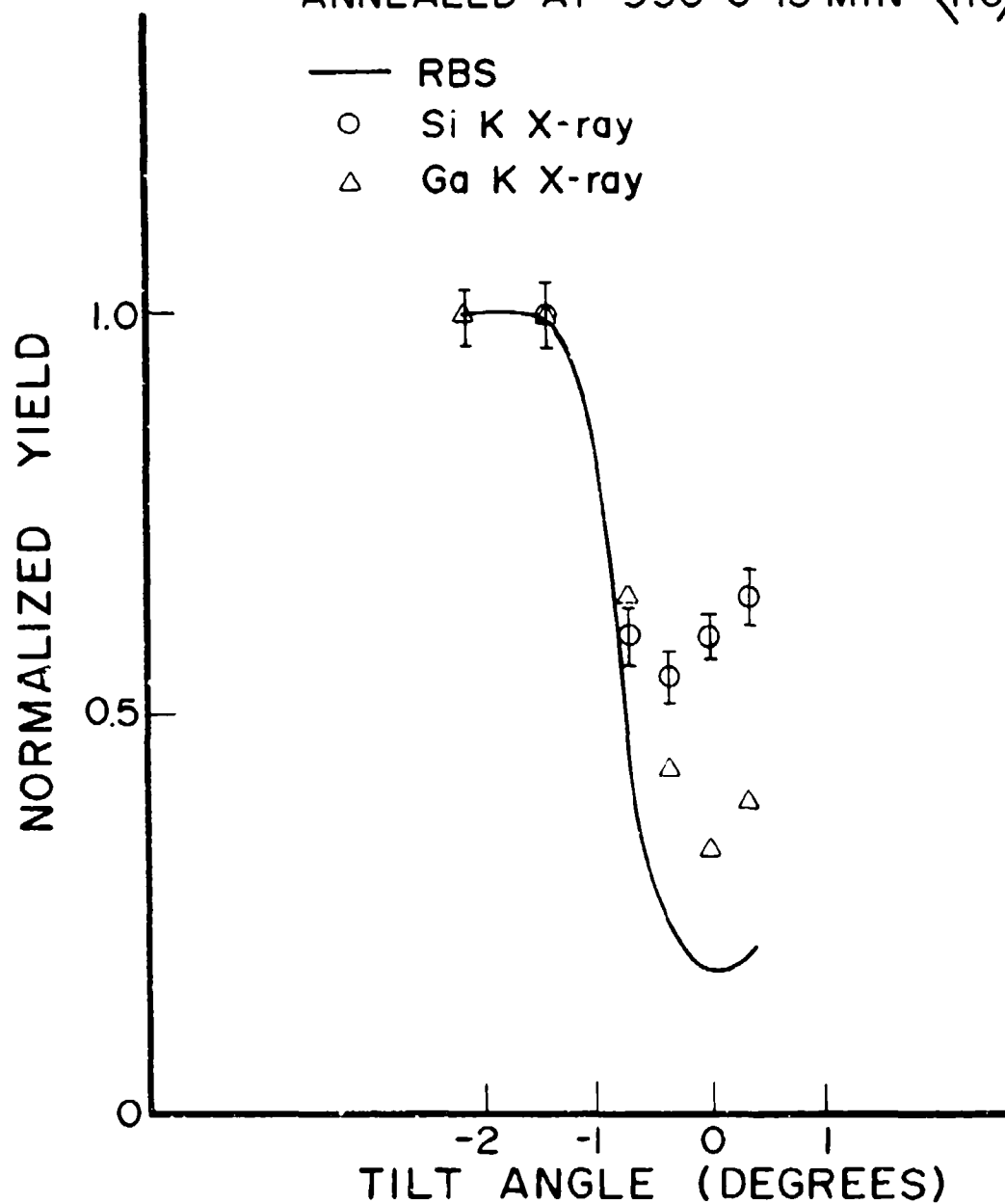


Figure 120 (a) $\langle 110 \rangle$ Channeling Dips for GaAs:Si Annealed at 950°C

120 keV Si \rightarrow GaAs

DOSE: $3 \times 10^{15} \text{ cm}^{-2}$

UES-723-205

ANNEALED AT 950°C 15 MIN $\langle 100 \rangle$

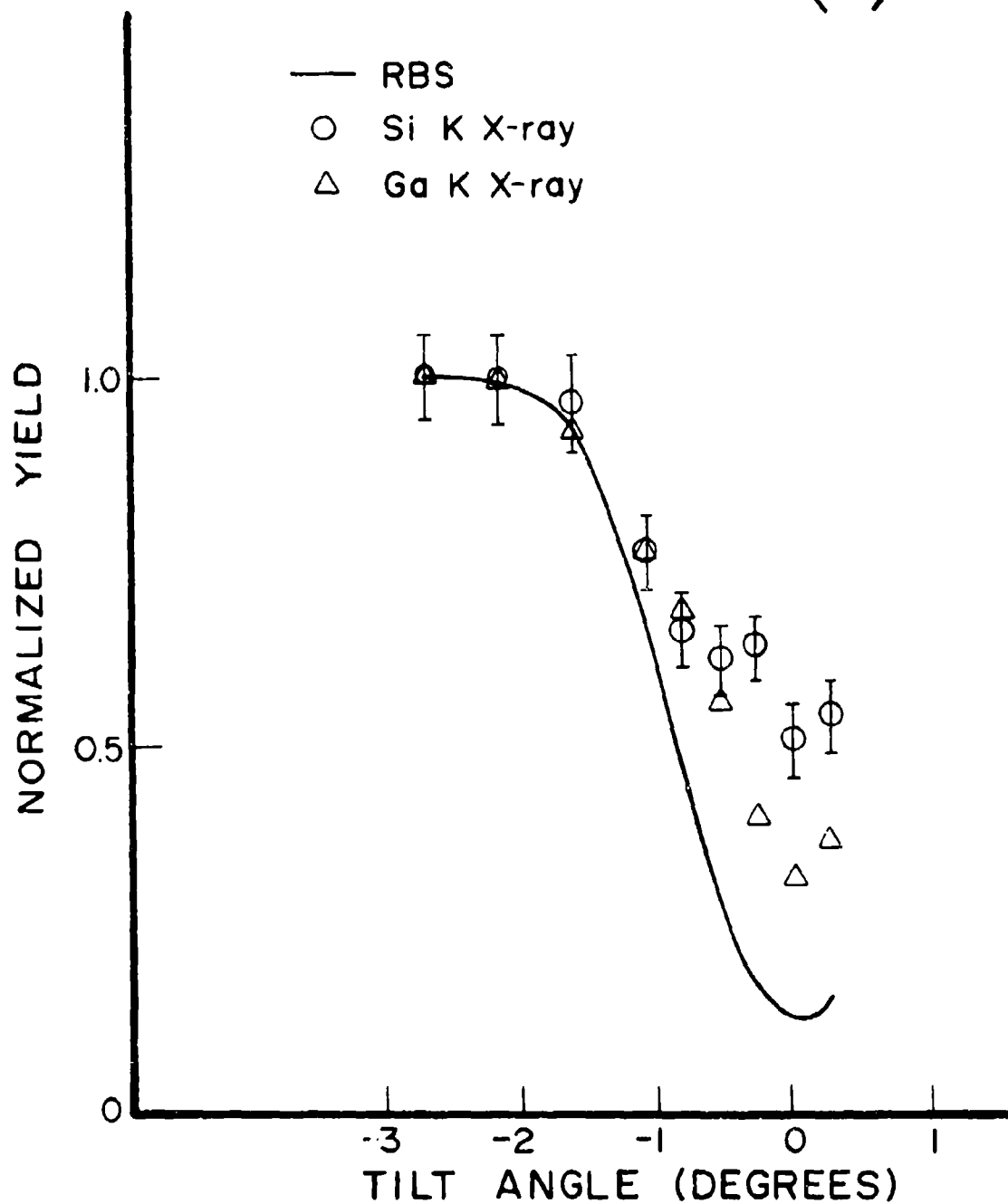


Figure 120 (b) $\langle 110 \rangle$ Channeling Dips for GaAs:Si Annealed at 950°C

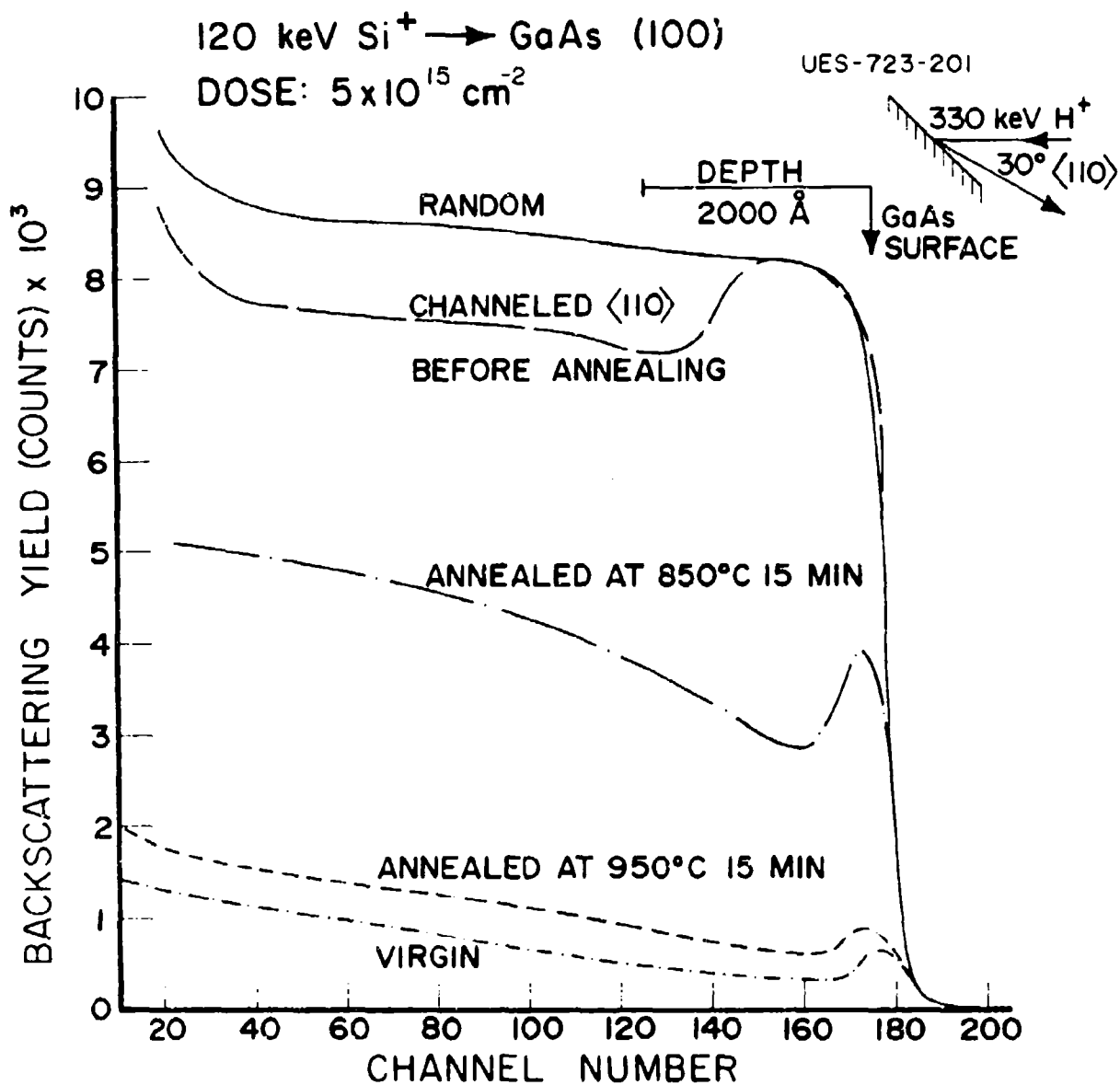


Figure 121 Backscattering spectra for GaAs:Si⁺($5 \times 10^{15} \text{ cm}^{-2}$)

channeling spectrum with that of a virgin crystal (Figure 121) reveals that considerable amount of damage remained. TEM analyses were conducted on the same sample. Figure 122(a) shows the transmission electron diffraction (TED) pattern of this sample. Diffraction analysis shows that the extra spots are due to twins lying on $\langle 111 \rangle$ planes. Bright field micrograph, Figure 122(b), shows the presence of twins together with dislocations loops. Figure 122(c) is a dark field micrograph imaged with one of the twin spots. The twin sizes were found to lie between 860 and 2,850 \AA measured along the $\langle 110 \rangle$ direction.

An angular scan across $\langle 100 \rangle$ shows near 100% channeling attenuation of the Si-K signal. However, the attenuation along $\langle 110 \rangle$ is only about 35% [Figures 123(a) and (b)]. Annealing the same sample at 950°C for 15 min results in further recovery of damage as observed by channeling (Figure 121). A TED pattern of the same specimen does not, under these annealing conditions, show any extra spots. The BF micrograph (Figure 124) shows the presence of dislocation loops together with the fine scale defects of average diameter $\sim 50 \text{\AA}$. These defects show black-white contrast under dynamical diffraction conditions and were determined to be precipitates. The level of precipitation was determined to be approximately 2%. Lattice location measurements now show about $70 \pm 7\%$ substitutionality [Figure 125 (a) and 125 (b)].

Sample 3

RBS-C measurement of the as-implanted (unannealed) sample shows that the layer is crystalline with some residual disorder characterized by a higher minimum yield and dechanneling as a function of depth (Figure 126). From our experience in the studies of low temperature annealing behavior of ion implanted GAAs, we feel that the sample temperature must have risen to about 500°C during implantation.

UES-723-219

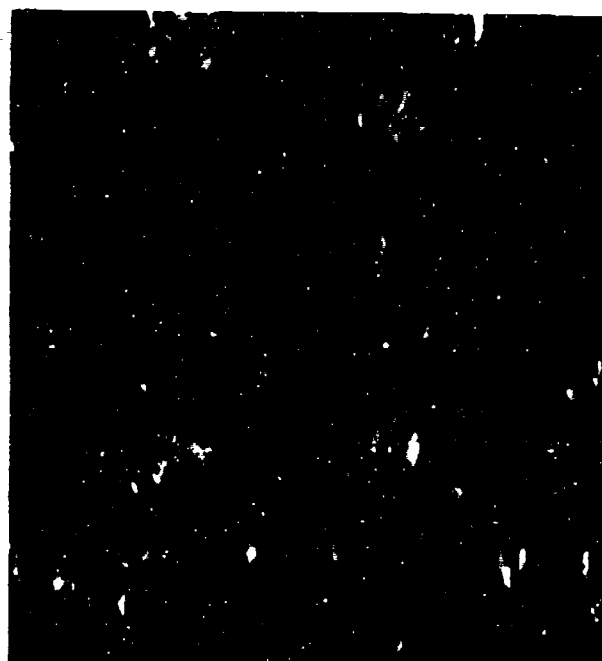


Figure 122 (a) TED Pattern in $\langle 114 \rangle$ Orientation, GaAs:Si⁺, $5 \times 10^{15} \text{cm}^{-2}$ 850°C, 15 Min, (b) and (c) are the Bright and Dark-Field Micrographs, Respectively

120 keV Si \rightarrow GaAs
 DOSE: $5 \times 10^{15} \text{ cm}^{-2}$
 ANNEALED AT 850°C 15 MIN $\langle 110 \rangle$

UES-723-158

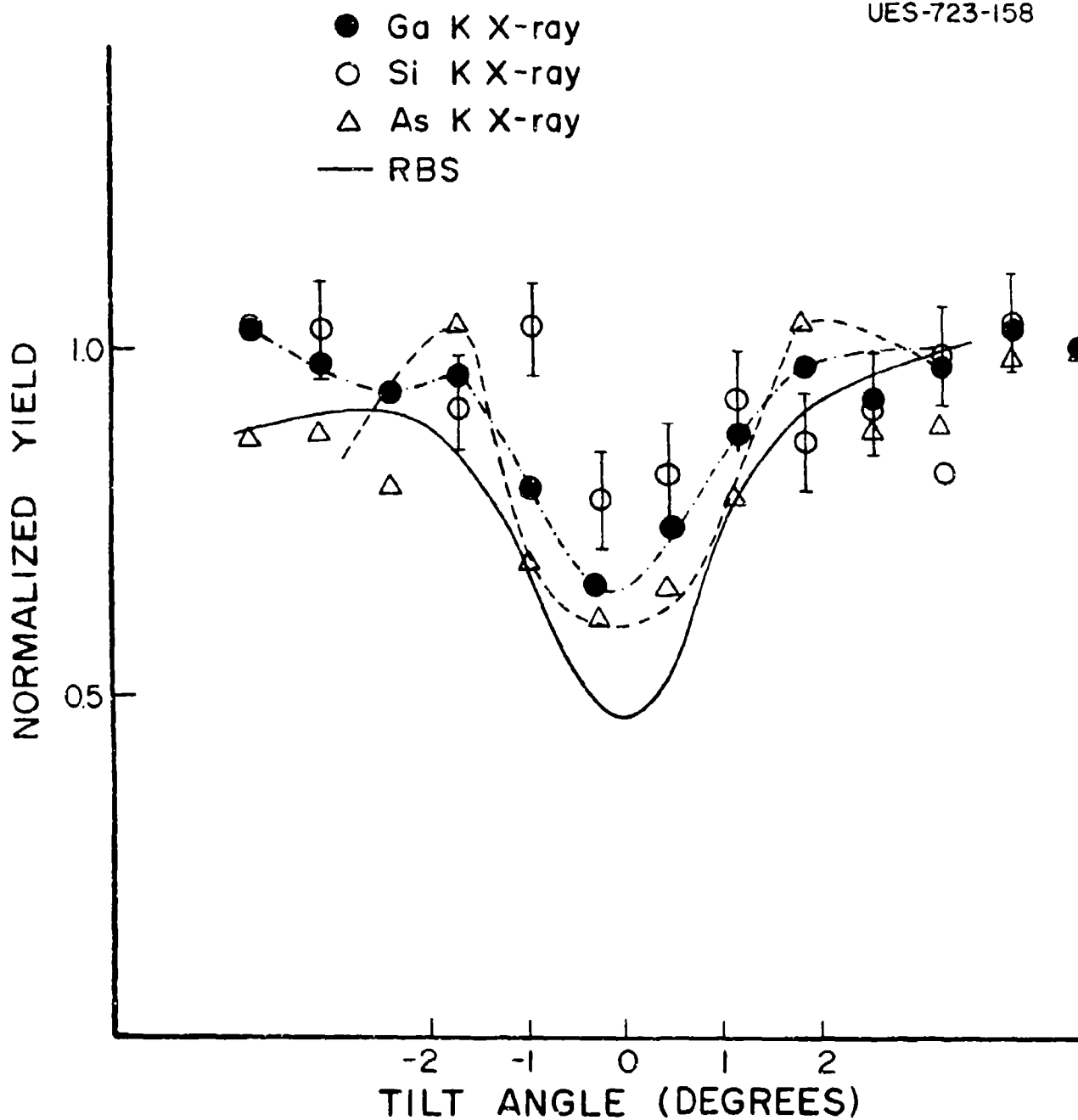


Figure 123 (a) $\langle 110 \rangle$ Channeling Dips for GaAs:Si Annealed at 850°C

120 keV Si \rightarrow GaAs

DOSE: $5 \times 10^{15} \text{ cm}^{-2}$

UES-723-157

ANNEALED AT 850°C 15 MIN $\langle 100 \rangle$

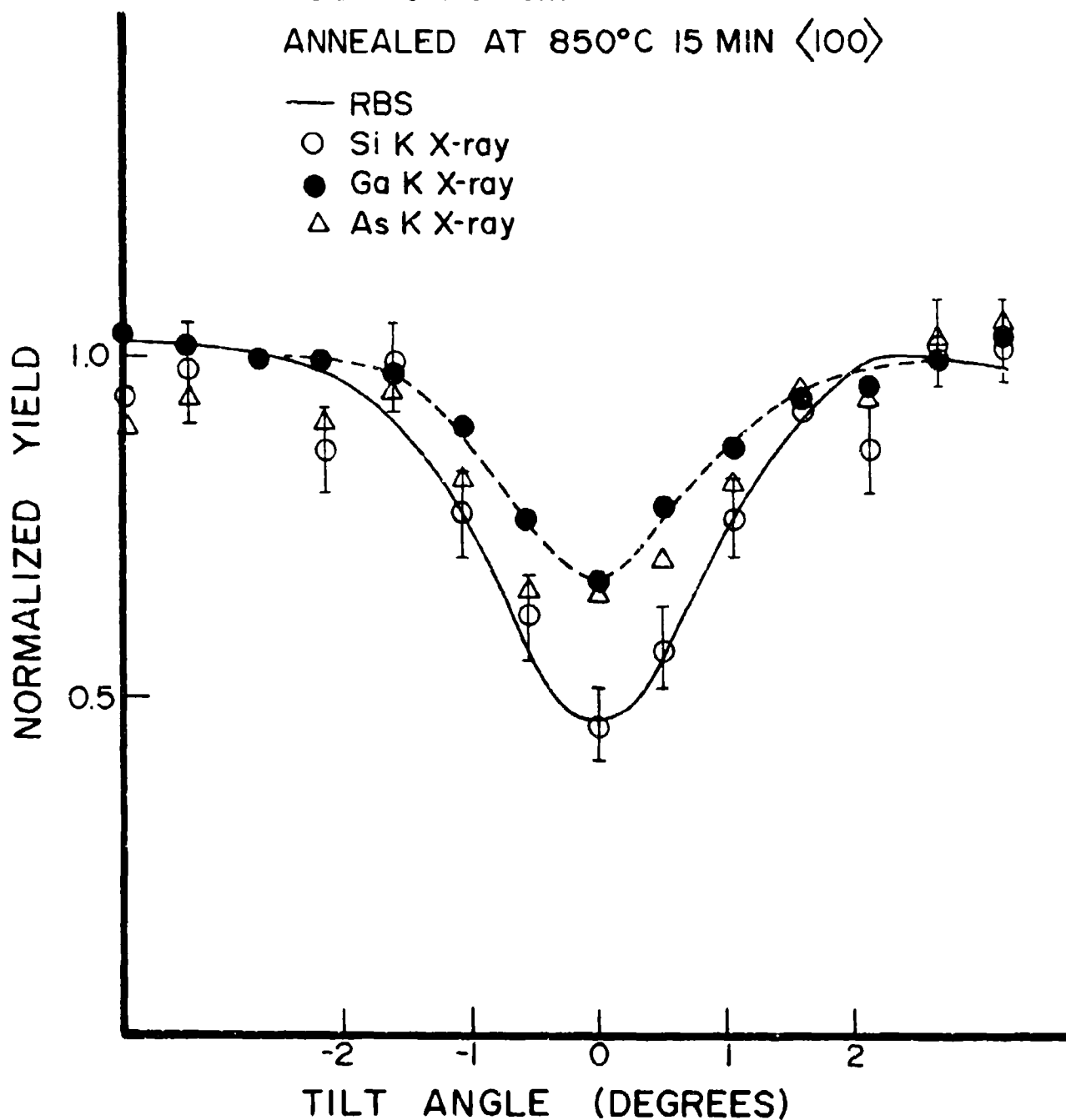


Figure 123 (b) $\langle 110 \rangle$ Channeling Dips for GaAs:Si Annealed at 850°C
231

UES-723-220



Figure 124 Bright-Field Micrograph of 120 keV Si^+ ,
 $5 \times 10^{15} \text{cm}^{-2}$, 950°C for 15 Min

120 keV Si \rightarrow GaAs
DOSE: $5 \times 10^{15} \text{ cm}^{-2}$

UES-723-155

ANNEALED AT 950°C 15 MIN $\langle 110 \rangle$

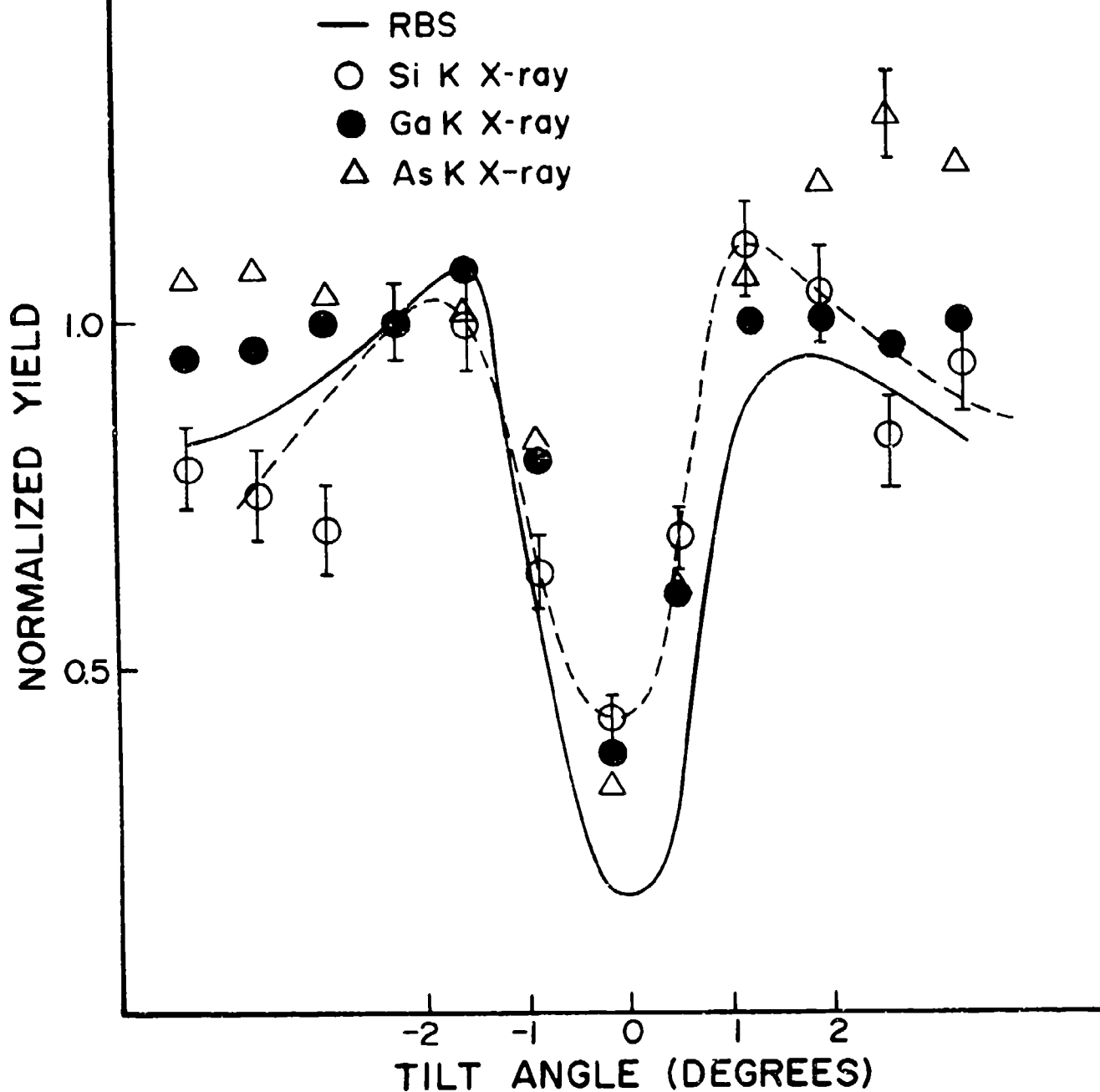


Figure 125 (a) $\langle 110 \rangle$ Channeling Dips for GaAs:Si⁺,
 $5 \times 10^{15} \text{ cm}^{-2}$, 950°C

120 keV Si \rightarrow GaAs

DOSE: $5 \times 10^{15} \text{ cm}^{-2}$

UES-723-156

ANNEALED AT 950°C 15 MIN $\langle 100 \rangle$

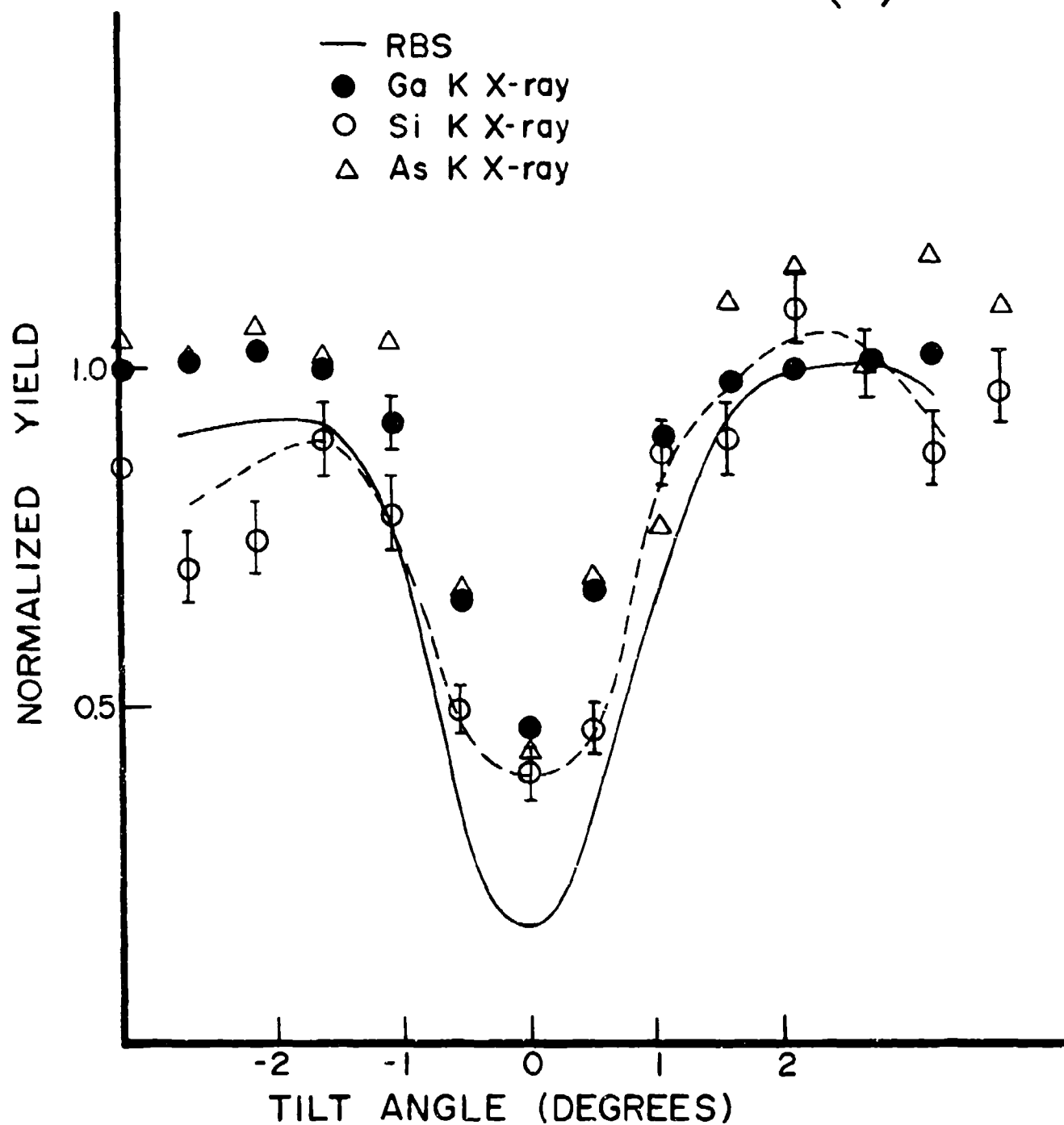


Figure 125 (b) $\langle 110 \rangle$ Channeling Dips for GaAs:Si⁺,
 $5 \times 10^{15} \text{ cm}^{-2}$, 950°C
234

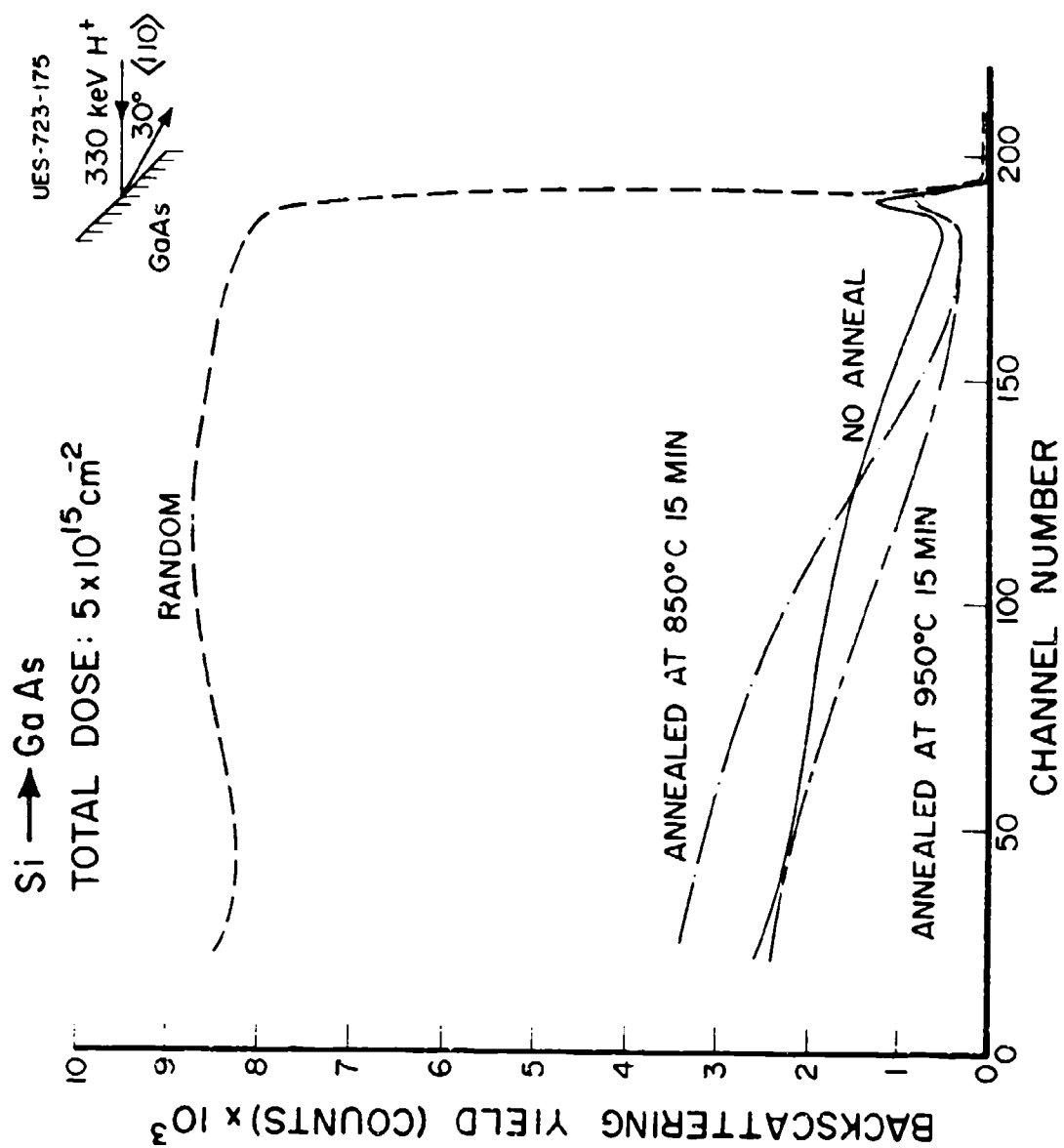


Figure 126 Backscattering Spectra for GaAs:Si, $5 \times 10^{15} \text{ cm}^{-2}$

TEM investigations shows the layer is crystalline with dislocation loops as the major residual defects. The dislocation density has been found to be of the total line length of $2.3 \times 10^5 \text{ cm/cm}^2$. PIXE angular scans for the non annealed sample show about 50% attenuation of the Si K x-ray dips. These dip curves are narrow by a substantial amount compared to the RBS-C dips indicating that the Si atoms are initially displaced considerably from the lattice positions before annealing occurs.

RBS-C measurements after annealing the samples at 850°C for 15 minutes show (Figure 126) that the surface region up to about 1300 μ became as good as virgin material. A rather sharp increase in dechanneling at this depth indicates a build up of disorder from that point inward. TEM analysis of the same sample (Figure 127) indicated a lower density of dislocations near the surface region; however, a sharp increase in dislocation density is observed as the electron beam is focused into a thicker region of the wedge shaped sample. Figure 127 shows the series of micrographs taken at various points starting from the surface region up to a thicker region of the wedge shaped sample. In planar channeling, the dechanneling gets amplified because of the presence of dislocation loops that give rise to enhanced dechanneling with very little direct scattering. Therefore, we have done channeling measurements along a $\{110\}$ plane with the results being shown in Figure 128. The data in this figure are for both 850°C and 950 °C anneals. Similar to the case of axial channeling, there again is a sharp increase in dechanneling at a depth of 1300 μ . A depth distribution of the disorder is extracted from the planar channeling analyses following the procedure of Picraux et al.⁸² The density of disorder as a function of depth Z is given by

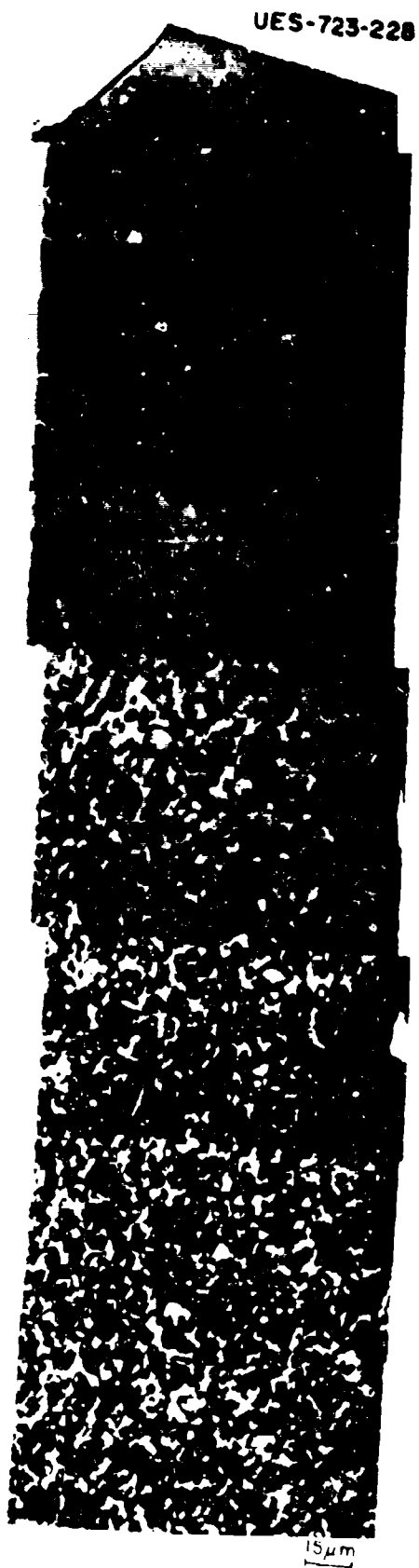


Figure 127 Bright-Field Micrographs of Sample 3 After Annealing at 850°C for 15 Min

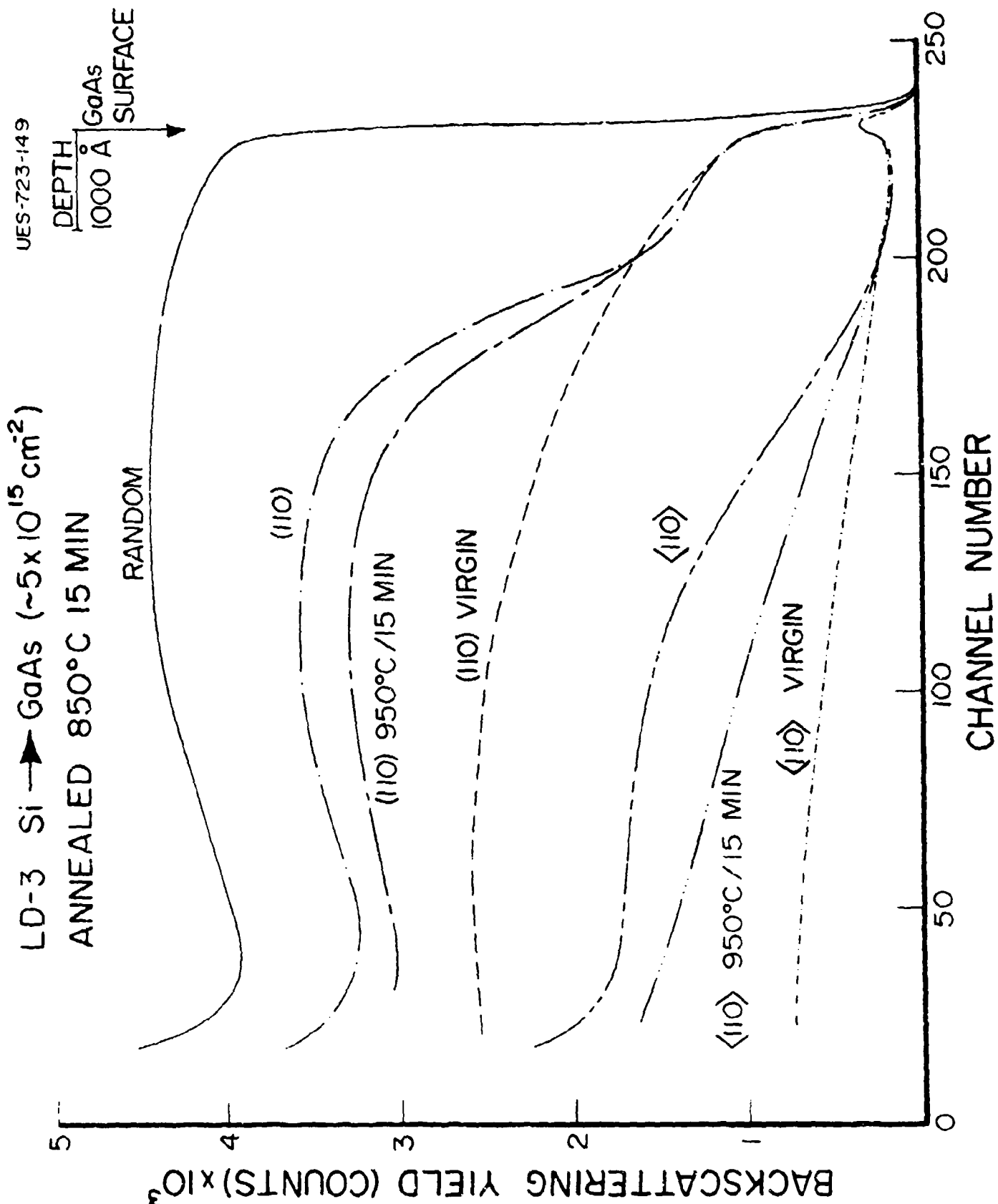


Figure 128

$\langle 110 \rangle$ Axial and (110) Planar Channeling Spectra for
 GaAs:Si⁺, $5 \times 10^{15} \text{ cm}^{-2}$
 238

$$\int_0^Z n(Z') dz' = \frac{1}{\lambda} \ln \frac{(1-\chi_D)}{(1-\chi_V)} \quad (1)$$

where n is the density of defects with a dechanneling cross section λ , χ_D and χ_V are the channeled yields in the damaged crystal and in the virgin crystal, respectively. A depth distribution is obtained by differentiating Equation (1). The results are shown in Figure 129 which indicate that the disorder region is confined to a depth between 1300 and 3760 Å. Thus, it appears that the annealing took place from the surface region inward as well as from the interface region outward. Further annealing of this sample at 950°C for 15 minutes has removed some of the damage, as indicated by lower dechanneling (Figure 126) as well as by the TEM weakbeam dark field micrograph of Figure 130. The dislocation density, in this case, is found to be $0.6 \times 10^3 \text{ cm}^{-2}$.

Lattice location measurements after annealing at 850°C are shown in Figure 131(a) and 131(b). The Si <110> has nearly the same half-width as that of the RBS dip. However, the shape of the Si <100> dip is slightly narrower and asymmetric as compared to the RBS dip. After annealing at 950°C, the shape of the <100> dip becomes symmetrical with half-width almost equal to the half-width of the corresponding RBS dip [Figures 132(a) and 132(b)]. The substitutional fraction can be calculated from these figures and found to be about 65% and 75% after 850°C and 950°C respectively.

Experiments so far have provided the information on total substitutionality of implanted Si in GaAs under various implantation and

UES-723-227

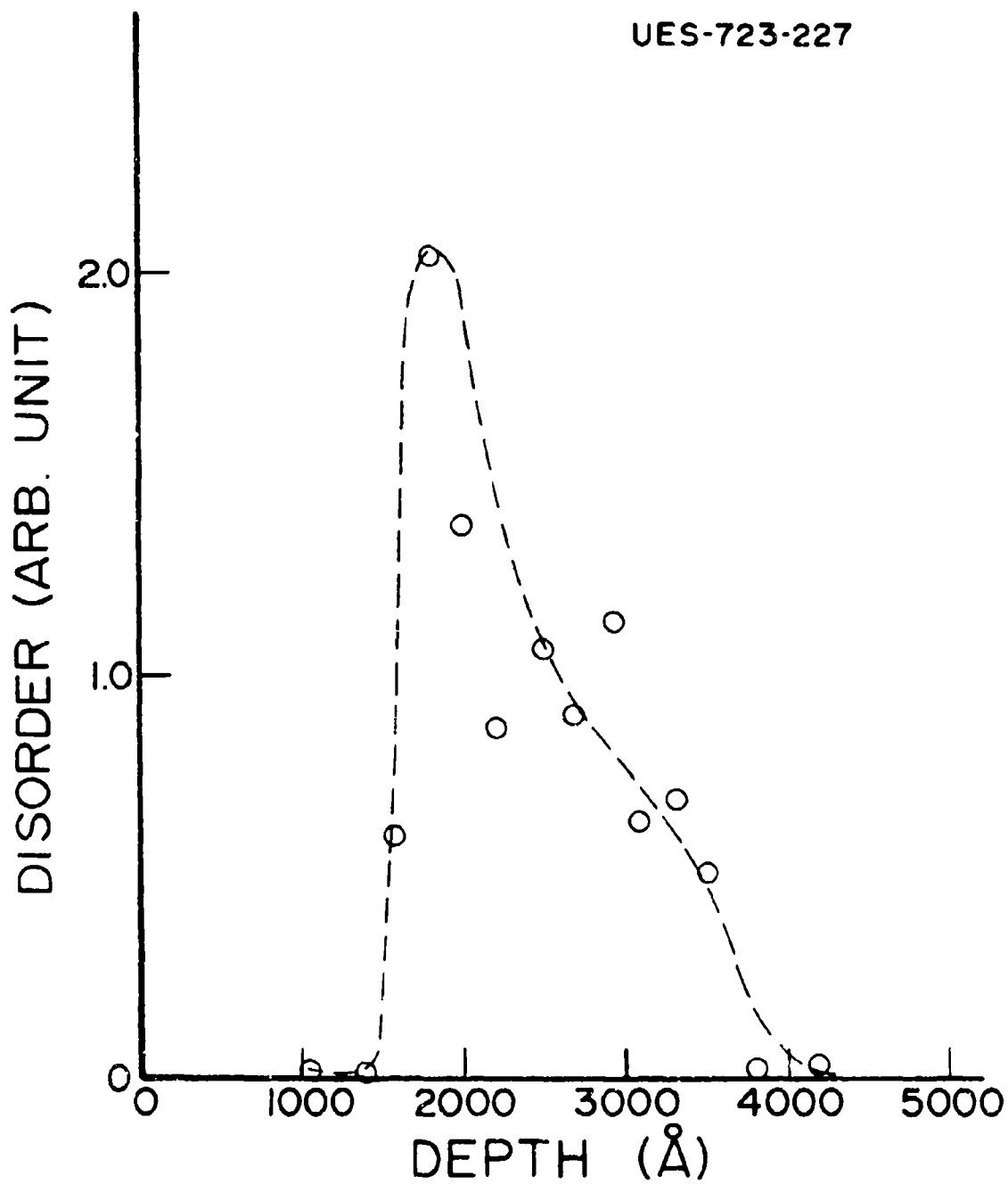


Figure 129 Depth Distribution of Disorder of Sample 3 after 850°C
Annealing for 15 min

UES-723-221



Figure 130 Weak Beam Dark-Field Micrograph of Sample 3,
After Annealing at 950°C for 15 Min

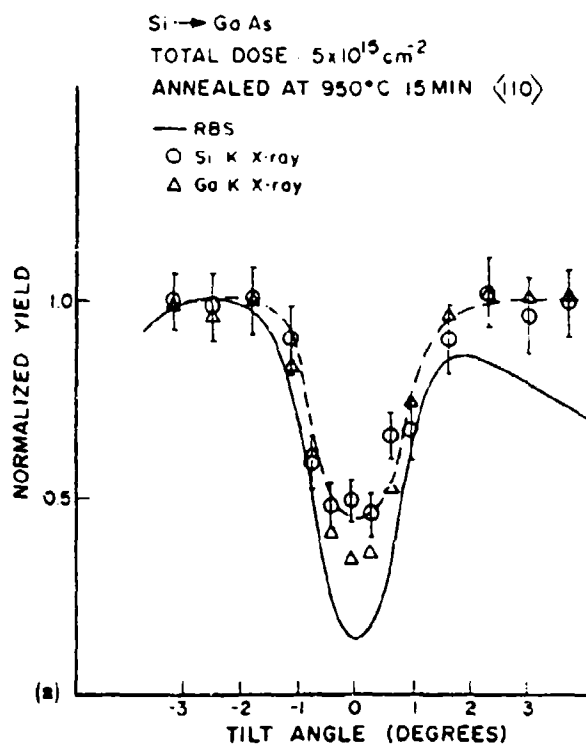
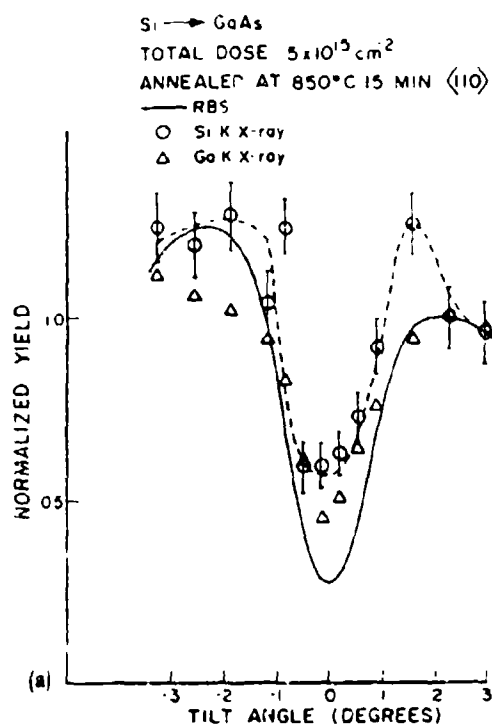


Figure 131 (a) $\langle 110 \rangle$ and (b) $\langle 100 \rangle$ Channeling Dips for GaAs:Si⁺, $5 \times 10^{15} \text{ cm}^{-2}$, 850°C

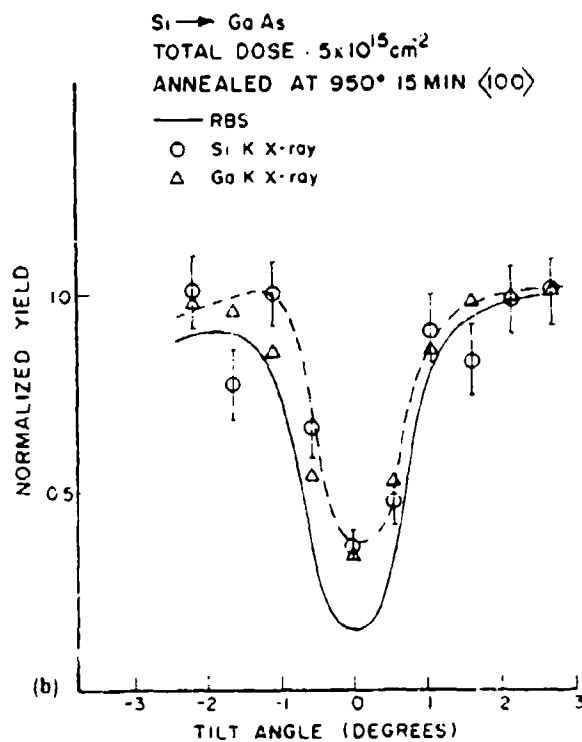
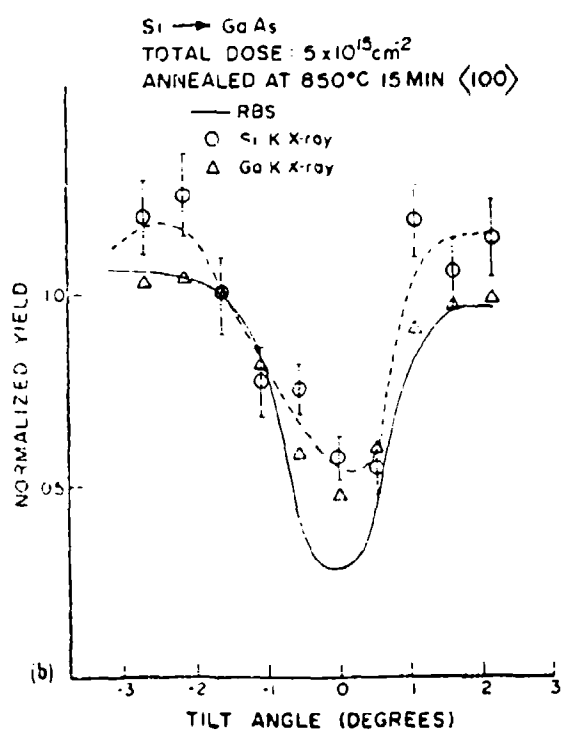


Figure 132 (a) $\langle 110 \rangle$ and (b) $\langle 100 \rangle$ Channeling Dips of Sample 3, Annealed at 950°C

annealing conditions. However, no attempt was made in those experiments to determine the specific site location of the implanted atoms. This can be done if one makes use of the fact that the $\langle 110 \rangle$ axis in a zinc-blende structure is made up of atomic strings containing only one of the two types of matrix atoms. When an ion beam is incident parallel to the $[1\bar{1}0]$ plane but at an angle $+\theta_0$ with respect to the $\langle 110 \rangle$ axis (see Figure 133), it has a higher probability of initially striking an A rather than B row. The opposite will happen if the beam is incident at an angle $-\theta_0$ to the $\langle 110 \rangle$ axis. Thus, if a complete angular scan is taken, an asymmetric channeling dip will result. When a substitutional impurity shows an asymmetry under these circumstances, it can be concluded that the impurity predominantly occupies one sublattice site. From a comparison of the associated asymmetry of the host atoms, the specific site can be identified.

We have first demonstrated this asymmetrical effect in the PIXE angular scan for unimplanted GaP and then the application was made for Si implanted GaAs.

Figure 134 shows the random and $\langle 110 \rangle$ channeling spectra of unimplanted GaP crystal. In addition to the surface peaks of Ga and P in the channeling spectrum, O peak has appeared showing the presence of oxygen on the surface. The integrated backscattering yields from a layer of thickness $\sim 400 \text{ \AA}$ have been measured behind the surface peaks of Ga and P as a function of tilt angle. The results are shown in Figure 135 where reverse asymmetries of Ga and P channeling dips are clearly visible. This is expected as discussed in relation to Figure 133. Figure 136 shows a typical PIXE spectrum of GaP. the area under the peaks of Ga and P K X-rays are measured as a function of tilt angle. The results are shown in Figure 137. A strong

UES-723-277

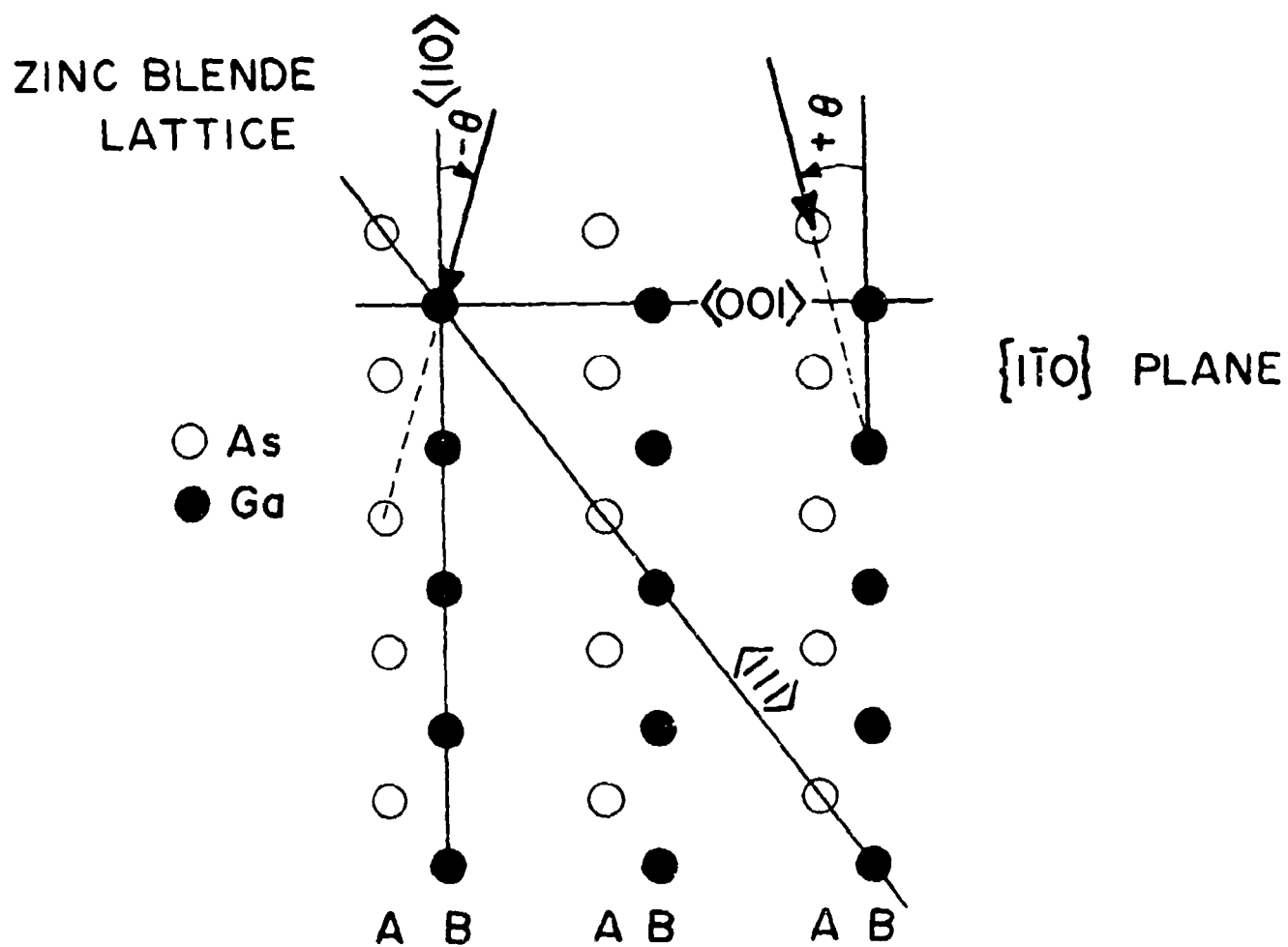


Figure 133 Positions of Ga and As Atoms in the $[110]$ Plane of the GaAs

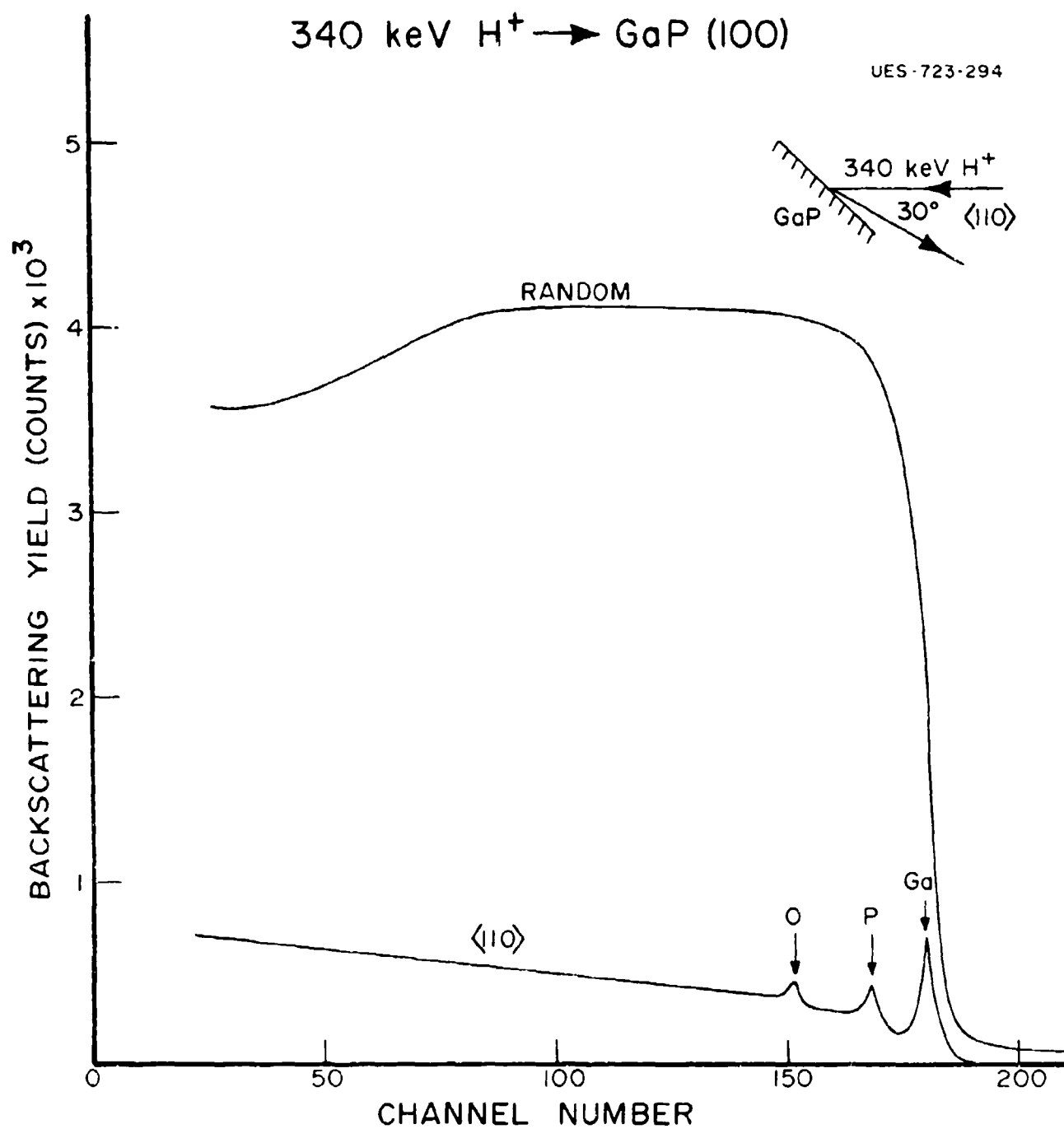


Figure 134 Channeling Spectrum of GaP

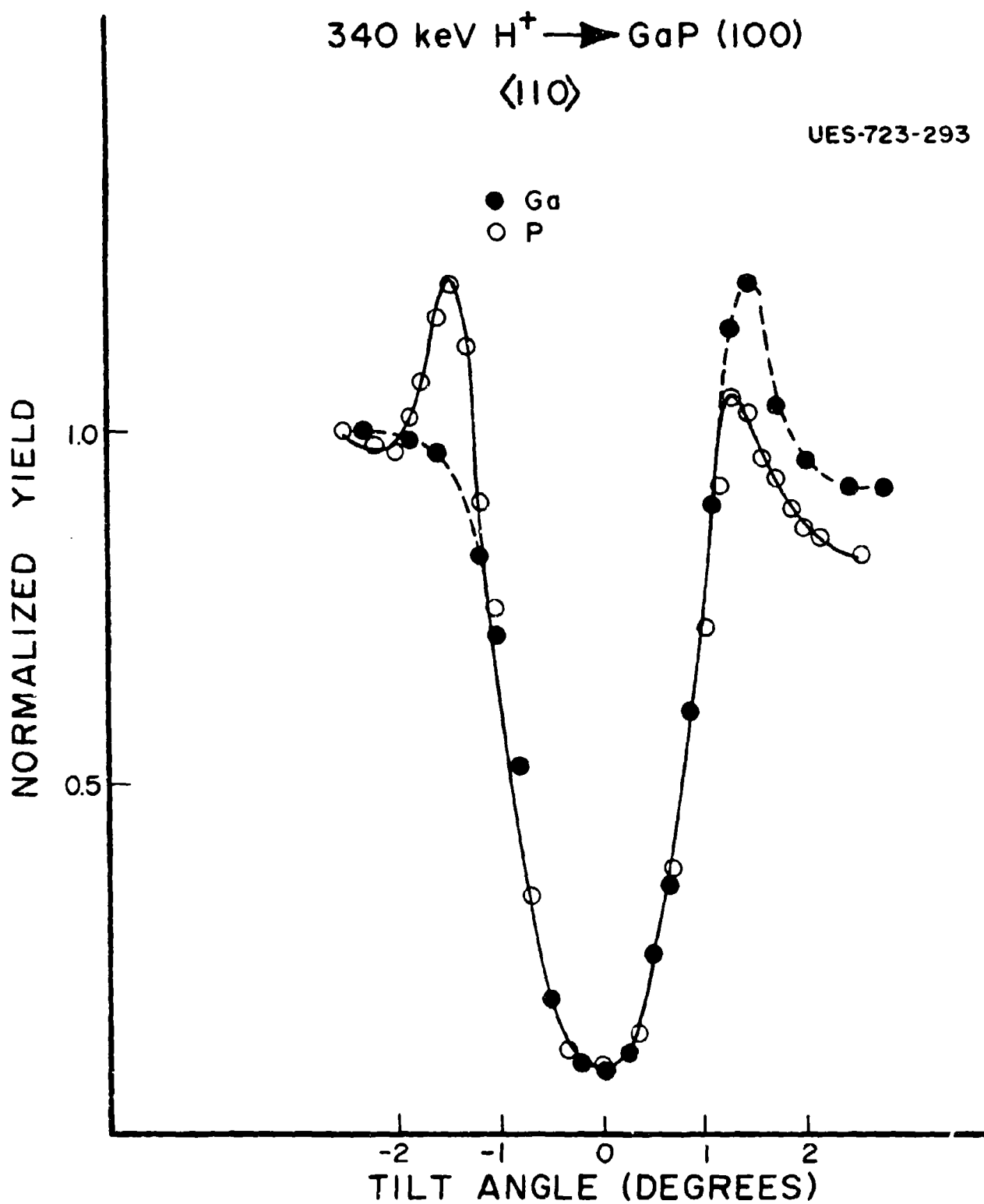


Figure 135

$\langle 110 \rangle$ Channeling Dip of GaP (RBS)
246

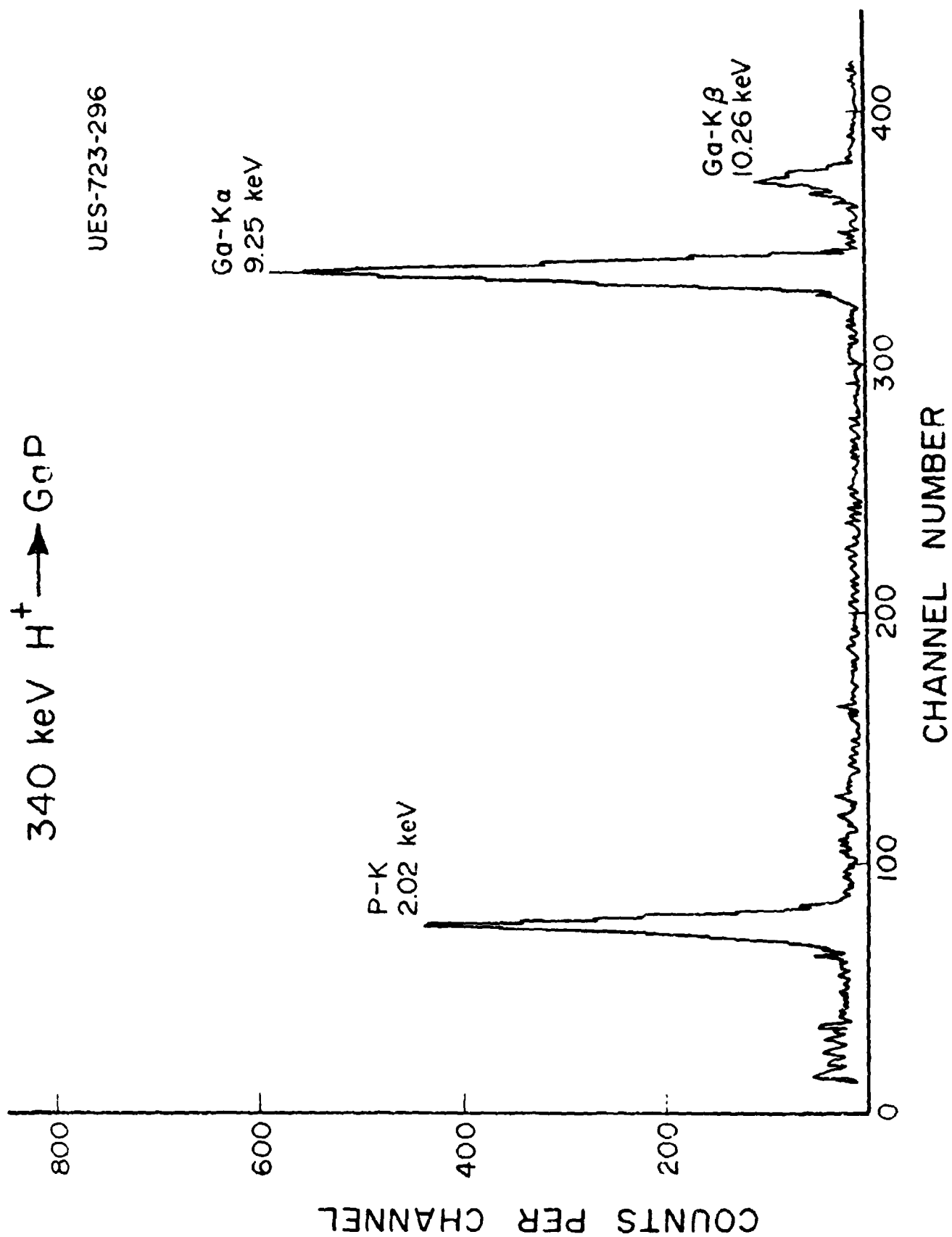


Figure 136 Characteristic X-ray Spectrum of GaP

340 keV $H^+ \rightarrow GaP$
 $\langle 110 \rangle$

UES-723-292

● P-K X-ray
 ○ Ga-K X-ray
 --- RBS

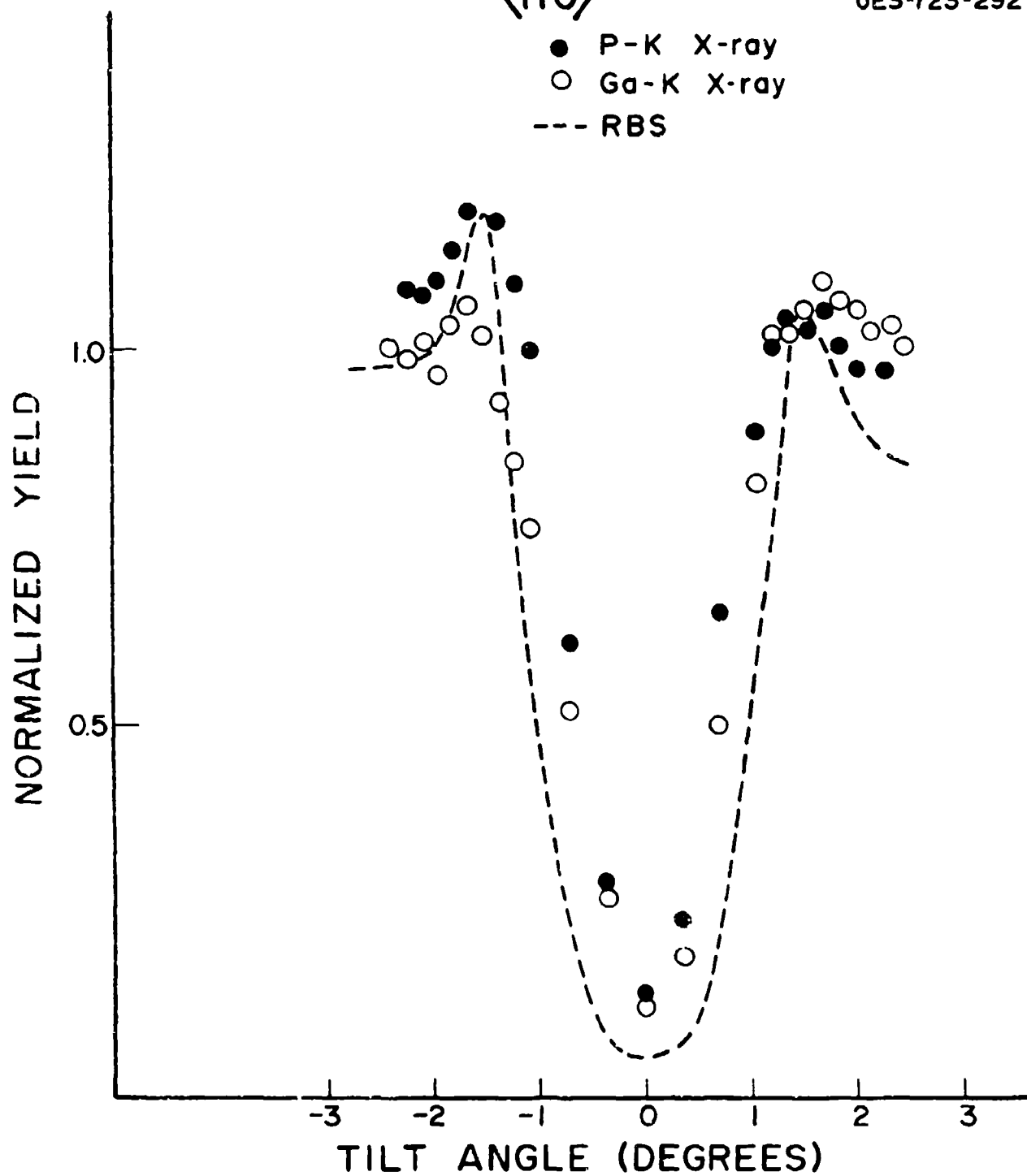


Figure 137

$\langle 110 \rangle$ Channeling Dip of GaP (RBS and PIXE)

asymmetry is observed in the case of P signal whereas no asymmetry is found for Ga signal. The asymmetry in the P K X-ray dip is about the same as in the RBS dip measured behind the P peak and integrated over a depth $\sim 2000 \text{ \AA}$. P K X-ray (2.02 keV) is originating from a thickness $\sim 200 \text{ \AA}$ near the surface of GaP and therefore the magnitude of asymmetry of P K X-ray dip and RBS dip for P signal are nearly the same. However, the Ga K X-ray (9.25 keV) is originating from a thickness ~ 2 microns. Since the preferential interaction^{83,84} between the beam and one of the sublattice atomic rows is most pronounced close to the surface only and gradually becomes less observable as the depth increases and finally disappears at larger depth due to the establishment of statistical equilibrium of channeling beam, the asymmetry effect for Ga K X-ray signal is not observable. Once the asymmetry effect of PIXE signal from P in GaP is established, the principle can be applied to S and Si implanted in GaAs. This is because S and Si have K X-ray energies in the neighborhood of P-K = 2.02 keV; S-K and Si-K being 2.31 keV and 1.74 keV respectively. The emission depths ($\sim 200 \text{ \AA}$) of these X-ray from GaAs are also about the same as for P K X-ray in GaP.⁵⁴

GaAs crystal implanted with Si at a dose of $5 \times 10^{15} \text{ cm}^{-2}$ and annealed at 950°C for 15 minutes was chosen for this study. The result of the S implanted sample will be described in the next section. The angular scan is shown in Figure 138. Si K X-ray dip is quite symmetrical indicating that the implanted Si is occupying both Ga and As sites.

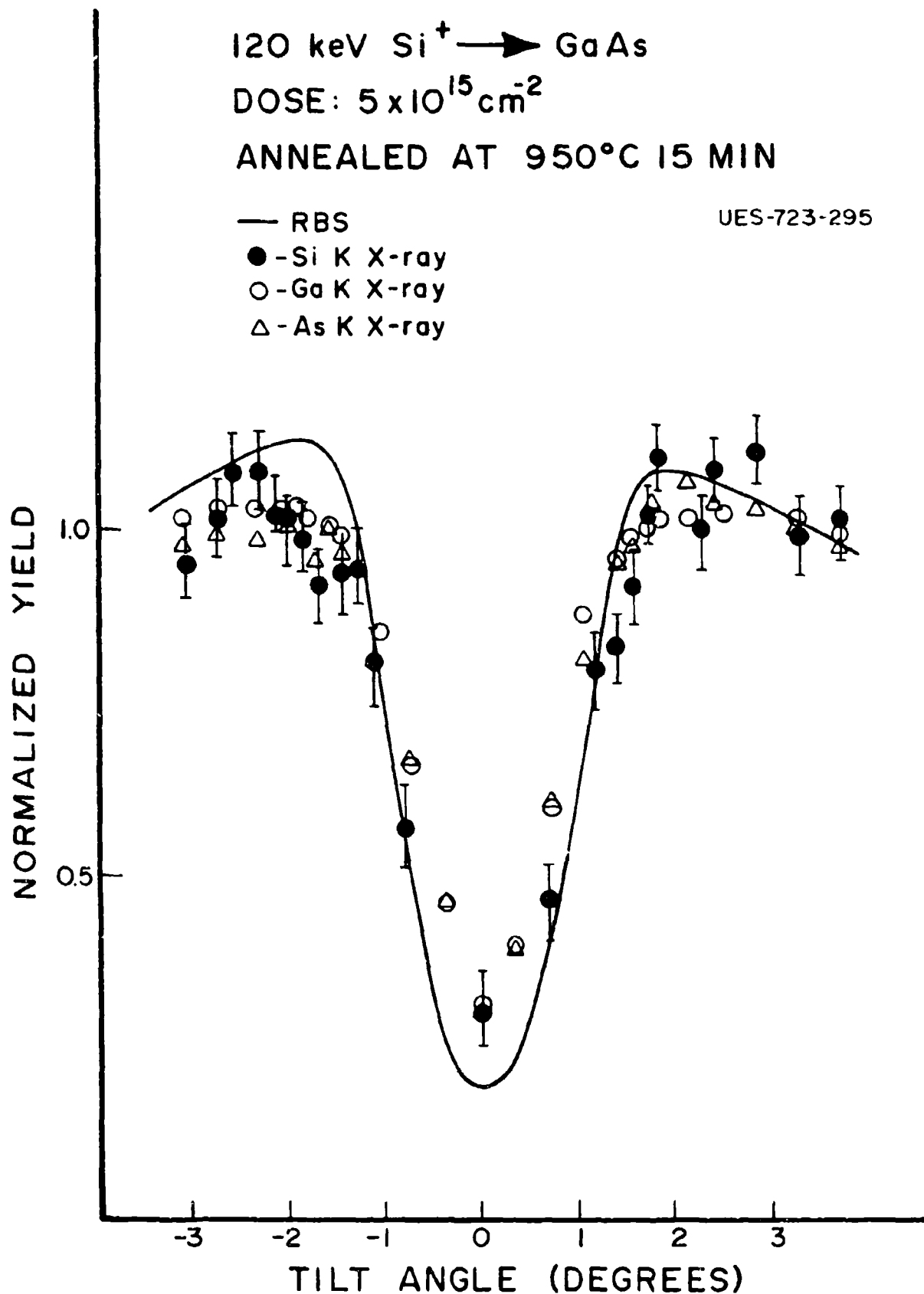


Figure 138

<110> Channeling Dip of GaAs:Si ($5 \times 10^{15} \text{ cm}^{-2}$)
Annealed at 950°C
250

4.4.5 Discussion

From the results reported so far, it is evident that about 60-85% Si occupies substitutional lattice sites in GaAs after high temperature annealing. Also, the TEM analysis reveals that the amount of precipitation is very low ($\sim 2\%$). Our results of electrical measurements as well as the results reported in the literature show that the activation efficiency for high doses is very poor ($< 10\%$). Comparing the Si K X-ray intensity from as-implanted and annealed samples we found that there were no measureable loss (within $\sim 10\%$) of Si after high temperature annealing. Similar results have also been reported by Masuyama et al.⁵¹ from SIMS measurement. Therefore the poor electrical activation cannot be attributed to the loss of Si after high temperature annealing. However, Masuyama et al.⁵¹ have observed that for $1 \times 10^{15} \text{ cm}^{-2}$, 300 keV Si implant, annealed at $900^\circ\text{C}/30$ minutes, Si atoms redistributed as compared to as-implanted distribution in such a way that the peak concentration decreased by about 45% (from $3.6 \times 10^{19} \text{ cm}^{-3}$) and the tail of the distribution extended to about $0.85 \mu\text{m}$ as compared to $0.67 \mu\text{m}$ for as-implanted sample. The free electron concentration was found to be flat, $\sim 2 \times 10^{18} \text{ cm}^{-3}$, up to that depth.

In the case of Sample 1 we have carried out the measurements of carrier concentration (N) and Hall mobility (μH) as a function of depth after 850 and 950°C annealing. The results are shown in Figure 139. A dip in the N is observed at a depth where the maximum concentration of Si is expected. Some redistribution of Si is evident from the measured N of $\sim 3 \times 10^{18} \text{ cm}^{-3}$ at a depth larger than $0.3 \mu\text{m}$. However, it is obvious that such a low electrical activation cannot be explained from the occurrence of redistribution alone. Si, being an amphoteric dopant in GaAs, may occupy both Ga and As lattice

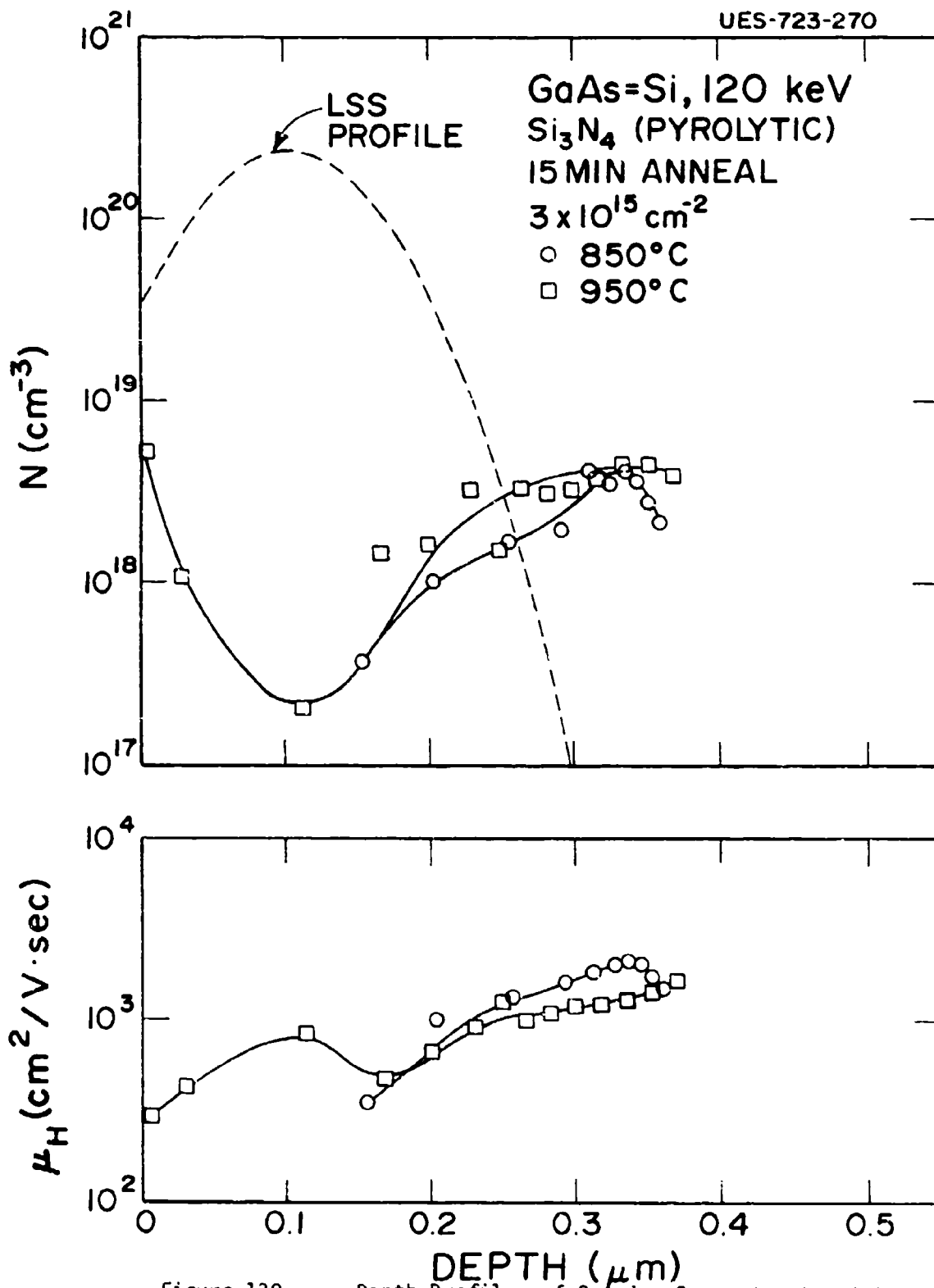


Figure 139

Depth Profiles of Carrier Concentration (N) and
Mobility (μ_H) for GaAs:Si⁺

sites, although at low doses they seem to occupy more Ga sites inferred from higher n-type electrical activation efficiency. The absence of asymmetry in the angular scan indicates that Si is occupying both Ga and As sites. Skolnik et al.⁸⁵ have performed infrared (IR) absorption studies on high energy (1-1.15 MeV), high dose ($4 \times 10^{16} \text{ cm}^{-2}$) Si implanted GaAs. They observed IR absorption bands corresponding to substitutional Si with site location being identified as Si on Ga sites (Si_{Ga}), Si on As sites (Si_{As}) and neutral neighbors pairs of substitutional Si ($\text{Si}_{\text{Ga}}\text{-Si}_{\text{As}}$). The presence of the pair complexes explains, in a qualitative sense, the poor electrical activation for high dose Si in GaAs. Our results of high substitutionality, very low precipitation, and absence of asymmetry are in support of this explanation. The dip in the carrier concentration around a depth of $\sim 0.1 \mu\text{m}$ is probably caused by such a mechanism of neighboring site occupation because of the highest concentration of Si around that depth.

4.5 S IMPLANTATION IN GaAs

Both Cr-doped and undoped GaAs wafers with (100) orientation were implanted with 120 keV S^+ ions in a nonchanneling direction at room temperature to doses of 1×10^{15} and $3 \times 10^{15} \text{ cm}^{-2}$.

4.5.1 Damage Analysis

RBS-C measurements after implantation show that (Figure 140) the layer has become amorphous up to a thickness of $\sim 1450 \text{ \AA}$ for a dose of $1 \times 10^{15} \text{ cm}^{-2}$. For a $3 \times 10^{15} \text{ cm}^{-2}$ implant the amorphous layer thickness was somewhat larger; $\sim 1530 \text{ \AA}$. After annealing at 800°C for 15 minutes, the layer recovers its crystallinity as characterized by a channeled spectrum lying almost on top of the virgin spectrum. Similarly, very good damage annealing took place for $3 \times 10^{15} \text{ cm}^{-2}$ implants annealed at 800°C .

120 keV S⁺ → GaAs
DOSE: 1 × 10¹⁵ cm⁻²

UES-723-226

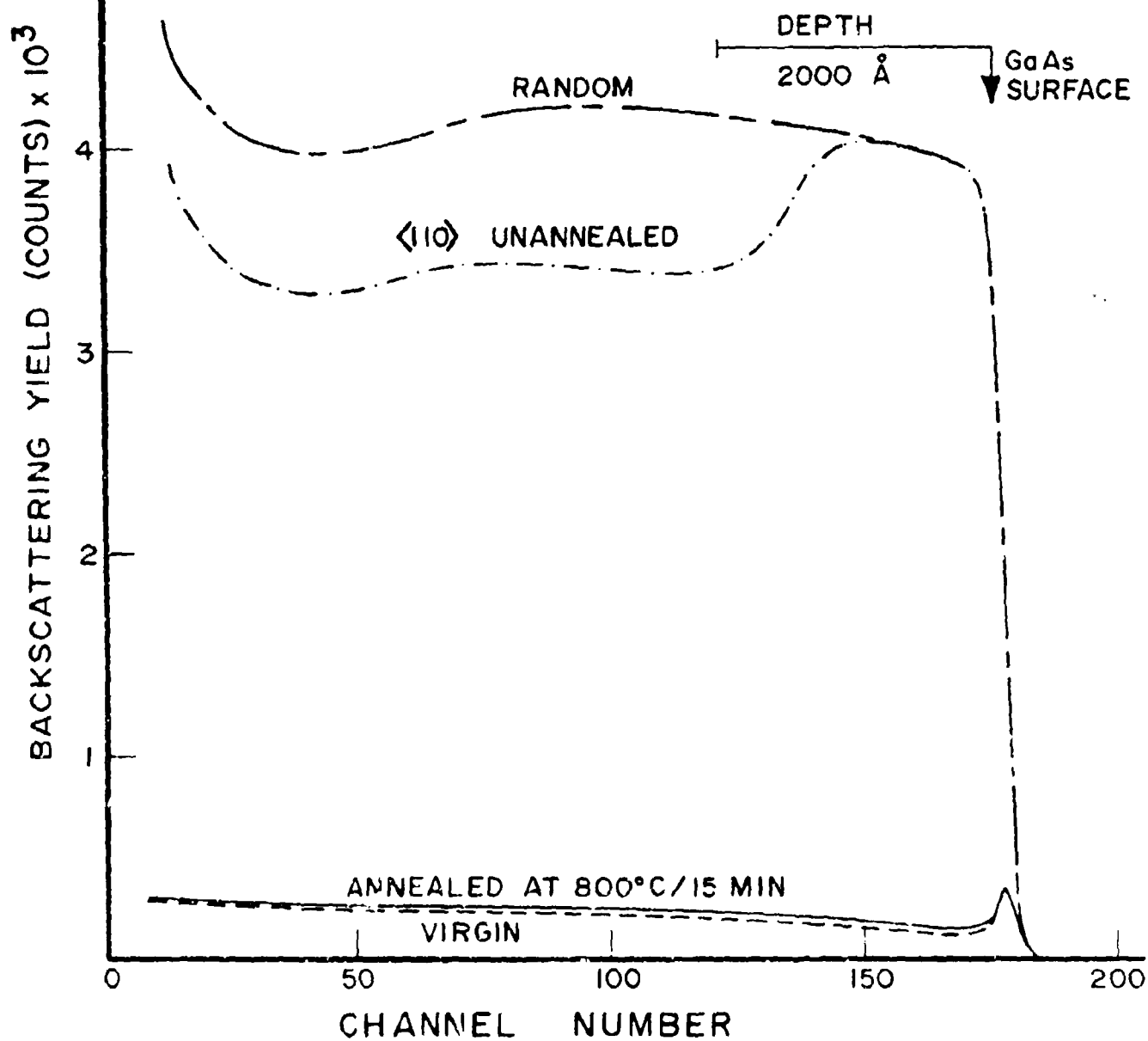
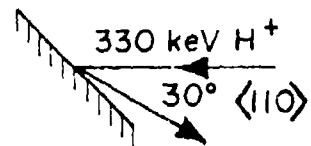


Figure 140 Backscattering Spectrum for GaAs:S⁺, 1 × 10¹⁵ cm⁻²

and 900°C for 15 minutes. The minimum yield (x_{\min}) measured behind the surface peak for the annealed implants ($3 \times 10^{15} \text{ cm}^{-2}$) were found to be .038 as compared to .037 for the virgin crystal. Figure 141(a) shows the TEM bright field micrographs of S implanted GaAs with a dose of $1 \times 10^{15} \text{ cm}^{-2}$ at 120 keV. Figure 141(b) shows the weak beam dark field micrograph of $3 \times 10^{15} \text{ cm}^{-2}$ implant. Examination reveals that there is some residual damage constituting principally of dislocation loops. The size of the loops varies in the case of $1 \times 10^{15} \text{ cm}^{-2}$ implant annealed at 800°C/15 minutes from 200 Å to 600 Å. In the case of $3 \times 10^{15} \text{ cm}^{-2}$ implant however, the sizes were found to vary from 200 Å to 2800 Å. There are an insignificant number of these near the surface, however at larger depths TEM reveals a line length of $3.84 \times 10^{15} \text{ cm}^{-1}$ of both perfect and faulted loops for the $1 \times 10^{15} \text{ cm}^{-2}$ implant.

4.5.2 Lattice Location

The location of the implanted S atoms were determined from channeling experiments in which X-ray emission spectra were collected as a function of tilt angles around the axis. Examples of X-ray emission spectra collected in a random and in a channeling direction are shown in Figure 142 for a GaAs sample implanted with 120 keV S^+ at a dose of $1 \times 10^{15} \text{ cm}^{-2}$ and annealed at 800°C for 15 minutes. The area under the peaks of S-K, Ga-K and As-K are measured as a function of tilt angle. Simultaneous measurements of RBS yield corresponding to a depth on the order of the range of 120 keV S^+ ions ($\sim 2000 \text{ Å}$) were also taken. Figures 143(a) and 143(b) show the angular scans around $\langle 110 \rangle$ and $\langle 100 \rangle$ respectively for the $1 \times 10^{15} \text{ cm}^{-2}$ implant. Very good substitutionality of S is clearly seen from these scans. Also the half width of the S signal is almost the same as the RBS signal



Figure 141 TEM Micrographs of Samples Implanted with 120 keV S^+ Ions to Doses of (a) $1 \times 10^{15} \text{ cm}^{-2}$, Bright-Field and (b) $3 \times 10^{15} \text{ cm}^{-2}$, Weak Beam Dark-Field. The Samples Were Annealed at 800°C for 15 Min

120 keV $S^{+} \rightarrow GaAs$
DOSE: $3 \times 10^{15} \text{ cm}^{-2}$

UES-723-229

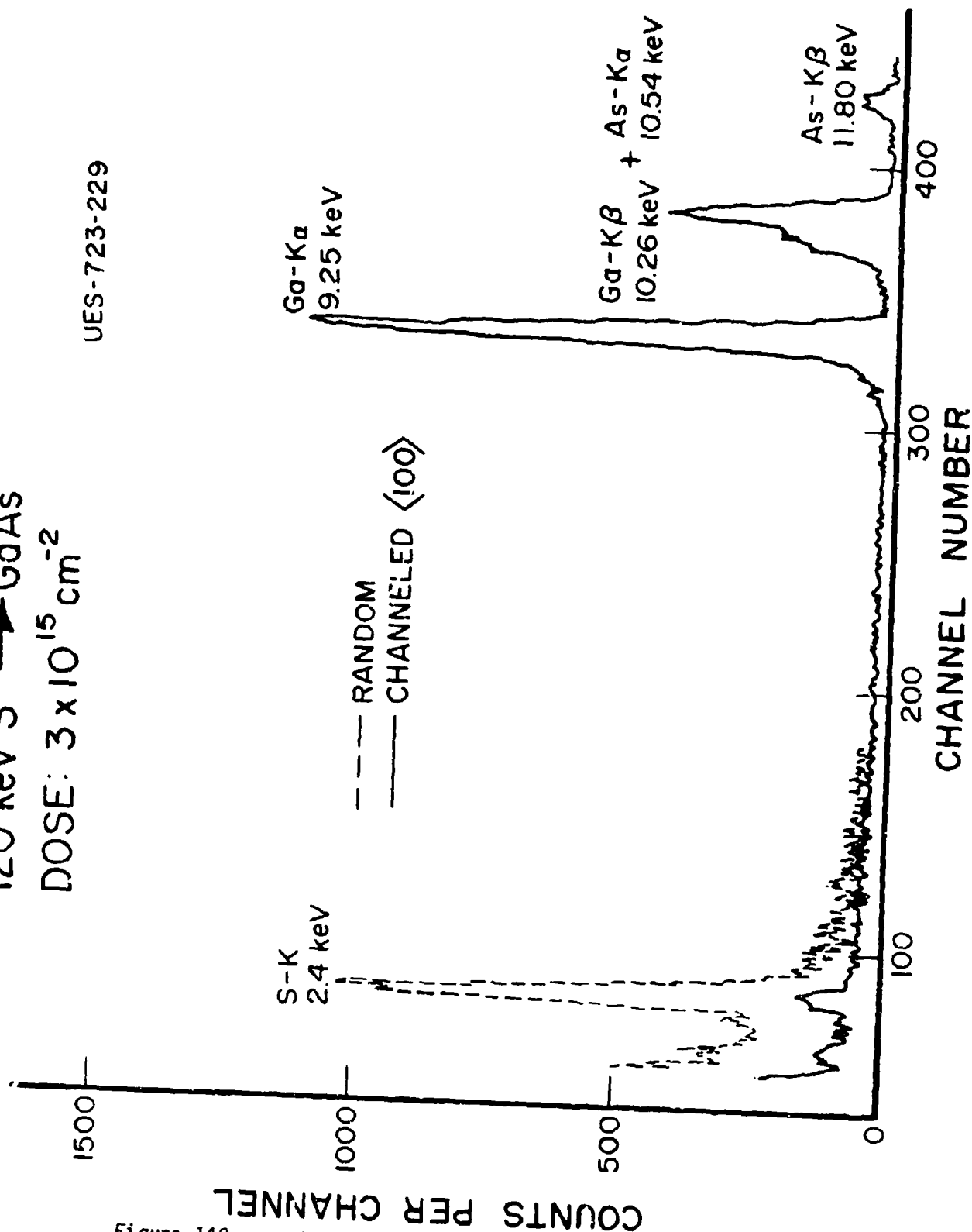


Figure 142

Characteristic X-ray Spectra for GaAs:S⁺
($3 \times 10^{15} \text{ cm}^{-2}$) Random and Channeled

120 keV S \rightarrow GaAs

UES-723-192

DOSE: $1 \times 10^{15} \text{ cm}^{-2}$

ANNEALED AT 800°C/15 MIN $\langle 110 \rangle$

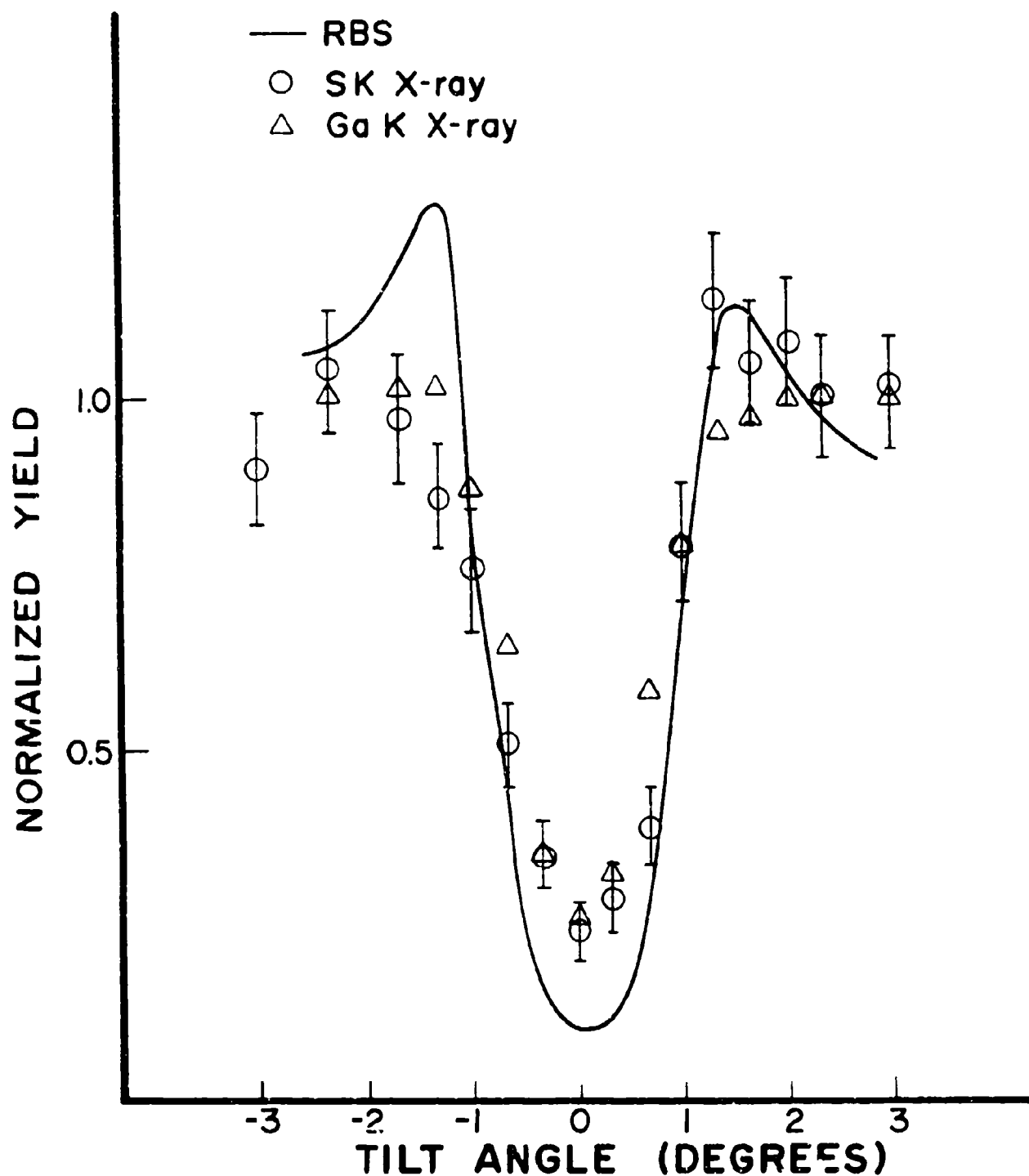


Figure 143 (a) $\langle 100 \rangle$ Channeling Dips of GaAs:S⁺ ($3 \times 10^{15} \text{ cm}^{-2}$, 800°C)

120 keV S \rightarrow GaAs

DOSE: $1 \times 10^{15} \text{ cm}^{-2}$

UES-723-194

ANNEALED AT 800°C/15 MIN $\langle 100 \rangle$

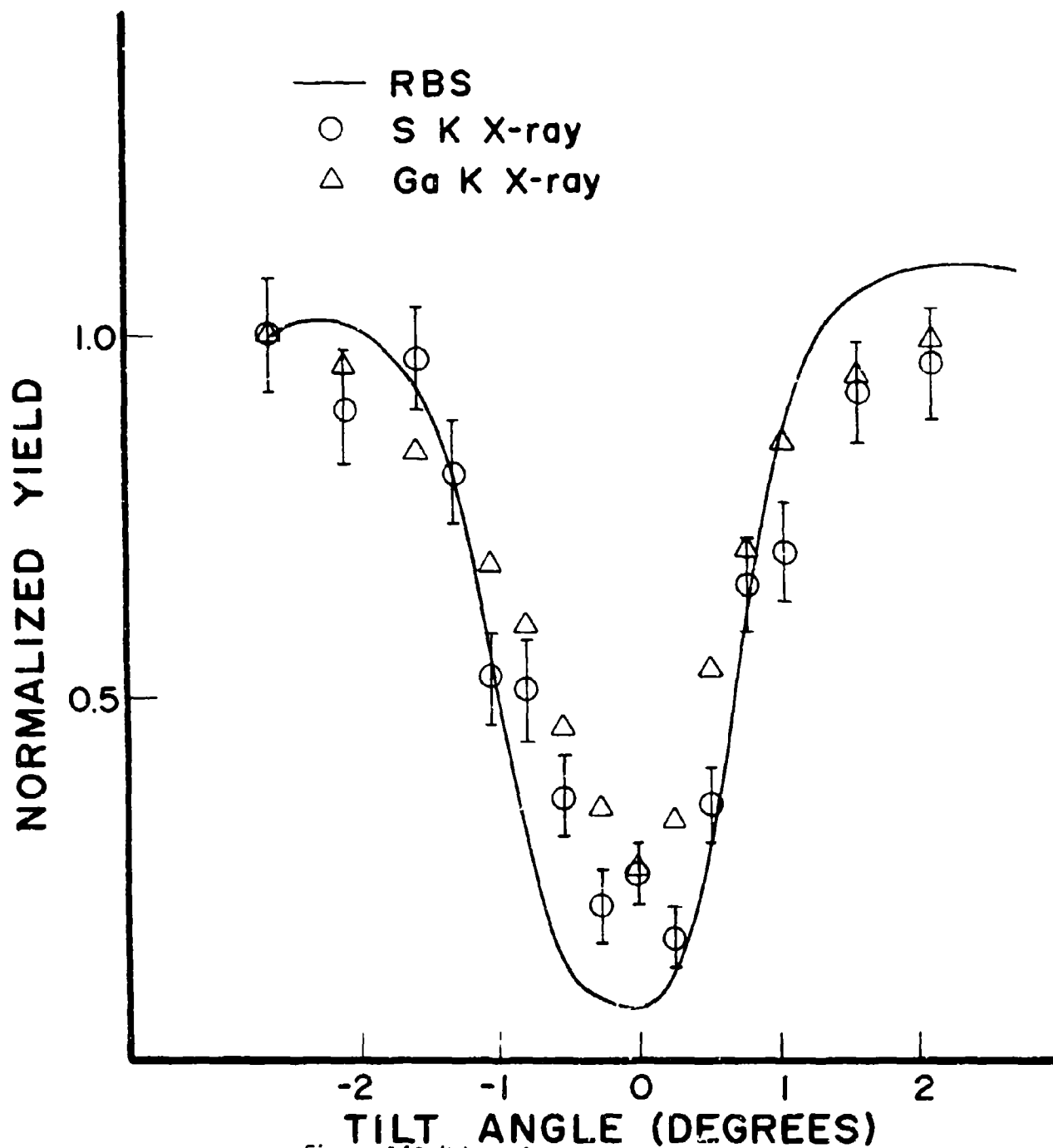


Figure 143 (b) $\langle 100 \rangle$ Channeling Dips of GaAs:S⁺
($3 \times 10^{15} \text{ cm}^{-2}$, 800°C)
259

indicating good alignment of S atoms along the string. It can be seen that the X-ray dip of Ga is narrower than the RBS minimum. Similar results were reported for P and S implants in Ge.⁸⁶ Experiments with an unimplanted GaAs crystal also resulted in narrower X-ray dips as compared to RBS and a higher minimum yield for X-rays.⁸⁷ The reason for this is associated with the greater depth of sampling done for Ga X-rays compared to the depths being analyzed in RBS. From Figure 143 one calculates that substitutional S accounts for 90% of the total S concentration.

Figures 144(a) and 144(b) show the angular scans of the $3 \times 10^{15} \text{ cm}^{-2}$ implant annealed at 800°C/15 minutes. Here also similar substitutional concentration as in the previous case is observed. However, the $\langle 110 \rangle$ dip for S is slightly narrow as compared to RBS dip. In order to obtain a rough estimation of the lateral displacements of the S atoms, the transverse kinetic energy of the incident beam at $\psi_{\frac{1}{2}}^S$ is equated to the Lindhard's continuum potential at a distance r from the GaAs atomic rows.⁸⁸

$$E(\psi_{\frac{1}{2}}^S) = U(r) = \frac{z_1 z_2 e^2}{d} \ln \left(\left(\frac{3a}{r} \right)^2 + 1 \right)$$

Using the $\psi_{\frac{1}{2}}^S$ value from the $\langle 110 \rangle$ angular scan; one can solve the above equation for r which gives an S displacement of 0.28 Å. A similar angular scan around the $\langle 100 \rangle$ direction shows that the displacement there must be 0.1 Å. The above results indicate the formation of preferentially oriented complexes such that the displacement of S takes place primarily along the $\langle 100 \rangle$ direction. However, angular scans after annealing the same sample at 900°C for 15 minutes do not show any measureable S displacement for both $\langle 100 \rangle$ and

120 keV S^+ \rightarrow GaAs

UES-723-223

DOSE: $3 \times 10^{15} \text{ cm}^{-2}$

ANNEALED AT $800^\circ\text{C}/15 \text{ MIN}$ $\langle 110 \rangle$

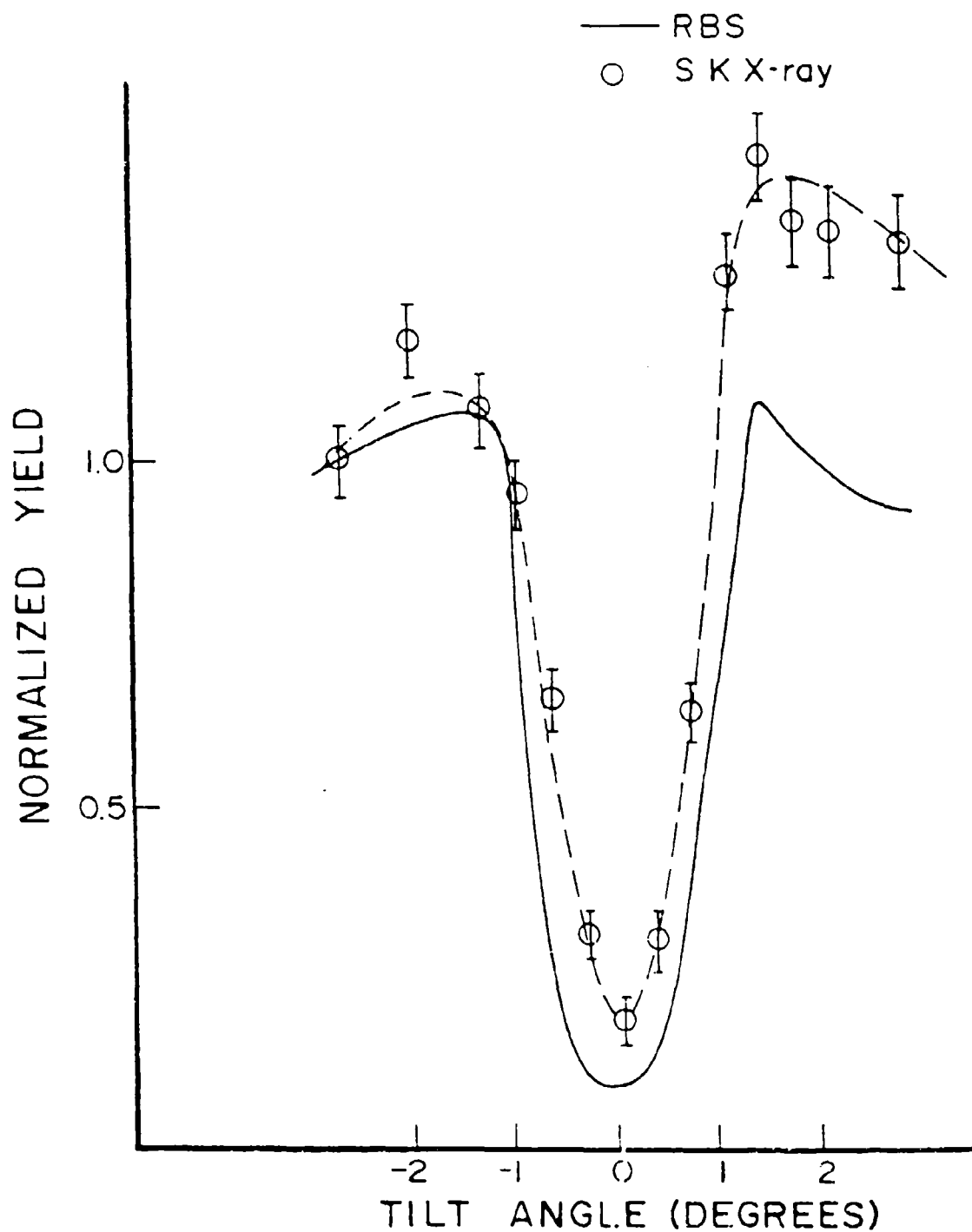


Figure 144 (a) $\langle 110 \rangle$ Channeling Dips of GaAs: S^+ ($3 \times 10^{15} \text{ cm}^{-2}$), 800°C

120 keV S^+ \rightarrow GaAs

UES-723-225

DOSE: $3 \times 10^{15} \text{ cm}^{-2}$

ANNEALED AT $800^\circ\text{C}/15 \text{ MIN}$ $\langle 100 \rangle$

— RBS

○ S K X-ray

NORMALIZED YIELD

1.0

0.5

-2

-1

0

1

2

TILT ANGLE (DEGREES)

Figure 144 (a) $\langle 100 \rangle$ Channeling Dips of GaAs: S^+
($3 \times 10^{15} \text{ cm}^{-2}$), 800°C

$\leq 100 \rangle$ directions [Figure 145(a) and Figure 145(b)] implying a reorientation of the final configuration at the higher temperature.

In order to obtain information about the specific site occupation, we have performed $\langle 110 \rangle$ angular scan parallel to the $\langle 110 \rangle$ plane as described earlier in connection to the Si implanted GaAs. Figure 146 shows a pronounced asymmetry in the S dip indicating that S is occupying one sublattice site. However, the RBS dip, which is made up of signals from both Ga and As, is symmetrical thus confirming the symmetry of the incidence angles about the $\langle 110 \rangle$ direction. A small but noticeable asymmetry is present in the Ga and As PIXE dips. The preferential interaction between the beam and one of the sublattice atomic rows is most pronounced close to the surface only and gradually becomes less observable as the depth increases and finally disappears at larger depth⁸⁴ due to the establishment of statistical equilibrium of the channeling beam. The Ga and As K X-rays are generated over a total depth $\sim 1.5 \mu\text{m}$, in the presnet experiment⁸⁹, of which about 50% is produced in the surface layer of thickness $\sim 400 \text{ \AA}$. This explains the much reduced asymmetry effect in the Ga and As K X-ray dips although a clear asymmetry, $\sim 10\%-12\%$, in the As signal intensity is observable in Figure 145(a). The S asymmetry is in the same tilt direction as the As asymmetry indicating that the implanted S is occupying As lattice sites. The asymmetry for S is very much greater than for As since the S X-rays are being generated in the first 200 \AA from the surface. The asymmetry in the case of S and As is further confirmed by channeling in another $\langle 110 \rangle$ direction at 90° to the previous direction. This results in a reversal of the type of atoms in a string with reference to the beam and the tilt plane. Expected reversal in the asymmetry has been observed for the S and As signals.

UES-723-224

120 keV S^+ \rightarrow GaAs (100)

DOSE: $3 \times 10^{15} \text{ cm}^{-2}$

ANNEALED AT 900°C 15 MIN $\langle 100 \rangle$

— RBS

○ S K X-ray

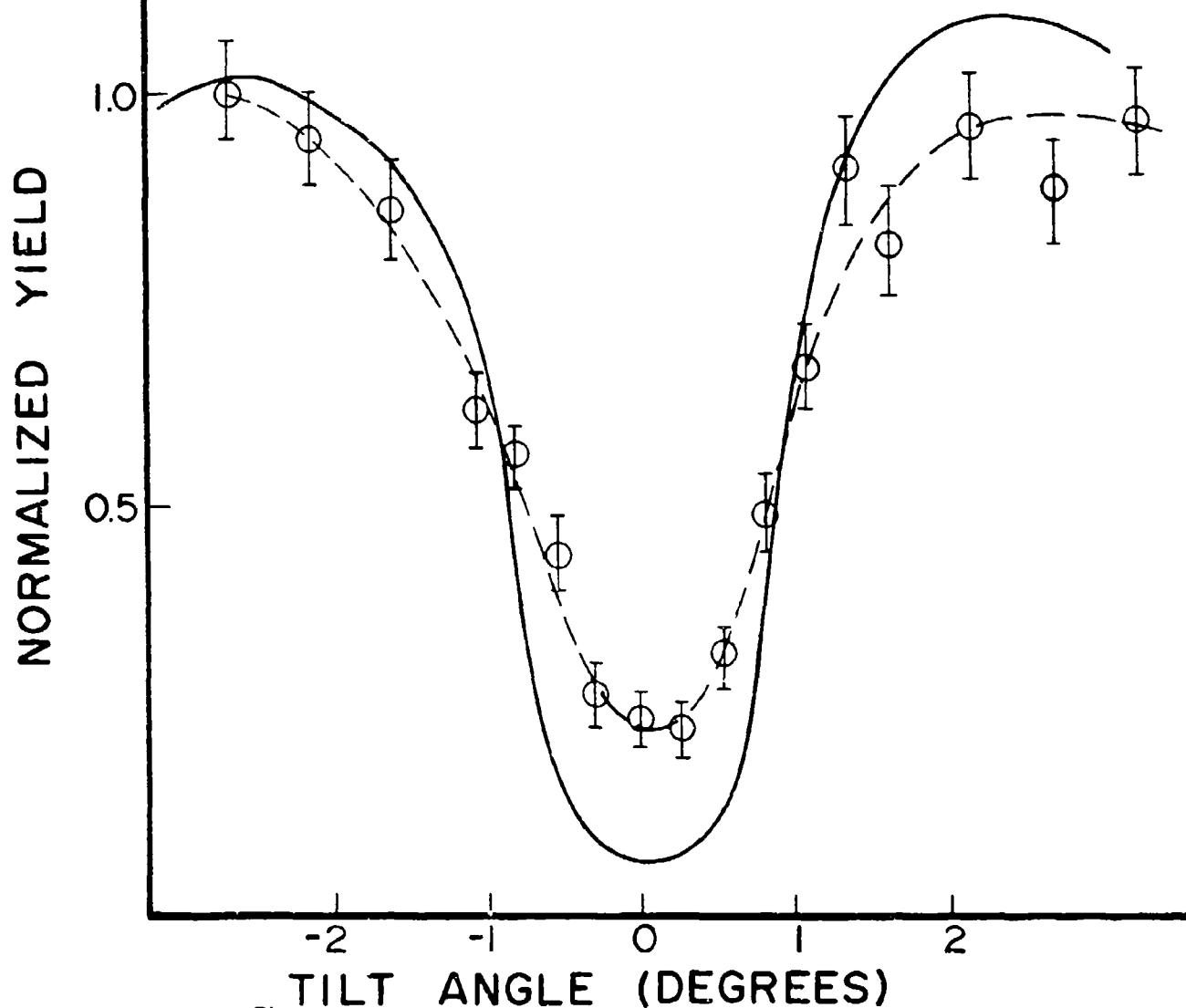


Figure 145 (a) $\langle 100 \rangle$ Channeling Dips of GaAs: S^+
($3 \times 10^{15} \text{ cm}^{-2}$), 900°C
264

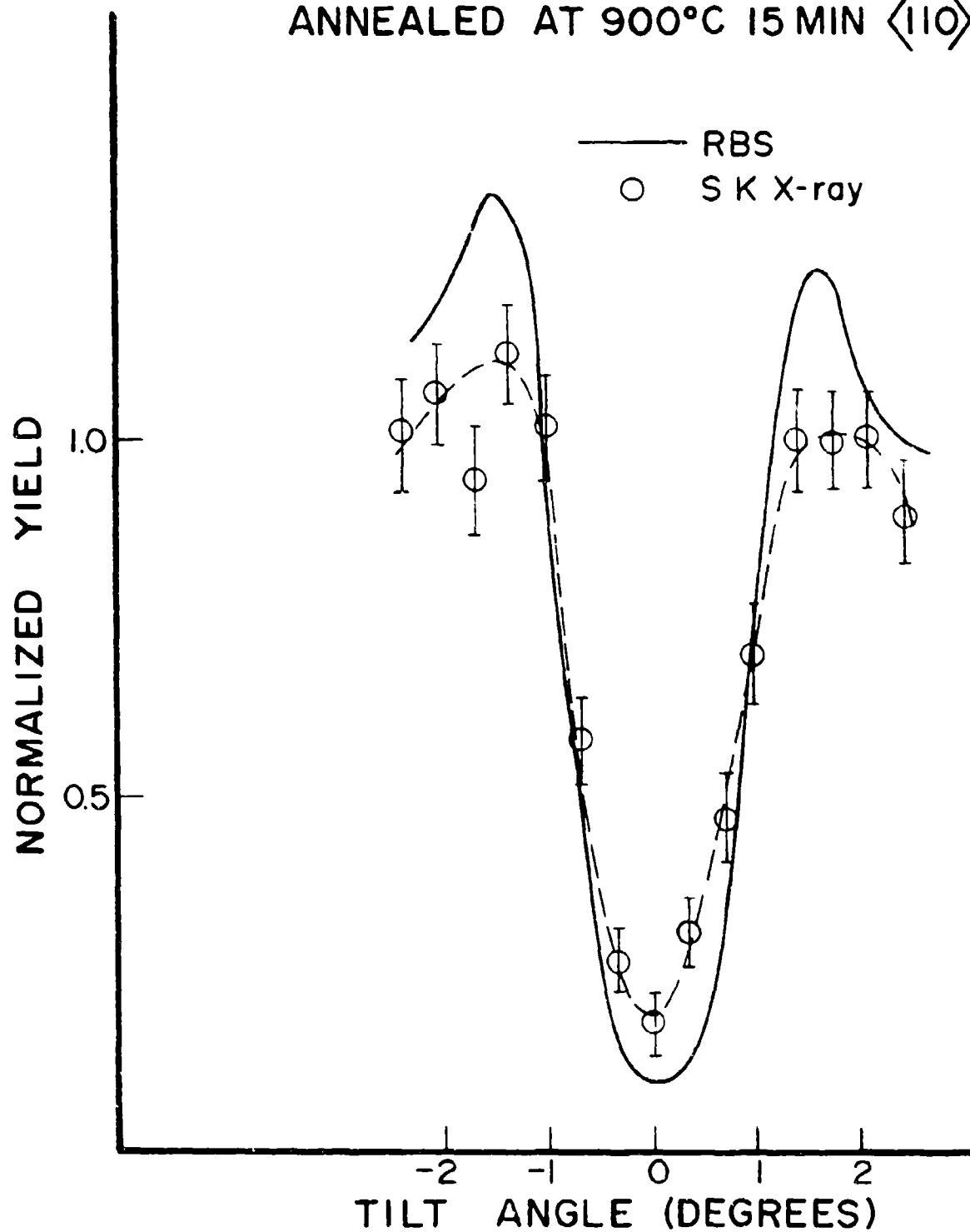
120 keV $S^+ \rightarrow$ GaAsDOSE: $3 \times 10^{15} \text{ cm}^{-2}$ ANNEALED AT 900°C 15 MIN $\langle 110 \rangle$ 

Figure 145 (b) $\langle 100 \rangle$ Channeling Dips of GaAs: S^+ ($3 \times 10^{15} \text{ cm}^{-2}$), 900°C

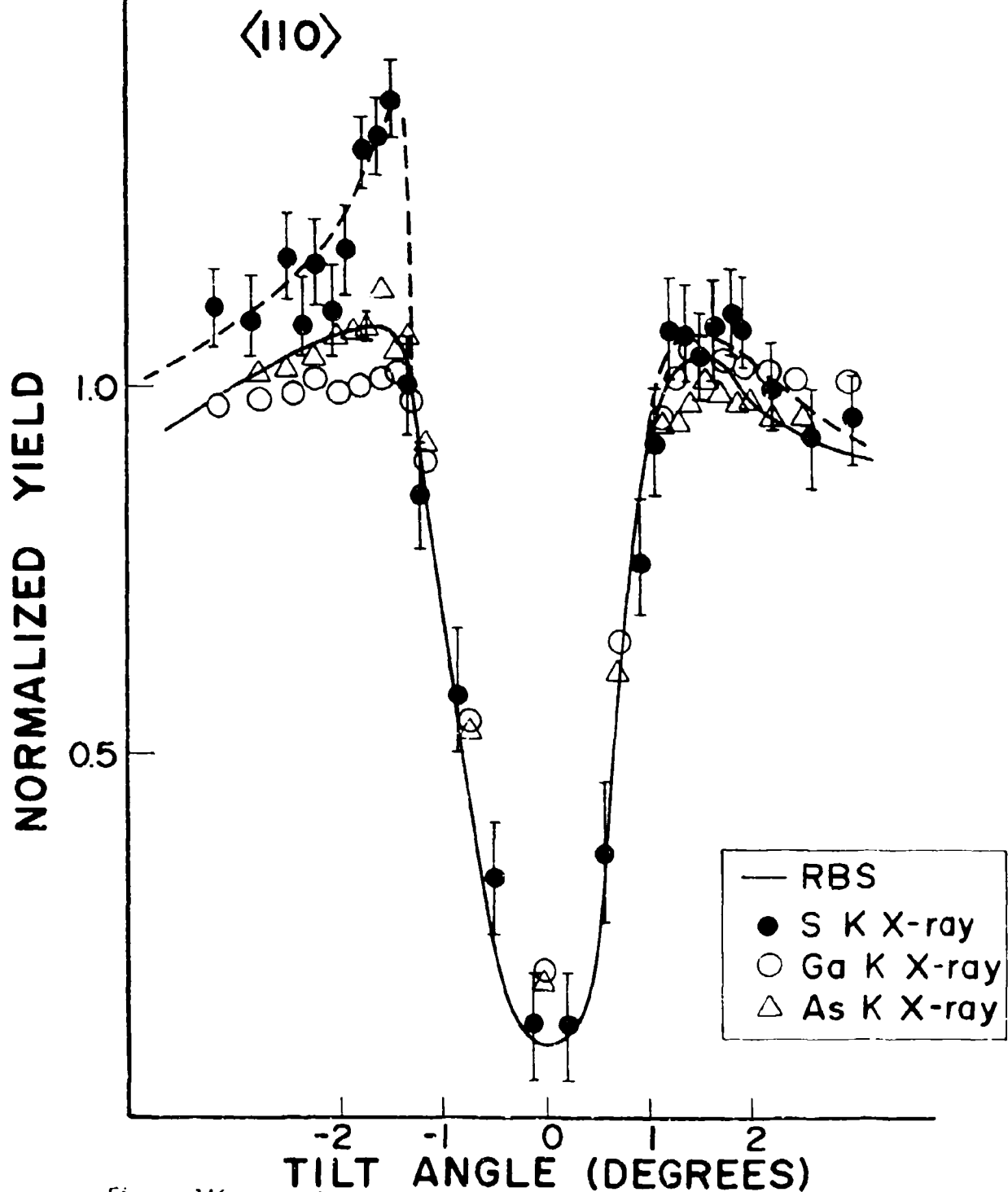
120 keV S^+ \rightarrow GaAs (100)DOSE: $3 \times 10^{15} \text{ cm}^{-2}$ ANNEALED AT $900^\circ\text{C} / 15 \text{ min}$ 

Figure 146

 $\langle 110 \rangle$ Channeling Dip Scanned Parallel to $\langle 110 \rangle$ Plane

4.5.3 Precipitation

A systematic approach was used in evaluating the amount of precipitation for each sample. In the transmission electron diffraction (TED) pattern second phases or precipitates can usually be identified by the presence of extra spots. However, if the volume concentration of the precipitates is not large enough then there will be no extra spots in the TED pattern. Contrast analysis methods are therefore needed to identify this type of precipitate. A spherical particle of dimension $<100> \text{\AA}$ exhibits black-white contrast when observed by TEM under dynamical diffraction conditions ($S \sim 0$). This type of contrast however, is also exhibited by small dislocation loops, i.e., Frank loops.⁹⁰ But due to the three dimensional nature of the precipitates, their black-white vector (\vec{r}) will always be parallel to the \vec{g} vector. This will not be the case for dislocation loops as a consequence of their two dimensional strain distribution. Thus, a distinction between the two entities is possible.

Quantitative evaluation of the percentage of dopant precipitation has been done in the following way. We assumed a spherical nature for the precipitates and then measured the average diameter of the particles in terms of the width of the region separating the black-white lobes. Using this diameter we calculated the total number of implanted atoms associated with the particles in a given area. This number divided by the area will give the area density which can be directly compared with the dose of the implanted ions.

Following the above mentioned identification procedure, we find that the small defects close to the surface in Figure 141(a) are precipitates. Similar defects were observed in bright field pictures of

$3 \times 10^{15} \text{ cm}^{-2}$ implants which are not shown here. The average diameter of these precipitates was found to be $\sim 5 \text{ nm}$. Precipitate analysis shows that only about 4%-6% of the implanted S is precipitated out of solid solution of the implantation doses of $1-3 \times 10^{15} \text{ cm}^{-2}$. The rest of the S is on substitutional lattice sites are measured by PIXE in combination with channeling.

4.5.4 Electrical Measurements

Surface carrier concentration and Hall mobility (μ_H) were measured for both samples and the results are shown in Table 6.

TABLE 6
SURFACE CARRIER CONCENTRATION AND HALL MOBILITY OF 120 keV S^+
IMPLANTED SAMPLES

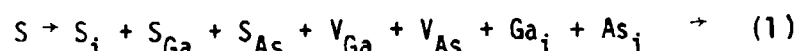
(keV) Energy	Dose (cm^{-2})	Anneal Temperature($^{\circ}\text{C}$)	$N_S(\text{cm}^{-2})$	Activation Efficiency (%)	($\text{cm}^2/\text{V}\cdot\text{sec}$)
	1×10^{15}	800	1.29×10^{13}	1.29	3087
120	3×10^{15}	800	1.75×10^{13}	0.58	3174
	3×10^{15}	900	6.4×10^{13}	2.14	2332

From Table 4, one can see that the electrical activation efficiencies are very low ($\sim 2\%$) even though very high substitutionality ($\sim 90\%$) and low precipitation ($\sim 6\%$) were recorded for these implants.

Very low dopant precipitation and residual damage and very high substitutionality for S measured in the present experiments demonstrate that the precipitation and/or non-substitutionality of S is not the cause of poor

electrical activation. The problem must lie in the formation of complexes involving S atoms on As sites (S_{As}) and vacancies and/or antisite lattice defects that compensate the n-type activity.

We present the following arguments for complex formation based on the information of high substitutionality and low precipitation of S in GaAs. Implantation of S creates vacancies and interstitials and may occupy various possible sites which can be described by the following simplified equation:



where S_i , Ga_i , and As_i represent S, Ga, and As atoms residing in interstitial (non-lattice) sites; S_{Ga} , S_{As} are S on Ga and As sites respectively and V_{Ga} , V_{As} are Ga and As vacancies respectively.

After annealing, since S atoms occupy As sites, both S_i and S_{Ga} will have to combine with V_{As} :



Then all the displaced As atoms (As_i) will not find a vacancy (V_{As}) to occupy resulting in an excess As_i . On the other hand, from equation (1) we see that after annihilation of S_{Ga} and Ga_i , excess V_{Ga} should remain because of the reaction of equation (3). The V_{Ga} may form complexes with S_{As} while As_i may diffuse to the surface. Another possibility, however, is that the As_i may occupy V_{Ga} and form As_{Ga} which is a deep donor and is

doubly positively charged when empty. Electron trapping by this center at room temperature will reduce the electrical activation efficiency of shallow donors.

The displacement of S by $\sim 0.28 \text{ \AA}$ from lattice sites as observed in the case of $3 \times 10^{15} \text{ cm}^{-2}$ implant annealed at 800°C for 15 minutes may be due to the $V_{\text{Ga}}\text{-S}_{\text{As}}$ complex formation which decomposes at 900°C and forms $\text{As}_{\text{Ga}}\text{-S}_{\text{As}}$ complexes.

4.6 Cr IMPLANTATION IN GaAs

4.6.1 Introduction

The physical behavior of chromium in GaAs has been a subject of past and present research interest because of its technological value as an active compensating deep acceptor in as-grown material.⁹¹ Historically, its function has been to compensate native n-type impurities such as Si in GaAs to produce semi-insulating substrate material. As such, it is added to the growth melt in low level, controlled amounts at volume concentrations of about 10^{15} to 10^{17} cm^{-3} . While it is generally accepted that at these levels Cr can be retained in solid solution, volume concentrations much above this are expected to result in some degree of precipitation within the normal GaAs lattice. The extent to which this happens and the characteristics of the precipitation within the normal GaAs lattice. The extent to which this happens and the characteristics of the precipitated material, however, have remained unclear. Little or no information exists on this problem either in the case of ion-implanted Cr or in Cr-doped, as grown GaAs, where Cr can segregate and be trapped in regions of damage caused by implantation of other dopants.

Studies of the redistribution of bulk Cr in GaAs under ion implantation of dopants have shown that chromium undergoes strong segregation

into regions of maximum displacement damage generating volume concentrations from the high 10^{17} cm^{-3} to the low 10^{18} cm^{-3} range.^{67,92} Although it is often assumed that precipitation of Cr will occur under these conditions, no systematic studies have been reported showing that this is the case. Therefore, the objective of the present set of experiments has been to determine the circumstances under which ion-implanted Cr in GaAs will remain in solution under annealing cycles where it is able to interact with the original displacement damage. Such studies are valuable in determining the extent to which Cr could be used as a compensating implant to produce isolation zones between active devices having n-type layers. Chromium implants may also have value as a way of trimming resistivity in selected regions of devices. Previous studies have reported on the behavior of ion-implanted Cr in GaAs in the range of 10^{15} to 10^{21} cm^{-3} .^{92,94} Those investigations were directed at understanding the initial profile of the implanted Cr in the host matrix and its redistribution after annealing. The present study approaches the subject through an investigation of the physical state and materials properties of ion-implanted Cr in moderate dose levels and the microstructural stability of this system under thermal annealing.

The experiments were carried out at Oak Ridge National Laboratory in collaboration with the Solid State Science Division. Protons at 1 meV were used for ion beam analysis. The experimental set up used in these experiments has been described earlier in the equipment section.

The X-ray detector was a windowless Si(Li) detector which could be inserted directly into the target chamber. However, it is necessary to collimate the detector to minimize effects and to eliminate spurious background due to fluorescence of the stainless steel chamber by the ion-induced target X-rays. The magnitude of the fluorescence problem is seen in Figure 147, which contrasts the characteristic X-ray spectra obtained from

UES-723-160

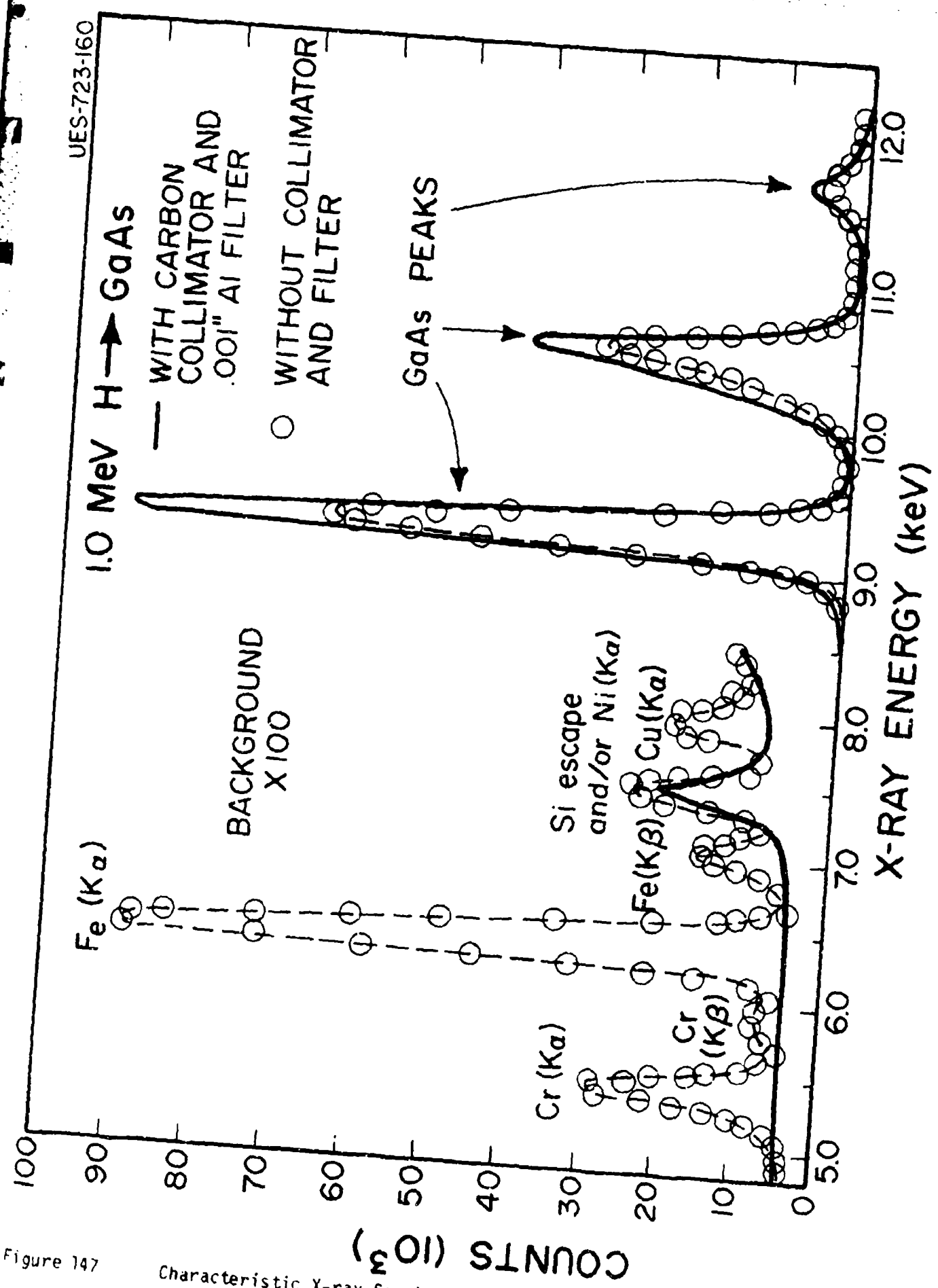


Figure 147

Characteristic X-ray Spectra of GaAs With and Without Collimator

a virgin GaAs sample as acquired with and without the collimator. It is clear that without collimation it would be impossible to distinguish real, quantitative Cr signals in the implanted GaAs from fluoresced X-rays. A 2.5-cm long graphite rod with a 0.5-cm-diam hole through the center served as the collimator. The collimator allowed only X-rays emitted from the ion-bombarded target area to reach the detector and acted as an infinite absorber for any other source of X-rays. Additionally, a 0.001-in Al absorber foil was used to attenuate low-energy X-rays. Figure 148 shows the X-ray features observed, under proper detector collimation, for a chromium-implanted GaAs single crystal. Both the Cr (K_α) and Cr (K_β) X-ray peaks from the implanted species are observable.

A calibration curve was established in order to confirm the accuracy of the implantation dose and the extent to which implanted Cr is retained in GaAs after annealing. As distinct from RBS, PIXE analysis requires a calibration curve for consistent determination of impurity concentration levels. Figure 149 is an example of how such a curve is established. Vapor-deposited calibration foils of Cr on mylar were used at varying concentrations to generate an initial linear relationship between the Cr peaks counts and the areal concentration density. The quantity of Cr on these foils was determined by microbalance weighing. This method has $\pm 10\%$ accuracy for areal densities in the range of 10 to 100 $\mu\text{g}/\text{cm}^2$. These concentrations are equivalent to implantation doses in the range of 10^{17}cm^{-2} , which is very much greater than most implant doses of practical interest in semi-conductors. In order to extend these to lower doses, a log-log plot of areal density versus X-ray counts was established and then extrapolated into the low-dose region of interest. Utilizing a well defined

PIXE SPECTRUM-1 MeV PROTON BEAM

Cr^+ ($120 \text{ keV}, 5 \times 10^{16} \text{ cm}^{-2}$) GaAs (100)

UES-723-142

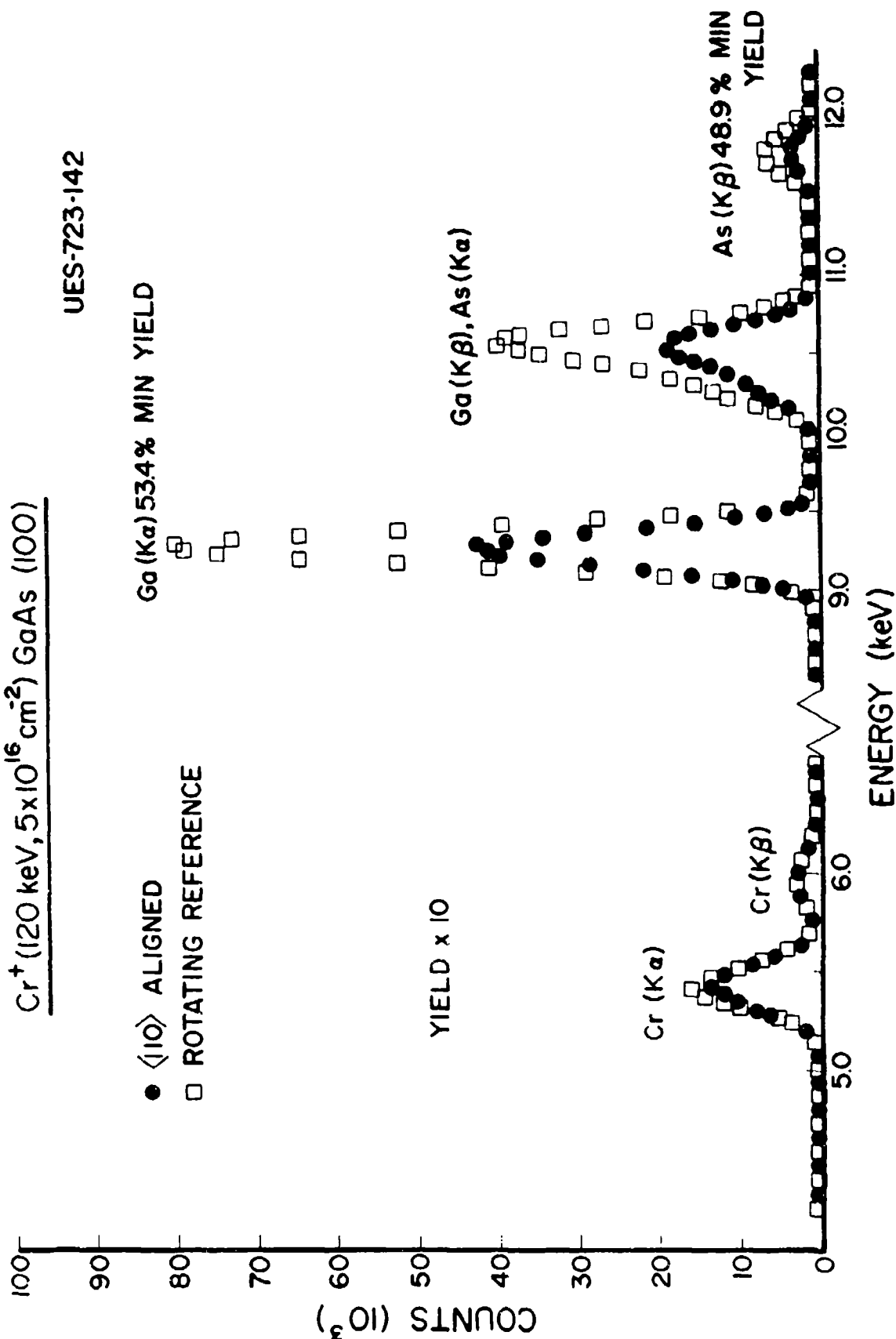


Figure 148

Characteristic X-ray Spectra of GaAs:Cr⁺
($5 \times 10^{16} \text{ cm}^{-2}$)

JAR '10X 1/24H053 / FIG 3 / 40%

set of implants obtained from accurate current integration, a complete set of points is obtained in order to establish a calibration curve extending from the 10^{17} to $1 \times 10^{15} \text{ cm}^{-2}$. An example of a point taken from a specimen implanted with $5 \times 10^{15} \text{ Cr/Cm}^{-2}$ is shown in Figure 149. Once having established this curve, it can be used to check all subsequent concentrations before and after annealing.

4.6.2 Observations and Experimental Results

A sequence of implanted samples was studied that started with a high dose of Cr implanted to $5 \times 10^{16} \text{ cm}^{-2}$ and then systematically reduced through doses of 1×10^{16} , 5×10^{15} , 1×10^{15} , 5×10^{14} , and $1 \times 10^{14} \text{ cm}^{-2}$.

Figure 150 shows RBS channeling data from the three highest dose implants after annealing. These are measured spectra obtained by taking the ratio of the aligned yield along $\langle 110 \rangle$ to a reference random spectrum at equivalent depths. The channeling results from a virgin GaAs sample are included for comparison. The $5 \times 10^{16} \text{ cm}^{-2}$ implanted sample shows an increased scattering yield at and immediately below the surface and is indicative of poor crystal recovery during annealing. Additionally, the large dechanneling rate behind the surface (compared to the virgin sample) shows that a high density of defects remained in the epitaxially regrown layer. This also suggests that there is poor incorporation of the Cr into minimum strain configurations of the crystal lattice. Crystal recovery for the $5 \times 10^{15} \text{ cm}^{-2}$ implants is seen to be much better. The slightly higher than virgin dechanneling rates do suggest, however, the presence of a small density of extended defects. Results from TEM have been obtained for these cases as well as for lower doses and are presented below with data from PIXE analyses.

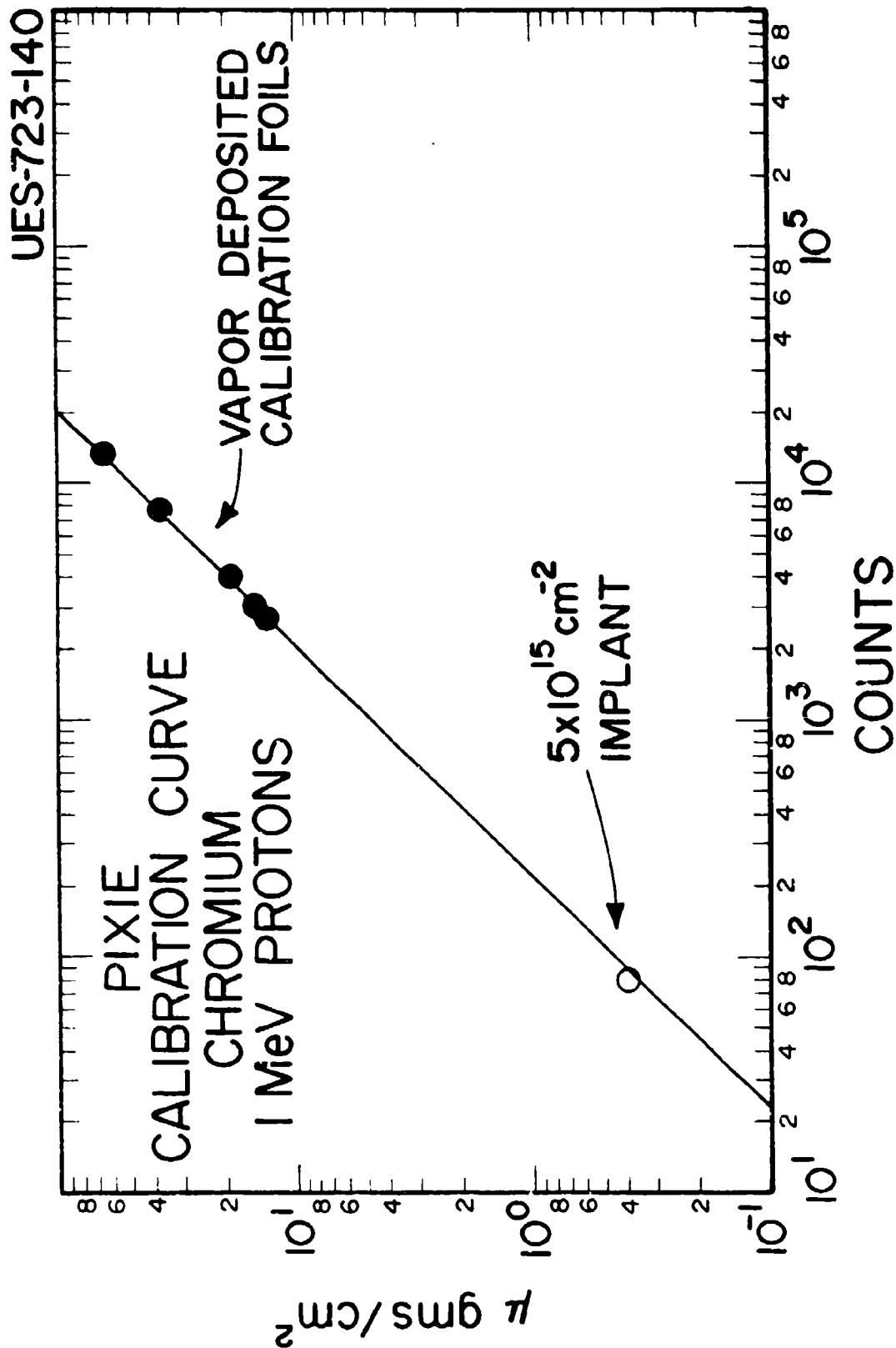


Figure 149

PIXIE Calibration Curve for GaAs:Cr⁺

JPV AUG 82 H053 / FIG 4 60°

Cr \rightarrow GaAs $\langle 110 \rangle$ ALIGNED

- Cr⁺ (120 keV, $5 \times 10^{16} \text{ cm}^{-2}$) GaAs (100) - ANNEALED
- Cr⁺ (120 keV, $5 \times 10^{15} \text{ cm}^{-2}$) GaAs (100) - ANNEALED
- Cr⁺ (120 keV, $1 \times 10^{15} \text{ cm}^{-2}$) GaAs (100) - ANNEALED

□ VIRGIN

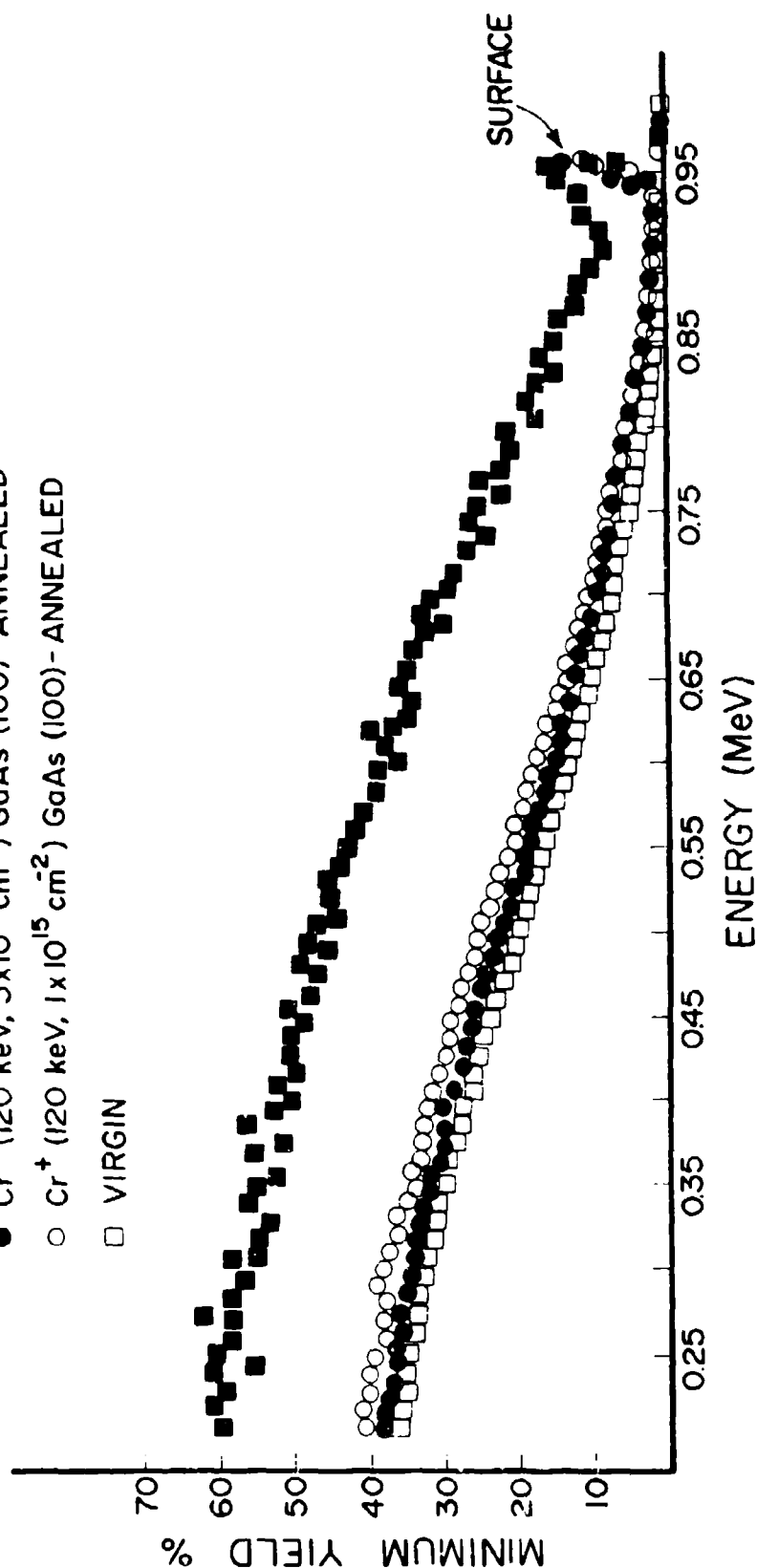


Figure 150

Channeling Spectra for GaAs:Cr⁺ Annealed at 900°C,
15 min

Figure 151 shows TEM results from the $5 \times 10^{16} \text{ cm}^{-2}$ specimen that yielded the large dechanneling in Figure 150. Figure 151(a) is a bright-field micrograph showing apparent coarse precipitation of the chromium. The diffraction pattern [Figure 151(c)] shows the presence of matrix spots superimposed on a ring pattern. An analysis of the diffraction pattern reveals that the ring pattern corresponds to that of chromium-rich particles oriented randomly within the host matrix. Figure 151(b) is a dark-field micrograph, imaged with the objective aperture on a part of the diffraction ring confirming the presence of chromium-rich precipitates. The dimensions of these second-phase particles appear to be in two general size categories of about 500- and 1000- Å diameter. Also, the precipitates are seen to be adjacent to or associated with dislocation lines in the GaAs and the precipitate. The plastic deformation associated with the formation of these dislocations is a consequence of the strain relief that occurs as the precipitates are incoherently incorporated into the lattice. These effects would account for the high dechanneling observed for this specimen in Figure 150. The results of combined RBS and PIXE angular scans are presented in Figure 152. The proton backscattering yield from the GaAs matrix is taken over a depth window set between 20 and 220 nm. The Cr X-ray signal is the integrated yield from all of the implanted chromium. It is expected that these atoms will be distributed within approximately the same depth range as was set for the backscattering window. As can be seen in Figure 152, the PIXE yield shows a flat distribution across the $\langle 110 \rangle$ scan direction, whereas the proton back-scattering shows a well defined channeling dip. These results are consistent with the damage analysis and TEM of Figure 150 and 151 showing poor lattice recovery and coarse precipitation of the chromium, with the

UES-723-188

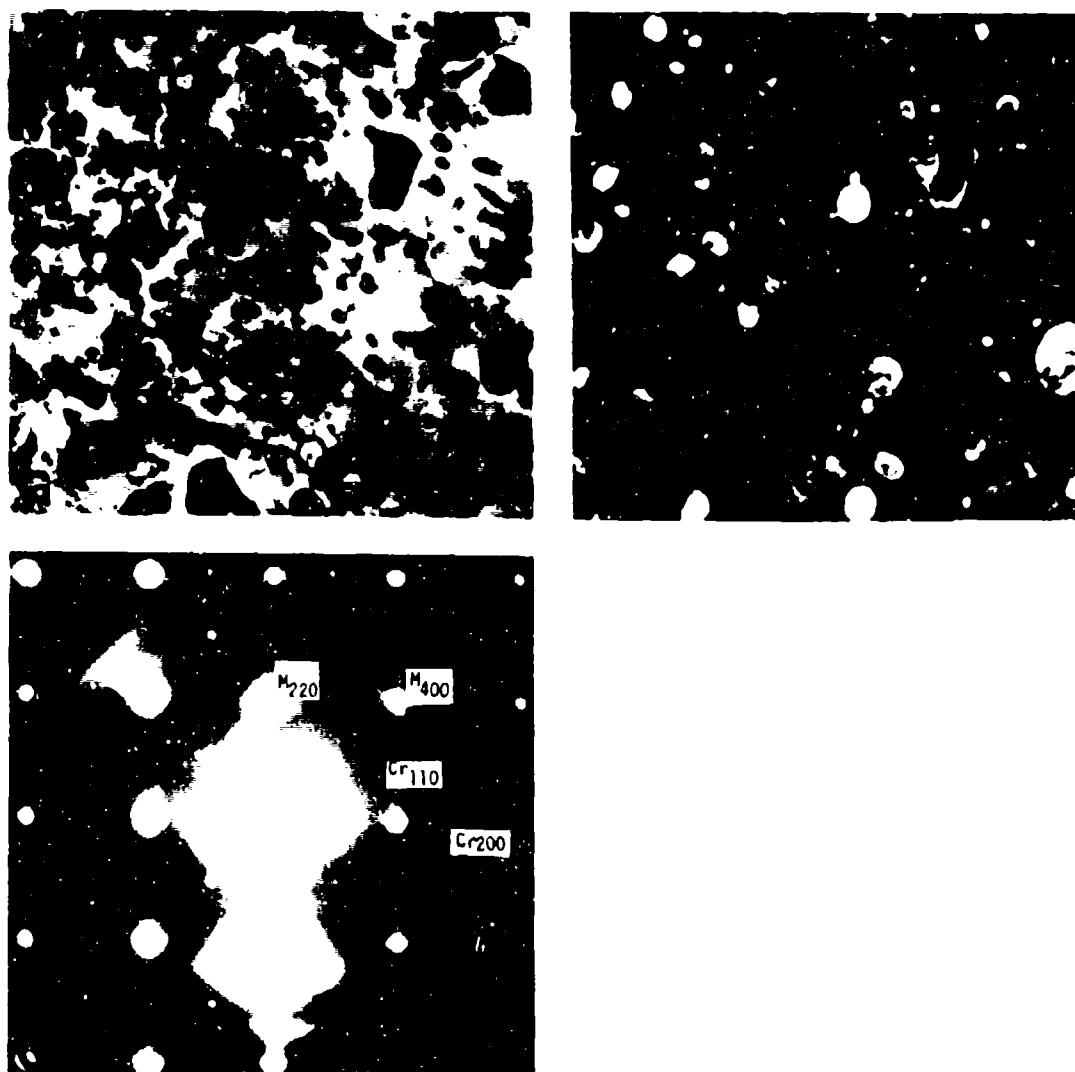


Figure 151 Electron Micrographs From Specimen Implanted with Chromium to a Dose of $5 \times 10^{16} \text{ cm}^{-2}$ and Annealed at 900°C for 15 min (a) Bright Field; (b) Dark Field; and (c) Diffraction Pattern

<110> ANGULAR SCAN 1.0 MeV $H^+ \rightarrow Cr^+$ (120 keV, $5 \times 10^{16} \text{ cm}^{-2}$)GaAs (100)● H^+ BACKSCATTERED YIELD
(window 20-220 nm)

□ Cr K X-RAY YIELD

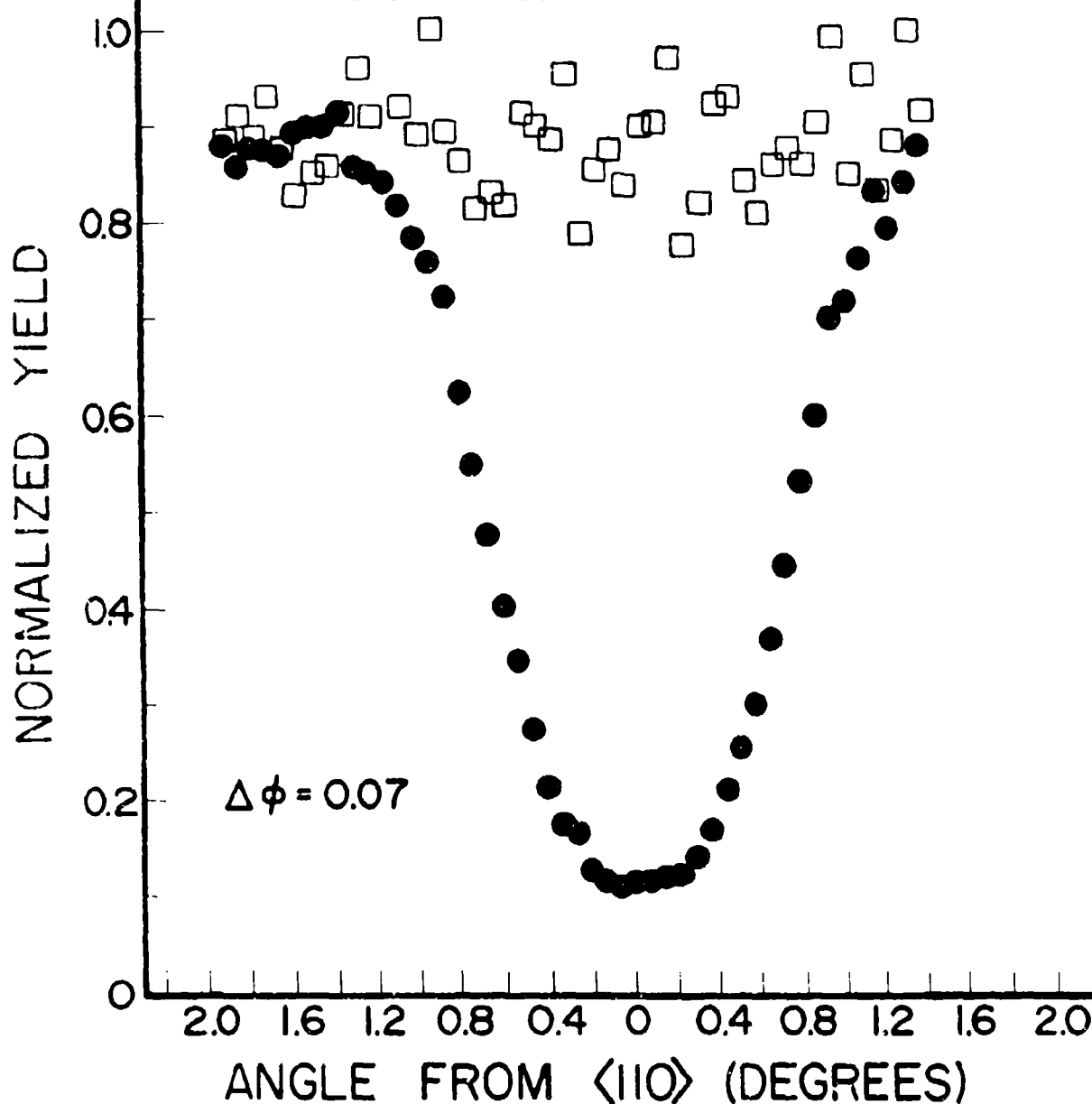


Figure 152

Combined RBS-PIXE Channeling Angular Scans for
Specimen Implanted with $5 \times 10^{16} \text{ Cr/cm}^2$ and
Annealed at 900°C for 15 min

precipitates being randomly oriented within the GaAs lattice. At this dose of $5 \times 10^{16} \text{ cm}^{-2}$ the material is basically a two-phase Cr-GaAs system.

The results associated with a 120-keV implant to a dose of $5 \times 10^{15} \text{ cm}^{-2}$ are presented in Figure 153. This sample, protected with a CVD pyrolytic Si_3N_4 cap, was annealed at 900 C for 15 minutes. The $5 \times 10^{15} \text{ cm}^{-2}$ sample shown in Figure 150 was annealed for the same temperature and time as that in Figure 153, however, it was protected by a plasma-deposited Si_3N_4 cap. (TEM results from a similar sample covered with a plasma-deposited Si_3N_4 cap showed the same microstructural features as those from the pyrolytically capped sample of Figure 153.) The micrographs in Figure 153 were taken in dynamical, two-beam diffraction with Figure 153(a) being conventional bright field ($g/220$). Figure 153(c) is a conventional dark-field image and Figure 153(b) is a weak-beam dark-field image ($g/311$) of the same area as Figure 153(a). The intensity distribution around the diffraction spots in the selected-area diffraction patterns obtained from these specimens indicated that the implanted region has recovered its crystal structure to a high degree of perfection in agreement with the results of Figure 150. The average size of the precipitates was determined to be 7.5 nm, and from contrast characteristics the strain distribution around the precipitates was found to be three dimensional, which corresponded to the spherical shape of the precipitates. From the micro-diffraction patterns obtained from individual precipitates, it was determined that they are chromium precipitates. In order to determine the extent to which the pyrolytic capping process was responsible for these precipitation effects, we prepared and examined a similar sample using the plasma-deposition procedure. The results were essentially the same showing similar chromium precipitate

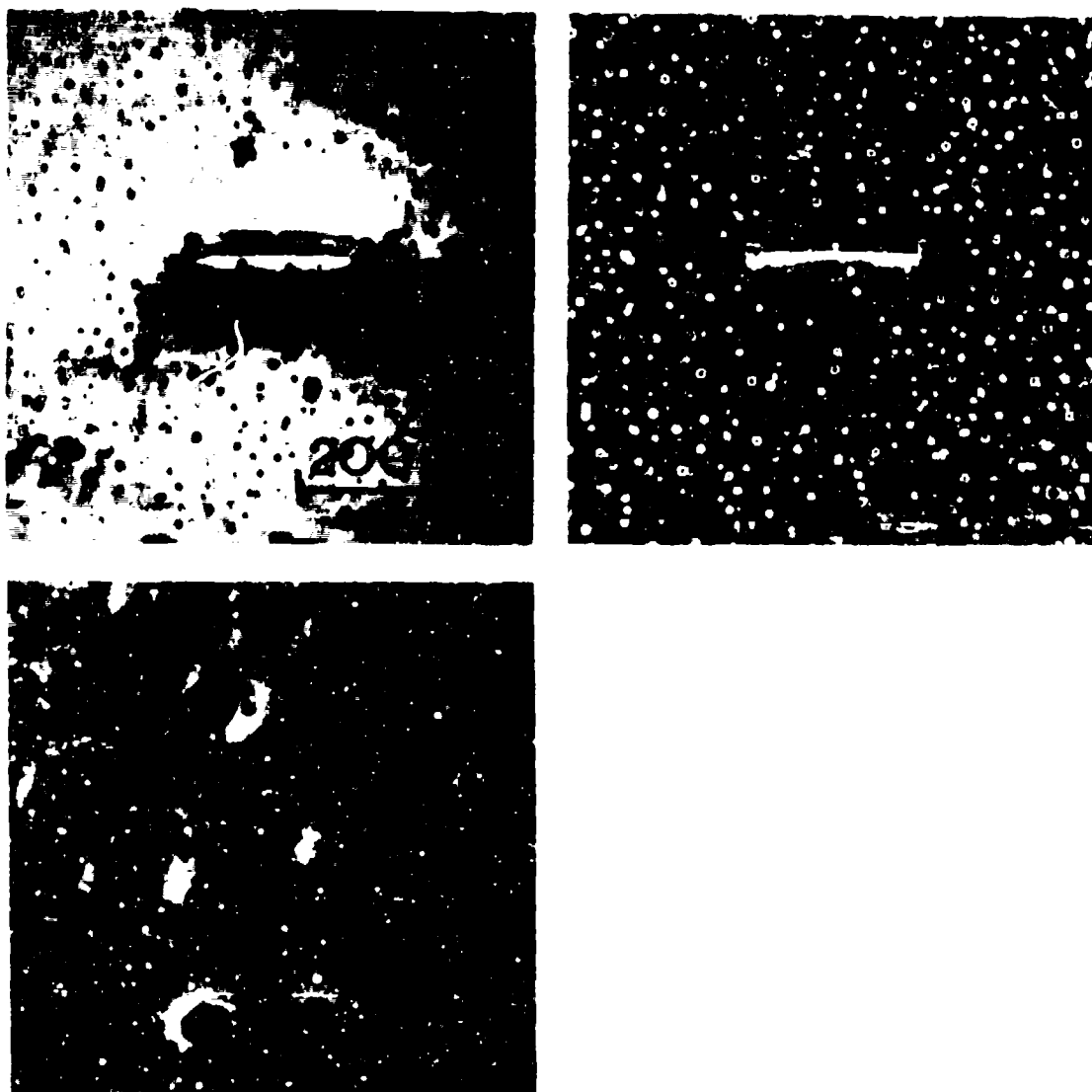


Figure 153 Electron Micrographs for Specimen Implanted with Chromium to a Dose of $5 \times 10^{15} \text{cm}^{-2}$ and Annealed at 900°C for 15 Min (a) Bright Field; (b) Weak Beam Dark Field; and (c) Standard Dark Field

distributions. We concluded that the capping procedure had little or no effect on the primary structure observed in Figure 153(b). The results of detailed angular scans in RBS-PIXE were also similar for the two different capping procedures. Such an angular scan is shown in Figure 154, where it is seen that the Cr yield is approximately flat across the scan but with a small broad flux peak component. This suggests that the fraction of Cr that is in solid solution has an interstitial-like behavior in GaAs.

Continuing downward in concentration, the results from a 120-keV implant of Cr in GaAs to a dose of $1 \times 10^{15} \text{ cm}^{-2}$ are shown in the electron micrographs of Figure 155. Figure 155(a) is a weak-beam dark-field image ($g/3g$ in dynamical diffraction with $S=0$). Figure 155(b) is a bright-field (dynamical $S=0$) micrograph. Figure 155(c) is also bright-field but in $9/220$ under $S=1$ conditions. In this particular case, the dose of $1 \times 10^{15} \text{ cm}^{-2}$ at 120 keV results in microstructure that is significantly different from the previously discussed higher dose implants. In addition to the dislocation lines, loops, and faulted loops scattered throughout the zone of observation, there is a very fine scale distribution of defect spots that are also observable. These could be small clusters of defects, such as interstitial or vacancy loops, or they could be precipitates and thereby have three-dimensional character. In order to distinguish which of these is the case, reference is made to Figure 155(b) where, under dynamical diffraction conditions, black-white contrast is observed. It has been determined from this figure that the black-white vector is aligned parallel to the operating 220 _ vector. This indicates that the spots seen in the micrograph are three dimensional in nature⁹⁰ and are therefore precipitates.

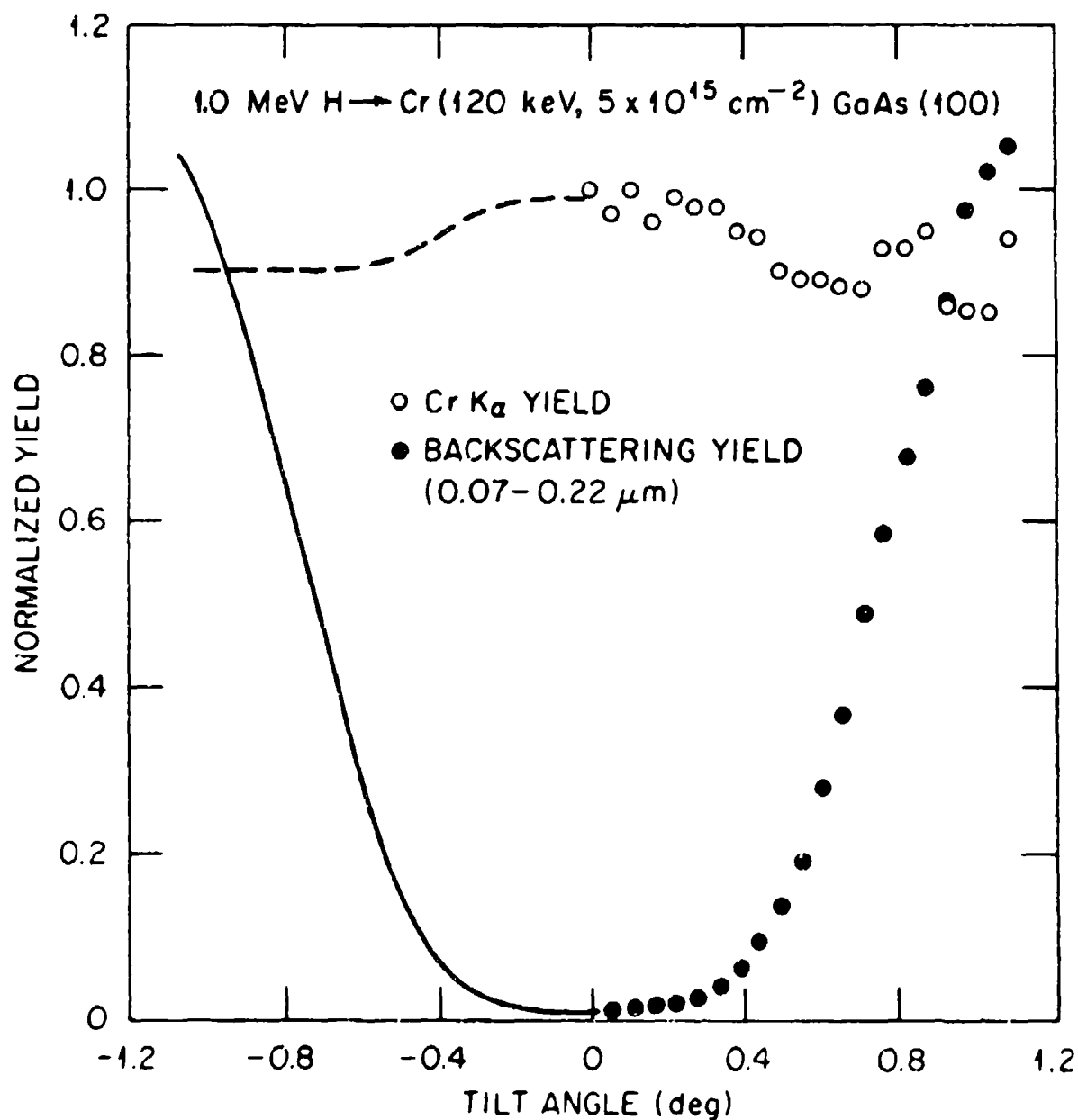


Figure 154

Combined RBS-PIXE Channeling Angular Scans for
Specimen of Figure 153 Implanted with
 $5 \times 10^{15} \text{ Cr/cm}^2$ and Annealed at 900°C for 15 min

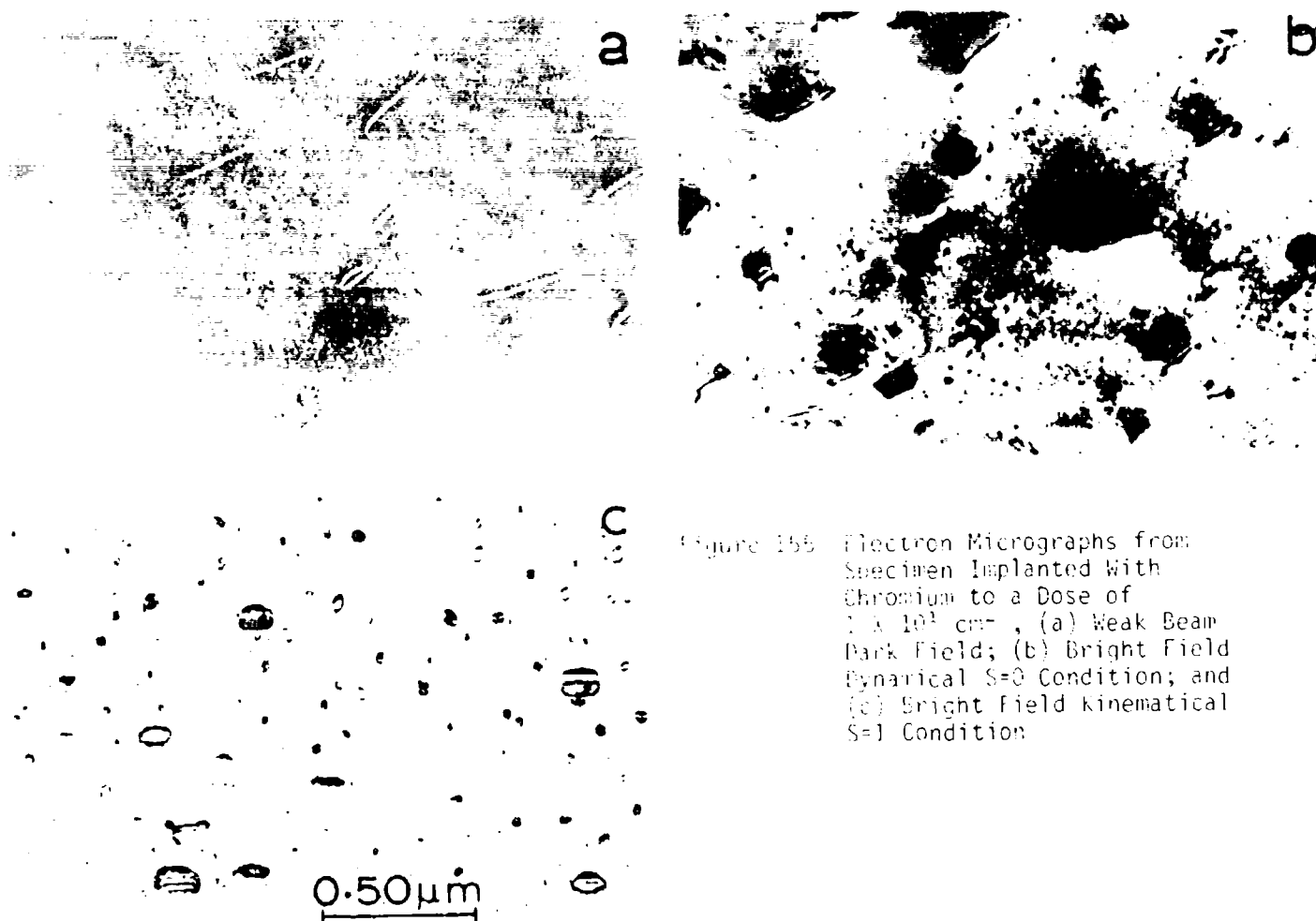


Figure 155 Electron Micrographs from Specimen Implanted With Chromium to a Dose of $1 \times 10^{17} \text{ cm}^{-2}$, (a) Weak Beam Dark Field; (b) Bright Field Dynamical $S=0$ Condition; and (c) Bright Field kinematical $S=1$ Condition



Figure 156 Bright-Field Micrograph from Specimen Implanted with Chromium to a dose of $1 \times 10^{17} \text{ cm}^{-2}$

In the case of the $1 \times 10^{15} \text{ cm}^{-2}$ implant, the observed areal density of chromium associated with these clusters is $0.4 \times 10^{15} \text{ cm}^{-2}$, with the average cluster diameter being 6.4 nm. This result demonstrates that on the order of 40% of the $1 \times 10^{15} \text{ cm}^{-2}$ implant of chromium has precipitated after annealing and that about 60% was absorbed into the GaAs matrix. Within the experimental uncertainties associated with such a measurement one would expect, on the basis of the above result, that a similarly prepared sample implanted to a dose of $5 \times 10^{14} \text{ cm}^{-2}$ would show a greatly reduced relative percentage of precipitated material. This is in fact observed to be the case. Figure 156 shows the observations made on a $5 \times 10^{14} \text{ cm}^{-2}$ chromium implant in GaAs that had been plasma capped with Si_3N_4 . The defect spots observable in black-white contrast are confirmed to be precipitates through the parallel nature of the g and l vectors. An analysis of these clusters shows that the average diameter is 5.6 nm (which is slightly smaller than the previous case); however the number density accounts for only $0.43 \times 10^{14} \text{ cm}^{-2}$ of the chromium atoms compared to an implant dose of $5 \times 10^{14} \text{ cm}^{-2}$. Thus an approximate precipitation level of 9% has occurred, with remaining Cr having been absorbed into solution in the GaAs lattice. Thus, a factor of 5 reduction in dose resulted in a similar factor of 5 reduction in precipitated fraction. This suggests that at $5 \times 10^{13} \text{ cm}^{-2}$ there would be less than 1% precipitated after a similar annealing cycle. Work that we have performed⁹⁵ indicates that for an implant fluence of $1 \times 10^{14} \text{ cm}^{-2}$, the Cr concentration profile redistributes extensively during annealing. The peak concentration in the as-implanted distribution ($R_p \sim 50 \text{ nm}$) is expected to be about $1 \times 10^{19} \text{ cm}^{-3}$ for such an implant. However, after annealing there is observed

a narrow near-surface peak concentration reaching $8 \times 10^{18} \text{ cm}^{-3}$ in the first few hundred angstroms and then, after a small depleted region at 500 \AA with a concentration $\sim 10^{18} \text{ cm}^{-3}$ for depths of 1000 to 3000 \AA . This rapid diffusional redistribution during an annealing should significantly reduce precipitation effects at doses in the range of $1 \times 10^{14} \text{ cm}^{-2}$. It is likely that chromium will be nearly 100% atomically distributed for such an implant dose under the annealing conditions used here. These concentrations, however, are in excess of the normal solubility limit of Cr in GaAs.⁹⁶ Electrical measurements on the compensating properties of Cr implanted at $1 \times 10^{14} \text{ cm}^{-2}$ are needed to determine the effective number of carriers that are removed by an individual implanted chromium atom. It is possible that Cr may be in tiny clusters smaller than the observational limit of the microscope (i.e., $< 10 \text{ \AA}$) and as such would have indeterminate consequences on the electrical properties.

4.7 Ar IMPLANTATION IN GaAs

It can be noted from the studies described so far that, although a complete epitaxial regrowth of the implantation induced amorphous layer takes place in the temperature range of $300\text{--}500^\circ\text{C}$, the regrown layer always contains a high density of defects in the form of microtwins. The origin of these microtwins is not known and could not be related to the implanted impurity. However, most of these studies were done with GaAs crystals implanted with various ions which are also used as dopants. After annealing, these dopants are likely to occupy a particular sublattice site. In a compound semiconductor, the displaced sublattice atoms may cause bonding error at the regrowth front by occupying wrong lattice positions thus forming a nucleation center for microtwins. Studies with the implantation of inert gas ion, on the

other hand, will eliminate the above mentioned possibility because it is not likely to occupy any particular lattice position. In addition, recent experiments⁹⁷ have shown enhanced electrical activation efficiency for GaAs preimplanted with argon and then subsequently implanted with Si and annealed at 825°C. thus, there is good reason to establish a general understanding of the behavior of argon implantation in GaAs.

Undoped semi-insulating liquid encapsulated Czochralski (LEC) grown GaAs wafers with $\langle 100 \rangle$ orientation were implanted with 700-keV Ar^+ ions in a nonchanneling direction at a dose of 5×10^{15} ions/cm².

4.7.1 Results and Discussion

The transmission electron diffraction (TED) pattern of the as-implanted specimen, Figure 157(a) shows the presence of amorphous rings and single crystal spots, indicating therefore the presence of a buried amorphous layer. The strong beam bright field micrograph, Figure 157(b), shows the presence of point defect clusters. We tried to see the presence of bubbles by underfocusing the image, but no bubbles were found. Figure 158(c) shows the bright field micrograph of the same specimen after annealing at 200°C for 30 minutes. No change in the microstructure was observed. The TED pattern (not shown here) still shows the presence of an amorphous layer.

The TED pattern in a $\langle 100 \rangle$ orientation (not shown here) of the same specimen, after annealing at 400°C for 30 minutes, shows the presence of extra spots together with the matrix spots. The origin of these extra spots was determined by tilting the specimen to a (114) orientation. Figure 159(a) shows the TED pattern in this (114) orientation. The extra spots are observed to be present at $1/3$ (511) and $2/3$ (511) positions. Following the analysis of Pashley and Stowell,⁷⁶ it was found that the extra spots are due to twins

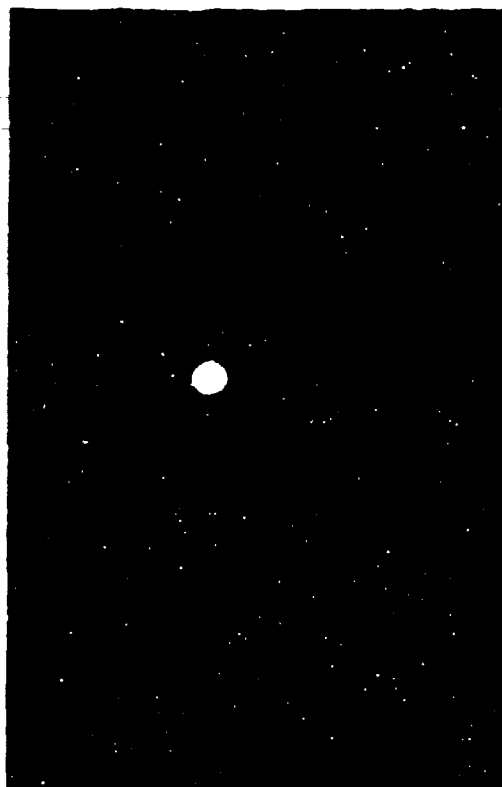


Figure 157 (a) TED Pattern of $\langle 001 \rangle$ orientation of Ar^+ Implanted GaAs (700 keV, $5 \times 10^{15} \text{ cm}^{-2}$). Strong Beam Bright Field Micrographs ($g=220$);

(b) As Implanted



(c) Annealed At 200°C for 30 Min



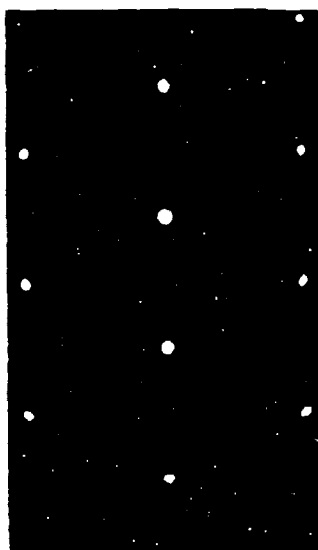
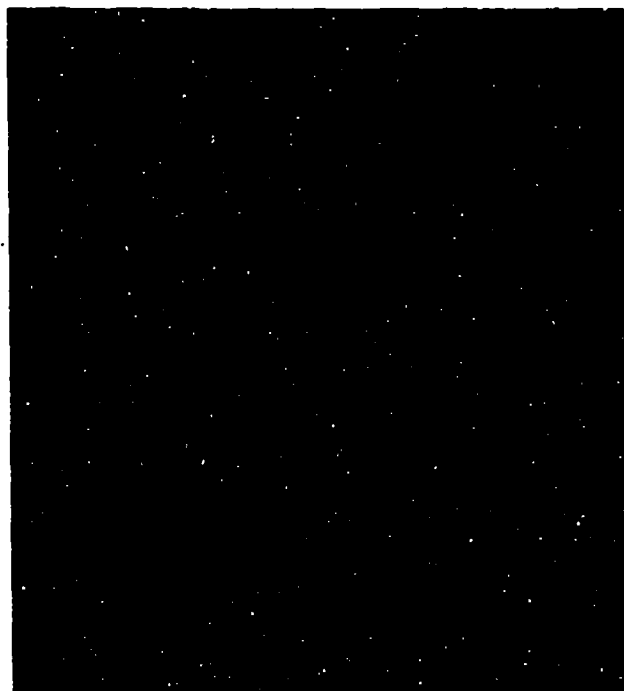


Figure 158 (a) TED Pattern in $\langle 114 \rangle$ Orientation of Ar^+ Implanted GaAs (700 keV, $5 \times 10^{15} \text{ cm}^{-2}$) after Annealing at 400°C for 30 Min. Strong Beam Bright Field Micrographs ($g=220$);

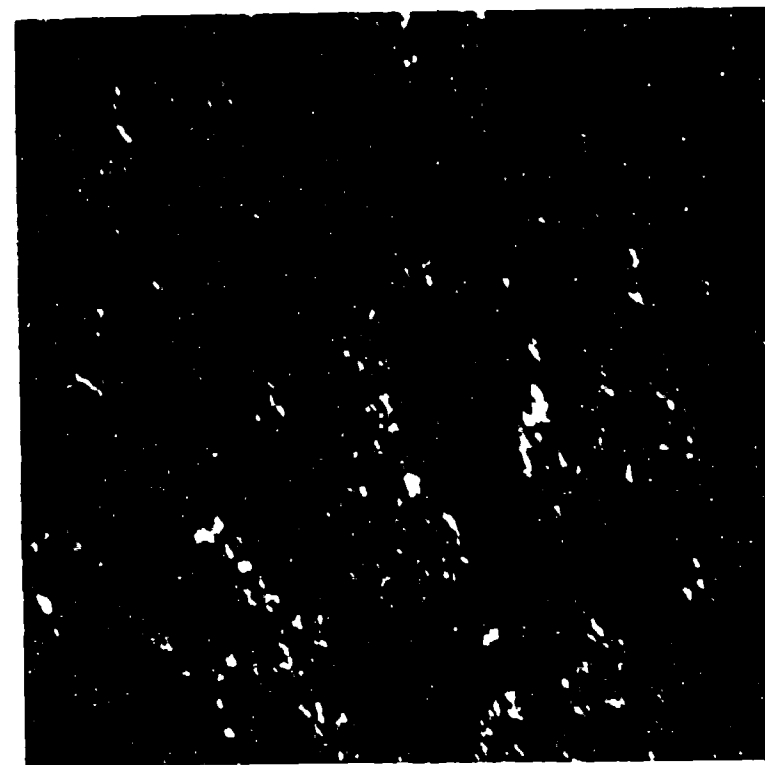
(b) Annealed at 400°C for 30 Min;



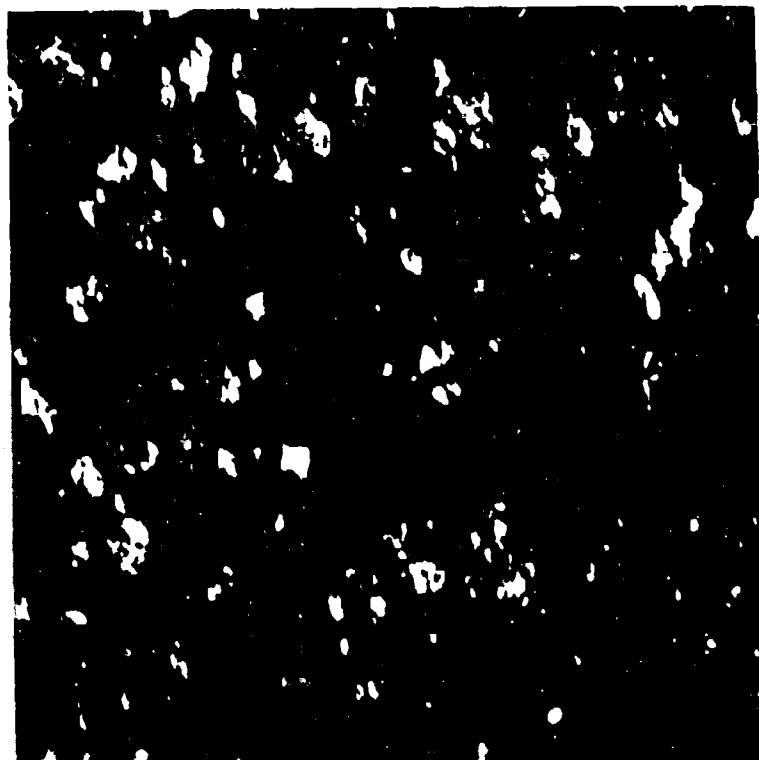
(c) Annealed at 600°C for 30 Min



UES-723-25I



(a)



(b)

Figure 159 Dark Field Micrographs of Ar^+ Implanted GaAs (700 keV , $5 \times 10^{15} \text{ cm}^{-2}$) Imaged with the Twin Spots
(a) Annealed at 400°C for 30 Min; (b) Annealed at 600°C for 30 Min

lying on (111) planes. Figure 159(b) is a strong beam bright field micrograph showing that all the point defect clusters have been annealed out with only the microtwins remaining. Figure 159(c) is a strong beam bright field micrograph of the same specimen after further annealing at 600°C for 30 minutes. No bubbles have been observed after 400 and 600°C annealing. Figure 160(a) and 160(b) are the dark field micrographs (as imaged with one of the twin spots), of the specimen after annealing at 400 and 600°C for 30 minutes, respectively. It is clearly evident that a greater volume of the implanted layer is occupied by twins in the 400°C anneal as compared to the 600°C case. It is concluded therefore that considerable annealing of the twins has taken place after annealing the specimen at 600°C.

Annealing at 850°C for 15 minutes has been performed on a different specimen, after encapsulating it with Si_3N_4 . The channeling spectrum of this specimen, Figure 106 shows that the damage level is rather low near the surface extending to a depth of about 900 Å. A sharp increase of dechanneling at this depth indicates the presence of high density of crystalline defects. The TED pattern (not shown here) of this specimen shows that only GaAs matrix spots are present, indicating that at 850°C the twins are completely annealed out. Figure 161(a) shows the strong beam bright field micrograph close to the surface region. The circular feature seen in this micrograph are the internal gas bubbles caused by the simultaneous condensation of vacancies and inert gas atoms. Figure 161(b) is a bright field micrograph of the same area but slightly underfocused. Under these circumstances the bubbles are clearly visible. The size distribution of these bubbles varies from 130 to 400 Å. Figure 161(c) is a strong beam bright field micrograph that images the region just inside the surface. Dislocations

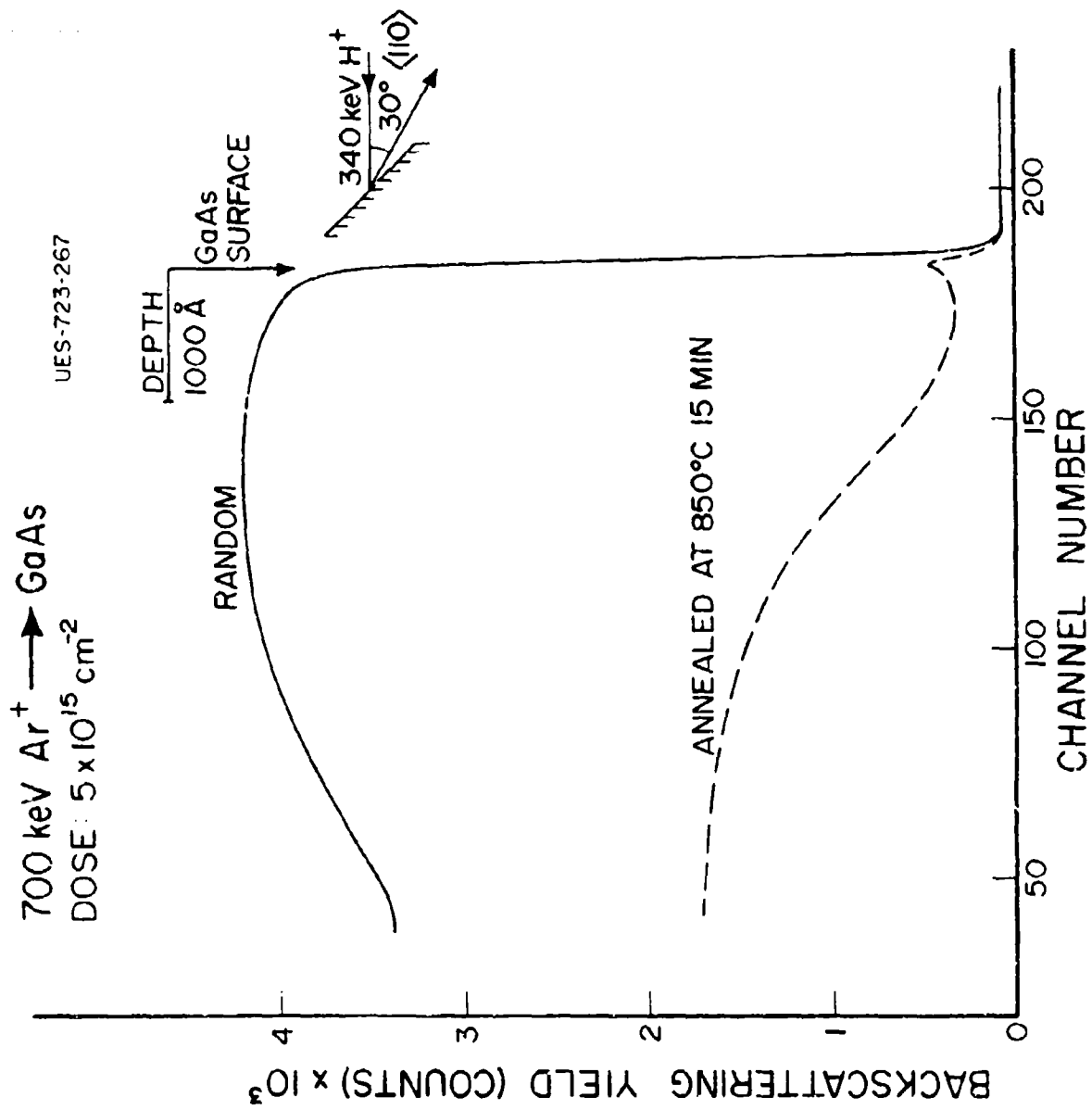


Figure 160 Channeling Spectrum of GaAs:Ar^+

UES-723-252

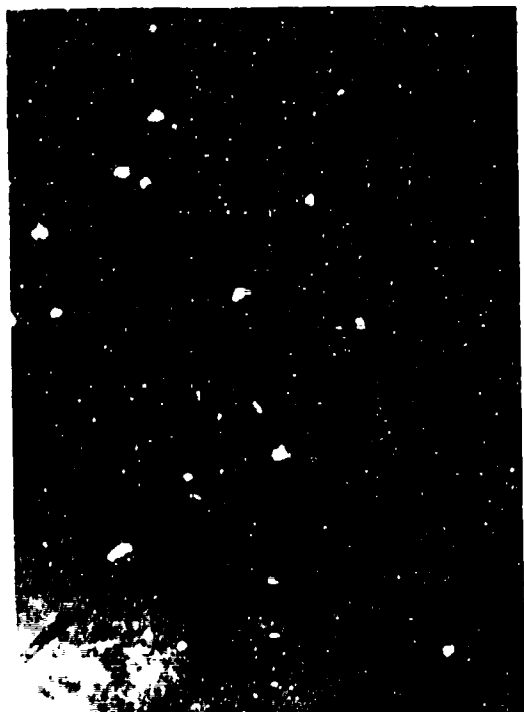
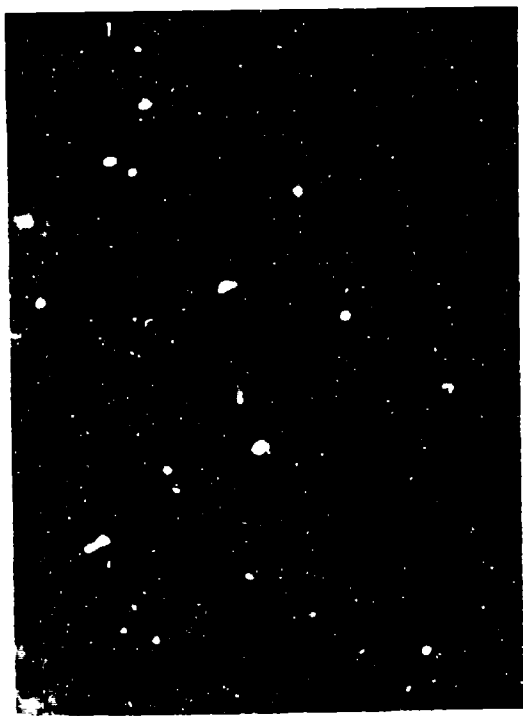


Figure 161 Strong Beam Bright Field Micrographs of The Ar^+ Implanted GaAs Specimen After Annealing At 850°C for 15 Min. (a) Close to the Surface, in Focus; (b) Same as (a), but Slightly Underfocus; (c) Slightly Inside the Implanted Layer; (d) Further Inside the Implanted Layer

were found to be present together with the bubbles. Many of the bubbles are found to be present in association with and/or attached to dislocations. Those bubbles that are associated with dislocations are found to be bigger in size than the ones which are not. The bubble sizes in this region vary from 200 to 600 Å. Figure 161(d) is a strong beam bright field micrograph of the same specimen further inside the implanted layer. Dislocation tangles are present together with bubbles. The dislocation density is found to be much higher in the deeper layer as compared to that in the near surface region. Thus the sharp rise in the dechanneling at ~ 900 Å can be explained as due to the onset of the dense dislocation tangles. Figure 162 is a weak beam dark field micrograph of the deeper implanted layer showing the dense dislocation tangles.

The precipitation of Ar in GaAs, i.e. the formation of bubbles is confirmed by lattice location experiments using RBS channeling in combination with PIXE. The location of the Ar atoms was determined by channeling experiments in which angular scans around $\langle 100 \rangle$ and $\langle 110 \rangle$ were performed. Examples of PIXE spectra in random and channeling $\langle 110 \rangle$ directions are shown in Figure 163.

It should be noted that the Ar-K signal remained almost unaltered while the beam direction changed from channeling to random. An angular half scan is shown in Figure 164 again showing that the Ar atoms are not occupying any unique lattice positions such as specific interstitial or substitutional sites thus confirming the TEM observations.

From these results it became clear that the formation of twins and therefore a defective regrowth of amorphous GaAs cannot be avoided by the implantation of higher influences of Ar^+ ions. It can thus be concluded that the nucleation of microtwins in GaAs is not related to the implanted

UES-723-253

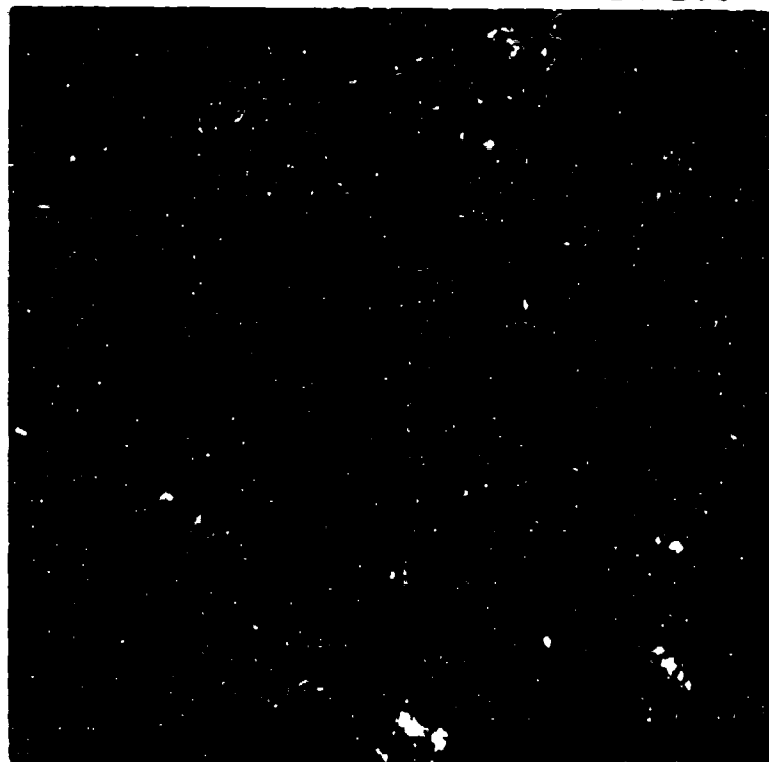


Figure 162 Weak Beam Dark-Field Micrograph of GaAs:Ar⁺ After
Annealing at 850°C, 15 Min

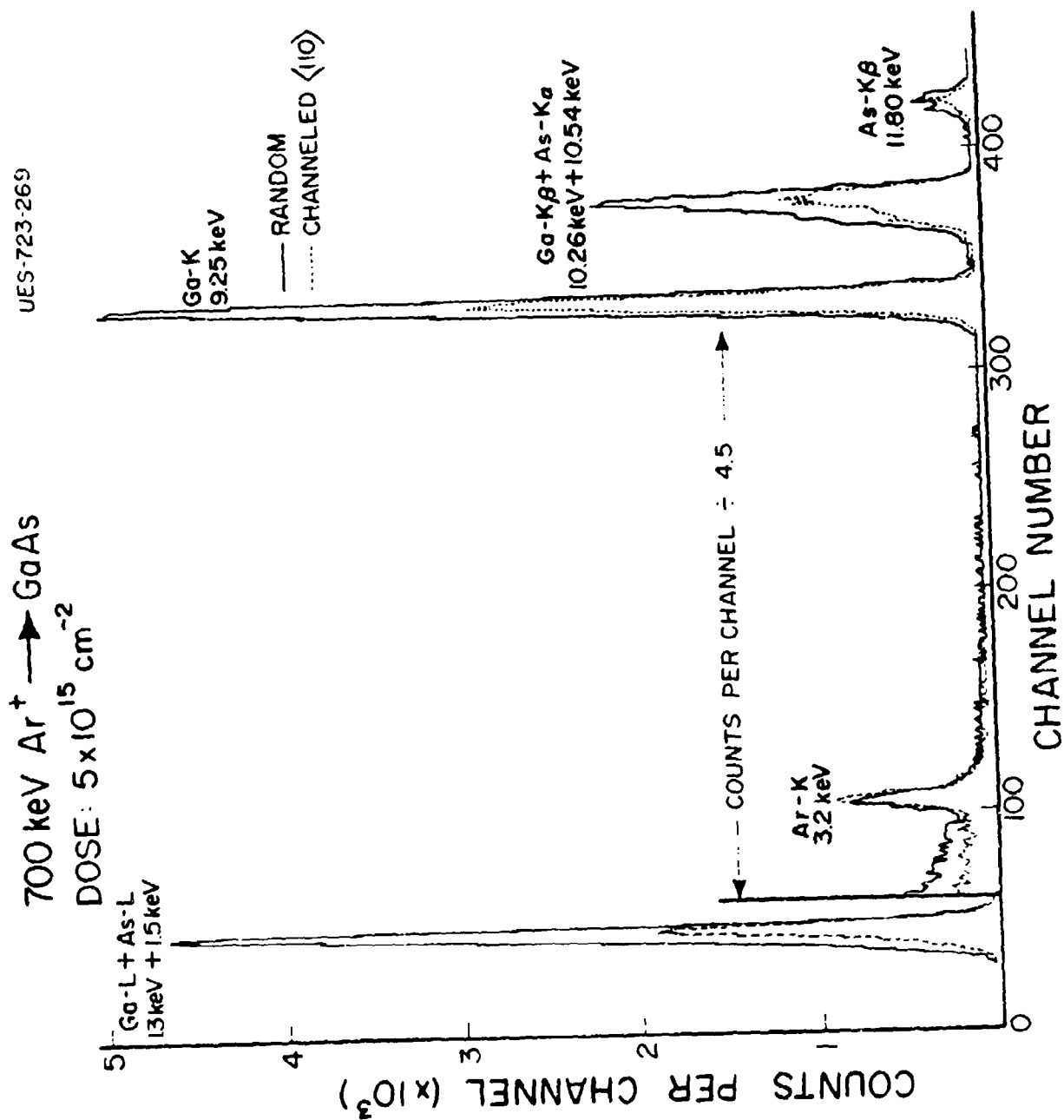


Figure 163

Characteristic X-ray spectra for GaAs:Ar⁺
297

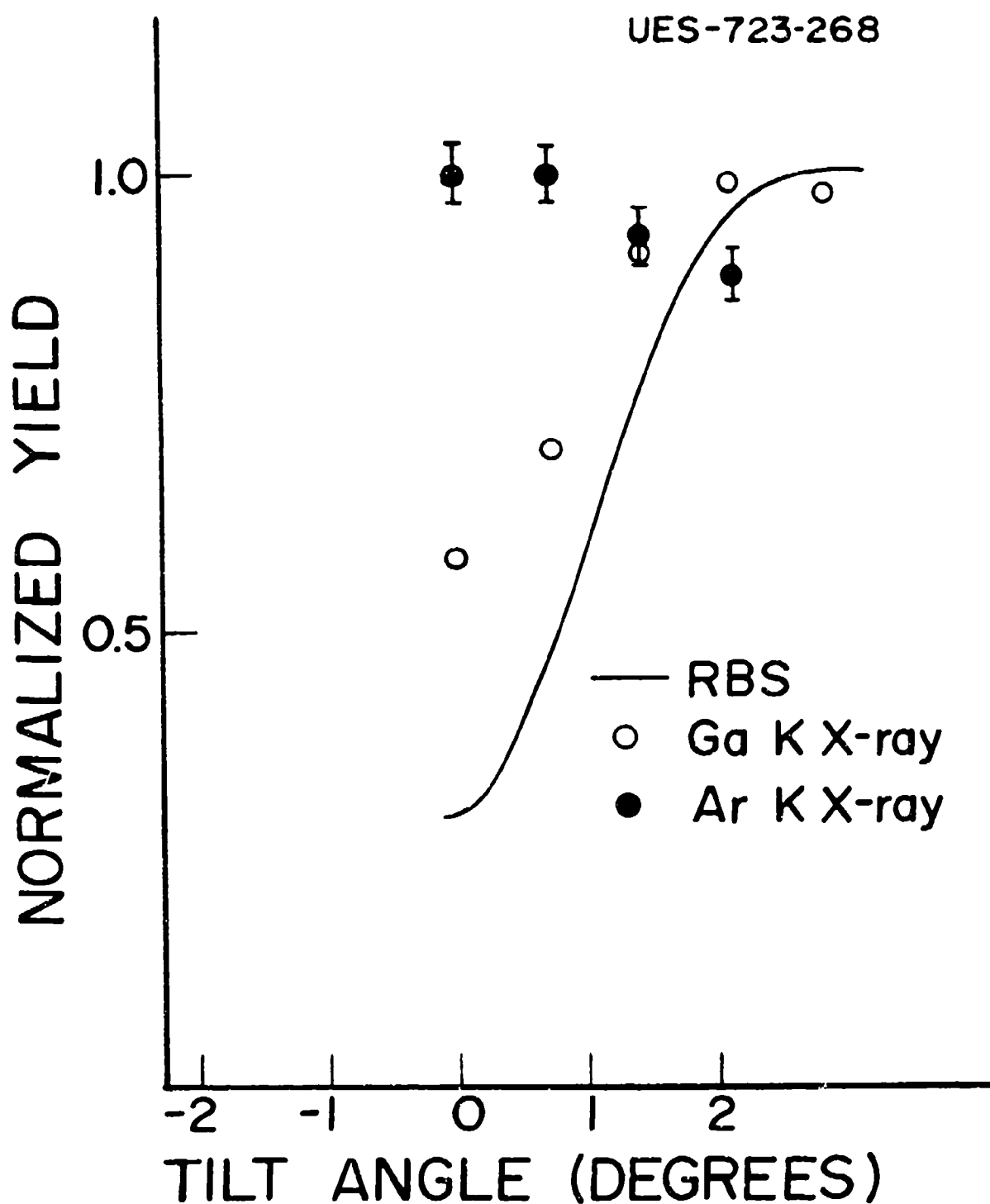


Figure 164

<110> Angular Half Scan of GaAs:Ar⁺ (700 keV,
5 X 10¹⁵ cm⁻², 850°C, 15 min)
298

impurity and its preferential occupation of any particular sublattice position. In the case of Ar implanted Si, low temperature annealing studies reported in the literature⁹⁸⁻¹⁰⁰ indicate that the bubbles of Argon gas form in both as-implanted and annealed samples along with microtwins. The formation of microtwins in Si recrystallization was explained as due to the formation of these bubbles at the crystalline-amorphous boundary where the symmetry of the regrowth is broken during annealing thus promoting the formation of microtwins. Since the microtwins in GaAs form at lower temperatures (200-600°C) than the temperature at which bubbles form (850°C) the nucleation of microtwins cannot be related to the presence of bubbles. It should be noted also that the microtwins anneal out at about 700°C. Above this temperature, dislocation tangles are the major residual defects.

It has been found that the bubbles which are associated with the dislocations are slightly larger than the rest [Figure 161(c)]. This indicates that the dislocations is higher than the mobility of isolated bubbles thus allowing smaller bubbles to coalesce to form larger ones. Note, for example, the size of the bubbles in the near surface region, which is of good crystalline quality, is smaller than the bubbles in the deeper region of the implanted layer. This observation is in agreement of Beere's model¹⁰¹ according to which a step introduced in a bubble surface by an intersecting dislocation reduces the energy required for nucleation of atomic planes thus promoting the bubble mobility by internal surface atom diffusion. The presence of argon filled bubbles in ion implanted GaAs is indirect proof of trapping of argon at vacant lattice sites since the nucleation of these gas bubbles requires that a strain relief trapping of the gas atoms at single or multivacancies occurs. According to Norgett and Lidiard,¹⁰² the capturing

of an inert gas atom at a vacant lattice site will act to reduce its interstitial strain energy to some small value. If the temperature is high enough for vacancy migration to occur then the attachment of a second vacancy will further eliminate the residual strain completely; however, there is now created a situation where the divacancy with one inert gas atom can absorb a second gas atom to reduce its interstitial strain energy. Thus, as this process repeats itself a gas bubble eventually forms. If the concentration of inert gas atoms is low enough, then simple vacancy or divacancy trapping can dominate. This mechanism of absorption into vacancies is one possible way in which argon atoms can act to reduce the number of compensating defects formed in n-type implanted GaAs if those complexes involve the attachment of vacancies to the n-type ion implanted dopants.

SECTION V
DEVICE ISOLATION BY ION IMPLANTATION IN
GaAs O^+ AND H^+ IMPLANTATION IN GaAs

It is known¹⁰³⁻¹⁰⁶ that ion bombardment produces high resistivity layers in GaAs through the creation of lattice defects which form deep trapping levels that compensate free carriers. Most commonly, protons and oxygen ions are used for implantation. It has been found¹⁰⁶ that oxygen has a definite advantage over protons in compensating that electrical activity. The compensation achieved by proton bombardment is not very stable above a temperature on the order of 500°C because of the annealing of those defects created by ion implantation, whereas the oxygen implanted layers have been found to remain compensated up to 900°C ¹⁰⁷. This is thought to be caused by a doping effect of oxygen resulting in deep levels of GaAs.¹⁰⁸

A dose dependence in the compensation effect has also been observed for O^+ implanted layers. For instance, a dose of less than $1 \times 10^{14} \text{ cm}^{-2}$ has been found¹⁰⁹ to result in a conducting layer upon annealing above 700°C . A dose of the order of 10^{15} cm^{-2} is required to obtain a stable compensated layer after annealing above 700°C . Recently, Favennac et al.¹¹⁰ has shown from secondary ion mass spectroscopic analyses that for doses below 10^{14} cm^{-2} , oxygen diffuses very quickly at 900°C , whereas for high dose 10^{15} cm^{-2} , oxygen piles up around its projected range during annealing. The results were identical in the case of both Cr-doped and undoped substrate materials. It was suspected that the pile up is caused by the precipitation of oxygen upon annealing at high temperature. However, no experimental evidence was presented to support this hypothesis. Also, there is not report

of any detailed investigation of the damage as a function of dose and anneal temperatures.

We have carried out an investigation of damage production as a function of dose for both O^+ and H^+ implantation in GaAs. The residual damage after annealing of O^+ implanted samples were analyzed by both RBS and TEM. Anisotropy in the displacement rate of Ga and As has been characterized.

Undoped semi-insulating liquid encapsulated Czochralski (LEC) grown GaAs wafers with (100) orientation were implanted with $^+$ ions in a non-channeling direction. Two different energies, 350 keV and 80 keV were used. The doses ranged from $5 \times 10^{13} \text{ cm}^{-2}$ to $5 \times 10^{15} \text{ cm}^{-2}$. RBS-channeling analysis has been performed using 340 keV H^+ ions. For H^+ implantation, 340 keV H^+ from the V de Graaff has been used.

5.1 RESULTS AND DISCUSSION

Figure 165 shows the $\langle 100 \rangle$ channeling spectra obtained from samples implanted with 80 keV O^+ ions to various doses before and after annealing. The damage produced by implantation before annealing increases with dose as expected. The dechanneling for implantation doses below $5 \times 10^{14} \text{ cm}^{-2}$ is very close to the virgin level and, therefore, not shown in the Figure. Although the damage level increased with dose, the layer remained crystalline even after implantation with $5 \times 10^{15} \text{ cm}^{-2}$, the highest dose employed in the present experiment. After annealing at 700°C for 15 minutes, samples with doses below $1 \times 10^{15} \text{ cm}^{-2}$ show a dechanneling rate nearly the same as that for the virgin crystal thereby indicating a good recovery of damage. However, for $5 \times 10^{15} \text{ cm}^{-2}$ implant, the residual damage is quite high as indicated by significantly higher dechanneling as compared to that in the virgin crystal. Spectra (Figure 166) collected in a high resolution geometry reveal

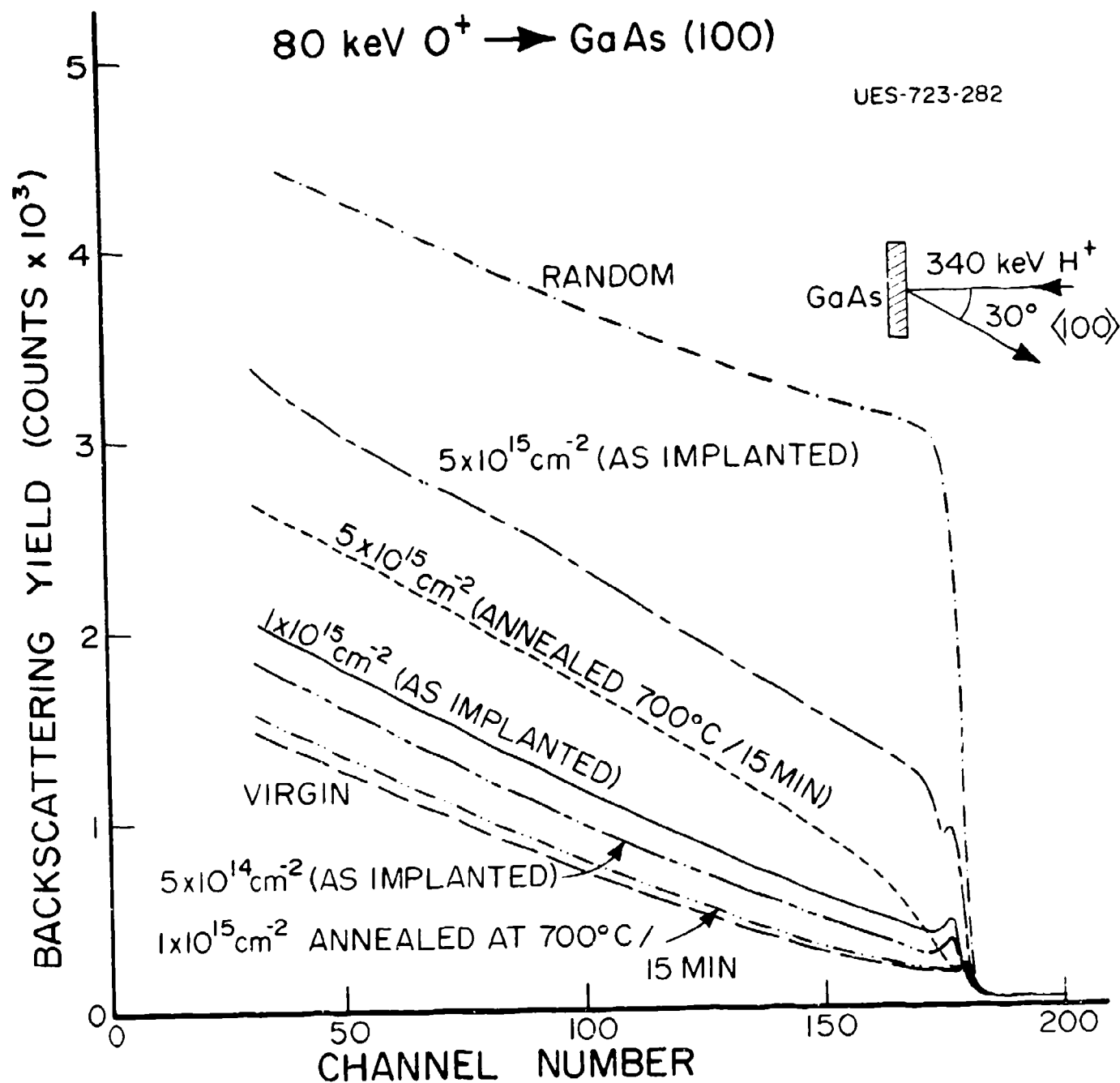


Figure 165

$\langle 100 \rangle$ Channeling Spectra of GaAs: O^+ (80 keV)

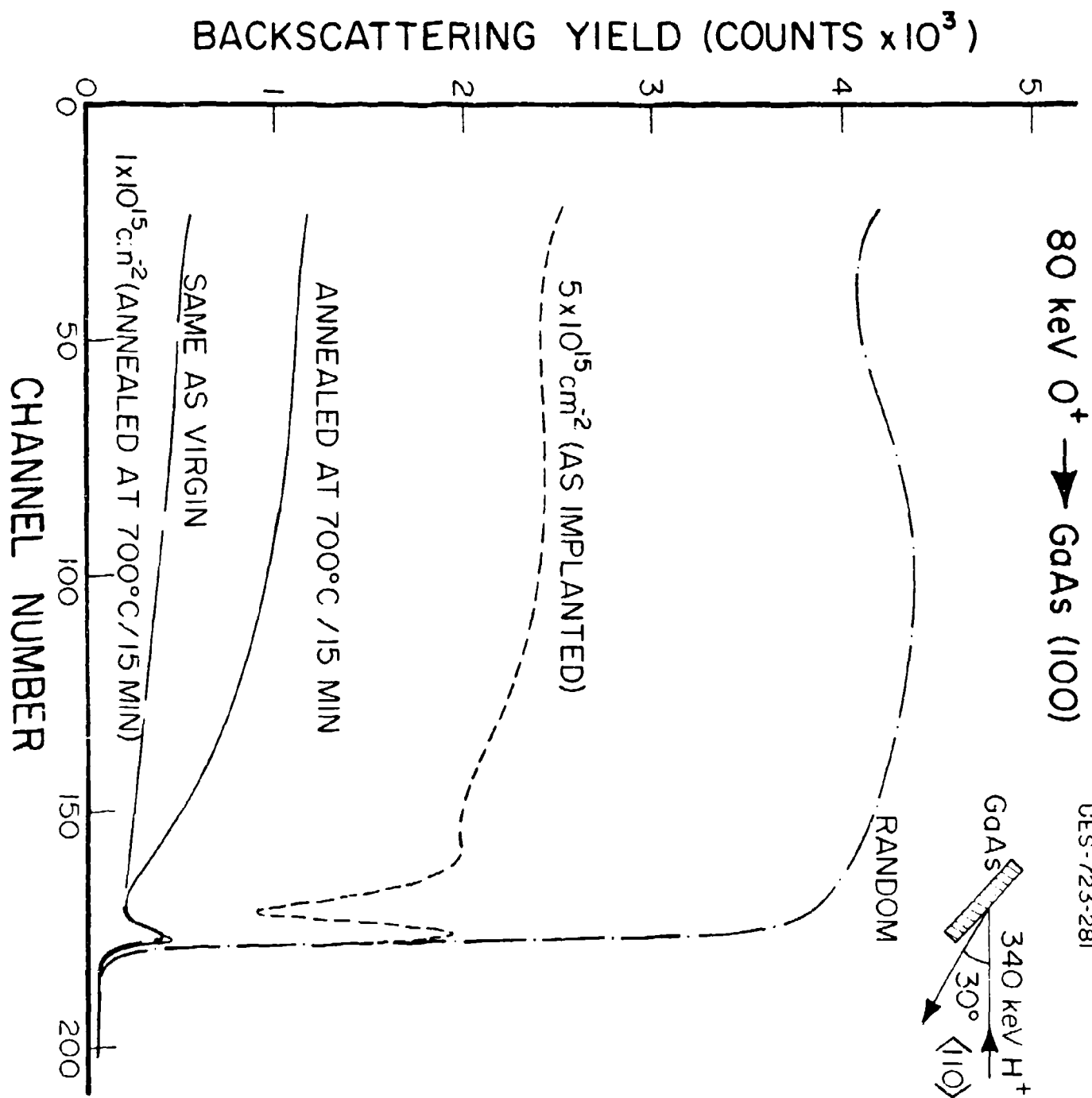


Figure 166

$\langle 110 \rangle$ Channeling Spectra of GaAs: O^+ (80 keV)

clearly that the damage in the $1 \times 10^{15} \text{ cm}^{-2}$ implant and in the lower dose implants anneals out completely after annealing at 700°C for 15 minutes. For $5 \times 10^{15} \text{ cm}^{-2}$ implant, the recovery is very good near the surface region (/cs300A) as observed from a comparison of the channeling spectrum with that of a virgin crystal. However, the damage increases as a function of depth as indicated by a sharp rise in dechanneling at this depth.

Figure 167 shows the $\langle 100 \rangle$ channeling spectra of 350 keV O^+ implanted samples. As compared to 80 keV implants, the surface region is less damaged for the same dose. The damage is maximum around a depth $\sim 600 \text{ \AA}$ which compares well with the projected range of 5350 \AA as tabulated in Gibbons et al.¹¹¹ Annealing at 700°C for 15 minutes again leads to a similar result as that for 80 keV implants (see Figure 168). Some defects are found to be present only in the case of $5 \times 10^{15} \text{ cm}^{-2}$ implant. The damage recovery was very good for $1 \times 10^{15} \text{ cm}^{-2}$ and lower dose implants.

TEM investigations of the samples described above were carried out in detail. The examination of the as-implanted samples confirm the crystallinity of the implanted layer as observed by the channeling technique. Bright field micrographs did not show any evidence of precipitation or defect clusters. The annealed specimens, for doses below $1 \times 10^{15} \text{ cm}^{-2}$, also do not show any observable damage. However, the bright field micrograph of the $5 \times 10^{15} \text{ cm}^{-2}$ O^+ implanted sample annealed at 700°C for 15 minutes shows (Figure 169) dislocation loops. The sizes of these loops vary from $50 - 1000 \text{ \AA}$. There was no evidence for precipitation of the implanted species. The corresponding transmission electron diffraction pattern shows the presence of only GaAs matrix spots.

350 keV $O^+ \rightarrow GaAs (100)$

UES-723-283

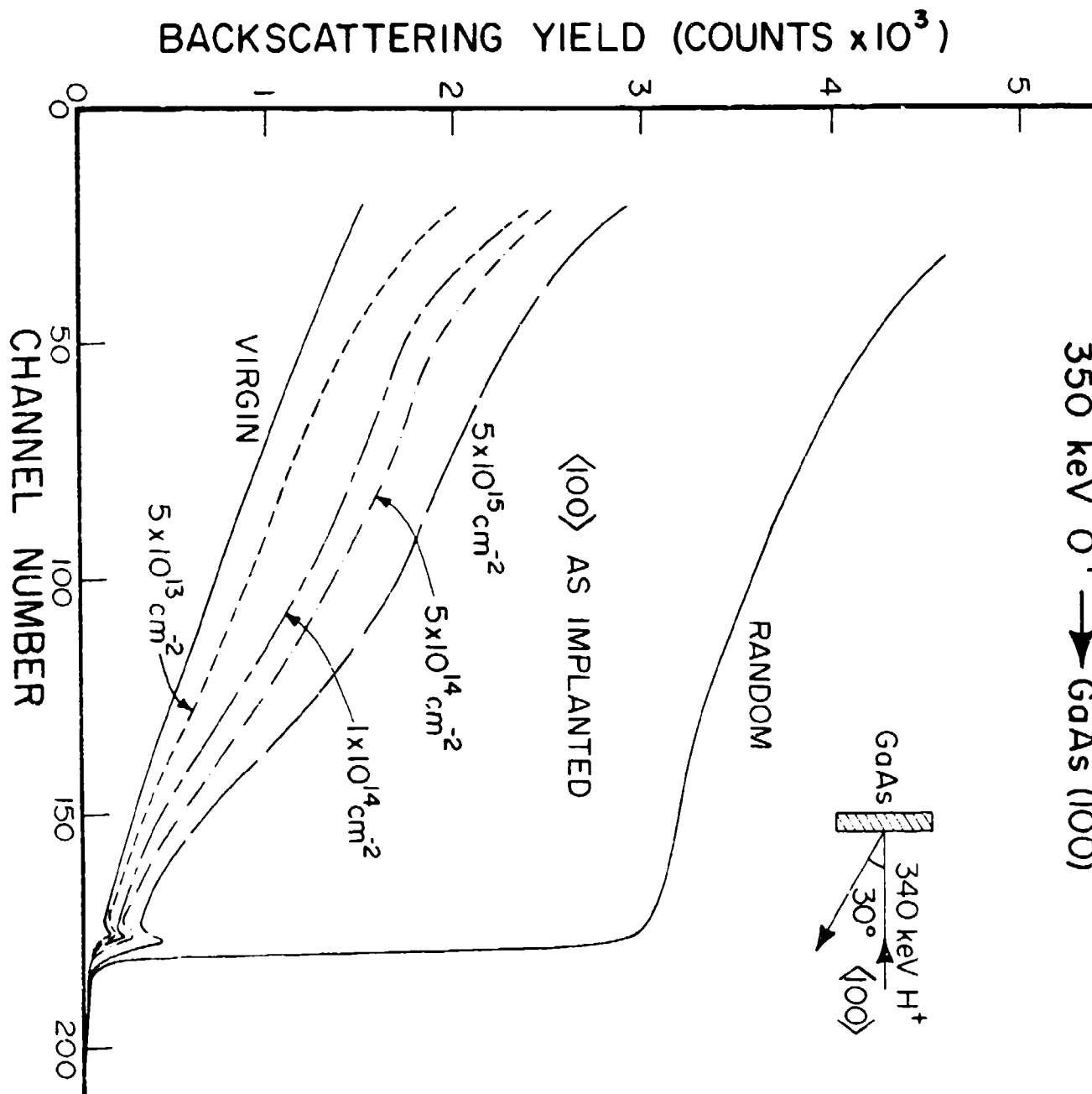


Figure 167

$\langle 100 \rangle$ Channeling Spectra of GaAs: O^+ (350 keV)

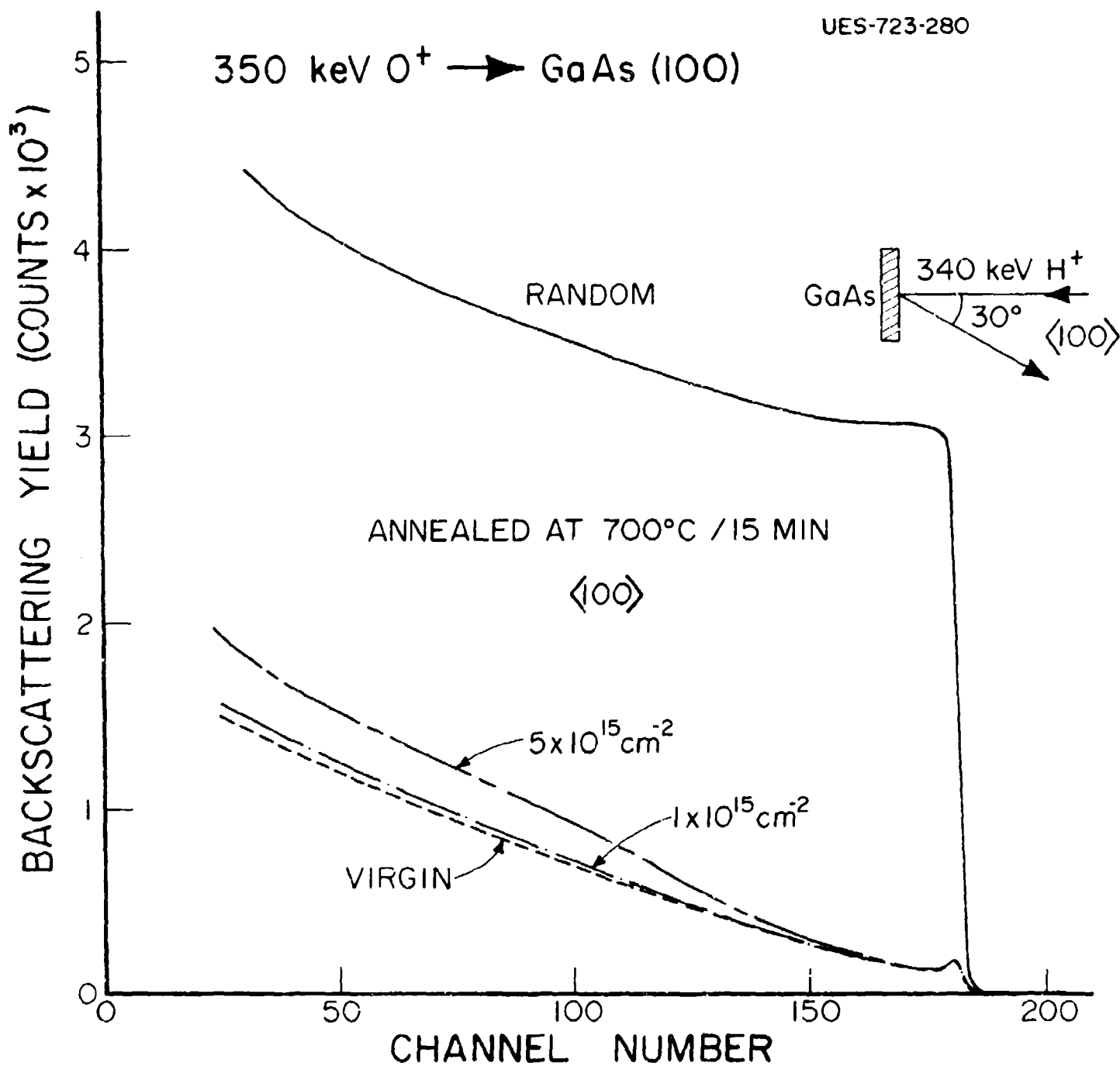


Figure 168

$\langle 100 \rangle$ Channeling Spectra of GaAs: O^+ (350 keV)
annealed at 700°C/15 min

UES-723-284

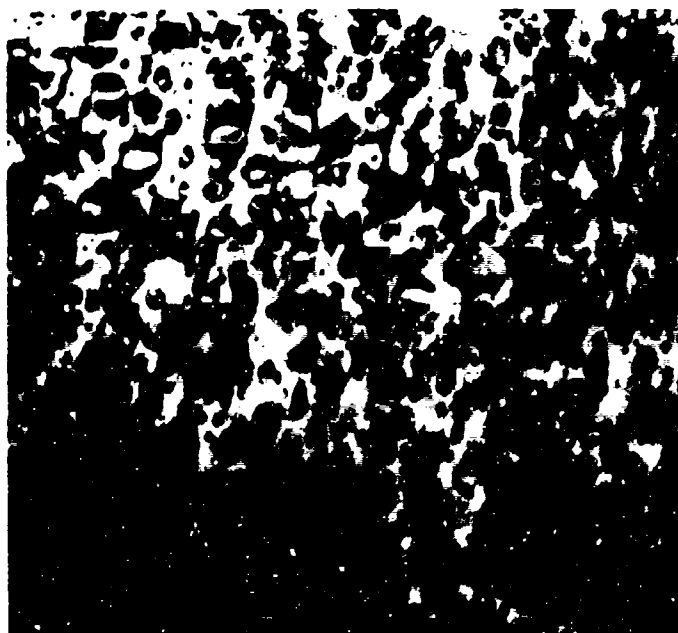


Figure 169 Strong Beam Bright Field Micrograph with $g=220$ for 80 keV
 O^+ Implanted to $5 \times 10^{15} \text{cm}^{-2}$ and Annealed at 700°C for 15 Min

The present experiments show that the damage created by oxygen implantation in GaAs recovers very well after annealing at 700°C for 15 minutes for doses below $1 \times 10^{15} \text{ cm}^{-2}$. It can, therefore, be concluded that the decrease of electrical conductivity due to oxygen implantation for doses in the range of $10^{14} - 10^{15} \text{ cm}^{-2}$ after annealing at high temperature¹⁰⁹ is not due to damage but must be due to a doping effect as discussed in the introduction. However, at higher dose residual damages in the form of dislocation loops are observed which may have some small contribution to the compensation effect. On the other hand, chemical doping is probably the major compensating factor at these higher fluences as well. Precipitates, if present, as suggested by Favennec et al.¹⁰⁶ must be of sizes smaller than 10 Å as we were unable to detect any by TEM.

In the case of H^+ implantation, the crystals were bombarded in a random direction and the RBS-C and PIXE spectra were collected after a certain interval to record the damage. A dose of $<100 > \text{C/cm}^2$ was needed to collect an RBS-C spectrum which has been found to produce no measurable damage when incident along a channeling direction. However, a dose of $\sim 650 \mu\text{C/cm}^2$ was required to collect a PIXE spectrum which produced some damage along channeling directions as observed by a small increase in dechanneling after the bombardment. Therefore, separate beam spots were used for RBS-C and PIXE analyses.

Figure 170(a) and (b) show the $<100 >$ and $<110 >$ channeling spectra respectively before and after random bombardment of 330 keV H^+ . Considerable increase in dechanneling is observed in both directions after irradiation in a random equivalent orientation. The minimum yield ρ (defined as the ratio of channeled yield to random yield) behind the surface peak as a

330 keV $H^+ \rightarrow$ GaAs
 $\langle 100 \rangle$

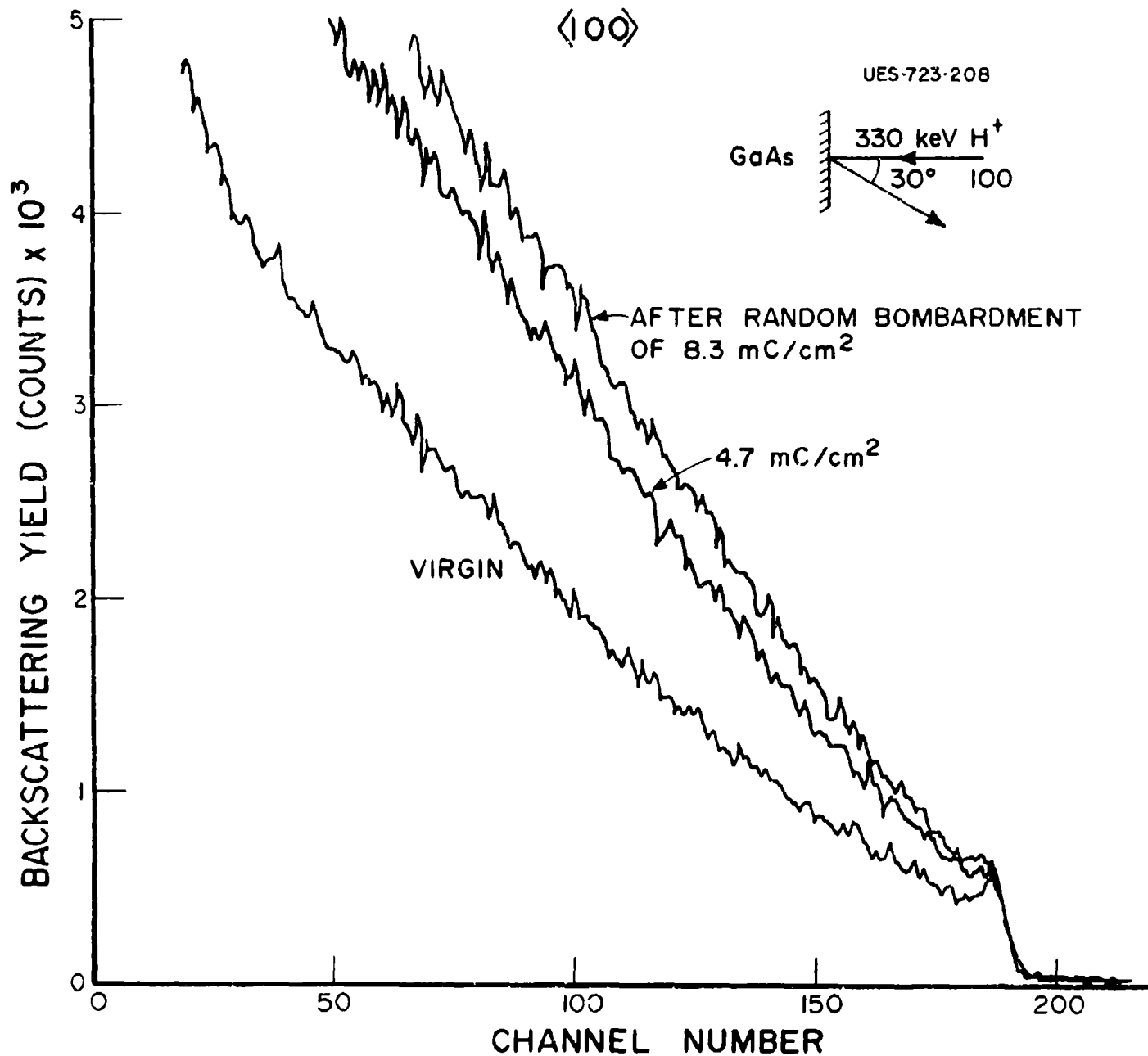


Figure 170 (a) $\langle 110 \rangle$ Channeling Spectra of GaAs Before and After Proton Bombardment

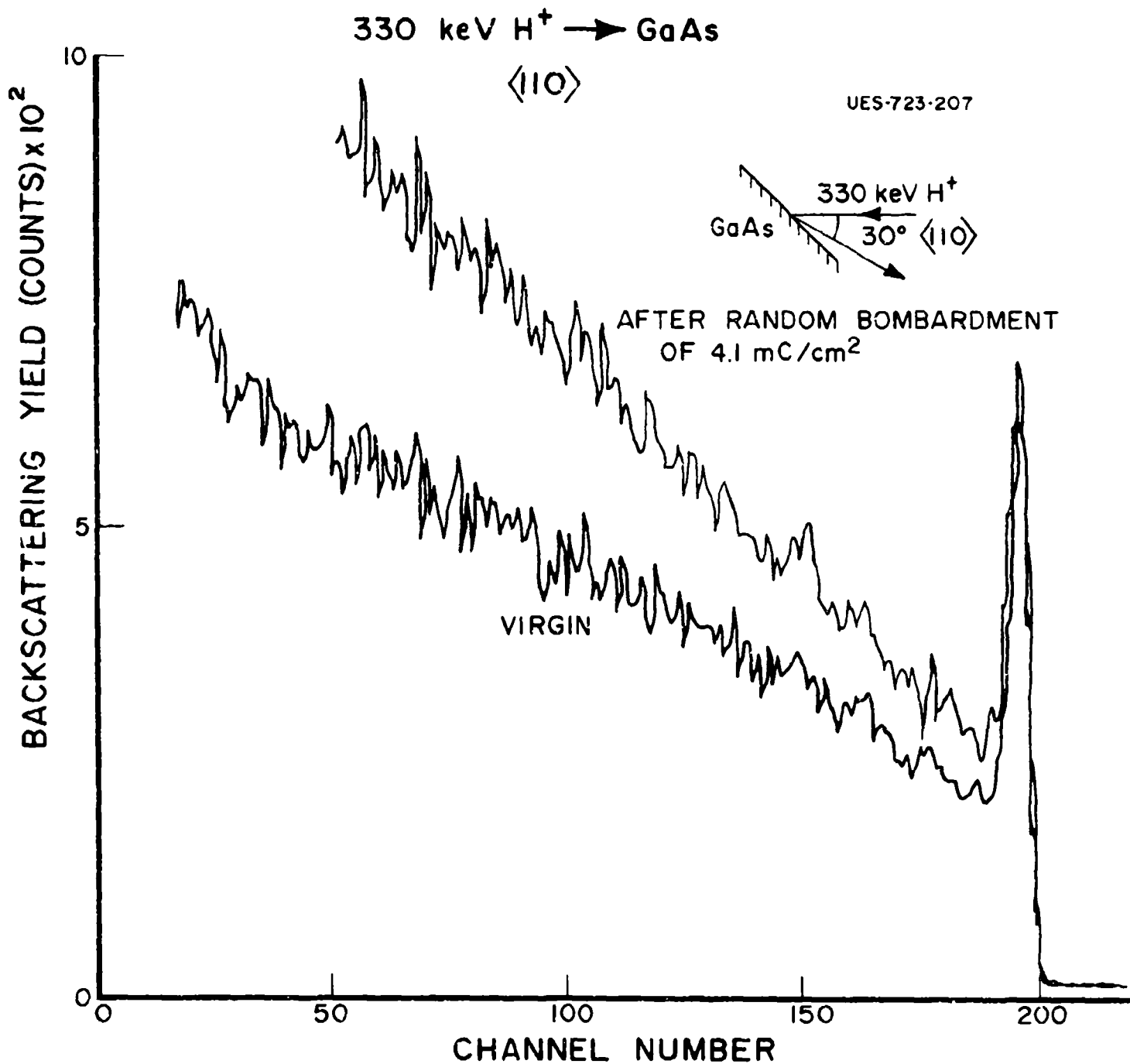


Figure 170 (b) $\langle 110 \rangle$ Channeling Spectra of GaAs Before and After Proton Bombardment

function of H^+ dose is plotted in Figure 171. As expected the rate of increase of χ has been found to be the same in both directions. The cross section for the displacement of GaAs atoms can be determined from the slope of the change in σ (i.e., $\Delta\chi$) vs. dose (ϕ) at zero dose:

$$\sigma = \frac{d\Delta\chi}{d\phi} \quad \phi = 0 \quad (1)$$

In this analysis, the contribution of dechanneling in defects is neglected because we consider χ in the region close to the surface ($\sim 1000 \text{ \AA}$). The cross section thus obtained is $8.2 \times 10^{-19} \text{ cm}^2$.

The displacement of atoms from their original lattice sites during the impact of energetic particles generally occurs due to the elastic energy transfer to the lattice atoms. An atom is displaced when an energy more than the threshold energy E_d is transferred to the lattice atom. According to reference 112, threshold displacement energy of Ga is 8.8 eV, whereas As is 10.1 eV. From electron irradiation measurements, Pons and Bourgoïn¹¹³ have shown that the threshold energy can vary in the range 7-11 eV depending on the direction of displacement. If we assume an average threshold displacement energy of 9 eV, we can calculate the cross section for displacement according to the theory of Kinchin and Pease.¹¹⁴

$$\sigma_{KP} = \frac{2\pi a_0^2 M_1 Z_1^2 Z_2^2 E_R^2 \ln(\gamma E_1/E_d)}{M_2 E_1 E_d} \quad (2)$$

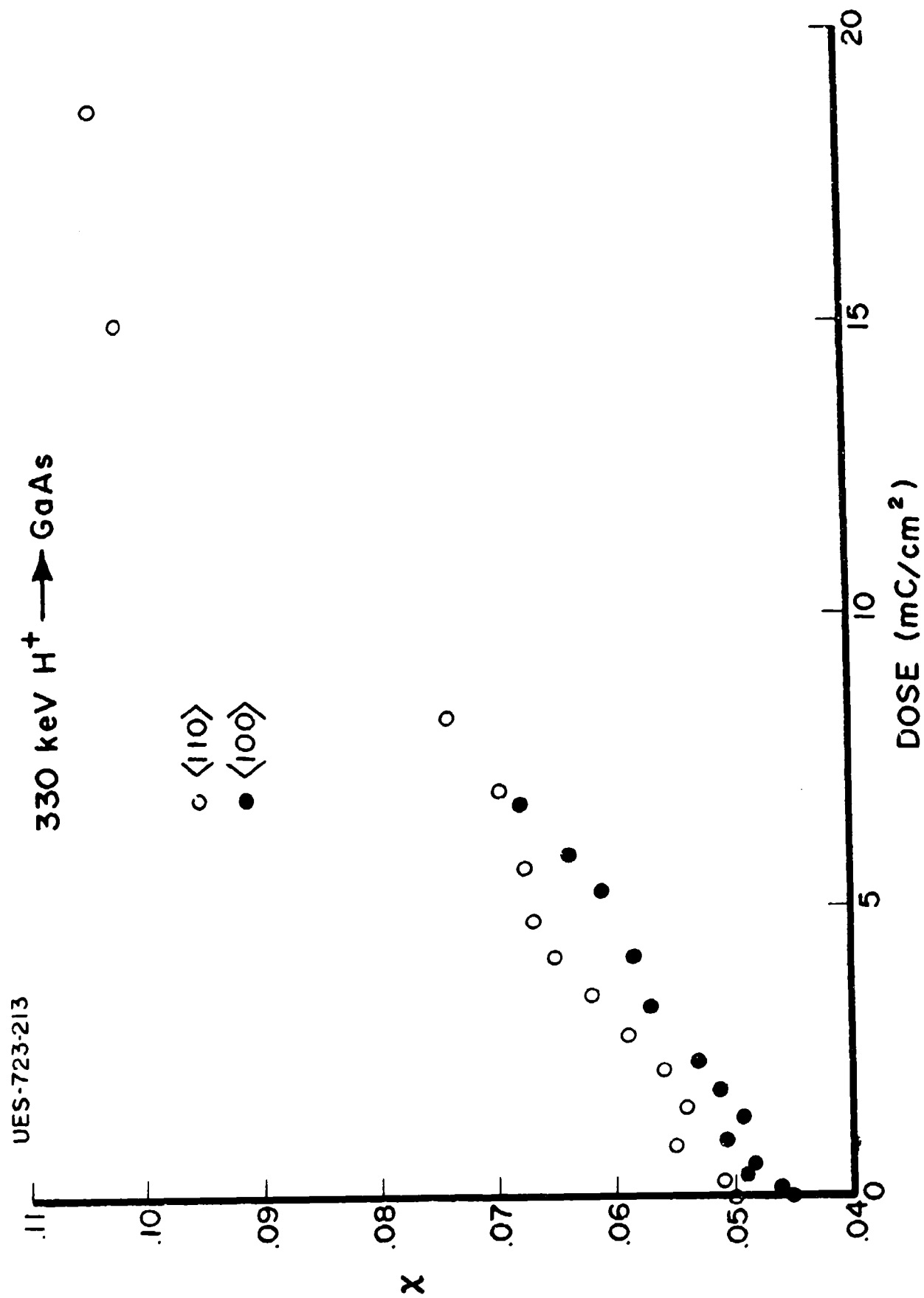


Figure 171 Minimum Yield X Behind the Surface Peak ($\sim 1000 \text{ \AA}^0$)
Versus Dose of 330 keV H^+

where

a_0 = Bohr radius

M_1 and Z_1 = Mass and atomic number of the projectile

M_2 and Z_2 = Mass and atomic number of the target atoms

E_R = Rydberg Energy

E_0 and E_d are the primary energy of the beam and
displacement energy respectively

and
$$\gamma = \frac{4M_1M_2}{(M_1 + M_2)^2}$$

This yields $\sigma_{kp} = 1.7 \times 10^{-18} \text{ cm}^2$ which compares quite well with the experimental value of $8.2 \times 10^{-19} \text{ cm}^2$. As Kinchin and Pease's theory does not consider annealing due to the recombination of Frenkel pairs, σ_{kp} should be larger than the experimentally derived value.

Lower E_d and Ga as compared to As, imply that more Ga atoms should be displaced as compared to As atoms. Assuming $E_d = 8.8 \text{ eV}$ for Ga and 10.1 eV for As, one can easily see from equation (2) that about 11% more Ga atoms as compared As atoms should be displaced from lattice sites. We have made an effort to establish this by measuring the non-substitutional fraction of Ga and As as a function of H^+ dose using PIXE in combination with channeling. Figure 172 shows the region of the PIXE spectrum, which is of present interest. Two spectra shown in Figure 172 were collected by bombarding along the $\langle 110 \rangle$ channeling direction before and after a random bombardment of 16.2 mC/cm^2 . A spectrum was collected also in a random direction.

330 keV $H^+ \rightarrow GaAs$

UES-723-214

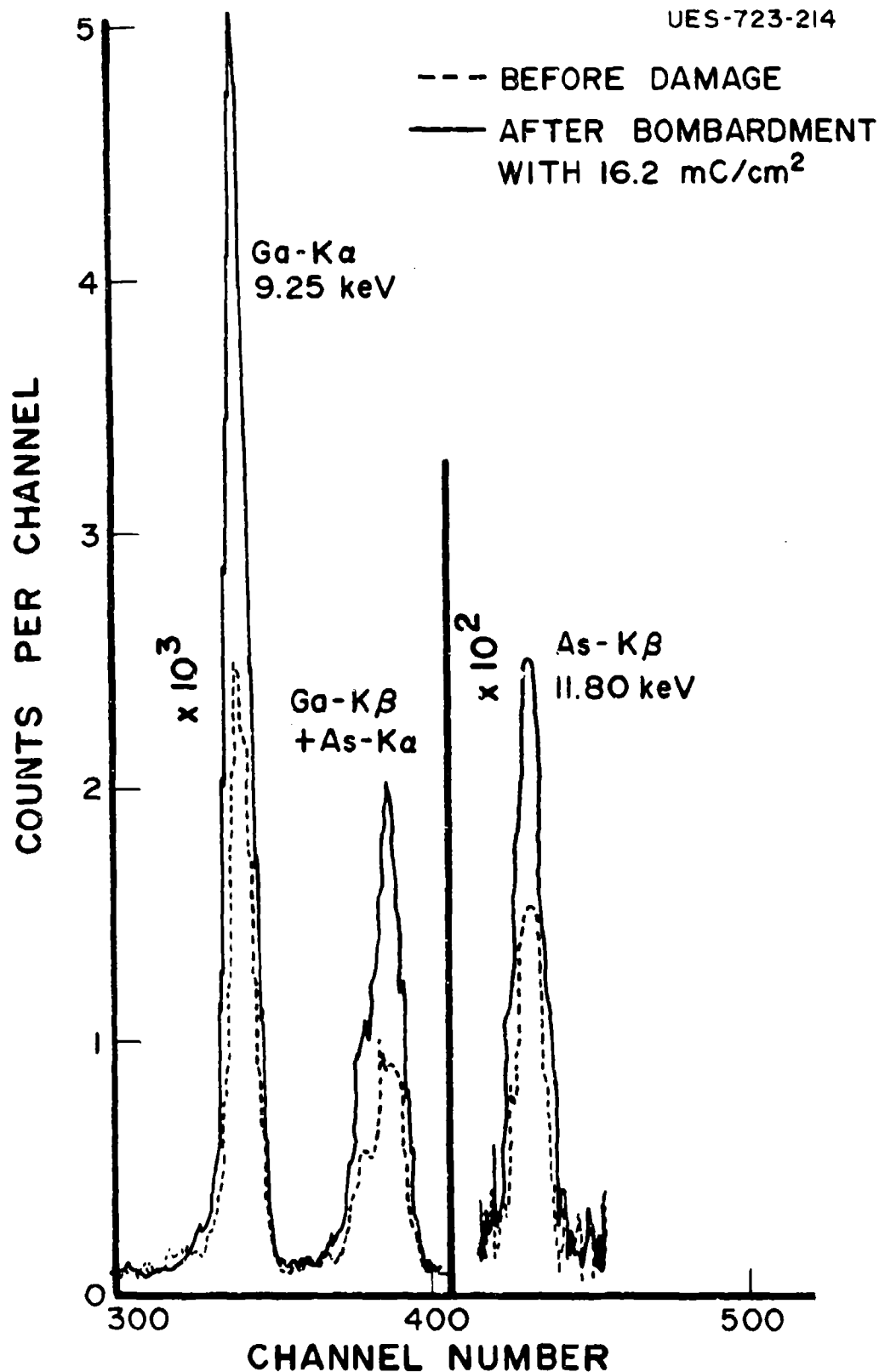


Figure 17: PIXE Spectra of GaAs in <110> Direction

The area under the peaks of Ga-K α and As-KB were used to calculate the minimum yield (χ) which is plotted in Figure 173 as a function of proton dose. It can be seen that χ increases as a function of dose and reaches a saturation after bombardment of about 15 mC/cm². This is consistent with the results obtained by RBS-C. From the minimum yields, one can determine the non-substitutional fraction, f_{ns} , of the Ga and As atoms:

$$f_{ns} = \frac{\chi_d - \chi_v}{1 - \chi_v} \quad (3)$$

where χ_d and χ_v are the minimum yields of damaged and virgin crystal respectively. Figure 173 shows that at saturation about 22% \pm .5% of the Ga atoms are nonsubstitutional as compared to $\sim 16 \pm 2.25\%$ As atoms. As the As signal is smaller than the Ga signal by an order of magnitude or more, the error in the determination of f_{ns} for As is larger. Even so, it is very clear that more Ga atoms are displaced as compared to As atoms as expected from the theoretical considerations discussed above. It may be noted that the X-ray signal is obtained across a depth $\sim 2 \mu\text{m}$ as compared to the mean projected range $\sim 2.5 \mu\text{m}$, of the 330 keV H⁺ in GaAs and deeper along a channeling direction.

In conclusion, we have demonstrated that the displacement of Ga and As atoms in GaAs due to proton irradiation can be described by the theory of Kinchin and Pease. We have also shown that about 7% \pm 2.5% more Ga atoms are displaced as compared to As atoms during proton irradiation as would be expected from a reduced threshold displacement energy for Ga atoms. Also, in the case of O⁺ implantation in GaAs, we have found slightly higher displacement (<4%) of Ga than As.

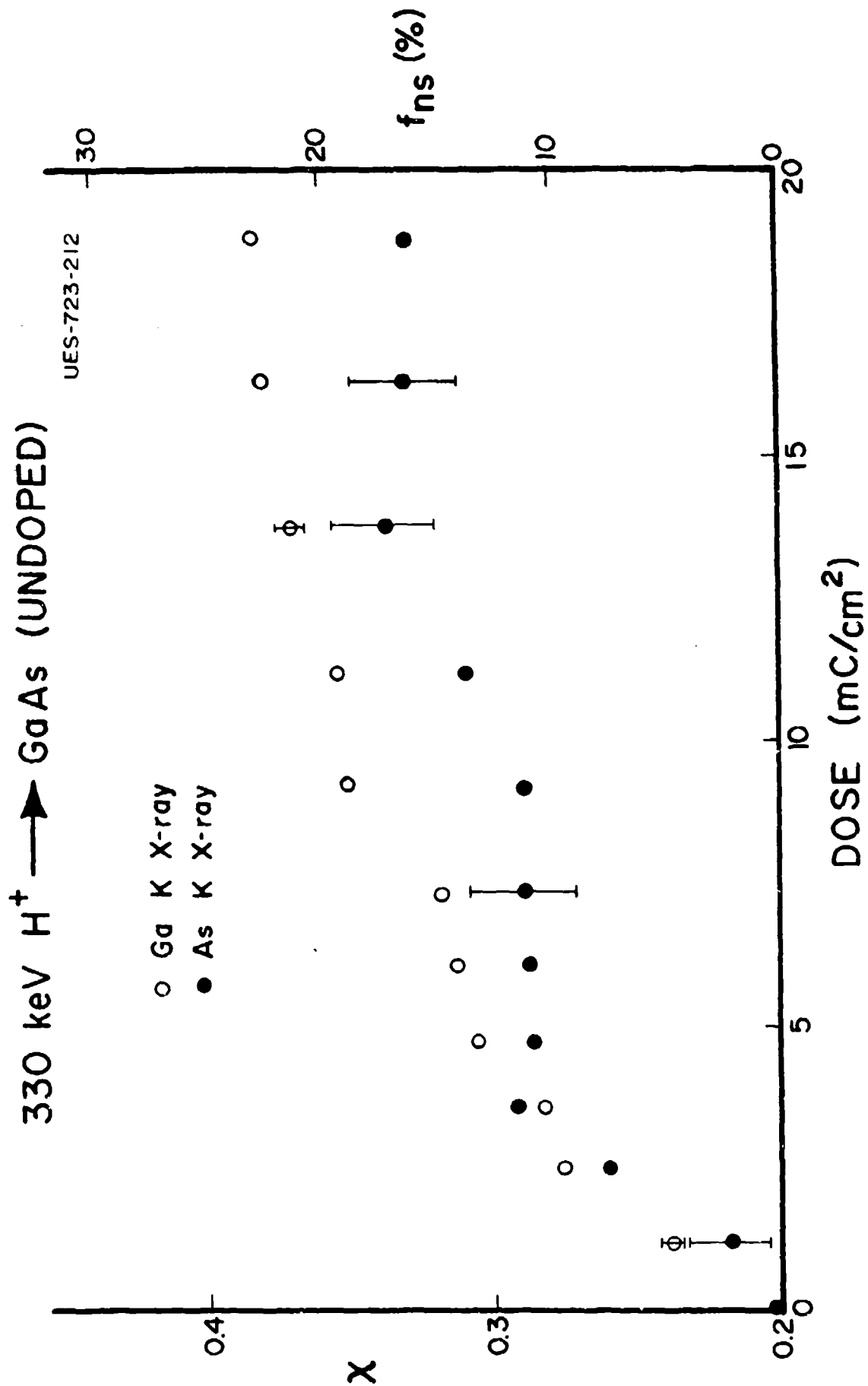


Figure 173 X-ray Minimum Yield as a Function of 330 keV H^+ Dose. The Percentage of Non-Substitutional Atoms (f_{ns}) are Given on the Top Right Hand Scale.

5.2 ELECTRICAL MEASUREMENTS OF Si^+ and O^+ IMPLANTED GaAs

It has been shown by Favennec¹⁰⁷ that oxygen implantation into GaAs can produce high-resistivity layers either by defect-induced compensation or by oxygen-doping-induced compensation. He suggested that the defect-induced compensation was dominant at annealing temperature below 600°C, while the oxygen-doping-induced compensation was dominant at higher annealing temperatures. Since the oxygen-ion bombardment into GaAs can be used in device isolation applications, many studies¹⁰⁶⁻¹¹⁰ have been done. However, most studies have been made on epitaxially grown uniformly doped GaAs and for high temperature annealing behavior. In this work we have studied the electrical properties of Si-implanted GaAs after bombarding with oxygen ions.

First, Si ions were implanted into semi-insulating GaAs at ion energies of 100 and 200 keV with doses of 3×10^{13} and $2 \times 10^{14} \text{ cm}^{-2}$, respectively. Prior to the oxygen-ion implantation, the Si-implanted samples were annealed at 850°C for 15 min. with CVD Si_3N_4 caps, and Hall-effect/sheet-resistivity measurements were made. The samples implanted at 100 keV with a dose of $3 \times 10^{13} \text{ cm}^{-2}$ showed an average sheet resistivity (R_{\square}) of $2.2 \times 10^2 \Omega/\square$ and an average surface-carrier concentration (N_s) of $1.23 \times 10^{13} \text{ cm}^{-2}$. The samples implanted at 200 keV with a dose of $2 \times 10^{14} \text{ cm}^{-2}$ showed an average sheet resistivity of $1.54 \times 10^2 \Omega/\square$ and an average surface-carrier concentration of $2.1 \times 10^{13} \text{ cm}^{-2}$. The sheet resistivity of the GaAs substrate itself was about $10^{10} \Omega/\square$.

Next, oxygen ions were implanted into the above mentioned 100- and 200-keV Si-implanted GaAs samples at ion energies of 57 and 113 keV, respectively. The ion energies of O were chosen in such a way that the projected ranges of both O and Si are about the same. For each oxygen-ion

energy, three different O-ion doses were chosen. After oxygen-ion bombardment, the samples were annealed at temperatures ranging from 100 to 400°C for 2 hours without any protective caps in flowing argon gas.

The results of Hall-effect/sheet-resistivity measurements are shown in Figure 174 and 175. For the 100 keV Si-implanted GaAs, the oxygen-ion dose of $6.5 \times 10^{12} \text{ cm}^{-2}$ is about one half of the surface-carrier concentration, the $1.5 \times 10^{13} \text{ cm}^{-2}$ dose is one half of the Si-ion dose which is also about the same value as the surface-carrier concentration, and the $3 \times 10^{13} \text{ cm}^{-2}$ dose is exactly the same as the Si-ion dose. For the 200 keV Si-implanted GaAs, the oxygen dose of $2.15 \times 10^{13} \text{ cm}^{-2}$ is about the same as the surface-carrier concentration, the $1 \times 10^{14} \text{ cm}^{-2}$ dose is one half of the Si dose, and the $2 \times 10^{14} \text{ cm}^{-2}$ dose is the same as the Si-ion dose.

As shown in Figure 174 and 175, the sheet resistivity increased dramatically from the initial value of the GaAs=Si samples after bombarding with oxygen ions. The sheet resistivity increased further sharply with annealing temperatures up to 400°C for all oxygen doses, and the samples showed neither n- nor p-type conductivity. However, the sheet resistivities are lower for the higher oxygen doses at a given annealing temperature. This higher level of electrical conduction for the higher oxygen doses may be attributed to residual oxygen-implantation related radiation damage. The results also indicate that the samples implanted with lower-dose Si can be compensated more effectively than those implanted with higher Si doses. It has been found that the sheet resistivity also increases gradually with annealing time at a given annealing temperature, but the sheet resistivity does not increase as dramatically as for the case of increasing annealing temperature. The sample implanted with oxygen at an energy of 57 keV to a

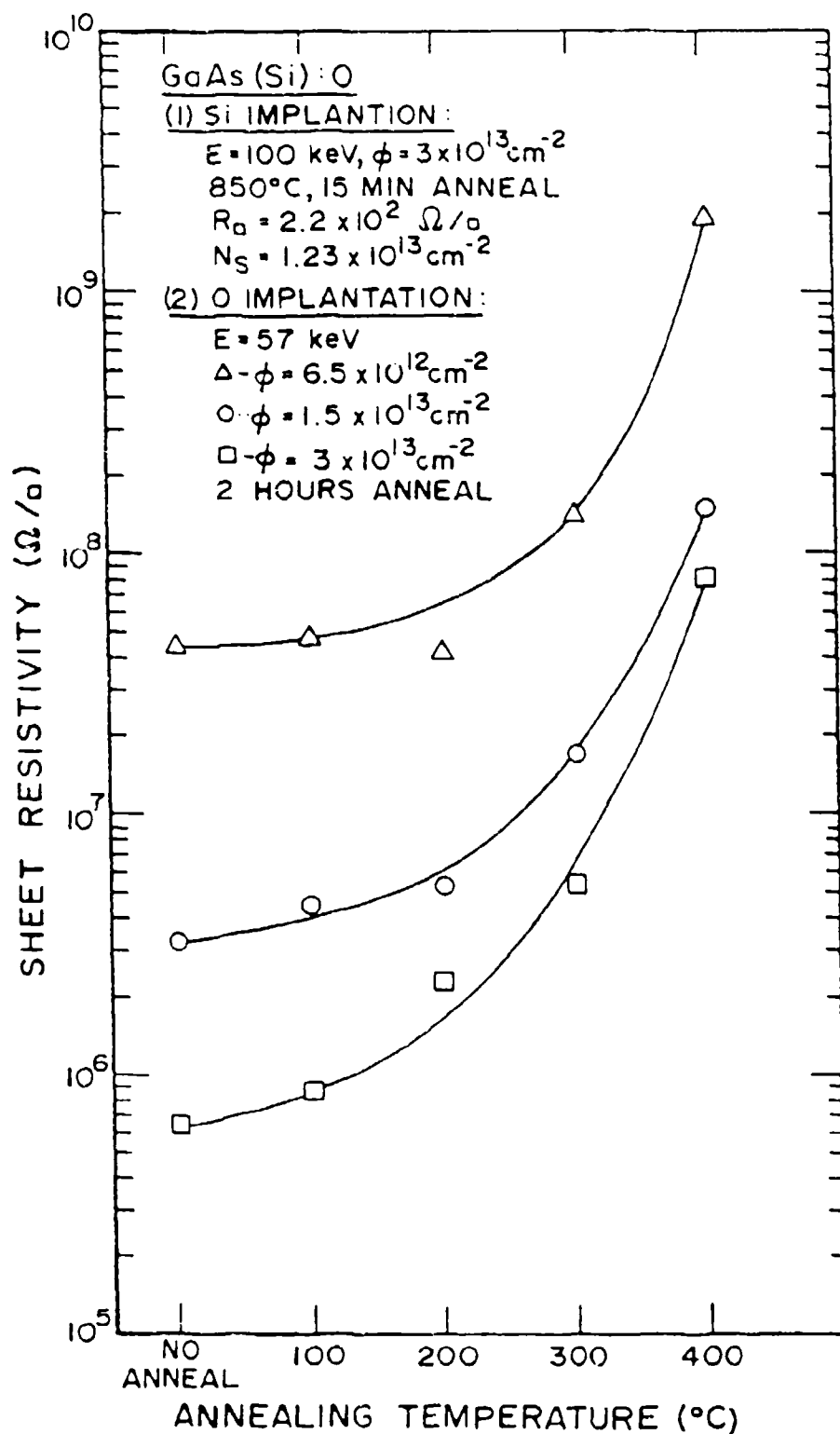


Figure 174

Sheet Resistivity versus Annealing Temperature for the
 100 keV Si-Implanted GaAs Samples Bombarded with 57-keV
 Oxygen Ions

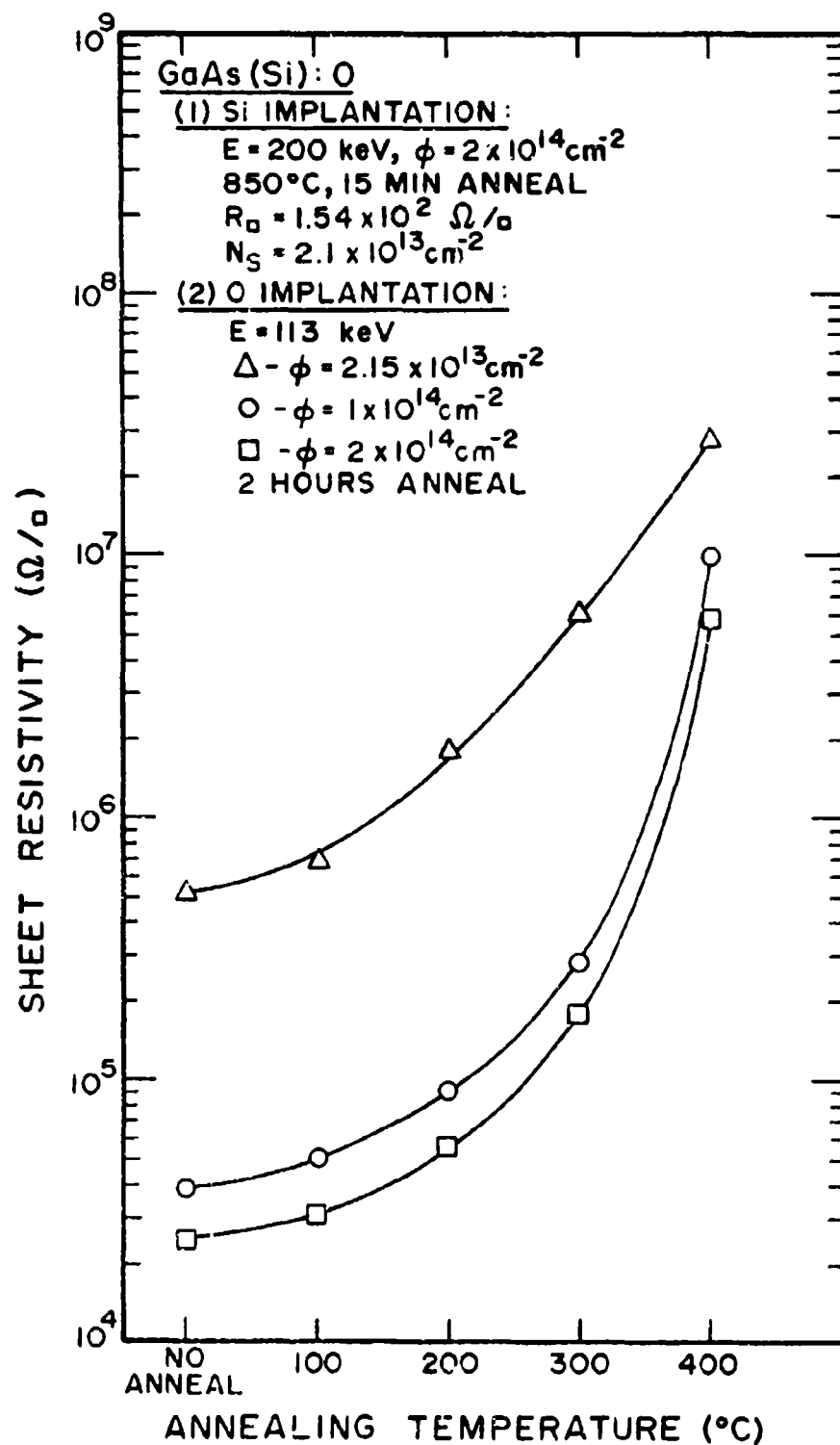


Figure 175 Sheet Resistivity Versus Annealing Temperature for the 200 keV Si-Implanted GaAs Samples Bombarded with 113 keV Oxygen Ions

dose of $6.5 \times 10^{12} \text{ cm}^{-2}$ and annealed at 400°C produces the highest sheet resistivity ($2 \times 10^9 \Omega/\square$), which is about the same value of the semi-insulating GaAs substrate itself. We may point out that the 400°C anneal of GaAs samples without any protective cap may create some extent of decomposition of the host lattice, although no visual sign of surface degradation of the samples was observed.

Although we do not understand the exact nature of defects or compensating centers created by the oxygen-ion bombardment, the defect-induced compensation may be dominant at the annealing temperatures below or at 400°C . The oxygen bombardment may create several compensating defects and each of which may anneal out at a different annealing temperature. It is therefore expected that the compensating defects with lower activation energies will anneal out at lower temperatures leaving those with higher activation energies. However, quite contrary to the above mentioned expectation, the sheet resistivity increases monotonically with annealing temperature up to 400°C . Probably most compensating defects created by oxygen bombardment are not only thermally stable at temperatures up to 400°C , but also some defects which contribute to the electrical conductivity may be annealed out gradually as the annealing temperature increases. Another possibility may be that the implanted oxygen related electron traps may increase with the annealing temperature. Although we can not find the exact correlation of compensating effects between O- and Si-dose levels, it appears that a much lower dose of oxygen than that of Si is required to produce a higher resistivity layer.

Also, oxygen ions alone were implanted into semi-insulating GaAs substrates for comparison. The results show that the value of sheet resistivity decreases initially from that of GaAs substrate itself after

oxygen bombardment. This may indicate that the disordered layer may contribute to the electrical conductivity. However, the value of sheet resistivity increases with annealing temperature up to 400°C as in the case of oxygen bombardment into Si-implanted GaAs, which may indicate that the defects contributing to the electrical conductivity anneal out gradually as the annealing temperature increases. Also, it has been observed that the value of sheet resistivity obtained from oxygen implantation alone is generally higher than that of the GaAs(Si):O at a given annealing temperature.

We have also investigated high temperature annealing behavior of Si-implanted GaAs after oxygen implantation. In this case, both Si and O were implanted into semi-insulating GaAs sequentially. The samples were then capped with CVD Si₃N₄ caps and annealed at temperatures ranging from 500 to 900°C for 15 minutes in flowing hydrogen gas. For this high temperature annealing, no high resistivity layer was produced, and the sheet resistivity remained below about $10^3 \Omega/\square$ at all annealing temperatures. Moreover, all samples showed n-type conductivity, indicating very poor oxygen-doping-induced compensation.

In summary, we can successfully produce high-resistivity layers by oxygen-ion bombardment into Si-implanted conducting GaAs layer as long as the annealing temperature remains at or below 400°C. However, the samples implanted with both Si and O and annealed at or above 500°C failed to produce high-resistivity layers, showing n-type conductivity for all cases.

SECTION VI

OHMIC CONTACT STUDY

Introduction

Alloyed Au-Ge or Au-Ge-Ni films are widely used for making Ohmic contacts to n-type GaAs.¹¹⁵⁻¹¹⁸ The reliability of the contact has been found to depend on the stability of the metallurgical grain structure and on the uniformity of the alloying behavior (surface morphology). It has been discovered that, in the case of Au-Ge, the alloying has a tendency to be non-uniform. Aina et al.¹¹⁶ has shown that by sintering Au-Ge films with GaAs at 315°C and 330°C for several hours, it is possible to get a uniform surface morphology and at the same time a very low contact resistance ($\sim 3 \times 10^{-6} \Omega \text{ cm}^2$). Another way of improving the surface morphology and hence a better Ohmic contact behavior is to deposit an overlayer of Ni on AuGe before alloying. Heiblum et al.¹¹⁷ has reported the presence of dark clusters on the surface of Au-Ge-Ni Ohmic contacts to n type MBE grown GaAs. These dark clusters were identified as Ge-Ni rich and Au deficient regions. Ogawa¹¹⁵ has described the microscopic grain structure as Ni-As-Ge rich and Au-Ga rich regions. So far, no systematic study has been done to compare and characterize the surface morphologies, compound formation and diffusion behavior of various contact systems on GaAs. We have made a detailed investigation of the alloying behavior of Au/GaAs, Au-Ge/GaAs and Au-Ge-Ni/GaAs using Scanning Electron Microscopy (SEM), Transmission Electron Microscopy (TEM), Rutherford Backscattering Techniques (RBS), and Energy Dispersive Analysis of X-rays (EDAX).

6.1 Au/GaAs

Figure 176 (a,b) shows the SEM pictures of the surface of Au/GaAs system after annealing at 350°C for 15 minutes. The presence of dark clusters are clearly evident. Figure 176 (c,d) shows the SEM picture of Au/GaAs after annealing at 425°C for 30 seconds. Not much change has been noticed in the surface morphology as compared to the 350°C anneal. Figure 177 (a,b) represents the SEM pictures of the surface of Au/GaAs after annealing at 450°C for 15 minutes. A very ordered surface morphology can be seen in the form of elongated (rectangular) patches. These patches are all parallel and aligned in a particular direction. Figure 178 (a,b,c) represents the transmission electron diffraction (TED) patterns of the Au/GaAs system after annealing at 350°C for 15 minutes, 425°C for 30 seconds, and 450°C for 15 minutes respectively. As is evident, well defined Au diffraction rings are present for 350°C and 425°C anneal indicating that Au has not reacted with GaAs at these temperatures. Figure 178 (d) shows the bright-field micrograph of Au/GaAs after annealing at 450°C at very low magnifications. The elongated structures, as observed at the surface by SEM (Figure 177) are clearly visible. Diffraction analysis shows that they lie along $\langle 110 \rangle$ directions of GaAs and they are Au rich regions. A similar result has been reported recently by Magee and Peng.¹¹⁹

The random energy spectra of backscattered He ions from Au-GaAs samples before and after annealing at 350°C for 15 minutes and 450°C for 15 minutes are shown in Figure 179. Assuming a stopping power of 3 MeV He⁺ in bulk Au as 124 eV/A°, we can estimate the thickness of the film which turns out to be 125 A°. When comparing these spectra, it can be seen that after annealing at 350°C for 15 minutes, Au has diffused into the GaAs at the interface up to a

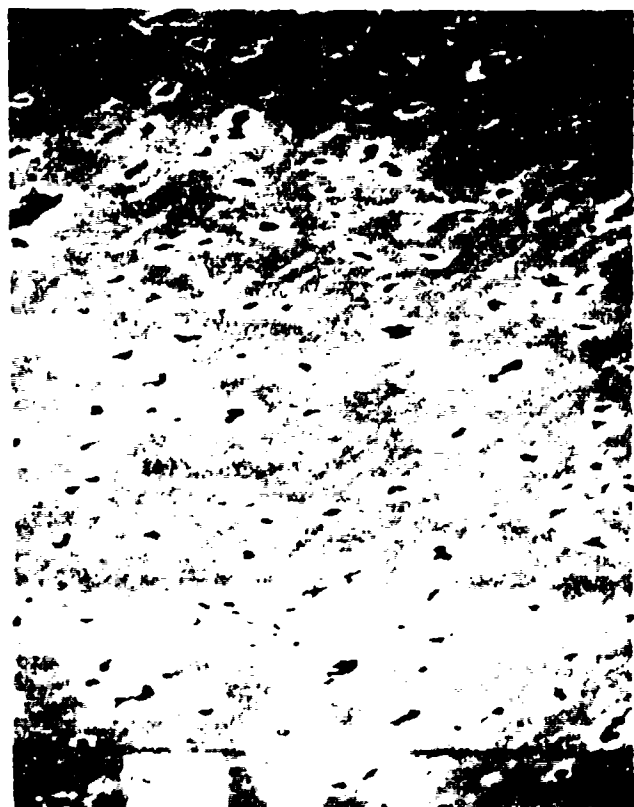
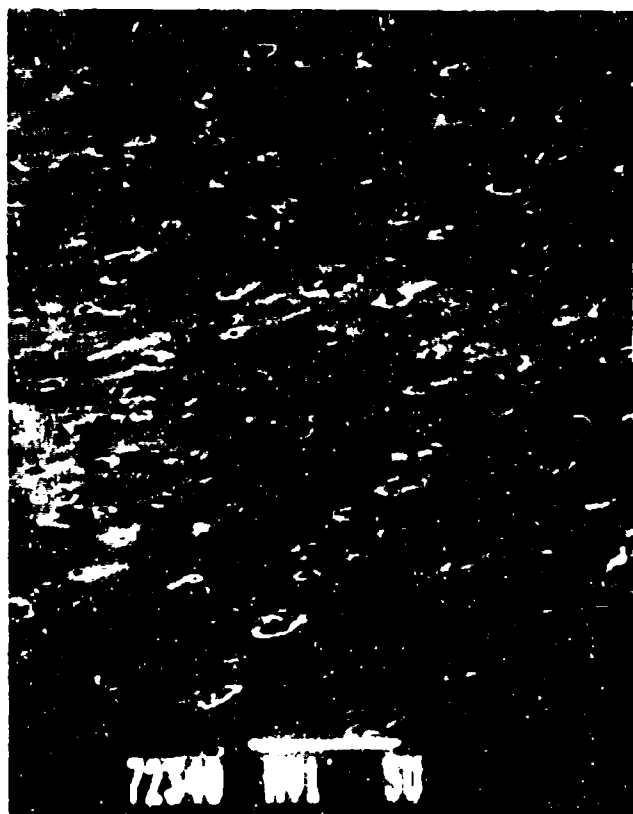


Figure 176 SEM Micrographs of Au/CaAs (a) and (b) annealed at 350 °C for 15 Minutes; (c) and (d) annealed at 425 °C for 0.5 Minutes.



Figure 177 SEM Micrographs of Au/GaAs After Annealing at 450°C for 15 Minutes (a) Mag. X2k; (b) Mag. X5k.

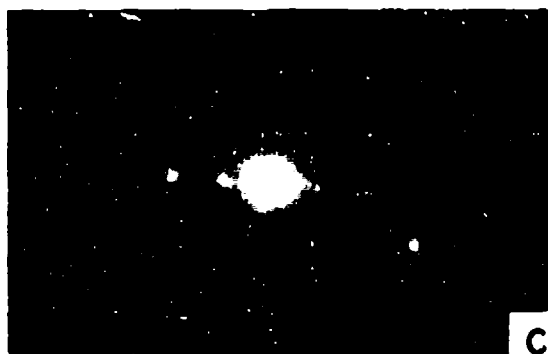


Figure 178 TED Pattern of Au/GaAs (a) Annealed at 350°C for 15 Minutes; (b) Annealed at 425°C for 0.5 Minutes; (c) Annealed at 450°C for 15 Minutes; (d) Bright-Field Micrograph After Annealing at 450°C for 15 Minutes.

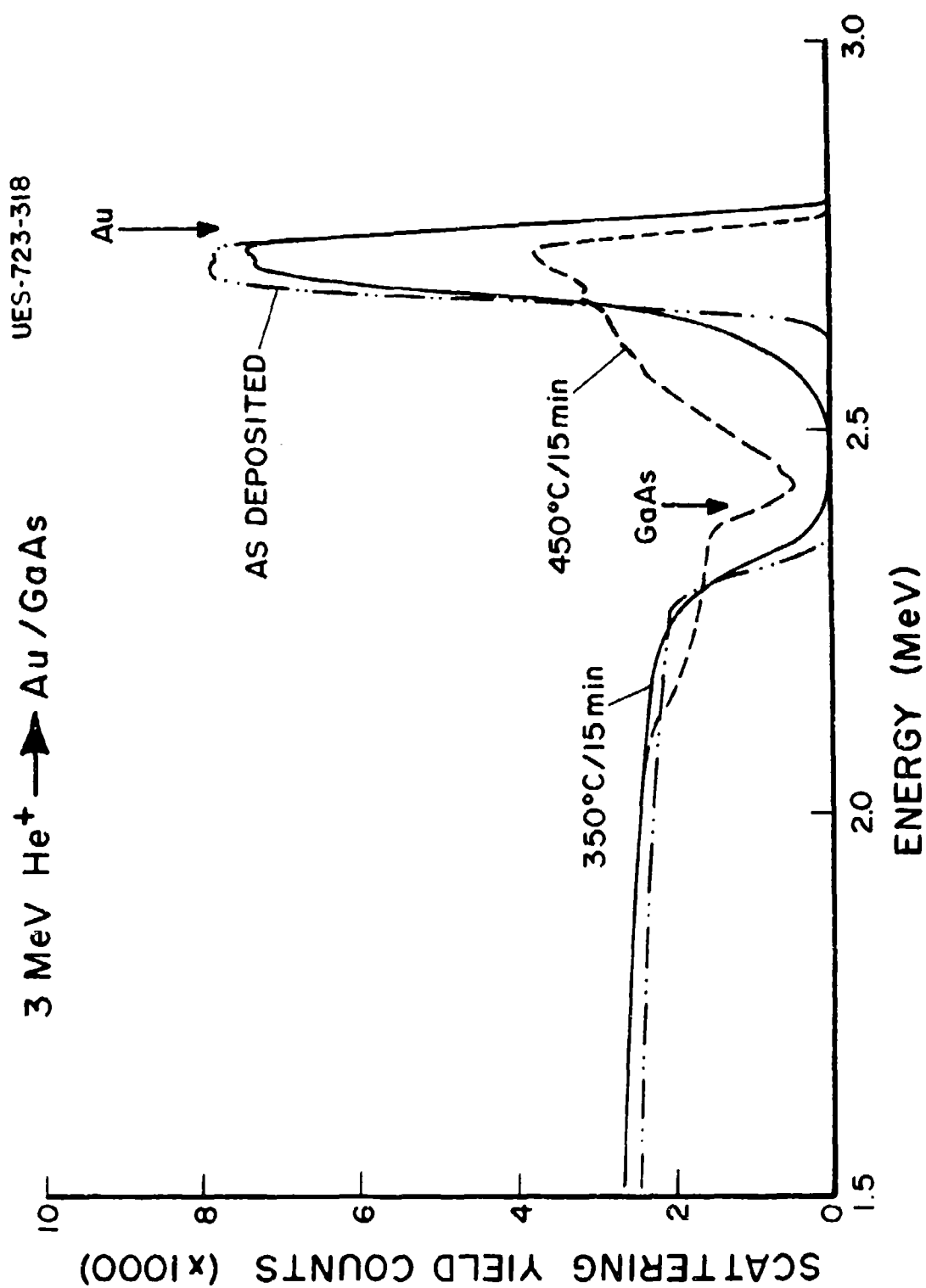


Figure 179 Rutherford Backscattering Spectra of He ions from Au-Ge-Ni/GaAs system before and after annealing at 350°C for 15 minutes at 450°C for 15 minutes.

depth $\sim 1400 \text{ \AA}$. It should be noted that this depth scale is determined by assuming that very little Au is present in GaAs after 350°C anneal and therefore the stopping power of GaAs can be used. The GaAs edge has moved only very slightly indicating that some outward diffusion of GaAs has taken place. After 450°C , 15 minute anneal, Au has diffused completely into the GaAs as can be seen from the presence of GaAs at the surface and the shift of Au edge inward. It shows that about $200\text{--}300 \text{ \AA}$ of GaAs is on the surface and then a mixed layer of Au and GaAs at thickness $\sim 2800 \text{ \AA}$ is present. This thickness is obtained by assuming an average stopping power of Au and GaAs and therefore can be off by about 20-30%. After annealing at 425°C for 30 seconds, RBS spectra (Figure 180) shows that Au has diffused only slightly into the GaAs. The surface has remained unaltered.

6.2 Au-Ge/GaAs

Figure 181 (a,b) shows the SEM picture of Au-Ge/GaAs surface annealed at 350°C for 15 minutes and 425°C for 0.5 minutes respectively. Presence of rectangular dark regions within the white region can be easily seen. These rectangular dark regions are found to contain Au-Ge; however, the white regions are found to be an Au rich region from EDAX analysis. Figure 181 (c) represents the SEM picture of Au-Ge/GaAs surface after annealing at 450°C for 15 minutes. The rectangular dark regions are still present at the edges of the white regions. Again the rectangular regions are found to contain Au-Ge and the white regions are rich in Au-Ga.

Figure 182 (a,b,c,d) represents the TED patterns of as deposited 350°C for 15 minutes, 425°C for 0.5 minutes and 450°C for 15 minutes annealed samples respectively. In the as deposited case, the diffraction rings of both Au and Ge are found to be present. The diffraction analysis of 350°C annealed

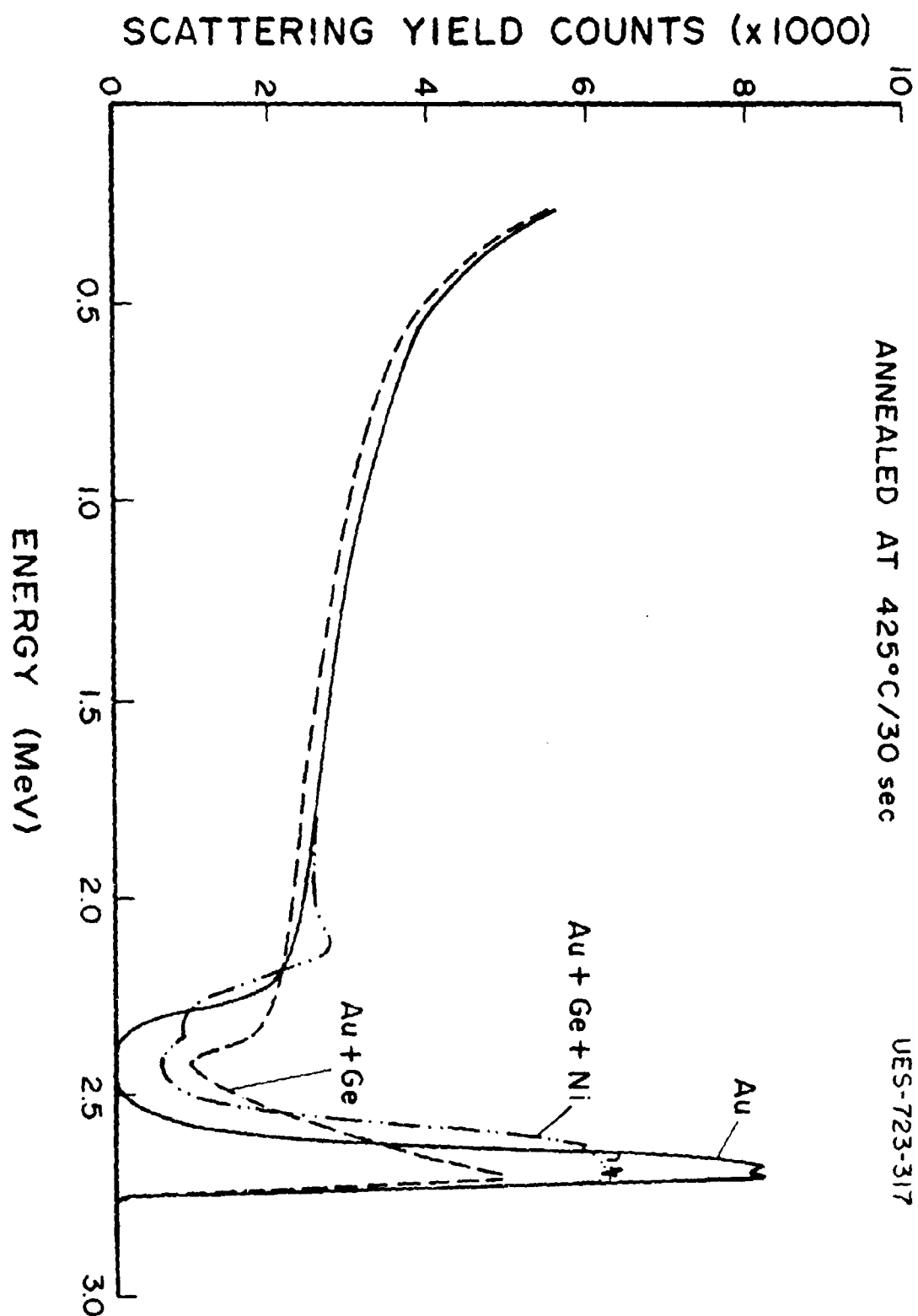


Figure 180 Rutherford Backscattering Spectra of He ions from Au/GaAs, Au-Ge/CaAs and Au-Ge-Ni/GaAs systems after annealing at 425°C for 15 minutes.

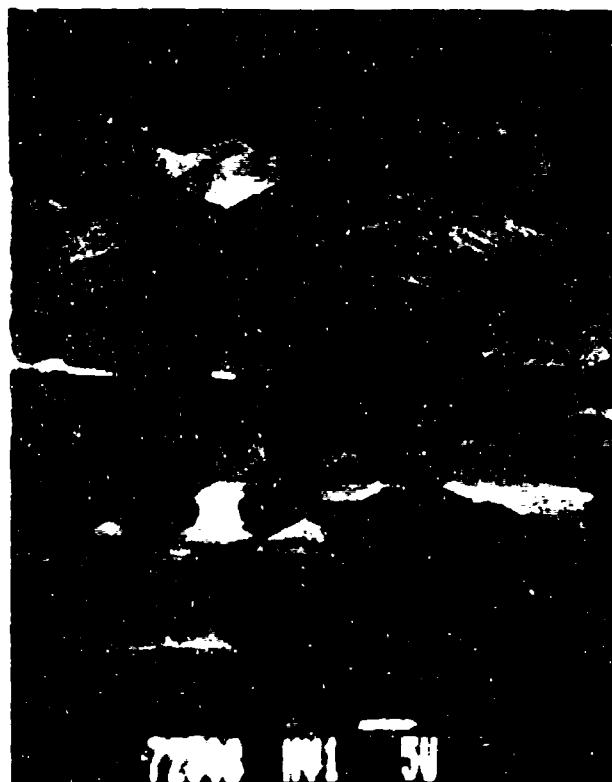


Figure 181 SEM Micrographs of Au-Ge/GaAs System (a) Annealed at 350°C for 15 Minutes; (b) Annealed at 425°C for 0.5 Minutes; (c) Annealed at 450°C for 15 Minutes.

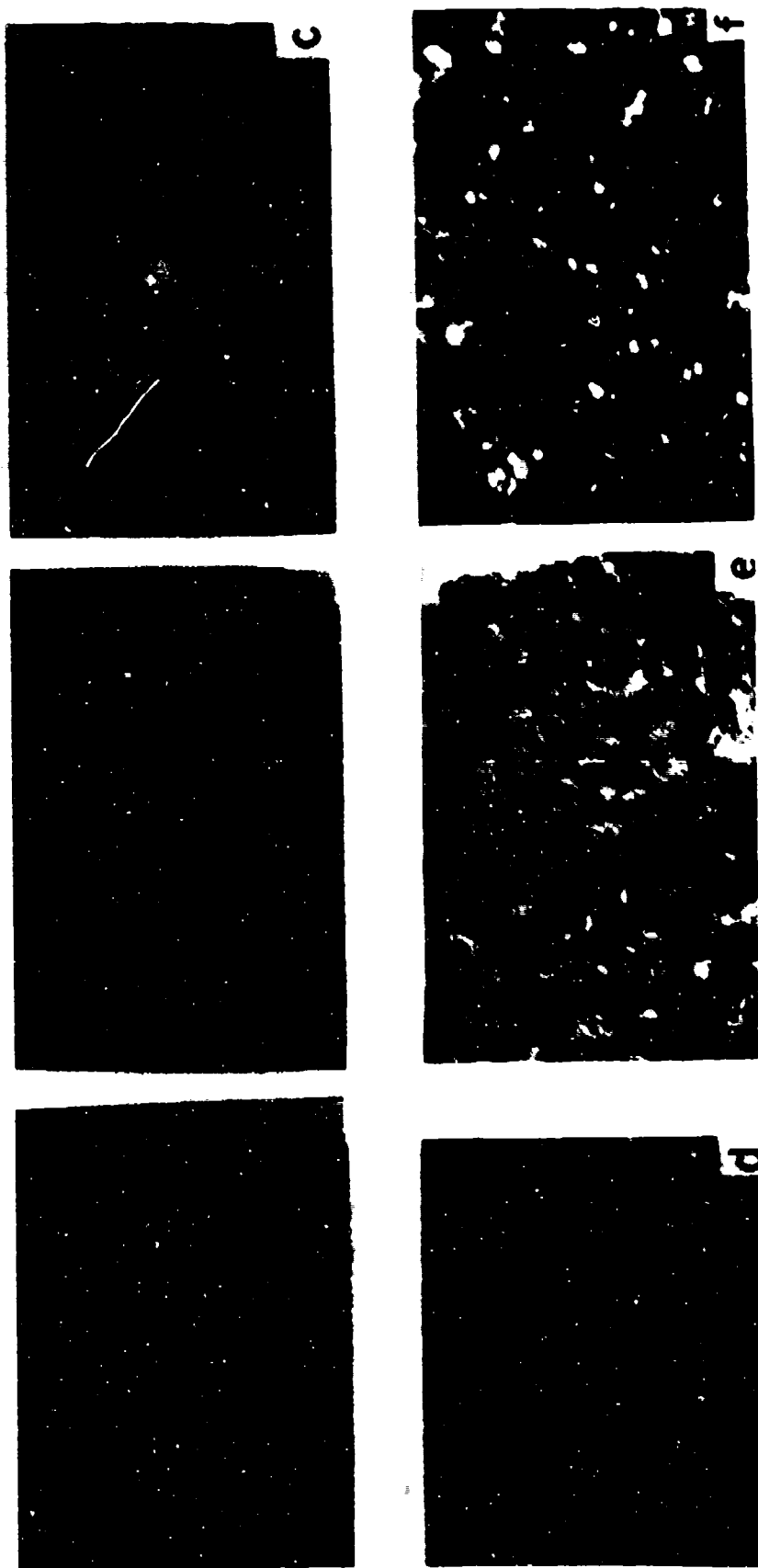


Figure 182 TEM Pattern of the Au-Ge/GaAs System (a) As Deposited; (b) Annealed at 350°C for 15 Minutes; (c) Annealed at 425°C for 0.5 Minutes; (d) Annealed at 450°C for 15 Minutes; (e) Bright and (f) Dark-Field Micrographs After Annealing at 450°C for 15 Minutes.

specimen reveals the presence of some diffraction rings of metastable γ -(Au-Ge) compound. Figure 182 (c) shows the TED pattern after annealing at 425°C for 0.5 minutes. Analysis of this diffraction pattern shows the presence of hexagonal Au_7Ga_2 compound. The analysis of the TED pattern after annealing at 450°C for 15 minutes, Figure 182d shows the formation of Ga_2O_3 compound. Figure 182 (e,f) shows the bright-field and dark-field micrographs of Au-Ge/GaAs system after annealing at 450°C.

Figure 183 shows the random spectra of backscattered He ions from Au-Ge film on GaAs before and after annealing at 350°C/15 minutes and 450°C/15 minutes. The thickness of the layer is found to be $\sim 1150 \text{ \AA}$ by assuming a weighted stopping power of Au (88%) and Ge (12%). Annealing at 350°C/15 minutes has caused a complete consumption of Au in GaAs, although some Au is still present at the surface in addition to GaAs. Because of the small mass difference between Ge, Ga and As atoms, signals could not be separated. Compared to Figure 179, it can be seen that the presence of 12% of Ge has made a significant difference in the diffusion rate of Au in GaAs. Annealing at 450°C/15 minutes has caused further diffusion of Au in to the GaAs. An edge has shifted inward indicating that only GaAs is present at the surface. However, nothing can be said about Ge from this spectra except its presence in the as deposited layer. Annealing at 425°C for 30 seconds resulted in the complete diffusion of Au-Ge in to GaAs, as indicated by the presence of GaAs and the reduction of Au yield at the surface (Figure 180).

6.3 Au-Ge-Ni/GaAs

Figure 184 (a,b,c,d) shows the SEM micrographs of Au-Ge-Ni/GaAs system after annealing at 350°C for 15 minutes, 425°C for 30 seconds. Figure 185 (a,b) shows the SEM micrographs of Au-Ge-Ni/GaAs system after annealing at

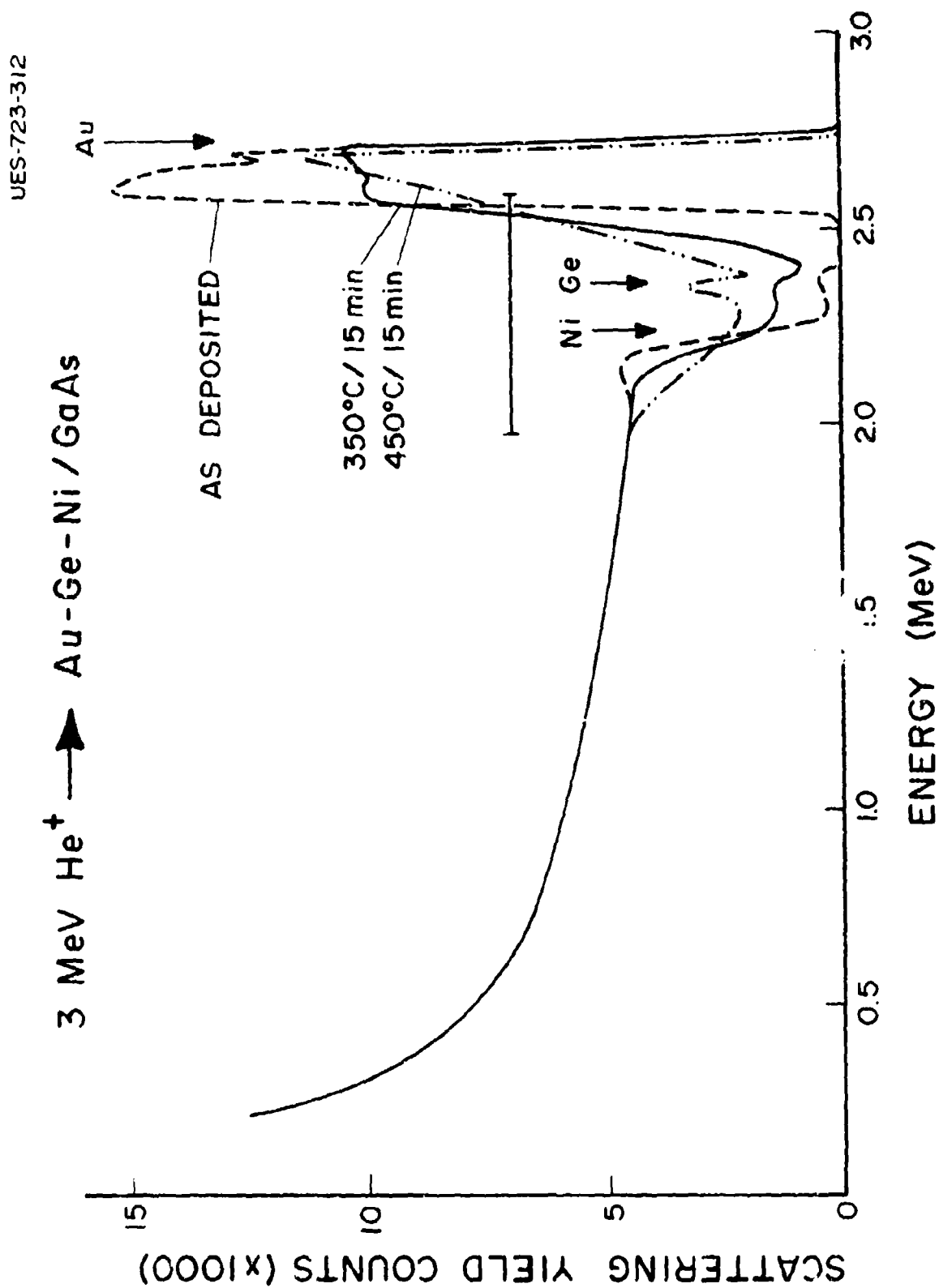


Figure 183 Rutherford Backscattering Spectra of He ions from Au-Ge/GaAs system before and after annealing at 350°C for 15 minutes and 450° for 15 minutes.

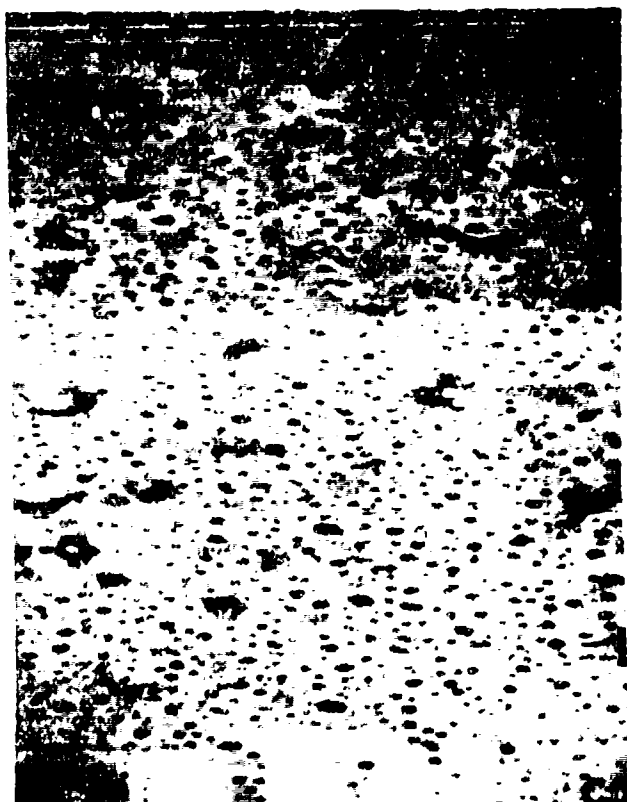


Figure 1-1. JPL Micrograph of the high-temperature system (a) and (b) showing the surface of the 15 Wm/m² (c) and (d) after 1000 hr of 15 Wm/m² (e) and (f) after 1000 hr of 15 Wm/m².



Figure 1a5 SEM Micrographs of Au-Ge-Ni/GaAs System After Annealing at 450 °C for 15 Minutes (a) Mag. X1k (b) Mag. X2k.

450°C for 15 minutes. The dark circular patches are clearly visible at all anneal temperatures. These patches are distributed very uniformly throughout the surface. The sizes of these dark patches are found to be larger at 450°C as compared to low temperature anneals.

Figure 186 (a) are the bright-field micrograph after annealing at 350°C for 15 minutes. As in the case of SEM micrograph (Figure 184), circular patches are clearly visible. Evidence of Au_7Ga_2 and isolated Au particle has also been found. Similar results have been found for 425°C anneal. Figure 186 (c) represents the TED pattern of the Au-Ge, Ni/GaAs system after annealing at 450°C for 15 minutes. The analysis of the TED pattern shows the presence of Ga_2O_3 compound.

The RBS spectra from Au-Ge-Ni/GaAs are shown in Figure 187 (a,b). The thickness of the layer is about 1400 Å. The small bump near the GaAs is due to the backscattering signal from Ni. After annealing at 350°C/15 minutes, Au has diffused in to GaAs up to a depth ~ 1200 Å. It appears from the spectrum after 350°C anneal that the Ge remained unchanged. However, after 450°C/15 minutes anneal, a narrower peak appears, the energy of which corresponds to Ga at the surface. It could be mixed up with both Ge and As signals. Au has diffused further into the GaAs as compared to the 350°C anneal (~ 2400 Å) and GaAs has covered the surface completely as indicated by the slight shift of the Au edge inward.

The spectrum after annealing at 425°C/30 seconds is comparable to that after annealing at 350°C/15 minutes. Au has diffused into GaAs to a thickness 1000 Å. Also Ge and Ni appear to have diffused into the GaAs to a depth ~ 400 Å (see Figure 188 a,b).

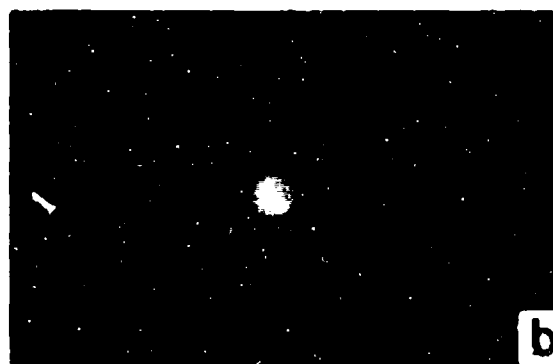


Figure 186 (a) Bright-Field Micrograph and (b) TED Pattern of the Au-Ge-Ni/GaAs System After Annealing at 350°C for 15 Minutes; (c) TED Pattern of Au-Ge-Ni/GaAs System After Annealing at 450°C for 15 Minutes.

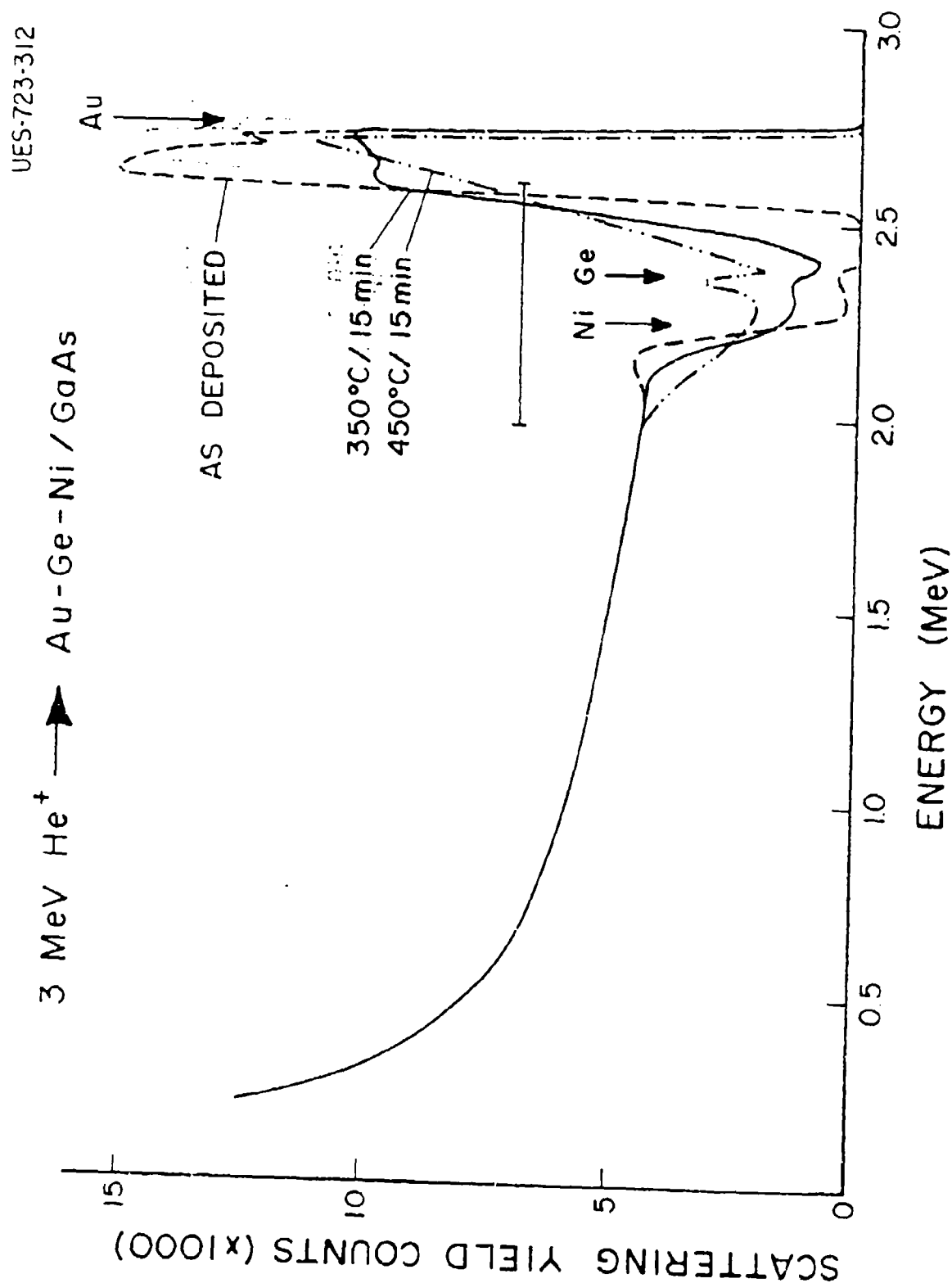


Figure 187 (a) Rutherford Backscattering Spectra of He Ions From Au-Ge-Ni/GaAs System After Annealing at 350°C for 15 Minutes and 450°C for 15 Minutes.

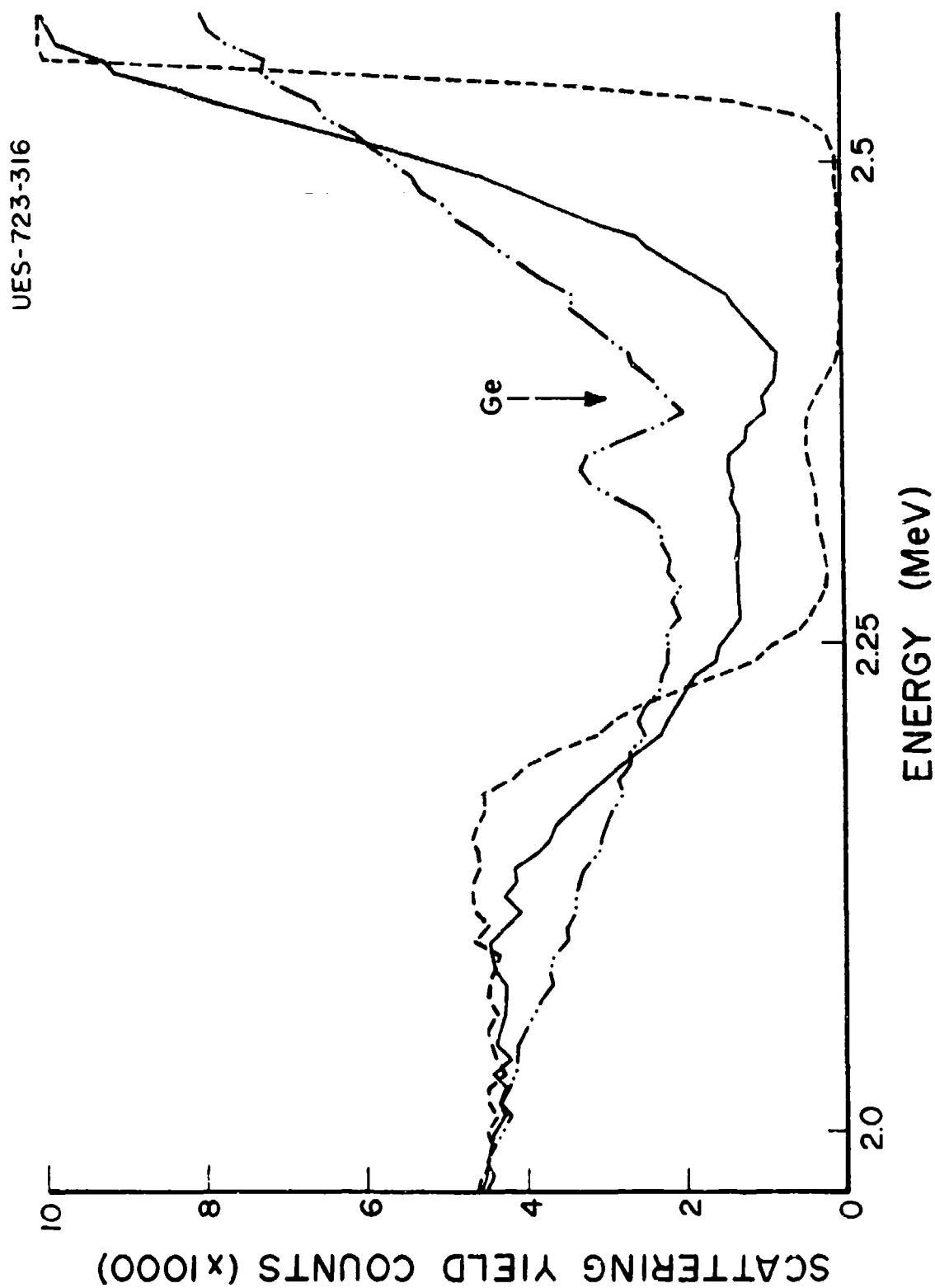


Figure 188 (a) Rutherford Backscattering Spectra of He ions from Au-Ge-Ni/GaAs system before and after annealing at 425°C for 0.5 minutes.

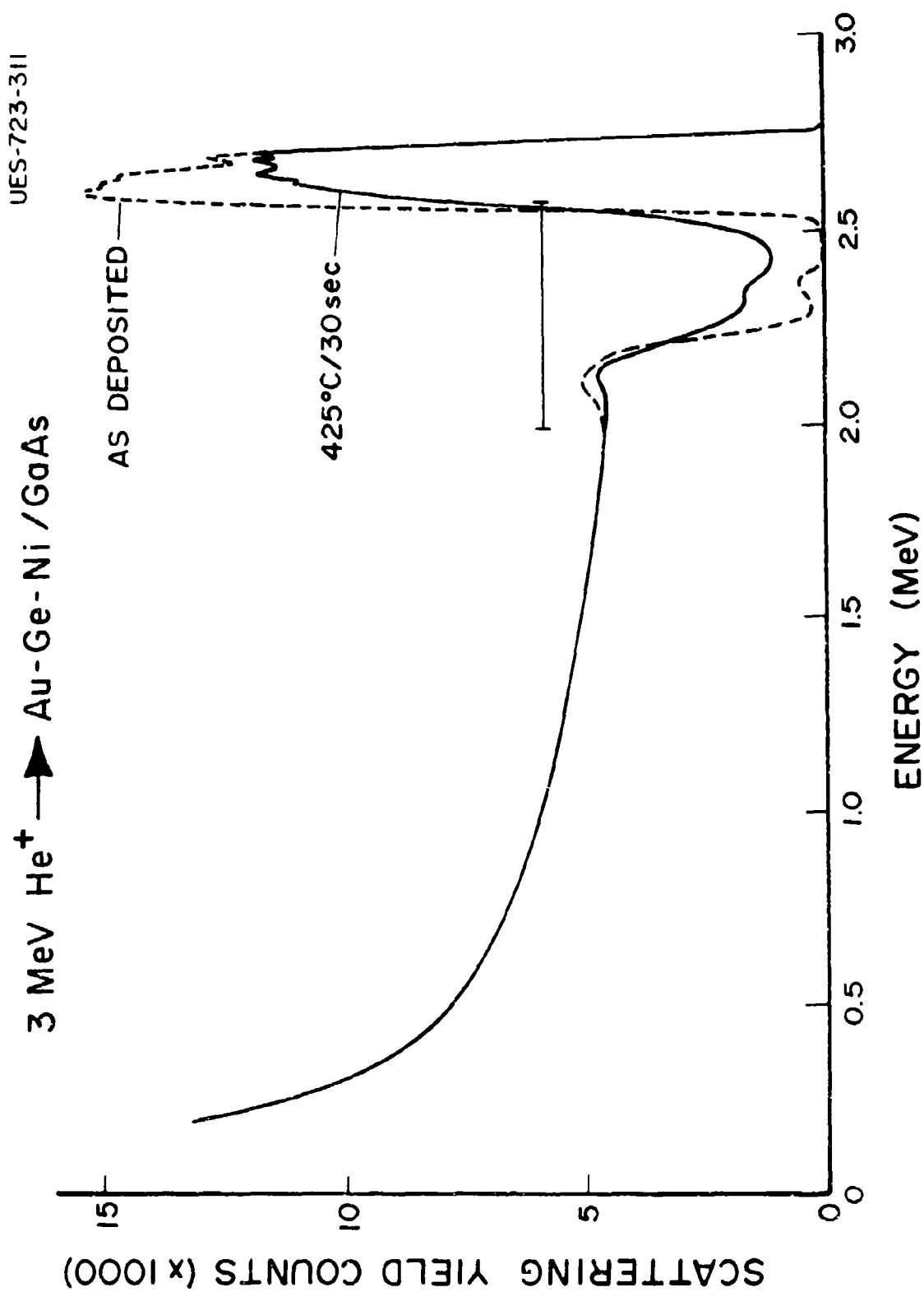


Figure 188

(b) Rutherford backscattering spectra of He ions from Au-Ge-Ni/GaAs system before and after annealing at 425°C for 0.5 minutes

Presenting data indicate that a good Ohmic contact is obtained with Au-Ge-Ni/GaAs after annealing at 425°C/30 seconds. Comparing to 450°C/15 minutes anneal, the surface morphology is uniform consisting of dark clusters which have been identified as Ge and Ni rich areas. The low density of these particles after 450°C/15 minute anneal indicate that the contact resistivity would be higher than the 425°C/30 second anneal. The 350°C/15 minute anneal may result in a lower contact resistivity than 450°C/15 minute anneal. However, this may still be higher than the 425°C/30 second anneal because of the presence of less dense dark clusters.

REFERENCES

1. P. M. Hemenger, Rev. Sci. Instrum. 44, 698(1973).
2. L. J. van der Pauw, Philips Res. Repts. 13, 1(1958).
3. J. W. Mayer, O. J. Marsh, G. A. Shifrin, and R. Baron, Can. J. Phys. 45, 4073(1967).
4. N. G. E. Johansson, J. W. Mayer, and O. J. Marsh, Solid State Electron. 13, 317(1970).
5. See, for example, W. V. McLevige, M. J. Helix, K. V. Vaidyanathan, and B. G. Streetman, J. Appl. Phys. 48, 3342(1977); Y. Yuba, K. Gamo, K. Masuda, and S. Namba, Jpn. J. Appl. Phys. 13, 641(1974); B. K. Shin, D. C. Look, Y. S. Park, and J. E. Ehret, J. Appl. Phys., 47, 1574(1976).
6. R. G. Hunsperger, R. G. Wilson, and D. M. Jamba, J. Appl. Phys. 43, 1318(1972).
7. R. Zölch, H. Ryssel, H. Kranz, H. Reichl, and I. Ruge, Ion Implantation in Semiconductors, ed. by F. Chernow, J. A. Borders, and D. K. Brice (Plenum, New York, 1977), p. 593.
8. Y. K. Yeo, Y. S. Park, and Phil Won Yu, J. Appl. Phys. 50, 3274(1979).
9. Byung Doo Choe, Y. K. Yeo, and Y. S. Park, J. Appl. Phys. 51, 4742(1980).
10. Y. K. Yeo, Y. S. Park, and Byung Doo Choe, Nucl. Instrum. Methods 182/183, 609(1981).
11. J. Lindhard, M. Scharff, and H. Schiott, Mat. Fys. Medd. Dan. Vid. Selsk. 33, 1(1963).
12. Y. K. Yeo, Y. S. Park, T. L. Pedrotti, and B. D. Choe, J. Appl. Phys. 53, 6148(1982).
13. W. K. Hofker, Philips Res. Rep. Suppl No. 8 (1975).
14. P. K. Vasudev, R. G. Wilson, and C. A. Evans, Jr., Appl. Phys. Lett. 36, 837(1980).
15. R. Heckingbottom and T. Ambridge, Rad. Eff. 17, 31(1973).
16. J. M. Woodcock, Appl. Phys. Lett. 28, 226(1976).
17. T. Ambridge, R. Heckingbottom, E. C. Bell, B. J. Sealy, K. G. Stephens, and R. K. Surridge, Electron. Lett. 11, 314(1975).

REFERENCES (con't)

18. C. A. Stolte, Ion Implantation in Semiconductors, edited by F. Chernow, J. A. Borders, and D. K. Brice (Plenum, New York, 1977), p. 149.
19. B. K. Shin, J. E. Ehret, Y. S. Park, and M. Stefaniw, J. Appl. Phys. 49, 2988(1978).
20. A. A. Gavrilou, G. A. Kachurin, N. B. Pridachin, and G. S. Snirov, Sov. Phys. Semicond. 8, 1455(1975).
21. K. Aoki, K. Gamo, K. Masuda, and S. Namba, Ion Implantation in Semiconductors, edited by F. Chernow, J. A. Borders, and D. K. Brice (Plenum, New York, 1977), p. 123.
22. Y. S. Park, Y. K. Yeo, and F. L. Pedrotti, Nucl. Instr. and Meth. 182/183, 617(1981).
23. M. N. Yoder, Solid St. Electron. 23, 117(1980).
24. K. Ploog, A. Fischer, and H. Kunzel, Appl. Phys. 18, 353(1979).
25. Y. K. Yeo, J. E. Ehret, F. L. Pedrotti, Y. S. Park, and W. M. Theis, Appl. Phys. Lett. 35, 197(1979).
26. F. L. Pedrotti, Y. K. Yeo, J. E. Ehret, and Y. S. Park, J. Appl. Phys. 51, 5781(1980).
27. Y. K. Yeo, F. L. Pedrotti, and Y. S. Park, J. Appl. Phys. 51, 5785(1980).
28. R. K. Surridge, and B. J. Sealey, J. Phys. D 10, 911(1977).
29. J. L. Tandon, M-A. Nicolet, and F. H. Eisen, Appl. Phys. Lett. 34, 165(1979).
30. J. P. Donnelly, Gallium Arsenide and Related Compounds, St. Louis, 1976, Inst. Phys. Conf. Ser. No. 33b (Institute of Physics and Physical Society, London, 1977), p. 166.
31. F. H. Eisen. Ion Implantation in Semiconductors, edited by S. Namba, (Plenum, New York, 1975), p. 3.
32. R. G. Hunsperger, and O. J. Marsh. Radiat. Eff. 6, 263(1970).
33. D. E. Davies, S. Roosild, and L. Lowe, Solid-State Electron. 18, 733(1975).
34. F. H. Eisen and M. B. Welch, Ion Implantation in Semiconductors, edited by F. Chernow, J. A. Borders, and D. K. Brice (Plenum, New York, 1977), p. 97.

REFERENCES (con't)

35. M. Fujimoto, H. Yamazaki, and T. Honda, Ion Implantation in Semiconductors, edited by F. Chernow, J. A. Borders, and D. K. Brice (Plenum, New York, 1977), p. 89.
36. J. M. Woodcock, J. M. Shannon, and D. J. Clark, Solid-State Electron. 18, 267(1975).
37. J. D. Sansbury and J. F. Gibbons, Radiat. Eff., 6, 269(1970).
38. H. Mueller, J. Gyulai, J. W. Mayer, F. H. Eisen, and B. M. Welch, Ion Implantation in Semiconductors, edited by S. Namba (Plenum, New York, 1975), p. 19.
39. F. H. Eisen, B. M. Welch, K. Gamo, T. Inada, H. Mueller, M-A. Nicolet, and J. W. Mayer, Application of Ion Beams to Materials 1975, edited by G. Carter, J. S. Colligon, and W. A. Grant (The Institute of Physics, London, 1976), p. 64.
40. J. Kasahara, M. Arai, and N. Watanabe, J. Appl. Phys. 50, 541(1979).
41. Y. K. Yeo, R. Kwor, and Y. S. Park, J. Appl. Phys. 53, 1812(1982).
42. Y. K. Yeo, Y. S. Park, and R. Kwor, J. Appl. Phys. 53, 1815(1982).
43. R. Kwor, Y. K. Yeo, and Y. S. Park, J. Appl. Phys. 53, 4786(1982).
44. R. G. Wilson and D. M. Jamba, Appl. Phys. Lett. 39, 715(1981).
45. C. A. Evans, Jr., C. G. Hopkins, J. C. Norberg, V. R. Deline, R. J. Blattner, R. G. Wilson, D. M. Jamba, and Y. S. Park, Semi-Insulating III-V Materials, edited by G. J. Rees (Shiva, Kent, England, 1980), p. 138.
46. A. Lidow, J. F. Gibbons, V. R. Deline, and C. A. Evans, Jr., Appl. Phys. Lett. 32, 149(1978).
47. A. Lidow, J. F. Gibbons, V. R. Deline, and C. A. Evans, Jr., Appl. Phys. Lett. 51, 4130(1978).
48. A. Lidow, J. F. Gibbons, V. R. Deline, and C. A. Evans, Jr., Appl. Phys. Lett. 32, 572(1978).
49. J. P. Donnelly, W. T. Lindley, and C. E. Hurwitz, Appl. Phys. Lett. 27, 41(1975).
50. R. M. Malbon, D. H. Lee, and J. M. Whelan, J. Electrochem. Soc. 123, 1413(1976).

REFERENCES (con't)

51. A. Masuyama, M-A. Nicolet, I. Golecki, J. L. Tandon, D. K. Sadana, and J. Washburn, App. Phys. Lett. 36, 749(1980).
52. S. G. Liu, E. C. Douglas, C. P. Wu, C. W. Magee, S. Y. Narayan, S. T. Jolly, F. Kolondra, and S. Jain. RCA Rev. 41, 227(1980).
53. W. K. Chu, J. W. Mayer and E. Rimini, Backscattering Spectrometry, (Academic Press, 1978).
54. J. W. Mayer and E. Rimini. Ion Beam Handbook For Material Analysis, ().
55. K. Gamo, T. Inada, J. W. Mayer, F. H. Eisen, and G. G. Rhodes, Radiation Effects 33, 85(1977).
56. J. S. Williams and M. W. Austin, Applied Physics Letter 36, 994(1980).
57. S. S. Kular, B. J. Sealy, K. G. Stephens, D. K. Sadana, and G. R. Booker, Solid State Electron. 23, 831(1980).
58. M. G. Grimaldi, B. M. Paine, M. Maenpaa, M. A. Nicolet, and D. K. Sadana, "Applied Physics Letter," 39, 70, (1981); "J. Applied Physics," 52, 4038, (1981).
59. R. S. Bhattacharya, P. P. Pronko, and S. C. Ling, "J. Applied Physics," 53, 1803, (1982).
60. G. Foti, L. Scepregi, E. F. Kennedy, J. W. Mayer, P. P. Pronko, and M. D. Rehtin, Phil. Mag A37, 591(1978).
61. D. V. Morgan, F. M. Eisen, and A. Ezis, IEEE Proc. 128, 109(1981).
62. V. S. Speriousu, B. M. Paine, M. A. Nicolet, and H. L. Glass, Applied Physics Letters.
63. R. S. Bhattacharya, P. P. Pronko, S. C. Ling, and S. R. Wilson, Applied Physics Letters 40, 502(1982).
64. I. L. Singer, J. S. Murday, and R. L. Cooper, Surface Science 7, 108(1982).
65. L. A. Christel and J. F. Gibbon, J. Applied Physics 52, 5050(1981).
66. R. Z. Bauerlein, Physik 176, 498, (1963).
67. T. J. Magee, H. Kawayoshi, R.D. Ormond, L. A. Christel, J. F. Gibbons, C. G. Hopkins, C. A. Evans, Jr., and D. S. Day, Applied Physics Letter 39, 906(1981).

REFERENCES (con't)

68. R. Drosd and J. Washburn, J. Applied Physics 53, 397(1982).
69. M. W. Thompson, Defects and Radiation Damage in Metals, (Cambridge University, New York, 1969).
70. S. T. Picraux, W. H. Weisenberger, and F. L. Vook, Radiation Effect 7, 101(1971).
71. L. C. Feldman and J. W. Rodgers, J. Applied Physics 41, 3776(1970).
72. R. R. Hart, Radiation Effect 6, 51(1970).
73. H. E. Rossendall, thesis, University of Amsterdam, 1974.
74. J. P. Biersack and L. G. Hagmark, Nuclear Instrum. Methods 174, 257(1980).
75. K. Gamo, T. Inada, S. Krekeler, J. W. Mayer, F. H. Eisen, and B. M. Welch, Solid-State Electron. 29, 213(1977).
76. D. W. Pashley and M. J. Stowell, Phil. Magazine 8, 1605(1963).
77. R. S. Bhattacharya, A. K. Rai, P. P. Pronko, J. Narayan, S. C. Ling, and S. R. Wilson, J. Phys. Chem. Solids 44, 61(1983).
78. L. Scepregi, J. W. Mayer, and T. W. Sigmon, Applied Phys. Letter 29, 92(1976).
79. P. Revesz, M. Wittmer, J. Roth, and J. W. Mayer, J. Appl. Phys. 49, 5199(1978).
80. S. T. Picraux, In Defects in Semiconductors, edited by J. Narayan and T. Y. Tan, (North Holland Publ. Co., 1981), p. 135.
81. A. K. Rai, R. S. Bhattacharya, and P. P. Pronko, Appl. Phys. Lett. 41, 1086(1982).
82. S. T. Picraux, D. M. Follstaedt, P. Baeri, S. V. Campisano, G. Foti, and E. Rinini, Radiation Effect 49, 75(1980).
83. A. Bontemps, J. Fontenille, and A. Guivarc'h, Phys. Lett. A. 55, 373(1976).
84. J. U. Andersen, N. G. Chechenin, and Z. Z. Hua, Appl. Phys. Lett. 39, 758(1981).
85. L. H. Skolnik, W. G. Spitzer, A. Kahan, F. Euler, and R. G. Hunsperger, J. Applied Phys. 43, 2146(1972).

REFERENCES (con't)

86. J. F. Chemir, I. V. Mitchell, and F. W. Saris, J. Appl. Phys. **45**, 537(1974).
87. R. S. Bhattacharya, unpublished.
88. J. A. Davies, in: Channeling-Theory, Observations and Application, ed. D. V. Morgan, (Wiley, New York, 1973), p. 391.
89. P. P. Pronko and R. S. Bhattacharya, IEEE Trans. Nucl. Sci., (to be published).
90. M. Wilkins, in: Diffraction and Imaging Techniques in Material Science, eds., S. Amelinckz, R. Geuens, J. Van Landuyt, (North-Holland, Amsterdam, 1978), p. 185.
91. Semi-Insulating III-V Materials, edited by G. J. Rees, (Shiva, Nottingham, 1980).
92. H. Kanber, M. Feng, V.K. Eu, and J. M. Whelan, Electrochemical Society meeting, Denver, October, 1981.
93. R. G. Wilson, P. K. Vasudev, and D. M. Jamba, Appl. Phys. Lett. **36**, 215(1980).
94. R. G. Wilson, J. Appl. Phys. **52**, 3954(1981).
95. P. P. Pronko and W. Christie, Oak Ridge National Laboratory, (unpublished).
96. R. W. Haisty and G. R. Cronin in: Proceedings of the 7th International Conference on the Physics of Semiconductors, (Dunod, Paris, 1964), p. 1161.
97. S. C. Liu, S. Y. Narayan, C. W. Magee, and C. P. Wu, Appl. Phys. Lett. **41**, 72(1982).
98. A. G. Cullis, T. E. Seider, and R. L. Meek, J Appl. Phys. **49**, 5199(1978).
99. P. Revesz, M. Wittmer, J. Roth, and J. W. Mayer, J. Appl. Phys. **49**, 5199(1978).
100. M. Wittmer, J. Roth, P. Revesz, and J. W. Mayer, J. Appl. Phys. **49**, 5207(1978).
101. W. B. Beéré, Philos. Magazine **25**, 189(1972).
102. M. J. Norgett and A. B. Lidiard, Philos. Magazine **18**, 1193(1968).

REFERENCES (con't)

103. A. G. Foyt, W. T. Lindley, C. M. Wolfe and J. P. Donnelly, Solid-State Electron. 12, 209(1969).
104. B. R. Pruniaux, J. C. North and A. V. Payer, IEEE TRANS. ELECTRON DEVICES ED-19 672, (1972).
105. J. D. Speight, P. Leight, N. McIntyre, J. G. Groves and S. O'Hara, Electron Lett 10, 88(1974).
106. P. N. Favennec, G. P. Pelons, M. Binet, and P. Bandet, Ion Implantation in Semiconductors and Other Materials, ed. B. L. Crowder, (Plenum, New York, 1973).
107. P. N. Favennec, J. Appl. Phys. 47, 2532(1976).
108. B. Deveaud and P. N. Favennec, Inst. Phys. Conf. Ser. No. 45, 1979, p. 492.
109. S. Gecim, B. J. Sealy, and K. G. Stephens, Electron Lett. 14, 306(1978).
110. P. N. Favennec, B. Deveaud, M. Salvi, A. Martinez, and C. Armand, Electron. Lett. 18, 202(1982).
111. J. F. Gibbons, W. S. Johnson, and S. W. Mylorie, Projected Range Statistics - Semiconductors and Related Materials, (2nd ed.), (Halsted Press, 1975).
112. J. W. Corbett, J. C. Bourgoin, Chapter 1 in Point Defects in Solids, ed., J. H. Crawford, L. M. Slifkin, (Plenum Press, 1975), Page 118.
113. D. Pons and J. Bourgoin, Phys. Rev. Letters 47, 1293(1981).
114. G. H. Kinchin and R. H. Pease, Rep. Progr. Phys. 18, 1(1955).
115. M. Ogawa. J. Applied Phys., 51, 406, (1980)
116. O. Aina, W. Katz, B. J. Baliga, and K. rose. J. Applied Phys., 53, 777, (1982)
117. M. Heiblum, M. I. Nathan, and C. A. Chang. Solid State Electronics, 25, 185, (1982)
118. G. S. Marlow, M. B. Das, and Uis Tongson. Solid State Electronics, 26, 259, (1983)
119. T. J. Mayce and J. Peng. Phys. Stat. Soli.(a), 32, 695, (1975)